Data-Driven and HVDC Control Methods to Enhance Power System Security

Thams, Florian

Publication date:
2018

Document Version
Publisher's PDF, also known as Version of record

Technical University of Denmark

Florian Thams

Data-Driven and HVDC Control Methods to Enhance Power System Security

Dissertation, September 2018

Kgs. Lyngby, Denmark

Center for Electric Power and Energy
Department of Electrical Engineering

DANMARKS TEKNISKE UNIVERSITET
Center for Electric Power and Energy (CEE)
DTU Electrical Engineering

Data-Driven and HVDC Control Methods to Enhance Power System Security

Data-drevne og HVDC-kontrolmetoder til forbedring af strømsystemets sikkerhed

Dissertation, by Florian Thams

Supervisors:
Associate Professor Spyros Chatzivasileiadis, Technical University of Denmark
Robert Eriksson, Swedish National Grid
Associate Professor Arne Hejde Nielsen, Technical University of Denmark

DTU - Technical University of Denmark, Kgs. Lyngby - September 2018

Data-Driven and HVDC Control Methods to Enhance Power System Security

This thesis was prepared by:
Florian Thams

Supervisors:
Associate Professor Spyros Chatzivasileiadis, Technical University of Denmark
Robert Eriksson, Swedish National Grid
Associate Professor Arne Hejde Nielsen, Technical University of Denmark

Dissertation Examination Committee:
Senior Researcher Nicolaos Cutululis (Chairman)
Department of Wind Energy, Technical University of Denmark, Denmark

Professor Oriol Gomis-Bellmunt
Centre of Technological Innovation in Static Converters and Drives, Universitat Politècnica de Catalunya, Spain

Professor Louis Wehenkel
Department of Electrical Engineering and Computer Science, University of Liège, Belgium

Center for Electric Power and Energy (CEE)
DTU Electrical Engineering
Elektrovej, Building 325
DK-2800 Kgs. Lyngby
Denmark

Tel: (+45) 4525 3500
Fax: (+45) 4588 6111
E-mail: cee@elektro.dtu.dk

Release date: 30. September 2018

Edition: 1.0

Class: Internal

Field: Electrical Engineering

Remarks: The dissertation is presented to the Department of Electrical Engineering of the Technical University of Denmark in partial fulfillment of the requirements for the degree of Doctor of Philosophy.

ISBN: 000-00-00000-00-0

To my family

Preface

This thesis is prepared at the Department of Electrical Engineering of the Technical University of Denmark in partial fulfillment of the requirements for acquiring the degree of Doctor of Philosophy in Engineering. The Ph.D. project was co-funded by the European Unions Seventh Framework Programme for Research, Technological Development and Demonstration under the grant agreement no. 612748 and by the ForskEL-projekt 12264 Best Paths for DK.

This dissertation summarizes the work carried out by the author during his Ph.D. project. It started on 1st June 2015, and it was completed on 30th September 2018. During this period, he was hired by the Technical University of Denmark as a Ph.D. student at the Center for Electric Power and Energy (CEE).

The thesis is composed of 8 chapters and 6 attached scientific papers, 5 of which have been peer-reviewed and published, whereas the remaining one is currently under review.

Florian Thams
30. September 2018

Acknowledgements

I like to take this opportunity to thank Robert Eriksson for having accepted me as a PhD Student at DTU and, for his support and feedback. I appreciate that even after leaving DTU, he took the time and continued to supervise me and was available for discussions whenever needed. I would also like to thank Spyros Chatzivasileiadis for 'taking me over' when he joined DTU and, for his support and feedback. I appreciate that both, Spyros and Robert, gave me the freedom to explore different research topics, encouraged me to try new things and gave their advice whenever needed. I would also like to thank Arne Hejde Nielsen for his support.

During my PhD studies I spent 5 months at ETH Zurich working with Gabriela Hug. I would like to thank Gabriela for accepting me as guest researcher and, for her support and feedback during that time. Special thanks goes also to all PSL members, for the great time I had in Zurich.

I would also like to thank Lejla Halilbašić for the proof reading of parts of my thesis, the numerous discussions, and the great collaboration within the BestPaths project and beyond. I would also like to thank Andreas Venzke for our discussions and good collaboration. Special thanks goes to Theis Bo Rasmussen for helping me with the Danish abstract. Further, I would like to thank all my colleagues for the entertaining discussions during lunch and coffee breaks.

Special thanks also goes to Nicolaos Cutululis, Oriol Gomis-Bellmunt and Louis Wehenkel for accepting to be the examiners of this thesis. I highly appreciate the time they devoted in reading the manuscript.

Finally, I'd like to thank my family and friends for their constant support.

Florian Thams

Kgs. Lyngby, Denmark, 30.09.2018

Table of Contents

Abstract

The development of High-Voltage Direct Current (HVDC) transmission based on Voltage Source Converters (VSCs) and its advantages compared to HVDC based on Line Commutated Converter (LCC), such as black-start capability and the capability to supply weak grids, has increased the interest in HVDC technology in Europe. Moreover, it is seen as enabling technology for Multi-Terminal High-Voltage Direct Current (MT-HVDC) grids. As such a MT-HVDC grid would most likely not be built at once in Europe but be developed by a step-wise integration of already existing on- and offshore inter-connectors, this raises potential multi-vendor interoperability issues. Furthermore, new methods are needed which take advantage of (i) the flexibility such a grid can offer and (ii) the high-resolution, real-time data available through the increasing deployment of Phasor Measurement Units (PMUs) in order to enhance the system stability of the interconnected AC-HVDC system.

This thesis covers five aspects of these developments: we investigate the potential of HVDC transmission lines in Europe; we found that several new HVDC lines are indispensable in the future European transmission network to meet the renewable energy source (RES) integration targets of the European Union. Ideally, these lines must become parts of a MT-HVDC grid to minimize costs and increase reliability.

In order to enable an MT-HVDC network consisting of installations from multiple suppliers, we investigate potential multi-vendor interoperability issues and the impact of different control structures on the power system stability.

Further, with the ability to control active and reactive power independently within milliseconds, VSC-HVDC systems do not only introduce new challenges but also new opportunities, such as controllable power flows and corrective control. Considering the increasing availability of measurement data, and the recent advances in data-driven approaches, we develop methods allowing us to enrich and use the available measurement data to increase power system security. As historical data often contain limited number of abnormal situations, simulation data are necessary to accurately determine the security boundary. Therefore, we developed a modular and highly scalable efficient database generation method for data-driven security assessment of power systems.

Moreover, using these databases, we take a more holistic view, and we combine the data-driven security assessment with optimization for operations and markets. Thereby, we leverage the advantages of the controlability of VSC-HVDC, the efficient data generation and data-driven methods to minimize power system operation costs.

Finally, inspired by the development of the data-driven security assessment, we developed a first proof-of-concept of how such methods can not only assess security, but also predict the criticality of faults based on local measurements only without requiring communication. Ideally, such a method could be developed into a local control support method for HVDC terminals enabling the

HVDC terminal potentially not only to react to measurements but act on stability predictions and thereby potentially prevent fast evolving short-term voltage stability problems.

Resumé

Udviklingen af Voltage Source Converter (VSC) teknologi inden for jævnstrømsforbindelser (HVDC) og dets fordele sammenlignet med Line Commutated Converter (LCC) teknologi har øget den Europæiske interessen i HVDC teknologi, bl.a. gennem mulighed for start fra dødt net og forsyning af svage net. Derudover anses VSC teknologien som en muliggørelse af Multi-Terminal jævnstrømsforbindelser (MT-HVDC). Et MT-HVDC netværk vil højst sandsynligt ikke blive bygget som en ny installation men snarere som en løbende sammensætning af eksisterende land- og havbasered HVDC forbindelser. Dette medfører en potentiel udfordring i sammenspillet mellem installationer fra forskellige leverandører. Yderligere er det nødvendigt at udvikle nye metoder der udnytter, (i) den fleksibilitet et MT-HVDC netværk kan tilbyde og (ii) den tilgængelige mængde af realtids data fra et stigende antal af Phasor Measurement Units (PMUs). Disse metoder skal have som mål at forbedre netværks stabiliteten i et sammenkoblet AC-HVDC net.

Denne afhandling dækker over fem dele af denne udvikling: Vi undersøger potentialet for HVDC forbindelser i Europa og identificerer adskillige forbindelser der i fremtiden er uundværlige for det Europæiske transmissionsnet, hvis målene fra den Europæiske Union (EU) omkring omstillingen til vedvarende energi (VE) skal nås. Ideelt set skal de identificerede forbindelser blive del af et MT-HVDC netværk.

For at muliggøre et MT-HVDC netværk bestående af installationer fra flere leverandører, har vi undersøgt kompatibilitets vanskeligheder samt samspillet af forskellige kontrolstrukturers betydning for stabiliteten af elnettet.

Med evnen til, indenfor millisekunder, at bestemme aktiv og reaktiv effekt uafhængigt, vil VSC-HVDC forbindelser ikke blot skabe nye problemer men også nye muligheder. Disse inkluderer påvirkning af effektstrømninger og udførelse fejlrettende styring. Som en reaktion på den øgede datamængde og udviklingen i den datadrevne tilgang til problemer, har vi udviklet metoder der kan udnytte den tilgængelige data og tilføre den værdi, som samlet kan forøge forsyningssikkerheden. På grund af den begrænsede repræsentation af unormale situation i historiske data, er brugen af simulerings data nødvendig for at klarlægge de tilstedeværende sikkerhedsgrænser. Derfor har vi udviklet en effektiv metode til skabelse af databaser til datadreven sikkerhedsvurdering af elnet, som både er modulær og skalerbar.

Ved brug af de skabte databaser opnås et helhedsbillede, som vi bruger til at kombinere den datadrevne sikkerhedsvurdering med optimeringsstrategier inden for elnet drift og markeder. Derved udnyttes fordelene i VSC-HVDC forbindelsers regulerbarhed, den effektive skabelse af databaser samt datadrevne metoder til at minimere elnettets driftsomkostninger.

Endelig har vi, inspireret af udviklingen af den datadrevne sikkerhedsvurdering, udviklet en indledende proof-of-concept af hvordan denne slags metoder ydermere kan forudse kritiske fejl udelukkende baseret på lokale målinger. Ideelt set kan sådan en metode blive videreudviklet til en lokal reguleringsmetode til understøttelse af HVDC terminaler. Derved kan HVDC terminalen

potentielt set både reagere på målinger og samtidig på stabilitetsforudsigelser. Dette giver mulighed for at forhindre en hurtig udbredelse af korttids spændings ustabilitet.

Acronyms

AC Alternating Current

ANN Artificial Neuro Network

APTC Active Power Transfer Capability

ATC Available Transfer Capacity

BaU Business-as-Usual

BF Brute Force

CS Control Structure

ENTSO-E European Network of Transmission System Operators for Electricity

DW Directed Walk

DFIG Doubly-Fed Induction Generator

DLR Dynamic Line Rating

DSA Dynamic Security Assessment

DT Decision Tree

ELM Extreme Learning Machine

FACTS Flexible Alternating Current Transmission System

FBMC Flow-Based Market Coupling

FIDVR Fault Induced Delayed Voltage Recovery

GSC Grid Side Voltage Source Converter

HIC High Information Content

HTLS High Temperature Low Sag

HVDC High-Voltage Direct Current

ICT Information and Communication Technology

IPM Interior Point Method

IS Importance Sampling

ISO Independent System Operator

LCC Line Commutated Converter

LS Load Shedding

LSTM Long Short-Term Memory

MILP Mixed-Integer Linear Programming

MIMO Multiple Input Multiple Output

MINLP Mixed-Integer Non-Linear Programming

MIP Mixed-Integer Programming

MISO Multiple Input Single Output

MISOCP Mixed-Integer Second Order Cone Program

MMC Modular Multilevel Converter

MT-HVDC Multi-Terminal High-Voltage Direct Current

NERC North American Electric Reliability Corporation

NLSDP Nonlinear Semi-Definite Programming

NSCOGI North Seas Countries Offshore Grid Initiative

NSWPH North Sea Wind Power Hub

NTC Net Transfer Capacity

NTF Notified Transmission Flow

OPF Optimal Power Flow

PLL Phase Locked Loop

PMU Phasor Measurement Unit

PSS Power System Stabilizer

PTDF Power Transfer Distribution Factor

PTP Point-To-Point

RAM Remaining Available Margin

RES Renewable Energy Sources

SCADA Supervisory Control and Data Acquisition

SC-OPF Security-Constrained Optimal Power Flow

SISO Single Input Single Output

SOC Second Order Cone

SQP Sequential Quadratic Programming

SRF Synchronous Reference Frame

SSSSC-OPF Small-Signal Stability Security Constrained Optimal Power Flow

SV Singular Value

SVM Support Vector Machine

SRF Synchronous Reference Frame

TEP Transmission Expansion Planning

TRM Transmission Reliability Margin

TSO Transmission System Operator

TTC Total Transfer Capacity

TYNDP Ten Year Network Development Plan

VSC Voltage Source Converter

WAMC Wide-Area Monitoring and Control

WFC Wind Farm Side Voltage Source Converter

List of Figures

List of Tables

List of Symbols

Variables used in the multi machine model (chapter 2)

α_{ik}	Angle of the ik-th entry of the network bus admittance matrix
δ_i	Rotor angle of generator i
$\mathbf{A}_{sys}$	System matrix
$\mathbf{e}'_{g_i}$	Transient voltage of generator i
$\mathbf{i}_{g_i}$	Current of generator i
$\mathbf{J}_{AE}$	Network algebraic Jacobian
ω_i	Rotor speed of generator i
ω_s	Synchronous rotor speed
ψ_{d,q_i}	Magnetic flux of generator i
d_i	Additional damping Torque of generator i
e_{fd_i}	Field voltage of generator i
h_i	Inertia constant of generator i
k_{A_i}	Amplifier gain of generator i
k_{E_i}	Self-excited constant used for of generator i
k_{F_i}	Stabilizer gain used for of generator i
N_g	Number of generators in the grid
N_{Bus}	Number of buses in the grid
r_{a_i}	Armature resistance of generator i
r_{F_i}	Output of the stabilizer of generator i
S_b^{ac}	Three-phase power base value
$S_{E_i}(e_{fd_i})$	Saturation function of generator i
$t''_{d0,q0_i}$	Sub-transient time const. of d-/q-axis of gen. i
$t'_{d0,q0_i}$	Transient time const. of d-/q-axis of generator i
t_{A_i}	Time constant of the voltage regulator of gen. i

t_{E_i} Exciter time constant of generator i

t_{F_i} Time constant of the stabilizer of generator i

t_{M_i} Mechanical torque of generator i

V_b^{ac} Phase-to-phase voltage base value

v_i Bus Voltage of Bus i

$v_{R,max}$ Limit of the voltage regulator of generator i

v_{R_i} Output of the voltage regulator of generator i

v_{ref_i} Reference voltage of generator i

$v_{s,i}$ Signal of Power System Stabilizer (PSS) at gen i

x''_{d,q_i} Sub-transient reactance of gen. i in d-/q-axis

x'_{d,q_i} Transient reactance of generator i in d-/q-axis

x_{d,q_i} Synchronous reactance of gen. i in d-/q-axis

x_{l_i} Leakage reactance of generator i in d-/q-axis

Y_{ik} Magnitude of the ik-th entry of the network bus admittance

Variables used in the MT-HVDC model and control structure analysis (chapter 2 & 4)

$\Delta\omega_{PLL}$ AC grid frequency deviation

$\Delta\Theta_{PLL}$ Phase angle deviation between the grid voltage and the orientation of the phase locked loop

ϵ_{PLL} Integrator state of the PLL

$\eta_{\alpha,i}$ Overall participation of each subsystem α in mode i

Γ Participation matrix

κ Selectable threshold in percent

λ Eigenvalue

$\mathbb{S}^{\alpha}$ Set of interaction modes $\mathbb{S}^{\alpha}$

χ Integrator states of the outer controller of a VSC

γ Integrator states of the current controller of a VSC

$\mathbf{\Gamma}_{ki}^{n}$ Normalized participation factors

ϕ Integrator states of damping controller of a VSC

$\mathbf{E}_w(s)$ System transfer function matrix - uncontrolled disturbances to outputs

$\mathbf{i}_{dc,meas}$ DC current considering measurement delay

$\mathbf{i}_g$ AC grid current

$\mathbf{i}_{l,meas}$ Converter AC current considering measurement delay

$\mathbf{i}_l$ Converter AC current

$\mathbf{k}_{i,PLL}$ Integrator Gain of the PLL controller

$\mathbf{k}_{p,PLL}$ Proportional Gain of the PLL controller

$\mathbf{p}_{ac,meas}$ Active power measured on the AC side considering measurement delay

$\mathbf{p}_{dc,meas}$ Active power measured on the DC side considering measurement delay

$\mathbf{r}$ Vector of reference values

$\mathbf{U}_w^{uiq}(s)$ System transfer function matrix - uncontrolled disturbances to active current loop references

$\mathbf{u}_{iq}$ Active current loop references of the current loops of the different GSCs

$\mathbf{v}_g$ AC grid voltage

$\mathbf{v}_{AD}^*$ Output signal of Active Damping Controller

$\mathbf{v}_{cv}$ Converter AC voltage

$\mathbf{v}_{cv}^*$ Converter Output Voltage reference of a VSC

$\mathbf{v}_{dc,meas}$ DC voltage considering measurement delay

$\mathbf{v}_{o,meas}$ AC voltage at the filter considering measurement delay

$\mathbf{v}_o$ AC voltage at the filter

$\mathbf{v}_{PLL,d/q}$ Low-Pass Filter States of the PLL

$\mathbf{w}_i$ Uncontrolled disturbances

$\mathbf{y}$ Vector of measurements values

$\mathbf{z}_i$ Output measurements

ω_b Base angular frequency

ω_d Damped circular frequency

ω_g Per unit grid frequency

ω_{AD} Cut-off frequency of low-pass filter of a VSC

$\overline{\sigma}$ Maximum singular value

$\overline{\sigma}(G(j\omega))$ Maximum singular value of the transfer function $G(j\omega)$

Σ_i Current error

Σ_v Voltage error

Θ_{PLL} Actual voltage vector phase angle

ζ Damping ratio

$c_{dc,line}$ Capacitances of DC lines

c_{dc} DC capacitance of voltage source converter

c_f Filter capacitance of VSC

$d_{x,y}$ Length of cable between VSC x and VSC y

$E_w(j\omega)$ System transfer function matrix

i_{ac} AC current

$i_{dc,cv}$ DC current at the voltage source converter

i_{dc} DC current

k_{AD} Proportional gain of damping controller of a VSC

k_{droop} Droop parameter

$k_{icd/q}$ Integrator gain of the outer controller of a VSC

k_{ic} Integrator gain of the current controller of a VSC

$k_{pcd/q}$ Proportional gain of the outer controller of a VSC

k_{pc} Proportional gain of the current controller of a VSC

l_{dc} DC line inductance

l_{dc} Inductance of DC lines in per unit

l_f Filter inductance of VSC

l_g Grid inductance of a Thévenin equivalent

p^*_{wf} Active power reference value of the wind farm converter

p_{ac} Active power measured on the AC side of the converter

p_{dc} Active power measured on the DC side of the converter

r_{dc} DC line resistance

r_f Filter resistance of VSC

r_g Grid resistance of a Thévenin equivalent

v_{dc} DC voltage

v^*_{dc} DC voltage set point

Variables used in the double-fed induction machine model (chapter 2)

$\mathbf{i}_s$ Stator current

$\mathbf{v}_r$	Rotor voltage
ω_s	Synchronous angle speed
$e_d^{'}$	Voltage behind transient reactance (d-axis)
$e_q^{'}$	Voltage behind transient reactance (q-axis)
h_{tot}	Inertia constant of turbine and generator
k_0	Coefficient for maximum power production operation
k_{i1}	Integrator gain (power regulator)
k_{i2}	Integrator gain (rotor-side current regulator)
k_{i3}	Integrator gain (grid voltage regulator)
k_{p1}	Proportional gain (power regulator)
k_{p2}	Proportional gain (rotor-side current regulator)
k_{p3}	Proportional gain (grid voltage regulator)
l_m	Mutual inductance
l_{rr}	Rotor self-inductance
N_{WT}	Number of wind turbines
p_{ref}	Active power control reference
p_s	Active power output
q_{ref}	Specified reactive power reference
q_s	Reactive power at stator terminal
r_r	Rotor resistance
s_r	Rotor slip
$t_0^{'}$	Rotor circuit time constant
t_e	Electromagnetic torque
t_m	Wind torque
x_s	Stator reactance
$x_s^{'}$	Transient stator reactance
Z_{awt}	Equivalent impedance for the common network of the aggregated wind turbines in the complete wind farm
Z_e	Impedance of the equivalent wind farm
Z_{wt}	Wind turbine impedance

Variables used in the gird expansion scenario development (chapter 3)

$\mathcal{G}^{(RES)}$ Set of (renewable) generators

$\mathcal{L}^{\mathcal{AC}}$ Set of AC lines

$\mathcal{N}$ Set of nodes

c^{shed} Cost of load shedding

c^{year} Installed generation capacities in a specific year

c_g Marginal cost of generator g

CL^{AC} Congestion level of the AC grid

E_x^{DL} Energy generated by the different RES types x on the distribution level

$E_{consumed,country}(h)$ Hourly electricity consumption profiles of the different countries

$E_{g_x,country}^{2016}(h)$ Hourly energy generation profile of the RES type x in a specific country

$E_{g_x,DL,country}^{2016,fitted}(h)$ Hourly energy generation profile of the RES type x at the distribution level in a specific country fitted to the data of 2016

$E_{g_x,DL,country}^{2016}(h)$ Hourly energy generation profile of the RES type x at the distribution level in a specific country

$E_{g_{i,x},country}^{2016}(h)$ Hourly energy generation profile of the RES type x in country i

E_g Annual energy produced by generator g

E_g^{max} Annual available energy of generator g

$e_{high-cost,i}$ Indicator for the potential utilization of a HVDC line interconnecting the marginal generator i

$e_{low-cost,i}$ Indicator for the potential utilization of a HVDC line interconnecting the marginal generator i

$E_{netdemand,country}(h)$ Hourly net demand curves of the different countries

E_n^{shed} Annual energy demand not supplied at node n

$E_{x,country}^{DL}$ RES energy of type x generated at the distribution level in a specific country

$h_{marg,i}$ Number of hours generator i is a marginal generator

$N_{country}$ Number of nodes in the corresponding country

$P_{l,Node\ k,country}$ Load values of the different nodes given in ENTSO-E's grid model

$P_{min,i}$ Minimum generation capacity of generator i

$up_{x,country}^{2030}$ Upscaling factor per generation type x on a per country basis

Variables used in the efficient database generation method (chapter 5)

α Discretization interval

η	Set of initialization points
Γ	Set of contingencies
γ	Security boundary
κ_{max}	Maximum number of steps
Λ	Number of different load profiles
λ_i	Eigenvalue i
ϕ_i	Right eigenvector associated with eigenvalue λ_i
ψ_i^T	Left eigenvector associated with eigenvalue λ_i
$\mathbf{P}^{max}$	Vector of generator maximum capacities
$\mathcal{C}$	Set of line outages
$\mathcal{G}$	Set of generator buses
$\mathcal{N}$	Set of buses
$\nabla d(OP_k)$	Gradient of $d(OP_k)$
Ω	Set of operating points in the vicinity of the security boundary γ
ω_i	Imaginary part of eigenvalue i
$\overline{P}_{G_i}$	Maximum active power limits of generator i
$\overline{Q}_{G_i}$	Maximum reactive power limits of generator i
$\overline{V}_i$	Maximum bus voltage limits of bus i
Ψ	Set of all operating points
ρ_i	System parameter i
σ_i	Real part of eigenvalue i
$\underline{P}_{G_i}$	Minimum active power limits of generator i
$\underline{Q}_{G_i}$	Minimum reactive power limits of generator i
$\underline{V}_i$	Minimum bus voltage limits of bus i
ζ_i	Damping ratio of eigenvalue i
A	System matrix
d	Distance from current OP_k to security boundary γ
$f_{ij,actual}^{(k)}$	Active power flow of operating point OP_k
$f_{max}^{(k)}$	Maximum possible flow between global source and global sink node for OP_k
N_G	Number of generators

OP_k Operating point k

P^* Generation dispatch set-point

P_{D_i} Active power demand at bus i

Q_{D_i} Reactive power demand at bus i

R Radius around the operating point P^* that does not contain any points belonging to the non-convex feasible region

W^0 Matrix representing the intact system state

Y^c Bus admittance matrix for outage c

Variables used in the data-driven methods for market-clearing (chapter 6)

Γ Set of contingencies

$\mathbb{O}_{ac}$ Set of ac operating points

$\mathcal{N}$ Set of buses

$\mathcal{P}$ Set of full paths representing the decision tree

θ_i Voltage angle at bus i

B_{nm} Susceptance of the line between nodes n and m

$c_{G,i}$ Costs of generator i

c_{ij} Second Order Cone transformation variable

$F_{L,i}^{min}$ Minimum line transfer limit of line i

$F_{L,p}^{max}$ Maximum line transfer limit of line i

F_{nm} Active power flow between nodes n and m

G_{nm} Conductance of the line between nodes n and m

I_n Set of nodes connected to node n

N_B Number of buses

N_G Number of generators

P^i Active power generation of generator i

Q^i Reactive power generation of generator i

s_{ij} Second Order Cone transformation variable

u_i Second Order Cone transformation variable

V_i Voltage at bus i

y_i Binary variable associated with path i

y_p Binary variable corresponding to the decision tree path

Variables used in the data-driven security assessment (chapter 2 & 7)

α Cost factor

$c(T)$ Accuracy of tree T

$C_\alpha(T)$ Cost-complexity metric

$G(V, E)$ Graph G consisting of vertices V and edges E

$N_V^e(G)$ Set of extended neighbours of a vertex V in a graph G

$N_V(G)$ Set of neighbours of a vertex V in a graph G

P_{nm} Active power flow between node n and m

V_y Voltage magnitude of node i

x_{nm} Reactance of line between node n and m

CHAPTER 1

Introduction

1.1 Background and Motivation

Over the last decades, the operation of a power system faced new challenges following the liberalization of the energy market and the changes in the energy mix. The liberalization led to the involvement of more stakeholders and more competition [17]. The shift in generation towards Renewable Energy Sources (RES) led the power system to be operated under increasingly stressed conditions. There are several reasons for that: the variability of the generation and the difficulty of precise forecasts, a large number of newly developed generation sites leading to new load flow patterns as well as high RES penetration in distribution grids causing potentially reverse power flows and voltage violations. At the same time, Transmission System Operators (TSOs) installed Flexible Alternating Current Transmission System (FACTS) devices enhancing flexibility and power transfer capability of the system [18]. Many High-Voltage Direct Current (HVDC) transmission system projects are being developed and planned around the world enabling controllable bulk power transfer over long distances. Moreover, with the increasing deployment of Phasor Measurement Units (PMUs) TSOs obtain high-resolution, real-time dynamic state information of the power grid allowing the development of methods to monitor, predict and enhance the system stability in real-time.

As the system is operated under increasingly stressed conditions and closer to its security boundaries, the TSOs are more often required to interfere with the initial market outcome, i.e. the power plant dispatch, in order to ensure a secure operation of the network. The redispatching measures, as these adjustments are called, consists mostly of readjusting the generation of single power plants or RES plants resulting in changed power flows complying with the determined stability limits. Taking the example of Germany, the shift in generation in terms of type but also location, i.e. from nuclear power plants located close to the load centers in the south/south-west of Germany towards a high wind penetration in the north, far away from the load centers, combined with a delayed grid expansion to cope with the changed power flows, led to a more difficult grid operation scenario requiring significantly more costly redispatching measures by the TSOs (volume of redispatched energy increased between between 2010 ($306\,\mathrm{GWh}$) and 2017 ($18.455\,\mathrm{GWh}$) by factor 60; costs increased by factor 30 ($13\,\mathrm{M€}$ vs. $396.5\,\mathrm{M€}$) [19, 20]. However, it is important to emphasize here that simultaneously the cost of reimbursing down-regulated RES as well as the use of reserves increased significantly leading to overall costs of $1.4\,\mathrm{B€}$ in 2017 in Germany alone [19].

Looking in the future, following the Paris climate agreement [21] the trend of an increasing share of RES will continue and even more challenges will appear due to the electrification of other sectors as transport or heating [22]. This will confront the power system not only with a higher share of variable generation and a growing demand but will also provoke a higher variability of the load requiring a higher flexibility of the system. The limited acceptance of the European citizens for new transmission lines demands a better utilization of existing assets. Still, additional grid capacity will

be required even with an optimal use of the existing grid [17]. With vast potential of wind energy located offshore in the North Sea region, new transmission corridors between load and generation are required to harness this energy. While wind power plants are being built further from the shore, the use of Alternating Current (AC) technology to interconnect them with the continent becomes less feasible. On the other hand, the transmission lines onshore could be built with HVAC or HVDC technology. Recent project developments in Germany show, however, higher public acceptance to new transmission corridors with an as small footprint as possible resulting in more cost intensive underground solutions [23] which are more suitable for long distances using HVDC technology [17]. HVDC offers other benefits as well. Power flows on HVDC lines are controllable increasing the grid flexibility and causing lower losses over long distances compared to AC. This led to an increasing interest in HVDC technology over the last decades.

A significant driver of this interest, in particular in Europe, was the appearance and development of HVDC transmission based on Voltage Source Converter (VSC) and its advantages compared to HVDC based on Line Commutated Converter (LCC). The black-start capability, the capability to supply weak grids, the comparable small footprint and the ability to control active and reactive power independently made this technology also feasible for offshore applications. Furthermore, it is seen as an enabler for Multi-Terminal High-Voltage Direct Current (MT-HVDC) grids allowing to interconnect several HVDC converters. In Europe, ten countries of the North sea region formed the North Seas Countries Offshore Grid Initiative (NSCOGI) in order to explore the best way to establish an offshore HVDC grid [24]. More recently, the three TSOs TenneT TSO B.V., Energinet and TenneT TSO GmbH signed an agreement to investigate the development of an artificial island in the North sea, the so called North Sea Wind Power Hub (NSWPH) [25]. Such an island would allow to harness the large offshore wind potential far away from the coasts serving as an energy collection point and would potentially be interconnected with the continent via several HVDC lines. In China, two MT-HVDC grids have already been commissioned [17, 26].

Due to the little experience with MT-HVDC grids, the control, operation and potential interaction of such a MT-HVDC grid with the connected AC grids are open research questions. Moreover, new methods enhancing the grid stability by taking advantage of the flexibility such a grid can offer and the high-resolution, real-time data of the connected AC-grids are needed.

In light of these developments, this thesis develops methods to identify potential grid upgrade scenarios and HVDC transmission corridors using a highly detailed European system model of about 8000 nodes. Further, this work provides an in-depth analysis of different proposed control structures for a potential MT-HVDC. Given the growing importance of multi-vendor interoperability, our studies focused on different proposed DC voltage control structures and their impact on interactions between systems, stability and interoperability. Moreover, we propose a methodology enabling the assessment of the operation space of an arbitrary MT-HVDC considering small-signal stability and other freely selectable requirements. Furthermore, this work develops methods allowing us to enrich and use the increasing amount of available measurement data to increase power system security. To this extent, we propose a highly scalable efficient database generation method to enrich historical data, as these data often lack information of all credible abnormal situations. Through, simulation data we are able to accurately determine the security boundary. Additionally, using data-driven methods on these simulation and measurement data, we extract the security boundary and incorporate it as constraints into the market clearing aiming to minimize redispatching actions and costs by considering more detailed security considerations

and the true non-convex feasible space. Moreover, we take the potential of HVDC corridors and MT-HVDC grids into account considering corrective control actions offered by HVDC terminals within the market clearing enabling an even more cost-efficient market-clearing. Finally, we investigate data-driven local control support methods enabling fast instability predictions with high accuracy based on local post-disturbance measurements. This method could support and enhance local control and protection systems enabling potentially fast local corrective control actions.

1.2 Contributions

The main contributions of this thesis are:

- A classification and in-depth study of different DC voltage droop control structures proposed in literature. The disturbance rejection capability, the impact of the Control Structures (CSs) on interactions with connected AC grids and potential issues due to the interoperability of different CSs in a multi-vendor scenario have been analyzed.
- Development of a methodology for a stability analysis of different DC voltage droop control implementations. The methodology enables to determine the operation space of an arbitrary MT-HVDC grid.
- Development of a modular and highly scalable efficient database generation method for data-driven security assessment of power systems. As historical data often contain limited number of abnormal situations and therefore limited information on the actual security boundary, simulation data are necessary to accurately determine the security boundary. This method creates simulation data with high information content and outperforms existing approaches requiring less than 10% of the time other methods require.
- Development of market-clearing algorithms which incorporate preventive / preventive-corrective security considerations. Using data-driven techniques, both small signal stability and steady-state security have been addressed and tractable decision rules in the form of line flow limits have been derived from large databases obtained though an offline security assessment. The resulting constraints have been incorporated in the market clearing.
- Development of data-driven control support methods for HVDC terminals enabling fast instability predictions with high accuracy based on using local measurement data only. Such a control support method could support and enhance local control and protection systems by allowing the local controller not only to react to measurement but act in advance on accurate predictions enabling potentially faster local corrective control actions.
- Development of methods to identify potential grid upgrade scenarios and HVDC transmission corridors maximizing social welfare and RES penetration in Europe using a highly detailed European system model of about 8000 nodes.

1.3 Outline of the Thesis

This thesis is structured as follows:

Chapter 2: Background The motivation behind multi-terminal HVDC grids and the use of data to enhance system security is described. The basic power system modeling and stability concepts used throughout the thesis are introduced.

Chapter 3: Development of Grid Expansion Scenarios for the European Power System: Scalability Analysis of AC and HVDC Technologies As part of the scalability assessment of the AC and HVDC technologies developed within BEST PATHS, grid expansion scenarios for the European power system were investigated analyzing the RES integration potential of the different technologies developed within BEST PATHS.

Chapter 4: MT-HVDC Control Structures This chapter provides a classification of different DC voltage control structures proposed in literature. An in-depth comparison of the impact on small signal stability, disturbance rejection and the interaction level is performed. Furthermore, a methodology for a stability analysis of different DC voltage droop control implementations determining the operation space of an arbitrary MT-HVDC grid is presented.

Chapter 5: Efficient Database Generation for Data-driven Security Assessment of Power Systems A modular and highly scalable efficient database generation method for data-driven security assessment of power systems is presented. As historical data often contain limited number of abnormal situations, simulation data are necessary to accurately determine the security boundary.

Chapter 6: Data-driven Methods for Market-clearing and Power System Operation Data-driven small-signal stability and preventive / preventive-corrective security-constrained optimal power flow algorithms are presented. Using simulation data, we incorporate both small signal stability and steady-state security in form of line flow constraints into the market clearing algorithm aiming to maximize the feasible space and to minimize redispatching actions.

Chapter 7: Data-driven Control Support Methods A data-driven control support method enabling fast instability predictions with high accuracy based on local post-disturbance measurements is presented. This method could support and enhance local control and protection systems enabling potentially fast local corrective control actions.

Chapter 8: Conclusion and Outlook The key findings of this thesis are presented and an outlook to future research directions is given.

1.4 List of Publications

Over the course of the PhD project the following articles were published:

Journals

[**Pub. A**] F. Thams, R. Eriksson, and M. Molinas, "Interaction of Droop Control Structures and its Inherent Effect on the Power Transfer Limits in Multi- terminal VSC-HVDC," IEEE Transactions on Power Delivery, vol. 32, no. 1, pp. 182-192, 2017.

[**Pub. B**] F. Thams, A. Venzke, R. Eriksson, and S. Chatzivasileiadis, "Efficient Database Generation for Data-driven Security Analysis of Power Systems," IEEE Transactions of Power Systems, 2018, under review.

Conferences

[**Pub. C**] F. Thams, S. Chatzivasileiadis, E. Prieto-Araujo, and R. Eriksson, "Disturbance Attenuation of DC Voltage Droop Control Structures in a Multi-Terminal HVDC Grid," in Power Tech, Manchester, 2017.

[**Pub. D**] F. Thams, S. Chatzivasileiadis, and R. Eriksson, "DC Voltage Droop Control Structures and its Impact on the Interaction Modes in Interconnected AC-HVDC Systems," in International Conference on Innovative Smart Grid Technologies (ISGT) Asia, Auckland, 2017.

[**Pub. E**] F. Thams, L. Halilbašić, P. Pinson, S. Chatzivasileiadis, and R. Eriksson, "Data-Driven Security-Constrained OPF," in 10th Bulk Power Systems Dynamics and Control Symposium - IREP, Espinho, 2017.

[**Pub. F**] L. Halilbašić, F. Thams, A. Venzke, S. Chatzivasileiadis, and P. Pinson, "Data-Driven Security-Constrained AC-OPF for Operations and Markets," 20th Power Systems Computation Conference, Dublin, 2018.

Further Publications

[**Pub. G**] L. Halilbašić, F. Thams and S. Chatzivasileiadis, "BEST PATHS Deliverable 13.1: Technical and economical scaling rules for the implementation of demo results," Technical Report, Technical University of Denmark, 2018, under review.

1.5 Division of Work between the Authors

[Pub. A] F. Thams formulated the outline, and researched and wrote the paper under the supervision of R. Eriksson. M. Molinas contributed with discussion on the content.

[Pub. B] F. Thams formulated the outline, and researched and wrote the paper under the supervision of R. Eriksson and S. Chatzivasileiadis. A. Venzke contributed with the code and section of the convex relaxation as well as with discussion on the content.

[Pub. C] F. Thams formulated the outline, and researched and wrote the paper under the supervision of R. Eriksson and S. Chatzivasileiadis. E. Prieto-Araujo contributed with discussion on the content.

[Pub. D] F. Thams formulated the outline, and researched and wrote the paper under the supervision of R. Eriksson and S. Chatzivasileiadis. E. Prieto-Araujo contributed with discussion on the content.

[Pub. E] F. Thams and L. Halilbašić formulated the outline and jointly wrote the article under the supervision of R. Eriksson, S. Chatzivasileiadis and P. Pinson. F. Thams developed the model, created the database, and was responsible for the knowledge extraction while L. Halilbašić developed the OPF formulation.

[Pub. F] L. Halilbašić formulated the outline and wrote the article under the supervision of S. Chatzivasileiadis and P. Pinson. F. Thams developed the model, created the database, and was responsible for the knowledge extraction while L. Halilbašić developed the OPF formulation and A. Venzke contributed with the convex relaxation formulation.

[Pub. G] F. Thams and L. Halilbašić formulated the outline and jointly wrote the report under the supervision of S. Chatzivasileiadis and P. Pinson. The problem formulation and its solution were jointly and equally performed by L. Halilbašić and F. Thams.

CHAPTER 2

Background

This chapter provides background information on power system stability, power system security, security considerations in market clearing, supervised machine learning methods and power system modeling with focus on state-space modeling.

2.1 Introduction

With focus on HVDC control and data-driven methods, this thesis investigates potential benefits offered by these methods within different aspects of power systems. These topics range from an high-level grid expansion scenario development over optimal power system operation and market-clearing algorithms to detailed low-level analyses of how specific methods impact the interaction between and the stability of power systems. Moreover, by leveraging an efficient data generation method, we achieve to include detailed stability analyses and security considerations into high-level optimization problems used within power system operation and market-clearing. Therefore, this chapter provides the reader with an introduction to power system security, the different types of power system stability and how power system security is currently taken into account during market-clearing. Then, we introduce the different supervised learning methods used within this thesis and we motivate the focus on HVDC and data-driven methods. Finally, the power system models used in this thesis are introduced.

2.2 Definition of Important Concepts

Due to the tremendous importance of electricity in our society nowadays, the secure operation of the power system and, thus, the stability of the power system is crucial. It is, however, important to distinguish between power system security, power system stability, the stability margin and the stability of an operating (equilibrium) point in a power system [27]:

- A set of equilibria is defined as stable if as a response to inputs or disturbances the system motion converges to the equilibrium set while the operating constraints are satisfied for all relevant variables along the trajectory [1].
- The power system is considered as *stable* if the power system remains intact after being subject to a physical disturbance by regaining a state of operating equilibrium with most system variables being bounded [1].
- The margin between the stability limit and the actual operating point of the power system is then defined as the stability margin [27].

- Power system security "refers to the degree of risk in its ability to survive imminent disturbances (contingencies) without interruption of customer service. It relates to robustness of the system to imminent disturbances and, hence, depends on the system operating condition as well as the contingent probability of disturbances. [...] System security can be further distinguished from stability in terms of the resulting consequences. For example, two systems may both be stable with equal stability margins, but one may be relatively more secure because the consequences of instability are less severe" [1].

Furthermore, with more and more complex control devices (e.g. HVDC links and FACTS devices) being installed to counteract the more stressed and uncertain operating conditions [28], it is important to distinguish between preventive security and preventive-corrective security in power system operation:

- Preventive security takes only preventive (i.e. pre-contingency) actions into account to ensure that in the event of a contingency no limit will be violated and there exists a stable operating point [29].
- Preventive-corrective security on the other hand considers both preventive and fast corrective (post-contingency) actions to ensure that in the event of a contingency no limit will be violated and there exists a stable operating point [29].

Thus, the secure operation of a power system involves operating the power system in a stable operating region consisting of a stable set of equilibria. Further, it usually involves the estimation of stability margins for the different types of (in)stability phenomena and a security assessment.

2.3 Power System Security Assessment

The power system security assessment is an important part of power system operation which involves the evaluation of the security of the system as defined in the previous section. Thus, it determines the robustness of the power system to imminent disturbances and consists of two important parts [1]:

- Static security analysis which consists of a post-disturbance system conditions analysis verifying that no equipment ratings or voltage constraints are violated [1].
- Dynamic security analysis which consists of the analysis of all different types of system stability shown in Fig. 2.1 [1]. It involves the simulation of a number of contingencies to determine the secure operating region in terms of the system dynamics [27].

Thus, for a secure operation of the power system, a clear understanding of the different types of instability and how they are interrelated is essential [1]. Hence, they are briefly introduced in the following subsection.

Moreover, due to the importance of the power system and in order to guarantee the customers reliability although it is impossible to eliminate all potential faults, power systems are usually operated according to various security criteria ensuring a sufficient security margin of the system [27]. One of these criteria is the N-1 criterion which is described after the introduction of the different types of power system stability.

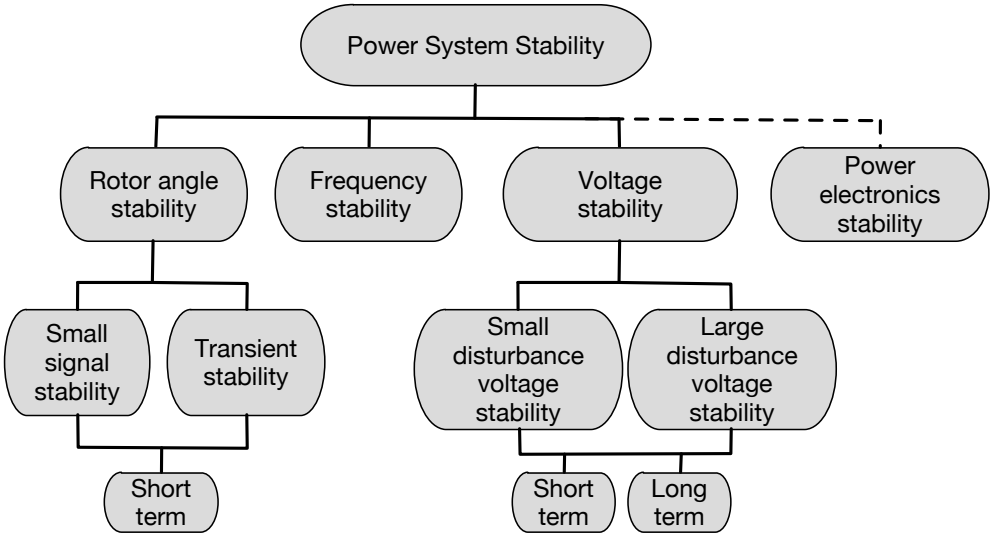

Figure 2.1: Classification of power system stability. Source: Adapted from [1].

2.3.1 Power System Stability

The authors of [1] divide power system stability into three types: rotor angle, frequency and voltage stability. This classification is based on (i) the physical nature of the resulting mode of instability, (ii) the size of the disturbance and (iii) the time span taken into consideration [1]. While rotor angle stability is related to the ability of synchronous machines to remain in synchronism after a disturbance, frequency stability is related to the ability of a power system to maintain steady frequency after a disturbance resulting in imbalance between generation and load [1]. Voltage stability, on the other hand, refers to the ability of a power system to maintain steady voltages at all buses in the system after a disturbance [1]. Thus, voltage instability describes the failure of the power system to maintain/restore equilibrium between load demand and load supply. The instability is often driven by the loads, which tend to be restored after a disturbance by the action of motor slip adjustment, distribution voltage regulators, tap-changing transformer, and thermostats [1].

Additionally, more recently with the increasing amount of power electronics in the system, a fourth type of (in)stability driven by power electronics has been observed, e.g. at VSCs in weak grid conditions [30]. An overview is shown in Fig. 2.1.

This thesis focuses mainly on small-signal stability, for which the damping ratio usually serves as metric used as stability margin. Usually, TSOs set certain threshold values of estimated damping ratios and operate the system in that way that the estimated damping ratio is over that threshold. While e.g. EirGrid uses a threshold of $5\,\%$ [31], Svenska kraftnät uses a threshold of $3\,\%$. The mathematical background of small-signal stability and the damping ratio will be discussed after the introduction of the corresponding models in section 2.7.4.

In contrast to the remaining thesis, the work presented in Chapter 7 focuses on short-term voltage stability issues which are driven by fast recovering load components (e.g. induction motor) that tend to restore power consumption in the time scale of a second following a large disturbance [32]. The stalling of induction motors has been identified as main reason for Fault Induced Delayed Voltage

Recovery (FIDVR) which is the phenomenon whereby system voltage remains at significantly reduced levels for several seconds after a transmission fault has been cleared [33]. FIDVR events are known to cause large amounts of bulk power system loads to trip on undervoltage potentially causing cascading events [34]. A FIDVR event is defined by North American Electric Reliability Corporation (NERC) as:

> Fault-Induced Delayed Voltage Recovery - a voltage condition initiated by a fault and characterized by:
>
> - Stalling of induction motors
> - Initial voltage recovery after the clearing of a fault to less than 90 percent of pre-contingency voltage
> - Slow voltage recovery of more than two seconds to expected post-contingency steady-state voltage levels
>
> [35]

2.3.2 N-1 Criterion

The N-1 criterion defines that after occurrence of a single contingency, the elements remaining in operation within a TSO's control area are capable of accommodating the new operating situation without violating operational security limits [36].

2.4 Security Considerations in Market Clearing

As the European Union is striving for the completion of a liberalized single electricity market, the electricity markets in Europe are gradually integrating [3]. As TSOs are responsible for a reliable operation of their control area, they perform extensive contingency analyses using load flow calculations in order to determine the available cross-border capacities, i.e. the transfer capacities of the tie-lines, which they provide to the market in order to include security considerations into the day-ahead market clearing [2]. Until May 2015, this was mostly done using Available Transfer Capacity (ATC) in Europe while today the Central Western European (CWE) day-ahead markets (i.e., Belgium, the Netherlands, France, Germany, Luxembourg and Austria) use a flow-based approach [3]. In the region Central Eastern Europe (CEE) the introduction of the Flow-Based Market Coupling (FBMC) is planned for 2019 [37].

Thus, the following subsection will briefly introduce the concept of transfer capacities while afterwards the ATC method and the FBMC method are described which are used to incorporated security considerations into the market-clearing.

2.4.1 Transfer Capacity

Any power system has a maximum transfer capacity of electric power reflecting its ability to transmit power from one area to another over the available transmission lines [38]. This transfer capacity is limited by the physical and electrical characteristics of the transmission lines or the entire system. Thus, the knowledge and the enforcement of these limits is an important aspect to ensure a secure operation of the power system. However, the maximum transfer capacities are difficult to determine in highly meshed interconnected power systems as they depend on the

specific topology and the current operating condition, i.e. the maximum transfer capacity of a line may vary depending on whether another line has been taken offline for e.g. maintenance, the current load level and which generators are currently dispatched. This is due to the fact that maximum transfer capacity of a line is bounded by one or more of the following limits depending on which is currently the lowest. These limits have been defined by the North American Electric Reliability Council in [38] as follows:

> **Thermal Limits** - Thermal limits establish the maximum amount of electrical current that a transmission line or electrical facility can conduct over a specified time period before it sustains permanent damage by overheating or before it violates public safety requirements.
>
> **Voltage Limits** - System voltages and changes in voltages must be maintained within the range of acceptable minimum and maximum limits. For example, minimum voltage limits can establish the maximum amount of electric power that can be transferred without causing damage to the electric system or customer facilities. A widespread collapse of system voltage can result in a blackout of portions or all of the interconnected network.
>
> **Stability Limits** - The transmission network must be capable of surviving disturbances through the transient and dynamic time periods (from milliseconds to several minutes, respectively) following the disturbance. [...]. Immediately following a system disturbance, generators begin to oscillate relative to each other, causing fluctuations in system frequency, line loadings, and system voltages. For the system to be stable, the oscillations must diminish as the electric systems attain a new, stable operating point. If a new, stable operating point is not quickly established, the generators will likely lose synchronism with one another, and all or a portion of the interconnected electric systems may become unstable. The results of generator instability may damage equipment and cause uncontrolled, widespread interruption of electric supply to customers. [38]

The test systems described in this thesis do not have thermal limits as limiting factor since those are comparably 'easy' to determine. This thesis proposes methods to determine the maximum transfer capacity (considering security requirements) as exact as possible using dynamic models and simulation data. By implementing the knowledge in optimization tools, this knowledge can be considered at the market stage mitigating the need for costly redispatching actions.

Note that the terms *transfer capacity* (used by European Network of Transmission System Operators for Electricity (ENTSO-E)) and *(active power) transfer capability* (used by NERC) are synonyms and can be used interchangeably.

2.4.2 Available Transfer Capacity (ATC)

The ATC method uses a simplified grid model reducing all nodes within a zone to an equivalent node (Fig. 2.3a) and ATC calculations are based on assumptions on the eventual market outcome [3]. The procedure of determining the ATCs usually involves determining the Total Transfer Capacity (TTC) which is basically the maximum power that can be transferred through the tie-lines connecting the TSO's operating area and the adjacent operating areas [2]. As aforementioned, these TTCs are set by physical and electrical limitations as thermal limits, voltage limits and stability limits,

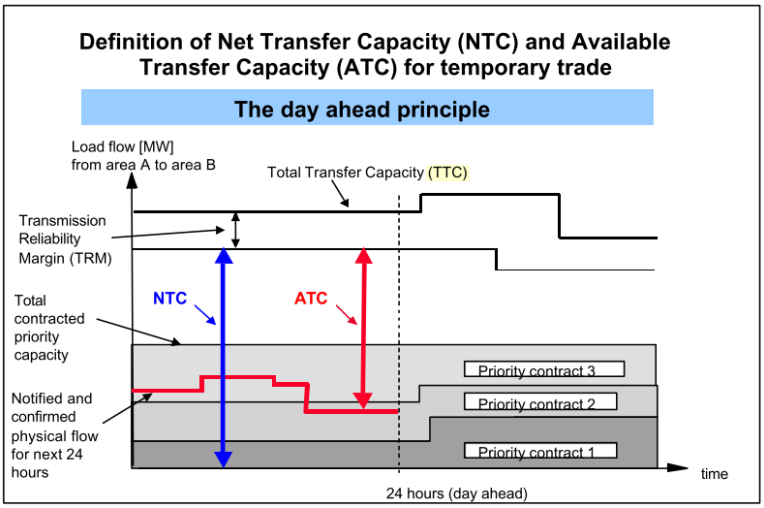

Figure 2.2: Day-ahead principle using NTC and ATC in the Nordel-area. Source: [2].

however, without considering contingencies (i.e. N-1 security). Combined with the Transmission Reliability Margin (TRM), which basically covers the forecast uncertainties of the tie-line power flows due to imperfect information from market players and unexpected real-time events (e.g. contingencies) [2], the Net Transfer Capacities (NTCs) can be determined as:

$$NTC = TTC - TRM. \tag{2.1}$$

Thus, the NTC value can be interpreted as "the expected maximum volume of generation that can be wheeled through the interface between the two systems, which does not lead to violations of the network constraints in either systems, respecting some technical uncertainties on future network conditions" [2].

The ATC is then determined by considering also the Notified Transmission Flow (NTF), which relates to "the already occupied part of the NTC by the already accepted transfer contracts at the studied time frame" [2]:

$$ATC = NTC - NTF. \tag{2.2}$$

The differences between ATC, NTC, NTF, TRM and TTC are illustrated in Fig. 2.2.

The drawback of this concept is that the ATCs are determined beforehand independent of the actual operating point while the actual stability limits vary with the actual flows in the system. Moreover, the ATC limits are given as constant values representing linear cuts of the feasible space, as visualized in Fig. 2.3c, which do not reflect the true feasible space of the system, excluding parts of the true feasible space with potentially cheaper operating points. Finally, the ATCs are determined using ac power-flow simulations while the market clearing in Europe is based on dc optimal power-flow simulations. In section 6.4.5, it is shown that by translating security considerations from the ac to the dc space the inaccuracy may be increased causing either too conservative or too loose limits requiring redispatching actions.

2.4.3 Flow-Based Market Coupling (FBMC)

In the FBMC, the physical transmission constraints are taken into account in the market clearing by using an Optimal Power Flow (OPF) formulation with Power Transfer Distribution Factors (PTDFs)

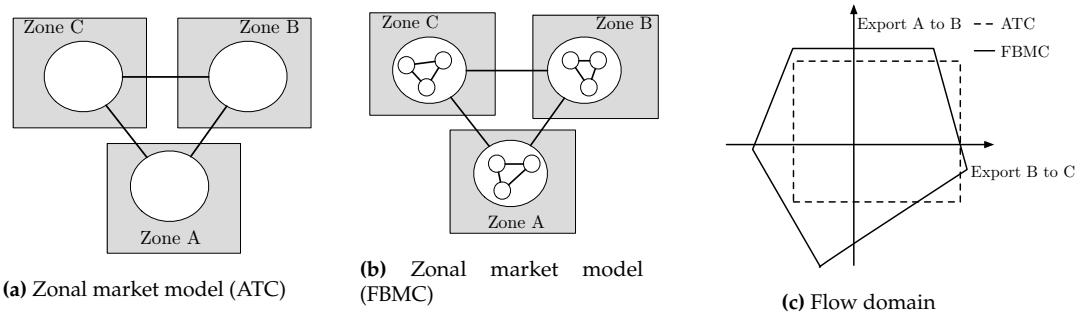

(a) Zonal market model (ATC)

(b) Zonal market model (FBMC)

(c) Flow domain

Figure 2.3: Comparison of the zonal market model of (a) the ATC model, (b) the FBMC model and (c) a visualisation of the resulting transfer limits. Source: Adapted from [3].

considering the tie-lines and all critical lines in normal and N-1 state (Fig. 2.3b) [3]. The zonal PTDFs and the Remaining Available Margin (RAM) are determined by the TSOs. The zonal PTDFs are an approximation of the real physical characteristics of the (simplified) grid while the RAM is the line capacity that can be used in the day-ahead market. However, in order to be able to calculate these parameters, the day-ahead market outcome has to be known already. Hence, it is a circular problem, in which the day-ahead market outcome has to be known to determine the FBMC parameters, and the FBMC parameters are needed to clear the day-ahead market outcome [3]. Thus, the parameters are calculated in advance based on a forecast of the state of the electricity system and then communicated to the day-ahead market clearing algorithm [3].

The advantage of this approach is visualized in Fig. 2.3c. Here, the line limits are not constant but depend on the operating point and are less conservative than with the ATC approach allowing a more efficient operation of the power system. The weakness of this approach lies in the convexity of the determined security boundary, which depending on the system under investigation does not necessarily reflect the true feasible space. This may cause the exclusion of feasible and potentially cheaper operating points due to the fact that they are not part of the largest feasible convex space. Furthermore, the considered security limits are based on a simplified model focusing on tie-lines and the most critical lines and the parameters are calculated based on a forecast of the state of the electricity system.

2.5 Supervised Machine Learning Methods

All data-driven methods used within this thesis can be classified as supervised machine learning methods. In supervised learning, an algorithm is used to learn the mapping function from known input variables to a known output variable in order to predict the output for unseen inputs. A brief introduction to the different methods used in this work is given in this subsection. For more details the interested reader is referred to [4, 39, 40]. After the description of the different methods the evaluation of the created classifiers are discussed.

2.5.1 Classification Tree

A classification tree is a subset of decision trees (DTs) where the decision outcome, called "target variable", can take a finite set of values. A introduction to DT theory for power systems can be found in [39].

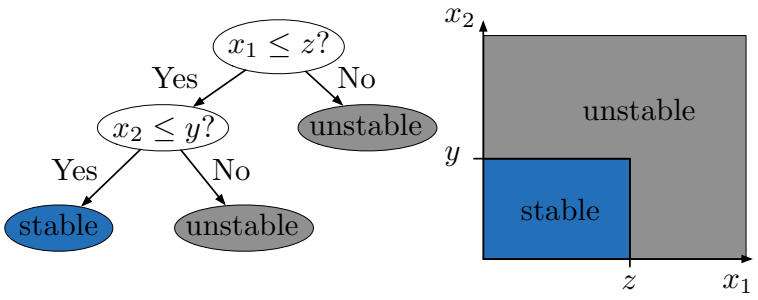

Figure 2.4: Simple example of a decision tree and a visualization of partitioning the data set.

The classification tree is used to reveal patterns of the interconnection between observed measurements (or artificially created signals) and target variables with the goal of using these patterns as decision rules to predict the decision outcome of new observations. The measurements used as decision variables are called 'predictors' or 'features'. A simple example of a DT is shown in Fig. 2.4. It contains nodes, branches and terminal decisions. At each node a test of a predictor splits the data set into subsets according to the test result. The branches connecting this node with the nodes one level below represent the possible test outcomes. The leaf nodes with terminal decisions constitute the final classification of the input observation [**Pub. E**]. This thesis uses the Statistics and Machine Learning Toolbox in Matlab 2017b [41] applying the standard CART algorithm for the creation of decision trees.

Splitting Criteria

The Statistics and Machine Learning Toolbox in Matlab 2017b [41] allows to choose between three different splitting criteria. As we focus on binary classifications within this thesis, two options, i.e. the gini index and cross entropy / deviance reduction, are of main interest which we will briefly introduce here. For more details the reader is referred to the documentation of the toolbox [42].

In a node m, representing a region R_m with N_m observations the proportion of class k observations in node m can be described as [40]:

$$\hat{p}_{mk} = \frac{1}{N_m} \sum_{x_i \in R_m} I(y_i = k). \tag{2.3}$$

The observations in node m can be classified to class $k(m)$ by:

- Gini index: $\sum_{k \neq k'} \hat{p}_{mk}\hat{p}_{mk'} = \sum_{k_1}^{K} \hat{p}_{mk}(1 - \hat{p}_{mk})$
- Cross entropy or deviance: $-\sum_{k=1}^{K} \hat{p}_{mk}\ log\ \hat{p}_{mk}$.

Moreover, the Statistics and Machine Learning Toolbox allows to vary the costs of misclassifying a data point into a certain class. This allows to create rather conservative decisions trees aiming at - in the particular case of power system security - rather misclassifying more *stable* points as *unstable* (false negative misclassifications) while minimizing misclassifications of *unstable* points as stable (false positive misclassification).

Tree Pruning

In order to avoid over-fitting of the classifiers, i.e. to fit the classifier too closely to a particular set of data while reducing its generalization capability, the depth of decision trees can be controlled. Moreover, after growing a tree, it can be pruned, i.e. the size reduced, to mitigate the over-fitting.

There exist several different pruning approaches including top down (i.e. starting at the root) and bottom up (i.e. starting at the leaf nodes) methods. One of the most popular is cost-complexity pruning which aims at minimizing a cost-complexity metric $C_\alpha(T) = c(T) + \alpha \times |T|$ which combines the tree size $|T|$ (complexity) and the accuracy (or error rate) $c(T)$ of the tree T for a selectable cost factor α. Thus, depending on the choice of α either complex and accurate or less complex and less accurate trees are preferred. The optimal α, i.e. also the optimal subtree T_i, can be determined by cross validation.

However, it is also possible to manually investigate the grown tree and prune specific nodes based on test results.

2.5.2 Support Vector Machine

Support Vector Machine (SVM) is one of the most famous supervised machine learning methods. It classifies the data by finding the best hyperplane separating all data points of one class from those of the other class. The best hyperplane is determined based on the largest margin, i.e. the maximum width of the slab parallel to the hyperplane without interior data points [40] which is determined by an optimization problem. The basic idea for a two-dimensional problem is shown in Fig. 2.5. This example is using a linear classifier in the ideal case where the data points of the different classes can be perfectly separated. However, in case simple hyperplanes are not a useful splitting criterion for the given data, nonlinear kernels (e.g. polynomial, cubic or radial) can be used to transform the problem into some space S where the resulting classifiers are hypersurfaces [40].

2.5.3 Ensemble Tree Algorithms

Ensemble-based decision making is based on the idea of combining several classifiers with relatively fixed bias to derive a decision by e.g. averaging their output [4]. Simply speaking: The intelligence of the mass is used instead of the individual classifier, as illustrated in Fig. 2.6.

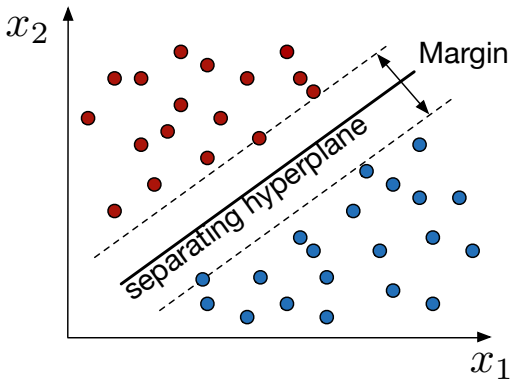

Figure 2.5: Linear hyperplane of a SVM.

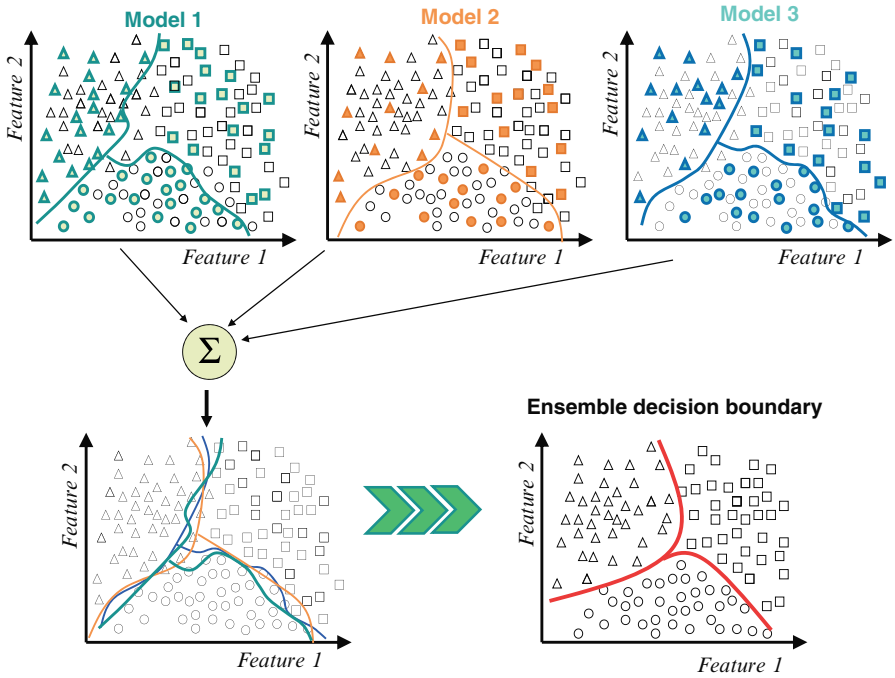

Figure 2.6: Variability reduction using ensemble systems. Source: [4].

A rich collection of ensemble tree classifiers has been developed, however, most of them are variations of two examples: Bagging and Boosting. While both combine an ensemble of weak learners using simple majority voting, they differ in the way the training sets of the weak learners are chosen. In bagging, each instance has the same chance of being in each training set. In boosting, however, the training set for each subsequent weak learner is increasingly focused on misclassified instances by previous classifiers [4].

While there exist countless different adaptations of ensemble tree algorithms, in this work we used three of the most popular ones: AdaBoost (short for Adaptive Boosting), LogitBoost and RUSBoost, i.e. three boosting examples. AdaBoost is the classical boosting algorithm, LogitBoost is an adaptation using a logistic regression model as cost function, while RUSBoost is an adaptation, which is expected to perform especially well for data-sets with skewed classes, i.e. uneven amount of samples for the different classes.

2.5.4 Classifier Assessment

In order to estimate the performance of the trained classifier, they need to be evaluated on data which has not been used during the training of the classifier. There exist different approaches to split the available data in training and test sets to create useful estimates of the performance of the created classifiers. Here, we focus on two methods used within this thesis: k-fold cross-validation and splitting into train and test sets.

Split into Train and Test Set

The simplest method to evaluate the performance of the trained classifiers is to split the data set into a training and a test set. The classifier is trained on the training set and evaluated on the test set. The size of the split depends on the size and the specifics of the data set. Given that the

classifier is only trained on part of the data, this method is suitable for very large data sets where both data sets, i.e. the training and the test set, are representative for the underlying problem [43].

K-fold Cross Validation

K-fold cross validation works by splitting the data set into k-parts (folds). The classifiers are trained on $k-1$ folds with one held back on which the classifier is tested. This is repeated until each part of the data set has been held back and used to test the trained classifier. Thus, this method leads to k different performance scores which are usually summarized by a mean and a standard deviation [43].

2.6 Motivation for focusing on Data-driven Approaches and HVDC Transmission

The following subsections will shed light on why we focused on data-driven approaches and VSC-HVDC transmission.

2.6.1 Benefits of VSC-HVDC

HVDC transmission is in general used for economic reasons for bulk power transfer over long distances due to lower line costs despite the converter stations being more costly than the ac substations. The break-even distance depends on the rating and the distance and is usually between $600-800\,\mathrm{km}$ (overhead lines) [44] but in specific studies it can also be significantly shorter ($310\,\mathrm{km}$) [17].

Moreover, HVDC transmission has additional benefits compared to AC transmission, such as controllable power flows, a lower environmental impact, the capability to interconnect asynchronous areas and the possibility to use long (submarine) cables ($> 200\,\mathrm{km}$) for offshore wind farms [17]. The break-even distance for submarine transmission depends on the rating and the number of conductors and lies between $50-200\,\mathrm{km}$ [17, 45].

A significant driver of this interest, in particular in Europe, was the appearance and development of HVDC transmission based on VSC and its advantages compared to HVDC based on LCC. The black-start capability, the capability to supply weak grids, the comparable small footprint and the ability to control active and reactive power independently made this technology also feasible for offshore applications. The drawbacks are, however, higher costs, higher losses and lower power ratings at the moment [17, 46]. However, it is also seen as an enabler for MT-HVDC grids allowing to interconnect several HVDC converters. While in China two MT-HVDC grids have already been commissioned [17, 26], there exists different initiatives investigating potential MT-HVDC in Europe. However, due to the little experience with MT-HVDC grids, the control, operation and potential interaction of such a MT-HVDC grid with the connected AC grids are open research questions. Moreover, new methods enhancing the grid stability by taking advantage of the flexibility such a grid can offer are needed, as each HVDC terminal is capable of performing fast corrective control actions providing reactive power support and / or a rerouting of the active power flow.

2.6.2 Benefits of the Use of Data

Power systems are one of the largest and most complex man-made nonlinear systems on earth, whose operation becomes increasingly challenging due to the shift in generation towards varying generation in form of RES. At the same time, with the increasing deployment of PMUs, TSOs obtain high-resolution, real-time dynamic state information of the power grid. Although these data contain only limited information of abnormal situations, the data could be enriched with simulation data, which is, however, a huge challenge by itself considering the complexity of the system (see section 5.3 for details). Nevertheless, such a database of measurement and simulation data allows the development of methods to monitor, predict and enhance the system stability in real-time. The large amount of data already helps to increase TSO situational awareness in the control center providing the TSOs with a better understanding of the actual stability limits, however, ideally, this knowledge could already be used within the market clearing leading to a more secure dispatch and reducing the need for costly re-dispatch.

Furthermore, real-time data could be used locally to support local control structures avoiding communication delay and enabling the controllers to act on accurate trajectory predictions based on the most recent measurement data instead of just react to actual measurements. This could potentially enable fast(er) corrective control actions.

2.7 Power System Modeling

This section introduces the power systems models used within the thesis. First, a generic mathematical model of a classical multi-machine model is described which is used in chapter 5 and 6. Then, a generic mathematical model of a MT-HVDC grid based on VSCs is presented which is used in chapter 4 and 6. After the introduction of a model of a wind farm based on Double-Fed Induction Generators (DFIGs) used in chapter 6, the concept of linearizing the derived state-space models and the definitions of small-signal stability and participation factors are introduced. Finally, it is explained how contingencies are reflected in the corresponding models.

As the work in chapter 7 is not focusing on small-signal stability but short-term voltage stability, that work was performed using PSS/e and a more detailed load modeling approach. However, as the load modeling approach is not related to any other chapter, the corresponding model is described within that chapter to improve the readability.

2.7.1 Mathematical Model of a Multi-Machine System

This section summarizes briefly the multi-machine model used in different sections of the thesis. For a more detailed description the interested reader is referred to [15, 47]. The model is denoted in a per-unit system using the three-phase ac power S_b^{ac} and the phase-to-phase ac voltage V_b^{ac} as base values.

Several different kind of synchronous machine models have been proposed which can be distinguished by the level of detail or the dynamic order of the model, respectively. A collection of the different models can be found in [15]. This thesis adapts the most common assumptions by most power system books neglecting flux dynamics and considering rotor speed deviations to be small as we are focusing on small-signal stability. Thus, a sixth order synchronous machine model (2.4)-(2.11) [47] with an Automatic Voltage Regulator (AVR) Type I ((2.13)-(2.15)) is used

throughout this thesis. All generators are additionally equipped with Power System Stabilizers (PSS) type 1 adding an additional state per generator (2.16). With an additional state for the bus voltage measurement delay (2.12) this leads to a state-space model of $11 \cdot N_G$ states, with N_G representing the number of generators in the grid. The small signal models were derived using Mathematica [48], the initialization and small signal analysis were carried out using Matpower 6.0 [49] and Matlab 2017b [41]. Reactive power limits of the generators are enforced.

Thus, the multi-machine model can be described with $11 \cdot N_G$ differential algebraic equations (2.4)-(2.16) and $4 \cdot N_G + 2 \cdot N_{Bus}$ algebraic equations: $2 \cdot N_G$ equations defining stator fluxes (2.18)-(2.19), $2 \cdot N_G$ stator equations (2.20)-(2.21), and $2 \cdot N_{Bus}$ network equations (2.22)-(2.23). N_{Bus} describes the number of buses in the power system.

$$\frac{d\delta_i}{dt} = \omega_b(\omega_i - \omega_s) \tag{2.4}$$

$$\frac{d\omega_i}{dt} = \frac{1}{2h_i}\left(t_{M_i} - \psi_{d_i} i_{g,q_i} + \psi_{q_i} i_{g,d_i} - d_i(\omega_i - \omega_s)\right) \tag{2.5}$$

$$\frac{de'_{g,q_i}}{dt} = (-e'_{g,q_i} - (x_{d_i} - x'_{d_i})(i_{g,d_i} - \gamma_{d2_i}\psi''_{d_i} \tag{2.6}$$

$$- (1 - \gamma_{d1_i}) i_{g,d_i} + \gamma_{d2_i} e'_{g,q_i}) + e_{fd_i})/t'_{d0_i} \tag{2.7}$$

$$\frac{de'_{g,d_i}}{dt} = (-e'_{g,d_i} - (x_{q_i} - x'_{q_i})(i_{g,q_i} - \gamma_{q2_i}\psi''_{q_i} \tag{2.8}$$

$$- (1 - \gamma_{q1_i}) i_{g,q_i} - \gamma_{q2_i} e'_{g,d_i}))/t'_{q0_i} \tag{2.9}$$

$$\frac{d\psi''_{d_i}}{dt} = (-\psi''_{d_i} + e'_{g,q_i} - (x'_{d_i} - x_{l_i}) i_{g,d_i})/t''_{d0_i} \tag{2.10}$$

$$\frac{d\psi''_{q_i}}{dt} = (-\psi''_{q_i} - e'_{g,d_i} - (x'_{q_i} - x_{l_i}) i_{g,q_i})/t''_{q0_i} \tag{2.11}$$

$$\frac{dv_{h_i}}{dt} = \frac{v_i - v_{h_i}}{t_{r_i}} \tag{2.12}$$

$$\frac{dv_{R_i}}{dt} = \frac{k_{A_i}((v_{s_i} + v_{ref_i}) - v_{h_i} - r_{f_i} - \frac{k_{f_i}}{t_{f_i}} e_{fd_i}) - v_{R_i}}{t_{A_i}} \tag{2.13}$$

$$\frac{dr_{f_i}}{dt} = -\frac{r_{F_i}}{t_{F_i}} - \frac{k_{F_i}}{(t_{F_i})^2} e_{fd_i} \tag{2.14}$$

$$\frac{de_{fd_i}}{dt} = -\frac{k_{E_i} + s_{E_i}(e_{fd_i})}{t_{E_i}} e_{fd_i} + \frac{v_{R_i}}{t_{E_i}} \tag{2.15}$$

$$\frac{dv_{1_i}}{dt} = -\left(k_\omega \omega_i + k_p p_{gen} + k_v v_i + v_{1_i}\right)/t_\omega \tag{2.16}$$

$$0 = k_\omega \omega_i + k_p p_{gen} + k_v v_i + v_{1_i} - v_{s_i} \tag{2.17}$$

$$0 = \psi_{d_i} + x''_{d_i} i_{g,d_i} - \gamma_{d1_i} e'_{g,q_i} - (1 - \gamma_{d1_i})\psi''_{d_i} \tag{2.18}$$

$$0 = \psi_{q_i} + x''_{q_i} i_{g,q_i} + \gamma_{q1_i} e'_{g,d_i} - (1 - \gamma_{q1_i})\psi''_{q_i} \tag{2.19}$$

$$0 = r_{a_i} \cdot i_{g,d_i} + \psi_{q_i} + v_{d_i} \tag{2.20}$$

$$0 = r_{a_i} \cdot i_{g,q_i} - \psi_{d_i} + v_{q_i} \tag{2.21}$$

for $i = 1, 2, 3, \ldots, N_G$.
and

$$0 = \quad p_{G_i} + p_{L_i}(v_i) - \textstyle\sum_{k=1}^{n} v_i v_k Y_{ik} \cos(\theta_i - \theta_k - \alpha_{ik}) \tag{2.22}$$

$$0 = \quad q_{G_i} + q_{L_i}(v_i) - \textstyle\sum_{k=1}^{n} v_i v_k Y_{ik} \sin(\theta_i - \theta_k - \alpha_{ik}) \tag{2.23}$$

for $i = 1, 2, 3, \ldots, N_G, N_G + 1, \ldots, N_{Bus}$.
with

$$p_{G_i} = i_{g,d_i} v_i \sin(\delta_i - \theta_i) + i_{g,q_i} v_i \cos(\delta_i - \theta_i) \tag{2.24}$$
$$q_{G_i} = i_{g,d_i} v_i \cos(\delta_i - \theta_i) - i_{g,q_i} v_i \sin(\delta_i - \theta_i) \tag{2.25}$$

for $i = 1, 2, 3, \ldots, N_G$.
The $11 \cdot N_G$ differential algebraic equations and $4 \cdot N_G + 2 \cdot N_{Bus}$ algebraic equations can be combined and rewritten in matrix notation as:

$$\dot{\mathbf{X}} = f(\mathbf{X}, \mathbf{Y}, \mathbf{U}) \tag{2.26}$$
$$\mathbf{0} = g_1(\mathbf{X}, \mathbf{Y}) \tag{2.27}$$
$$\mathbf{0} = g_2(\mathbf{X}, \mathbf{Y}) \tag{2.28}$$

with the state vector $\mathbf{X} = [\mathbf{X}_1^T \ \mathbf{X}_2^T \ \ldots \mathbf{X}_{N_G}^T]^T$ where $\mathbf{X_i} = [\delta_i \ \omega_i \ e'_{g,q_i} \ e'_{g,d_i} \ \psi''_{d_i} \ \psi''_{q_i} \ v_{h_i} \ v_{R_i} \ r_{f_i} \ e_{fd_i} \ v_{1_i}]^T$. $\mathbf{Y} = [\mathbf{Y_C}^T \mathbf{Y_B}^T]^T = [\theta_1 \ v_1 \ \ldots v_{N_G} \vdots \theta_2 \ldots \theta_{N_{Bus}} \ v_{N_G+1} \ \ldots v_{N_{Bus}}]^T$ is the set of algebraic variables with $\mathbf{Y_B}^T$ being the set of load-flow variables and $\mathbf{Y_C}^T$ representing the remaining algebraic variables. The input vector is defined as $\mathbf{U} = [\mathbf{U}_1^T \ \mathbf{U}_2^T \ \ldots \mathbf{U}_{N_G}^T]^T$ with $\mathbf{U_i} = [v_{ref_i} \ t_{M_i}]^T$. While $\mathbf{f}(\mathbf{X}, \mathbf{Y}, \mathbf{U})$ denotes the $11 \cdot N_G$ differential algebraic equations of the generators, $\mathbf{g}_1(\mathbf{X}, \mathbf{Y})$ denotes the $2 \cdot N_G$ algebraic network equations corresponding to the buses where the generators are connected to. $\mathbf{g}_2(\mathbf{X}, \mathbf{Y})$ denotes the $2 \cdot (N_{Bus} - N_G)$ algebraic network equations corresponding to the remaining buses.

After the introduction of the mathematical models of a VSC based MT-HVDC Grid and a wind farm, we will introduce the concept of linearizing such systems in matrix notation. Moreover, a few detailes of the linearization process of a multi-machine model will be briefly discussed. For a detailed description of the linearization process of a multi-machine model the interested reader is referred to [47, 50].

2.7.2 Mathematical Model of a VSC based MT-HVDC Grid

Although recently the projects under development using HVDC based on VSCs tend to use mostly Modular Multilevel Converters (MMCs), most of the projects already commissioned use two- / three- or multi-level VSCs. Due to the fact that a MT-HVDC will most likely not be built at once but involve a step-wise integration of already existing on- and offshore interconnectors [51], this thesis will use a generic mathematical model of a VSC-HVDC terminal. All methodologies presented in this thesis could, however, also be used with a mathematical model of a MMC. Thus, a general mathematical model of a VSC-HVDC terminal with simplified AC grid is presented in this subsection. This model is based on the single VSC configuration introduced in [6]. In order to develop a multi-terminal grid, an arbitrary number of those terminals and lines can be connected.

This model was used in **[Pub. A]**, while a slightly different model [9] was used in **[Pub. C]** and **[Pub. D]** due to a collaboration with Eduardo Prieto-Araujo from the Universitat Politècnica de Catalunya. The differences are highlighted in section 4.5.2. Thus, most parts of the model description are taken from **[Pub. A]**. The dc cable model description is adjusted due to the fact that the later work did not only focus on π-equivalent models but also took a frequency dependent π cable model into account as described in subsection 2.7.2.

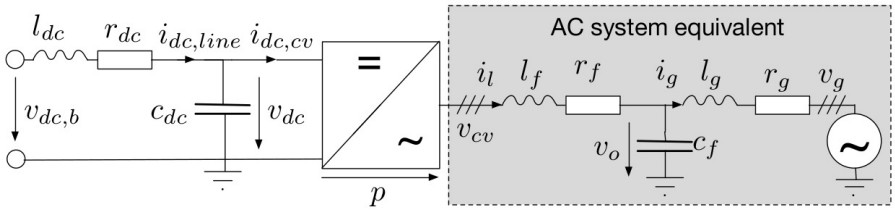

Figure 2.7: Model of a VSC-HVDC terminal connected to a single DC line. Source: **[Pub. A]**.

Model Conventions

Upper case letters represent physical values of the electrical circuit, whereas lower case letters define per unit quantities. The apparent power rating of the converter and the peak value of the rated phase voltage serve as base values for the used per unit system. The modelling of the electrical system and the control of the AC-side will be presented in a Synchronous Reference Frame (SRF), using the amplitude-invariant Park Transformation. The d-axis voltage vector is aligned with the voltage vector, v_o, at the corresponding filter capacitor, c_f, and the q-axis is leading the d-axis by $90°$ [52]. SRF equations will be noted in complex space vector notation according to

$$\mathbf{x} = x_d + j \cdot x_q. \tag{2.29}$$

Electrical System

As shown in Fig. 2.7, a simplified but appropriate model for the analyses presented in the following chapters is used. The focus on the outer control loop, as well as the emphasis on small-signal analysis, justifies this simplification for a multi-terminal grid in order to minimize the large computational burden.

Electrical System on the AC side: As shown in Fig. 2.7, a simplified model of the AC grid is assumed, using an LC filter as the grid interface of the VSC and a Thévenin equivalent representation of the grid. The state-space equations can be obtained as given below, where the per unit grid frequency is denoted as ω_g and the base angular frequency as ω_b [53, 54]. Considering the aforementioned model convention ($\mathbf{v}_{cv} = v_{cv,d} + jv_{cv,q}$), the equations are given as follows:

$$\frac{d\mathbf{i}_l}{dt} = \frac{\omega_b}{l_f}\mathbf{v}_{cv} - \frac{\omega_b}{l_f}\mathbf{v}_o - \left(\frac{r_f\omega_b}{l_f} + j \cdot \omega_g\omega_b\right)\mathbf{i}_l \tag{2.30}$$

$$\frac{d\mathbf{v}_o}{dt} = \frac{\omega_b}{c_f}\mathbf{i}_l - \frac{\omega_b}{c_f}\mathbf{i}_g - j \cdot \omega_g\omega_b\mathbf{v}_o \tag{2.31}$$

$$\frac{d\mathbf{i}_g}{dt} = \frac{\omega_b}{l_g}\mathbf{v}_o - \frac{\omega_b}{l_g}\mathbf{v}_g - \left(\frac{r_g\omega_b}{l_g} + j \cdot \omega_g\omega_b\right)\mathbf{i}_g \tag{2.32}$$

The power balance between AC and DC side is given below. It is based on the assumption of an ideal lossless average model for the converter.

$$v_{cv,d} \cdot i_{l,d} + v_{cv,q} \cdot i_{l,q} = v_{dc} \cdot i_{dc,cv} \tag{2.33}$$

Electrical system on the DC side: Depending on the required model fidelity the DC cables can be modeled either as π-equivalent or as so-called frequency dependent π-models.

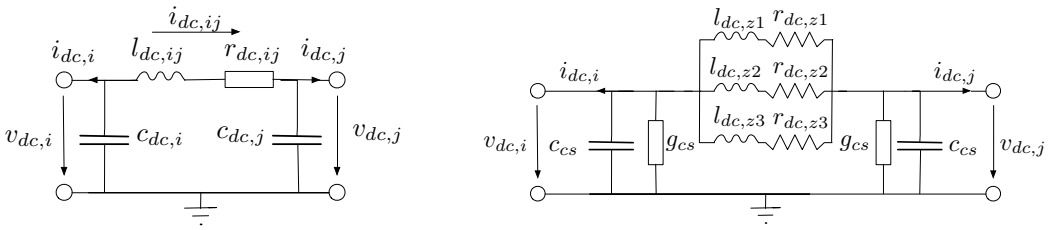

Figure 2.8: DC cable models: a) classic π-equivalent, b) approximation of frequency dependent π DC cable model. Source: Adapted from [5].

π-equivalent cable model: In this case, the lines are represented as single π-equivalents. The cable resistance and inductance are modeled as single elements in series while the cable capacitances, $c_{dc,line}$, are incorporated in the DC capacitance of the corresponding converter, c_{dc}, as given in (2.34).

$$c_{dc} = \frac{c_{dc,line}}{2} + c_{dc,vsc} \tag{2.34}$$

It is worth to note that this is a simplified model, which can approximate only the lowest frequency resonant peak of the cable [55]. But, on the other hand, D'Arco argues in [6], that this approach also resembles the worst case scenario with respect to LC oscillations. This is due to the fact that the oscillatory effects are condensed in a single frequency, instead of being spread on several frequencies as in a real cable. This modeling approach can also be justified by the results of [56], indicating that for an appropriate sizing of the capacitor the impedance seen by the VSC is almost identical. The equations for the dynamics at the DC capacitors are given by:

$$\frac{dv_{dc}}{dt} = \frac{\omega_b}{c_{dc}} i_{dc,line} - \frac{\omega_b}{c_{dc}} i_{dc,cv} \tag{2.35}$$

Whereas the DC line dynamics according to the defined current flow are given by:

$$\frac{di_{dc,line}}{dt} = \frac{\omega_b}{l_{dc}} v_{dc,b} - \frac{\omega_b}{l_{dc}} v_{dc} - \frac{\omega_b r_{dc}}{l_{dc}} i_{dc,line} \tag{2.36}$$

Frequency dependent π cable model: The 'frequency dependent π' cable model was introduced in [5]. The model, shown in Fig. 2.8b, is called 'frequency dependent π' since the additional parallel branches are calculated to fit the frequency response of a wide-band cable model [14, 57]. The equations for the dynamics at the DC capacitors are given by:

$$\frac{dv_{dc}}{dt} = \frac{\omega_b}{c_{dc}} (i_{dc,1} + i_{dc,2} + i_{dc,3}) - \frac{\omega_b}{c_{dc}} i_{dc,cv} \tag{2.37}$$

Whereas the DC line dynamics according to the defined current flow are given by:

$$\frac{di_{dc,1}}{dt} = \frac{\omega_b}{l_{dc,z1}} v_{dc,b} - \frac{\omega_b}{l_{dc,z1}} v_{dc} - \frac{\omega_b r_{dc,z1}}{l_{dc,z1}} i_{dc,1} \tag{2.38}$$

$$\frac{di_{dc,2}}{dt} = \frac{\omega_b}{l_{dc,z2}} v_{dc,b} - \frac{\omega_b}{l_{dc,z2}} v_{dc} - \frac{\omega_b r_{dc,z2}}{l_{dc,z2}} i_{dc,2} \tag{2.39}$$

$$\frac{di_{dc,3}}{dt} = \frac{\omega_b}{l_{dc,z3}} v_{dc,b} - \frac{\omega_b}{l_{dc,z3}} v_{dc} - \frac{\omega_b r_{dc,z3}}{l_{dc,z3}} i_{dc,3} \tag{2.40}$$

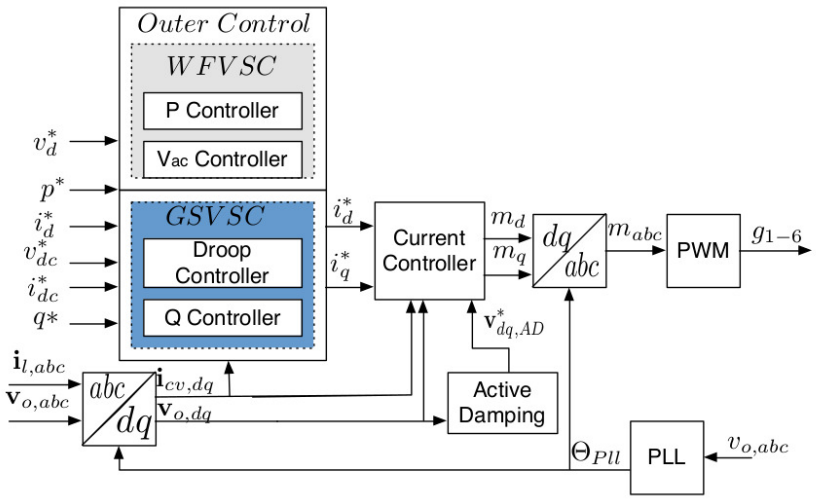

Figure 2.9: Control system - GSC and WFC differ by outer controllers, GSCs differ by chosen droop CS. Source: [**Pub. A**].

Control System

The control system consists of a damping controller against LC filter oscillations, a current controller, a Phase Locked Loop (PLL) and an outer controller. The outer control depends on the connected AC grid, which is explained in more detail in the outer loop controller subsection. An overview of the control system is given in Fig 2.9. The corresponding equations are given in the following subsections.

Phase Locked Loop (PLL): The VSC is assumed to be synchronized with the corresponding AC grid through a PLL, modelled as shown in Fig. 2.10 [54, 58]. An inverse tangent function is used on the low-pass filtered estimated phase voltages $\mathbf{v}_{PLL} = v_{PLL,d} + jv_{PLL,q}$ to approximate the actual phase angle error $\Delta\Theta_{v,PLL}$. Followed by a PI controller in order to derive the frequency of the tracked voltages. The corresponding equations are given as:

$$\frac{d\mathbf{v}_{PLL}}{dt} = -\omega_{LP,PLL}\mathbf{v}_{PLL} + \omega_{LP,PLL}\mathbf{v}_o \tag{2.41}$$

$$\frac{d\epsilon_{PLL}}{dt} = \tan^{-1}\left(\frac{v_{PLL,q}}{v_{PLL,d}}\right) \tag{2.42}$$

$$\frac{d\Delta\Theta_{v,PLL}}{dt} = \omega_b\Delta\omega_{PLL} \tag{2.43}$$

with ϵ_{PLL} representing the integrator state of the PI controller and $\Delta\Theta_{PLL}$ the phase angle deviation between the grid voltage, $\mathbf{v}_g$, and the orientation of the PLL. $\Delta\omega_{PLL}$ describes the grid frequency deviation. The deviation variables are necessary for the modeling of the PLL in the SRF. The actual voltage vector phase angle, Θ_{PLL}, is needed for the transformation between stationary and rotating reference frame.

In case the VSC is connected to a weak grid, the PLL which is commonly used for grid synchronization can negatively affect the dynamic performance and stability range of the VSC. The stability problems associated with the PLL are in general related to the influence of the converter operation on the voltage measurements used for grid synchronization [59]. Different approaches have been proposed to mitigate this problem as e.g. an impedance-conditioned PLL (IC-PLL) [59]

or power-synchronization control [60] which introduces a power-balanced-based synchronization mechanism similar to the operation principle of traditional synchronous machines. This thesis, however, focuses on situations where the grid connected to all VSCs is strong enough for the use of PLLs.

Active Damping of LC Filter Oscillations: An active damping of LC filter oscillations is implemented, based on injecting a component, $\mathbf{v}^*_{AD}$, to the converter output voltage, which is in counter-phase with the detected oscillations [61, 62].

$$\mathbf{v}^*_{AD} = k_{AD}\left(\mathbf{v}_o - \boldsymbol{\phi}\right) \tag{2.44}$$

$$\frac{d\boldsymbol{\phi}}{dt} = \omega_{AD}\mathbf{v}_o - \omega_{AD}\boldsymbol{\phi} \tag{2.45}$$

While ω_{AD} represents the cut-off frequency and $\phi = \phi_d + j\phi_q$ the integrator states of the low-pass filter, k_{AD} is used as tuning parameter depending on the dynamic response of the system. The controller is visualized in Fig. 2.11.

Inner Current Control Loop: The inner current control is based on vector control in the synchronous reference frame, tuned by modulus optimum criterion [63]. Considering two conventional PI controllers with decoupling terms and voltage feed-forward, the converter output voltage reference, $\mathbf{v}^*_{cv}$, can be defined as:

$$\mathbf{v}^*_{cv} = k_{pc}(\mathbf{i}^*_l - \mathbf{i}_l) + k_{ic}\gamma + jl_f\omega_{PLL}\mathbf{i}_l + \mathbf{v}_o - \mathbf{v}^*_{AD} \tag{2.46}$$

with γ, k_{pc} and k_{ic} representing the integrator state, the proportional and integral gain of the PI controller.

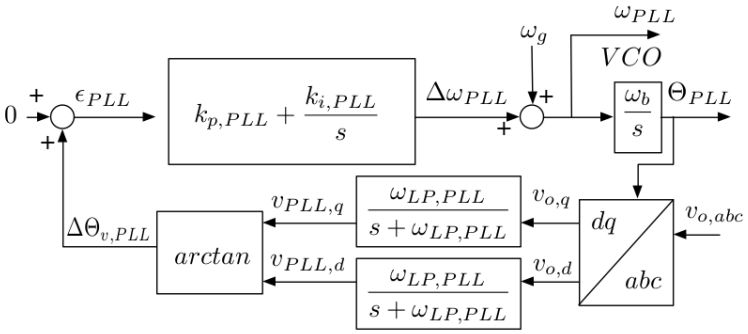

Figure 2.10: Phase Locked Loop. Source: **[Pub. A]**.

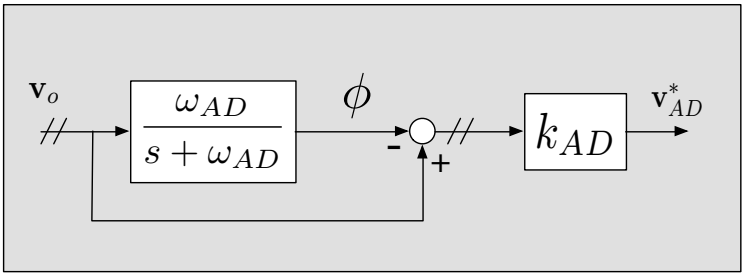

Figure 2.11: Active Damping of LC-Oscillations. Adapted from: [6].

Outer loop controller: The outer loop control structure is the main difference between the terminals. Here, a distinction is made between VSC terminals, which are supposed to take part in the dc voltage control, and those which are not. The former are most likely connected to rather strong grids, hence those terminals are called Grid Side Converters (GSCs) in the following. The latter are most likely connected to rather weak grids, where the focus lies on maximizing the power output as it is for wind farms, hence those are called Wind Farm Converters (WFCs) in the following.

Wind farm converter (WFC): For a VSC terminal representing a wind farm, a conventional active power controller is providing the d-axis current reference. The q-axis reference is provided by an ac voltage controller. The equations are given as:

$$i^*_{l,d,wf} = k_{pcd,wf}\left(p^*_{wf} - p_{wf,ac}\right) + k_{icd,wf}\chi_{d,wf} \tag{2.47}$$

$$i^*_{l,q,wf} = k_{pcq,wf}\left(v^*_{o,d,wf} - v_{o,d,wf}\right) + k_{icq,wf}\chi_{q,wf} \tag{2.48}$$

with $\chi_{d/q}$, $k_{pcd/q}$ and $k_{icd/q}$ representing the integrator state, the proportional and integral gain of the PI controller.

Grid side converter (GSC): The q-axis current reference for a VSC terminal connected to a strong grid is provided by a reactive power controller.

$$i^*_{l,q,g} = k_{pcq,g}\left(q^*_g - q_g\right) + k_{icq,g}\chi_{q,g} \tag{2.49}$$

The d-axis current reference is provided by one of the various DC voltage droop controllers. The different types have been identified and categorized in section 4.4. They are shown in Fig. 2.12. The block diagrams of the corresponding droop controller indicate that these droop controllers differ with respect to (i) power or current based droop implementations, (ii) the choice of the second variable (besides DC voltage): current / power measured on AC or DC side and (iii) the choice on which variable the droop gain k_{droop} is applied, i.e. which variable is controlled in the first and which in the second loop.

The corresponding equations of those controllers are given in (2.51)-(2.58) in the order of CS 1 to 8.

$$\text{CS1: } i^*_{l,d,g} = k_{pcd,g}\left(\frac{v_{dc} - v^*_{dc}}{k_{droop}} + i^*_{dc} - i_{dc}\right) \tag{2.50}$$

$$+ k_{icd,g}\chi_{d,g} \tag{2.51}$$

$$\text{CS2: } i^*_{l,d,g} = \frac{v_{dc} - v^*_{dc}}{k_{droop}} + i^*_{ac} \tag{2.52}$$

$$\text{CS3: } i^*_{l,d,g} = k_{pcd,g}\left((i^*_{dc} - i_{dc}) \cdot k_{droop} + v_{dc} - v^*_{dc}\right) \tag{2.53}$$

$$+ k_{icd,g}\chi_{d,g}$$

$$\text{CS4: } i^*_{l,d,g} = k_{pcd,g}\left((i^*_{ac} - i_{ac}) \cdot k_{droop} + v_{dc} - v^*_{dc}\right) \tag{2.54}$$

$$+ k_{icd,g}\chi_{d,g}$$

$$\text{CS5: } i^*_{l,d,g} = k_{pcd,g}\left(\frac{v_{dc} - v^*_{dc}}{k_{droop}} + p^*_{dc} - p_{dc}\right) \tag{2.55}$$

$$+ k_{icd,g}\chi_{d,g}$$

$$\text{CS6: } i^*_{l,d,g} = k_{pcd,g}\left(\frac{v_{dc} - v^*_{dc}}{k_{droop}} + p^*_{ac} - p_{ac}\right) \tag{2.56}$$

$$+ k_{icd,g}\chi_{d,g}$$

$$\text{CS7: } i^*_{l,d,g} = k_{pcd,g}\left((p^*_{dc} - p_{dc}) \cdot k_{droop} + v_{dc} - v^*_{dc}\right) + k_{icd,g}\chi_{d,g} \tag{2.57}$$

$$\text{CS8: } i^*_{l,d,g} = k_{pcd,g}\left((p^*_{ac} - p_{ac}) \cdot k_{droop} + v_{dc} - v^*_{dc}\right) + k_{icd,g}\chi_{d,g} \tag{2.58}$$

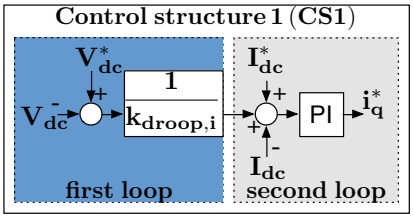

(a) CS1(V_{dc}-I_{dc})- [55, 64–69]

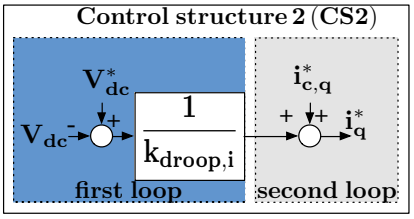

(b) CS2 (V_{dc}-I_{ac}) - [70, 71].

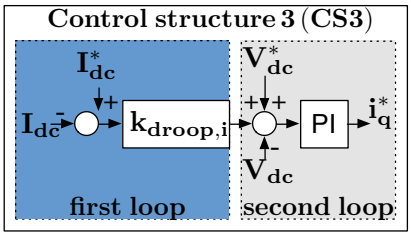

(c) CS3 (I_{dc}-V_{dc}) - [72–74].

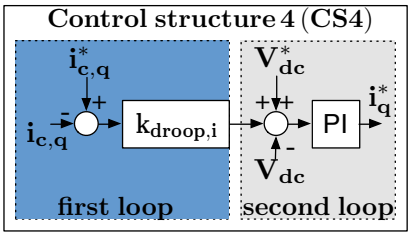

(d) CS4 (I_{ac}-V_{dc}) - [75].

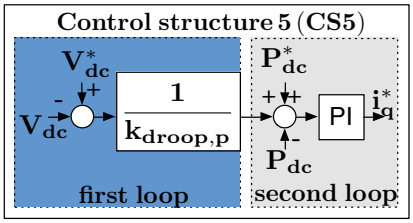

(e) CS5 (V_{dc}-P_{dc}) - [76–79].

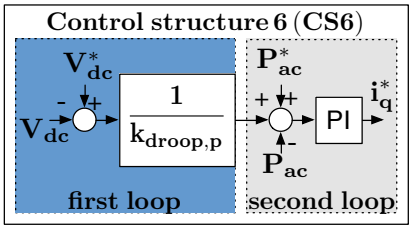

(f) CS6 (V_{dc}-P_{ac}) - [79].

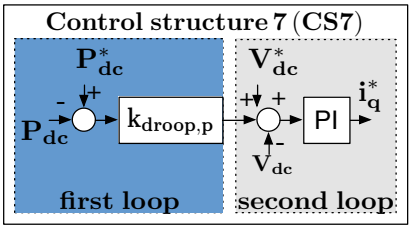

(g) CS7 (P_{dc}-V_{dc}) - [80, 81].

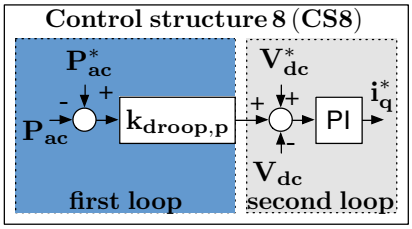

(h) CS8 (P_{ac}-V_{dc}) - [81].

Figure 2.12: Analyzed DC voltage droop control structures. Source: [**Pub. C**].

State Space Model

By combining the equations presented in the previous subsections, a MT-HVDC grid can be modelled in a state space representation. The order of the model depends on the number of terminals within the MT-HVDC, the chosen outer control structures, the number of DC cables and the chosen DC cable model type. The state vector of each VSC is given as $\mathbf{x}_{VSC,i}=[v_{o,d}\ v_{o,q}\ i_{l,d}\ i_{l,q}\ \gamma_d\ \gamma_q\ \chi_d\ \chi_q\ i_{g,d}\ i_{g,q}\ \phi_d\ \phi_q\ v_{pll,d}\ v_{pll,q}\ \epsilon_{PLL}\ \Delta\Theta\ v_{dc}]^T$, the state vector of each dc cable is given as $\mathbf{x}_{dc,pi,i}=[i_{dc}]^T$ for the classical π model and $\mathbf{x}_{dc,freq,i}=[i_{dc,1}\ i_{dc,2}\ i_{dc,3}]^T$ for the frequency dependent π model respectively.

2.7.3 Mathematical Model of a Wind Farm with Doubly-Fed Induction Generators

This section presents a mathematical model of a DFIG as proposed in [7, 82–85]. The model neglects the stator transients and uses a one-mass model of the drive train [82]. It is visualized in Fig. 2.13. Given that a wind farm model consisting of full order models of every single wind turbine is computationally extremely demanding, it is common practice in power system stability studies to use simplified equivalent models. Thus, an aggregated model of a single DFIG wind turbine is used to represent a wind farm following the approach proposed in [86]. A wind farm based on DFIGs is used because this type of generator has one of the highest market shares resulting in a high frequency of occurrence in existing wind farms [87, 88].

The one-mass drive train model is given in (2.59) and the induction generator neglecting stator transients is given in (2.60)-(2.61) while the control loops of the back-to-back converter are given in (2.62)-(2.65). Corresponding algebraic equations are given in (2.66)-(2.69). The grid side converter

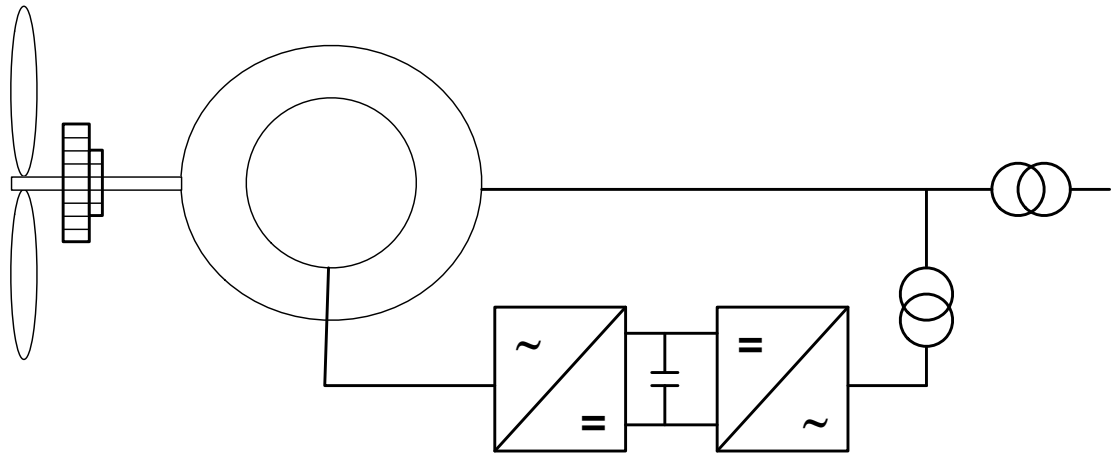

Figure 2.13: Double-Fed Induction Generator. Adapted from: [7].

is assumed to operate at unity power factor and the dc-link capacitor dynamics are neglected.

$$\frac{ds_r}{dt} = \frac{t_m - t_e}{2h_{tot}} \tag{2.59}$$

$$\frac{de_d^{'}}{dt} = s_r\omega_s e_q^{'} - \omega_s \frac{l_m}{l_{rr}} v_{qr} - \frac{1}{t_0^{'}}(e_d^{'} + (x_s - x_s^{'})i_{qs}) \tag{2.60}$$

$$\frac{de_q^{'}}{dt} = -s_r\omega_s e_d^{'} + \omega_s \frac{l_m}{l_{rr}} v_{dr} - \frac{1}{t_0^{'}}(e_q^{'} - (x_s - x_s^{'})i_{ds}) \tag{2.61}$$

$$\frac{dx_1}{dt} = p_{ref} - p_s \tag{2.62}$$

$$\frac{dx_2}{dt} = k_{p1}(p_{ref} - p_s) + k_{i1}x_1 - i_{qr} \tag{2.63}$$

$$\frac{dx_3}{dt} = q_{ref} - q_s \tag{2.64}$$

$$\frac{dx_4}{dt} = k_{p3}(q_{ref} - q_s) + k_{i3}x_3 - i_{dr} \tag{2.65}$$

$$t_m = ((k_0 * ((1 - s_r)^3)/\omega_s) \tag{2.66}$$

$$t_e = \frac{p_s}{\omega_s} \tag{2.67}$$

$$v_{qr} = k_{p2}(k_{p1}(p_{ref} - p_s) + k_{i1}x_1 - i_{qr}) + k_{i2}x_2 + s_r\omega_s l_m i_{ds} + s_r\omega_s l_{rr} i_{qr} \tag{2.68}$$

$$v_{dr} = k_{p2}(k_{p3}(q_{ref} - q_s) + k_{i3}x_3 - i_{dr}) + k_{i2}x_4 - s_r\omega_s l_m i_{qs} - s_r\omega_s l_{rr} i_{dr} \tag{2.69}$$

Combining these equations we obtain a state space model with the states $x_{DFIG} = [s_r, e_d, e_q, x_1, x_2, x_3, x_4]^T$.

The equivalent wind farm model including the calculated equivalent impedance of the collector system and the aggregated model of wind turbines is obtained following the approach proposed in [8, 89, 90] and visualized in Fig. 2.14. It is represented by the same complete model as the individual wind turbines. Moreover, with this aggregated model we assume an equivalent wind at every wind turbine of the wind farm. This is a simplified but appropriate assumption for large-scale power system steady-state analysis as the authors showed in [89]. For a wind farm consisting of N_{WT} equivalent wind turbines, equivalent parameters can be expressed as follows:

$$S_{eq} = \sum_{j=1}^{N_{WT}} S_j = N_{WT} \cdot S_j \tag{2.70}$$

$$Q_{ref,eq} = \sum_{j=1}^{N_{WT}} Q_{ref,j} \tag{2.71}$$

The equivalent impedance is calculated in that way that the short-circuit impedance of the equivalent wind farm must be equal to the short-circuit impedance of the complete wind farm [8]:

$$Z_e = Z_{awt} - \frac{Z_{wt}}{N_{WT}} \tag{2.72}$$

where Z_{awt} is the equivalent impedance for the common network of the aggregated wind turbines and Z_{wt} is the wind turbine impedance.

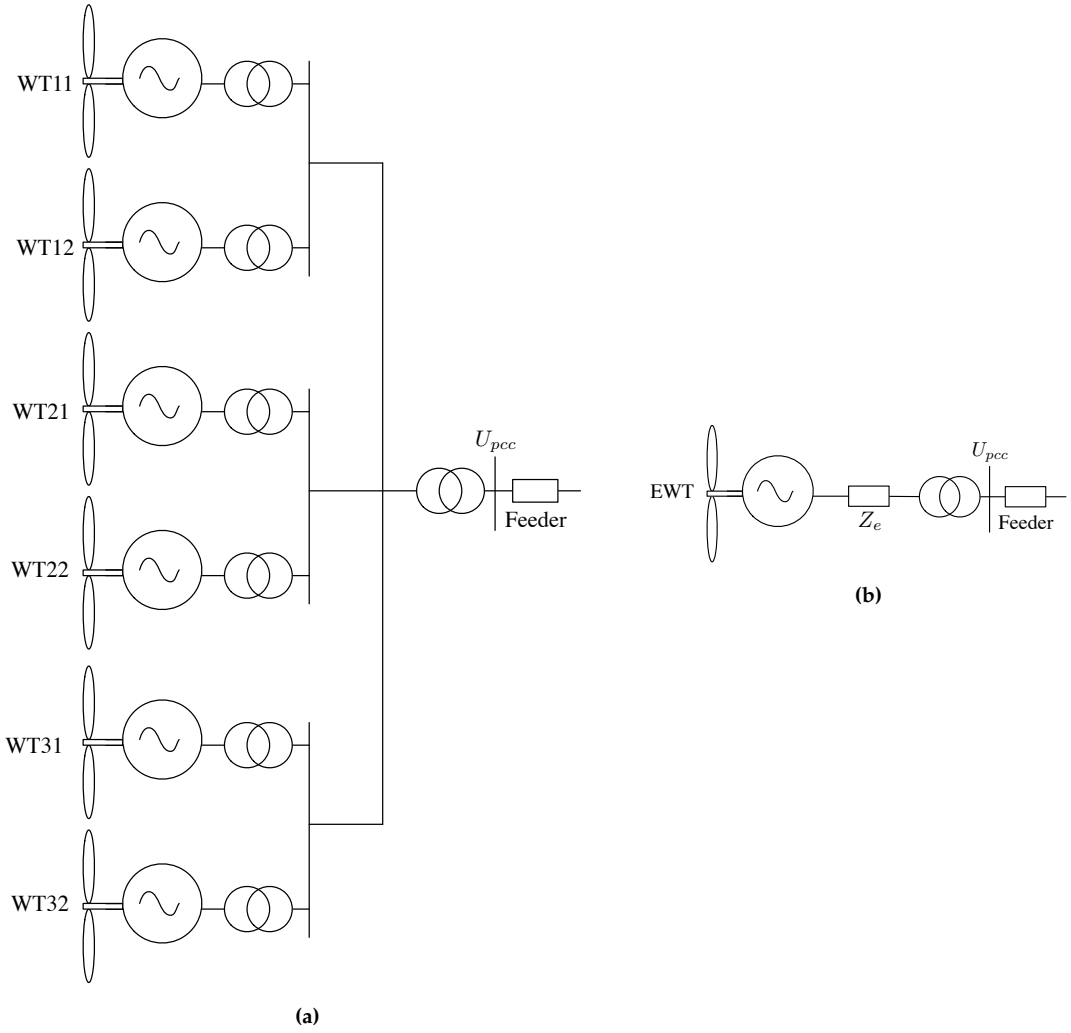

Figure 2.14: Visualization of a (a) complete wind farm and (b) an equivalent wind farm. Adapted from: [8]

.

2.7.4 System Linearization

A set of nonlinear equations describing a dynamic system, such as a power system, can be expressed in vector matrix notations as [52]:

$$\dot{\mathbf{x}} = \mathbf{f}(\mathbf{x}, \mathbf{u}) \tag{2.73}$$

$$\mathbf{y} = \mathbf{g}(\mathbf{x}, \mathbf{u}) \tag{2.74}$$

with $\mathbf{x}$ and $\mathbf{u}$ representing the state, respectively input vector.

Given an equilibrium point of this system, we have

$$\dot{\mathbf{x}}_\mathbf{0} = \mathbf{f}(\mathbf{x}_\mathbf{0}, \mathbf{u}_\mathbf{0}) = \mathbf{0}. \tag{2.75}$$

For small perturbations from the equilibrium the nonlinear functions $\mathbf{f}(\mathbf{x}, \mathbf{u})$ can be expressed as

$$\begin{aligned}\dot{\mathbf{x}}_\mathbf{i} = \dot{\mathbf{x}}_{\mathbf{i0}} + \mathbf{\Delta}\dot{\mathbf{x}}_\mathbf{i} &= f_i[(\mathbf{x}_{\mathbf{i0}} + \mathbf{\Delta}\mathbf{x}_\mathbf{i}), (\mathbf{u}_{\mathbf{i0}} + \mathbf{\Delta}\mathbf{u}_\mathbf{i})] \\ &= f_i(\mathbf{x_0}, \mathbf{u_0}) + \frac{d\mathbf{f}_i}{dx_1}\Delta x_1 + \ldots + \frac{d\mathbf{f}_i}{dx_n}\Delta x_n \\ &\quad + \frac{d\mathbf{f}_i}{du_1}\Delta u_1 + \ldots + \frac{d\mathbf{f}_i}{du_r}\Delta u_r.\end{aligned} \tag{2.76}$$

$$\begin{aligned}\mathbf{y}_\mathbf{j} = \mathbf{y}_{\mathbf{j0}} + \mathbf{\Delta}\mathbf{y}_\mathbf{j} &= g_j[(\mathbf{x}_{\mathbf{j0}} + \mathbf{\Delta}\mathbf{x}_\mathbf{j}), (\mathbf{u}_{\mathbf{j0}} + \mathbf{\Delta}\mathbf{u}_\mathbf{j})] \\ &= g_j(\mathbf{x_0}, \mathbf{u_0}) + \frac{d\mathbf{g}_j}{dx_1}\Delta x_1 + \ldots + \frac{d\mathbf{g}_j}{dx_n}\Delta x_n \\ &\quad + \frac{d\mathbf{g}_j}{du_1}\Delta u_1 + \ldots + \frac{d\mathbf{g}_j}{du_r}\Delta u_r.\end{aligned} \tag{2.77}$$

With $\dot{\mathbf{x}}_{\mathbf{i0}} = \mathbf{f}_\mathbf{i}(\mathbf{x}_0, \mathbf{u}_0)$ and $\mathbf{y}_{\mathbf{j0}} = \mathbf{g}_\mathbf{j}(\mathbf{x}_0, \mathbf{u}_0)$, we obtain

$$\mathbf{\Delta}\dot{\mathbf{x}}_\mathbf{i} = \frac{d\mathbf{f}_i}{dx_1}\Delta x_1 + \ldots + \frac{d\mathbf{f}_i}{dx_n}\Delta x_n + \frac{d\mathbf{f}_i}{du_1}\Delta u_1 + \ldots + \frac{d\mathbf{f}_i}{du_r}\Delta u_r \tag{2.78}$$

$$\mathbf{\Delta}\mathbf{y}_\mathbf{j} = \frac{d\mathbf{g}_j}{dx_1}\Delta x_1 + \ldots + \frac{d\mathbf{g}_j}{dx_m}\Delta x_m + \frac{d\mathbf{g}_j}{du_1}\Delta u_1 + \ldots + \frac{d\mathbf{g}_j}{du_r}\Delta u_r \tag{2.79}$$

with $i = 1, \ldots, n$ and $j = 1, \ldots, m$. Thus, the linearized forms of (2.73)-(2.74) are

$$\mathbf{\Delta}\dot{\mathbf{x}} = \mathbf{A}\mathbf{\Delta}\mathbf{x} + \mathbf{B}\mathbf{\Delta}\mathbf{u} \tag{2.80}$$

$$\mathbf{\Delta}\mathbf{y} = \mathbf{C}\mathbf{\Delta}\mathbf{x} + \mathbf{D}\mathbf{\Delta}\mathbf{u} \tag{2.81}$$

with $\mathbf{A} \in \mathbb{R}^n \times \mathbb{R}^n$, $\mathbf{B} \in \mathbb{R}^n \times \mathbb{R}^r$, $\mathbf{C} \in \mathbb{R}^m \times \mathbb{R}^m$ and $\mathbf{D} \in \mathbb{R}^m \times \mathbb{R}^r$ the known coefficient matrices of the steady state linearization around $\mathbf{x_0} \in \mathbb{R}^n$.

Linearization process of the multi-machine model

For a detailed description of the linearization process a multi-machine model, the interested reader is referred to [50, 91]. Here, we will briefly summarize the main steps starting from the matrix notation

$$\dot{\mathbf{X}} = f(\mathbf{X}, \mathbf{Y}, \mathbf{U}) \tag{2.82}$$

$$\mathbf{0} = g_1(\mathbf{X}, \mathbf{Y}) \tag{2.83}$$

$$\mathbf{0} = g_2(\mathbf{X}, \mathbf{Y}) \tag{2.84}$$

with the state vector $\mathbf{X} = [\mathbf{X}_1^T\ \mathbf{X}_2^T\ \ldots \mathbf{X}_{N_G}^T]^T$ where $\mathbf{X_i} = [\delta_i\ \omega_i\ e'_{g,q_i}\ e'_{g,d_i}\ \psi''_{d_i}\ \psi''_{q_i}\ v_{h_i}\ v_{R_i}\ r_{f_i}\ e_{fd_i}\ v_{1_i}]^T$. $\mathbf{Y} = [\mathbf{Y_C}^T \mathbf{Y_B}^T]^T = [\theta_1\ v_1\ \ldots v_{N_G} \ldots \theta_2 \ldots \theta_{N_{Bus}}\ v_{N_G+1}\ \ldots v_{N_{Bus}}]^T$ is the set of algebraic variables with $\mathbf{Y_B}^T$ being the set of load-flow variables and $\mathbf{Y_C}^T$ representing the remaining algebraic variables. The input vector is defined as $\mathbf{U} = [\mathbf{U}_1^T\ \mathbf{U}_2^T\ \ldots \mathbf{U}_{N_G}^T]^T$ with $\mathbf{U_i} = [v_{ref_i}\ t_{M_i}]^T$. While $\mathbf{f}(\mathbf{X}, \mathbf{Y}, \mathbf{U})$ denotes the $11 \cdot N_G$ differential algebraic equations of the generators, $\mathbf{g}_1(\mathbf{X}, \mathbf{Y})$ denotes the $2 \cdot N_G$ algebraic network equations corresponding to the buses where the generators are connected to. $\mathbf{g}_2(\mathbf{X}, \mathbf{Y})$ denotes the $2 \cdot (N_{Bus} - N_G)$ algebraic network equations corresponding to the remaining buses.

With $\mathbf{A} = \frac{d\mathbf{f}}{d\mathbf{X}}$, $\mathbf{B_1} = \frac{d\mathbf{f}}{d\mathbf{Y_C}}$, $\mathbf{B_2} = \frac{d\mathbf{f}}{d\mathbf{Y_B}}$, $\mathbf{E} = \frac{d\mathbf{f}}{d\mathbf{U}}$, $\mathbf{C_1} = \frac{d\mathbf{g}_1}{d\mathbf{X}}$, $\mathbf{D_{11}} = \frac{d\mathbf{g}_1}{d\mathbf{Y_C}}$, $\mathbf{D_{12}} = \frac{d\mathbf{g}_1}{d\mathbf{Y_B}}$, $\mathbf{C_2} = \frac{d\mathbf{g}_2}{d\mathbf{X}}$, $\mathbf{D_{21}} = \frac{d\mathbf{g}_2}{d\mathbf{Y_C}}$, $\mathbf{D_{22}} = \frac{d\mathbf{g}_2}{d\mathbf{Y_B}}$ the notation of the linearized system is given as:

$$\begin{bmatrix}\mathbf{\Delta}\dot{\mathbf{X}} \\ \mathbf{0} \\ \mathbf{0}\end{bmatrix} = \begin{bmatrix}\mathbf{A}\ \mathbf{B_1}\ \mathbf{B_2} \\ \mathbf{C_1}\mathbf{D_{11}}\mathbf{D_{12}} \\ \mathbf{C_2}\mathbf{D_{21}}\mathbf{D_{22}}\end{bmatrix} \begin{bmatrix}\mathbf{\Delta X} \\ \mathbf{\Delta Y_C} \\ \mathbf{\Delta Y_B}\end{bmatrix} + \begin{bmatrix}\mathbf{E} \\ 0 \\ 0\end{bmatrix} \mathbf{\Delta U} \tag{2.85}$$

The system matrix A_{sys} with dimension $11 \cdot N_G \times 11 \cdot N_G$ fulfilling the equation

$$\mathbf{\Delta \dot{X}} = \mathbf{A}_{sys}\mathbf{\Delta X} + \mathbf{E}\mathbf{\Delta U} \tag{2.86}$$

can be obtained as:

$$\mathbf{A}_{sys} = \mathbf{A} - [\mathbf{B}_1\ \mathbf{B}_2][\mathbf{J}_{AE}]^{-1}\begin{bmatrix}\mathbf{C_1}\\ \mathbf{C_2}\end{bmatrix} \tag{2.87}$$

with

$$[\mathbf{J}_{AE}] \quad = \quad \begin{bmatrix}\mathbf{D_{11}} & \mathbf{D_{12}}\\ \mathbf{D_{21}} & \mathbf{D_{22}}\end{bmatrix} \tag{2.88}$$

representing the network algebraic Jacobian.

In this work, the small-signal models are derived symbolically until equation (2.7.4), due to the fact that the symbolic inversion of the Jacobian given in (2.88) is computationally extremely demanding, if not impossible (for larger systems). The symbolic derivation enables us to initialize the model for every possible combination of load and generation using Matpower 6.0 [49].

Small Signal Stability

Small signal stability or small disturbance stability refers to the system's ability to maintain synchronism and steady state voltages under small disturbances [1]. It is based on Lyapunov's linearized method [52] stating that a linear model $\mathbf{A}$ is asymptotically stable if all eigenvalues λ of $\mathbf{A}$ given by (2.89) have negative real parts.

$$(\mathbf{A} - \lambda\mathbf{I})\mathbf{\Phi} = 0 \tag{2.89}$$

Each eigenvalue $\lambda_i = a_i + ib_i$ is commonly associated with a mode providing valuable information on the system behavior. The damping of the i^{th} mode is defined as:

$$\zeta_i = \frac{-a_i}{\sqrt{a_i^2 + b_i^2}} \tag{2.90}$$

Participation Factors

The participation factors Γ_{ki} measuring the relative participation of the k-th state variable in the i-th mode are determined by:

$$\mathbf{\Gamma} = \{\Gamma_{ki}\} = \{\Phi_{ki}l_{ik}\} \tag{2.91}$$

where $\mathbf{\Phi}_{ki}$ and $\mathbf{l}_{ki}$ are the k-th entry of the i-th right ($\mathbf{\Phi}_i \in \mathbb{R}^{n_t}$) respective left ($\mathbf{l}_i \in \mathbb{R}^{n_t}$) eigenvectors of $\mathbf{A}$. The normalized participation factors are defined as $\Gamma^n_{ki} = \frac{\Gamma_{ki}}{\|\mathbf{\Gamma}_i\|}$. $\mathbf{\Gamma}_i \in \mathbb{R}^{n_t}$ contains the participation factors associated with mode i for all system states, whereas $\|\cdot\|$ denotes the L_1-norm [52, 92].

2.7.5 Modeling of Contingencies

As the following chapters will present studies considering contingencies, we will briefly discuss how these are reflected by the small-signal model. In case of contingencies, the small-signal model is adjusted by explicitly incorporating the outage of a single component. Thus, the multi-machine

model of the base case, i.e. without any contingency, is adapted for every credible contingency resulting in $|\Gamma| + 1$ different small signal models. Variable Γ represents the set of considered contingencies.

While line outages do not require explicit changes of the small-signal model, i.e. the use of the base case in combination with the changed admittance matrix is sufficient to represent the outage, a bus outage requires an adaption of the matrices $\mathbf{A}$, $\mathbf{B}$, $\mathbf{C}$, $\mathbf{D}$. In particular, the rows and columns of the matrices $\mathbf{A}$, $\mathbf{B}$, $\mathbf{C}$, $\mathbf{D}$ corresponding to the specific bus need to be deleted.

In order to evaluate the N-1 security of the system, the small signal model is initialized for all Ψ operating points with a power flow of the base case. Then, the small signal model is adjusted for the n_{cont} different contingencies and the adjusted small signal models are initialized with an corresponding ac power flow reflecting the post-disturbance system state of the corresponding contingency. Then, the small signal stability is analyzed. The choice of the slack bus may differ between the contingencies considered. Ideally the distributed slack buses should be chosen according to the location of the primary reserves which balance the power mismatch in case of the specific contingency, based on the experience of the TSO.

CHAPTER 3

Development of Grid Expansion Scenarios for the European Power System: Scalability Analysis of AC and HVDC Technologies

*This chapter describes the work performed within the EU-project BEST PATHS which has been published in [**Pub. G**]. As part of the scalability assessment of the BEST PATHS technologies, grid expansion scenarios for the European power system were developed analyzing the performance boundaries of the different technologies developed within the project in terms of their RES integration potential. This chapter is structured as follows: After a brief introduction and literature review, the different technologies developed within the project are introduced and the contributions of this work are highlighted. Then, the development of the Business-as-Usual 2030 scenario is described, followed by the different methodologies used to determine the performance boundaries of the different technologies. In particular, we consider three different methodologies to determine the different transmission upgrade scenarios: (i) only technologies for repowering AC transmission lines (ii) extending the existing grid with DC transmission technology only and (iii) a combined approach. Finally, a case study is presented.*

3.1 Background

Following the goal of the European Union to cut greenhouse gas emission by $80-95\,\%$ by 2050, significant changes in the energy system can be expected. Besides energy efficiency, the already visible shift towards renewable energy sources will be boosted demanding an almost emission free electricity production in 2050 [93]. In Europe, vast potential of wind energy is located in the North Sea region [94] due to the comparable high average wind speed. Due to higher capacity factors of wind farms located offshore ($40-50[\%]$ (offshore) vs $20-30[\%]$ (onshore) [95, 96]) and the available onshore locations being restricted by limited social acceptance [97], more and more offshore wind farms are being built [98]. The increasing generation capacity in the North sea region, far away from traditional load centers, e.g. in the south/south-west of Germany, requires also additional transmission capacity, i.e. new transmission corridors, between load and generation enabling to harness this energy. Considering the forecasted electrification of sectors such as transport and heating [22] the power system will not only face more variability and uncertainty of the generation but also more variability and uncertainty of the load. The limited acceptance of the European citizens for new transmission lines demands a higher flexibility of the power system and a better utilization of existing assets. However, additional grid capacity will be required even with an optimal use of the existing grid [17]. Recent project developments in Germany show higher

public acceptance to new transmission corridors with an as small footprint as possible resulting in more cost intensive underground solutions [23] which for long distances are more suitable for HVDC technology [17].

ENTSO-E has recognized that significant transmission upgrades and expansions will be required to strengthen the power system and to keep pace with the climate goals of the European Union. ENTSO-E started tackling the challenge through investments in new transmission projects developed within the framework of the Ten Year Network Development Plan (TYNDP) [22], which provides the most up to date reference for upcoming transmission investments in Europe [**Pub. G**]. This analysis requires a holistic approach taking into account the entire European transmission grid to evaluate the demand for grid reinforcements or a grid expansion considering the current and projected power flows and limitations of the system. Moreover, the analysis has to assess which available technology is the most suitable for the specific application considering the specific conditions.

Thus, the EU-project BEST PATHS[1] project was funded to develop novel transmission technologies to increase the pan-European transmission network capacity and electric system flexibility. The investigated technologies comprise Dynamic Line Rating (DLR) and High Temperature Low Sag (HTLS) conductors, superconducting DC cables and the upgrade of existing and the building of new DC lines (overhead lines, underground or submarine cables) to even multi-terminal HVDC grids. The different technologies developed within the five demonstrations (DEMOs) are introduced in Section 3.3.

The focus of this chapter is to assess the scalability of the novel transmission technologies developed within the BEST PATHS project and to analyze how they can contribute to higher levels of renewable energy integration, social welfare and security of supply. Facilitating the assessment of the performance boundaries of the different technologies, the analysis is split into a DC upgrade and an AC upgrade scenario. Based on this assessment, policy recommendations are developed.

3.2 Literature Review

Although, the focus of our work does not lie on investment cost optimality nor on an overall optimal transmission expansion planning but on determining the performance *boundaries* of the developed technologies for a given generation and load development scenario, we still need to determine the optimal grid expansion / grid reinforcement using the specific technology. Thus, this work still lies in the domain of Transmission Expansion Planning (TEP). TEP is a large-scale, complex and nonlinear combinatorial problem of mixed integer nature which increases exponentially with system size [99]. The objective is to minimize investment and operational cost while satisfying the increasing demand and operational constraints such as generation output power or transfer limits of transmission lines. As one of the most important issues in power system planning, TEP has been widely investigated as a non-detachable part of long-term power system planning [100]. Different TEP problem formulations can be distinguished by several aspects such as the modeling (dc vs ac), the solving method (optimization vs heuristic) or considered constraints. The interested reader is referred to [99–101] for a comprehensive literature review of existing methods. Here, we concentrate on approaches focusing on large-scale TEP. Given the model size ($\approx$ 8000 nodes) and

[1] BEST PATHS: "BEyond State-of-the-art Technologies for rePowering Ac corridors and multi-Terminal HVDC Systems", www.bestpaths-project.eu, funded by the European Union

the available simulation data (i.e. hourly demand and RES production profiles for a whole year), dc power flow modeling is the only viable option considering computational time.

Moreover, in [102], the authors emphasize that the application of optimization to solve large-scale TEP is often unmanageable even with high-performance computing tools and that TSOs often resort to manual or partially manual approaches that rely on their intuition. As part of the e-HIGHWAYS 2050 project [103], they propose a *reduce-expand-develop* methodology which as a first step consists of condensing most information of the system, i.e. among other things this includes network reduction as well as a specific snapshot selection. As a second step, they optimize the grid expansion at a zonal level before optimizing the grid expansion as a final step at a nodal level. In their case study, however, the most detailed network model used consists of 1025 nodes, i.e. $\approx \frac{1}{8}$ of our system size, demanding a computational time of $37\,\mathrm{h}$.

In [104], the authors propose a decomposition framework for solving large-scale transmission capacity expansion planning with security constraints under uncertainties. They present the capability of their approach on a reduced ERCOT system with 3179 buses solving the problem in around 2.8 days considering 10 scenarios.

An example for TEP in the context of cross-national regional planning is the TYNDP developed by ENTSO-E every two years. It is an analysis of the electricity grid development in the coming ten years considering the national TEPs. Grid bottlenecks are identified and used as candidates for grid reinforcements. These candidates (and additional candidates submitted by third parties) are analyzed in an extensive evaluation according to several criteria. However, the reinforcements are analyzed individually and no optimization is performed [101].

3.3 Technologies developed within the BEST PATHS Project

The technologies developed within the BEST PATHS project are focusing either on repowering AC transmission lines or on DC technology. Here, we briefly introduce the technologies:

3.3.1 AC Technologies

The technologies for repowering AC transmission lines developed within BEST PATHS focus on HTLS transmission lines and DLR, both of which can increase the transmission capacity of existing lines.

As we focus on the performance boundaries of these technologies, we sent out questionnaires to the demo leaders of the BEST PATHS technologies to collect data on the capabilities of these technologies. The questionnaires revealed that DLR and HTLS can increase the transmission capacity of a line by up to 20% and 100%, respectively.

3.3.2 DC Technolgies

Four of the five demonstrations within the BestPaths project focus on DC technology:

- DEMO 1 aims on reducing risks of HVDC links connecting offshore wind farms.
- DEMO 2 focuses on multi-vendor interoperability.

- DEMO 3 investigates potential upgrade scenarios of multi-terminal HVDC links with the specific example of the SACOI link.
- DEMO 5 works on a prototype scale validation of the technical feasibility of integrating DC superconducting cable links within an AC meshed network.

We collected DEMO 1-3 within the DC scalability assessment, because given the aim of the study, as well as the size of the test network, a clear separation between the demonstrators becomes infeasible. In fact, the combined success of all three demonstrators is a prerequisite for our assumption of being able to up-scale single HVDC links to an pan-European network.

The superconducting cables developed within DEMO 5 are not considered in this study given the limited length of the cables and their area of application being dense populated areas, which are represented as single nodes in the high-resolution European transmission grid model. Thus, the following analysis also highlights the importance of multi-vendor interoperability for future grid development plans, as it is seen as a prerequisite for the development of a pan-European network. Therefore, we will investigate potential multi-vendor interoperability issues in the next chapter.

3.4 Contribution

In contrast to existing work, this work determines the performance *boundaries* of the technologies developed within BEST PATHS for a given generation and load development scenario. That means, we developed methodologies to evaluate the maximum achievable RES penetration with the different technologies for a given generation and load development scenario. We collected the different technologies developed within BEST PATHS in technologies aiming at repowering existing AC transmission lines and in DC technologies. For each of these technologies we determine the performance *boundaries* as visualized in Fig. 3.1.

Hence, this work contributes with (i) a high-level analysis of a large-scale deployment of the technologies developed within BEST PATHS in the pan-European transmission network. Focusing on the capability of each BEST PATHS technology and not investment cost-optimality, (ii) the performance boundaries of each technology are identified when applied on a pan-European scale as visualized in Fig. 3.1. By using a 8,000 node model of the European system reflecting the expected system topology of 2030, hourly wind, solar and generation profiles, and adopting the generation capacity and demand projection of the EUCO30 scenario of the European Commission [105],

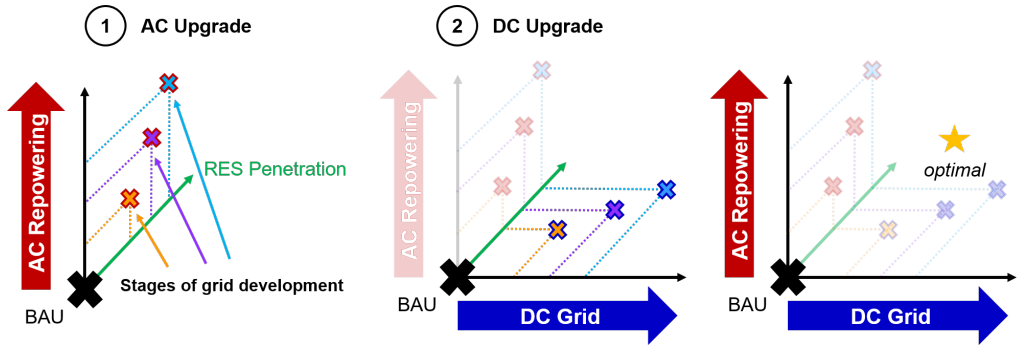

Figure 3.1: Schematic illustration of how the scalability assessment provides the bounds of the future European grid development. Source: **[Pub. G]**.

(iii) a detailed picture of transmission bottlenecks in the year 2030 is obtained. (iv) A rigorous analytical approach for the identification of new HVDC corridors is presented, which guarantees the maximum performance of each newly placed dc line, in term of increasing RES penetration, reducing RES curtailment and Load Shedding (LS), and decreasing generation. Moreover, (v) the dc grid expansion scenario is compared to a scenario focusing on the reinforcement of the ac system and a combined upgrade scenario, i.e. dc grid expansion and ac reinforcement. Based on this assessment, (vi) policy recommendations are developed.

3.5 Development of the Business-as-Usual 2030 Scenario

This thesis uses the data set developed within the framework of the deliverable “13.2 Definition and Building of BestPaths Scenario" led by CIRCE. The deliverable describes the development of the Business-as-Usual (BaU) data set using a combination of a grid model provided by the European Network of Transmission System Operators (ENTSO-E), the ten year network development plan 2016 (TYNDP) [106] and data from the e-Highway 2050 project [103]. The load and generation data for 2016 are based on ENTSO-E’s statistical factsheet [107] and ENTSO-E’s power statistic data base [108], while the projections for 2030 are based on the EUCO30 scenario developed by the European Commission [105]. The model development is out of the scope of this thesis, therefore the interested reader is referred to the deliverable for more details. All results obtained from the simulations and conclusions drawn from them are subject to these input data and dependent on their validity.

3.5.1 Adjusting Load and Generation Data to ENTSO-E Data for 2016

Due to the inclusion of the TYNDP projects, the data set already contains the transmission system data for 2030, while the load and generation data still corresponds to the year 2016. In order to fully represent a 2030 scenario, this data needs to be adjusted to consider the nuclear phase-out in Germany [109] as well as the projected increase in electricity consumption and installed capacity of renewable energy sources (RES) [22].

Furthermore, the data set developed within the framework of deliverable 13.2 consists of the network model for voltage levels 220 kV and above. Thus, the connected loads at the transmission buses represent net demand at the different nodes and already consider (RES) generation at lower voltage levels in the form of lower or negative demand. In Germany for example, 96 % of the wind generation [110] and almost 100 % of the PV generation [111] is connected to the distribution grid, which means that this share of RES generation is not visible in the data set and only represented through lower net demand at the nodes. This also entails that the installed generation capacities in the data set do not correspond to the official values provided by ENTSO-E [107]. However, in order to be able to upscale the load to projection levels for the year 2030, a more detailed differentiation is required. Otherwise, the upscaling of RES and load could not consider the generation on the distribution level.

To this end, this work takes the grid provided by CIRCE as basis and considers the RES sources in the data set as the share of RES connected to the transmission system. Then, using the power statistics database [108] and the ENTSO-E statistical factsheet [107], we derive the share of installed generation capacity on the transmission level by comparing the currently installed generation capacity in the original data set (for each type of generation separately) with the actual total installed capacity (given in [107]) on a per country basis. This gives us an estimate of how much

energy is generated by the different generation types on the transmission and distribution level, respectively, which in turn allows us to determine the share of RES production in the net demand. Note that we do not assume any conventional generation on the distribution level but adjust the installed capacities of conventional generators on the transmission level (and thus, in the data set) to fully reflect the total installed capacity of conventional generation for each country individually. The data on electric energy generation and consumption per country are obtained from ENTSO-E's monthly domestic values reports [108]. Combined with the hourly RES profiles given in CIRCE's data set, the energy E generated by the different RES types x on the distribution level (E_x^{DL}), which is 'hidden' in the net demand, can be computed per country as given in (3.1)-(3.2).

$$E_{x,country}^{CIRCE} = \sum_{h=1}^{8760} \sum_{i=1}^{N_{country}} E_{g_{i,x},country}^{2016}(h), \tag{3.1}$$

$$E_{x,country}^{DL} = E_{x,country}^{ENTSOE} - E_{x,country}^{CIRCE}, \tag{3.2}$$

$$x \in \Psi = \{\text{wind, solar, geo-thermal, hydro, bio fuel, other RES}\},$$

where $N_{country}$ represents the number of nodes in the corresponding country. The net demand of the entire country $E_{netdemand,country}$ is calculated by fitting the wind $E_{wind,country}^{DL}$ and solar energy $E_{PV,country}^{DL}$ on the distribution level to wind and solar generation profiles taken, if available, from the CIRCE database or from [112–114], otherwise. If the data set already contains more than one profile for a specific country, these profiles are interpolated and then fitted to the required energy level:

$$E_{g_x,DL,country}^{2016,fitted}(h) = E_{g_x,country}^{2016}(h) \cdot \frac{E_{x,country}^{DL}}{\sum_{h=1}^{8760} E_{g_x,country}^{2016}(h)} \tag{3.3}$$

Generated energy from other RES sources in the distribution level (geothermal, hydro, bio-fuel, renewable waste, others [108]) is uniformly distributed over the whole year due to missing generation profiles. The hourly net demand curves of the different countries $E_{netdemand,country}(h)$ can be computed by subtracting the different hourly distribution level profiles from the hourly electricity consumption profile obtained from ENTSO-E's power statistic data base $E_{consumed,country}(h)$:

$$E_{netdemand,country}(h) = E_{consumed,country}(h) - \sum_{x=1}^{|\Psi|} E_{g_x,DL,country}^{2016,fitted}(h) \tag{3.4}$$

The total load of Germany as well as the net demand and the power produced by different RES sources on the distribution level over the course of a whole year is visualized in Fig. 3.2. The computed net demand is distributed among the different nodes in the countries according to the load values $P_{l,Node\ k,country}$ given in ENTSO-E's grid model.

$$E_{netdemand,Node\ k,country}(h) = E_{netdemand,country}(h) \cdot \frac{P_{l,Node\ k,country}}{\sum_{i=1}^{N_{country}} P_{l,Node\ i,country}} \tag{3.5}$$

As pumped hydro power plants can either operate as generator or as a motor / load pumping water into a reservoir, the operation time of each of these operation modes need to be determined. This is due to the fact that the plants can only generate power as long as there is water in the reservoir and they can only pump water up as long there is space in the reservoir left. Given that a

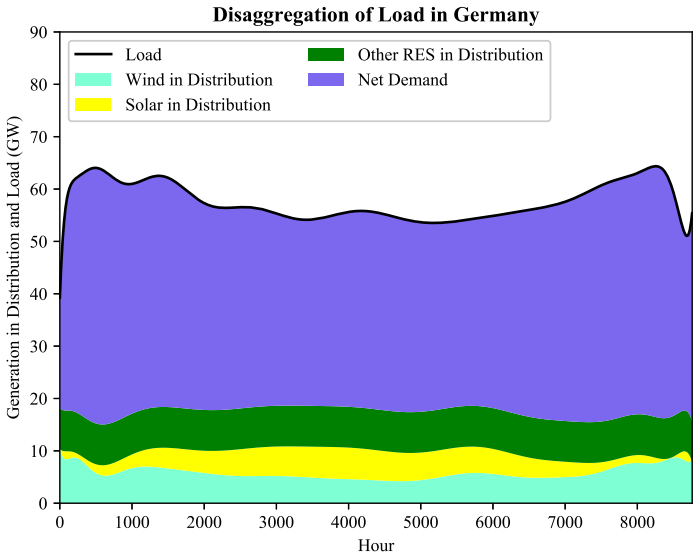

Figure 3.2: Visualization of the disaggregation of the total load in net demand and RES production on distribution level for the example of Germany. Source: **[Pub. G]**

detailed analysis would require time demanding sequential simulations with detailed reservoir size modeling for each pump hydro plant, we use a simplified assumption in which pumped hydro storage power plants are assumed to be able to operate annually for a limited number of hours. This also enables parallelizing the simulations. We determine the number of hours during which pumped hydro storage power plants are allowed to operate based on the actual generated energy provided in the ENTSO-E statistical factsheet for 2016 [107] and the installed pumped hydro capacity per country. The hours are allocated to the periods with high demand and low availability of other renewable energy (i.e., wind and solar).

The electricity production of run-of-the-river and other hydro power plants depends on seasonal river flows and reservoir/pondage limitations, which often prevent the hydro power plant from operating (at higher output levels). Hence, most hydro power plants are not always dispatchable to their maximum possible level. In order to consider these limitations, we reduce their installed capacities, such that even when operating during each hour of the year at maximum capacity, their production would not exceed the observed hydro energy production in 2016 [107] on the transmission level. The alternative approach to limit the number of operating hours as applied to pumped hydro storages leads to a lot of infeasible hours due to the lack of sufficient base generation. Not changing the installed capacity of run-of-the-river and other hydro power plants (except for pumped storages) while considering them dispatchable throughout the entire year leads to unrealistically high hydro production levels and would not reflect the actual 2016 production levels as listed by ENTSO-E. Therefore, we choose to adjust their installed capacity levels instead while assuming them dispatchable during each hour of the year.

Following this approach, the RES penetration level can be evaluated accurately considering not only the 'visible' RES generation on the transmission level but also the 'hidden' generation on the distribution level. Furthermore, this approach allows us to (a) adjust the load and generation data as accurately as possible to the ones given in the 2016 monthly domestic values reports from ENTSO-E [108] and (b) better include 2030 load and generation projections, as shown in the following section.

3.5.2 Including Load and Generation Projections for 2030

The scenario for 2030 is based on the EUCO 2030 scenario developed by the European Commission [105]. The scenario reflects the achievements of the 2030 climate and energy targets as agreed by the European Council in 2014 and includes an energy efficiency target of 30 % [22]. This section describes the required upscaling of the load and the different RES generation sources.

ENTSO-E provides a detailed list of installed capacity projections per generation technology on a per country basis for the EUCO 2030 scenario [22]. We adjust the installed generation capacities in our data set c^{2016} to the projected levels for 2030 c^{2030} by determining an upscaling factor per generation type on a per country basis, $up^{2030}_{x,country}$:

$$up^{2030}_{x,country} = \frac{c^{2030}_{x,country}}{c^{2016}_{x,country}} \tag{3.6}$$

$$P^{2030}_{g_x,node\ y,country}(h) = up^{2030}_{x,country} \cdot P^{2016}_{g_x,node\ y,country}(h). \tag{3.7}$$

Furthermore, the actual load within the net demand is also upscaled according to the given values using the same approach. Finally, the installed capacity P_{max} of all nuclear power plants in Germany is set to zero considering the planned nuclear phase-out.

Thus, this approach allows to fit the model as accurately as possible to the EUCO 2030 scenario developed by the European Commission [105]. The data for 2016 and 2030 is given on a per country basis in the Appendix in Tables A.1 - A.2.

3.6 Methodology for the Transmission Upgrade Scenarios

Within this work, we consider three different methodologies to determine the different transmission upgrade scenarios: (i) only technologies developed within BestPaths for repowering AC transmission lines (ii) extending the existing grid with DC transmission technology only or (iii) a combined approach.

All transmission upgrade scenarios are performed for an entire year (i.e., 8760 hours) using DC optimal power flow (DC-OPF) simulations and annual time series for load and renewable energy generation. The DC-OPF is a linear optimization problem widely used in power system operations and electricity market clearing, which minimizes total generation cost and thus, determines the optimal active power generation dispatch, which satisfies all demand under consideration of generator active power limits and active power line flow limits. Note that reactive power and transmission losses are neglected. This simplification is, however, not expected to have a big impact. In fact, in [115], the authors compared the use of DC optimal power flow models with the full AC system model to reveal congestion patterns and emphasized the good performance of the DC-OPF method while highlighting the speed advantage.

Despite the availability of sufficient generation capacities, line congestions might prevent to fully supply all demand during certain hours of the year. Therefore, we include the possibility of shedding load, which is a reasonable assumption given that it is common practice to disconnect contracted industrial loads with own generation capabilities in case of a transmission capacity shortage. We minimize, however, the amount of unsupplied load by penalizing the corresponding variable with a high cost in the objective function. This way, load shedding is only applied as a last resort to ensure feasibility and thus, a guaranteed solution of the optimization problem.

Due to the fact that detailed investment costs of the different technologies are not available and very project specific, our assessment does not consider investment costs but aims at increasing social welfare by a reduction of operating costs. This reduction of operating costs per year serves as an indicator for maximum acceptable investment costs. Furthermore, by aiming at maximizing social welfare, we simultaneously maximize the RES penetration level as RES have zero marginal cost and are ranked first in the marginal cost curve. In [116], the author showed that increasing social welfare is equivalent to relieving congestions, which is visualized in Fig. 3.3. The Figures visualize the impact of congestions in the system on the dispatch of generators. If sufficient transmission capacity is available (i.e., no congestions; Fig. 3.3a), the generators are dispatched according to the merit order curve to supply the demand. In this case, there is only one marginal generator, which is the last one in the merit order to be dispatched to satisfy the demand, i.e., the most expensive one, which sets the price and is only dispatched as much as needed (usually below its capacity limit) to cover the remaining demand. A single congestion, however, might prevent a cheaper generator with sufficient capacity to supply the remaining demand to be dispatched to the required levels as the grid cannot absorb higher power injection levels at the generator's connection point. Given that the congestion prevents a cheap generator in the merit order curve (often a renewable energy generator with very low marginal cost) to produce as much power as required to satisfy the demand, another more expensive 'out-of-merit-order' generator is additionally required to be dispatched, as visualized in Fig. 3.3b. This increases the total generation cost and thus, reduces social welfare as well as renewable energy penetration. Therefore, the primary target of all upgrade scenarios is to increase the transmission capacity and reduce grid congestions, so that the cheapest set of generators can be dispatched.

3.6.1 AC Upgrade Scenario

The technologies for repowering AC transmission lines developed within BEST PATHS have been introduced in section 3.3. As introduced in that section, the developed technologies include HTLS transmission lines and DLR, and as the questionnaires from DEMO leaders revealed they can increase the transmission capacity of a line by up to 20% and 100%, respectively **[Pub. G]**. As the technologies focus on AC line repowering only, we do not consider the development of new AC transmission lines but only focus on repowering existing ones. The benefits of the technologies

(a) Merit-order curve without a congestion in the system **(b)** Merit-order curve with a congestion in the system

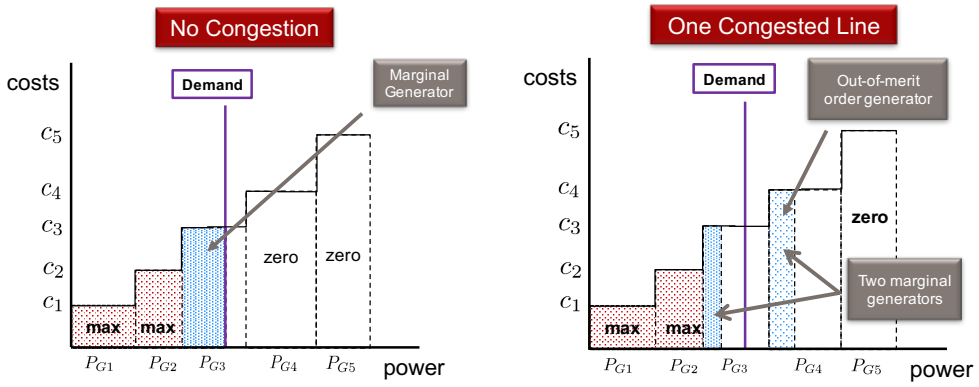

Figure 3.3: Impact of a congestion in the system on the merit-order curve. Source: **[Pub. G]**.

developed within the Best Paths project focusing on repowering AC lines are also constrained by the capabilities of the substations, which are the determining factor for the improvement potential of existing lines.

The optimal bound along the *AC upgrade axis*, which the Best Paths technologies could facilitate, are determined by allowing the flow on all transmission lines (i.e., not including transformers) to exceed the capacity limit by 100% and evaluate the required capacity increase ex-post. Any required increase below 20% could be facilitated by both HTLS and DLR, while HTLS is the only upgrade option for increases above 20%.

Additionally, we perform two theoretical analyses serving as a benchmark for the 2030 AC grid development. Fist, we analyze the theoretical bounds of using Best Paths technologies for repowering AC lines but having no limitations imposed by transformers and substations (i.e., leaving them unconstrained in the optimization problem). Secondly, we assume no limitation by neither AC lines nor transformers and substations at all (i.e., only considering the limitation of the DC lines). These analyses help to put the results of the analysis of the Best Paths technologies into context and serve as a benchmark for the 2030 AC grid development.

3.6.2 DC Upgrade Scenario

The technologies focusing on DC technology developed within BEST PATHS have been introduced in section 3.3. As discussed in that section, we collected them all within the DC scalability assessment except the superconducting cables, because given the aim of the study, as well as the size of the test network, a clear separation between the demonstrators becomes infeasible. The superconducting cables are not considered in this study given the limited length of the cables and their area of application being dense populated areas, which are represented as single nodes in the high-resolution European transmission grid model **[Pub. G]**.

Within the DC Scalability assessment the focus lies on expanding the current European electricity network by building new HVDC interconnections enabling controllable high power flows over long distances with comparably low losses. Thus, besides offering additional transmission capacity to relieve congestions, HVDC interconnections increase the controlability of the system enabling to route power directly from one specific node to the other allowing to circumvent congestions in the vicinity of the low-cost marginal generator. Furthermore, HVDC interconnections allow a higher integration of offshore wind energy, due to the fact that many locations located far away from shore are only accessible by HVDC technology. Finally, additional transmission capacity with controllable flows will enhance the trading capacity between the different countries which is expected to result in significant cost reductions. However, due to the significant investment cost for new HVDC interconnections, every new line should carefully be planned in order to result in a high utilization of the new asset and in an operating cost reduction which will make the investment feasible. Thus, even without taking all non-technical issues as e.g. social acceptance of new lines into account, the transmission expansion planing, or specifically in this case the problem of choosing the right location for new HVDC interconnections is not trivial considering the size of the European transmission network.

In [116], the author showed that increasing social welfare is synonymous to the relief of existing congestions considering only energy costs. The author relate the number of congestions in a network to the number of marginal generators, i.e. generators which are dispatched neither at their

minimum nor at the maximum limit. They prove that in any system an additional line connecting a low-cost marginal generator, i.e with a cost equal or lower than the system marginal cost, with a high-cost marginal generator, i.e. with a cost higher than the system marginal cost, will relieve at least one congested line and enable the low-cost marginal generator to substitute the high-cost marginal generator and by that increase social welfare. Based on this observation the authors developed a methodology for HVDC placement for maximizing social welfare which is based on adding a line with the objective of setting the dispatch of the out-of-merit order generator to zero.

Following this approach, we adapt it to our system under investigation. We analyze a high-resolution European transmission grid model with varying production and demand over a time frame of a whole year. Therefore, we observe varying congestions and marginal generators over the year. We determine for every generator the number of hours ($h_{marg,i}$) it is neither producing at its minimum nor at its maximum limit. Within these hours, we determine the amount of energy it could potentially produce additionally (in case of low-cost marginal generator) and the amount of energy we potentially need to substitute respectively (in case of a high-cost marginal generator). Finally, by combining these two features, i.e. the number of hours and the amount of energy of the marginal generator, we create two parameters $e_{low-cost,i}$ and $e_{high-cost,i}$. These parameters determine the potential value for every generator i to be interconnected with an marginal-generator of the opposite type (low-cost / high-cost). These parameters basically weight the amount of energy available / needed at the specific node with the proportion of time in which this energy is available / needed. Hence, the factors are higher if the same amount of energy is available over many hours within a year compared to the case in which this energy is only available within a few hours a year. Thus, these parameters serve as a good indicator for the potential utilization of a HVDC line interconnecting marginal generators:

$$h_{marg,i} = \{h = 1, \ldots, 8760 \quad \forall\, P_i^{min}(h) < P_i(h) < P_i^{max}(h)\} \tag{3.8}$$

$$e_{low-cost,i} = \frac{|h_{marg,i}|}{8760} \cdot \sum_{h=1}^{|h_{marg,i}|} \left(P_i^{max}(h_{marg,i}(h)) - P_i(h_{marg,i}(h))\right) \tag{3.9}$$

$$e_{high-cost,i} = \frac{|h_{marg,i}|}{8760} \cdot \sum_{h=1}^{|h_{marg,i}|} \left(P_i(h_{marg,i}(h)) - P_i^{min}(h_{marg,i}(h))\right) \tag{3.10}$$

As a result, parameter $e_{low-cost,i} \geq \epsilon_1$ and $e_{high-cost,i} \geq \epsilon_2$ justify the significant investment of building a new HVDC inter-connection between these marginal generators. After ranking the marginal generators according to $e_{low-cost}$ and $e_{high-cost}$, we determine heuristically the top ranked marginal generators to be interconnected based on the distance between them. Given the potential large distances between low-cost and high-cost marginal generators, an inter-connection of a low-cost and a high-cost marginal generator may be performed by inter-connecting another high-/low-cost marginal generator in between.

Thus, for example, in case we determine a low-cost marginal generator with a high $e_{low-cost,i}$ value in the North Sea. That means, this generator could produce significant more energy but is often curtailed. Further, we determine two high-cost marginal generators with comparably high $e_{high-cost,i}$ values, one in the North of Germany and one in the South of Germany. Thus, these generators are often dispatched with less than their maximum capacity (but above their minimum capacity). Then, it is feasible to inter-connect the low-cost marginal generator with the high-cost marginal generator in the North because the currently curtailed energy of the low-cost marginal generator will substitute the energy produced by the more expensive high-cost marginal

generator. Moreover, depending on the values of the parameters, it may be feasible to inter-connect the high-cost marginal generator in the North with the high-cost marginal generator in the South because (i) the available energy of the low-cost marginal generator may exceed the energy required to substitute the energy produced by the high-cost generator in the North allowing to transmit the exceeding energy towards the South. (ii) The two high-cost marginal generators might be marginal in different hours, i.e. in some hours the low-cost marginal generator could substitute the high-cost marginal generator in the North while in other hours the one in the South. (iii) In case of potential cost differences, the cheaper high-cost marginal generators can substitute the more expensive high-cost generator within hours in which the low-cost generator is not marginal.

The DC scalability assessment is performed step-wise in order to be able to react to changed power-flows due to the added transmission capacity.

3.6.3 Combined Upgrade Scenario

The *combined upgrade scenario* is based on the *DC upgrade scenario* and examines potential improvements for each stage of DC grid development by also upgrading the underlying AC grid. Similarly to the AC scalability assessment, we first evaluate the benefits of deploying the Best Paths technologies for AC line repowering at each step performed during the DC scalability analysis. We then look at the additional benefits to be gained when neglecting transformer limitations and in a third step, when neglecting the AC grid limitations as a whole. This allows us to assess the impact of the added DC lines on the AC grid and the interactions between the two transmission upgrade/expansion approaches.

3.7 Case Study - The European Transmission System

We perform the scalability assessment of the Best Paths technologies on a network model representing the European transmission system in 2030. It includes impending transmission projects from the TYNDP 2016 to be commissioned before 2030 as well as projections for load and generation based on the EUCO30 scenario. The AC grid of the network model consists of 7474 buses, 8787 transmission lines, 1148 transformers, 1269 generators and 3361 loads. The DC system consists of 72 point-to-point DC lines with 144 converters stations and 144 DC buses. There is no load or generation connected to the DC system. The generators are grouped in the following six categories with the number of generators belonging to the corresponding category indicated in parentheses: conventional (765), run-of-the-river hydro power plants and hydro reservoirs (87), pumped hydro storage power plants (84), solar power plants (42), offshore wind generators (43) and onshore wind generators (248). The data for (net) demand, renewable energy production on the distribution level (which is accounted for in the net demand) and maximum achievable RES penetration level are listed in Table 3.1. The maximum RES penetration level is calculated based on the renewable energy available from hydro, solar and wind generators and already accounts for the time periods during which renewable energy availability exceeds the demand and needs to be spilled in order to maintain power balance across the entire network. The DC-OPF simulations are carried out on an hourly basis for a whole year (i.e., 8760 hours). Generator cost functions are assumed to be

Table 3.1: Characteristics of European transmission network 2030. Source: [**Pub. G**].

Net demand (TWh)	RES production in distribution (TWh)	Demand (TWh)	Max. RES penetration (%)
2733.10	786.60	3519.70	56.47

linear. Load shedding is penalized with 300 €/MWh, which is higher than the maximum cost of generation (162.79 €/MWh) and thus, incentivizes to supply the load rather than to disconnect it. Note that the cost of LS is usually assumed much higher but in this case needs to be appropriately scaled as high values out of scale with the rest of the cost parameters might raise numerical issues.

3.7.1 Performance Indicators of the Scalability Assessment

The primary target of the scalability assessment is to increase the transmission capacity and reduce grid congestions, which in the context of this case study is equivalent to increasing social welfare and RES penetration levels. To this end, we use the key performance indicators (KPIs) defined in WP2 of the Best Paths project and listed in Table 3.2 for evaluating the results of the different upgrade scenarios.

3.7.2 Evaluation of the Business-as-Usual 2030 Scenario

The main results of the BaU2030 without any grid reinforcements are visualized in Figs. 3.4 and 3.5. Fig. 3.4 shows the annual dispatch of the different generation categories and the amount of load shedding. 22.35% of the demand is covered by distributed generation on lower voltage levels, while the remainder is covered by generators on the transmission level. The RES penetration level reaches 52.84% and exceeds the penetration level of 50%, which has been projected by the EUCO30 scenario, mainly due to different modeling approaches. The EUCO30 projections have been evaluated using a high-level energy modeling approach based on a mixed complementarity problem, which simultaneously accounts for several different energy objectives (such as energy efficiency targets etc.) and does not account for a high-resolution transmission grid model. Additionally, our assumption on the share of renewable energy generation in the transmission and distribution systems might be another source causing discrepancies. 0.94% of the total load is shed due to grid congestions. Specifically, most of the LS occurs in Sweden, Norway and Finland (67.78%), where a simplified grid representation developed within the eHighway 2050 project is used and which consists primarily of DC lines, which exhibit a high congestion level due to large

Table 3.2: Performance indicators of the scalability assessment. Source: **[Pub. G]**.

RES Penetration (%)	Share of total load supplied by renewable energy sources: $\frac{\sum_{g\in\mathcal{G}^{RES}} E_g}{\sum_{n\in\mathcal{N}} E_n^D}$
RES Curtailment (%)	Share of available renewable energy not dispatched due to congestions: $\frac{\sum_{g\in\mathcal{G}^{RES}} E_g^{max}-E_g}{\sum_{g\in\mathcal{G}^{RES}} E_g^{max}}$
Load Shedding (LS) (%)	Share of energy demand not supplied due to congestions: $\frac{\sum_{n\in\mathcal{N}} E_n^{shed}}{\sum_{n\in\mathcal{N}} E_n^D}$
Generation Cost (€)	Annual generation cost: $\sum_{g\in\mathcal{G}} c_g \cdot E_g$
Objective Function Value (€)	Annual cost of generation and load shedding: $\sum_{g\in\mathcal{G}} c_g \cdot E_g + \sum_{n\in\mathcal{N}} c^{shed} \cdot E_n^{shed}$

E_g	Annual energy produced by generator g (MWh).	E_g^{max}	Annual available energy of generator g (MWh).
E_n^{shed}	Annual energy demand not supplied at node n (MWh).	E_n^D	Annual energy demand at node n (MWh).
$\mathcal{G}^{(RES)}$	Set of (renewable) generators.	$\mathcal{N}$	Set of nodes.
c_g	Marginal cost of generator g (€/MWh).	c^{shed}	Cost of load shedding (€/MWh).

exports of hydro and other renewable power to continental Europe. Most of the remaining LS occurs in France (30.66%) due to AC grid congestions and particularly transformer congestions.

Fig. 3.5 depicts the dispatched renewable energy with respect to the available energy for each renewable generation category. The bottom subplot contains all sources of hydro power. As expected, solar power has a peak during the summer months whereas both offshore and onshore wind power are largely available during the winter months. Hydro power has a fairly constant generation profile due to our modeling assumptions of run-of-the-river power plants and hydro reservoirs described in section 3.5. Pumped hydro storages do not have a significant impact on the hydro generation profile due to relatively low installed capacities supplying only 1.89% of the total load. The dark areas represent renewable energy curtailment, which amounts to 138.31 TWh or 12.10% of the total renewable energy available. It can be seen that there is still potential for increased levels of RES penetration if the available renewable energy could be transported away from where it is generated. Specifically, offshore wind farms and solar generators curtail 36.39% and 15% of their available energy, respectively, which largely accounts for the gap between the current RES penetration level and the maximum achievable of 56.47%. Table 3.3 lists the main results of the BaU2030 including the annual generation cost and the objective function value, which additionally to the generation cost also includes the cost of LS.

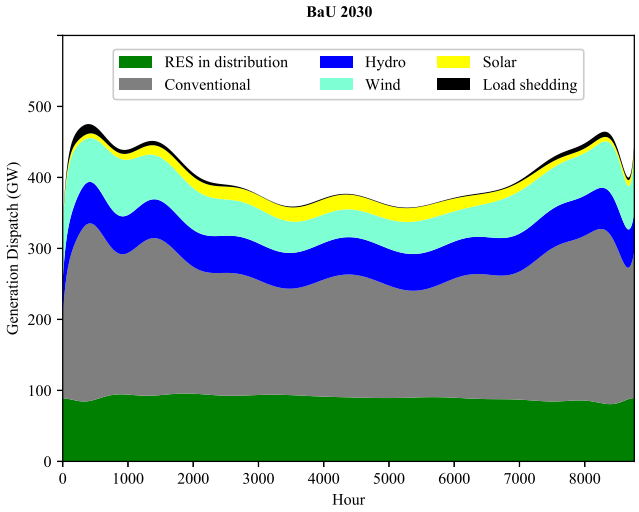

Figure 3.4: Load and generation 2030. Source: [**Pub. G**].

Table 3.3: Results of BaU 2030. Source: [**Pub. G**].

RES penetration (%)	RES curtailment (%)	LS (%)	Generation cost (B€/a)	LS cost (B€/a)	Obj. fct. value (B€/a)
52.84	12.10	0.94	50.08	7.86	57.94

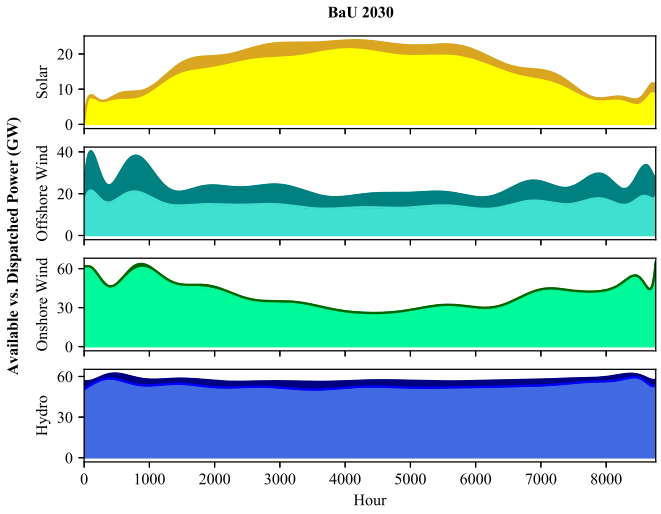

Figure 3.5: Available vs. dispatched power of the different RES. The dark areas represent RES spillage. Source: [**Pub. G**].

3.7.3 AC Upgrade Scenario

Grid congestions are the main cause for not being able to fully dispatch all renewable power which is available. Within the AC scalability assessment we evaluate how Best Paths technologies for AC reinforcements could contribute to releasing congestions and thus, increasing both the RES penetration level and social welfare. Table 3.4 lists the main results, where *BP reinforcements* denotes the results considering transmission upgrades using Best Paths technologies for AC line repowering only. *BP reinforcements w/o transformer limits* denotes the case using BP reinforcements but neglecting substation and transformer limitations which *BP reinforcements* do not upgrade. *AC* $\rightarrow \infty$ represents the outermost bound on the *AC upgrade axis* without any AC grid limitations at all.

Load shedding remains unchanged in the *BP reinforcements* case as the increased levels of load shedding in France are due to transformer congestions, while the load shedding in Scandinavia is caused by congestions on DC lines, which remain largely unaffected by AC grid reinforcements. This becomes apparent in the *BP reinforcements w/o transformer limits* scenario, where load shedding in France is completely avoided and only remains in Scandinavia.

Fig. 3.6 shows the change in RES curtailment for each RES generation category individually. Solar, onshore wind and hydro power curtailment is decreased to a greater degree than offshore wind, which indicates that AC grid reinforcements alone cannot accommodate the available offshore energy and benefit mostly the dispatch of continental generation distributed throughout the AC grid.

An increase in RES penetration level of 0.19 % can be achieved under the *BP reinforcements* scenario, while additionally 0.13 % can be added to that under the assumption of sufficient capacity in the substations. Note that transformer upgrades without any additional AC line repowerings cause an increase in RES penetration of 0.15 % showing that transformer upgrades are not as effective as the *BP reinforcements*, which alone achieve 0.19 %. However, in combination the effect of both upgrade measures are reinforced resulting in an increase of 0.5% to 53.34 %. The RES penetration level

Table 3.4: Results of AC Scalability. Source: [**Pub. G**].

	RES pen. (%)	RES curtail. (%)	Load shedding (%)	Gen. cost (B€/a)	LS cost (B€/a)	Obj. fct. value (B€/a)
BP reinforcements	53.03	11.56	0.94	49.77	7.67	57.44
BP reinforcements w/o transformer limits	53.34	10.82	0.63	48.70	5.19	53.89
AC $\rightarrow \infty$	54.00	8.58	0.63	47.10	5.27	52.37

increases as expected through added transmission capacity but cannot exceed 54 % through AC grid reinforcements only and thus, cannot reach the maximum possible penetration level. This and the fact that most of the RES curtailment occurs offshore highlights the need for new transmission corridors, which will transport the power produced from remote offshore locations to consumption centers. Nonetheless, the *BP reinforcements* case results in annual generation cost savings of 310 M€ at a required total transmission capacity increase of 11.83 GW distributed among 21 AC lines. The required increase corresponds to only 0.03 % of the current installed AC transmission capacity.

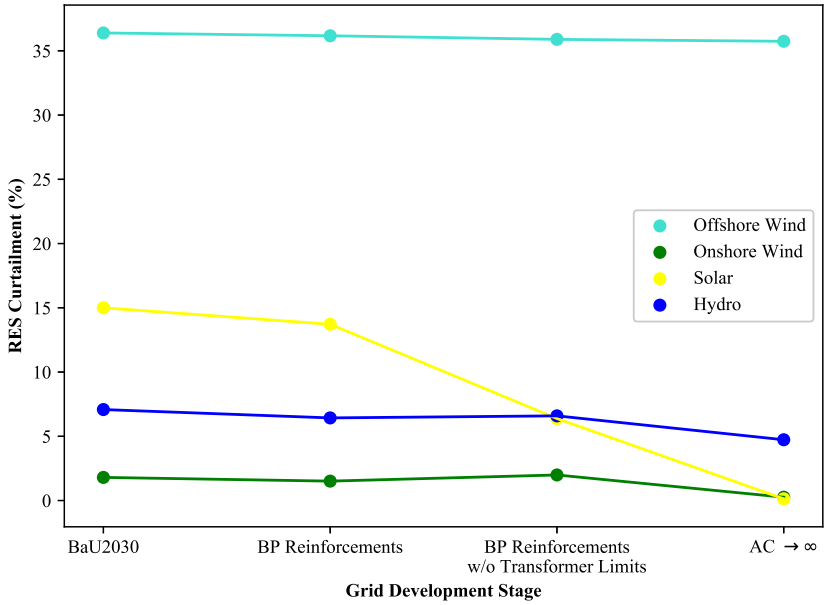

Figure 3.6: Renewable energy curtailment for each renewable generation category. Source: [**Pub. G**].

3.7.4 DC Upgrade Scenario

The DC upgrade scenario is developed in a step-wise approach allowing to account for the change in power flows due to the added transmission capacity. The development is stopped as soon as $e_{low-cost} \leq \epsilon$, which indicates that the highest ranked low-cost marginal generator does not offer enough spillage throughout the year to justify the significant investment costs of an additional DC line. The following subsections will present the step-wise placement of the DC lines, while the main findings of all steps will be summarized in the last subsection as well as in Section 3.7.5, where we discuss the results of the combined upgrade scenario.

All lines are considered to be built as bipole with a total transmission capacity of 3 GW, which has been identified as upper bound for HVDC interconections in Europe by the BestPaths partners. Based on the load duration curves obtained from the simulations the sizing of the lines can potentially be improved afterwards.

Step 1

The first step of the DC scalability assessment uses the BaU 2030 scenario as base case to determine the marginal generators (listed in Tab. 3.5 and Tab. 3.6). This list include the parameters h_{marg}, i.e. the number of hours the generators are marginal, and $e_{low-cost}$ and $e_{high-cost}$, respectively, i.e. the parameters serving as a good indicator for the potential utilization of a HVDC line connected to that node as introduced in Section 3.6.2. The added HVDC interconnections are visualized in Fig. 3.7 (note that the connection points shown on the map is a rough approximation of the actual locations). The analysis of the BaU 2030 scenario already showed that the highest spillage of energy over the year can be observed at the offshore wind farms which is reflected by the top ranked low-cost marginal generators. The high-cost marginal generators on the other hand are located mainly in the UK / Scandinavia and Eastern Europe, i.e. far away from the low-cost marginal generators. Given the large distance between the offshore wind farms in the North sea and the high-cost marginal generators, two lower ranked low-cost marginal generators ('84NO', 'DK916183') are taken as intermediate points allowing to transfer the generated power from the North sea to Sweden and Eastern Europe.

All added dc lines combined transfer 260.26 TWh over the whole year which corresponds to an average utilization of 71 %. This indicates a high usage of the assets and an increased trading between the countries. The load duration curve of every added DC line is shown in Fig. 3.8. Most of the new assets are used throughout the entire year at a high rate achieving average rates of $P_{dc} \geq$

Table 3.5: List of top ranked low-cost marginal generators in step 1. Source: [**Pub. G**]

Name	Bus ID	h_{marg} [h]	Energy spillage [TWh]	$e_{low-cost}$
'ES916537'	2169	2627	21.79	6.53
'offshore2'	7465	6662	7.37	5.61
'offshore3'	7469	7008	5.72	4.58
'offshore22'	7466	6333	5.52	3.99
'offshore14'	7460	6681	4.84	3.69
'offshore8'	7474	6620	4.42	3.36
'offshore5'	7471	6671	4.05	3.13
'offshore4'	7470	6563	4.04	3.03
'84NO'	30	1999	0.28	0.06
'DK916183'	2046	619	0.48	0.034

Table 3.6: List of top ranked high-cost marginal generators in step 1. Source: **[Pub. G]**.

Name	Bus ID	h_{marg} [h]	Energy production of marg. gen. in h_{marg} exceeding P_{min} [TWh]	$e_{high-cost}$
'AC_95uk'	78	4218	3.98	1.92
'AC_92uk'	67	1916	8.03	1.76
'PL925636'	6664	3832	3.33	1.45
'AC_94uk'	77	2066	5.39	1.27
'AC_96IE'	81	3336	3.10	1.18
'BG911342'	389	8712	0.86	0.86
'74FI'	1	8195	0.74	0.70
'88SE'	47	6542	0.91	0.68
'CZ912108'	652	1679	2.92	0.56
'ES917371'	2769	2310	1.22	0.32

60 % of the line rating. Only two lines ('88SE'-'74FI' / 'offshore3'-'AC_95uk') indicate a comparable low usage with average usage rates of $P_{dc} \approx 40$ % of the line rating. In these cases a lower line rating might be feasible considering potential cost reductions.

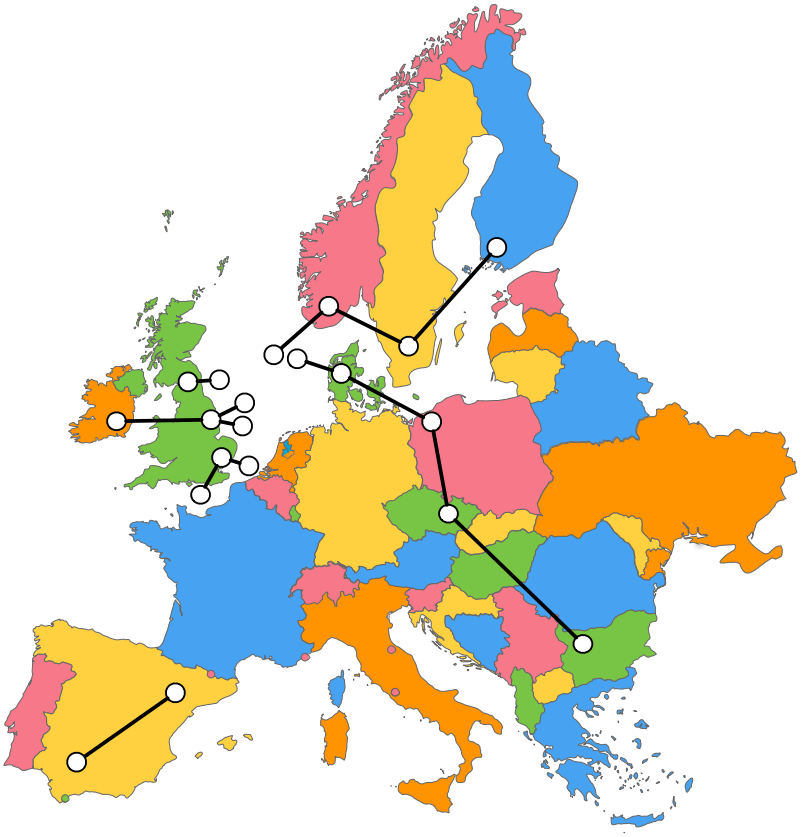

Figure 3.7: Step 1 of the DC upgrade scenario. Source: **[Pub. G]**.

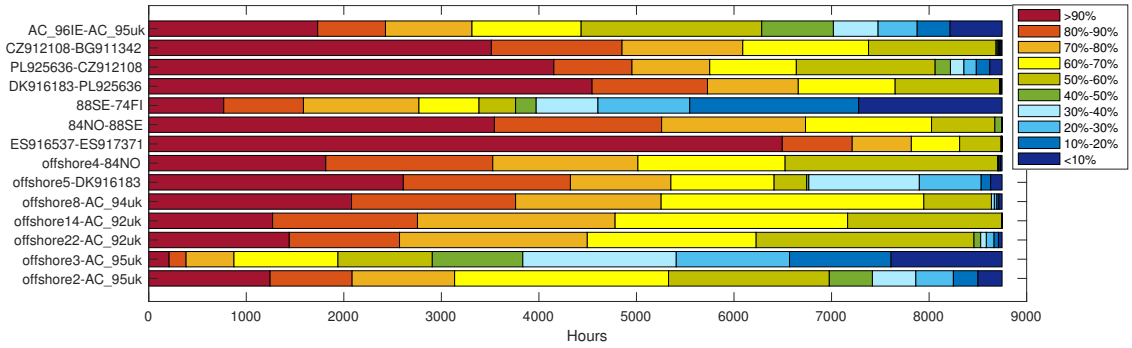

Figure 3.8: Load duration curve of DC lines added during step 1 of the DC scalability assessment. Source: [**Pub. G**].

Step 2

The second step of the DC scalability assessment uses the simulation results of step 1 as base case to determine the marginal generators (listed in Tab. 3.7 and Tab. 3.8). The added HVDC interconnections are visualized in Fig. 3.9 (note that the connection points shown on the map is a rough approximation of the actual locations). The top ranked low-cost marginal generators still reflect the high spillage of energy at the offshore wind farms observed in the BaU 2030 scenario. However, it is worth emphasizing that the spillage at the marginal generators of stage 1 is significantly reduced and other offshore nodes are identified as marginal generators (with lower $e_{low-cost}$ values). The majority of the high-cost marginal generators on the other hand are located in Eastern Europe, i.e. far away from the low-cost marginal generators. Given the large distance between the offshore wind farms in the North sea and the high-cost marginal generators in Eastern Europe, the node 'PL925636', in the previous step identified as high-cost marginal generator, serves as interconnection point between Denmark ('DK916155') and the Czech Republic ('CZ912108'/'CZ911895'). All added dc lines (step 1 & 2) combined transfer 530.6 TWh over the whole year which corresponds to an average utilization of 70 %. This indicates a high usage of the assets and an increased trading between the countries. The load duration curve of every added DC line is shown in Fig. 3.10. Note that the addition of 'offshore6'-'AC_92uk' reduced the usage of the previously installed line 'offshore14'-'AC_92uk'. Thus, the installed capacity of those lines may be optimized with respect to asset usage rate but this is out of the scope of this analysis. Furthermore, note that the low usage rate of the line 'offshore10'-'DK916155' is not indicating its redundancy

Table 3.7: List of top ranked low-cost marginal generators in step 2. Source: [**Pub. G**].

Name	Bus ID	h_{marg}	Energy spillage	$e_{low-cost}$
'ES916537'	2169	2575	20.35	5.74
'offshore1'	7457	6574	4.04	3.03
'Offshore11'	6476	6500	3.73	2.77
'offshore10'	7458	6586	3.45	2.59
'offshore6'	7472	6669	3.40	2.59
'offshore12'	7459	6518	3.43	2.55
'offshore7'	7473	6682	3.55	2.71
'offshore18'	7464	6437	3.49	2.57
'offshore17'	7463	6493	3.32	2.46

Table 3.8: List of top ranked high-cost marginal generators in step 2. Source: [**Pub. G**].

Name	Bus ID	h_{marg} [h]	Energy production of marg. gen. in h_{marg} exceeding P_{min} [TWh]	$e_{high-cost}$
'BG911091'	373	6103	0.8913	0.6210
'CZ912108'	652	7371	0.7311	0.6152
'ES917371'	2769	1809	2.8493	0.5884
'AC_92uk'	67	1107	4.3101	0.5447
'DK916155'	2040	7713	0.2642	0.2326
'HU922598'	5.533	6374	0.3149	0.2291
'CZ911895'	596	4903	0.3129	0.1752
'HU922547'	5504	8601	0.1738	0.1706
'PT925931'	6794	8097	0.1817	0.1680
'DK916424'	2114	8290	0.1247	0.118

but it is due to insufficient transmission capacity away from 'DK916155' / 'PL925636' / 'CZ912108' as indicated by the high usage of the corresponding lines and the following development steps of the dc upgrade scenario.

Figure 3.9: Step 2 of the DC upgrade scenario. Lines added in step 1 are marked in black, while lines added in step 2 are marked in blue. Source: [**Pub. G**].

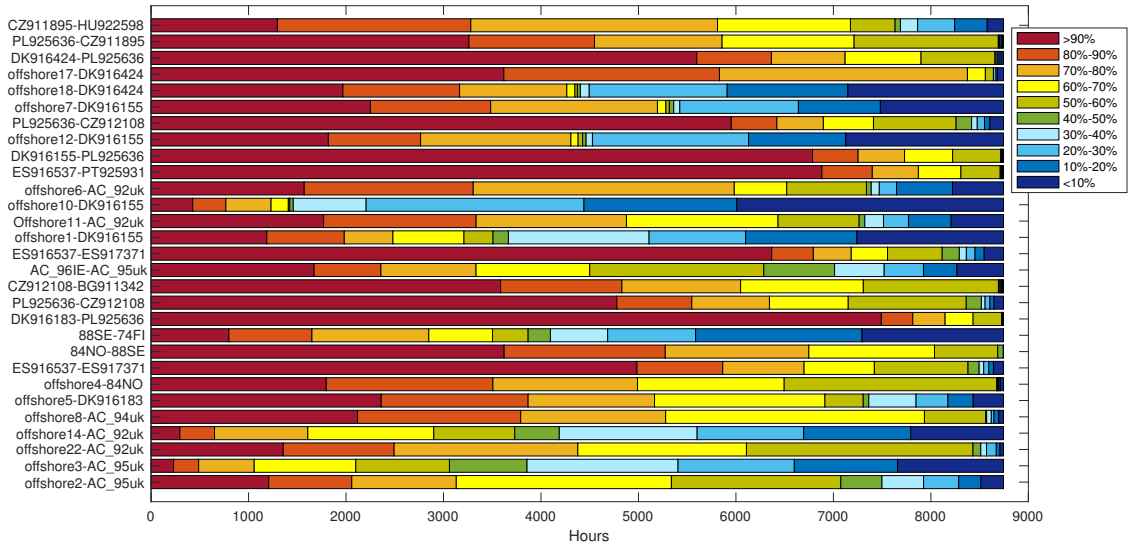

Figure 3.10: Load duration curve of DC lines added during step 1 and 2 of the DC scalability assessment. Source: [**Pub. G**].

Step 3

The third step of the DC scalability assessment uses the simulation results of step 2 as base case to determine the marginal generators (listed in Tab. 3.9 and Tab. 3.10). The added HVDC interconnections are visualized in Fig. 3.11 (note that the connection points shown on the map is a rough approximation of the actual locations). The top ranked low-cost marginal generators still reflect the high spillage of energy at the offshore wind farms observed in the BaU 2030 scenario. However, it is worth emphasizing that the spillage at the marginal generators of stage 1 & 2 is significantly reduced and other offshore nodes are identified as marginal generators (with lower $e_{low-cost}$ values). Furthermore, note that the spillage at the spanish generator ('ES916537') was significantly reduced from 21 TWh (BaU) to 16.8 TWh (step 2) (also indicated by high usage of the installed lines) but will be reduced further by adding additional transmission capacity. The high-cost marginal generators on the other hand are located in Eastern Europe and South Western Europe.

Given the large distance between the offshore wind farms in the North sea and the high-cost marginal generators in Eastern Europe the node 'DK916183' previously identified as marginal generator node serves as interconnection point between the North sea and Eastern Europe. All added dc lines (step 1-3) combined transfer 938.3 TWh over the whole year which corresponds to

Table 3.9: List of top ranked low-cost marginal generators in step 3. Source: [**Pub. G**].

Name	Bus ID	h_{marg}	Energy spillage	$e_{low-cost}$
'ES916537'	2169	2302	16.84	4.42
'offshore15'	7461	6654	2.972	2.26
'Offshore9'	6478	6007	3.28	2.25
'offshore16'	7462	6674	2.90	2.21
'Offshore13'	6477	6648	2.91	2.21
'AC_96IE'	81	830	0.7932	0.08
'PT925871'	6776	1119	0.52	0.066

Table 3.10: List of top ranked high-cost marginal generators in step 3. Source: **[Pub. G]**

Name	Bus ID	h_{marg} [h]	Energy production of marg. gen. in h_{marg} exceeding P_{min} [TWh]	$e_{high-cost}$
'BG911091'	373	6834	0.66	0.51
'ES917371'	2769	1482	2.75	0.46
'BG911342'	389	8739	0.32	0.32
'CZ912108'	652	7712	0.34	0.30
'AC_92uk'	67	732	2.70	0.23
'CZ912114'	655	3061	0.46	0.16
'PT925931'	6794	8229	0.15	0.14
'SK928311'	7173	7260	0.15	0.12
'ES916669'	2266	6572	0.15	0.12
'PL925276'	6506	6197	0.16	0.11

an average utilization of 76.1 %. This indicates a high usage of the assets and an increased trading between the countries. The load duration curve of every added DC line is shown in Fig. 3.12. Note that the usage of 'offshore10'-'DK916155' increased significantly due to the added transmission capacity.

Figure 3.11: Step 3 of the DC upgrade scenario.Lines added in step 1 and step 2 are marked in black and blue respectively, while lines added in step 3 are marked in green. Source: **[Pub. G]**.

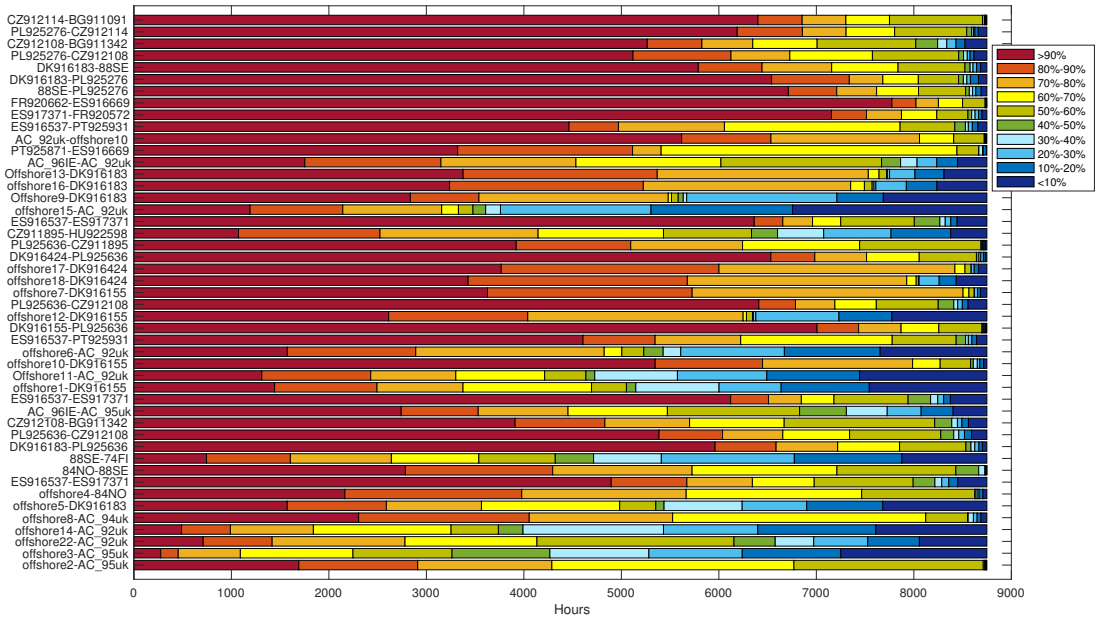

Figure 3.12: Load duration curve of DC lines added during step 1-3 of the DC scalability assessment. Source: **[Pub. G]**.

Step 4

The fourth step of the DC scalability assessment uses the simulation results of step 3 as base case to determine the marginal generators (listed in Tab. 3.11 and Tab. 3.12). The added HVDC interconnections are visualized in Fig. 3.13 (note that the connection points shown on the map is a rough approximation of the actual locations). Note that the energy spillage is already significantly reduced so that the last low-cost marginal generator listed in Tab. 3.11 only offers 0.2 TWh in comparably few hours resulting in $e_{low-cost} < \epsilon_1$ and is therefore not considered anymore.

All added dc lines (step 1-4) combined transfer 999.98 TWh over the whole year which corresponds to an average utilization of 76.22 %. This indicates a high usage of the assets and an increased trading between the countries. The load duration curve of every added DC line is shown in Fig.

Table 3.11: List of top ranked low-cost marginal generators in step 4. Source: **[Pub. G]**.

Name	Bus ID	h_{marg}	Energy spillage	$e_{low-cost}$
'ES916537'	2169	1622	8.790	1.627
'FR920572'	5139	928	1.815	0.192
'FR918995'	3775	823	0.195	0.018

Table 3.12: List of top ranked high-cost marginal generators in step 4. Source: **[Pub. G]**.

Name	Bus ID	h_{marg} [h]	Energy production of marg. gen. in h_{marg} exceeding P_{min} [TWh]	$e_{high-cost}$
'ES917371'	2769	1034	1.84	0.22
'FR920662'	5222	4485	0.24	0.12

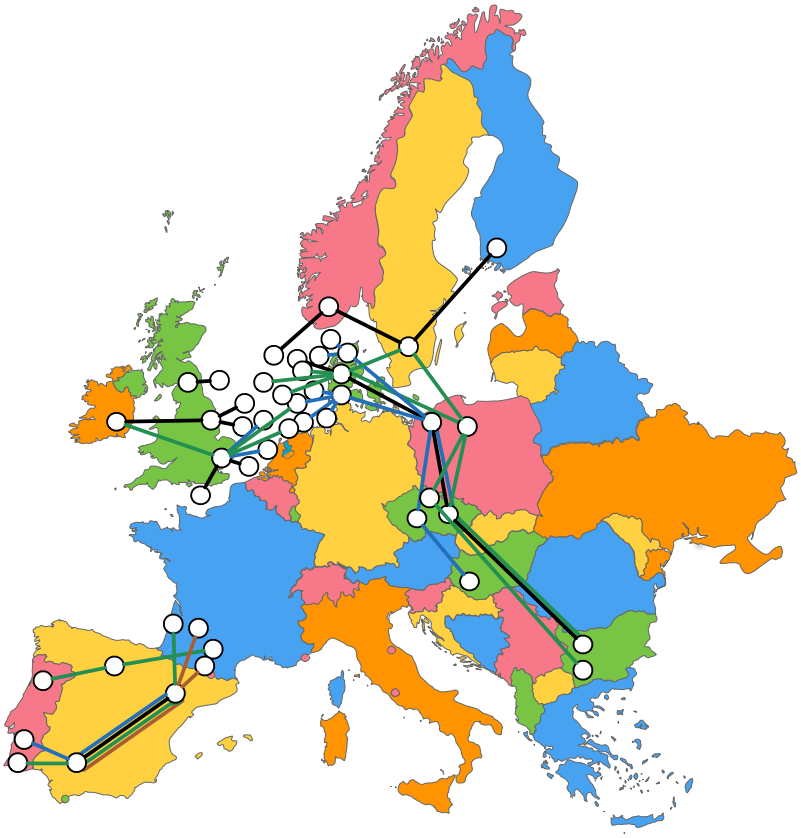

Figure 3.13: Step 4 of the DC upgrade scenario.Lines added in step 1 and step 2 are marked in black and blue respectively, while lines added in step 3 are marked in green. Lines added in step 4 are highlighted in orange. Source: **[Pub. G]**.

3.14. Note that some lines connecting offshore nodes with the main grid (e.g. 'offshore3'-'AC_95uk' / 'offshore8'-'AC_94uk') show lower usage rates. The capacity for all connected lines of the specific nodes could be optimized, which is, however, out of the scope of this work.

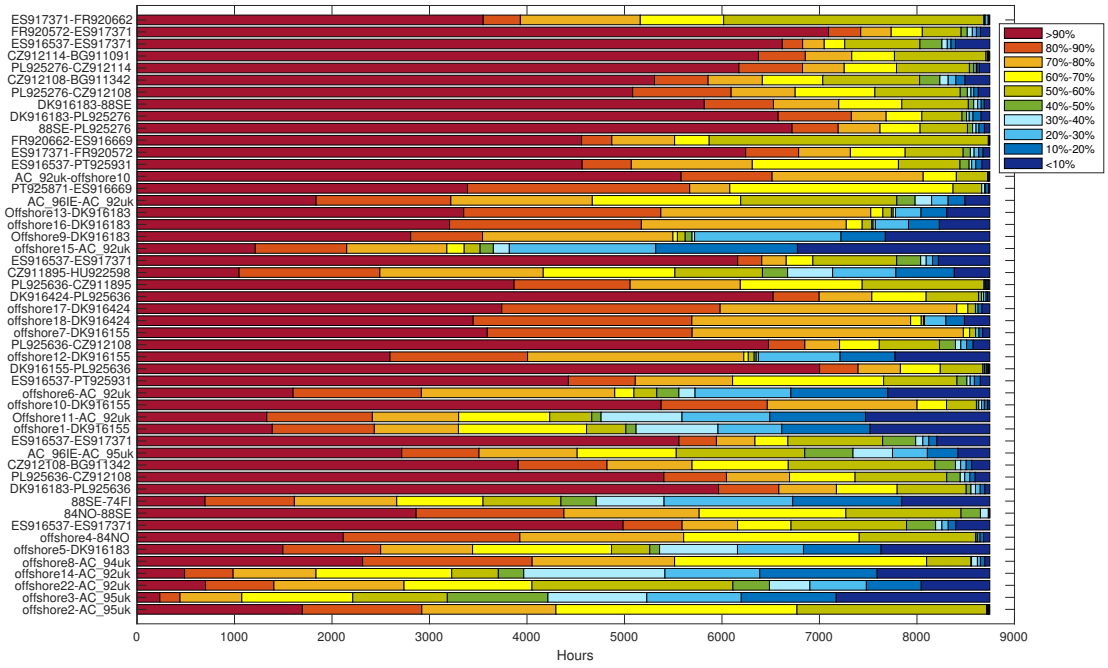

Figure 3.14: Load duration curve of DC lines added during step 1-4 of the DC scalability assessment. Source: **[Pub. G]**.

Evaluation of the DC Upgrade Scenario

The previous subsections provided insights on which lines have been built and why, and visualized the utilization of the added lines. The following subsection discusses the impact this grid development has on specific key performance indicators as the renewable energy penetration level, the curtailment of renewable energy sources, the energy not served, and the operating costs.

The development of the RES penetration level is shown in Fig. 3.15 while the curtailment of each

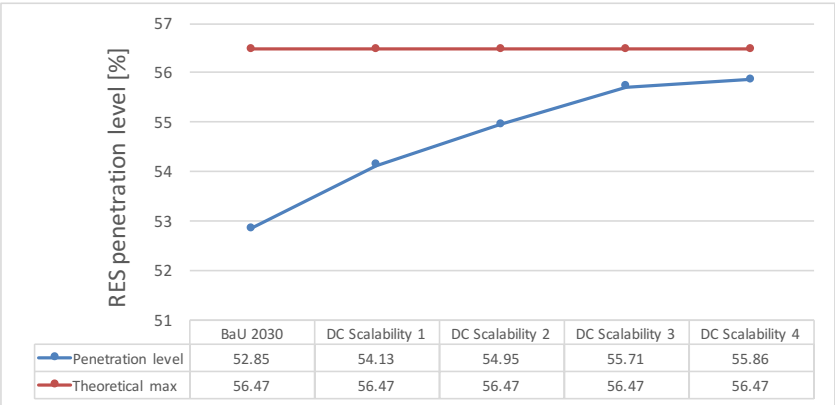

Figure 3.15: Renewable energy penetration level for each step of DC upgrade. Source: **[Pub. G]**.

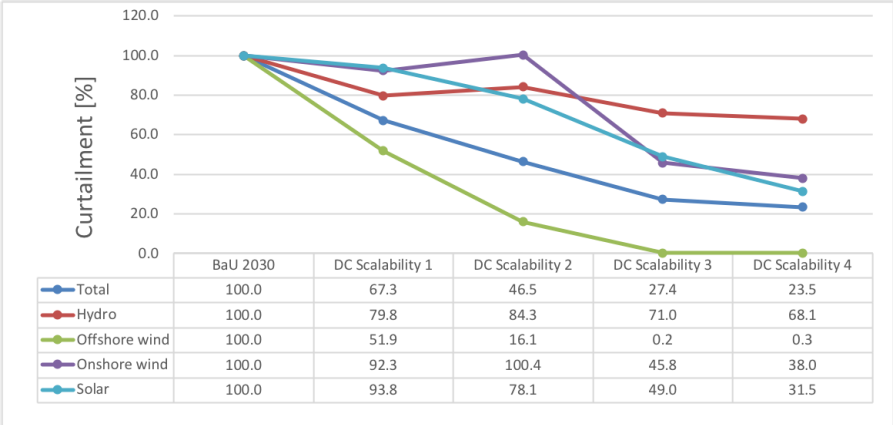

	BaU 2030	DC Scalability 1	DC Scalability 2	DC Scalability 3	DC Scalability 4
Total	100.0	67.3	46.5	27.4	23.5
Hydro	100.0	79.8	84.3	71.0	68.1
Offshore wind	100.0	51.9	16.1	0.2	0.3
Onshore wind	100.0	92.3	100.4	45.8	38.0
Solar	100.0	93.8	78.1	49.0	31.5

Figure 3.16: Renewable energy curtailment for each renewable generation category. Source: [**Pub. G**].

RES technology is shown in Fig. 3.16 with the BaU scenario as a base level. Fig. 3.15 shows that the RES penetration increases from 52.85 % up to 55.86 % in step 4 approaching the theoretical maximum of 56.47 % considering the theoretical maximum production of all RES sources. As discussed in the previous subsections, most of the low-cost marginal generators are offshore wind farms located in the North sea region which is based on the fact that most spilled RES energy is offshore wind energy as observed in the BaU scenario analysis. The effect of establishing higher transmission capacities from offshore locations to high-cost locations in Eastern Europe is well captured in Fig. 3.16 indicating the significant reduction of curtailment of offshore wind. Furthermore, Fig. 3.16 indicates the benefits of the added lines in South West Europe resulting in reductions of solar energy and onshore energy curtailment. Moreover, Fig. 3.16 indicates that, in particular in step 3, cheap offshore wind substitutes partially more expensive hydro power plants. Note that during the selection of the high-cost marginal generators we neglected hydro power plants aiming to increase RES penetration. However, for every HVDC line connecting a cheap marginal generator with an expensive marginal generator, the potential low-cost energy injection at the expensive marginal generator node may exceed the energy required to completely substitute the expensive marginal generator. Therefore, the results show that the excess energy may additionally substitute hydro power plants located in the vicinity of the expensive marginal generator because hydro power plants have higher marginal costs. Although this reduces the gain in terms of RES penetration level, it still reduces the generation costs of the system, i.e. our

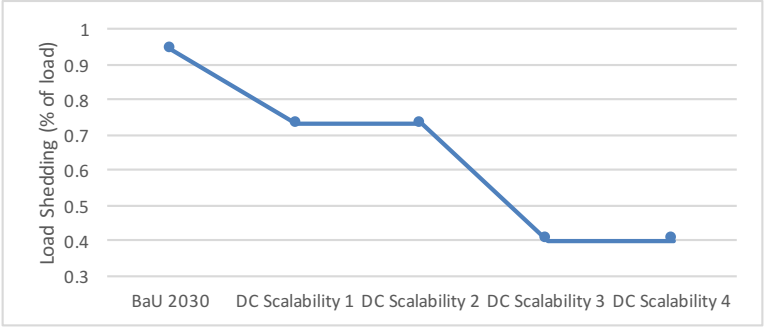

Figure 3.17: Development of the load shedding for each step of DC upgrade. Source: [**Pub. G**].

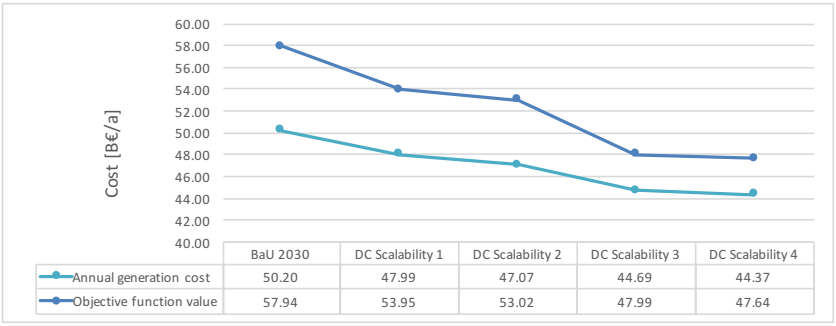

	BaU 2030	DC Scalability 1	DC Scalability 2	DC Scalability 3	DC Scalability 4
Annual generation cost	50.20	47.99	47.07	44.69	44.37
Objective function value	57.94	53.95	53.02	47.99	47.64

Figure 3.18: Development of generation costs for each step of DC upgrade. Source: [**Pub. G**].

objective function of the OPF.

Furthermore, a significant reduction of load shedding is achieved in particular due to the steps between BaU - DC Scalability 1 and DC Scalability 2 - DC Scalability 3, as shown in Fig. 3.17. Thus, as it may have been expected, we show through our method that relieving congestions results in a reduction of load shedding.

Although, a detailed cost-benefit analysis is out of the scope of this analysis, we briefly want to discuss the potential generation cost reduction by a dc upgrade scenario. The generation costs of the European system as well as the objective function value for the different DC upgrade steps are shown in Fig. 3.18. A significant cost reduction can be achieved reducing the generation costs from 50.2 B€ per year to 44.37 B€ in step 4. This is a cost reduction of 11.61 %. The reduction of load shedding is reflected by the objective function value curve approaching the generation costs curve. Considering a life-time of the required DC installations of approx. 30-40 years [117], the cost savings sum up to 233.2 B€ (40 years) and considering the (not optimized) additionally installed HVDC capacity (150 GW) it resembles a break-even point for a potential investment decision of 1.56 B€/ GW. However, considering a capacity optimization and a more realistic AC and DC grid development, this factor can probably be further increased.

3.7.5 Combined Upgrade Scenario

Within the combined upgrade scenario we take a broader view on the AC and DC upgrade possibilities by combining the AC upgrades with each DC grid development stage. The main results of the AC, DC and combined upgrade scenarios are visualized and compared in Fig. 3.19 to 3.20. Fig. 3.20 clearly shows that connecting more DC lines to the grid increases the congestion level of the AC grid as the grid tries to accommodate the increased injections from offshore wind farms. While DC lines do act as a congestion relief method [116] in some parts of the grid, they also increase the total amount of power flows in the underlying AC grid by allowing to supply previously disconnected load. We define the congestion level of the AC grid (CL^{AC}) based on the lines' congestion duration $T_l^{100\%}$ throughout the year,

$$CL^{AC} = \frac{\sum_{l \in \mathcal{L}^{AC}} \frac{T_l^{100\%}}{8760}}{|\mathcal{L}^{AC}|}, \tag{3.11}$$

where $\mathcal{L}^{AC}$ represents the set of AC lines. Hence, the Best Paths technologies for repowering AC lines can have a more profound impact in combination with a concurrent DC grid development and even more so with additional transformer upgrades than when deployed alone. The orange

dot in the *DC 4* grid development stage represents the highest grid development stage for the 2030 network conditions developed within this case study, which can be facilitated by Best Paths technologies only. 56 AC lines europewide would require a total capacity increase of 63.62 GW, out of which 20 require an upgrade of less than 20 %. The RES penetration level is increased from 52.85 % (BaU2030) to 56.06 % approaching the maximum possible level of 56.47 % as depicted in Fig. 3.20. RES curtailment is significantly reduced from 12.10 % to 2.17 %, which can greatly affect the economics of renewable energy projects and increase the revenue of wind and solar energy projects improving their competitiveness on the electricity market and possibly allowing for the discontinuation of feed-in tariffs and other subsidies. At the same time, the total cost (including the cost of load shedding) is reduced by 10.84 B€. Fig. 3.19 depicts the change in generation cost and the change in objective function value (i.e., the cost of generation plus the cost of load shedding) for the different stages of grid development. Even though the objective function only considers a fictitious value for load shedding, which at a value of 300 e/MW is still considered low, it is more representative of the actual cost development and makes the different stages of grid development

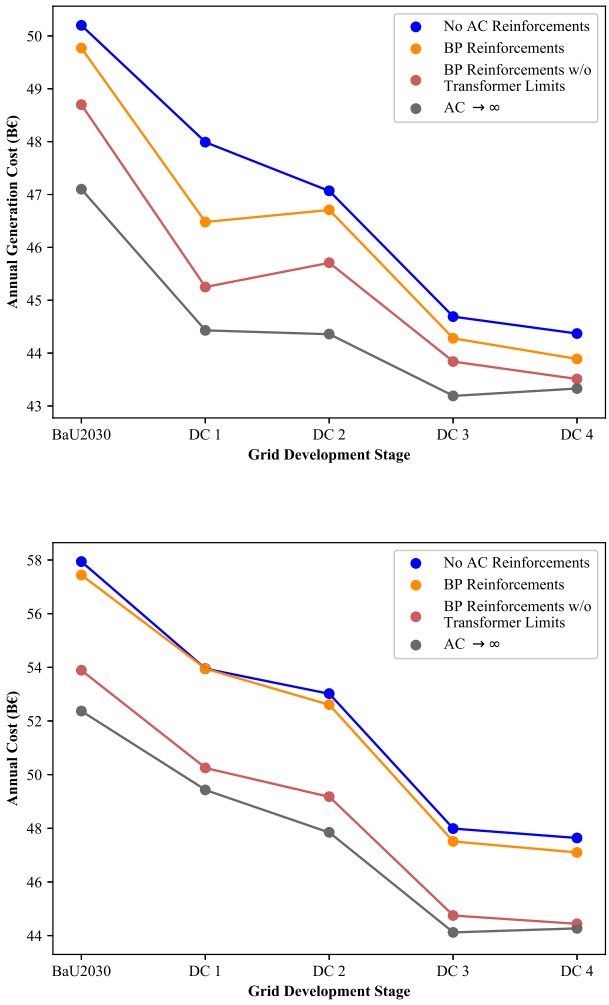

Figure 3.19: Annual generation cost (excl. cost of load shedding) and annual cost including load shedding for AC, DC and combined upgrade scenarios. Source: **[Pub. G]**.

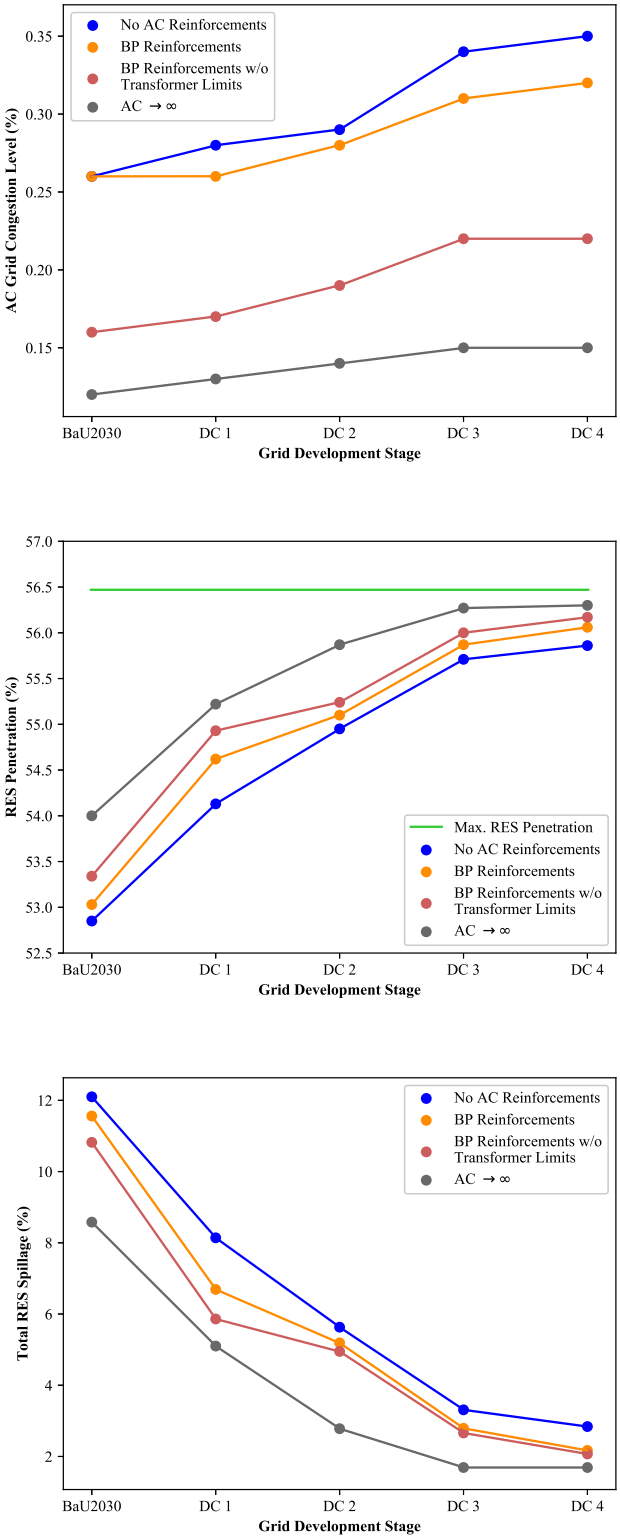

Figure 3.20: Congestion level of the AC grid, RES penetration and total RES spillage for AC, DC and combined upgrade scenarios. Source: **[Pub. G]**.

comparable to each other. This is due to the fact that unlike the generation costs, the objective function value considers the same load level at each stage through either dispatched generation or load shedding. The generation cost, however, does not reflect the reduction in load shedding from one stage to the next, which might lead to an increase in generation cost despite higher RES penetration levels due to higher load levels that need to be supplied as becomes apparent through the increase in generation cost from *DC 1* to *DC 2*. The objective function value still decreases, though. Load shedding is reduced by almost 60 % from 0.94 % to 0.39 % of the total load. Most of the remaining load shedding (i.e.,68.84 %) needs to be carried out in France, where the new DC line connections to Spain increase the stress on the already highly loaded transformers as discussed in Section 3.7.3. Nonetheless, load shedding is also reduced in France from 7.89 TWh to 7.33 TWh, which can be further improved with appropriate transformer upgrades.

3.8 Conclusion

We adapt the notion of optimality bounds from optimality theory, where relaxations (i.e., approximations) can provide bounds on the optimal solution of NP-hard problems, to the context of the future European mixed AC/DC grid development. We consider the grid development for the AC and DC transmission technologies separately and evaluate their individual potential to relieve congestions, increase social welfare and contribute to a more renewable electricity supply. This approach allows us to determine the bounds of the future European grid development as visualized in Fig. 3.21. Our results show that congestions within the AC grid can be partially relieved using technologies for repowering AC lines developed within the Best Paths project. However, we also show that the positive impact of these Best Paths technologies is highly constrained by the transformer limitations and that their benefits can be reinforced if they were deployed along with transformer upgrades.

Given the RES development projections of the EUCO30 scenario, which considers a substantial increase in offshore wind power capacity (11.7 GW in 2016 to 41 GW in 2030), a big share of the RES potential is not deployable without additional HVDC lines (or AC lines for offshore wind farms near shore). Therefore, the potential for improvements with AC reinforcements only is relatively small given the mentioned EUCO30 assumptions. The benefits of the AC reinforcements become more apparent when combining them with concurrent DC upgrades. In this way, the already substantial increase in RES penetration level and reduction in cost achieved by placing new HVDC transmission corridors can be further reinforced by relieving AC grid congestions in

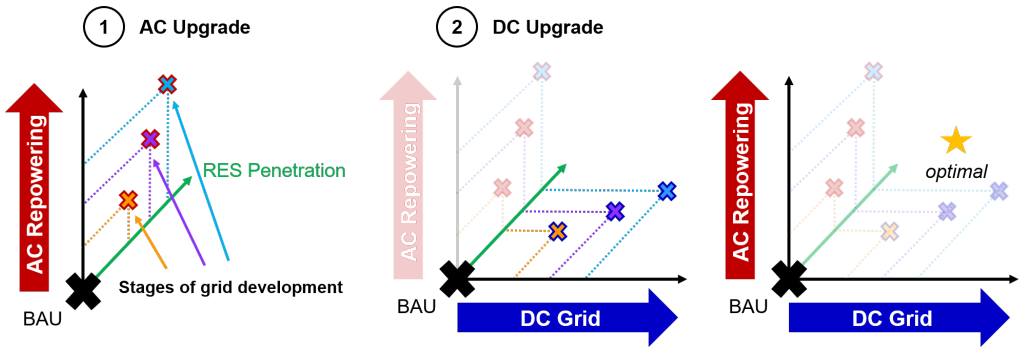

Figure 3.21: Schematic illustration of how the scalability assessment provides the bounds of the future European grid development. Source: **[Pub. G]**.

the vicinity of the new injection points, which further reduces the annual cost by 4.2 B€ (BestPaths AC reinforcements + transformer upgrades at DC Scalability step 4). 23.7 % of the total reduction in cost are related to the AC reinforcements. This also highlights that an optimal grid development will consist of both AC reinforcements and new DC transmission assets. The study also emphasizes the benefits of HVDC lines to reroute power flows from low-cost to high-cost marginal generators in a fully controllable way demonstrating their ability to substitute more expensive generators. Despite the fact that DC lines can reduce congestions in the underlying AC grid, additional AC reinforcements in the vicinity of their injection points are often required in case of increased power injections at that point. As a result, substituting larger expensive generators, which already inject a substantial amount of power at their node, will require less AC reinforcements.

Thus, the following policy recommendation was developed:

New transmission lines based on HVDC technology are indispensable in the future European transmission network, as they allow for highly flexible power transmission and the transport of large amounts of renewable energy from remote generation sites to load centers. At the same time, reinforcements of the existing AC grid are necessary to accommodate increased injections of HVDC lines. Thus, a coordinated upgrade of both AC and DC network is essential to achieve the full potential of either technology.

3.9 Future Work

The future work in this area may include the improvement of the simplified system representing Scandinavia and Great Britain. As the network model provided by ENTSO-E, did not include any data for these systems, these models were taken from the e-HIGHWAYS 2050 project and consist of various DC links.

Moreover, future work could focus on a more detailed representation of the pumped hydro storage plants and investigate the impact of potential upgrades of existing hydro plants to pumped hydro storage plants, possibly while also considering other storage systems as e.g. power-to-gas.

CHAPTER 4

MT-HVDC Control Structures

Following our policy recommendation that new HVDC lines are indispensable in the future European transmission system, this chapter deals with the challenges arising when such lines are potentially interconnected to form a MT-HVDC grid. Due to the little experience with MT-HVDC grids, the control, operation and potential interaction of such a MT-HVDC grid with the connected AC grids are open research questions. Thus, this chapter investigates various dc voltage droop control structures in terms of stability, disturbance rejection and interaction with connected ac systems as well as multi-vendor interoperability. A methodology is presented to determine the operating space of an arbitrary MT-HVDC system which is used to compare the impact of the various dc voltage droop control structures on the power transfer capability. This chapter is structured as follows: First, the background of this chapter is discussed and a brief literature review is provided. Then, the contributions of this chapter are emphasized and the different dc voltage droop control structures are classified in a simple framework, followed by a description of the work published in ***[Pub. A]***, ***[Pub. C]***, ***[Pub. D]***.

4.1 Background

So far most High-Voltage Direct Current (HVDC) systems have been built as Point-To-Point (PTP) connections. However, with the emergence of HVDC based on Voltage Source Converter (VSC) the development of Multi-Terminal High-Voltage Direct Current (MT-HVDC) is seen as a feasible option. A crucial aspect for the operation of such a large MT-HVDC is the operational reliability, since any malfunction could have a significant economic impact. In this perspective, it should be avoided that the regulation of the dc voltage and the intertwined regulation of the power flow between the terminals should rely on an approach where one single unit is assigned a dominant role. Instead, a distributed control architecture where multiple units are actively participating in the control of the dc voltage based on local measurements is preferable [75]. Indeed, a decentralized architecture is inherently more robust against outages and more effective in case of power fluctuations that exceed the available control range of a single terminal [118]. Several alternative strategies for distributed dc voltage control have been proposed in the technical literature. A common element in most of these control strategies is the presence of a dc voltage droop mechanism [72, 76, 119, 120]. Despite that the general operating principle of dc droop is identical for the different implementation schemes, the use of different control objectives and different feedback signals can have significant impact on the dynamic performance and the stability properties [75, 121]. Moreover, these differences may also lead to different kind of interactions with the connected ac grids which have already been observed for PTP-connections in different projects (e.g. BorWin1 [122], INELFE [123]).

Furthermore, unlike in China, a MT-HVDC grid in Europe would most likely not be built at once but be developed by a step-wise integration of already existing on- and offshore interconnectors [51]. This, however, would raise the question of the interoperability of HVDC systems from different vendors.

4.2 Literature Review

Over the last decades, large projects and many publications have addressed the control of a MT-HVDC grid, its impact on the stability and the system interactions as well as potential interoperability issues.

The European HVDC Grid Study Group including Transmission System Operators (TSOs) as well as vendors of HVDC technology was founded in 2010 to develop "Technical Guidelines for first HVDC Grids" including proposals to start standardization work [51]. Among other things they concluded the necessity to study potential interactions between different converters and recommended to apply vendor-specific parameter and control concepts to study the stability of MT-HVDC systems [51]. They also stated that standardization of HVDC equipment as well as control concepts and communication could enhance the development of MT-HVDC grids [51]. The European HVDC Grid Study Group identified dc voltage droop control and droop control with deadband as suitable control concepts for MT-HVDC [51]. The applicability of droop control and its preference by vendors of HVDC technology is also proven by its use in the Nanao MT-HVDC grid [26].

In technical literature several alternative droop control schemes have been proposed [55, 64–68, 70, 72, 76, 119, 120, 124]. These dc droop implementations, however, are usually analyzed separately or by comparing only a few selected cases. In [125] for example, Vrana compares the general principles and relation of power and current based droop schemes but does not consider droop control methods using ac current or active power measured on the ac side. Haileselassie on the other hand differentiates in [79] between active power measured on the ac and the dc side but does not consider any current based droop control methods. In 2018, 1-2 years after our studies, the authors of [121] published a comparative study of five different droop control structures analyzing their impact on the relative stability, performance and robustness of the overall MT-HVDC system. Similar to our work they perform an eigenvalue analysis comparison, a multivariable frequency response analysis of the different structures, and the impact of the cable modeling.

Similarly, interactions between converters or between converters and the connected ac grid have been studied, as e.g. by Beerten et al. in [92]. They investigate the influence of droop parameters (NB: not different kinds of droop control structures) and dc breaker inductors on the system interactions. In [126], Endegnanew et al. investigate interactions between asynchronous ac grids in a hybrid ac/dc power system for a specific power based droop scheme. In [9, 127, 128], different damping schemes have been proposed to mitigate observed harmonic stability problems caused by interactions between the converters and resonances from the system [122, 123]. In each case, however, a specific droop control scheme is used without analyzing which influence other options could potentially have. The final report of the MEDOW[1] project (2013-2017) highlights the novelty of harmonic instability problems due to AC/HVDC (converter) interactions in the power system community and emphasizes the need for detailed studies [129].

As one of the first initiatives, the EU-project BEST PATHS[2] (2014-2018) focuses among other things on the HVDC-VSC multi-vendor interoperability. The main objective was to investigate conditions allowing a maximum of interoperability and contribute with recommendations to

[1] MEDOW: "Multi-terminal DC Grid for Offshore Wind", www.medow.engineering.cf.ac.uk, funded by the European Union

[2] BEST PATHS: "BEyond State-of-the-art Technologies for rePowering Ac corridors and multi-Terminal HVDC Systems", www.bestpaths-project.eu, funded by the European Union

the standardization of interoperability requirements for multi-vendor MT-HVDC grids. Experts involved in the projects conclude that "the existing technology delivered by the main HVDC vendors is not directly interoperable" [130] and see "interoperability [of different vendors] as one of the greatest challenge" [130] in the development of MT-HVDC grids. In fact, Olivier Despouys from RTE[2] involved in the BEST PATHS[1] project stated in May 2018 [130] that the main problem of investigating and improving multi-vendor interoperability is related to testing the interaction of potentially protected intellectual property of different vendors as e.g. control algorithms determining the behaviour of the converters.

The on-going efforts of the European Union funding recently two new projects on MT-HVDC (PROMOTioN[3] (2016-2019), InnoDC[4] (2017-2021)) and the conclusions from previous projects emphasize the importance of more detailed studies of the different Control Structures (CSs) and their potential interactions with each other in order to ensure the stability of future MT-HVDC. Although two MT-HVDC grids have been commissioned in China [17, 26], Olivier Despouys from RTE expects significant more difficulties in a European competitive market context with multiple vendors, due to the fact that in China “a specific manufacturer was in charge of the whole control and protection for all converters delivered by other suppliers” [130]. He does, however, not anticipate “this kind of set-up [as] the expected way forward in western countries where HVDC is a competitive market.”

4.3 Contributions

Several alternative droop control concepts have been proposed in the literature. It is, however, a business secret how each vendor has exactly set up its control scheme and experts identified the interoperability of potentially different control concepts as key challenges for future MT-HVDC grids. Furthermore, these dc droop implementations are usually analyzed separately or by comparing only a few selected cases. Therefore, this work addresses the analysis and comparison of different control schemes systematically, using a simple classification framework we proposed in [75]. Furthermore, this work contributes with

- an in-depth comparison of the impact of the different CSs on small signal stability, disturbance rejection, the interaction level and multi-vendor interoperability (section 4.5-4.8),
- the uncovering that limits frequently used in literature for CS analysis and tuning (e.g. [9, 69]) are not sufficient to maintain the impact of specific disturbances within a certain boundary (section 4.6),
- a methodology for stability analysis of different dc voltage droop CSs determining the operation space of an arbitrary MT-HVDC grid (section 4.7).

[2]RTE: Réseau de transport d’électricité

[3]PROMOTioN: “PROgress on Meshed HVDC Offshore Transmission Networks”, www.promotion-offshore.net, funded by the European Union

[4]InnoDC: “Innovative tools for offshore wind and direct current (dc) grids”, www.innodc.org, funded by the European Union

4.4 Classification of dc Voltage Droop Control Structures

In general, a droop control scheme introduces a linear relationship between two electrical variables. In the specific case of dc voltage droop control for MT-HVDC, the dc voltage is used in each implementation, so that the droop gain, k_{droop}, defines the deviation of V_{dc} for a variation of the other electric variable:

$$V_{dc} = V_{dc}^{*} + k_{droop}(y^{*} - y) \tag{4.1}$$

y^{*} and V_{dc}^{*} are the set points and V_{dc}, y are the measured electric variables respectively. The second electric variable, y, can either represent the dc current, I_{dc}, one component of the ac current, I_{ac}, the active power measured on the dc side, P_{dc}, or the active power measured on the ac side, P_{ac}. They can be categorized by two different types of generalized structures, depending on whether the dc voltage is used within the first loop (Type2 (V_{dc}-y)) or the second loop (Type1 (y-V_{dc})) as shown in Fig. 4.1. This leads to a total of 8 different dc voltage droop control structures, shown in Fig. 2.12. We introduced this classification first in [75].

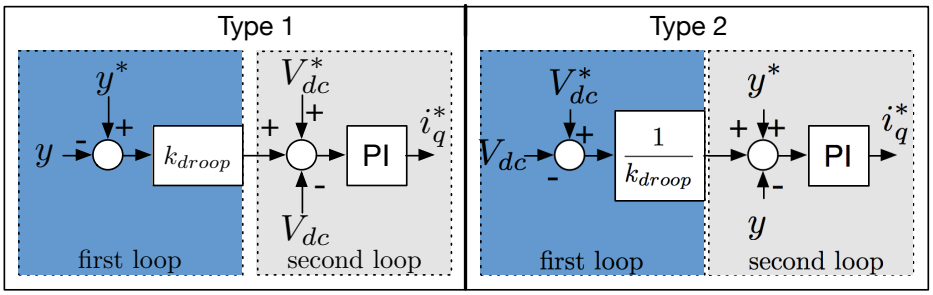

Figure 4.1: Generalized droop control structures. Source: **[Pub. C]**.

4.5 DC Voltage Droop Control Structures and its Impact on the Interaction Modes in Interconnected AC-HVDC Systems

As a first step of the assessment of the different dc voltage droop control structures, we investigate how the usage of the different structures impacts the interaction modes between the different sub-systems. That means, we analyze how the choice of the control structure influences the level of interaction between the different converters and between the ac and the dc subsystem since it is preferred to have those systems as decoupled as possible to minimize a potential spread of disturbances from one system into the other. This work has been published in **[Pub. D]**. In [92], the authors analyze interaction modes and their sensitivity to droop parameters and dc breaker inductances in a MT-HVDC system. However, there does not exist an analysis of the impact of the various CSs on the interaction modes between different subsystems. Thus, it remains unknown whether the choice of a certain CS results in an unfeasible stronger coupling of subsystems, as for instance the dc and the ac subsystems. In general, it is preferred to have those systems as decoupled as possible to minimize a potential spread of disturbances from one system into the other.

The contributions of this work include the following: First, an analysis of the quantitative and qualitative coupling between the different subsystems will be provided for two different tunings

of the converters, i.e. whether a certain CS imposes a higher degree of coupling reflected by a higher percentage of interaction modes and whether this also influences the damping ratio of the interaction modes. In particular, we will focus on the coupling between the dc and the ac systems and the coupling between the different HVDC converters. We will show how a faster response time impacts the coupling of the different subsystems. Further, we will discuss how a generalized feedback influences the coupling of those subsystems.

4.5.1 Methodology

In order to evaluate how the choice of the CS influences the coupling of the different subsystems, a methodology, initially proposed in [92] to identify and analyze interaction modes between converters in a HVDC system, is adapted [**Pub. D**].

Given a general linearized model of a HVDC system, which is composed of various subsystems for every connected converter terminal and every HVDC cable, and the definition of the normalized participation factors Γ^n_{ki}, as given in section 2.7.4, we define a criterion to distinguish between local modes and interaction modes.

Here, interaction modes are defined as modes where at least two subsystems participate. Hence, local modes, on the other hand, are defined as modes where only a single subsystem participates. The vector $\mathbf{\Gamma}^n_{\alpha,i} \in \mathbb{R}^{n_\alpha}$ contains all normalized participation factors associated with mode i for all states of the subsystem α.

The overall participation of each subsystem α in mode i is defined as [92]:

$$\eta_{\alpha,i} = \frac{\|\mathbf{\Gamma}^n_{\alpha,i}\|}{\|\mathbf{\Gamma}^n_{i}\|} \tag{4.2}$$

with $\|\cdot\|$ denoting the L_1-norm. Focusing on interaction between specific subsystems $\mathbb{I}^\alpha$ a set of interaction modes $\mathbb{S}^\alpha$ can be defined as:

$$\mathbb{S}^\alpha = \{i \mid \eta_{\alpha,i} \geq \kappa,\ \forall\, \alpha \in \mathbb{I}^\alpha\} \tag{4.3}$$

with $\mathbb{S}^\alpha \subseteq \mathbb{S}$, the set of all modes, and κ resembling a threshold chosen equal to 5%, following the example in [92].

Here, two subsets of interaction modes are of particular interest:

- the interaction modes of the subset $\mathbb{S}^{ac,dc} = \{i \mid (\eta_{dc,i} \geq \kappa) \wedge ((\eta_{ac_1,i} \geq \kappa) \vee \cdots \vee (\eta_{ac_N,i} \geq \kappa)),\ \forall\, dc, ac_j \in \mathbb{I}^{ac,dc}\}$. That means interaction modes with participation of at least one of the connected ac systems and the dc system, since it is preferred to have those systems as decoupled as possible to minimize a potential spread of disturbances from one system into the other.
- the interaction modes of the subset $\mathbb{S}^{gsc} = \{i \mid (\eta_{gsc_1,i} \geq \kappa) \wedge (\eta_{gsc_2,i} \geq \kappa) \wedge \cdots \wedge (\eta_{gsc_N,i} \geq \kappa),\ \forall\, gsc_j \in \mathbb{I}^{gsc}\}$, i.e. interaction modes between all Grid Side Voltage Source Converters (GSCs), indicating the degree of coupling within the dc grid.

These two subsets will be evaluated quantitatively, i.e. how many of all modes show this type of coupling, and qualitatively, i.e. where are the corresponding eigenvalues located, how critical are they and which states participate in particular?

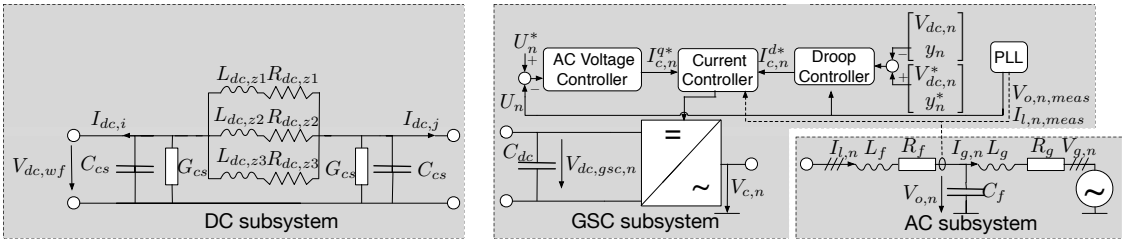

Figure 4.2: Splitting of the different subsystems. Adapted from: **[Pub. D]**.

4.5.2 Modeling particularities

For the analysis of this section a slightly different generic MT-HVDC model derived in [9] was used. The detailed state representation of this model is presented in the following subsection where the model is divided into different subsystems. The main differences to the model described in section 2.7.2 are (i) the modeling is done in absolute values not in per-unit (ii) the absence of the active damping controllers, (iii) the use of ac voltage controllers instead of reactive power controllers, (iv) the introduction of measurement delays and (v) the use of different Phase Locked Loops (PLLs) based on [9], where the angle deviation is computed as

$$\Theta_{PLL} = \frac{K_{p,PLL}s + K_{i,PLL}}{s^2 + V_{o,q,0}K_{p,PLL}s + V_{o,q,0}K_{i,PLL}} V_{o,d}. \tag{4.4}$$

Note that in this model the q-axis, not the d-axis, voltage vector is aligned with the voltage vector, V_o.

4.5.3 Subsystem Definition

This model is derived for every of the eight different droop control structures as well as for a case with a generalized feedback signal which is described in detail below. Each of these models consists of a number of three different kind of subsystems, shown in Fig. 4.2. Due to space limitations, the variables are shown in complex space vector notation, i.e. for example $\mathbf{V}_o = V_{o,q} + jV_{o,d}$.

The ac subsystems are modeled as Thévenin equivalents with an LC-filter interface to the GSCs. Thus, the states corresponding to the ac subsystems, $\mathbb{I}^{ac_j}$, with $j = 1, \ldots, N$, are the following:

$$\mathbf{x}_{ac,j} = \Big[I_{g,d,j}, \quad I_{g,q,j}, \quad V_{o,d,j}, \quad V_{o,q,j}, \quad I_{l,d,j}, \quad I_{l,q,j}, \\ V_{o,d,meas,j}, \quad V_{o,q,meas,j}, \quad I_{l,q,meas,j}, \quad P_{ac,meas,j} \Big]^T. \tag{4.5}$$

Variables $I_{g,d/q,j}$, $I_{l,d/q,j}$ represent the grid current and the line current flowing through the converter. $V_{o,d/q,j}$ represents the voltage at the point of common coupling (PCC) and $V_{o,d/q,meas,j}$ the delayed voltage measurement at the PCC. Further, $P_{ac,meas,j}$ and $I_{l,q,meas,j}$ represent the delayed active power measurement at the PCC and the delayed measurement of q- component of the current flowing though the converter used in the control loops.

The dc grid subsystem includes all dc cables, modelled as 'frequency dependent' π model where the additional parallel RL branches are calculated to fit the frequency response of a wide-band cable model [5, 14]. In general, in a dc grid, wind farm side converters (WFC) work as grid forming

converters for the connected ac grid without controlling V_{dc}. Hence, due to the focus on the GSC control WFCs can be simplified to dc current sources representing an uncontrolled disturbance for the dc grid [9]. Thus, the states corresponding to the dc subsystem, $\mathbb{I}^{dc}$, are:

$$\mathbf{x}_{dc} = \Big[I_{dc,z(l)}, \quad I_{dc,z(l+1)}, \quad I_{dc,z(l+2)}, \quad \cdots, \quad I_{dc,z(3M-2)}, \quad I_{dc,z(3M-1)}, \quad I_{dc,z(3M)}, \quad I_{dc,meas,l}, \quad \cdots, \quad I_{dc,meas,M}, \quad V_{dc,wf,k}, \quad \cdots, \quad V_{dc,wf,K} \Big]^T \tag{4.6}$$

with $I_{dc,z(l)}$ - $I_{dc,z(l+2)}$ representing the currents in the different branches of the $l = 1, \cdots, M$ different dc cables. Further, $I_{dc,meas,l}$ represents the delayed dc current measurements at the GSCs, shown in Fig. 4.2 as $I_{dc,i}$. The variable $V_{dc,wf,k}$ denotes the dc voltage at the $k = 1, \ldots, K$ Wind Farm Side Voltage Source Converters (WFCs).

The GSCs are assumed to be synchronized to the ac grids through a PLL and operated with conventional current controllers in the Synchronous Reference Frame (SRF). As cascade control requires the speed of response to increase towards the inner loop, the internal loop is designed to achieve a fast response [63]. Thus, the current controllers of the GSCs are tuned by the Internal Model Control (IMC) technique designed to track references with a settling time of $10\,\mathrm{ms}$ [131]. Saturation limits are included in the control scheme, in order not to exceed the maximum current ratings of the converters.

Both GSCs are assumed to use dc voltage droop control. the different structures have been introduced in section 2.7.2 and visualized in Fig. 2.12. Further, to better control the power sharing between the converters after a converter outage, the use of a generalized feedback signal using communication between the GSCs has been proposed [132] as an alternative to the eight CSs using local measurements only. The idea here is, to use a multiple-input feedback controller using all measured voltages deviations as inputs at every terminal, as given in:

$$\begin{bmatrix} \mathbf{\Delta I_{dc,1}} \\ \mathbf{\Delta I_{dc,2}} \\ \vdots \\ \mathbf{\Delta I_{dc,N}} \end{bmatrix} = \begin{bmatrix} g_{11} & g_{12} & \cdots & g_{1N} \\ g_{21} & g_{22} & \cdots & g_{2N} \\ \vdots & \vdots & \ddots & \vdots \\ g_{N1} & g_{N2} & \cdots & g_{NN} \end{bmatrix} \begin{bmatrix} \mathbf{\Delta V_{dc,1}} \\ \mathbf{\Delta V_{dc,2}} \\ \vdots \\ \mathbf{\Delta V_{dc,N}} \end{bmatrix}. \tag{4.7}$$

Thus, $\mathbf{G}$ represents a matrix of droop gains interconnecting the current and voltage measurements at the different terminals. In case all entries of the matrix are zero except the entries on the main diagonal, this approach corresponds to the case where each droop controlled terminal uses CS1 (V_{dc}-I_{dc}). Then, each entry on the diagonal corresponds to the inverse of the droop gains, $\frac{1}{k_{droop}}$ and there is no generalized feedback. Otherwise, all matrix entries are determined by an optimization problem considering the line resistances. Hence, the proposed generalized feedback controller is similar to CS1 (V_{dc}-I_{dc}) but differs by the fact that the generalized feedback controller uses measurements of all GSCs and additional corresponding droop gains.

A comparable performance of power and current based droop control structures and the generalized feedback controller is ensured by the following:

- The droop gains were chosen as $k_{droop,p} = \frac{1}{25}\,\frac{\mathrm{V}}{\mathrm{kW}}$ as suggested in [9].
- The droop gains used within the power and current based droop controller should be comparable. Thus, the relation derived in [125] is used to determine the current based droop

gains, $k_{droop,i_{dc}}$, that are equivalent to the power based droop gains, $k_{droop,p}$:

$$k_{droop,i_{dc}} = \frac{V^*_{dc,j}}{\frac{1}{k_{droop,p}} - I^*_{dc,j}}. \tag{4.8}$$

The current based droop gain used for the CSs combining $V_{dc,j}$ and $I_{ac,j}$ needs to be scaled additionally, due to the higher range of $I_{ac,j}$. However, due to the non-linearity of power based droop control, the approximation holds only for a small deviation of the voltage:

$$k_{droop,i_{ac}} = \frac{I^*_{dc,j}}{I^*_{c,q,j}} \cdot k_{droop,i_{dc}}. \tag{4.9}$$

- For a comparable performance of the generalized feedback control g_{11} and g_{22} are chosen as $\frac{1}{k_{droop,i} - \frac{k_{droop,i}}{2}}$, while g_{12} and g_{21} are chosen as $\frac{1}{k_{droop,i}/2}$.
- For all droop control structures, we analyze two different tunings. Each of these tunings, is comparable for all droop control structure enabling comparability between the different structures. We analyze two different tunings for each structure to show the impact of the tuning on the coupling of the different subsystems. The fast tuning leads to a fast rise time of approx. $17\,\mathrm{ms}$ and a settling time of approx. $60\,\mathrm{ms}$ with an overshoot of approx. $5\,\%$. The slow tuning leads to an over-damped response without overshoot, a rise time of approx. $23\,\mathrm{ms}$ and a settling time of approx. $40\,\mathrm{ms}$.

Only the response of CS2(V_{dc}-I_{ac}) differs, due to the absence of a PI controller (see Fig. 2.12), since the droop gain already serves as proportional controller connecting $V_{dc,j}$ and $I_{q,j}$ creating the necessary reference variable for the current controller. Hence, the dynamics of CS2(V_{dc}-I_{ac}) are determined by the current controller, which was tuned independently of the outer CS.

Thus, the GSC subsystems, $\mathbb{I}^{gsc_j}$, with $j = 1, \ldots, N$, consist of the following states:

$$\mathbf{x}_{gsc,j} = \left[\epsilon_{d,j},\ \epsilon_{q,j},\ \gamma_{d,j},\ \gamma_{q,j},\ \chi_{d,j},\ \chi_{q,j},\ V_{dc,j},\ V_{dc,meas,j},\ P_{dc,meas,j}\right]^T \tag{4.10}$$

with $\epsilon_{d/q,j}$ corresponding to the integrator state of the phase-locked loop (PLL). Variables $\gamma_{d/q,j}$ and $\chi_{d/q,j}$ represent the integrator states of the current and outer controllers. $V_{dc,j}$ and $V_{dc,meas,j}$ represent the dc voltage at the converter and its delayed measurement. Further, $P_{dc,meas,j}$ represents the delayed active power measurement at the GSC.

4.5.4 Case study

A three terminal grid, shown in Fig. 4.3, is chosen to evaluate which impact has the choice of the CS on the coupling of the different subsystems. A WFC is connected over two submarine cables to

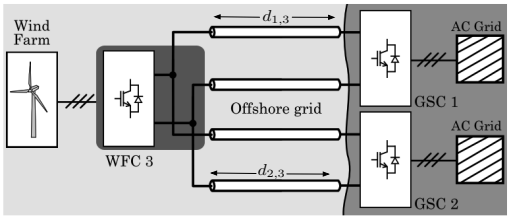

Figure 4.3: Three terminal VSC-HVDC grid. Source: [9].

two different GSCs on the shore. The length of both lines is assumed to be $100\,\mathrm{km}$, parameters are taken from [14]. Choosing the same droop control structure for both GSCs we obtain nine different scenarios (eight different droop CSs, one with generalized feedback). The parameters are given in the appendix. The WFC is assumed to inject maximum power into the HVDC grid with an equal power sharing between the converters. The linearized models are verified by equivalent non-linear models built in Matlab Simulink, which also provide the steady state initial values. As described in the methodology, we focus on two subsets of interaction modes, in particular $\mathbb{S}^{ac,dc}$ and $\mathbb{S}^{gsc}$.

AC/DC Interactions

Fig. 4.4 shows the size of the subset of AC/DC Interactions modes $\mathbb{S}^{ac,dc}$ with respect to the set of all modes $\mathbb{S}$ in percent in black (fast tuning) and red (slow tuning) respectively. Further, it indicates the minimum damping ratio of the interaction modes in that subset in percent in blue (fast tuning) and green (slow tuning). The first observation is that the coupling of the dc and ac subsystems is affected by the choice of the CS. In fact, depending on the CS and the tuning this subset includes between $11.8\,\%$ (CS7 (P_{dc}-V_{dc}) and CS8 (P_{ac}-V_{dc})) and $21.6\,\%$ (CS6 (V_{dc}-P_{ac}))) of all modes in case of the fast tuning. For the slow tuning it is spread between $0\,\%$ (CS3 (I_{dc}-V_{dc}) and CS7 (P_{dc}-V_{dc})) and $13.7\,\%$ (CS8 (P_{ac}-V_{dc})), considering that there exists no different tuning for (CS2 (V_{dc}-I_{ac}) due to the fact that the CS does not include a PI-controller within the droop controller. Further, unlike it might be intuitively expected the use of an ac measurement within the droop control structure does not necessarily lead to a higher degree of coupling. Further, Fig. 4.4 also indicates that the damping ratio of the most critical eigenvalue of this subset differs significantly for every CSs as well as for the different tunings (between $16.4\,\%$ (CS6 (V_{dc}-P_{ac})) and $29.3\,\%$ (CS3 (I_{dc}-V_{dc})) for the fast tuning and between $15\,\%$ (CS8 (P_{ac}-V_{dc})) and $100\,\%$ (CS1 (V_{dc}-I_{dc})) for the slow tuning, CS2 (V_{dc}-I_{ac}): $14.8\,\%$). This indicates that the choice and tuning of the CS does not only influence the degree of coupling of the ac and dc grid, but also the damping of the disturbances, which can potentially spread between the subsystems.

It is remarkable that for all CSs but CS8 (P_{ac}-V_{dc}) an increased transient response (faster tuning) leads to a higher coupling and lower damping ratio, while it is the other way around for CS8 (P_{ac}-V_{dc}).

The analysis of the participation factors of the lowest damped modes indicates that CSs using the q-component of the ac current within the droop control structure (CS2 (V_{dc}-I_{ac}) and CS4 (I_{ac}-V_{dc}))

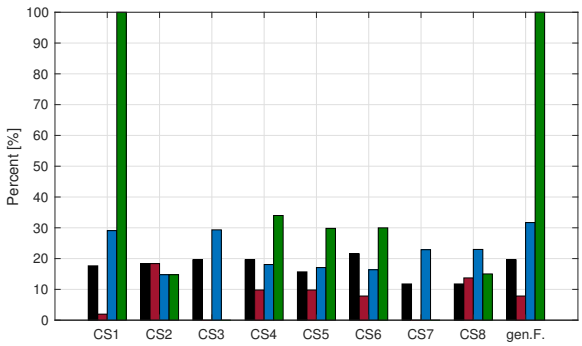

Figure 4.4: Size of subset $\mathbb{S}^{ac,dc}$ with respect to $\mathbb{S}$ in percent for the fast (black) and slow tuning (red). The minimum damping ratio of the corresponding eigenvalues of subset $\mathbb{S}^{ac,dc}$ is shown in percent in blue for the fast and in green for the slow tuning. Source: [**Pub. D**].

create a stronger coupling between the outer control loops and therefore for specific modes a stronger coupling between the dc and ac systems. The analysis shows that in this case the subset $\mathbb{I}^{dc}$ participates with $\eta_{dc} = 9.4\,\%$ (CS4 (I_{ac}-V_{dc}) (fast tuning)) respectively $\eta_{dc} = 6.9\,\%$ (CS2 (V_{dc}-I_{ac}) in those modes which have a high participation of both ac voltage controllers and corresponding ac states, while in case other CSs are used the dc participation in these modes is $\leq 2.2\,\%$ (fast tuning).

Further, it is worth mentioning that both CSs using the dc current (CS1 (V_{dc}-I_{dc}) and CS3 (I_{dc}-V_{dc})) lead to almost complete decoupling of the ac and dc systems in case of the slow tuning, i.e. there exists no (CS3 (I_{dc}-V_{dc})), respectively only very few very well damped eigenvalues. Further, in the fast tuning case, they lead to a medium coupling but all interaction modes are very well damped. In fact, unlike the other CSs all eigenvalues but two corresponding to the interaction modes have a damping ratio of $100\,\%$ and the two remaining ones have significant higher damping ratios ($\geq 29\,\%$) than the lowest damped eigenvalues corresponding to the interaction modes of all remaining CSs.

The impact of the generalized feedback controller can be evaluated by comparing the results of CS1 (V_{dc}-I_{dc}) with the scenario where both GSCs use the generalized feedback controller since they differ only by the use of the measurement signals and additional corresponding droop gains as indicated in section 4.5.3. Figure 4.4 shows that this leads to a slightly higher number of interaction modes ($21.6\,\%$ to $17.7\,\%$ (fast tuning), $7.8\,\%$ to $2\,\%$ (slow tuning)), hence a higher coupling between the subsystems as intuitively expected due to the communication between the converters. Further, in the fast tuning case, it leads to a slightly higher damping of that aforementioned pair of eigenvalues $31.6\,\%$ to $29.1\,\%$.

Thus, considering that it is preferable to have the ac and dc grid as decoupled as possible with as well damped interaction modes as possible CS7 (P_{dc}-V_{dc}) shows the best properties. For the slow tuning it leads to a complete decoupled system while for the fast tuning it leads to the most decoupled system and a medium damping (together with CS8 (P_{ac}-V_{dc})). Further, CS3 (I_{dc}-V_{dc}) leads to a complete decoupled system with the slow tuning as well. However, in case of the fast tuning a higher coupling of the system (with even though very well damped interaction modes) can be observed. Hence, the best results in particular for the slow tuning are observed for both CSs, combining V_{dc} with dc variables and controlling V_{dc} in the second loop.

On the other hand, CS2 (V_{dc}-I_{ac}) leads to a medium coupling of the systems (size of $\mathbb{S}^{ac,dc}$= $18.3\,\%$ of $\mathbb{S}$) and the lowest damping of the most critical interaction mode ($14.8\,\%$). However, considering that TSOs allow damping ratios as low as 3% in their systems, the values of all CSs are not critical in terms of system security. Nevertheless, significant differences between the CSs have been shown.

Converter Interactions

Fig. 4.5 shows the size of the subset $\mathbb{S}^{gsc}$ with respect to the set of all modes $\mathbb{S}$ in percent in black (fast tuning) and red (slow tuning) respectively. Further, it indicates the minimum damping ratio of the interaction modes in that subset in percent in blue (fast tuning) and green (slow tuning). The figure shows a high degree of coupling of the two converters and that also the degree of coupling between the different converters depends on the choice of the CS and the tuning, since the size of the subset $\mathbb{S}^{gsc}$ varies between $43.1\,\%$ (CS4 (I_{ac}-V_{dc}) and CS6 (V_{dc}-P_{ac})) and $54.9\,\%$ (CS5 (V_{dc}-P_{dc}) and CS7 (P_{dc}-V_{dc})) of $\mathbb{S}$ (fast tuning) and between $41.2\,\%$ (CS1 (V_{dc}-I_{dc}) and CS3 (I_{dc}-V_{dc})) and $54.9\,\%$ (CS5 (V_{dc}-P_{dc})) of $\mathbb{S}$. The choice of CS2 (V_{dc}-I_{ac}) leads to $38.8\,\%$ of $\mathbb{S}$ being interaction modes of the subset $\mathbb{S}^{gsc}$.

Further, it is shown that the choice of the CS and its tuning influences the degree of coupling between the converters and also how well those interaction modes are damped. The blue (fast) and green (slow) bars in Fig. 4.5 indicate minimum damping ratios between $3.3\,\%$ (CS4 (I_{ac}-V_{dc})) and $10\,\%$ (CS6 (V_{dc}-P_{ac})) (fast) and between $10.1\,\%$ (CS7 (P_{dc}-V_{dc})) and $14.3\,\%$ (CS8 (P_{ac}-V_{dc})) (slow), hence significant differences and close to critical damping ratios for CS4 (I_{ac}-V_{dc}). The choice of CS2 (V_{dc}-I_{ac}) leads to a minimum damping ratio of $5.4\,\%$.

Thus, the best performing CS from the previous subset, CS7 (P_{dc}-V_{dc}), leads to a comparably medium (slow) / high (fast) degree of coupling between the GSCs and a comparably low (slow) / medium (fast) level of damping ratio with respect to the other CSs. The second place, CS3 (I_{dc}-V_{dc}), leads to a low (slow) / medium (fast) degree of coupling and comparably low (slow) / medium (fast) damping ratios.

The analysis of the participation factors of the least damped modes indicates that all least damped modes are related to the outer control loops (mostly ac voltage controllers) and the corresponding ac variables. Thus, the previously observed stronger coupling between the outer control loops in case the q-component of the ac current is used within the droop control structure (CS2 (V_{dc}-I_{ac} and CS4 (I_{ac}-V_{dc}) (fast tuning)) also leads to a lower damping of the most critical interaction modes of the system. However, apart from this and the fact that CSs combining I_{dc} with V_{dc} with a slow tuning lead to a comparably low degree of coupling of the GSCs, there is no clear tendency that a specific combination of variables or order of control loops is better or worse in general within this subset.

The generalized feedback leads to a higher degree of coupling ($49\,\%$ to $45.1\,\%$) as intuitively expected due to communication between the converters, however, it does not improve the damping of the most critical interaction mode.

4.5.5 Discussion

It has been shown that the choice of the CSs as well as the tuning influences the degree of coupling between the different subsystems. Further, a CS leading to a low degree of coupling of dc and ac systems does not consequently also lead to a lower degree of coupling within the dc grid.

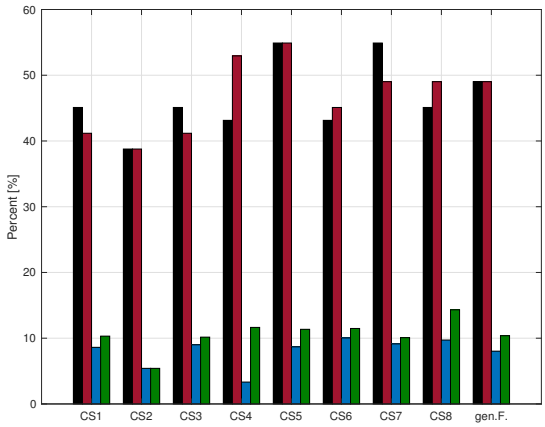

Figure 4.5: Size of subset $\mathbb{S}^{gsc}$ with respect to $\mathbb{S}$ in percent for the fast (black) and slow tuning (red). The minimum damping ratio of the corresponding eigenvalues of subset $\mathbb{S}^{gsc}$ is shown in percent in blue for the fast and in green for the slow tuning. Source: **[Pub. D]**.

Additionally, a trade-off between the degree of coupling of the subsystems, the damping of the interaction modes and the response time of the converters was observed.

A CS controlling V_{dc} in the second loop and combining it with a second dc variable (I_{dc}/P_{dc}) is especially with a slow tuning preferable for decoupling the dc and ac subsystems. On the other hand, a CS combining V_{dc} with I_{dc} and a slow tuning leads to a comparably low degree of coupling within the dc grid. Thus, CS3 (I_{dc}-V_{dc}) achieves overall the best results with a comparably slow transient response. For a fast response the results are not as clear as for the slow response. In that case different CSs have advantages in different subsets. Considering the higher importance of the subset $\mathbb{S}^{ac,dc}$, CS8 (P_{ac}-V_{dc}) is a good candidate for a fast transient response, since it leads to the most decoupled dc and ac subsystems with a comparably medium damping ratio.

Finally, a generalized feedback increases the coupling of the subsystems and the damping of specific but not all interaction modes.

To sum up, the impact of the choice of the droop control structure and its tuning on the degree of coupling of different subsystems in an interconnected AC/MT-HVDC system has been analyzed. It has been highlighted that the choice of the droop control structure and its tuning influence the degree of coupling of the dc grid with the connected ac grids as well as the degree of coupling between the GSCs. Moreover, it has been shown that the damping of these interaction modes also depends on the choice of the droop control structure and its tuning.

4.6 Disturbance Attenuation of DC Voltage Droop Control Structures in a MT-HVDC Grid

After the assessment of the impact on the interaction modes, we continue with an in-depth analysis of how well uncontrolled disturbances in the dc grid are damped using the different control structures. In a MT-HVDC grid, WFC usually do not participate in the dc voltage control but serve as grid forming units of the offshore collection grid, and thus can be interpreted as uncontrolled disturbances for the dc grid, exporting as much power as available. The GSCs, on the other hand, use dc voltage droop control to control the dc voltage while balancing the active power. Thus, the GSCs continuously respond to the uncontrolled disturbances due to the wind-infeed fluctuations, ideally without violating any current or voltage limitations even in the worst case scenario. This work investigates how well the different control structures perform in the worst case scenario and how important a detailed dc cable modeling is. Moreover, we reveal that maximum singular value limits, frequently used in literature for Multiple Input Multiple Output (MIMO) analysis, are not sufficient to prove that the impact of specific disturbances on analyzed outputs are within a certain boundary. The work presented in this section has been published in [**Pub. C**].

In this work, we adapt a methodology, proposed in [69]. Initially, the methodology was used to analyse the multi-variable frequency response for one specific dc voltage droop CS. It was further extended in [9] using the methodology to design a droop controller using certain requirements based on maximum Singular Value (SV) limits. In our work, we adapt the methodology to compare the disturbance attenuation of the different dc voltage droop control structures. This provides insight on potential differences between the CSs and the suitability of the different structures in combination with e.g. offshore nodes.

Thus, the contributions of this work include the following: (i) an analysis and comparison of the multi-variable frequency response of the eight different CSs is performed. Further, (ii) the

results for a frequency dependent and a conventional π-equivalent dc cable model are compared, indicating how the usage of the latter might lead to overrated resonance peaks. The result is verified by a participation factor analysis of the eigenvalues corresponding to the resonance peaks in order to determine the origin of resonance peaks observed in the singular value representation. Finally, (iii) we point out that the maximum SV limits frequently used in literature (e.g. [9], [14]) for MIMO analysis are not sufficient to prove that the impact of specific disturbances on analyzed outputs is within a certain boundary. Due to the fact that these maximum SV limits implicitly assume the same amplification at every output, it is necessary to verify them by a Multiple Input Single Output (MISO) analysis of the transfer functions connecting the inputs with the highest amplified output [**Pub. C**].

This section is structured as follows: First, the methodology will be introduced, then the analyzed model will be presented followed by a discussion of the results.

4.6.1 Methodology

The methodology enables the analysis of the different dc voltage droop control structures considering all the dynamics of a generic multi-terminal HVDC system. The control structure of a generic multi-terminal HVDC system is illustrated in Fig. 4.6. The wind farms are assumed to control the ac grid voltage and angle and to export all available active power. Thus their active power in-feed into the dc grid is considered as uncontrolled disturbance for the distributed droop voltage control scheme. Based on this scheme the closed loop transfer function matrices combining the converters and both ac and dc grid dynamics can be calculated:

$$\mathbf{E}_w(s) = \frac{\mathbf{z}(s)}{\mathbf{w}(s)} = \frac{(\Delta V_{dc,1}(s) \ \cdots \ \Delta V_{dc,M}(s))^T}{(P_{wf,N+1}(s) \ \cdots \ P_{wf,M}(s))} \tag{4.11}$$

$$\mathbf{U}_w^{uiq}(s) = \frac{\mathbf{u}_{iq}(s)}{\mathbf{w}(s)} = \frac{(i_{c,1}^{q*}(s) \ \cdots \ i_{c,N}^{q*}(s))^T}{(P_{wf,N+1}(s) \ \cdots \ P_{wf,M}(s))} \tag{4.12}$$

where $\mathbf{E}_w(s)$ is the transfer function matrix relating the power induced into the HVDC grid by the wind farms, $\mathbf{w}_i$, with the dc voltage deviations at all terminals, $\mathbf{z}_i$. Indices $k = 1 \dots N$ represent the GSCs, while $k = N+1 \dots M$ represent the connected wind farms. The transfer function matrix $\mathbf{U}_w^{uiq}(s)$ relates accordingly the wind farm power, $\mathbf{w}$, with $\mathbf{u}_{iq}$, the active current loop references of the current loops of the different GSCs.

The performance of the control structures is evaluated by analyzing the frequency response of the system transfer function matrices, using the singular values representation. The method can be understood as an expansion of the Bode frequency representation for multi-variable systems [9]. The operation requirements, such as the desired power sharing among the different converters

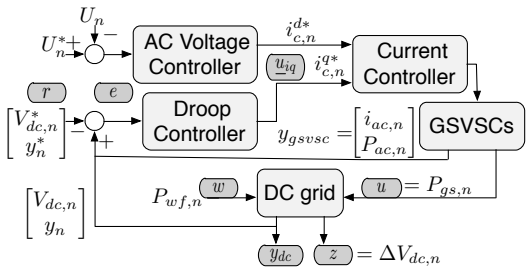

Figure 4.6: Control structure of multi-terminal HVDC grid. Source: [**Pub. C**].

controlling the DC voltage, the maximum voltage error allowed at the grid terminals and the maximum converter current ratings, can be transferred as gain boundaries in the multi-variable frequency response of the overall system [69].

The singular value representation of the system transfer function matrix, $\mathbf{E}_w(s)$, can be obtained as:

$$\sigma_i(\mathbf{E}_w(j\omega)) = \sqrt{\lambda_i(\mathbf{E}_w^T(j\omega)\mathbf{E}_w(j\omega))} \tag{4.13}$$

where λ_i is the i-eigenvalue of the matrix. The maximum SV $\overline{\sigma}(\mathbf{E}_w(j\omega))$ indicates the maximum amplification of the corresponding inputs by the system seen from a specific output. Here, we analyse which effect the wind power input ($\mathbf{w}$ in Fig. 4.6) has on the dc voltage deviations ($\mathbf{z}$) at all HVDC terminals.

As aforementioned, the operation requirements can be translated into gain boundaries of the singular value frequency response. The energy of the error e, caused by any disturbance w of bounded energy, is given by [9]:

$$\max_{v\neq 0} \frac{\|\mathbf{e}\|_2}{\|\mathbf{w}\|_2} = max_\omega \overline{\sigma}(T_{ew}(j\omega)) \tag{4.14}$$

where $\|\mathbf{e}\|_2^2 = \int e^T e$ is the 2-norm of e. Thus, for instance ensuring that the effects of a disturbance w on the voltage error e is under defined limits can be expressed as $\overline{\sigma}(E_w(j\omega))$ is bounded at the frequencies of interest [9].

In case a maximum voltage error of 10% (Σ_v) of the nominal value at each terminal should not be exceeded, the maximum singular value $\overline{\sigma}(\mathbf{E}_w(j\omega))$ can be derived as [9]:

$$\overline{\sigma}(\mathbf{E}_w(j\omega)) \leq \frac{\|\mathbf{z}(j\omega)\|_2}{\|\mathbf{w}(j\omega)\|_2} = 20\log_{10}\left(\frac{\sqrt{\sum_{k=1}^{M}(V_{dc,k}\cdot\Sigma_v)^2}}{\sqrt{\sum_{k=N+1}^{M}P_{wf,k}^2}}\right) \tag{4.15}$$

In addition, in [9] the authors derive the maximum gain the SV representation of the transfer function $\mathbf{U}_r^{uiq}(j\omega)$ should not exceed. As given in (4.12), these transfer functions indicate the impact of the wind power in-feed on the active current loop references of the different GSCs. This maximum gain corresponds to a maximum allowed current flowing through the GSCs of $110\,\%$ (Σ_i) of the nominal current value, $i_{l,n}$.

$$\overline{\sigma}(\mathbf{U}_w^{uiq}(j\omega)) \leq \frac{\|\mathbf{u}_{iq}(j\omega)\|_2}{\|\mathbf{w}(j\omega)\|_2} = 20\log_{10}\left(\frac{\sqrt{\sum_{k=1}^{N}(i_{l,n,k}\cdot\Sigma_i)^2}}{\sqrt{\sum_{k=N+1}^{M}P_{wf,k}^2}}\right) \tag{4.16}$$

However, by using the L_2-norm these limits calculate the maximum energy of the error caused by the disturbances that would lead to a $10\,\%$ voltage deviation / $110\,\%$ nominal current at each terminal. Hence, these limits assume implicitly that the deviation of the outputs is the same for all outputs, i.e. in our case that the dc voltage deviation is the same at each terminal in the whole grid. However, this is not true and since the exact deviation at the less deviating terminals is not known in advance it can therefore not be considered in the calculation. Therefore, we will show that it is necessary to validate the results by analysing the transfer functions from the chosen disturbances to that output which experiences the highest deviation. That means, to calculate the maximum error, Σ, of the most deviating output by using $\overline{\sigma}$ of the MISO analysis one has to solve (4.15) and

(4.16) for Σ while neglecting the sum in the numerator considering only the single most deviating output.

Extending the SV analysis, we analyzed the eigenvalues, λ_i, in terms of their damping ratio, ζ, and damped circular frequency, ω_d, in order to determine those eigenvalues corresponding to the resonance peaks in the SV representation. Then, we used the participation factor analysis described in section 2.7.4 allowing us to determine the origin of the resonance peaks.

4.6.2 Modeling particularities

The modeling is done according to the generic MT-HVDC model described in section 4.5.2-4.5.3. The only differences are that (i) a generalized feedback controller was not considered and that (ii) the tuning of the outer controllers is based on optimization based robust control techniques [133] determining the tuning of the controllers $K(s)$ minimizing the H_∞ norm $\|T_{w,r\to y}(K)\|_\infty$, where $T_{w,r\to y}(K)$ denotes the closed loop transfer functions from the disturbance, $\mathbf{w}$, respectively the references, $\mathbf{r}$, to the measurements, $\mathbf{y}$. A comparable tuning for a chosen settling time of $100\,\mathrm{ms}$ [131] was achieved using pre- and post-compensators.

Furthermore, this work compares the impact of two different dc line models. First, the results are discussed for a conventional π-equivalent model. As discussed in section 2.7.2, this is a simplified model, but it is considered appropriate, as D'Arco also argues in [6], since the chosen model represents the worst case scenario with respect to LC oscillations [**Pub. C**]. In [14], however, the authors argue that for SV decomposition studies the conventional π model is not sufficient. Therefore, in a second step, the results are compared to the case where a 'frequency dependent π' cable model is used. The model, introduced in section 2.7.2, is called 'frequency dependent π' since the additional parallel branches are calculated to fit the frequency response of a wide-band cable model [14, 57].

4.6.3 Case study

The analysis is performed for a three terminal grid shown in Fig. 4.7 for a scenario where both GSCs use the same dc voltage droop control structure and the same droop gain values. The parameters are given in the appendix. The results are compared for the different dc cable models and examined with a participation factor analysis in order to detect the origin of the resonance peaks.

The wind farm is assumed to inject maximum power into the HVDC grid, since this leads to the highest gains of the SV representation. Thus, it represents the worst case scenario. The linearized

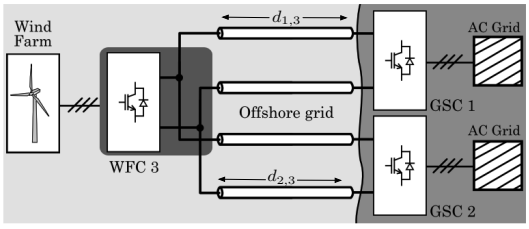

Figure 4.7: Three terminal VSC-HVDC grid. Source: [9].

model is verified by an equivalent non-linear model built in Matlab Simulink, which also provides the steady state initial values.

The results of the SV analysis of $\mathbf{E}_w(j\omega)$ and $\mathbf{U}_r^{uiq}(j\omega)$ for both dc cable models are shown in Fig. 4.8. The maximum SV leading to a maximum of $10\,\%$ voltage deviation at each terminal ($\overline{\sigma}(\mathbf{E}_w(j\omega))$) and to maximum $110\,\%$ of the nominal current flowing through the GSCs ($\overline{\sigma}(\mathbf{E}_w(j\omega))$) can be calculated following (4.15)-(4.16):

$$\overline{\sigma}(\mathbf{E}_w(j\omega)) \leq 20\log_{10}\left(\frac{\sqrt{\sum_{k=1}^{M}(V_{dc,k}\cdot\Sigma_v)^2}}{\sqrt{\sum_{k=N+1}^{M}P_{wf,k}^2}}\right) = 20\log_{10}\left(\frac{(\sqrt{(4\cdot10^5\cdot0.1)^2\cdot3}}{700\cdot10^6}\right) = -80.09\,\mathrm{dB} \tag{4.17}$$

$$\overline{\sigma}(\mathbf{U}_w^{uiq}(j\omega)) \leq 20\log_{10}\left(\frac{\sqrt{\sum_{k=1}^{N}(i_{l,n,k}\cdot\Sigma_i)^2}}{\sqrt{\sum_{k=N+1}^{M}P_{wf,k}^2}}\right) = 20\log_{10}\left(\frac{\sqrt{(1465.5\cdot1.1)^2\cdot2}}{700\cdot10^6}\right) = -109.74\,\mathrm{dB} \tag{4.18}$$

In order to visualize these limits and put them into context to the performance of the different CSs, we faded the area exceeding those limits gray in Fig. 4.8.

Cable model: conventional π

The SV representations of $\mathbf{E}_w(j\omega)$ (Fig. 4.8a) are very similar for all CSs besides CS2($V_{dc}-I_{ac}$), which, however, is the only droop control structure without a PI-controller. All CSs besides CS2($V_{dc}-I_{ac}$) exceed the limit of $-80.09\,\mathrm{dB}$ already for $\omega \ll 1$ with values around $-79.3\,\mathrm{dB}$. CS2($V_{dc}-I_{ac}$) stays at approx. $-89\,\mathrm{dB}$ for $\omega \leq 1$. For higher frequencies the SV representations of all CSs indicate a peak at a resonance frequency: CS2($V_{dc}-I_{ac}$) at $145.5\,\mathrm{rad/s}$ (=23.2 Hz), all remaining CSs: at approx. $180\,\mathrm{rad/s}$ (=28.6 Hz). Here, all CSs exceed the limit with a maximum $\overline{\sigma}(\mathbf{E}_w(j\omega))$ of approx. $-73.6\,\mathrm{dB}$. Hence, all CSs would exceed the limit of a maximum dc voltage deviation of 10% in case those frequencies are excited.

The SV representations of $\mathbf{U}_r^{uiq}(j\omega)$ (Fig. 4.8c) show that all CSs achieve in steady state a $\overline{\sigma}(\mathbf{U}_r^{uiq}(j\omega))$ of $-110.8\,\mathrm{dB}$. Thus, all CSs comply with the limit. However, similar to the previous analysis, the SV representations of $\mathbf{U}_r^{uiq}(j\omega)$ indicate a resonance peak for all CSs at the same resonance frequencies leading to maximum SVs of $-102.2\,\mathrm{dB}$ (CS2($V_{dc}-I_{ac}$)) to $-106.8\,\mathrm{dB}$ (all remaining CSs). Thus, none of the CSs complies with the limit for the whole frequency range.

The deviation from the results obtained in [9], where only CS6(V_{dc}-P_{ac}) was analyzed, are due to the varied cable length (here $d_{1,3}=200\,\mathrm{km}$, $d_{2,3}=300\,\mathrm{km}$ instead of $d_{1,3}=100\,\mathrm{km}$, $d_{2,3}=150\,\mathrm{km}$) as well as the fact that the dc voltage deviation at the wind farm is also considered. Here, a smaller droop gain would be necessary to comply with the derived limits. Hence, the analysis shows that with this cable model the choice of the droop gains is closely related to the length of the cables as well as the capacitance size of the wind farm converter.

In the Single Input Single Output (SISO) case, the SV analysis is equivalent to the bode diagram of the corresponding transfer function. In the MIMO case, however, the maximum SV is the maximum gain for any input direction, hence the SV representation is not just the sum of the bode diagrams of the corresponding transfer functions. Nevertheless, it is possible to determine the eigenvalues causing the resonance peaks by examining the damped circular frequencies and ratios of the corresponding transfer functions. The corresponding eigenvalues have been examined by a

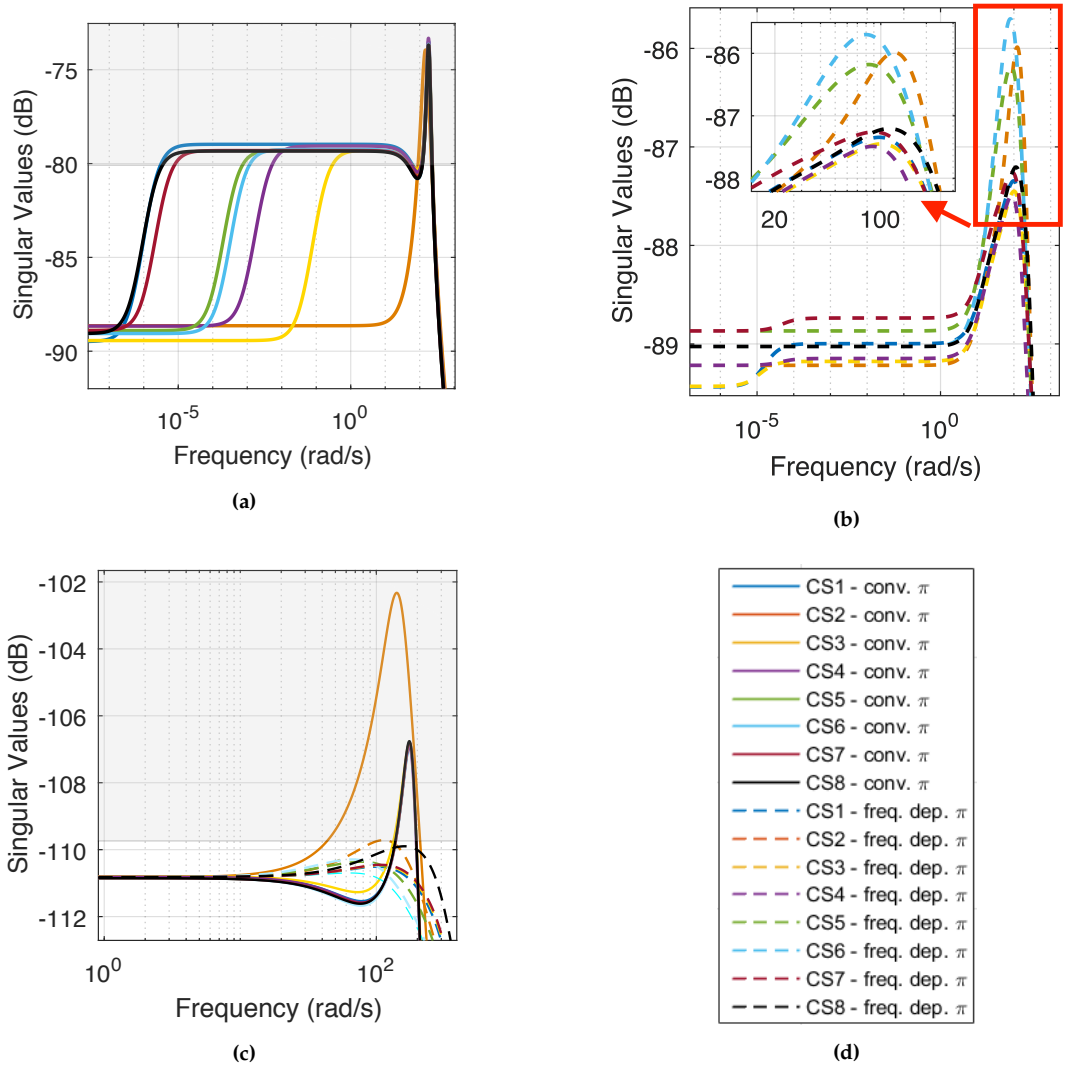

Figure 4.8: Singular value representation of a) $E_w(j\omega)$ (wind power input - dc voltage deviation) for a π-equivalent dc cable model and b) $E_w(j\omega)$ for a 'frequency dependent π' cable model, c) $\mathbf{U}_r^{uiq}(j\omega)$) (wind power input - current controller reference) for both models and d) the legend for all graphs. Source: [**Pub. C**].

participation factor analysis in order to identify the source of the resonance peak. The analysis is done for the case where both GSCs use CS1(V_{dc}-I_{dc}). However, further analyses showed that the results can be generalized for the remaining CSs.

The analyses showed that the resonance peak of CS1(V_{dc}-I_{dc}) in Fig. 4.8a is related to a pair of complex eigenvalues, with a damping ratio of $14.5\,\%$. The participation factor analysis of this pair of complex eigenvalues causing the resonance peak is shown in Fig. 4.9. It indicates, that the peak is mainly related to the dc voltage at the wind farm, $V_{dc,3}$, the currents in the dc lines, $I_{dc,13}$ and $I_{dc,23}$ as well as the dc voltage at GSC1, V_{dc}. Similar results with varying damping ratios are obtained for the analysis of the resonance peaks of the remaining GSCs. Hence, the resonance peaks, i.e. the maximum possible amplifications of dc voltage oscillations, are always related to dc values at the wind farm. The results are also similar for the analysis of eigenvalues corresponding to the peaks of the SV representation of the transfer function matrix $\mathbf{U}_w^{uiq}(s)$, which resembles the control action. Hence, in contrast to the usual practice that the wind farm converter does

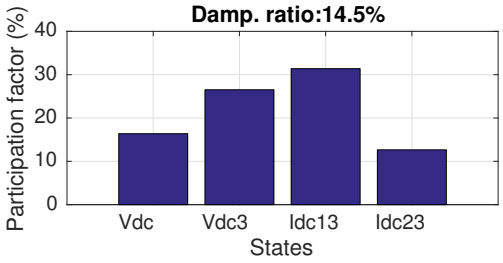

Figure 4.9: Participation factor analysis of the complex pair of eigenvalues causing the resonance peak in case of CS1(V_{dc}-I_{dc}). Source: [**Pub. C**].

not participate in the dc voltage control, the results indicate that a participation or an additional damping of dc voltage oscillations at this point could be feasible.

Cable model: frequency dependent π

Compared with the conventional π model, the frequency dependent π model enables the droop control structures to react faster without causing instability, which results in a better disturbance attenuation. Hence, the results for $E_w(j\omega)$ (Fig. 4.8b) indicate lower SVs for the whole frequency range for all CSs, however, with slightly bigger differences between them. Still, in steady state, the maximum SVs of all CSs are comparable, with CS1(V_{dc}-I_{dc}) achieving the lowest with $-89.5\,\mathrm{dB}$. The differences are caused by the different tunings and the fact that (4.8) is only an approximation of the non-linear control behavior of active power and dc voltage [125].

For frequencies $\geq 10\,\frac{\mathrm{rad}}{\mathrm{s}}$, CS4($I_{ac}$-$V_{dc}$) achieves the lowest $\overline{\sigma}(\mathbf{E}_w(j\omega))$ with $-87.49\,\mathrm{dB}$ at a frequency of $88\,\mathrm{rad/s}$ (=$14\,\mathrm{Hz}$). The highest maximum singular value is obtained by CS6($V_{dc} - P_{ac}$) with $-85.7\,\mathrm{dB}$, closely followed by CS2(V_{dc}-I_{ac}) ($-85.99\,\mathrm{dB}$) and CS5(V_{dc}-P_{dc}) ($-86.18\,\mathrm{dB}$).

Although it seems, as if all CSs stay far below the $10\,\%$ voltage deviation limit ($-80.09\,\mathrm{dB}$), it is not possible to calculate the maximum dc voltage deviation from these dB values using (4.15), since the dc voltage deviation at each converter differs. Assuming the same deviation for all outputs, as (4.15) and (4.16) do, a maximum deviation of $4.27\,\%$ (CS4(I_{ac}-V_{dc})) and $5.26\,\%$ (CS6($V_{dc} - P_{ac}$)) would be achieved. However, the deviations are not the same. In fact, the highest deviation can be observed at the wind farm, due to the fact that there is no dc voltage control at this point and the input is not damped by a cable. Hence, if we only consider the transfer function from wind power input to dc voltage deviation at the wind farm converter we can calculate a maximum voltage deviation of $5.74\,\%$ (CS4(I_{ac}-V_{dc})) and $6.73\,\%$ (CS6($V_{dc} - P_{ac}$)) using (4.15). Thus, in contrast to what is implicitly assumed in (4.15) and (4.16), when deriving a maximum SV limit in the MIMO analysis, it always needs to be considered that the output deviation might not be the same at every output. Since the deviation at the less deviating terminals is not known in advance and can therefore not be considered in the calculation, the transfer functions from the disturbances to the highest deviating output (MISO analysis) should be analysed additionally in order to verify the results.

The analysis of the control action, i.e. the SV representation of $\mathbf{U}_w^{uiq}(j\omega)$ (Fig. 4.8c), for the various CSs indicates small differences between the different CSs. Here, only CS2($V_{dc} - I_{ac}$) exceeds the limit of $-109.74\,\mathrm{dB}$ slightly. Although the remaining CSs do not exceed the limit, it is necessary to analyse the transfer function from the wind power input to the highest deviating output, the current reference at the converter station closest to the wind farm, GSC1. It indicates that only

CS4(I_{ac}-V_{dc}) would comply with the boundary of max. $110\,\%$ of the nominal current flowing through GSC1. While - in case the frequencies corresponding to the resonance peaks are excited by the input signal - the current exceeds from $111\,\%$ (CS5(V_{dc}-P_{dc})) up to $120\,\%$ (CS8(P_{ac}-V_{dc})) of the nominal current for the remaining CSs.

Analysing the eigenvalues of CS1(V_{dc}-I_{dc}), a complex pair of eigenvalues with similar participation factors as the one leading to the resonance peak in the conventional π model can be identified at the damping frequency of $327.44\,\mathrm{rad/s}$ (=$52.1\,\mathrm{Hz}$) with a damping ratio of $52.2\,\%$. Hence, the different dc cable parameters lead to a change in the resonance frequency and a significantly higher damping.

4.6.4 Discussion

The results show that it is important to use a more accurate frequency dependent cable model as it allows to perform a more accurate design of the distributed droop voltage control.

Further, it was shown that the maximum dc voltage deviation depends on the chosen dc voltage droop CS. In fact, for the topology chosen in the case study it can be minimized to $5.74\,\%$ by using CS4($I_{ac} - V_{dc}$) instead of $6.73\,\%$ with CS6($V_{dc} - P_{ac}$), which would allow the operator to operate the system closer to the nominal values, thus more efficiently.

Only CS4($I_{ac} - V_{dc}$) managed to comply also with the requirement of limiting the current flowing through the GSCs to 110% of the nominal current. The choice of a higher droop gain would allow all CSs to comply with that requirement, however, at the same time it would increase the dc voltage deviation. The effect is the same for all CSs, hence, the differences between them are comparable for different droop gains. Finally, the need for MIMO analyses due to varying impact of the disturbance on the different HVDC terminals has been highlighted.

Thus, The impact of the various dc voltage droop control structures has been compared for two different dc cable models. It was shown that the possible amplification of dc oscillations depends up to a certain extent on the chosen dc voltage droop control structure. Finally, we showed that the maximum singular value limits, frequently used in literature for MIMO analysis, is not sufficient to prove that the impact of specific disturbances on analyzed outputs is within a certain boundary. In fact, it is necessary to verify them by an analysis of the transfer functions connecting the disturbances with the highest deviating output (MISO analysis) due to an uneven impact of the disturbances on the different outputs.

4.7 Interaction of Droop Control Structures and Its Inherent Effect on the Power Transfer Limits in Multi-Terminal VSC-HVDC

After having assessed the response of the different control structures to uncontrolled disturbances within the dc grid and the influence of the different control structures on the interaction modes, this work develops a methodology to determine the potential operation space of an arbitrary MT-HVDC for selectable requirements (e.g. voltage / current limits or robustness against disturbances). The work presented in this section has been published in **[Pub. A]**. The contributions enclose (i) a methodology enabling us to determine the potential operation space of an arbitrary MT-HVDC for freely selectable requirements. Since this methodology is not limited to the usage of simplified Thévenin equivalents as ac grid representation but could also be used with more detailed multi-machine models, it could be used for detailed grid expansion planing as well as for power system

security studies. In fact, this methodology is adapted and developed further in section 6.6 allowing us to incorporate potential preventive and corrective control actions of HVDC terminals and security considerations into market clearing.

In the case study of this chapter, the methodology is used (ii) for a stability analysis of different droop control implementations. It is applied to analyze a MT-HVDC grid, which extends the work in [75], to emphasize the impact of different control structures [**Pub. A**]. In particular, the flexibility against active power flow variations and robustness against disturbances will be compared and analyzed for all the various implementations.

Additionally, (iii) the stability limits of the most promising configurations will be analyzed and the limitations discussed in more detail. This will also provide further insight on how different droop controlled converters influence each other.

This work uses the general mathematical model described in section 2.7.2.

This section is structured as follows: After introducing the methodology, a case study of a three terminal grid will be presented and the findings will be discussed.

4.7.1 Methodology

The operation space of an arbitrary MT-HVDC is defined by the safe operation range of the MT-HVDC in terms of the maximum active power and reactive power flows in the MT-HVDC grid. The safe operation range is defined in this section as the set of operating points fulfilling the requirements set by the user applying the method. Examples for these requirements, as e.g. voltage and current limits, will be introduced in the following subsection. In this study, we propose a methodology focusing on the active power transfer capability considering a variation of the power sharing between the terminals, i.e. a variation of the droop gain. However, the methodology can easily be adjusted to also include the reactive power capabilities and an arbitrary number of terminals in an MT-HVDC grid.

The differences between the various dc voltage droop controllers are analyzed in terms of active power transfer capability as a function of the droop gains of the connected GSCs using droop control. That means by using eigenvalue analysis, the eigenvalue movement is analyzed for a variation of the disturbances (= power injection at uncontrolled dc nodes / WFCs) and a variation of the droop gains. The sensitivity of certain eigenvalues for a variation of these parameters is shown in Fig. 4.10.

For each combination of these parameters, the nonlinear system is linearized and the steady state is evaluated with respect to the chosen requirements for an acceptable operation point. These requirements can be chosen by the user applying the method and could include e.g. specific stability margins and / or current / voltage limitations. This analysis will basically result in a set of acceptable operation points, which are plotted with respect to the power transferred at a specific terminal (see Fig. 4.11). The surfaces of this area of acceptable operation points in this plot illustrate the upper and lower boundary (both directions of power flow) of acceptable operation for a specific combination of droop gains at each terminal. This set of acceptable operation points varies with respect to the chosen requirements. In contrast to other publications using small signal analysis, this methodology helps to determine the range of acceptable operation for a specific terminal within a multi-terminal grid for various control structures with all possible droop gain

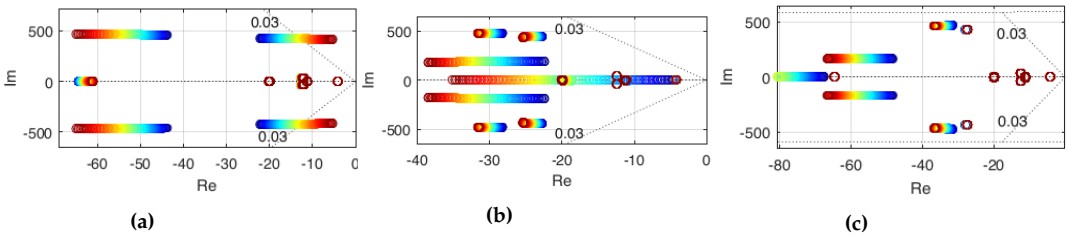

Figure 4.10: Visualization of the sensitivity of certain eigenvalues and the stability margin of a minimum damping ratio of 3%. The pole movement is shown for a variation of a) p_{wf} from 0 p.u. (blue) to 1 p.u. (red), b) k_{droop} from 0 (blue) to 0.1 (red) and c) k_{droop_gs2} from 0 p.u. (blue) to 0.1 p.u. (red) for otherwise fixed values of $p_{wf} = 0$ pu, $k_{droop} = 0.1$ p.u. and $k_{droop,gs2} = 0.1$ p.u.. Source: **[Pub. A]**.

combinations and any arbitrary requirement. This operating range is expressed as a range of possible power flows at that terminal for a specific droop gain combination. Therefore, it is referred to as Active Power Transfer Capability (APTC) in the following.

Finally, the steady states at the boundary of the Active Power Transfer Capability (APTC) are analyzed by a participation factor analysis, in order to identify the states associated with the modes causing the violation of a specific stability margin. This provides insight in determining the origin of the boundary and identifies which part of the system is provoking the limit.

Here, this analysis is used to illustrate the focus of this work: revealing the impact of the choice of the droop control structure on the APTC for different exemplary requirements for an acceptable operation point. Since the models differ only in terms of the droop control structures, this analysis allows to determine which effect each control structure has on the APTC of each terminal and the whole system. Further, it reveals which control structures are more beneficial than others in terms of the APTC. Additionally, in the planning phase of a multi-vendor MT-HVDC grid, probably using different kind of droop control structures, the analysis facilitates to determine more or less beneficial combinations of control structures. Moreover, by analyzing these boundaries along the variation of the droop gains, it provides insight on how the choice of the droop gain values affects

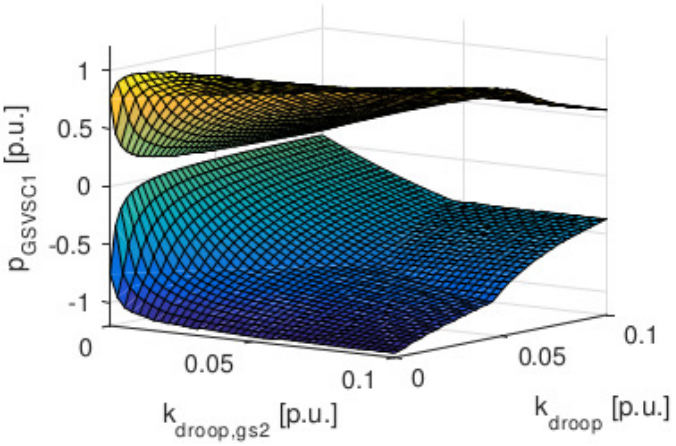

Figure 4.11: Visualization of the operation boundaries. Source: **[Pub. A]**.

the APTC during operation. Additionally, it indicates whether a certain ratio of the droop gain values may be beneficial for maximizing the APTC.

Flowchart of the Methodology

The methodology is shown in detail in Fig. 4.12, as an example for a three terminal model, as it is used in the case study. The methodology can, however, also be applied to other topologies, the visualization of the APTC just becomes more challenging in case of a higher number of terminals.

The methodology can also be used to determine the operating space of an arbitrary MT-HVDC considering its reactive power capability by varying the reactive power set-points. Furthermore, in section 6.6, it is demonstrated how this methodology is used in combination with N-1 security assessment to exploit the corrective control potential of HVDC terminals. Here, however, the focus is on a variation of the power flow (p^*_{wf}) and the power sharing between the converters ($k_{droop}/k_{droop,gs2}$), allowing us to study the impact of different CSs on the APTC of the system.

First, a range of values for the droop gains, as well for the disturbance resembled by the power injection of the uncontrolled dc node, needs to be defined. Here, the values of the disturbances will define the power flow, while the droop gains will define the power sharing between the terminals.

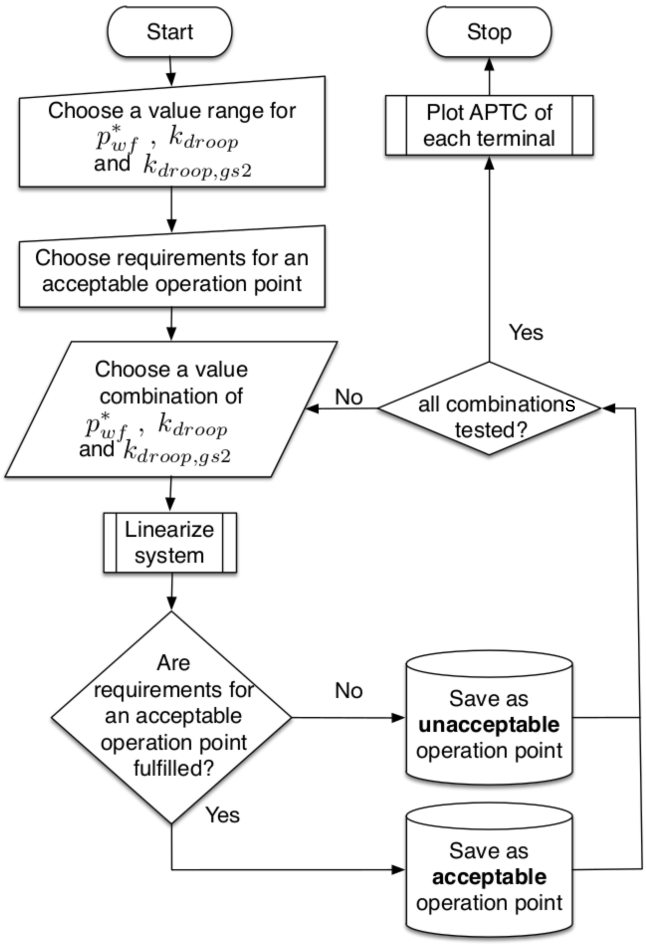

Figure 4.12: Flowchart of Methodology. Source: [**Pub. A**].

In the case study, a value range of $0.0001\,\text{p.u.} \leq k_{droop} \leq 0.1\,\text{p.u.}$ and $-2\,\text{p.u.} \leq p^*_{wf} \leq 2\,\text{p.u.}$ was chosen, however, the ranges can be chosen by the user applying the method according to the analyzed system. Additionally, any arbitrary requirement for an acceptable operation point can be chosen, which can include (several) stability margins and/or current/voltage requirements. Then, the first combination of values is chosen and the nonlinear system obtained from the aforementioned equations is linearized for the given inputs. It is analyzed whether the steady state meets current and voltage limits and whether the eigenvalues satisfy the requirements of various possible stability margins. Depending on the results, the operation points are saved correspondingly and the next combination of values is analyzed.

Requirements for an acceptable Operation Point

As aforementioned, any arbitrary requirement for an acceptable operation point can be chosen by the user applying the method. Since there are no grid codes or standardized requirements for acceptable operation points in MT-HVDC grids defined yet, in the case study the APTC is analyzed for three possible requirements in order to investigate whether a certain requirement (current/voltage limit or stability margin) limits specific control structures more than others. The three requirements are:

Voltage and Current Limits: First, the APTC are analyzed only with respect to the current and voltage limits. Here, these limits are chosen according to the Cigré B4 dc Grid test system, i.e. the dc voltage operational frame is assumed to be between 0.95 p.u. and 1.05 p.u., while the maximum current in the dc cable is set to 2265 A [134].

Damping Ratio $\geq 3\%$: A minimum damping ratio of 3% is required for all eigenvalues [135].

Maximum DC Voltage deviation of 5%: As we presented in section 4.6.1, the performance of the control structures can be analyzed by means of the singular value representation of the system transfer function matrices, $E_w(j\omega)$. As aforementioned, the maximum singular value, $\overline{\sigma}(G(j\omega))$, indicates the maximum amplification of the corresponding inputs by the system seen from a specific output. The analyzed inputs and outputs are the disturbance (wind power input) and the dc voltage errors at the GSCs. Thus, similarly as in section 4.6.1, we derive the maximum gain the singular value representation should not exceed reflecting a specific maximum voltage error. Here, it is adapted to the per unit system and a maximum deviation of 5% at the GSCs is chosen as stability margin:

$$\begin{aligned}\overline{\sigma}(E_w(0)) \leq \frac{\|e(0)\|_2}{\|w(0)\|_2} &= 20\log_{10}\left(\frac{\sqrt{e_{gsc1}+e_{gsc2}}}{p_{wfc}}\right)\\ &= 20\log_{10}\left(\frac{\sqrt{(1\cdot 0.05)^2\cdot 2}}{1}\right) = -23.01\,\text{dB}\end{aligned} \tag{4.19}$$

As the previous case study investigated also the dc voltage error at the wind farms, a wider voltage error was accepted (10%). In this case study, we narrowed our focus on the GSCs concentrating on the differences between the different droop control structures.

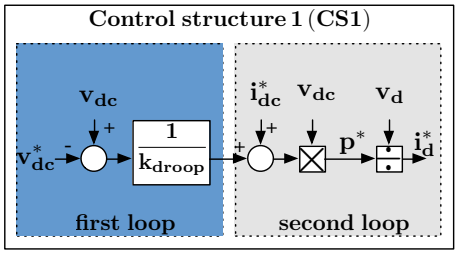

Figure 4.13: Visualization of CS1($V_{dc} - I_{dc}$) without PI controller. Source: **[Pub. A]**.

4.7.2 Modeling particularities

This work uses the model described in section 2.7.2. The only particularity is that this work follows [75] in modeling CS1($V_{dc} - I_{dc}$) as:

$$\text{CS1:}\quad i^*_{l,d,g} = \frac{\left(\frac{v_{dc}-v^*_{dc}}{k_{droop}} + i^*_{dc}\right)\cdot v_{dc}}{v_{o,d}}, \tag{4.20}$$

i.e. without a PI controller as visualized in Fig. 4.13.

4.7.3 Case Study

A symmetric three terminal grid is derived from the aforementioned model, as shown in Fig. 4.14 (the ac sides are equal for all terminals as indicated by the ac system equivalent of the general model). We chose a symmetric case study, because in this case, the same droop gain in both converters leads to an equal power sharing. Thus, it facilitates the comparison between the different CSs.

All used models are verified by time domain simulations with equivalent non-linear models built in Matlab SimPowerSystems. The validation was performed by comparing different step responses of the non-linear and the linearized models. Two validation plots are shown in Fig. 4.15.

The GSCs use each one of the eight different droop control structures. First, both GSCs use the same CSs in order to detect the ones with highest APTC and highest damping ratios. Then, the

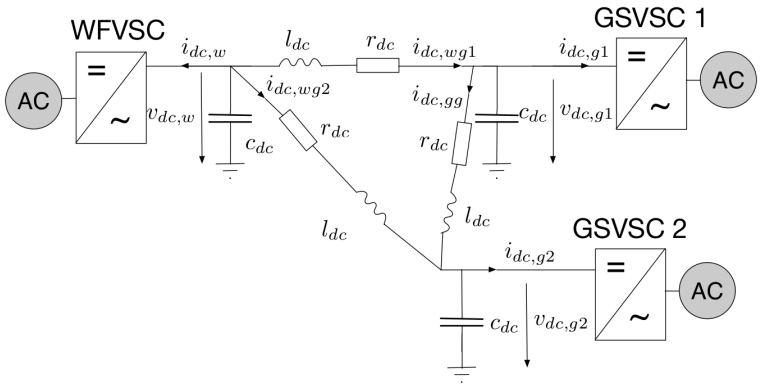

Figure 4.14: Model of the dc grid. Source: **[Pub. A]**.

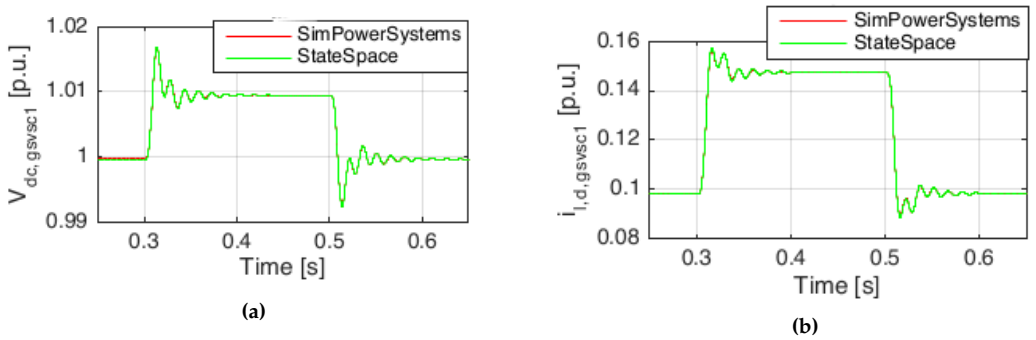

Figure 4.15: Validation of the small signal model by a time domain simulation and comparison with a non-linear model built in Matlab SimPowerSystems. (Response of a) $v_{dc,gs1}$ and b) $i_{l,d}$ to a 10% step in p^*_{wf}). Source: [**Pub. A**].

most promising ones are combined with each other in order to determine the most beneficial combination of droop control structures. Each of these models consists of 52-54 states depending on the dc voltage droop implementations used. All models have been derived using Maxima [136] as the symbolic derivation enables us to initialize the model for every possible operating point.

The analysis depends obviously on the given parameters and should therefore be selected as they appear in the system. In this case study, the dc voltage reference values for both GSCs are set to 1 p.u., while the current and active power reference values of the GSCs are set to 0.1 p.u.. The numerical values for the gains of the droop controller have been selected with respect to the aforementioned reference values to ensure a comparable performance. In particular, if a PI controller is present, its tuning has been set to achieve a 5% overshoot for a 5% step in the dc voltage reference with a fast rise time of approx. $8\,\mathrm{ms}$ and a settling time of a few tens of milliseconds. Thus, it is chosen to be very fast compared to suggestions in the literature of up to few 100 ms [51] in order to approach the limits of the VSC. Additionally, a second tuning with a rise time in the range of tens of milliseconds and a settling time of 100 ms is used as reference case.

In order to ensure comparability but also not to be limited by the VSC representing the wind farm, the active damping of both GSCs are tuned equally, whereas a higher damping factor is chosen for the WFC.

All parameter and base values are given in the appendix. The dc parameters are scaled into per unit by using the same base frequency as for the ac side, as shown in the appendix. This results in apparently high values for per unit inductance and capacitance, however, these parameters are corresponding to a dc cable of about $67\,\mathrm{km}$ [6].

Note that this study was performed before the negative impact of the conventional π cable model was identified and thus uses the conventional π model. As aforementioned, it can be assumed as the worst case scenario. The previous study also indicates that it negatively affects the results for all CSs similarly and thus the results are still comparable. The methodology itself can be used with any kind of model.

Analysis of the Case where both GSCs use the same CS

In this scenario the same control structure is used at GSC1 and GSC2. This is done in order to determine the operation ranges for each CS for the various requirements.

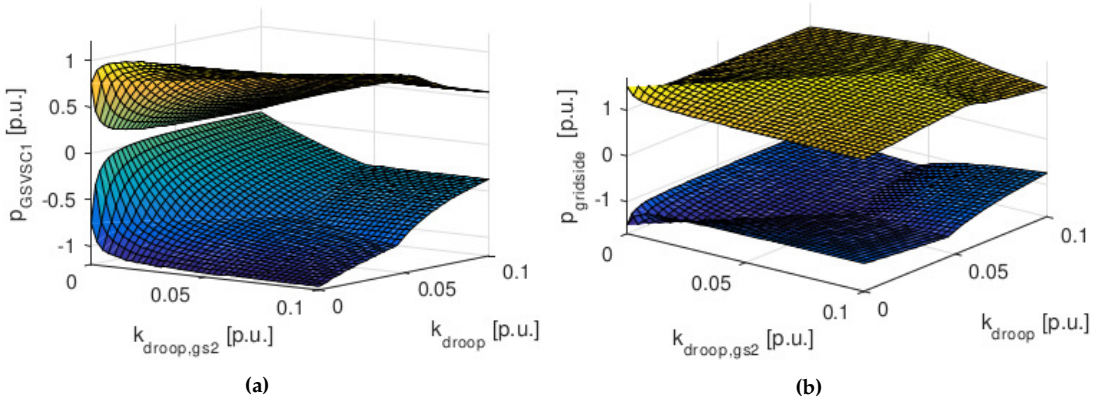

Figure 4.16: APTC of a) GSC1 and b) the sum of both GSCs ($p_{gridside}$). Source: **[Pub. A]**.

Below, the APTCs are given for the case where the only requirements considered are the system stability ($Re\{\lambda\} \leq 0$) and the voltage and current limits given in the subsection 4.7.1. The impact of the remaining requirements are discussed in the corresponding subsections and highlighted in the respective tables. The APTC of the case in which both GSCs use CS8($P_{ac} - V_{dc}$) is shown in Fig. 4.16. Fig. 4.16a shows the maximum power transfer in both directions of one terminal for all combinations of k_{droop} and $k_{droop,gs2}$. That means with the given current definition shown in Fig. 4.14, the upper surface resembles the inverter limit of that GSC while the lower surface resembles the rectifier limit of that GSC. The area between both surfaces is the area of stable and acceptable operation points. Thus, the APTC of a single terminal indicates for which power flow variations a stable and acceptable operation can be achieved for that terminal for all droop gain value combinations. In the optimal case, each terminal should achieve an APTC ≥ 2 p.u. for a wide range of droop gain combinations in order to be able to withstand disturbances and power flow variations up to its rated power in both power flow directions.

The APTC for the sum of both GSCs ($p_{gridside}$), shown in Fig. 4.16b, indicates how much power can be transferred from the WFC to the GSCs (upper limit) and how much could be transferred from both GSCs to an uncontrolled dc node (lower limit), i.e. to a converter not taking part in the dc voltage control. In this scenario, the WFC should be imagined as being connected to a weak grid (e.g. small island) instead of a wind farm.

When analyzing the APTC of the various CSs, it is of main interest to find the maximum APTC value of a single terminal, i.e. for example for CS8($P_{ac} - V_{dc}$) to determine the droop gain combination where the range between the upper and lower limit is the highest in Fig. 4.16a. Further, it is of main interest to find the maximum APTC value for the whole $p_{gridside}$ (Tab. 4.1 & Tab. 4.3), since in the case of just maximizing the APTC of a single terminal the APTC of the second terminal will be minimized at the same time, as shown in Fig. 4.16a (maximum at $k_{droop} = 0.0001$ and $k_{droop,gs2} = 0.1$, but minimum at $k_{droop} = 0.1$ and $k_{droop,gs2} = 0.0001$). Thus, the maximum APTC for the whole $p_{gridside}$ is represented by the maximum range between the upper and lower boundary in Fig. 4.16b.

Additionally, the eigenvalues with the lowest damping ratio at both limits have been analyzed in order to determine possible limitations and differences between the CSs (Tab. 4.2, Tab. 4.4).

Table 4.1: Comparison of Maximum APTC of a single GSCs for various CSs
Requirements: fulfilled, fulfilled but close to boundary, not fulfilled. Adapted from: **[Pub. A]**.

Control Structure	Fast Response Time					Slow Response Time				
	Max Range p_{gsc1}	Damping Ratio of lowest damped EV		$\overline{\sigma}(E_w(0))$		Max Range p_{gsc1}	Damping Ratio of lowest damped EV		$\overline{\sigma}(E_w(0))$	
		l. limit	u. limit	lower limit	upper limit		l. limit	u. limit	lower limit	upper limit
CS1($V_{dc} - I_{dc}$)	1.14 p.u.	0.14%	13.88%	-46.1 dB	-46.3 dB					
CS2($V_{dc} - I_{ac}$)	1.17 p.u.	5.27%	0.02%	-54.4 dB	-54.5 dB					
CS3($I_{dc} - V_{dc}$)	2.23 p.u.	6.86%	7.62%	-51 dB	-51.6 dB	2.23 p.u.	0.35%	6.19%	-50.8 dB	-51.4 dB
CS4($I_{ac} - V_{dc}$)	2.23 p.u.	7.26%	7.72%	-51.4 dB	-52 dB	2.16 p.u.	0.41%	6.14%	-51.1 dB	-51.8 dB
CS5($V_{dc} - P_{dc}$)	1.34 p.u.	0.05%	13.1%	-27.2 dB	-27.4 dB	1.87 p.u.	0.03%	9.49%	-30.5 dB	-30.8 dB
CS6($V_{dc} - P_{ac}$)	1.38 p.u.	0.15%	15.41%	-26 dB	-26.3 dB	1.87 p.u.	0.08%	10.31%	-30.5 dB	-30.8 dB
CS7($P_{dc} - V_{dc}$)	2.24 p.u.	8.6%	7.6%	-51 dB	-51.5 dB	2.24 p.u.	4.9%	6.7%	-50.8 dB	-51.4 dB
CS8($P_{ac} - V_{dc}$)	2.24 p.u.	6.8%	7.6%	-51 dB	-51.6 dB	2.24 p.u.	0.32%	6.15%	-50.8 dB	-51.4 dB

Both analyses have been carried out once for each investigated tuning in order to be able to point out the consequences of a different tuning.

Analysis of the maximum APTC of a single terminal The results of the analysis of the maximum APTC of a single terminal in the case both terminals use the same CS is given in Tab. 4.1. The participation factor analysis of the lowest damped eigenvalues at both limits is given in Tab. 4.2.

The results indicate that the four CSs, where the dc voltage is controlled in the second loop, outperform the remaining CSs. That means, CS3($I_{dc} - V_{dc}$), CS4($P_{ac} - V_{dc}$), CS7($P_{dc} - V_{dc}$) and CS8($P_{ac} - V_{dc}$) achieve a significantly larger APTC. Additionally, they achieve significantly lower maximum singular values in steady state, $\overline{\sigma}(E_w(0))$. However, all CSs fulfill the requirements of the stability margin minimizing the voltage deviation ($\overline{\sigma}(E_w(0)) \geq -23.01\,\mathrm{dB}$). The tables indicate further that the results are almost the same for the slow tuning.

For all CSs the APTC of a single terminal is maximized in case the difference of the droop gains is high, which minimizes the APTC of the second terminal at the same time, as shown above in Fig. 4.16a. The reason for this is the current limit of 2265 A (= 0.755 p.u.), which limits the current for each line and therefore makes it necessary to minimize the power transfer of the second terminal, in order to transfer as much power as possible from the WFC through all three cables to one specific terminal. This might make the results rather specific for this topology, however, the analysis still points out which CSs are capable of withstanding large droop gain deviations

Table 4.2: Participation Factor Analysis for Maximum APTC of a single GSC
GSC1 + ac grid 1, GSC2 + ac grid 2, WFC +ac grid, dc grid. Adapted from: **[Pub. A]**.

Control Structure	Fast Response Time: Highest participation factors of lowest damped EV							
	lower limit				upper limit			
CS1($V_{dc} - I_{dc}$)	32% $i_{g,d,g1}$	30% $v_{o,d,g1}$	18% $v_{o,q,g1}$	17% $i_{g,q,g1}$	45% $v_{o,q,g1}$	43% $i_{g,q,g1}$	5% $i_{l,q,g1}$	3% $\chi_{q,g1}$
CS2($V_{dc} - I_{ac}$)	50% $i_{l,d,g1}$	50% $v_{dc,g1}$	\	\	37% $i_{g,d,wf}$	26% $v_{o,d,wf}$	11% $\chi_{d,wf}$	8% $v_{o,q,wf}$
CS3($I_{dc} - V_{dc}$)	25% $i_{dc,wg2}$	22% $v_{dc,w}$	21% $v_{dc,g2}$	13% $i_{dc,wg1}$	31%$v_{o,d,g1}$	26% $i_{g,d,g1}$	17% $v_{o,q,g1}$	16% $i_{g,q,g1}$
CS4($I_{ac} - V_{dc}$)	24% $i_{dc,wg2}$	23% $v_{dc,w}$	21% $v_{dc,g2}$	13% $i_{dc,wg1}$	31%$v_{o,d,g1}$	26% $i_{g,d,g1}$	17% $v_{o,q,g1}$	16% $i_{g,q,g1}$
CS5($V_{dc} - P_{dc}$)	39% $i_{g,d,g1}$	29% $v_{o,d,g1}$	10% $v_{dc,g1}$	8% $v_{o,q,g1}$	32% $v_{o,d,g2}$	26% $i_{g,d,g2}$	16% $v_{o,q,g2}$	15% $i_{g,q,g2}$
CS6($V_{dc} - P_{ac}$)	39% $i_{g,d,g1}$	29% $v_{o,d,g1}$	8% $v_{dc,g1}$	8% $v_{o,q,g1}$	32% $v_{o,d,g2}$	25% $i_{g,d,g2}$	18% $v_{o,q,g2}$	16% $i_{g,q,g2}$
CS7($P_{dc} - V_{dc}$)	30% $v_{o,q,g2}$	27% $i_{g,q,g2}$	19% $v_{o,d,g2}$	19% $i_{g,d,g2}$	31% $v_{o,d,g1}$	26% $i_{g,d,g1}$	18% $v_{o,q,g1}$	16% $i_{g,q,g1}$
CS8($P_{ac} - V_{dc}$)	25% $i_{dc,wg2}$	23% $v_{dc,w}$	21% $v_{dc,g2}$	13% $i_{dc,wg2}$	31% $v_{o,d,g1}$	26% $i_{d,g,g1}$	18% $v_{o,q,g1}$	16% $i_{g,q,g1}$
Slow Response Time								
CS3($I_{dc} - V_{dc}$)	23% $v_{dc,w}$	23% $i_{dc,wg2}$	17% $i_{dc,wg1}$	16% $v_{dc,g2}$	24% $v_{dc,g1}$	24% $i_{dc,gg}$	23% $v_{dc,g2}$	7% $\chi_{d,g1}$
CS4($I_{ac} - V_{dc}$)	23% $v_{dc,w}$	22% $i_{dc,wg2}$	17% $i_{dc,wg1}$	16% $v_{dc,g2}$	23% $i_{dc,gg}$	23% $v_{dc,g1}$	23% $v_{dc,g2}$	7% $\chi_{d,g1}$
CS5($V_{dc} - P_{dc}$)	39% $v_{dc,w}$	20% $i_{dc,wg1}$	12% $i_{dc,wg2}$	9% $v_{dc,g2}$	38% $v_{o,d,g1}$	27% $i_{g,d,g1}$	10% $v_{o,q,g1}$	9% $i_{g,q,g1}$
CS6($V_{dc} - P_{ac}$)	39% $v_{dc,w}$	20% $i_{dc,wg1}$	12% $i_{dc,wg2}$	9% $v_{dc,g2}$	28% $v_{o,d,g2}$	24% $i_{g,d,g2}$	22% $v_{o,q,g2}$	20% $i_{g,q,g2}$
CS7($P_{dc} - V_{dc}$)	34% $v_{dc,g1}$	21% $i_{dc,wg1}$	11% $v_{dc,w}$	11% $\chi_{d,g1}$	34% $v_{dc,g1}$	24% $i_{dc,wg1}$	12% $v_{dc,w}$	11% $\chi_{d,g1}$
CS4($P_{ac} - V_{dc}$)	23% $i_{dc,wg2}$	23% $v_{dc,w}$	17% $i_{dc,wg1}$	16% $v_{dc,g2}$	25% $v_{dc,g1}$	24% $i_{dc,gg}$	23% $v_{dc,g2}$	8% $\chi_{d,g1}$

within a MT-HVDC grid without leading to instability (in rectifier mode). This is indicated by the very low damping ratios of the lowest damped eigenvalues at the lower limit for CS1($V_{dc} - I_{dc}$), CS2($V_{dc} - I_{ac}$), CS5($V_{dc} - P_{dc}$) and CS6($V_{dc} - P_{ac}$), as shown in Tab. 4.2. This means further that the APTC of those CSs decreases further for a stability margin demanding a minimum damping ratio of 3%, which leads to an even bigger deviation between the highest and lowest APTC of the various CSs.

The participation factor analysis in Tab. 4.2 shows further which states have a participation in the modes of those eigenvalues with the lowest damping ratio. In fact, in case of the fast tuning, the eigenvalues corresponding to the very low damping ratios at the lower limit (CS1($V_{dc} - I_{dc}$), CS5($V_{dc} - P_{dc}$) & CS6($V_{dc} - P_{ac}$)) are related to the GSC1, i.e. the GSC transferring as much power as possible from the ac to the dc side. Hence, the instability is caused by the terminal and the connected ac grid.

In case of the slower tuning, the damping ratios at the lower limit do not differ so much anymore, i.e. the ones of the better performing CSs decrease while the damping ratios of the remaining ones remain low. Only CS7($P_{dc} - V_{dc}$) still fulfills the stability margin in this case. Further, with the slower tuning, the lower limit is related to oscillation within the dc grid for all CSs, as the participation factor analysis indicates (Tab. 4.2). Thus, a faster tuning leads to better damped dc oscillations.

Analysis of the maximum APTC of the sum of both GSCs The results of the maximum APTC of all GSCs are given in Tab. 4.3. It is shown that CS3($I_{dc} - V_{dc}$) and CS8($P_{ac} - V_{dc}$) still outperform the others in case of the fast tuning. While CS4($I_{ac} - V_{dc}$) still achieves a comparable APTC, CS3($I_{dc} - V_{dc}$) and CS8($P_{ac} - V_{dc}$) achieve significant lower maximum singular values in steady state, $\overline{\sigma}(E_w(0))$, i.e. smaller voltage deviation induced by a variation of the active power of the WFC.

The results indicate further that in order to maximize the APTC of all GSCs equal droop gains (or small deviations) are preferable, the only exception here is CS7($P_{dc} - V_{dc}$).

The analysis additionally shows that with slower tuning the maximum singular values of CS3($I_{dc} - V_{dc}$), CS4($I_{ac} - V_{dc}$), CS7($P_{dc} - V_{dc}$) and CS8($P_{ac} - V_{dc}$) decrease, while the ones of CS5($V_{dc} - P_{dc}$) and CS6($V_{dc} - P_{ac}$) remain approximately constant. Further, with that tuning, the APTC of CS5($V_{dc} - P_{dc}$), CS6($V_{dc} - P_{ac}$) and CS7($P_{dc} - V_{dc}$) increase while the ones of CS3($I_{dc} - V_{dc}$) and CS8($P_{ac} - V_{dc}$) decrease, which brings the APTC of all CSs closer to each other. Hence, the various CSs tend to favor different tunings / the impact of the tuning on the CSs varies for the different CSs.

Table 4.3: Comparison of Maximum APTC of Sum of GSCs for various CSs
Requirements: fulfilled, fulfilled but close to boundary, not fulfilled. Adapted from: **[Pub. A]**.

	Fast Response Time					**Slow Response Time**				
Control Structure	Max Range $p_{gridside}$	Damping Ratio of lowest damped EV l. limit	Damping Ratio of lowest damped EV u. limit	$\overline{\sigma}(E_w(0))$ lower limit	$\overline{\sigma}(E_w(0))$ upper limit	Max Range $p_{gridside}$	Damping Ratio of lowest damped EV l. limit	Damping Ratio of lowest damped EV u. limit	$\overline{\sigma}(E_w(0))$ lower limit	$\overline{\sigma}(E_w(0))$ upper limit
CS1($V_{dc} - I_{dc}$)	1.97 p.u.	0.23%	13.92%	-26 dB	-27.3 dB					
CS2($V_{dc} - I_{ac}$)	1.95 p.u.	0.16%	0.19%	-23.7 dB	-24 dB					
CS3($I_{dc} - V_{dc}$)	3.02 p.u.	6.19%	8.22%	-61.3 dB	-62 dB	2.9 p.u.	0.002%	5.8%	-27.3 dB	-29 dB
CS4($I_{ac} - V_{dc}$)	2.97 p.u.	8.98%	7.99%	-36.6 dB	-37.3 dB	2.97 p.u.	2.21%	5.87%	-28.9 dB	-29.6 dB
CS5($V_{dc} - P_{dc}$)	2.48 p.u	0.06%	15.49%	-26.4 dB	-26.7 dB	2.76 p.u.	0.5%	11.12%	-26.4 dB	-26.7 dB
CS6($V_{dc} - P_{ac}$)	2.55 p.u	0.05%	17.04%	-26.4 dB	-26.7 dB	2.77 p.u.	0.03%	12.14%	-26.5 dB	-26.9 dB
CS7($P_{dc} - V_{dc}$)	2.47 p.u	0.1%	9.2%	-32 dB	-32.3 dB	2.59 p.u.	0.07%	7.26%	-28.8 dB	-29.1 dB
CS8($P_{ac} - V_{dc}$)	3.02 p.u	6.7%	8.37%	-53.5 dB	-53.9 dB	2.97 p.u.	0.08%	5.6%	-27.8 dB	-28.2 dB

Table 4.4: Participation Factor Analysis for Maximum APTC of the Sum of both GSCs ■ GSC1 + ac grid 1, ■ GSC2 + ac grid 2, ■ WFC +ac grid, ■ dc grid. Adapted from: [**Pub. A**].

Control Structure	Highest participation factors of lowest damped EV							
	lower limit				upper limit			
Fast Response Time								
CS1($I_{dc}-P_{ac}$)	37% $i_{g,d,g1}$	30% $v_{o,d,g1}$	11% $v_{o,q,g1}$	10% $i_{g,q,g1}$	45% $v_{o,q,g2}$	42% $i_{g,q,g1}$	5% $i_{l,q,g2}$	2% $\chi_{q,g2}$
CS2($I_{ac}-P_{ac}$)	46% $v_{dc,w}$	24% $i_{dc,wg1}$	24% $i_{dc,wg2}$	2% $v_{dc,g2}$	37% $i_{g,d,wf}$	26% $v_{o,d,wf}$	11% $\chi_{d,wf}$	8% $v_{o,q,wf}$
CS3($I_{dc}-V_{dc}$)	26% $v_{dc,w}$	15% $\chi_{d,g1}$	15% $\chi_{d,g2}$	11% $v_{dc,g1}$	15%$v_{o,d,g1}$	15% $v_{o,d,g2}$	13% $i_{g,d,g1}$	13% $i_{g,q,g2}$
CS4($I_{ac}-V_{dc}$)	19% $v_{dc,w}$	18% $i_{dc,wg1}$	17% $v_{dc,g1}$	16% $i_{dc,wg2}$	29%$v_{o,d,g2}$	25% $i_{g,d,g2}$	19% $v_{o,q,g2}$	17% $i_{g,q,g2}$
CS5($V_{dc}-P_{dc}$)	19%$i_{g,d,g1}$	19% $i_{g,d,g2}$	15% $v_{o,d,g1}$	15% $v_{o,d,g2}$	18% $v_{o,q,g1}$	18% $v_{o,q,g2}$	17% $i_{g,q,g1}$	17% $i_{g,q,g2}$
CS6($V_{dc}-P_{ac}$)	19% $i_{g,d,g1}$	19% $i_{g,d,g2}$	15% $v_{o,d,g2}$	15% $v_{o,d,g1}$	17% $v_{o,q,g1}$	17% $v_{o,q,g2}$	16% $i_{g,q,g1}$	16% $i_{g,q,g2}$
CS7($P_{dc}-V_{dc}$)	34% $i_{g,d,g2}$	31% $v_{o,d,g2}$	16% $v_{o,q,g2}$	14% $i_{g,q,g2}$	32% $v_{o,d,g1}$	26% $i_{g,d,g1}$	17% $v_{o,q,g1}$	15% $i_{g,q,g1}$
CS8($P_{ac}-V_{dc}$)	25% $v_{dc,w}$	15% $\chi_{d,g1}$	15% $\chi_{d,g2}$	11% $v_{dc,g1}$	15% $v_{o,d,g1}$	15% $v_{o,d,g2}$	13% $i_{g,d,g1}$	13% $i_{g,d,g2}$
Slow Response Time								
CS3($I_{dc}-V_{dc}$)	23% $v_{dc,w}$	19% $i_{dc,wg1}$	19% $i_{dc,wg2}$	13% $v_{dc,g1}$	24% $i_{dc,gg}$	23% $v_{dc,g1}$	23% $v_{dc,g2}$	6% $\chi_{d,g1}$
CS4($I_{ac}-V_{dc}$)	24% $v_{dc,w}$	17% $\chi_{d,g1}$	20% $\chi_{d,g2}$	13% $v_{dc,g1}$	24% $i_{dc,gg}$	24% $v_{dc,g1}$	24% $v_{dc,g2}$	7% $\chi_{d,g2}$
CS5($V_{dc}-P_{dc}$)	38% $v_{dc,w}$	16% $i_{dc,wg1}$	16% $i_{dc,wg2}$	8% $\chi_{d,g2}$	17% $v_{o,d,g1}$	17% $v_{o,d,g2}$	13% $i_{g,d,g1}$	13% $i_{g,d,g2}$
CS6($V_{dc}-P_{ac}$)	38% $v_{dc,w}$	16% $i_{dc,wg1}$	16% $i_{dc,wg2}$	7% $\chi_{d,g1}$	34% $v_{o,d,g1}$	26% $i_{g,d,g1}$	16% $v_{o,q,g1}$	14% $i_{g,q,g1}$
CS7($P_{dc}-V_{dc}$)	37% $i_{g,d,g2}$	32% $v_{o,d,g2}$	12% $v_{o,q,g2}$	11% $i_{g,q,g2}$	34% $v_{dc,g1}$	25% $i_{dc,wg1}$	13% $v_{dc,w}$	10% $\chi_{d,g1}$
CS8($P_{ac}-V_{dc}$)	21% $v_{dc,w}$	19% $i_{dc,wg1}$	19% $i_{dc,wg2}$	14% $v_{dc,g1}$	25% $i_{dc,gg}$	24% $v_{dc,g1}$	24% $v_{dc,g2}$	6% $\chi_{d,g1}$

The damping ratios of the lowest damped eigenvalues, given in Tab. 4.4, indicate significant difference between the CSs. In fact, a stability margin demanding a minimum damping ratio of 3% with a fast tuning will further decrease the APTC of all CSs except CS3($I_{dc}-V_{dc}$), CS4($I_{ac}-V_{dc}$) and CS8($P_{ac}-V_{dc}$). This will lead to even higher APTC deviation between the various CSs. The lowest damped eigenvalues of the lower limit of all these three cases are related to the dc grid and the droop controller. In all other cases (except CS2($V_{dc}-I_{ac}$)) the lowest damped eigenvalues of the lower limit are related to ac values of either GSC1 or GSC2. Given the low damping ratios of those eigenvalues, for CS1($V_{dc}-I_{dc}$), CS5($V_{dc}-P_{dc}$), CS6($V_{dc}-P_{ac}$) and CS7($P_{dc}-V_{dc}$) the lower limit is caused by the ac side oscillations of one of the GSCs.

The lowest damped eigenvalues of the upper limit on the other hand have for all CSs a comparable high damping ratio, except for CS2($V_{dc}-I_{ac}$), where the upper limit is apparently related to oscillations within the ac grid of the WFCs.

4.7.4 Discussion

Two important aspects of the APTC have been analyzed, first the maximization of power transfer of a single terminal and then the maximization of APTC of the whole system. CS3($I_{dc}-V_{dc}$), CS4($I_{ac}-V_{dc}$) and CS8($P_{ac}-V_{dc}$) outperform the remaining CSs in both aspects. In both cases, they obtain wider APTC, higher damping ratios of the lowest damped eigenvalue, as well significant lower maximum singular values. Furthermore, the maximum APTC is only limited by the current limitations.

Additionally, we investigated the impact of the tuning of the converters on the ATPC. Therefore, two different tunings have been compared. The tuning hardly impacts the analysis of maximizing the APTC of a single terminal, while the influence on the APTC between the WFC and the GSCs is not negligible. It is obvious that a faster damping leads to better damped dc oscillations. This is indicated by the comparison of the eigenvalue movement for a variation of k_{droop} in Fig. 4.17. It is obvious that both pairs of complex eigenvalues with $Im\{\lambda\} \approx \pm 400$ are moved to regions with higher damping ratio in the left half-plane. A participation factor analysis indicates that these eigenvalues are related to dc states.

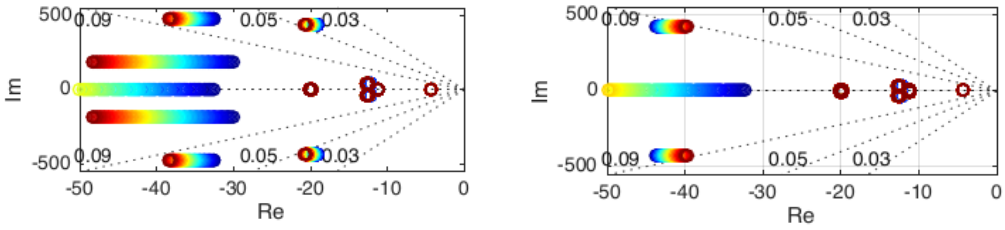

(a) Slow Tuning

(b) Fast Tuning

Figure 4.17: Movement of the EV and the damping ratios for a variation of $k_{droop} = 0\,\text{p.u.}$ (blue) to $0.1\,\text{p.u.}$ (red) in case both GSCs use CS3($I_{dc} - V_{dc}$). Source: **[Pub. A]**.

Further, it has been shown that all CSs are not limited by a set of maximum singular values. The damping ratio stability margin on the other hand is limiting specific CSs while others are fulfilling this stability margin without further limitation of the APTC. Hence, in case of demanding a minimum damping ratio of 3%, the differences between the APTC of the various CSs will be even more significant.

To sum up, a methodology to determine the operation range of an arbitrary MT-HVDC grid was presented. The methodology allows to determine the active power transfer capability of single terminals as well as the whole grid and e.g. how it is impacted by the choice of a specific CS or different turnings. A case study was used to analyze the impact of the choice of different dc voltage droop control structures and two different tunings on the APTC considering different stability margins. It was shown that a fast tuning leads to better damping of dc oscillations. Further, it was shown that three different CSs (CS3($I_{dc} - V_{dc}$), CS4($I_{ac} - V_{dc}$) and CS8($P_{ac} - V_{dc}$)) outperform the remaining five. Between these three, the performance within the single terminal analysis is almost identical. In the analysis of the maximum APTC of both GSCs, CS3($I_{dc} - V_{dc}$) and CS8($P_{ac} - V_{dc}$) achieve slightly higher ranges and lower voltage deviations.

4.8 Multi-Vendor Interoperability

The methodology presented in the previous section is also well suited to investigate potential multi-vendor interoperability issues. The different terminals can be modelled with different control structures and the operation spaces can be compared. Moreover, considering the analysis of the previous sections using the same models, the interaction level and frequency response can be compared. Furthermore, since HVDC projects are very unique, and the topologies are very project-specific with a plug-and-play solution usually not existing, this methodology also allows to investigate the operation space of specific topologies and could also be used within a security assessment.

As it remains unknown which control structure each vendor is using, as an example we combined the best performing CSs from the previous analysis using the same topology. Thus, this case study represents a multi-vendor scenario. Hence, the results will reveal whether a combination of different CSs has a positive or negative impact on the operation space.

Ideally, in a real project, this methodology could be used by a third party using the specific models of the different vendors in order to identify potential interoperability issues for the specific project topology. In [130], Oliver Despouys from RTE suggests such an approach as a way to circumvent any potential intellectual property theft threats which otherwise appear by demanding the vendors to exchange their control algorithms to ensure interoperability.

Table 4.5: Maximum APTC - Requirements: ■ fulfilled. Source: [**Pub. A**].

Control Structures	Max Range $p_{gridside}$	$\overline{\sigma}(E_w(0))$ l. limit	$\overline{\sigma}(E_w(0))$ u. limit	Low. Damp. Ratio l. limit	Low. Damp. Ratio u. limit
4 & 3	3.02 p.u.	-61.33 dB	-61.99 dB	6.2 %	8.2 %
8 & 3	3.02 p.u.	-53.5 dB	-53.95 dB	6.7 %	8.4 %
8 & 4	3.02 p.u.	-61.33 dB	-61.99 dB	6.2 %	8.2 %

4.8.1 Case Study

In order to determine the consequences of combining different CSs within one grid and finding the most beneficial combination, the most promising CSs from the previous analysis have been combined. Thus, GSC1 and GSC2 will use different droop control structures with the fast tuning in the following. In particular, the combinations of CS3($I_{dc} - V_{dc}$), CS4($I_{ac} - V_{dc}$) and CS8($P_{ac} - V_{dc}$) have been analyzed in detail, due to the most promising results in the previous section.

The analysis indicates that the results for a maximization of the APTC of the single terminal do not differ from the previous analysis for the specific CSs. Thus, the focus is put on the maximization of the APTC of the whole system, the results are given in Tab. 4.5. All the three combinations fulfill all requirements and achieve the same APTC. However, both combinations including CS4($I_{ac} - V_{dc}$) achieve lower maximum singular values than the combination of CS8($P_{ac} - V_{dc}$) & CS3($I_{dc} - V_{dc}$), which leads to lower voltage deviation at the GSCs induced by a power variation of the WFC. The maximum APTC of all these three combinations is limited by the current limit. Thus, with cables enabling a higher current limit the APTC will be further increased. However, this does not imply that for other current limitations different combinations of CSs might be more beneficial, since in the previous analysis it was already shown that these three CSs outperform the remaining ones already with this current limit.

4.8.2 Discussion

The three best performing dc voltage droop control CSs from the previous case study have been combined with each other in order to determine the most beneficial combination. It turns out that a combination of a control structure using the dc voltage and the ac current (CS4($I_{ac} - V_{dc}$)) with either a control structure using dc voltage and active power measured on the ac side (CS8($P_{ac} - V_{dc}$)) or using dc voltage and dc current (CS3($I_{dc} - V_{dc}$)) leads to even lower voltage deviation induced by power variations of the wind farm. However, it is important to emphasize that additional studies are needed to verify the results for other topologies. The main contribution of this work is a methodology that can be used for such additional studies. In fact, the methodology does not only allow to compare different CSs but allows to determine the operation space of any arbitrary MT-HVDC grid. This will be used in section 6.6 to determine the security boundaries of an interconnected AC-HVDC system enabling us to include security considerations into power system operation and market clearing algorithms.

4.9 Conclusion and Outlook

The control of MT-HVDC grids has not been standardized yet and although vendors agree that dc voltage droop control is a viable option, it is unknown what kind of control each vendor is exactly using. Given that a MT-HVDC grid in Europe will probably be developed in a step-wise

approach integrating existing inter-connectors, multi-vendor interoperability will be required. Thus, the interoperability of different vendors has been identified as a key challenge. As a first step, this work collected the different structures proposed in literature and developed a simple categorization framework. Then, the benefits and drawbacks of the various CSs were analyzed in detail and a method capable of determining the operation space of an arbitrary MT-HVDC grid was developed. This method has been used in a case study to analyze the impact of the different CSs on the APTC. Moreover, it has been revealed that limits frequently used in literature for CS analysis and tuning (e.g. [9, 69]) are not sufficient to maintain the impact of specific disturbances within a certain boundary and need to be verified by a MISO analysis of the highest amplified output.

The different studies have shown that the choice of the dc voltage droop CS has a significant impact on the stability, disturbance rejection and interaction level between connected AC-HVDC systems. It was shown that a dc voltage droop control structure using the dc voltage and the active power measured on the ac side, (CS8($P_{ac} - V_{dc}$)), leads to a comparable low-level of interactions between the dc and ac subsystems. Thus, this structure separates those system as much as possible mitigating the potential spread of disturbances from one system into the other. Moreover, this kind of structure also maximizes the APTC of a MT-HVDC system. While, a combination of dc voltage and ac current, (CS4($I_{ac} - V_{dc}$)), also maximizes the APTC, it, moreover, maximized the disturbance attenuation by a minimal dc voltage deviation in case of disturbances. However, compared to CS8($P_{ac} - V_{dc}$), it leads to a slightly higher interaction level between the ac and dc system. Although, these studies focused on quite specific systems within the case studies, these observations are supported by the observations of the recently published study in [121]. The authors conclude that two structures (almost) identical to CS4($I_{ac} - V_{dc}$) and CS8($P_{ac} - V_{dc}$) possess better stability and robustness than the other tested three structures (corresponding to CS3($I_{dc} - V_{dc}$), CS6($V_{dc} - P_{ac}$) and CS7($P_{dc} - V_{dc}$)).

Thus, the most beneficial CSs have been identified, however, it remains unknown what kind of CS each vendor is using. Although, between the best performing CSs no interoperability issue was identified, it can not be ruled out that there exist potential interoperability problems between the implementations of the different vendors. In fact, within the BestPaths project experts had access to control replicas of different vendors and concluded that "the existing technology delivered by the main HVDC vendors is not directly interoperable" [130]. Since the details are unknown due to intellectual property interests of the different parties, it can only be speculated what the reason is. Given the presented studies, supported by the results of [121], it may either be related to interoperability problems not visible within a study based on small-signal stability (e.g. requiring more detailed electro-magnetic studies) or to a not optimal choice of the droop CS or it is related to additional, not considered control features for e.g. protection purposes. Thus, future work should focus on collaborations with different vendors and use control replicas of the vendors to be able to study potential interoperability issues in detail.

CHAPTER 5

Efficient Database Generation for Data-driven Security Assessment of Power Systems

After the development of the method enabling to determine the operation space of an MT-HVDC for given security considerations, we extended our work to a more detailed representation of the ac grid. Motivated by the idea to enhance power system security with data-driven methods, we quickly realized that first a database generation method capable of producing high-quality databases for large systems is required to enable data-driven security assessments. Therefore, this chapter deals with the development of an efficient database generation method for data-driven security assessment of power systems. This chapter is structured as follows: First, the motivation for this work is discussed highlighting why such a method is needed and what the challenges are. Afterwards, a brief literature review is provided. Then, the contributions of this chapter are emphasized, followed by the description of the work published in ***[Pub. B]****.*

5.1 Background

A fundamental function for both short-term and long-term power system operation is the security assessment. TSOs need to balance the probability of system failure on a sub-hourly basis against the costs, and need to guarantee the security of supply in the long-term, having the required infrastructure and operating practices in place. Moreover, TSOs are required to provide transfer capacities representing the bounds of a feasible system operation to the market. All these functions require the assessment of thousands of possibilities with respect to load patterns, potential contingencies and active and reactive power generation ranges of generators leading to a large-scale combinatorial problem already for small systems. Millions of possible operating points violate operating constraints and lead to an insecure system, while millions satisfy all limitations and ensure safe operation. For systems exceeding the size of a few buses, however, it is impossible to assess all potential operating points, as the problem complexity explodes. Therefore, computationally efficient methods are necessary to perform a fast and accurate Dynamic Security Assessment (DSA).

The DSA usually consists of several methods evaluating the different types of (in)stability, e.g. transient, small-signal, or voltage stability. Numerous approaches exist in the literature proposing methods to assess or predict the different types of (in)stability. Recently, with the abundance of data from sensors, such as smart meters and Phasor Measurement Units (PMUs), machine learning approaches have emerged showing promising results in tackling this problem [10, 137]. Due to the high reliability of the power system operation, however, historical data are not sufficient to train such techniques, as information related to the security boundary or insecure regions is often missing. Thus, simulation data are necessary to fill this gap.

This work deals with the fundamental problem that most of the DSA methods are confronted with before the implementation of any algorithm: the generation of the necessary data set which is required for the development of dynamic security classification approaches. As the quality of this data set directly impacts the achievable quality of any data-driven dynamic security classification, a high quality database is of significant importance. The database quality influences the data-driven dynamic security classification quality of any method because these tools try to generalize the knowledge they extract from the available data points. If the database, however, does only contain a low percentage / a low number of operating points close to the security boundary, these tools will not be able to identify the real security boundary. In contrast, depending on the available data set, these tools will determine a boundary which is either too conservative or too risky in categorizing the operating points.

With this work we aim to propose a modular and scalable algorithm that can efficiently focus on simulating operating points close to the security boundary allowing to identify the security boundaries of large systems with data-driven tools in a computationally efficient manner.

5.2 Definitions

Before carrying on with a description of the challenges of a database creation and our proposed methodology, we define a set of terms that will be used throughout this work.

Security boundary

the boundary γ dividing the secure from the insecure region; (a) can correspond to a specific stability boundary, e.g. small-signal stability or voltage stability, (b) can represent a specific stability margin, i.e. all operating points not satisfying the stability margin belong to the insecure region, (c) can be a combination of security indices, e.g. the intersection of operating points that are both N-1 secure and small-signal stable. Note that our proposed method can apply to any security boundary the user needs to consider.

HIC – High Information Content

the set Ω of operating points in the vicinity of the security boundary γ, see (5.2) [138]. This is the search space of high interest for our methods as it separates the secure from insecure regions.

Infeasible Operating Points

in the remainder of this work, operating points, i.e. combinations of generator set-points and load values, which either do not comply with the voltage requirements or for which there exist no power flow solution are called infeasible. Naturally, all infeasible operating points are also insecure.

DW – Directed Walk

we use this term to denote the steepest descent path our algorithm follows, starting from a given initialization point, in order to arrive close to the security boundary.

5.3 Challenges of the Database Generation

Before describing the methodology in detail, we will briefly highlight the challenges of creating a high quality database for medium to large systems which suitable for data-driven approaches. There are two main challenges with the generation of such a database. First, the problem size. It is computationally impossible to assess all possible operating points for systems exceeding a few tens of buses. Second, the information quality. Dynamic security assessment is a non-convex and highly nonlinear problem. Generating an information-rich and not too large data set can lead to algorithms that can be trained faster and achieve higher prediction accuracy.

Determining the secure region of a power system is an NP-hard problem. In an ideal situation, in order to accurately determine the non-convex secure region we need to discretize the whole space of operating points with an as small interval as possible, and perform a security assessment for each of those points. For a given system topology, this set consists primarily of all possible combinations of generator and load setpoints (NB: if the system includes tap-changing transformers, and other controllable devices, the number of credible points increases geometrically). Thus, in a classical brute force approach, the number of points to be considered is given by:

$$|\Psi| = \Lambda \cdot \prod_{i=1}^{N_G - 1} \Big(\frac{\overline{P}_{G_i} - \underline{P}_{G_i}}{\alpha} + 1 \Big), \tag{5.1}$$

where N_G is the number of generators i, P_i^{max} and P_i^{min} is their maximum and minimum capacity, α is the chosen discretization interval between the generation setpoints, and Λ represents the number of different load profiles.

For example, for the IEEE 14 bus system [49] with 5 generators and a discretization interval of $\alpha = 1\,\mathrm{MW}$, a classical brute force approach requires $|\Psi| \approx 2.5 \cdot 10^6$ operating points to be assessed for a single load profile. It can be easily seen that security assessment of large systems can very fast result in an intractable problem. For example, in the NESTA 162 bus system [139], a brute force approach would require the analysis of $7 \cdot 10^{29}$ points. It becomes clear that the efficient database generation is one of the major challenges for the implementation of data-driven tools in power system security analysis. In this effort, we need to balance the trade-off between two partially contradicting goals: keep the database as small as possible to minimize computational effort, but contain enough data to determine the security boundary as accurately as possible. To better illustrate our approach, in Fig. 5.1 we show all possible operating points of two generators for a certain load profile in a system. Focusing on small-signal stability here, we define the security boundary γ as a certain level of minimum damping ratio, which corresponds to our stability margin. All safe operating points, with a damping ratio above γ, are plotted in blue, while operating points that do not fulfill the stability margin are plotted in yellow. From Fig.5.1, it is obvious that if we are able to assess all points close to γ, it is easy to classify the rest of the points. By that, the size of the required database can be significantly reduced. In the remainder of this chapter, we will call the set of operating points in the vicinity of γ as the set of *High Information Content* (*HIC*), defined as follows:

$$\Omega = \{OP_k \in \Psi \mid \gamma - \mu < \gamma_k < \gamma + \mu\}, \tag{5.2}$$

with γ_k denoting the value of the chosen stability margin for operating point OP_k and μ representing an appropriate small value to let $|\Omega|$ be large enough to describe the desired security boundary with sufficient accuracy. The value of μ depends on the chosen discretization interval in the vicinity

of the boundary. In Fig. 5.1, the HIC set, i.e. all points $OP_k \in \Omega$, is visualized as the grey area surrounding γ. In this small example, we were able to assess all possible operating points and accurately determine the HIC area. For large systems this is obviously not possible. As a result, in the general case, the main challenge is to find the points OP_k which belong to the HIC area $|\Omega|$.

To put the difference between $|\Psi|$ and $|\Omega|$ in perspective: for the small signal stability analysis of the IEEE 14 bus system, the classical brute force approach requires the analysis of $|\Psi| \approx 2.5 \cdot 10^6$ operating points (OPs) for a single load profile. By assuming a required damping ratio of $\gamma = 3\,\%$, and $\mu = 0.25\,\%$, the HIC set, defined as $\Omega = \{OP_k \in \Psi \mid 2.75\,\% < \gamma_k < 3.25\,\%\}$, reduces the analysis to only 1457 points (here, γ refers to the damping ratio of the lowest damped eigenvalue). In other words, by assessing only $0.06\,\%$ of all data points, we can accurately determine the whole secure region of this example.

This small amount of operating points that are required to assess in order to determine the security boundary has actually worked as an obstacle for one of the most popular approaches in previous works: importance sampling. Importance sampling re-orients the sampling process towards a desired region of interest in the sampling space, while also preserving the probability distribution. Thus, it requires that the initial sampling points include sufficient knowledge about the desired region of interest. However, the smaller the proportion of the region of interest is in respect to the entire multi-dimensional space, the larger the initial sample size needs to be to include a sufficient number of points within the desired region of interest. Therefore, the use of expert knowledge [138, 140, 141], regression models [10] or linear sensitivities [138] are proposed to determine the desired region and reduce the search space. However, since this search space reduction is based on a limited initial sample size, it entails the risk of either missing regions of interest not represented in the initial sample or requires a large initial sample which increases the computational burden. Similarly, expert knowledge has been used in previous works [138, 142] to reduce the burden of the N-1 security assessment to a few critical contingencies. Our proposed method does not require expert knowledge and avoids potential biases by not separating the knowledge extraction from the sampling procedure.

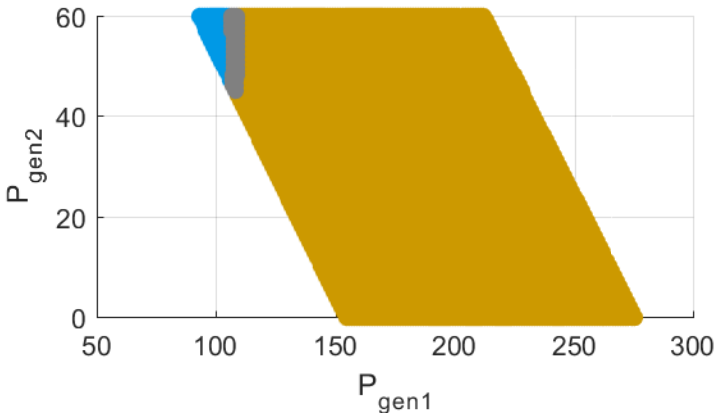

Figure 5.1: Scatter plot of all possible operating points of two generators for a certain load profile. Operating points fulfilling the stability margin and outside the high information content (HIC) region ($\gamma_x > 3.25\%$) are marked in blue, those not fulfilling the stability margin and outside HIC ($\gamma_x < 2.75\%$) are marked in yellow. Operating points located in the HIC region ($2.75\% < \gamma_k < 3.25\%$) are marked in grey. Source: **[Pub. B]**

Note, that this has been an illustrative example to demonstrate the computational gains of focusing only on the HIC area. In large systems, the main challenge is that it is not possible to know a priori which points x belong to the HIC area Ω. Thus, finding the HIC region and focusing on simulating points within that region is a major challenge which we will focus on later in this chapter.

5.4 Literature Review

The efforts to develop a systematic and computationally efficient methodology to generate the required database have been limited up to date: The aforementioned importance sampling based methods [10, 138, 143–145] are based on Monte-Carlo variance reduction (MCVR) technique, introducing a bias in the sampling process such that the representation of rare events increases in the assessment phase.

In [140, 141], the authors use re-sampling techniques based on post-rule validation to enrich the database with samples close to the boundary. In [142], the authors propose to enrich the database iteratively with additional points close to the security boundary by adding operating points at half the distance of the already existing operating points at the security boundary. This, however, requires additional computation to enrich the previously generated database. In [146], M. Sun et al. propose a composite modelling approach using high dimensional historical data. I. Konstantelos et al. propose in [147] to use the variable truncation C-Vine method to model complex dependencies extracted from historical measurement data. In [148], the authors provide an review of different multivariate dependence modeling techniques, namely parametric, non-parametric and copula functions.

5.5 Contributions

This work leverages advancements in several different fields to propose a highly scalable, modular, and computationally efficient method. Using properties derived from convex relaxation techniques applied on power systems, we drastically reduce the search space. Applying complex network theory approaches, we identify the most critical contingencies boosting the efficiency of our search algorithms. Based on steepest descent methods, we design the exploration algorithm in a highly parallelizable fashion, and exploit parallel computing to reduce computation time. Compared with existing approaches, our method achieves a speed-up of 10 to 20 times, requiring less than 10% of the time other approaches need to achieve the same results.

The contributions of this work are the following:

- We propose a computationally efficient and highly scalable method to generate the required datasets for the training or testing of dynamic security assessment methods. Our approach requires less than 10% of the time existing methods need for results of similar quality.
- Our method is modular and can accommodate several types of security boundaries, including transient stability and voltage stability. In this work, we demonstrate our approach considering the combination of N-1 security and small signal stability.
- Besides the database generation, the methodology we propose can be easily employed in real-time operation, where computationally efficient techniques are sought to explore the security region in case of contingencies around the current operating point.

5.6 Methodology

The Methodology is visualized in Fig. 5.2. We divide the proposed methodology in two main parts. First, the search space reduction by the elimination of a large number of infeasible (and insecure) operating points. Second, the directed walks: a steepest-descent based algorithm to explore the search space and accurately determine the security boundary. During the search space reduction, we exploit properties of convex relaxation techniques to discard large infeasible regions. In order to reduce the problem complexity, we employ complex network theory approaches which allow us to identify the most critical contingencies. Finally, designing the directed walks as a

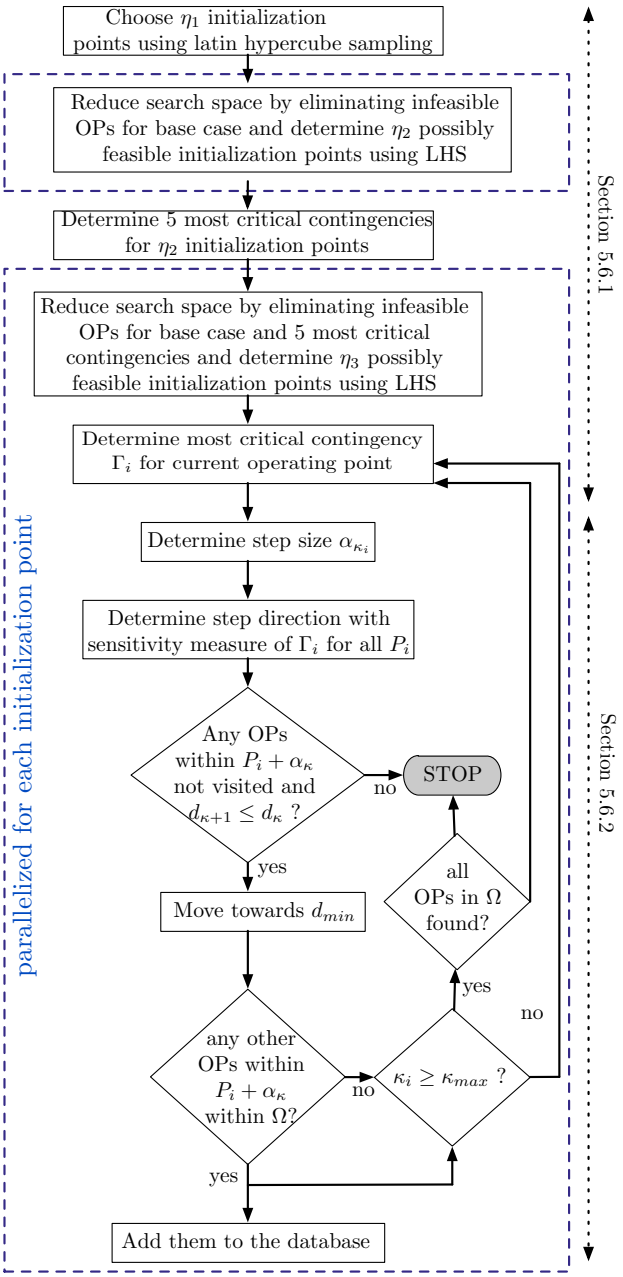

Figure 5.2: Flowchart of the proposed methodology. Adapted from **[Pub. B]**.

highly parallelizable algorithm, we use parallel computing capabilities to drastically reduce the computation time.

The different parts are described in detail in the following sections. Our algorithm starts by uniformly sampling the search space using the Latin Hypercube Sampling (LHS) method, to generate initialization points for the subsequent steps (Section 5.6.1). Following that, we propose a convex grid pruning algorithm, which also considers contingency constraints, to discard infeasible regions and reduce the search space (Section 5.6.1). In Section 5.6.1, we leverage complex network theory approaches to identify the most critical contingencies. The identified contingency set is crucial both for the grid pruning algorithm, and for subsequent steps within the Directed Walks. After resampling the now significantly reduced search space, we use these samples as initialization points for the Directed Walk (DW) algorithm, described in Section 5.6.2. In order to achieve an efficient database generation, the goal of the algorithm is to traverse as fast as possible large parts of the feasible (or infeasible) region, while carrying out a high number of evaluations inside the HIC region. This allows the algorithm to focus on the most relevant areas of the search space in order to accurately determine the security boundary. The DWs are highly parallelizable, use a variable step size depending on their distance from the security boundary, and follow the direction of the steepest descent. Defining the secure region as the N-1 secure *and* small signal stable region in our case studies, we demonstrate how our method outperforms existing importance sampling approaches, achieving a 10 to 20 times speed-up.

5.6.1 Reducing the Search Space

Choice of Initialization Points

An initial set of operating points is necessary to start our computation procedure. Using the Latin Hypercube Sampling (LHS), we sample the space of operating points to select the initialization points η. Besides the initialization points at the first stage, η_1, our method requires the finer selection of initialization samples, η_2 and η_3 during the reduction of the search space in two subsequent stages, as will be explained later. We use the same sampling procedure at all stages. The Latin hypercube sampling (LHS) aims to achieve a uniform distribution of samples across the whole space. Dividing each dimension in subsections, LHS selects only one sample from each subsection of each parameter, while, at the same time, it maximizes the minimum distance between the samples [10]. An even distribution of the initialization points over the multi-dimensional space is of high importance in order to increase the probability that our method does not miss any infeasible region or any HIC region. The number of initialization points $|\eta|$ is a tuning factor which depends on the specific system under investigation. In general, quite sparse discretization intervals are used for the search space reduction procedures in the first two stages of our approach, η_{1-2}, while a more dense discretization interval is used for the directed walks at a later stage, η_3. Suitable values are discussed in the case study. While LHS allows an even sampling, it is very computationally expensive for high-dimensional spaces and large numbers of initialization points. Thus, for larger systems there is a trade-off between initial sampling and computation time, that needs to be considered. A comparison of LHS and random sampling is shown in Fig. 5.3.

Grid Pruning Algorithm For Search Space Reduction

Given the η_1 initialization points from the first stage, the aim of this stage is to reduce the search space by eliminating infeasible operating regions. For that, we use a grid pruning algorithm

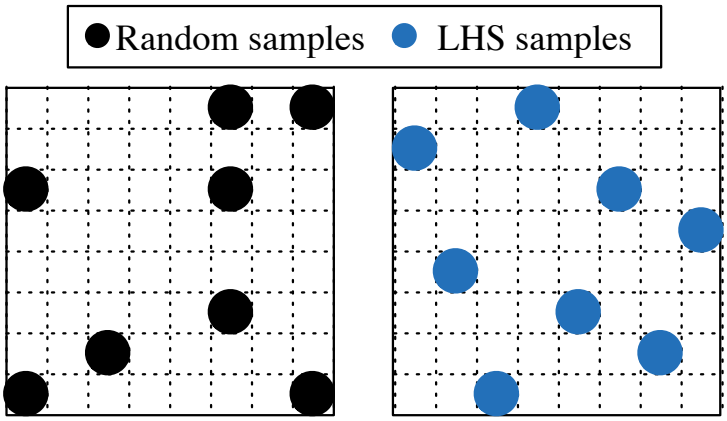

Figure 5.3: Comparison of an exemplary random and Latin hypercube sampling in two dimensions. In contrast to random sampling, every row and column is samples using LHS (adapted from [10]).

which relies on the concept of convex relaxations. The algorithm is inspired by [149], where it was developed to compute the feasible space of small AC optimal power flow (OPF) problems. In this work, we introduce a grid pruning algorithm which determines infeasible operating regions considering not only the intact system but also all N-1 contingencies.

Convex relaxations have been recently proposed to relax the non-convex AC-OPF to a semidefinite program [150]. A corollary of that method is that the resulting semidefinite relaxation provides an infeasibility certificate: If an initialization point is infeasible for the semidefinite relaxation, it is guaranteed to be infeasible for the non-convex AC-OPF problem. This property is used in our grid pruning algorithm.

The semidefinite relaxation introduces the matrix variable W to represent the product of real and imaginary parts of the complex bus voltages, (for more details the interested reader is referred to [150, 151]). Defining our notation, the investigated power grid consists of $\mathcal{N}$ buses, where $\mathcal{G}$ is the set of generator buses. We consider a set of line outages $\mathcal{C}$, where the first entry of set $\mathcal{C}$ corresponds to the intact system state. The following auxiliary variables are introduced for each bus $i \in \mathcal{N}$ and outage $c \in \mathcal{C}$:

$$Y_i^c := e_i e_i^T Y^c \tag{5.3}$$

$$\mathbf{Y}_i^c := \frac{1}{2}\begin{bmatrix} \Re\{Y_i^c + (Y_i^c)^T\} & \Im\{(Y_i^c)^T - Y_i^c\} \\ \Im\{Y_i^c - (Y_i^c)^T\} & \Re\{Y_i^c + (Y_i^c)^T\} \end{bmatrix} \tag{5.4}$$

$$\bar{\mathbf{Y}}_i^c := \frac{-1}{2}\begin{bmatrix} \Im\{Y_i^c + (Y_i^c)^T\} & \Re\{Y_i^c - (Y_i^c)^T\} \\ \Re\{(Y_i^c)^T - Y_i^c\} & \Im\{Y_i^c + (Y_i^c)^T\} \end{bmatrix} \tag{5.5}$$

$$M_i := \begin{bmatrix} e_i e_i^T & 0 \\ 0 & e_i e_i^T \end{bmatrix} \tag{5.6}$$

Matrix Y^c denotes the bus admittance matrix of the power grid for outage c, and e_i is the i-th basis vector. The initialization points η_1 from stage A (see Section 5.6.1) correspond to both feasible and infeasible operating points for the AC power flow. Given a set-point P^* for the generation dispatch (corresponding to initialization point η_1^*), (5.7) – (5.13) compute the minimum distance from P^* to the closest feasible generation dispatch. Obviously, if P^* is a feasible generation dispatch, the

minimum distance is zero.

$$\min_{W^c} \sqrt{\sum_{i\in\mathcal{G}} (\text{Tr}\{\mathbf{Y}_i^0 W^0\} + P_{D_i} - P_i^*)^2} \tag{5.7}$$

$$\text{s.t.}\ \underline{P}_{G_i} \leq \text{Tr}\{\mathbf{Y}_i^c W^c\} + P_{D_i} \leq \overline{P}_{G_i} \quad \forall i \in \mathcal{N}\, \forall c \in \mathcal{C} \tag{5.8}$$

$$\underline{Q}_{G_i} \leq \text{Tr}\{\bar{\mathbf{Y}}_i^c W^c\} + Q_{D_i} \leq \overline{Q}_{G_i} \quad \forall k \in \mathcal{N}\, \forall c \in \mathcal{C} \tag{5.9}$$

$$\underline{V}_i^2 \leq \text{Tr}\{M_i W^c\} \leq \overline{V}_i^2 \quad \forall i \in \mathcal{N}\, \forall c \in \mathcal{C} \tag{5.10}$$

$$W^c \succeq 0 \quad \forall c \in \mathcal{C} \tag{5.11}$$

$$\text{Tr}\{\mathbf{Y}_i^c W^c\} = \text{Tr}\{\mathbf{Y}_i^0 W^0\} \quad \forall i \in \mathcal{G}\backslash\{\text{slack}\}\, \forall c \in \mathcal{C} \tag{5.12}$$

$$\text{Tr}\{M_i W^c\} = \text{Tr}\{M_i W^0\} \quad \forall k \in \mathcal{G}\, \forall c \in \mathcal{C} \tag{5.13}$$

The matrix variable W^0 refers to the intact system state. The terms $\underline{P}_{G_i}, \overline{P}_{G_i}, \underline{Q}_{G_i}, \overline{Q}_{G_i}$ are the maximum and minimum active and reactive power limits of the generator at bus i, respectively. The active and reactive power demand at bus i is denoted with the terms P_{D_i} and Q_{D_i}. The bus voltages at each bus i are constrained by upper and lower bounds $\overline{V}_i$ and $\underline{V}_i$. In case of an outage, the generator active power and voltage set-points remain fixed (5.12) – (5.13), as traditional N-1 calculations do not consider corrective control. To reduce the computational complexity of the semidefinite constraint (5.11), we apply a chordal decomposition according to [151] and enforce positive semidefiniteness only for the maximum cliques of matrix W^c. To obtain an objective function linear in W^0, we introduce the auxiliary variable R and replace (5.7) with:

$$\min_{W^c, R} \quad R \tag{5.14}$$

$$\text{s.t.} \sqrt{\sum_{i\in\mathcal{G}} (\text{Tr}\{\mathbf{Y}_i^0 W^0\} + P_{D_i} - P_i^*)^2} \leq R \tag{5.15}$$

The convex optimization problem (5.8) – (5.15) guarantees that the hypersphere with radius R around the operating point P^* does not contain any points belonging to the non-convex feasible region, considering both the intact system state and the contingencies in set $\mathcal{C}$. Note that the obtained closest generation dispatch $P_i^0 = \text{Tr}\{\mathbf{Y}_i^0 W^0\} + P_{D_i}$ is feasible in the relaxation but not necessarily in the non-convex problem. Hence, with R we obtain a lower bound of the distance to the closest feasible generation dispatch in the non-convex problem.

In a procedure similar to [152], we apply an iterative algorithm for the grid pruning: First, given η_1 initialization points, we solve (5.8) – (5.15) without considering contingencies, i.e. $\mathcal{C} = \{0\}$. Using the determined hyperspheres, we eliminate the infeasible operating regions and, using LHS, we resample the reduced search space to select a reduced set of initialization points η_2. In the next stage, given η_2, we determine the five most critical contingencies (see section 5.6.1 for more details) and resolve (5.8) – (5.15). We remove all resulting infeasible regions from the set η_2, and using LHS we resample the remaining feasible region to determine the initialization set η_3. The number of considered contingencies is a trade-off between the amount of obtained infeasible points and the required computational time to solve the semidefinite relaxation.

As an example, we consider the IEEE 14 bus system in a scenario where all but three generators (P_{gen2-4}) are fixed to specific values. Considering the five most critical contingencies, and using our proposed convex grid pruning algorithm, the search space is reduced by $65.34\,\%$. This is visualized in Fig. 5.4: the colored area shows the discarded regions of infeasible points as determined by the superposition of the spheres.

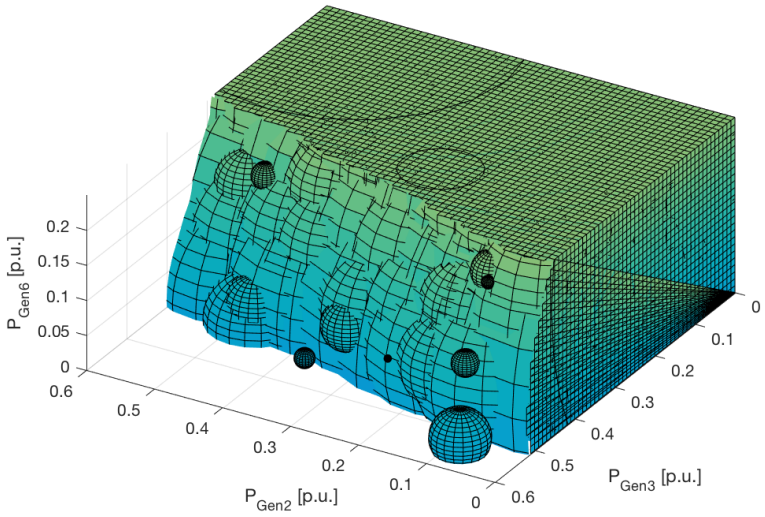

Figure 5.4: Search space reduction obtained by the proposed grid pruning algorithm for the IEEE 14 bus system. Operating points within the structure formed by superimposed spheres are infeasible considering N-1 security. Source: [**Pub. B**].

Determining the Most Critical Contingencies

From the definition of N-1 security criterion it follows that a single contingency suffices to classify an operating point as infeasible. Most of the unsafe operating points, however, belong to the infeasible regions of several contingencies. As a result, focusing only on a limited number of *critical* contingencies, we can accurately determine a large part of the N-1 insecure region, thus reducing the search space without the need to carry out a redundant number of computations for the whole contingency set. This drastically decreases the computation time.

The goal of this section is to propose a methodology that determines the most critical contingencies, which can then be used both in the convex grid pruning algorithm (5.8) – (5.15), and in the step direction of the DWs in Section 5.6.2.

Classical N-1 contingency analyses including time-domain simulations are computationally demanding. However, recent developments based on applying complex network theory in power systems showed promising results in identifying vulnerable lines and nodes at a fraction of the time using e.g. the (extended) betweeness [153] or centrality based on maximum flow approaches [154].

Complex network theory studies the structural properties of complex systems based on statistical physics and graph theory. Graphs are simple models of complex systems, defined as a set of vertices V connected by a subset of edges E. Mathematically, this can be represented as a graph, $G = (V, E)$, where E is a subset of non-zero elements in the $V \times V$ adjacency matrix [155]. The generators / loads represent source respectively sink nodes. Since we focus on specific operating points with specific power flow patterns, every edge has a direction leading to an directed graph G_d.

The betweeness of a node in a network is defined as the number of shortest paths that pass through it. Thus, it is a proxy for how much power each substation (node) is transmitting assuming that power is routed through the most direct path [153].

Similarly, the centrality index used in [154], and first proposed for power systems in [156, 157], refers to the portion of the flow passing through a specific edge in the network. Components with

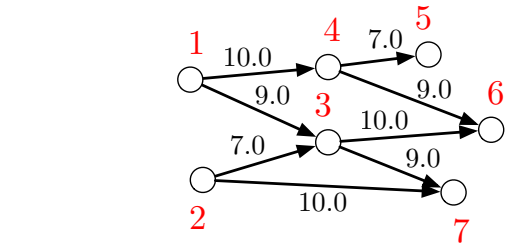

(a) Initial graph

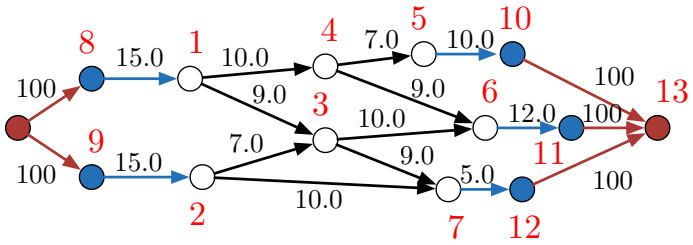

(b) Extended graph

Figure 5.5: Visualization of the graph extension. Node numbers are marked in red and edge weights in black.

higher centrality have a higher impact on the vulnerability of the system, and thus have higher probability to be critical contingencies. The index is based on a classical optimization problem in complex network theory, known as maximum flow problem.

Similar to [154], we adopt an improved max-flow formulation for the power system problem, which includes vertex weights, and extends the graph with a single global source and a single global sink node which has been visualized in Fig. 5.5. The initial graph is shown in Fig. 5.5a, while the extended graph is given in Fig. 5.5b. As a first step, the graph is extended in that way that one additional node is added to the graph for every generator and every load. Each of these nodes is connected with an edge to the corresponding node initially representing the bus of the corresponding generator / load. The generator capacity, respectively the load size (active power), is chosen as the weight of the corresponding, newly introduced edge. All nodes and edges of the first step of the extension are marked blue in Fig. 5.5b. As a second step, two additional nodes are introduced. The first one is connected to all previously introduced generator nodes, representing the global source node. The other one is connected to all previously introduced load nodes, representing the global sink node. The weights of the newly introduced edges are chosen as significantly higher than any other edge weight in order not to interfere with the maximum flow calculations. All nodes and edges of the second step of the extension are marked red in Fig. 5.5b.

The improved max-flow formulation using the extended graph accounts for the net load and generation injections at every vertex, avoids line capacity violations resulting from the superposition of different source-sink combinations, and decreases computation time. However, contrary to [154], we use a modified definition of the centrality index. While Fang et al. [154] analyze the most critical contingencies for all generation and demand patterns, we are interested in the most critical contingency for every *specific* load and generation profile, i.e. for every operating point OP_k. Thus,

for each operating point OP_k we define the centrality index as:

$$C_{ij}^{(k)} = f_{ij,actual}^{(k)} / f_{max}^{(k)}. \tag{5.16}$$

where $f_{ij,actual}^{(k)}$, are the actual flows for that operating point OP_k, and $f_{max}^{(k)}$ represents the maximum possible flow between global source and global sink node for the same case. Thus, at every operating point OP_k, the lines are ranked according to their contribution to the maximum flow in the system. The higher their centrality index is, the more vulnerable becomes the system in case they fail, and as a result they are placed higher in the list of most critical contingencies.

The case study includes a brief discussion about the performance of this vulnerability assessment for the investigated systems. Despite the drastic decrease in computation time and its general good performance, the proposed approach still includes approximations. As we will see in Section 5.6.2, we take all necessary steps to ensure that we have avoided any possible misclassification.

5.6.2 Directed Walks

Variable Step Size

As mentioned in Section 5.3, to achieve an efficient database generation our focus is to assess a sufficiently high number of points inside the HIC area, while traverse the rest of the space faster and with fewer evaluations. To do that, we propose to use a variable step size α depending on the distance d of the operating point from the security boundary γ. The distance $d(OP_k)$ of the operating point under investigation is defined as:

$$d(OP_k) = |\gamma_k - \gamma|, \tag{5.17}$$

with γ_k being the stability index value for operating point OP_k. Then, for OP_k we define the variable step size α_k as follows:

$$\alpha_k = \begin{cases} \epsilon_1 \cdot P^{max}, & \text{if } d(OP_k) > d_1 \\ \epsilon_2 \cdot P^{max}, & \text{if } d_1 \geq d(OP_k) > d_2 \\ \epsilon_3 \cdot P^{max}, & \text{if } d_2 \geq d(OP_k) > d_3 \\ \epsilon_4 \cdot P^{max}, & \text{otherwise} \end{cases}, \tag{5.18}$$

where $\mathbf{P}^{max}$ is the vector of generator maximum capacities, ϵ_{1-4} are scalars, and for distances d_{1-3} holds $d_1 > d_2 > d_3$. Since the system is highly nonlinear (in our case study for example we are searching for the minimum damping ratio considering N-1 security, i.e. $\Gamma + 1$ different nonlinear systems superimposed), the exact step size required to reach the HIC region cannot be constant and determined a-priori. Thus, the step size is gradually reduced as we approach the security boundary in order not to miss any points within the HIC region. This is illustrated in Fig. 5.6.

It follows that distances d_{1-3} and the corresponding ϵ_{1-4} are tuning factors, to be chosen depending on the desired speed, granularity, precision and given system size. Factors found useful for given systems are discussed in the case study.

Determining the Step Direction

After identifying the step size, we need to determine the direction of the next step. Our goal is to traverse the feasible (or infeasible) region as fast as possible, and enter the HIC region. To do that, at every step we follow the steepest descent of the distance metric $d(OP_k)$, as shown in (5.19).

$$OP_{k+1} = OP_k - \alpha_k \cdot \nabla d(OP_k) \tag{5.19}$$

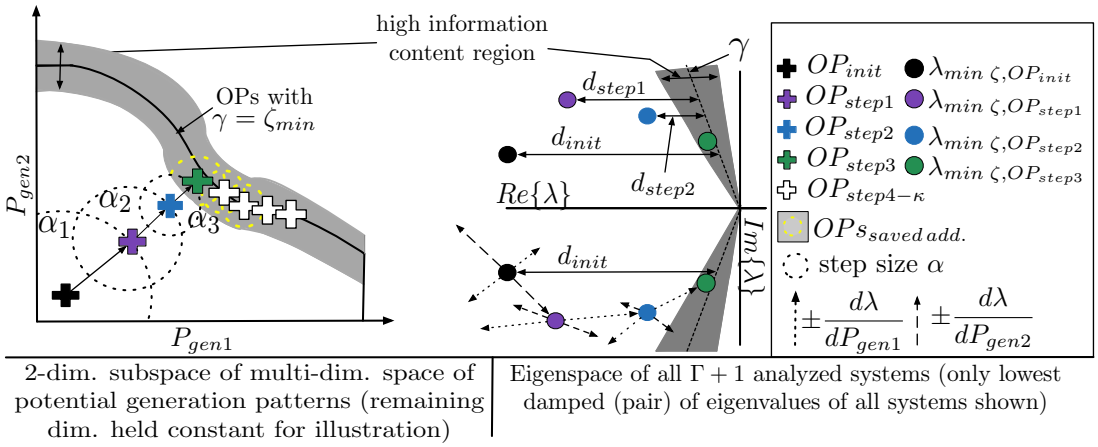

Figure 5.6: Illustration of the Directed Walk (DW) through a two dimensional space using varying step sizes, α_i, following the steepest descent of distance, d. Source: [**Pub. B**].

where α_k is the step size for OP_k, defined in (5.18), and $\nabla d(OP_k)$ is the gradient of $d(OP_k)$. As the distance is a function of the chosen stability index, it is user specific and $\nabla d(OP_k)$ in the discrete space shall be determined by a suitable sensitivity measure, which differs for different stability indices. If the focus is on voltage stability for example, the associated margin sensitivities could be used [158]. It is stressed that our method is suitable for any sensitivity capable of measuring the distance to the chosen stability index. In the case studies of this work, we focus on small-signal stability and, as described in the next paragraph, we pick the damping ratio sensitivity as a suitable measure.

Normally, at every step k we should measure distance d for all $N-1$ contingencies, select the minimum of those distances and based on that, determine the next step size and direction. Having thousands of initialization points η_3 implies checking along all possible dimensions and $N-1$ contingencies at every step of thousands of directed walks. Beyond a certain system size, this becomes computationally intractable. Instead, we take advantage of the critical contingency identification procedure described in Section 5.6.1, and at every step we measure distance d assuming the most critical contingency for OP_k. This reduces the required analysis from $\Gamma + 1$ systems to one system, which drastically decreases the computation time. Following steps in this procedure, as described later, ensure that this approximation is sufficient and there is an accurate detection of the security boundary as soon as we enter the HIC region.

Sensitivity Measure for Small-Signal Stability

We determine the step direction by the sensitivity of the damping ratio, ζ, of the system representing the most critical contingency, Γ_i. This requires to compute the eigenvalue sensitivity which, in turn, depends on the state matrix $\mathbf{A}_{\Gamma_i}$ (for more details about forming state matrix A the reader is referred to [52]). Thus, the sensitivity of eigenvalue λ_n to a system parameter ρ_i is defined as

$$\frac{\partial \lambda_n}{\partial \rho_i} = \frac{\psi_n^T \frac{\partial \mathbf{A}_{\Gamma_i}}{\partial \rho_i} \phi_{\mathbf{n}}}{\psi_n^T \phi_n}. \tag{5.20}$$

ψ_n^T and ϕ_n are the left and right eigenvectors, respectively, associated with eigenvalue λ_n [52]. Defining $\lambda_n = \sigma_n + j\omega_n$, and with $\zeta = \frac{-\sigma_n}{\sqrt{\sigma_n^2+\omega_n^2}}$, we can determine the damping ratio sensitivity,

$\frac{\partial \zeta_n}{\partial \rho_i}$ as

$$\frac{\partial \zeta_n}{\partial \rho_i} = \frac{\partial}{\partial \rho_i}\left(\frac{-\sigma_n}{\sqrt{\sigma_n^2+\omega_n^2}}\right) = \omega_n \frac{(\sigma_n \frac{\partial \omega_n}{\partial \rho_i} - \omega_n \frac{\partial \sigma_n}{\partial \rho_i})}{(\sigma_n^2+\omega_n^2)^{\frac{3}{2}}}. \tag{5.21}$$

Due to the fact that the computation of $\frac{\partial \mathbf{A}_{\mathbf{\Gamma_i}}}{\partial \rho_i}$ is extremely demanding, it is usually more efficient to determine the damping ratio sensitivity of ζ to ρ_i by a small perturbation of ρ_i. The whole process is illustrated in Fig. 5.6. The parameters ρ_i correspond to the power dispatch of two generators. The DW is illustrated following the steepest descent of damping ratio considering the lowest damped eigenvalue of the system representing the most critical contingency Γ_i.

Parallelization of the Directed Walks

Directed Walks are easily parallelizable. In our case studies, we have used 80 cores of the DTU HPC cluster for this part of our simulations. To ensure an efficient parallelization and not allow individual processes take up unlimited time, we set a maximum number of steps of DWs, κ_{max}. The tuning of κ_{max} is discussed in the case studies in Section 5.7.

Entering the HIC region

As soon as a DW enters the HIC region, two additional processes take place. First, all points surrounding the current operating point are assessed as well, as they may be part of Ω. This is indicated in Fig. 5.6 by the yellow circles. Second, we allow the DW to move along only a single dimension (the dimension is still selected based on the steepest descent) and with the minimum step size. This ensures that we collect as many points within the HIC region as possible.

Termination of the Directed Walks

Each DW terminates if the next step arrives at an operating point already existing in the database. The termination criterion excludes operating points that were collected as "surrounding points" of a current step (see Section 5.6.2).

Full N-1 contingency check

After all DWs have been performed for every initialization point in parallel, we evaluate all safe (and almost safe) operating points in the database against all possible contingencies to ensure that no violations occur. More formally, we assess all operating points in the final database with $\gamma_k \geq \gamma - \mu$ for all remaining Γ systems to ensure that a possible false identification of the most critical contingency does not affect the stability boundary detection. This allows us to guarantee a high level of accuracy in determining the security boundary. Despite, this being the most computationally expensive step of our method, accounting for over 50% of the required time, in absence of expert knowledge this procedure is required for any method reported in the literature [143, 144]. The difference is, however, that our approach manages to discard a large volume of not relevant data before this step, and, as a result, outperforms existing methods by being at least 10 to 20 times faster.

Final Set of Directed Walks

The maximum number of steps κ_{max}, although helpful for the efficient parallelization of the DWs, may result in DWs that have not sufficiently explored the search space. In this final step, for any

DWs that have reached κ_{max} while inside the HIC region, we perform an additional round of DW to explore as thoroughly as possible the HIC region. The final points from the previous round serve as initialization points.

5.7 Case Studies

In the first case study, the efficient database generation method is applied on the IEEE 14 bus system. We measure the efficiency improvement compared with the Brute Force (BF) approach, and we demonstrate how our method outperforms importance sampling techniques. It is impossible to carry out the comparison with the BF approach in larger systems, as BF becomes intractable. In the second case study, we demonstrate the scalability of our method to larger systems, such as the NESTA 162 bus system [139]. The case studies in this work use the combination of N-1 security and small-signal stability for the definition of the security boundary. It should be stressed though that the proposed methodology proposes a general framework and is applicable to a number of other stability metrics or power system models.

5.7.1 Small-Signal Model

The sixth order synchronous machine model [47] with an Automatic Voltage Regulator (AVR) Type I introduced in Section 2.7.1 is used in this study. In case of the NESTA 162 bus system, all generators are addtionally equipped with Power System Stabilizers (PSS) type 1. The small signal models were derived using Mathematica, the initialization and small signal analysis were carried out using Matpower 6.0 [49] and Matlab. Reactive power limits of the generators are enforced. Machine parameters are taken from [16] and given in the appendix.

5.7.2 IEEE 14 bus system

Carrying out the first case study on a small system, where the BF approach is still tractable, allows us to verify that our method is capable of finding $100\,\%$ of the points belonging to the HIC region. To ensure comparability, all simulations used 20 cores of the DTU HPC cluster.

Network data is given in [49], machine parameters are given in the appendix. The considered contingencies include all line faults (except lines 7-8 and 6-13[1]). Due to the BF approach, we know that 1457 operating points belong to the HIC set, i.e. with $2.75\,\% < \zeta < 3.25\,\%$. The grid pruning without considering any contingency does not reduce the search space in this case study; this is because all possible combinations of generation setpoints do not violate any limits for the given load profile. Thus, η_1 is chosen as 0 and we directly start with the contingency-constrained grid pruning considering the five most critical contingencies. Table 5.1 compares the performance of our method with the BF approach and an Importance Sampling (IS) approach [143]. The BF approach is serving as the benchmark, because we know that this approach finds all OPs in the HIC region as it just analyzes all potential OPs. Thus, it allows us to show that our method is capable of finding all OPs in the HIC region in significantly less time than the BF and the IS approach. In fact, our method is capable of creating a database including *all* points of interest in 3.77 min; that is 0.68 % of

[1]The IEEE 14-bus and the NESTA 162-bus systems, based on the available data, are not $N-1$ secure for all possible contingencies. The outage of those specific lines lead to violations (e.g. voltage limits, component overloadings, or small-signal instability) that no redispatching measure can mitigate. This would not have happened in a real system. In order not to end up with an empty set of operating points, and still use data publicly available, we choose to neglect these outages.

Table 5.1: Results: IEEE 14 Bus System. Source: **[Pub. B]**.

Required time	Time in % w.r.t. BF	OPs in Ω found	Method	η_1 / η_2 / η_3 / κ_{max}
2.56 min	0.46 %	95.13 %	DWs	0 / 200 / $2k$ / 10
2.99 min	0.54 %	98.9 %	DWs	0 / 200 / $2k$ / 15
2.94 min	0.53 %	97.80 %	DWs	0 / 200 / $2k$ / 20
3.77 min	0.68 %	100 %	DWs	0 / 200 / $2k$ / 25
2.94 min	0.53 %	97.80 %	DWs	0 / 200 / $1k$ / 20
3.48 min	0.74 %	99.93 %	DWs	0 / 200 / $3k$ / 20
4.80 min	0.86 %	100 %	DWs	0 / 200 / $5k$ / 20
37.0 min	6.66 %	100 %	Importance Sampling (IS)	
556 min	100 %	100 %	Brute Force (BF)	

the time required by the BF approach (9.26 hours; 147 times faster). The proposed method is also significantly faster (approx. 10 times) than an Importance Sampling approach (31.60 min).

One of the major advantages of our method is the drastic search space reduction through the grid pruning and the most critical contingency identification. In this case study, grid pruning eliminated up to 70.13 % of all $\approx 2.5 \cdot 10^6$ potential operating points (the number varies based on the number of initialization points). At the same time, performing every DW step for the single most critical contingency, we reduce the required assessment from $\Gamma + 1$ systems to 1 system. In larger systems the speed benefits will be even more pronounced, e.g. 14-bus: $\Gamma + 1 = 19$ contingencies are reduced to 1 (most critical); 162-bus: $\Gamma + 1 = 160$ contingencies reduced to 1.

Table 5.1 also compares the method's performance for different numbers of initialization points η_{1-3} and maximum number of DW steps κ_{max}. In this system, choosing a higher number of maximum steps instead of a higher number of initialization points leads to time savings. The same holds in larger systems, as shown in Table 5.2.

In the highlighted case of Table 5.1, the required computation time for the different parts of our method is split as follows: 26.67 % (60.31 s) for the grid pruning considering the 5 most critical contingencies (200 operating points); 53.1 % (120.12 s) for the Directed Walks; and 20.24 % (45.78 s) for the final N-1 check of all operating points. Grid pruning eliminates 1149 from the $\eta_3 = 2000$ initialization points, resulting in 851 feasible starting points for the DWs. The most critical contingency is detected correctly in 94.55 % of cases.

5.7.3 NESTA 162 bus system

A BF approach with a 1 MW step size for this system requires the assessment of $7.6 \cdot 10^{29}$ operating points for a single load profile; this is computationally intractable. The set of considered contingencies includes 159 line faults[1]. To ensure comparability, all simulations for the 162-bus system have been performed using 80 cores of the DTU HPC cluster.

Compared to the IEEE 14 bus system, the problem size (potential # of OPs) is 23 orders of magnitude larger while the problem complexity (# of faults) increased 6.2 times. Table 5.2 presents the results of our method compared with an Importance Sampling approach [143]. As the BF approach for this system is intractable, the exact number of points within the HIC region (set Ω) is unknown. Therefore, the focus here is on demonstrating that within similar time frames, our proposed method is capable of finding substantially more unique operating points inside Ω. Indeed, our approach

Table 5.2: Results: NESTA 162 Bus System. Source: **[Pub. B]**

Req. time	Unique OPs in Ω	Method	η_1 / η_2 / η_3 / κ_{max}
9.35 h	3118	Directed Walks	$30k$ / $120k$ / $800k$ / 5
13.17 h	4166	Directed Walks	$30k$ / $120k$ / $800k$ / 10
14.57 h	25046	Directed Walks	$30k$ / $120k$ / $800k$ / 20
29.78 h	150790	Directed Walks	$30k$ / $120k$ / $800k$ / 30
37.07 h	183295	Directed Walks	$30k$ / $120k$ / $800k$ / 40
13.36 h	16587	Directed Walks	$100k$ / $200k$ / $800k$ / 5
18.20 h	45040	Directed Walks	$100k$ / $200k$ / $800k$ / 10
35.70 h	901	Importance Sampling (IS)	

identifies approx. three orders of magnitude more HIC points that an Importance Sampling approach (183'295 vs 901 points).

In the highlighted case of Table 5.2, the computation time is split as follows: 3.44 h (9.28 %) for LHS (3 stages), 1.85 h (4.98 %) for both stages of grid pruning, 7.04 h (18.98 %) for the DWs, and 24.75 h (66.76 %) for the final N-1 check of all operating points of interest. This highlights that the most computationally expensive part is the complete N-1 analysis and shows why our proposed method is significantly faster than others: (i) we reduce the search space by eliminating infeasible N-1 points through the grid pruning algorithm, (ii) we evaluate most points only for one contingency and discard all with $\zeta < 2.75\,\%$, and (iii) the method can largely be scheduled in parallel.

5.8 Conclusion and Outlook

This work proposes an efficient database generation method that can accurately determine power system security boundaries, while drastically reducing computation time. Such databases are fundamental to any DSA method, as the information in historical data is not sufficient, containing very few abnormal situations. This topic has not received the appropriate attention in the literature, with the few existing approaches proposing methods based on importance sampling.

Our approach is highly scalable, modular, and achieves drastic speed-ups compared with existing methods. It is composed of two parts. First, the search space reduction, which quickly discards large infeasible regions leveraging advancements in convex relaxation techniques and complex network theory approaches. Second, the "Directed Walks", a highly parallelizable algorithm, which efficiently explores the search space and can determine the security boundary with extremely high accuracy. Using a number of initialization points, a variable step size, and based on a steepest descent method, the "Directed Walk" algorithm traverses fast through large parts of feasible (or infeasible) regions, while it focuses on the high information content area in the vicinity of the security boundary. Our case studies on the IEEE 14-bus and the NESTA 162-bus system demonstrate the high scalability and excellent performance of our algorithm, being able to identify up to 100% of the discrete operating points around the security boundary, while achieving computational speed-ups of over 10 to 20 times, compared with an importance sampling approach. Our approach is modular, not dependent on the initial sampling set (as importance sampling is), and agnostic to the security criteria used to define the security boundary. Criteria to be used include N-1 security, small-signal stability, voltage stability, or a combination of several of them. The method can find application in off-line security assessment, in real-time operation, and in machine learning and

other data-driven applications, providing a computationally efficient way to generate the required data for training and testing of new methods.

In future work, the methodology can be developed further in order to facilitate the generation of databases considering corrective control actions of HVDC terminals. The challenges are threefold: (i) increasing complexity of the model, (ii) increasing problem size since each HVDC terminal adds two degrees of freedom with an wide operating range ($\approx \pm P_{max}$ / $\pm Q_{max}$) to the problem. Moreover, (iii) an operating point cannot be classified by only evaluating the most critical contingency due to potential corrective control actions which complicates the operating point classification. This is described in more detail in Section 6.6.2. Although, the generation of such a database is in general possible with the proposed method, it would require an additional loop over operating ranges of the different HVDC terminals, i.e. adapting the method proposed in Section 4.7 to determine the operating space of MT-HVDC grids. This, however, could potentially be solved more elegantly and faster by developing the method further.

CHAPTER 6

Data-driven Methods for Market-clearing and Power System Operation

*After the development of an efficient database generation method enabling a data-driven power system security assessment, such databases are used within this chapter to develop data-driven methods for market-clearing and power system operation. In particular, we include security considerations into optimal power flow algorithms using data. This chapter is structured as follows: First, the background of this chapter is discussed and a brief literature review is provided. Then, the contributions of this chapter are emphasized, followed by a description of the work published in **[Pub. E]** and **[Pub. F]**. Finally, we bridge the gap to chapter 4 by incorporating corrective security into the market clearing considering corrective control actions of HVDC terminals.*

6.1 Background

As a consequence of the change in the energy mix and the liberalization of the energy market, the European power system is nowadays operated under increasingly stressed conditions. This is based on several factors which are among others: increased competition, the higher variability due to the more distributed generation and the difficulty of precise forecasts. As the system is operated under increasingly stressed conditions and closer to its security boundaries, the Transmission System Operators (TSOs) are more often required to interfere with the initial market outcome, i.e. the power plant dispatch, in order to ensure a secure operation of the network. The redispatching measures, as these adjustments are called, consists mostly of readjusting the generation of single power plants or RES plants resulting in changed power flows which comply with the determined stability limits. Taking the example of Germany, the shift in generation in terms of type but also location, i.e. from nuclear power plants located close to the load centers in the south/south-west of Germany towards a high wind penetration in the north, far away from the load centers, combined with a delayed grid expansion to cope with the changed power flows, led to a more difficult grid operation scenario requiring significantly more costly redispatching measures by the TSOs (volume of redispatched energy increased between between 2010 (306 GWh) and 2017 (18.455 GWh) by factor 60; costs increased by factor 30 (13 M€ vs. 396.5 M€) [19, 20]. However, it is important to emphasize that simultaneously the cost of reimbursing down-regulated Renewable Energy Sources (RES) as well as the use of reserves increased significantly leading to overall costs of 1.4 B€ in 2017 in Germany alone [19].

Nowadays, market-clearing processes and security assessment are separated in most electricity markets [159]. As introduced in section 2.4, the economic dispatch is determined by market

operators in an auction based on Optimal Power Flow (OPF) algorithms considering only a few limitations. These limits are provided by the TSOs with focus on the transfer capacities of the tie-lines. While the Flow-Based Market Coupling (FBMC) improved the market clearing using not constant but linear convex limits (based on a simplified model) compared to the Available Transfer Capacity (ATC) approach, these convex limits still do not reflect the true feasible space of the system which is non-convex.

The actual physical bounds are determined by TSOs which are in charge of the secure and reliable system operation. Depending on the result of their detailed security assessment considering their entire system and not only a few critical and tie-lines, TSOs carry out necessary redispatching measures.

While in the example of Germany, the problem of missing transmission lines / transfer capacity between the north and south of Germany can not be solved by smarter algorithms, market-clearing processes which include more detailed security considerations and forecast uncertainties may still be able to reduce the need for costly redispatching measures leading directly to a feasible and secure market outcome.

In order to optimally establish secure system operation, consider the whole true feasible space and avoid expensive redispatching actions, market-clearing processes need to account for more detailed security considerations and use limits which actually reflect the true feasible space of the system. To this end, algorithms are required, which capture the security requirements imposed by TSOs while at the same time being scalable and rapidly deployable in market-clearing auctions. For TSOs, on the other hand, Security-Constrained Optimal Power Flows (SC-OPFs), i.e. OPFs which explicitly account for security criteria, are an essential tool for the planning and real-time operation of their system [28]. Thus, SC-OPF is an important tool both for power system operation and market-clearing.

Following the distinction between preventive security and preventive-corrective security, introduced in section 2.3, preventive SC-OPFs identify optimal preventive control actions compliant with the N-1 security criterion leading to an operating point at which the system is able to withstand the loss of any major component without violating system constraints. However, in contrast to preventive-corrective SC-OPFs, preventive SC-OPFs do not consider the possibility of corrective actions in post-contingency states, apart from those taking place automatically (e.g. active power of generators participating in frequency control, secondary voltage control,...) [28].

Further, SC-OPFs can be distinguished by their application, by which kind of stability issues they consider, by the approach how they include stability constraints and by how many contingencies they consider [28]. Their application varies from the determination of the minimum number of control actions over identifying optimal redispatch actions to the identification of the optimal dispatch in case of market applications. While in Europe market-dispatch relies on DC approximations, the authors in [160] identified a security-constrained AC-OPF as "ultimate goal" for market software to be used by Independent System Operators (ISOs) across the US. They foresee up to $10\,\%$ cost savings worldwide based on improved modeling of voltage and stability constraints leading to more realistic dispatch decisions and better market signals, whereas they emphasize that the oversimplification of current software results in sub-optimal solutions [160]. The implementation of Mixed-Integer Programming (MIP) in day-ahead and real-time markets in the US already resulted in cost savings of half a billion dollars annually [161].

Major drawbacks of conventional SC-OPFs include the problem size and the negligence of stability requirements [28]. The classical SC-OPF formulation just implicitly assumes that the system will not lose stability after the occurrence of a contingency and (with or without post-contingency corrective actions) will reach a viable steady-state [28]. However, since the system dynamics are not modeled in the conventional SC-OPF, the assumptions are not verified. As the system dynamics are based on differential algebraic equations, they cannot be included in the OPF as linear or non-linear constraints in a straightforward way. Therefore, often linear heuristic constraints derived after running time domain simulations are used. They, however, may lead to sub-optimal solutions and generally require several iterations to refine the heuristic constraints [28]. Thus, the SC-OPF is usually formulated in a very conservative way leading potentially to sub-optimality and undetected risk of instability [28].

As aforementioned, SC-OPFs can be further distinguished by the kind of stability they consider. This thesis focuses on Small-Signal Stability Security Constrained Optimal Power Flows (SSSSC-OPFs), i.e. SC-OPFs which consider N-1 security and ensure that the pre- and post-contingency state is small-signal stable. In [162], the authors propose SSSSC-OPFs as commendable tool that can provide the complete redispatch information considering economic dispatch and technical constraints. They argue, that in contrast to SSSSC-OPFs, most commercial software such as PSS/e and NEPLAN only use particpation factors to perform offline redispatching studies and can therefore neither determine which generator should increase or decrease the generation nor how much generation should be dispatched. Thus, SSSSC-OPF seems like a good option. Solving a SSSSC-OPF problem is, however, in general very challenging because of the non-smooth nature of the small-signal stability constraint [162].

6.2 Literature Review

In literature several different methods have been proposed:

While an approach based on numerical eigenvalue sensitivity has been used in [163], the authors in [159] use eigenvalue-sensitivities with respect to OPF decision variables to maintain tractability of small-signal stability constraints. Thus, they keep the small-signal stability constraint feasible by successively solving SSSSC-OPF with Interior Point Method (IPM) [162]. However, the authors conclude that the required computational effort is a major challenge and the methods perform poorly when applied to larger systems.

An approximate singular value based IPM is proposed in [164] using the minimum singular value of the modified full Jacobian matrix as stability index. The gradient of this index is, however, approximated by first-order Taylor series expansion and the Hessian is evaluated numerically by perturbing the gradients [162].

In [165], the authors use a closed-form eigenvalue sensitivity based IPM which however require the derivation and calculation of the second-order eigenvalue sensitivities essential for forming the Hessian of the small-signal constraints. Thus, the authors also conclude that the required computational effort is a major challenge and the methods perform poorly when applied to larger systems.

In [166], the authors use an explicit small-signal stability constraint based on Lyapunov theorem and a Nonlinear Semi-Definite Programming (NLSDP) formulation. This approach may, however,

also be computationally problematic for large systems due to dense subsidiary semi-definite matrix variables [162].

In [162], the authors propose an approach using closed-form eigenvalue sensitivity and Sequential Quadratic Programming (SQP) combined with gradient sampling. In contrast to all IPM methods, which cannot guarantee convergence of the problem, even locally, due to the non-smoothness nature of the small-signal stability constraints [162], this methods achieves global convergence. The authors, however, do not consider N-1 security, thus reducing the problem size significantly.

In [167] a security boundary-constrained DC-OPF ensuring voltage and small-signal stability is proposed, where hyperplanes are used to linearly approximate the security boundary. Thus, operating points outside the convex space constructed by the hyperplanes are not considered in the OPF.

Compared to these more conventional approaches where small-signal stability is considered using sensitivities or hyperplanes, this thesis proposes to use data-driven approaches to determine the boundaries. While data-driven approaches have been used in power systems for online security assessments using decision trees [141, 142, 144, 168–170] or multiway decision trees [171] for years (an overview is given in [172]), the efforts to combine these approaches with a SC-OPF have been limited. In [173], the authors determine a online preventive control strategy accounting for contingencies and transient stability. The security considerations are translated to generator capacity limits of the most critical generators, which are included as hard constraints in the OPF. This approach, however, restrains the market participants from bidding all their available capacity and imposes very conservative bounds, which can prevent the deployment of cheaper generation capacity.

In [142], the authors propose also to translate the security considerations into generator capacity limits. Additionally, they propose to decompose the security regions into several secure convex regions. In order to determine preventive and corrective control actions, they propose to solve the OPF problems sequentially for every convex set.

In [144], the authors translate also the security considerations into generator capacity limits to derive two kind of decision trees, one to identify potential security issues focusing on transient stability and the other to provide online decision support on allowed preventive control strategies.

6.3 Contributions

The contributions of this chapter include the development of market clearing algorithms which incorporate both small-signal stability and N-1 security. First, a data-driven small-signal stability and preventive security constrained DC-OPF is developed which in contrast to previous work incorporates security and stability considerations and which does not limit any market participant in their bidding opportunities but does translate the security considerations into line flow limits. Different approaches to map the security considerations from the ac into the dc space are discussed. In contrast to current practices, we achieve less conservative limits and extend the feasible space to the true non-convex feasible space. Thus, we relieve artificial market constraints which prevent certain market outcomes while ensuring a N-1 secure and small-signal stable dispatch mitigating the need for redispatching measures.

Second, the data-driven small-signal stability and preventive SC-OPF is developed further to an AC-OPF extending the applicability to power system operation. Used either in market clearing or

in power system operation for e.g. determining redispatching measures, the method incorporates both small-signal stability and N-1 security considerations translated into line flow limits. More importantly, the method extends the feasible space represented in the SC-OPF compared to conventional methods, and can identify the global optimum as opposed to most previous work and tested Mixed-Integer Non-Linear Programming (MINLP) solvers. Furthermore, the approach we propose significantly reduces computation time due to a decreased problem size, which we obtain by separating both the small-signal stability and N-1 security analysis from the online assessment. Instead, the analysis is performed offline within the database creation / knowledge extraction.

Finally, we propose a data-driven small-signal stability and preventive-corrective security constraint DC-OPF. Thus, besides both small-signal stability and N-1 security, we incorporate also potential fast corrective control actions by HVDC terminals into the market-clearing. Hence, we propose to include corrective control actions, i.e. changes of the HVDC set-points, allowing for even less conservative limits resulting in an even more cost-efficient but still N-1 secure and small-signal stable dispatch.

6.4 Data-driven Small-Signal Stability and Preventive Security Constrained DC-OPF

In this work electricity market operations are unified with power system security considerations. Both small signal stability and steady-state security are addressed by using data-driven techniques. Tractable decision rules are derived in the form of line flow limits, and the resulting constraints are incorporated in market clearing algorithms. The goal is to enlarge the feasible space of the market clearing to a non convex region, thus minimizing redispatching actions, and instead allow the market to determine the most cost-efficient dispatch while considering all security constraints.

To maintain tractability of our approach we perform our security assessment offline, in order to determine stable and unstable operating regions. With the help of decision trees, we transform this information to linear decision rules for line flow constraints. We propose conditional line transfer limits, which can accurately capture security considerations, while being less conservative than current approaches. Our approach can be scalable for large systems, accounts explicitly for power system security, and enables the electricity market to identify a cost-efficient dispatch avoiding redispatching actions. Furthermore, we investigate the impact of different mapping approaches between the security considerations determined using an ac power flow and the market clearing using dc power flow algorithms.

Thus, the contribution of this section is a data-driven SC-OPF, which (a) incorporates the N-1 criterion, (b) ensures small-signal stability and compliance with stability margins, (c) avoids the complex reformulation of small-signal stability constraints inside the OPF by incorporating decision rules, (d) is applicable to large systems, (e) allows for a fast online solution as all computation related to the small-signal model is done offline and (f) encapsulates all security considerations for the OPF in conditional transfer limits of the lines. Traditionally, transfer limits, which are calculated by TSOs and provided to market operators, tend to be very conservative and can lead to an inefficient use of the network. In this work, we derive conditional transfer limits in the form of decision rules, which can be easily incorporated in OPF algorithms using Mixed-Integer Linear Programming (MILP) and allow the market to optimally decide on power flows which will always guarantee power system security. Furthermore, this SC-OPF is not limited to market operation but it can also be used to minimize losses in the system or for other objectives.

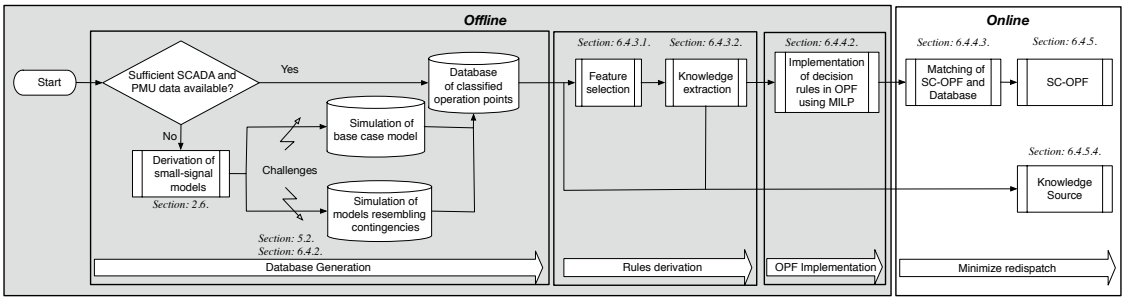

Figure 6.1: Proposed Methodology. Source: Adapted from [**Pub. E**].

For this purpose, a large database of operating points is created using a small-signal model of the system. The operating points are evaluated for small-signal stability and classified according to their compliance with required stability margins and the N-1 security criterion. Decision tree learning tools are then applied to derive decision rules suitable for implementation in OPF problems, thereby reducing the complexity of the SC-OPF. This allows for a more detailed modeling of the system given that all computations with respect to the small-signal model are done offline and not within the OPF. Less constraints are used compared to conventional SC-OPFs, which makes the method suitable for large systems.

The remainder of this section is organized as follows: An overview of the methodology to derive the SC-OPF is given in section 6.4.1. The database creation is described in section 6.4.2, followed by a summary of the methodology for feature selection and knowledge extraction in section 6.4.3. Section 6.4.4 describes the implementation of small-signal stability constraints in an OPF problem, while the application of the proposed method is demonstrated in section 6.4.5. Finally, section 6.4.6 concludes the work.

6.4.1 Methodology

The methodology to derive the data-driven preventive security constrained OPF is visualized in a flowchart in Fig. 6.1.

The first part consists of the data generation block. If available, data from Phasor Measurement Units (PMUs) could be used. Further, if Supervisory Control and Data Acquisition (SCADA) data is available a state estimator could be used to map the data into a power system model to perform the required simulations. However, due to the unavailability of such data we used data obtained by simulation of small-signal models in this work. The derivation of such models is described in section 2.7.1, while the consideration of N-1 security and the challenges of the data generation are discussed in section 2.7.5 and section 5.3, respectively. The result of this first part of the methodology is a large database of operating points which are classified for the base case as well as for credible contingencies. This is described in section 6.4.2. The second part of the methodology uses this database to derive rules, which can later be incorporated in the OPF formulation. The second part includes feature selection and knowledge extraction and is described in section 6.4.4. The third part consists of implementing such rules in the OPF algorithm using MILP (section 6.4.4). Finally, the SC-OPF is tested in a case study in section 6.4.5.

6.4.2 Database Generation

As shown in chapter 5, the IEEE 14 bus system is small enough to create a database using a classical brute force approach as database generation method. Here, we report on results from **[Pub. E]** which preceded the development of the method we proposed in chapter 5 and for this reason the brute force approach is used. However, as shown in chapter 5, we can generate an equally high-quality database in significant less time with the method we proposed in chapter 5. As a matter of fact, the intractability of the brute force approach for larger systems which we realized when carrying out this work is exactly what motivated us to develop the advanced method for an efficient database generation that we reported in chapter 5.

Each operating point is examined for small signal stability for the base case as well as for all $|\Gamma|$ contingencies considering the chosen stability margin and classified as *fulfilling the stability margin* or *not fulfilling the stability margin*. Γ is defined as the set of considered contingencies. The results are saved in a database together with the necessary information of the operating point. The necessary information depends on the chosen mapping of the operating points between the ac and dc power flow and is described in more detail in section 6.4.3.

However, in case that PMU and SCADA data is available for all credible operating points, the data could be used. In that case, noise reduction and data correction methods might be necessary and the data needs to be analyzed with respect to the stability margin of the operating points. However, it is very likely that there does not exist data for all credible contingencies, thus additional simulations will be necessary. Hence, a state estimator could be used to map the SCADA data into a power system model to perform additional simulations.

6.4.3 Feature Selection and Knowledge Extraction

After the database has been created, indicators need to be determined which are suitable to distinguish between operating points *fulfilling the stability margin* or *not fulfilling the stability margin*. These indicators are also called 'features'. In fact, the final accuracy of the data-driven SC-OPF depends on how well these features are suited to classify the operating points and how well these features translate the security considerations from the ac space into the dc space of the market clearing. Thus, determining the best features is key to obtain a low level of conservatism for the constraints representing the security boundary. The knowledge extraction constitutes the final step in the offline derivation of the decision rules.

Feature Selection

The goal is to implement the derived security constraints in the market clearing. In order to avoid the creation of constraints which target directly specific market participants by using constraints on specific generators as in previous works, we focus on deriving constraints on line flows. Thus, the goal is to incorporate all security considerations into conditional transfer limits, which provide the boundaries for the market and keep the complexity of the SC-OPF comparably low. Since line flow constraints do not directly prevent any generator of producing at its limit (which indirectly could of course happen), line flow constraints are less biased against certain market participants and market interfering. In fact, line flow limits are well in line with current practices of transfer capacities.

The transfer limits for the market-clearing are derived from the data obtained by using ac power flow as initialization for the small signal models. Since market operations are usually based on linearized dc power flow equations, the main issue here is to achieve a good mapping between the ac power flow operating points and the dc power flow points. This mapping is needed due to the fact that for the same generation pattern the line flows in an ac power flow can differ (significantly) from the ones in a dc power flow depending on the voltages and angles in the system. Thus, a better mapping of operating points leads to more accurate and less conservative line flow limits.

We focused on three different approaches to determine the active power transfer limits. Equation (6.1) shows the active power transfer over a line $n-m$ based on the full AC power flow equations.

$$F_{nm} = |V_n||V_m| \left(G_{nm}\cos(\theta_n - \theta_m) + B_{nm}sin(\theta_n - \theta_m)\right), \tag{6.1}$$

where F_{nm} and V_n denote the active power flow between nodes n and m and the voltages at node i, respectively. G_{nm} and B_{nm} correspond to the conductance and susceptance of the line.

Standard DC Approximation

- the resistance of the lines is very small compared to the reactance resulting in: $G = 0$ and $B_{nm} = \frac{-1}{x_{nm}}$
- the angle difference between adjacent nodes is small allowing for the sine to be replaced by its argument
- voltage magnitudes $|V_n|$ are equal to 1 p.u..

The line flows are then given by:

$$F_{nm} = \frac{\theta_n - \theta_m}{x_{nm}}. \tag{6.2}$$

Less conservative approximation More accurate line flows can be computed if nodal voltage magnitudes and the sine of the angle difference are accounted for:

$$F_{nm} = \frac{|V_n||V_m|\sin(\theta_n - \theta_m)}{x_{nm}}. \tag{6.3}$$

Exact Mapping of DC and AC operating points The most precise mapping of the dc and ac operating points has been achieved by incorporating the mapping into the data generation. We derived the line losses of the ac power flow of each generation pattern and included them as additional loads in a subsequent dc power flow. The losses are added to the nodes in the following way:

$$P_{Loss,n} = \frac{1}{2} \cdot \sum_{m \in I_n} \Big(F_{nm} + F_{mn}\Big), \tag{6.4}$$

where F_{nm} and F_{mn} represent the line flows obtained from the ac power flow analysis and I_n denotes the set of nodes connected to node n. The dc power flow is thus augmented by the loss approximation of the corresponding ac power flow and the obtained line flows of the dc power flow represent an exact mapping of operating points.

Knowledge Extraction

This work proposes classification trees as knowledge extraction/classification methods. A classification tree is a subset of decision trees (DT) where the decision outcome, called "target variable", can take a finite set of values. Decision Trees have been introduced in section 2.5.1. Within the generated databases containing all operating points, we distinguish between those "fulfilling the stability margin" and those "not fulfilling the stability margin". TSOs require stability margins to ensure sufficient damping of oscillations. The classification tree is used to reveal patterns of the interconnection between observation attributes and target variables with the goal of using these patterns as decision rules to predict the decision outcome of new observations. These attributes of observations used as decision variables are the previously introduced features. The use of a DT instead of other data mining or machine learning techniques provides a better understanding of the entire system's small-signal stability and what influence different parts of the system have. Moreover, we can define conditional transfer limits by using an appropriate feature selection and associating all full Decision Tree (DT) paths from the root to the leaves with binary decision variables. The optimal dispatch is then chosen by allowing only one path to be activated.

Note that before training the DT, the database should be analyzed with respect to the potential problem of skewed classes, i.e. it needs to be examined whether one class ("fulfilling the stability margin" / "not fulfilling the stability margin") is significantly over-represented compared to the other. If this is the case, three options exist: (a) limiting the number of the over-represented class by neglecting the appropriate amount of samples, (b) over-sampling the minority class or (c) raising the cost of misclassifying the minority class. While option (a) might leave out exactly the most important information close to the stability boundary, (b) degrades the learning speed due to duplicate instances. Option (c) allows to introduce risk-aversion, which might lead to more conservative and less cost-efficient transfer limits. This however, can be improved through smaller step sizes during the analysis described in section 5.3.

The DT is trained on a subset of the whole database, called training set A, as introduced in 2.5.4. The derived rules are tested using another subset B of the database with $A \cup B = \emptyset$. As the DT using cross entropy as splitting criteria achieved higher accuracies in our study, we continued

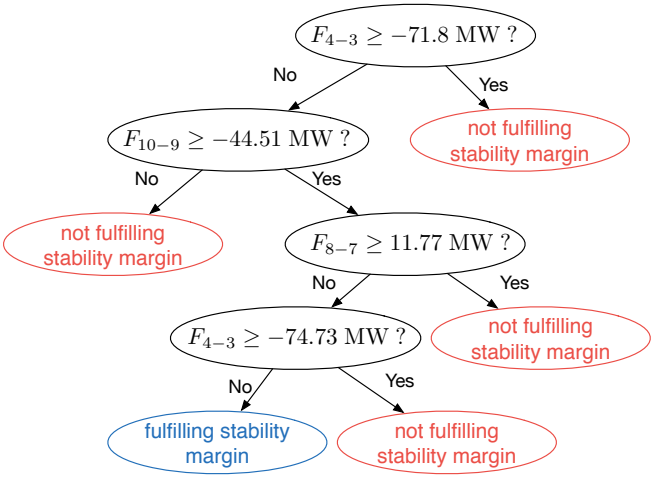

Figure 6.2: A simple example of a decision tree. Source: [**Pub. E**].

working with that DT.

It is worth mentioning that although DTs achieve pretty high accuracies, there will always be misclassifications, which in theory could cause unstable solutions of the proposed data-driven SC-OPF. However, actions have been taken to minimize, if not completely avoid this threat. First, by increasing the cost for misclassifications of unstable cases (see section 2.5.1), we reduce the misclassifications in this direction. This, however, might also cause less cost-efficient line flow limits. Further, by choosing a certain stability margin and differentiating between "fulfilling the stability margin" and "not fulfilling the stability margin", instead of "stable" and "unstable", we can reduce the risk even further, since misclassifications do not necessarily lead to instability, but just to lower stability margins than required - at least in all scenarios tested in this work. This is discussed in more detail in section 6.4.5.

Finally, in order to avoid over-fitting, the obtained trees need to be pruned appropriately. This work applies a manual approach of pruning specific nodes according to test results using the OPF.

6.4.4 OPF Implementation

The network is modeled using a linear DC approximation as it is usually done in market applications.

Standard DC Optimal Power Flow (DC-OPF)

The objective function to be minimized represents the total generation cost (6.5). The optimization problem is formulated as follows:

$$\min_{\mathbf{P_G}} \sum_{i=1}^{N_G} c_{G,i} P_{G,i}, \tag{6.5}$$

$$\text{s.t.} \sum_{i=1}^{N_G} P_{G,i} - \sum_{n=1}^{N_B} P_{D,n} = 0, \tag{6.6}$$

$$-\mathbf{F_L^{max}} \leq \mathbf{PTDF} \cdot \left(\mathbf{P_G} - \mathbf{P_D}\right) \leq \mathbf{F_L^{max}} \tag{6.7}$$

$$\mathbf{0} \leq \mathbf{P_G} \leq \mathbf{P_G^{max}}, \tag{6.8}$$

where symbols in bold denote matrices or vectors. N_G and N_B refers to the number of generators and buses, respectively. Equality constraint (6.6) ensures balance between total generation and total demand. Demand $\mathbf{P_D}$ is assumed to be inelastic and thus, not a decision variable. Power Transfer Distribution Factors (PTDFs) are used to translate net injections into line flows, which are constrained to their line flow limits $F_{L,i}^{max}$ in Eq. (6.7). Equation (6.8) constrains the generator outputs below capacity limits.

Security Constrained OPF (SC-OPF)

The SC-OPF ensuring N-1 security and small signal stability extends the standard DC-OPF by including additional constraints representing *conditional line transfer limits*, derived from the decision tree in section 6.4.3. The DT is incorporated into the optimization using MILP. Each full

path p from the root to a leaf node is represented by a set of minimum and maximum line transfer limits $\mathbf{F^{min}_{L,p}}$ and $\mathbf{F^{max}_{L,p}}$, respectively. Equation (6.7) is replaced by:

$$\mathbf{PTDF} \cdot \left(\mathbf{P_G} - \mathbf{P_D}\right) \leq \mathbf{F^{max}_{L,p}} y_p + \mathbf{F^{max}_{L}}(1 - y_p) \quad \forall p \in P \tag{6.9}$$

$$\mathbf{PTDF} \cdot \left(\mathbf{P_G} - \mathbf{P_D}\right) \geq \mathbf{F^{min}_{L,p}} y_p - \mathbf{F^{max}_{L}}(1 - y_p) \quad \forall p \in \mathcal{P}, \tag{6.10}$$

where $\mathcal{P}$ is the set of full paths representing the decision tree. Note that the conditional line transfer limits do not limit the flows symmetrically as in Eq. (6.7), i.e. the lower bound does not necessarily correspond to the negative upper bound. Each path is associated with a binary variable y_p, which, if chosen, ensures the activation of the corresponding conditional line flow limits or otherwise, leaves the usual line flow limits unchanged. The number of binary variables corresponds to the number of leaf nodes in the DT. The choice of line limits to one path only is constrained through $\sum_p y_p = 1$.

Matching of SC-OPF and Database

In contrast to the operating points saved in the database, losses are not inherently considered in the standard DC-OPF or SC-OPF described above. Thus, the operating points resulting from the OPFs need to be matched with the ones saved in the database by incorporating losses. Due to the fact that the optimal power flow is not known prior to delivering the line flow limits and the line flows and losses vary depending on the generation pattern, an initial best guess of the optimal operating point is crucial to achieve a good matching. By searching the database for the cheapest operating point (assuming that costs are known a priori), which fulfills the stability margin and meets the load level, we found a "best guess" operating point, whose losses were incorporated in the standard DC-OPF and the SC-OPF according to (6.4). The losses of the "best guess" OP are determined through an ac power flow analysis. The DC-OPF and SC-OPF are thus augmented by a loss approximation and yield more realistic results.

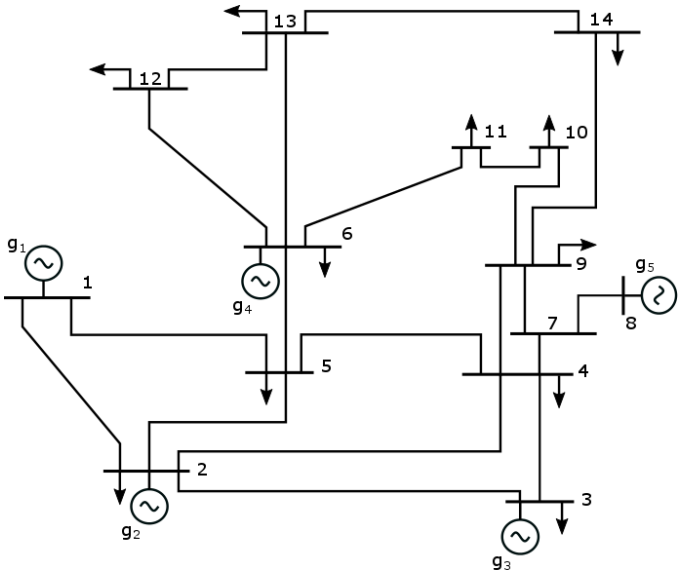

Figure 6.3: IEEE 14 Bus System. Source: [11].

Table 6.1: Results of standard DC-OPF and data-driven SC-OPF using different mapping approaches. Source: [**Pub. E**].

	DC-OPF (w. losses)	Best Guess (Data Based)	SC-OPF (clas. DC)		SC-OPF (less con. DC)		SC-OPF (exact)	
Dispatch (MW)			1. Run	2. Run	1. Run	2. Run	1. Run	2. Run
g_1	275.5509	183.73	165.962	165.262	176.535	176.297	184.106	184.127
g_2	0	55	60	60	60	60	60	60
g_3	0	27.5	26.603	26.671	22.51	22.616	24.628	24.906
g_4	0	2.5	16.17	15.687	9.689	9.582	0	0
g_5	0	0	0	0	0	0	0	0
Total Cost (€)	2755.5	2981.1	3091.63	3077.21	3022.56	3019.9	2960.48	2964.87
Min. damping ratio (%)	-20.33%	4.07%	9.73%	9.59%	6.59%	6.57%	2.98%	3.05%
Cost of Security (€)	-	225.59	336.12	321.7	267.05	264.39	204.97	209.36

6.4.5 Case Study

The proposed method ensuring small signal stability and N-1 security is applied to the IEEE 14 bus test system shown in Fig. 6.3. All parameters are given in the appendix.

The small signal multi-machine model used in this work is described in section 2.7.1, neglecting, however, the Power System Stabilizers (PSSs) at every generator. It is worth emphasizing that the methodology is independent of the model and can be used with any model with any level of detail. The small signal models were derived using Mathematica, the initialization and small signal analysis were carried out using Matlab and Matpower 6.0 [49]. All DC-OPF simulations were carried out in Python using the Gurobi Optimizer [174].

A minimum damping ratio of 3% is chosen as stability margin. We chose to require the same minimum damping ratio also for the steady states obtained after an outage of a single element during the N-1 security analysis. However, this could also be chosen differently by e.g. allowing lower damping ratios after certain faults.

The system has been simulated for several load levels ($\pm 20\%$) and various step sizes between the generation patterns. Generator g_1 has been chosen as the slack bus, also in all N-1 scenarios, due to the small size of the other generators. Since the IEEE 14 Bus system is not N-1 stable, a few contingencies and reactive power limits could not be considered for the N-1 security assessment. All line faults have been considered except for a fault on the line connecting bus 1 and bus 2. All bus faults have been analyzed, except for a fault at bus 1 and bus 2. These contingencies could not be considered because either they lead to instability / violation of the AVR limits for any operating point of the considered load patterns (bus 1) or the stable operating points are not stable for the remaining contingencies. Hence, this would leave us with an empty set of feasible operating points and therefore we had to neglect these contingencies.

First, we will compare the results of the novel data driven SC-OPF, when using different features for mapping the operating points of ac and dc power flows. Then, we will investigate the impact of various step sizes between the generation patterns on the results of the data-driven SC-OPF, i.e. different accuracies and database sizes. Finally, we will discuss additional benefits of data-driven approaches.

Comparison between Standard DC-OPF and Data-driven SC-OPF using different Mapping Approaches

The comparison between the data-driven SC-OPFs using different mapping approaches is done using a $2.5\,\mathrm{MW}$ step size during the data generation. Table 6.1 lists the results of both the standard

DC-OPF and the SC-OPF using different features of the database, in particular the three different mapping approaches described in section 6.4.3. Additionally, the database best guess operating point is listed, which is used for determining the losses to be incorporated in the OPFs.

Table 6.1 shows that the standard DC-OPF fails to ensure N-1 security, since for this generation pattern the most critical pair of eigenvalues of the most critical fault in the N-1 security assessment (Fault at Bus 5) indicates a negative damping ratio, i.e. instability. The most critical eigenvalues of those faults in the N-1 security assessment violating the minimum required stability margin of 3% are shown in Fig. 6.4. It shows that all SC-OPFs ensure N-1 security of the system by a change of the generation pattern resulting in the most critical eigenvalues of the same faults being moved into the left half-plane, i.e. in the safe area with a minimum damping ratio larger than the required stability margin.

The figure illustrates also that the operating points obtained by the SC-OPFs using different mapping approaches vary by their minimum damping ratio, which reflects the more conservative line flow limits in case of both dc approximations compared with the exact mapping approach. These more conservative line flow limits lead consequently also to higher cost of security, as indicated in Tab. 6.1.

Finally, Tab. 6.1 indicates also the importance of the matching of operating points, i.e. the importance of the best guess of power flow. While in the 1^{st} run of the SC-OPFs the losses are implemented according to the data based best guess, the 2^{nd} run uses the result of the 1^{st} run as initial best guess. In this case, the loss distribution and therefore the line flows are more accurate, i.e. more comparable to dc power flows obtained in the data generation. Thus, the matching of operating points is improved which leads to better results in all cases.

Comparison of different Step Sizes between the analyzed Generation Patterns

Various aspects and results for the database generation of a SC-OPF comparing different step sizes used during data generation are shown in Tab. 6.2.

Obviously, following the simple brute force approach with constant step size between each analyzed generation pattern the database size grows as indicated in Eq. (5.1). However, as discussed in section 5.3 there exist improvement potential which we leveraged in the development of the efficient database generation method presented in chapter 5. Further, the required simulation time is related to the database size. It naturally increases with the number of operating points. The database was generated using 20 cores in parallel on the high performance computing farm at DTU.

The tree accuracy is also related to the available database size. In general, it should be easier to differentiate between the case fulfilling the stability margin and not fulfilling the stability margin if there is a higher step size in between the analyzed generation patterns. This is reflected in Tab. 6.2 by the decreasing number of false prediction with risk with increasing step size. False predictions with risk are those predictions which falsely predict operating points not fulfilling the stability margin as "fulfilling the stability margin". The results show that the chosen risk averse approach, discussed in section 6.4.3, which increases the costs of this kind of false predictions, works fine since the vast majority of false predictions is made in the other direction. This is indicated by the small percentage of these kind of false predictions within the total number of false predictions.

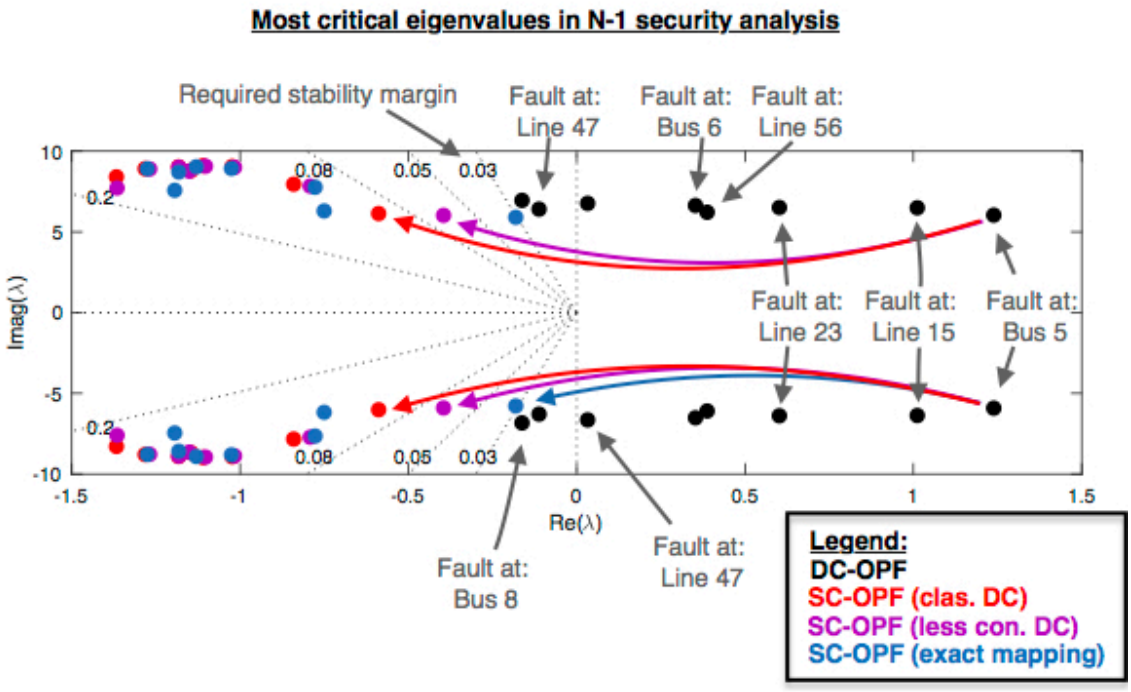

Figure 6.4: Visualization of the location of the most critical eigenvalues in the N-1 security analysis for the DC-OPF (black), SC-OPF using the classical dc approximation approach (red), SC-OPF using the less conservative dc approximation approach (purple) and SC-OPF using the exact mapping approach. The faults corresponding to the critical eigenvalues are denoted in grey. The small signal models resembling the faults differ by the base case in that way that they consider the disconnection of the corresponding elements. Any contingency not violating the stability margin requirement of 3% is neglected. Source: [**Pub. E**].

However, on the other hand there exists also less data for training which may decrease the tree accuracy as indicated in Tab. 6.2. This also leads to potentially shorter trees represented by a smaller number of binary variables and a faster execution time, shown in Tab. 6.3.

Table 6.2 supports also the discussion in section 5.3 about the importance of the step size, in

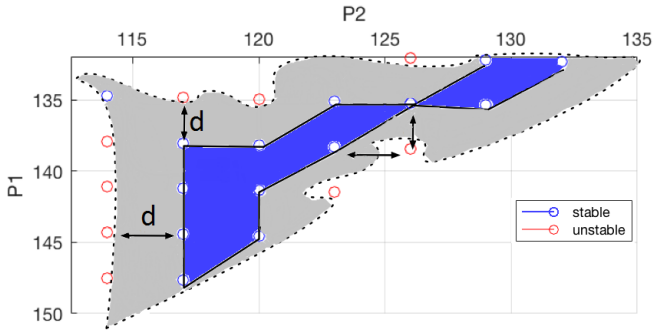

Figure 6.5: Step size (d) of simulation needs to be chosen in a way that the area of stable operating points (purple) is maximized while the area of uncertain/potentially stable operating points (grey) which lies between stable (blue) and unstable (red) operating points is minimized. Source: [**Pub. E**].

Table 6.2: Database Analysis for different Step Sizes. Source: [**Pub. E**].

step size	1 MW	2.5 MW	5 MW
# operating points, Ψ	2515396	75625	6084
Simulation time	8.17 h	15.11 min	1.29 min
Training set			
Tree accuracy	99.86%	99.77%	98.9%
False prediction w. risk	55	1	0
% of false pred.	1.54%	0.57%	0
Min. damp. ratio of risky false pred.	2.89%	2.76%	-
Using database of other step sizes as test set			
Tree accuracy	99.79%	99.03%	97.64%
False prediction w. risk	36	9111	13298
% of false pred.	23.08%	37.34%	22.44%
Min. damp. ratio of risky false pred.	2.73%	1.37%	0.82%

particular close to the boundary. This is reflected by the significantly increasing number of risky false predictions with increasing step size when the DTs are tested with the database of the other step sizes. Here, the DTs of $2.5\,\mathrm{MW}$ and $5\,\mathrm{MW}$ are tested on the $1\,\mathrm{MW}$ database while the $1\,\mathrm{MW}$ DT is tested on the $2.5\,\mathrm{MW}$ database. It is shown that a wider step size in between the generation patterns leads to potentially more and unsafer risky false predictions, as indicated by the increasing number of false predictions with risk and the decreasing minimum damping ratio of those false predictions.

However, the tree accuracy should not be confused with the cost efficiency of the line flow limits resembled by the generation costs. All SC-OPFs with the different step sizes lead to points fulfilling the required stability margin. Here, we used two runs using the 1^{st} run as initialization for the 2^{nd} run as described in the previous subsection.

Table 6.3 shows that in fact the SC-OPF using the widest step size leads to the cheapest operating point. This is due to the wider uncertain area in between the analyzed operating points (as visualized in Fig. 6.5) resulting in more relaxed line flow limits. However, the difference is very small (max. 6.2€). It is important to emphasize that, although the widest step size achieves the best performance in this particular scenario, smaller step sizes are safer as discussed before and indicated in Tab. 6.2.

Comparison with Available Transfer Capacity and Flow-Based Market Coupling

As already aforementioned and shown again in Tab. 6.4, a DC-OPF (with losses) leads to an operating point which is not N-1 stable. Thus, redispatching would be necessary if a secure operation of the power system is desired. Here, we compare the proposed SC-OPF with two other approaches used to include security into the market clearing.

First, we compare the proposed SC-OPF to a DC-OPF considering losses and using ATCs. In order to compare the proposed method with current approaches, it is assumed that there is no capacity reserved for already accepted transfer contracts, thus the Net Transfer Capacities (NTCs) equal the ATCs. Different ATCs ensuring a damping ratio of 3% have been tested and the least conservative

Table 6.3: Data-driven SC-OPF Results for different Step Sizes. Source: [**Pub. E**].

Data-driven SC-OPF			
step size	1 MW	2.5 MW	5 MW
Bin. var.	616	35	28
Exec. time	26.64s	1.08s	0.98s
Generation cost	2965.4€/h	2964.9€/h	2959.2€/h
Minimum margin	3.03%	3.05%	3.42%
Generation (MW)			
g_1	187	193.50	183.3213
g_2	60	42.72	58.0360
g_3	18.7	24.73	27.46
g_4	3.7	0	0
g_5	0	0	0

and cheapest results have been obtained for a single limit of $37.09\,\mathrm{MW}$ for the line connecting bus 2 and 3. It still leads to a comparably conservative and expensive operating point far away from the minimum required damping ratio. The proposed SC-OPF clearly outperforms the classical ATC approach.

Second, we compare the proposed SC-OPF to an approach where we determined the convex hull of the operating points with the minimum required damping ratio and derived linear constraints from the convex hull implementing them into a DC-OPF considering losses. This, can be seen as a very detailed version of the flow-based market coupling where only tie-lines and critical lines are considered. Nevertheless, the results indicate that this approach also leads to more conservative limits and higher costs than the proposed SC-OPF.

Thus, the enlargement of the feasible space, which will be discussed in more detail in section 6.5.2, allows to create less conservative limits and leads to a more cost efficient market clearing.

Additional Benefit of the Data-driven Approach

Besides the possibility to deliver cost-efficient line flow limits the data-driven approach provides the additional benefit of serving as an easy accessible source of knowledge for the TSO which could be useful during normal operation but in particular during training of new employees.

Table 6.4: Comparison of data-driven SC-OPF with standard DC-OPF, ATC limits and convex limits extracted from the database representing flow-based market coupling

	DC-OPF (w. losses)	ATC limits	Convex limits	SC-OPF (exact)
Dispatch (MW)				2. Run
g_1	275.5509	202.249	187.54	184.127
g_2	0	0	59.76	60
g_3	0	60	17.30	24.906
g_4	0	5.58	4.84	0
g_5	0	0	0	0
Total Cost (€)	2755.5	3020.1	2966.7	2964.87
Min. damping ratio (%)	-20.33%	7.15%	5.55%	3.05%
Cost of Security (€)	-	264.64	211.16	209.36

First, similar as visualized in Fig. 6.4, the database enables the user to get an overview which faults are the most critical for any operation point. Unlike for the specific generation pattern provided by the DC-OPF this may only be a single fault.

Second, the use of a DT instead of other knowledge extraction methods provides the user with additional knowledge about safe and unsafe line flows in the system which is easily to comprehend by human operators. By just visualizing the tree as e.g. in Fig. 6.2 the user is able to access this valuable comprehensive information, which would not be possible by most other knowledge extraction methods, such as Artificial Neuro Networks (ANNs), which work mostly like a black-box from the outside.

6.4.6 Discussion

A novel data-driven SC-OPF method ensuring small-signal stability has been proposed. It uses a small-signal model for data generation, and classification trees for the knowledge extraction. Conditional transfer limits in the form of decision rules are derived from the decision tree and implemented in the OPF problem by means of MILP. We investigated the impact of different features for the mapping of operating points from the ac to the dc space and emphasized specific aspects of this method, e.g. the importance of matching the operating points. Additionally, we discussed the challenges of this method, such as the problems arising when using a wide step size (in particular at the stability boundary). Finally, we emphasized the additional benefits of the data-driven approach as it serves as a source of knowledge of the system. The case study indicates a good performance.

6.5 Data-driven Small-Signal Stability and Preventive Security Constrained AC-OPF

This section describes the work published in [**Pub. F**] extending the work described in the previous section to an AC-OPF. Thus, it aims to bridge the gap between power system operation and markets. Using simulation data, we extract knowledge on system security using DTs and incorporate it into the AC-OPF using MIP. Furthermore, we relax the non-convex AC power flow equations with a Second Order Cone (SOC) relaxation and strengthen the relaxation using data. To our knowledge, this is the first SC-OPF formulated as a Mixed-Integer Second Order Cone Program (MISOCP) combining the advantages of convex MIP and data analytics. Besides allowing for a fast online solution, this method extends the feasible space reflecting the non-convexity area of operation and includes the true optimal solution.

Thus, the main contribution of this work is a data-driven small signal stability and preventive security constrained AC-OPF (SSSPS-AC-OPF) algorithm formulated as a MISOCP. This method incorporates the N-1 security criterion, small signal stability for the base case and all N-1 contingencies. It is scalable, can be solved fast as all security considerations are computed offline, and exploits the maturity of convex MIP solvers allowing to identify the optimal operating point within a non-convex and possibly disjoint stability area. Potential users of this tool are:

- system operators using it as a security analysis tool for e.g. redispatch
- market operators aiming for optimal solutions considering security evaluations.

The main advantage of this approach is that it can be solved to global optimality where tested non-convex solvers fail and it mitigates the need for iterative contingency analyses currently used by system operators.

6.5.1 Methodology

This methodology is similar to the one described in the previous section (6.4.1) in the sense that it consists of an offline security assessment, which includes the database generation and derivation of decision rules, and an online SC-OPF, which incorporates the decision rules ensuring power system security.

Preventive SC-AC-OPF - Current Practice

The traditional preventive SC-OPF (PSC-OPF) aims at finding the optimal least-cost dispatch ensuring N-1 security. It extends the conventional nonlinear and non-convex AC-OPF by including additional constraints to ensure feasibility of the identified solution after the occurrence of any specified contingency. The AC-OPF is given as follows:

$$\min_{\mathbf{x}} \sum_{i=1}^{N_G} C_i\Big(P_i^G\Big), \tag{6.11}$$

$$\text{s.t. } P_i^G - P_i^D = G_{ii}V_i^2 + \sum_{j=1,j\neq i}^{N_B} V_iV_j\Big(G_{ij}\cos(\theta_{ij}) + B_{ij}\sin(\theta_{ij})\Big), \qquad \forall i \in \mathcal{N} \tag{6.12}$$

$$Q_i^G - Q_i^D = -B_{ii}V_i^2 + \sum_{j=1,j\neq i}^{N_B} V_iV_j\Big(G_{ij}\sin(\theta_{ij}) - B_{ij}\cos(\theta_{ij})\Big), \qquad \forall i \in \mathcal{N}, \tag{6.13}$$

$$\underline{\mathbf{x}} \leq \mathbf{x} \leq \overline{\mathbf{x}}, \tag{6.14}$$

$$\theta_{\text{ref}} = 0, \tag{6.15}$$

where $\mathbf{x}$ represents the set of optimization variables including active power generation $\mathbf{P^G}$, reactive power generation $\mathbf{Q^G}$, voltage magnitudes $\mathbf{V}$ and voltage angles θ. $\mathcal{N}$ denotes the set of buses. The objective function (6.11) minimizes active power generation costs. Constraints (6.12) and (6.13) ensure active and reactive power balance at all nodes, where G_{ij} and B_{ij} represent the real and imaginary parts of the bus admittance matrix, respectively. Constraint (6.14) limits all decision variables within their upper and lower bounds. Equation (6.15) sets the voltage angle of the reference bus to zero. Line flow limits are not explicitly included here, as we derive limits from the security analysis, which will be introduced later.

Control variables (e.g., active and reactive power generation, transformer tap position etc.) in the PSC-OPF are not allowed to change from pre- to post-contingency states. The problem size of the OPF increases to $\Gamma + 1$ compared to the conventional AC-OPF, where Γ denotes the number of contingencies, rendering SC-OPFs computationally very demanding. The computational burden of SC-OPFs, especially for large systems with many considered contingencies, is a major challenge.

Another challenging factor is the inclusion of system dynamics, i.e. stability considerations, in SC-OPF algorithms. Given that they cannot be incorporated as linear or nonlinear constraints in a straightforward way, common practice is to impose tighter constraints. Such conservative bounds on the feasible space should allow the system to return to a steady-state equilibrium after a fault event, but also lead to costly and suboptimal solutions.

NTC constitute one example of such conservatism (see section 2.4). NTCs are fixed line flow limits, which are determined by TSOs in each direction of cross-border lines prior to the day-ahead

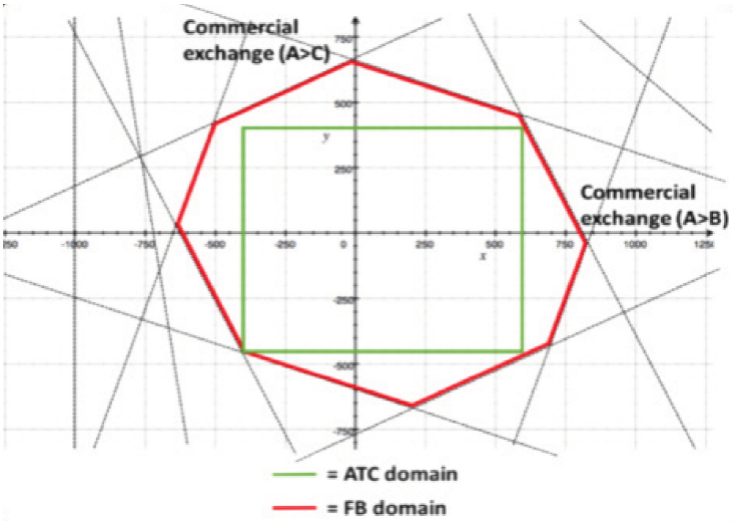

Figure 6.6: Security domain of Flow-Based Market Coupling (FBMC) and Available Transfer Capacity (ATC) [12]. ATCs are NTCs reduced by long-term capacity nominations. Source: [**Pub. F**].

market-clearing. Improvements towards a more accurate representation of the physical reality of power systems have been achieved by introducing FBMC, where a simplified European network representation is accounted for in the market-clearing. Critical branches (CBs) inside and between zones are identified, which could potentially be congested and limit the cross-border trade. All CBs are represented through PTDF and instead of assuming only one fixed NTC value for each cross-border line, all constraints imposed by the CBs are considered. Thus, a larger secure domain is offered to the market compared to static NTC approaches as depicted in Fig. 6.6. The market is then able to determine the optimal combination of commercial capacities between zones. Nonetheless, even flow based NTCs only capture one convex region of the entire feasible space and do not represent the non-convex reality of power system operations.

Improving the Preventive SC-AC-OPF Using Data

To address the challenges described above, we propose a data-driven approach to SC-AC-OPFs.

Database Generation As shown in chapter 5, the IEEE 14 bus system is small enough to create a database using a classical brute force approach as database generation method. Here, we report on results from [**Pub. F**] which preceded the development of the method we proposed in chapter 5 and for this reason the brute force approach is used. In order to achieve more detailed results we enriched the database with additional points close to the security boundary by running an additional run of the brute force approach with an discretization interval/step size of $0.5\,\mathrm{MW}$ focusing on the region close to the security boundary. However, as we discussed in 5.4, this approach proposed by Genc et al. in [142] requires additional computation to enrich the previously generated database with important scenarios close to the security boundary. Thus, this work strengthened our motivation to develop the advanced method for an efficient database generation that we reported in chapter 5. And as shown in chapter 5, we can generate an equally high-quality database in significant less time with the method we proposed in chapter 5.

Feature Selection and Knowledge Extraction As this work deals with an AC-OPF, the feature selection process from the previous section needs to be adapted.

Compared with the previous work, here we need to consider that the security considerations as well as the OPF are located in the AC space, i.e. we do not need a mapping from one space into the other. Thus, based on the lessons learned from the previous section, we use voltage angle differences $\theta_{ij} = \theta_i - \theta_j$ along transmission lines as features to determine the security boundary.

As knowledge extraction method, this work continues to use decision trees which are trained with cross entropy as splitting criteria. We apply a manual approach of pruning specific nodes according to test results using the OPF.

Thus, each branch p of the DT contains a set of minimum and maximum voltage angle differences and leads to a different region of the feasibility space, one of which contains the least-cost, optimal solution. A visual illustration of our approach is depicted in Fig. 6.7. Instead of defining bounds that contain only one of the three stable regions depicted in the shades of blue, conditional rules allow to capture the entire feasible region within the red frame.

OPF Implementation The DT is incorporated in the SC-OPF using Mixed-Integer Programming (MIP). Each full branch is associated with a binary variable y_p, which if chosen, activates the corresponding upper and lower bounds on angle differences, or otherwise, leaves the original bounds unchanged:

$$y_p \cdot \underline{\theta_{ij,p}} - (1 - y_p) \cdot \overline{\theta_{ij}} \leq \theta_{ij} \leq y_p \cdot \overline{\theta_{ij,p}} + (1 - y_p) \cdot \overline{\theta_{ij}}, \quad \forall (i,j) \in \mathcal{L}, \forall p \in \mathcal{P}. \tag{6.16}$$

$\mathcal{L}$ and $\mathcal{P}$ denote the set of lines and DT branches/paths, respectively. Only one DT branch, i.e. one set of minimum and maximum bounds on angle differences, can be chosen, which is imposed by adding constraint $\sum_{p \in \mathcal{P}} y_p = 1$.

The data-driven SC-OPF is thus formulated as a Mixed-Integer Non-linear Program (MINLP), which is a NP-hard problem. One of the main contributions of in this section is that we relax the non-convex AC power flow equations using a Second Order Cone relaxation and obtain a SC-OPF formulated as a Mixed-Integer Second Order Cone Program (MISOCP), which is a convex mixed-integer program that can be solved efficiently by already existing solvers.

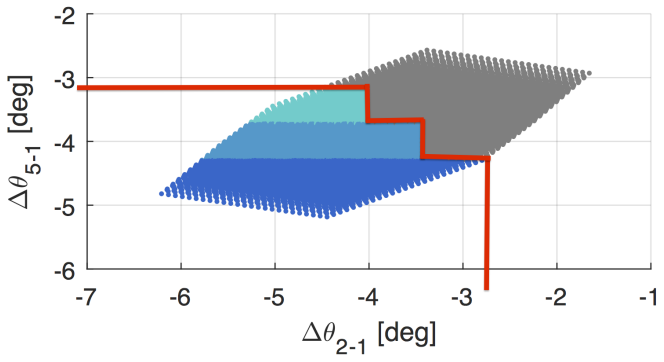

Figure 6.7: Illustrative example of non-convex space. Source: **[Pub. F]**.

Relaxing the Data-driven SC-OPF

The SOC formulation of the OPF problem is based on [175], [176] and [177]. New variables are introduced to capture the nonlinearities and non-convexities of the AC power flow equations: (a) $u_i := V_i^2$, (b) $c_{ij} := V_i V_j \cos(\theta_{ij})$ and (c) $s_{ij} := -V_i V_j \sin(\theta_{ij})$. The AC-OPF is transformed from the space of $\mathbf{x} := \{\mathbf{P^G}, \mathbf{Q^G}, \mathbf{V}, \theta\}$ variables to the space of $\mathbf{x_{SOC}} := \{\mathbf{P^G}, \mathbf{Q^G}, \mathbf{u}, \mathbf{c}, \mathbf{s}\}$ variables and is given by:

$$\min_{\mathbf{x_{SOC}}} \sum_{i=1}^{N_G} C_i\Big(P_i^G\Big) \tag{6.17}$$

$$\text{s.t. } P_i^G - P_i^D = G_{ii}u_i + \sum_{j=1, j\neq i}^{N_B} \Big(G_{ij}c_{ij} - B_{ij}s_{ij}\Big), \qquad \forall i \in \mathcal{N} \tag{6.18}$$

$$Q_i^G - Q_i^D = -B_{ii}u_i - \sum_{j=1, j\neq i}^{N_B} \Big(G_{ij}s_{ij} + B_{ij}c_{ij}\Big), \qquad \forall i \in \mathcal{N} \tag{6.19}$$

$$c_{ij} = c_{ji}, \quad s_{ij} = -s_{ji}, \qquad \forall (i,j) \in \mathcal{L} \tag{6.20}$$

$$c_{ij}^2 + s_{ij}^2 = u_i u_j, \qquad \forall (i,j) \in \mathcal{L} \tag{6.21}$$

$$\underline{V_i}^2 \leq u_i \leq \overline{V_i}^2, \qquad \forall i \in \mathcal{N}. \tag{6.22}$$

Active and reactive power generation are constrained by their usual limits and are not explicitly mentioned. The non-convex quadratic equality constraint (6.21) is relaxed through a second-order cone constraint: $c_{ij}^2 + s_{ij}^2 \leq u_i u_j$. The SOC formulation of the OPF problem (6.17)-(6.22) is exact for radial networks and the optimal voltage angles can be recovered by solving:

$$\theta_i - \theta_j = \text{atan2}(s_{ji}^*, c_{ij}^*), \quad \forall (i,j) \in \mathcal{L}, \tag{6.23}$$

where * indicates the optimal solution obtained from the SOC-OPF. For meshed networks the above formulation is a strict relaxation, potentially resulting in solutions, which are infeasible for the original AC-OPF [177]. Reintroducing voltage angle variables and constraint (6.23) in problem (6.17)-(6.22) would render the SOC formulation exact for meshed networks, but also non-convex. Various convex approximations of constraint (6.23) have been proposed [177], [175]. In this work we use a sequential conic procedure as proposed in [175], where the arctan function is linearized using a Taylor series expansion.

Conditional bounds on voltage angles are introduced using binary variables as described in section 6.5.1. Known limits on angle differences can also be used to define bounds on the SOC variables $\mathbf{c}$ and $\mathbf{s}$:

$$y_p \cdot \tan(\underline{\theta_{ij,p}}) \cdot c_{ij} - (1 - y_p) \cdot \tan(\overline{\theta_{ij}}) \cdot c_{ij} \leq s_{ji}, \qquad \forall (i,j) \in \mathcal{L}, \forall p \in \mathcal{P}, \tag{6.24}$$

$$y_p \cdot \tan(\overline{\theta_{ij,p}}) \cdot c_{ij} + (1 - y_p) \cdot \tan(\overline{\theta_{ij}}) \cdot c_{ij} \geq s_{ji}, \qquad \forall (i,j) \in \mathcal{L}, \forall p \in \mathcal{P}. \tag{6.25}$$

Otherwise, the SOC variables c_{ij} and s_{ij} are only constrained by their implied upper and lower bounds $\overline{V_i V_j}$ and $-\overline{V_i V_j}$, respectively, which in practice can be very loose. In order to tighten the relaxation, we determine minimum and maximum values of c_{ij} and s_{ij} along all lines (i, j) using the information from the generated database of operating points.

6.5.2 Case Study

We evaluate the performance of the proposed data-driven SC-OPF ensuring small-signal stability and N-1 security on a modified version of the IEEE 14 bus test system [11]. Our case study consists of three parts. First, we compare the convex MISOCP formulation of the algorithm to a data-driven MINLP implementation and a standard (i.e., not data-driven) preventive SC-OPF. Its low computational effort makes the proposed MISOCP suitable for AC based market-clearing auctions as envisaged in the US. In Europe, however, electricity markets will probably continue to rely on DC approximations. To this end, we show how the proposed method can also be used by TSOs for optimizing redispatching actions in order to ensure N-1 security and small-signal stability after the market-clearing. Finally, we analyze how the data-driven approach coupled with MIP notably extends the feasible space of the OPF.

The network data is given in [178] with some modifications introduced in **[Pub. E]**. Note that additionally the voltage setpoints of generators 4 and 5 are changed to 1.02 p.u. and 1.01 p.u., respectively, and the reactive power of generator 1 is limited within ± 990 Mvar. The considered contingencies include the same as in the previous section (all except Bus 1 and 2, line 1-2). Additionally, a fault at Bus 6 is neglected because compared to the previous work the voltage limits after a contingency are tightened ($0.94\,\text{p.u.} \leq V_i \leq 1.06\,\text{p.u.},\ \forall\, i \in \mathcal{N}$). Note that the standard PSC-OPF does not incorporate stability considerations, but only extends the constraint set to account for the defined N-1 contingencies. Bus 1 with generator g_1 has been chosen as the slack bus for the base case and all N-1 cases. A step size of $0.5\,\text{MW}$ was chosen for discretizing the possible operating range and generating the database of operating points used for deriving the decision tree. The minimum damping ratio of an operating point over the base case and all N-1 cases is used as a metric for small-signal stability. As usual in power system operation, we define a security margin by requiring a minimum damping ratio of $3\,\%$. The derived DT contains 136 leaf nodes, out of which 74 point to operating regions, which are small-signal stable for the base case and all considered contingencies. Thus, 74 binary variables are used to define conditional constraints on voltage angle differences along lines and incorporate the stable regions in the data-driven SC-OPF. Note that 1.34 million operating points have been evaluated for this case study, from which more than 88 000 fulfill the required minimum damping ratio. Three different load levels (base case, $\pm 20\%$) have been considered. The voltage magnitude at generator buses is set to the corresponding generator voltage setpoint in order to ensure an appropriate voltage profile, which is fundamental to a secure system operation. The small-signal analysis was performed using Matlab and Matpower 6.0 [49]. The data-driven SC-OPF based on MISOCP was implemented in Python using the Gurobi Optimizer. The standard preventive SC-OPF (i.e., NLP) and the MINLP implementation of the data-driven SC-OPF were carried out in GAMS. The open-source solvers BONMIN and COUENNE were used for the MINLPs, while CONOPT was used for the NLP.

Comparison of Preventive and Data-driven SC-OPFs

Table 6.5 lists the results of all three SC-OPF implementations. It can be observed that all implementations based on decision trees result in operating points, which exhibit minimum

Table 6.5: Results of standard PSC-OPF and data-driven SC-OPF implemented as MINLP and MISOCP. Adapted from: [**Pub. F**].

		Standard PSC-OPF		**Data-driven SC-OPF**					
		NLP		**MINLP**				**MISOCP**	
				COUENNE		BONMIN			
Cost	(€/h)	3022.83		3445.09		3381.21		3365.95	
Runtime	(s)	10.06		1000.16		96.16		5.58	
Iterations	(-)	-		-		-		4	
Min. damping ratio	(%)	unstable		3.27		2.97		2.53	
Leaf node	(-)	-		31		133		104	
Dispatch		**P** (MW)	**Q** (Mvar)	**P** (MW)	**Q** (Mvar)	**P** (MW)	**Q** (Mvar)	**P** (MW)	**Q** (Mvar)
	g_1	168.20	5.30	106.86	16.37	108.15	16.76	109.89	16.44
	g_2	60.00	50.00	52.19	38.08	60.00	37.55	60.00	37.97
	g_3	39.39	21.51	60.00	10.93	60.00	11.65	60.00	11.79
	g_4	0	6.91	25.00	0.40	25.00	0.74	25.00	0.82
	g_5	0	4.81	19.33	3.72	10.61	4.01	8.98	4.09

damping ratios that are non-negative and are thus stable for the base case and all considered N-1 contingencies. The solution of the standard PSC-OPF however is unstable for a fault at bus 5 and line 1-2, respectively. Thus, the identified preventive control actions do not fullfill the system's security requirements and would call for redispatching measures. As the PSC-OPF results in an operating point, which does not reflect the small-signal stability requirements, its total cost is lower than the other solutions.

All three data-driven implementations result in different leaf nodes of the DT and thus in different regions of the feasible space with various degrees of conservatism. Higher damping ratios are also reflected by higher costs. All solutions include a stability margin, but only the most conservative result achieves a minimum damping ratio of more than $3\,\%$. This can be explained by the fact that (a) the OPF is not limited to the specified discretization intervals of $0.5\,\mathrm{MW}$, as used for the database generation and (b) DTs are not $100\,\%$ accurate leading to missclassifications. For cases, where the minimum damping ratio is a hard constraint, higher values can be required when deriving the DT in order to avoid violations. Fig. 6.8 illustrates the stable domain covered by all DT leaf nodes as a function of the angle differences along lines 1 and 2. The rectangles indicate the domains covered by the three different leaf nodes obtained from the data-driven SC-OPF implementations with the location of the corresponding solution pointed out. It can be seen that the stable domain is non-convex and that safer operating points exhibiting higher damping ratios are located further away from the stability boundary.

The known scalability issues of COUENNE [179], which is a global optimization solver, lead to significantly higher execution times compared to BONMIN, which employs heurisitic methods for non-convex MINLPs. Also, the default settings for both solvers include a relative tolerance gap of $10\,\%$ terminating the computation as soon as a solution is found, which lies within $10\,\%$ of the true objective value. This explains the choice of different leaf nodes. However, even reducing the tolerance value does not change the outcome indicating that neither of the solvers is able to provide the best integer solution. The MISOCP is able to find the optimal integer solution, which has been verified by manually imposing the bounds defined by each DT branch. Specifically, we solved 74 AC-OPFs consecutively, one for each DT branch and imposed the corresponding bounds in order to determine the DT branch, which contains the least-cost, optimal NLP solution. Leaf node 104 actually contains the bounds, which result in the least-cost NLP solution. Notably, in this test case, the MISOCP relaxation is exact, i.e. its solution is feasible to the nonlinear, non-convex AC-OPF

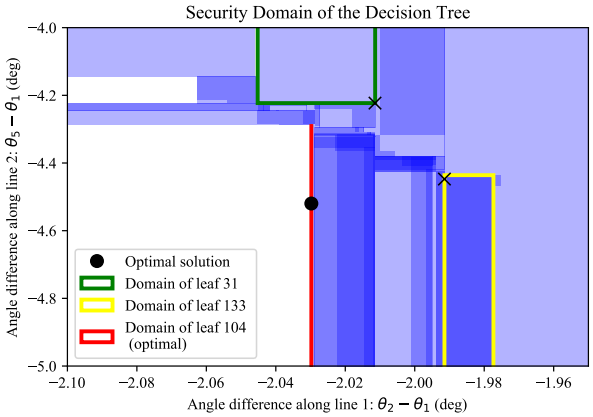

Figure 6.8: Non-convex security domain of the DT as a function of the angle differences along lines 1 and 2. The blue shaded areas represent the stable regions defined by all DT branches. The darker the color, the more domains of different DT branches overlap. Note that the actual security domains covered by the different leaf nodes do not overlap and might even be disjoint, which however cannot be depicted by only two dimensions. Source: **[Pub. F]**

formulation and corresponds to the global optimum of the non-convex problem. Nonetheless, given that the MISOCP formulation is still a relaxation, identified solutions can be infeasible for the original problem. Therefore, we propose to use the MISOCP primarily to identify the optimal DT branch and hence the linear bounds on the feasible space, such that the optimal solution is included. Once these are known and the feasible space has been reduced, the integer variables can be omitted and a common AC-OPF (i.e., NLP) with the previously identified bounds on angle differences imposed as linear constraints can be performed to identify feasible and secure preventive control actions. The MISOCP solution serves as a lower bound and can validate the optimality of the AC-OPF solution.

Table 6.5 also outlines the savings in online computation time of the proposed SC-OPF method. The data-driven approach outperforms the usual PSC-OPF by more than $40\,\%$, while at the same time incorporating more security requirements. Naturally, the computation time depends on the size of the DT and the number of binary variables used to represent it. Even though introducing binaries increases the OPF complexity, this side effect is offset by a signifincantly reduced overall size of the SC-OPF. While the PSC-OPF increases 32-fold when considering 31 contingencies, the proposed data-driven approach inreases less than 4-fold for the same amount of contingencies. As indicated by constraint (6.16), $(2 \times N_L \times N_P + 1)$ additional constraints are added, where N_L and N_P denote the number of network lines and DT paths, respectively.

Furthermore, given that the problem is a convex MIP, which can be solved efficiently by already exisiting solvers that are able to handle up to a few thousand binaries, the amount of discrete variables is not expected to be an obstacle. The size of the DT is directly determined by the size of the dataset, which it is derived from. Hence, a more efficient method to generate the database of operating points, appropriate pruning of the DT and techniques to decompose the data-driven optimization are aspects that require a deeper analysis and are promising approaches to enhance the scalability performance of the method.

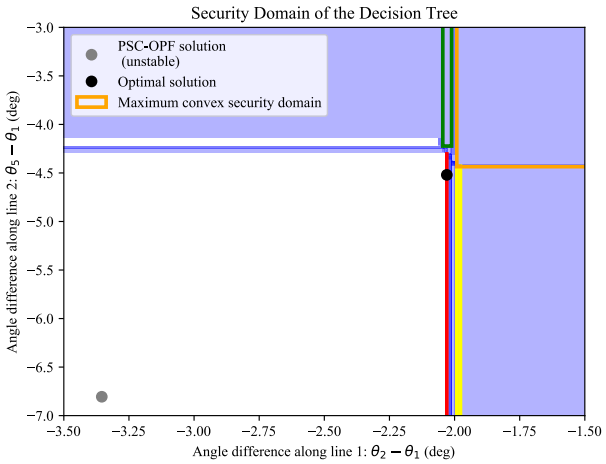

Figure 6.9: Visualization of redispatch and maximum convex security domain, which can be covered by one leaf node only. Source: **[Pub. F]**

Optimizing Redispatch

The method can be used by TSOs to identify optimal redispatching actions, where for example the market-based day-ahead dispatch, if identified as unstable, is redirected through the DT to a secure domain. We have reformulated the MISOCP in order to optimize redispatching actions, assuming that the costs of generator up- and down-regulation correspond to its marginal cost. Generators are assumed to be paid for up-regulation and charged for savings resulting from down-regulation. We have used the unstable solution of the standard PSC-OPF listed in Tab. 6.5 as an input to the redispatch and successfully shifted the operating point to leaf node 104. The cost of redispatch amounts to $343.12\,€$, which corresponds to the original difference in objective values between the PSC-OPF and MISOCP.

The MISOCP, if implemented at the market stage, could result in more than $10\,\%$ cost savings for the system operator and better reflects the locational impact of stability requirements.

Enlarging the Feasible Space

The generated database contains 1.34 million operating points, out of which $6.57\,\%$ fulfill the $3\,\%$ minimum damping ratio and define the feasible space of operation. We have evaluated how much of the entire stable region is covered by each individual leaf node, i.e. how many operating points fulfill the constraints imposed by the corresponding DT branch. All leaf nodes cover in total $99.91\,\%$ of the considered stability region, where leaf node 7 accounts for most of it, capturing $77.78\,\%$ of the entire feasible space. The implied bounds of leaf node 7 are depicted in Fig. 6.9. If we had considered the stability requirements in the OPF only by imposing bounds, which define a convex space, as it is currently done in practice, we would have been able to capture at most $77.78\,\%$ of the feasible space, thereby also missing the optimal solution as can be seen in Fig. 6.9. Thus, our approach to incorporate the information provided by the database in the optimization problem through binary variables allows us to enlarge the feasible space by more than $28\,\%$, enclosing the remaining $22.13\,\%$, which are covered by the DT.

6.5.3 Discussion

In this section we propose a data-driven approach to preventive SC-OPF, which ensures N-1 security and small-signal stability, it is scalable and uses decision trees to capture the non-convex and possibly disjoint space of stable operating points. We propose a new approach to translate data, which operators usually already have available from dynamic simulations, and include them in a simple way in an optimization framework. Binary variables are used to represent the knowledge extracted from the data giving rise to two levels of non-convexities: one that refers to the integrality of the binary variables and another one that concerns the AC power flow equations. We eliminate the latter using a SOC relaxation and obtain a convex MISOCP. MISOCPs generalize convex mixed-integer quadratic programs, for which solvers have already reached a high level of maturity. The proposed method reduces the overall problem size by avoiding to explicitly include all considered contingencies and incorporates stability requirements, both of which have been major challenges in SC-OPFs. Finally, we have shown that by using data coupled with MIP in (SC-)OPFs we can enlarge the feasible space represented in the OPF by more than $28\,\%$.

The relaxed data-driven SC-OPF can be used to determine the optimal bounds (i.e., the optimal DT branch) on the feasible space, such that secure preventive control actions are ensured. Considering that the DT represents a non-convex operating space, identified preventive actions can be less conservative than those determined by current approaches as described in section 6.5.1. The need for iterative contingency analyses to indentify suitable control actions are alleviated. The MISOCP formulation of the SC-OPF can be used by market operators as a market-clearing tool due to its low online computational effort but also by TSOs to determine optimal redispatching actions and the bounds on angle differences, which allow accommodating the redispatch.

6.6 Data-driven Small-Signal Stability and Preventive-Corrective Security Constrained DC-OPF

This work extends the data-driven security constrained DC-OPF presented in section 6.4 by incorporating corrective control offered by HVDC terminals. Moreover, it bridges the gap between the chapter on Multi-Terminal High-Voltage Direct Current (MT-HVDC) control structures and this chapter by adapting the methodology proposed in Section 4.7 to incorporate the flexibility offered by HVDC terminals into the security considerations already included in the previous sections. Considering corrective control by HVDC terminals already in the market-clearing allows for an even less conservative and more cost-efficient dispatch while keeping all the benefits of the presented data-driven security constrained DC-OPF, such as the incorporation of N-1 security and small-signal stability and the possibility of considering non-convex, possibly disjoint operating spaces.

The additional challenges of including corrective control of High-Voltage Direct Current (HVDC) terminals are threefold. First, the size and complexity of the small-signal model increases significantly with every HVDC terminal. Second, every HVDC terminal adds two additional degrees of freedom with a wide range of potential values ($\approx \pm P_{max}$, $\approx \pm Q_{max}$) to the problem complicating the database generation by significantly increasing the number of potential operating points. Finally, the benefit of corrective control, allowing HVDC terminals to change set-points in order to save the system in case of contingencies, complicates the data-point classification. As these challenges mainly concern the database generation and operating point classification, they are described in more detail in section 6.6.2.

6.6.1 Methodology

As this works extends the data-driven security constrained DC-OPF presented in section 6.4 we adapt the presented methodology. In order to include corrective control of HVDC terminals, the main changes lie in the database generation and the operating point classification.

6.6.2 Database Generation

In case of corrective control, the database generation faces the three aforementioned additional challenges: (i) increased small-signal stability model complexity leading to a higher computation time. Given the model complexity of HVDC terminals, the size of the small-signal model increases by approx. 20 states per terminal (depending on model fidelity of converter and dc cable). (ii) Two additional degrees of freedom per HVDC terminal increase the problem size significantly. Moreover, given the wide operating range of an HVDC terminal ($\approx \pm P_{max}$, $\approx \pm Q_{max}$), a single HVDC terminal corresponds to a problem size increase of four generators. (iii) Increased complexity of operating point classification. The necessity to analyze potential corrective actions for every contingency and every generation pattern (i.e. combination of generator outputs) complicates the operating point classification. It is not enough anymore to know that a combination of generator outputs does not fulfill the security requirements for the most critical fault, because there could potentially exist another combination of HVDC set-points for which the combination of generator outputs fulfills the requirements for a specific contingency and another combination for another contingency. Thus, we basically need to extend the method proposed in Section 4.7 to determine the operation boundaries of the HVDC terminals for the different network topologies and generator dispatches.

The complication of the operating point classification is visualized in Fig. 6.10. In case of preventive control, every generator set-point needs to be tested with every HVDC set-point for every contingency. If this combination of generator and HVDC set-points fulfills the stability requirements for every contingency, it is added to the set of 'set-points fulfilling the requirements'. If it does not fulfill the requirements for a single contingency, e.g. the most critical one, however, the remaining contingencies do not need to be evaluated to classify the operating point appropriately.

In case of corrective control, every combination of generator set-points needs also to be tested with every HVDC set-point for every contingency. However, if there exists a combination of generator set-points and HVDC set-points for which the stability requirements are fulfilled in the base case, the database needs to be evaluated whether there exists at least a single set of (possibly different) HVDC set-points fulfilling the stability requirements for the remaining contingencies. If there exists at least one set of HVDC set-points for every contingency, the initial combination of generator set-points and HVDC set-points can be added to the set of 'set-points fulfilling the requirements'.

An additional issue increasing the complexity of operating point classification is related to the HVDC integration and the mapping between the ac and dc space. As the reactive power set-points of the HVDC terminals are not part of the dc problem, a set of ac operating points $\mathbb{O}_{ac}$, whose size depends on the discretization interval of the HVDC set-points, needs to be mapped into a single dc operating point. That means for example, that the operating points $OP_{ac} = [P_{g_1} = 180\ P_{g_2} = 0\ P_{g_3} = 10\ P_{g_4} = 10\ P_{g_5} = 0\ P_{g_{wf}} = 20\ P_{g_{HVDC1}} = -20\ Q_{HVDC1} = \pm Q_{HVDC,max}\ Q_{HVDC2} = \pm Q_{HVDC,max}] \in \mathbb{O}_{ac}$ need to be mapped into a single dc operating point. Moreover, these ac operating points differ by the losses occurring in the system, i.e. also

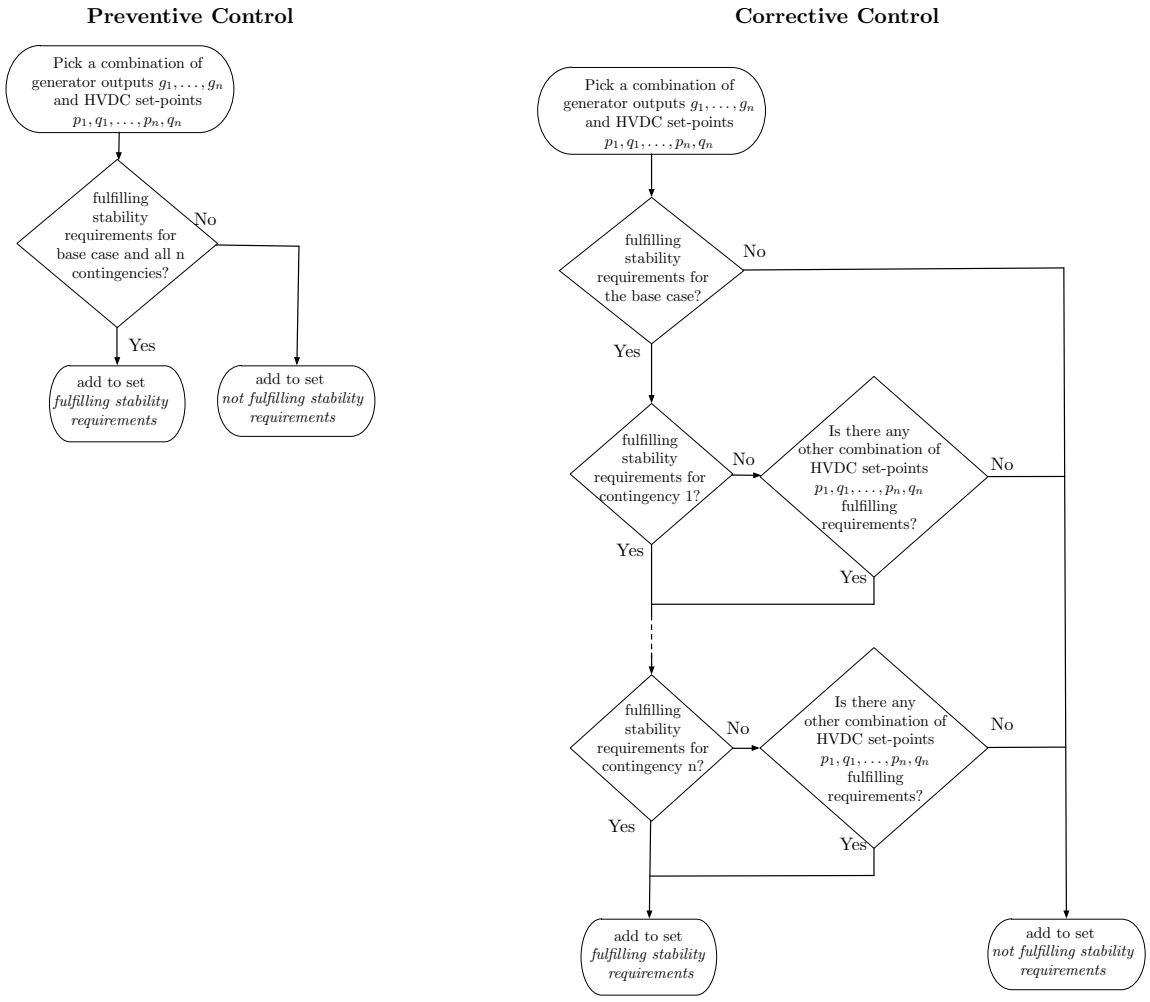

Figure 6.10: Visualization of the difference in data-point classification between preventive and corrective control.

by the line flows which serve as predictors in our study, and also by their classification. To this extent, we determine for every potential dc operating point whether there exists at least a single $OP_{ac} \in \mathbb{O}_{ac}$ allowing to classify it as fulfilling the requirements according to the preventive-corrective definition. Moreover, if there exists several OP_{ac} fulfilling the requirements (or all not fulfilling the requirements) we need to map all these ac operating points into the single dc operating point. Therefore, we average the corresponding lines flows in order to reduce memory requirements and classifier training time.

Thus, the database generation becomes significantly more complicated.

6.6.3 OPF Implementation

The OPF implementation remains the same as presented in 6.4.4. The implementation of the HVDC lines is realized in the form of virtual generators, i.e. two generators per HVDC line with $P_{g,1} = -P_{g,2}$. The losses of the HVDC line are considered as loads at the nodes of the virtual generators, evenly split between the nodes. Following the lessons learned from the previous

sections, the losses of the DC lines are also approximated by an ac power flow of the best guess of the database using MatACDC [180].

6.6.4 Feature Selection and Knowledge Extraction

Following the lessons learned from previous work, which are presented in the case study in section 6.4.5, this work uses as features the exact mapping of dc and ac operating points by augmenting the dc power flow by the losses approximation of the corresponding ac-power flow. The details are presented in section 6.4.3.

Following the previous work, this work also uses decision trees as knowledge extraction method.

6.6.5 Case Study

We evaluate the performance of the data-driven small-signal stability and preventive-corrective security constrained OPF by comparing it to a data-driven small-signal stability and preventive security constrained OPF, which corresponds to the data-driven SC-DC-OPF presented in section 6.4 with additionally considering HVDC lines and preventive control of HVDC terminals. As we have already shown in section 6.4.5 that our data-driven preventive SC-DC-OPF allows for a more cost efficient dispatch than current approaches, such as ATC and FBMC, this case study demonstrates that by considering the corrective control capabilities of HVDC terminals already in the market-clearing, an even more cost efficient dispatch can be obtained.

The IEEE 14 Bus system has been modified by integrating a HVDC line and a windfarm as visualized in Fig. 6.11. The parameters are given in the appendix. The small-signal models of the multi-machine model, the HVDC transmission system and the Doubly-Fed Induction Generator (DFIG) based wind farm have been introduced in section 2.7. The model has been built using Mathematica [48], as the symbolic derivation enables us to initialize the model for every possible combination of load and generation using MatACDC [180]. The small signal analysis is carried out using Matlab 2017b [41]. Reactive power limits of the generators are enforced. Note that although a $100\,\mathrm{MW}$ wind farm is connected, the ac network is not capable of absorbing $100\,\mathrm{MW}$ at bus 17 at the given load level $\sum_{i=1}^{N_B} P_{D_i} = 259\,\mathrm{MW}$. Hence, it is a simplified example resembling the problems currently observed in Germany. A comparable large installed wind power capacity is located in the north, while the load centers are in the south. Due to missing transmission lines from the north to the south because of delay in the project development, the wind power needs to be curtailed in case of high wind speeds. This setup allows us to show that our data-driven approach is capable of reducing the need for redispatching actions by incorporating the security considerations and potential corrective control actions offered by the HVDC terminals already in the market-clearing.

Note that within the N-1 security analysis, the HVDC line has been neglected as HVDC point-to-point links are usually not considered as N-1 secure. All ac line faults have been considered except those lines interconnecting the HVDC terminal with the ac grid / wind farm (line13-17 / line15-16) and line7-8.

As an extension of the efficient database generation method proposed in chapter 5 which allows the creation of databases considering corrective control is currently still under development, a brute force approach is used to enable the presentation of this small case study. Although a comparably wide grid discretization (i.e. a step size of $3\,\mathrm{MW}$ for the generators and $10\,\mathrm{MW}$ for the HVDC

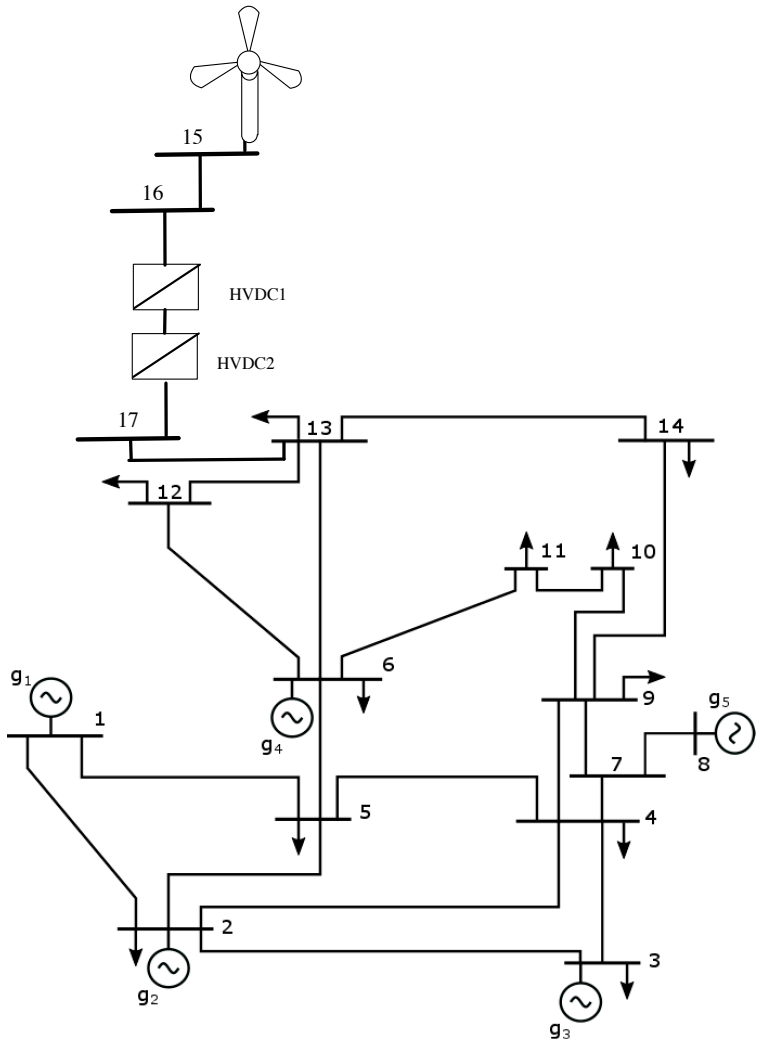

Figure 6.11: Visualization of the modified IEEE14Bus system.

set-points) was chosen, this requires the analysis of $173.3 \cdot 10^6$ data points with the brute force approach. Considering also the increased model size and number of faults we consider per data point, the database generation takes $\approx 140\,\mathrm{h}$ using the brute force approach with 200 cores on the HPC cluster at DTU for a single load level. This emphasizes the need for the extension of our efficient database generation method.

As a first step, both approaches, i.e. preventive security and the preventive-corrective security approach, can be compared by the size of the feasible space which becomes visible by an analysis of the database. Given the discretization and database reduction as described in Section 6.6.2, 392931 dc operating points are obtained in the database. Just by comparing the amount of feasible points for the preventive (13066, 3.33%) and the preventive-corrective (49640, 12.63%) case highlights the increase in feasible space obtained by considering corrective control actions offered by HVDC terminals. However, it needs to be emphasized that - as for all small-signal stability OPFs - the transition trajectory between the pre- and post-disturbance OPs is not considered and thus, it needs to be verified that the transition trajectory does not violate any dynamic limits. However, as the potential pre- and post-disturbance OPs are collected within the database, the data-driven

Table 6.6: Comparison of data-driven preventive and preventive-corrective approaches.

	$P_{wind} \leq P_{wind,max}$		$P_{wind} \leq 10\,\mathrm{MW}$	
	preventive	corrective	preventive	corrective
Dispatch (MW)				
g_1	106.8	133.0	166.2	218.8
g_2	60.0	60.0	60.0	20.4
g_3	60.0	28.7	7.6	17.0
g_4	13.6	25.0	25.0	6.0
g_5	12.1	0.0	3.6	0.0
g_{wf}	20.0	25.8	10.0	10.0
Total Cost (€)	3198.1	2948.6	3036.5	2807.7
Min. damping ratio (%)	7.3%	5.9%	8.9%	8.4%

approach also facilitates the time-domain verification. Ideally, the small-signal stability approach could be supported by time-domain simulations verifying the transition trajectories already within the database generation.

The decision trees are created using Matlab 2017b [41] with the gini-index as splitting criteria. We raise the cost for false positives by a factor 8, i.e. misclassifying an OP not complying with the requirements as stable. The initial accuracy using 5-fold cross-validation is for both approaches at $99.99\,\%$ with the only errors being false negative predictions. However, in order to mitigate the over-fitting, we pruned step-wise singular nodes based on OPF results. Thus, in the end the accuracy of the trees went significantly down to $96.68\,\%$ (preventive) and $89.45\,\%$ (preventive-corrective). Note, however, that also after the pruning zero false positives are detected, i.e. the whole pruning made the trees a bit more conservative without increasing the risk of false positive misclassifications.

Following the approach presented in section 6.4, we incorporate the system losses from a best guess operating point found by searching in the database for the cost optimal solution of each approach.

The results of both approaches, once for $P_{wind} = P_{wind,max}$ and once for $P_{wind} = 10\,\mathrm{MW}$ are shown in Tab. 6.6. Both approaches find N-1 secure operating points, however, the preventive-corrective security approach enlarges the feasible space and allows significant savings ($7.8\,\%$ and $7.5\,\%$, respectively) in both cases. Note that due to the small-signal stability considerations a maximum RES dispatch would not lead to the most cost efficient solution which can be observed in Tab. 6.6. Especially the preventive-corrective SC-OPF would be able to determine even cheaper operating points using less wind power, however, as RES are usually prioritized, high RES dispatch is enforced here. Still, as aforementioned the ac grid is not capable of absorbing $P_{wind,max}$ but the preventive-corrective security approach allows to maximize the RES dispatch compared to the preventive approach. Considering the results presented in Section 6.4.5, more cost efficient results could probably be achieved by using a database with smaller discretization intervals.

Thus, by incorporating security considerations and the corrective control capability of HVDC terminals into the market-clearing, a stable, cost efficient dispatch is achieved and the need for redispatching actions is mitigated.

6.6.6 Discussion

A data-driven small-signal stability and preventive-corrective security constrained DC-OPF has been presented. Compared with a data-driven small-signal stability and preventive security constrained DC-OPF the feasible space is enlarged allowing for a more cost efficient dispatch. By ensuring the small-signal stability and preventive(-corrective) security of the dispatched operating points, the need for redispatch is mitigated. Potential corrective control policies can be extracted from the database.

6.7 Conclusion and Outlook

Data-driven methods for market-clearing and power system operation have been developed which allow for a more cost efficient and secure dispatch determination by implementing more detailed security considerations and extending the feasible space to the real non-convex space. The proposed methods are scalable and computationally efficient due to the fact that the N-1 security and small-signal stability analysis is performed offline. Tractable decision rules are extracted from the database enabling their implementation into OPF algorithms. Moreover, we took the increasing interest in HVDC transmission in Europe into account and considered the benefits of corrective control offered by HVDC terminals enabling an even more cost efficient market-clearing. Further, the methods can potentially be used at different time horizons (e.g. day-ahead market, intra-day market or during operation). Case studies have highlighted the superior performance of the proposed methods compared to current approaches.

Although this work already shows promising results, we believe there exist a few opportunities to extend the proposed methods. (i) The database generation can be extended by adding time-domain simulations. Besides the safe operating condition before and after the fault, as small-signal stability and security constrained OPF guarantee, the additional time-domain simulation would ensure that the trajectory in between is also safe making it not only small-signal stable but transient and voltage stable. The advantage of extending our method with time-domain simulation instead of starting from scratch is that the database can be used to determine a significant reduced size of pre-disturbance states which need to be investigated.

Moreover, (ii) the proposed methods can be extended by including uncertainty within the OPF formulation by using chance constrains. So far the uncertainty of RES is separated from the problem in the sense that we rely on a precise forecast. However, the next step is to include the uncertainty within the OPF allowing us to include more detailed probabilistic forecasts. Then, using chance constrains the data-driven OPF formulation could ensure that the dispatch would e.g. with a violation probability of $5\,\%$ always be within the secure region.

CHAPTER 7

Data-driven Dynamic Stability Assessment based on Local Measurements

After the successful application of data-driven methods on a system wide level, this work investigates potential application on control level using local measurements only.

7.1 Background

In modern power systems voltage stability is an important issue since voltage instability has significantly contributed to some major blackouts around the world (e.g. USA-Canada blackout in 2003 [181], southern Sweden/ eastern Denmark 2003 [182] and Italy blackout in 2003 [183]). The IEEE and CIGRE joint task force defines 'voltage stability' as the ability of a power system to sustain voltage magnitudes at all buses after small or large disturbances [184]. Thus, voltage instability describes the failure of the power system to maintain/restore equilibrium between load demand and load supply. The instability is often driven by the loads, which tend to be restored after a disturbance by the action of motor slip adjustment, distribution voltage regulators, tap-changing transformer, and thermostats [1].

Voltage stability can be classified in two categories: small disturbance and large disturbance voltage stability. Further, based on the time frame of interest voltage stability can be distinguished by short-term and long-term voltage stability. The long-term phenomena involves slower acting equipment, such as tap-changing transformers, thermostatically controlled loads, and generator current limiters [1]. The short-term voltage stability is driven by fast recovering load components (e.g. induction motor) that tend to restore power consumption in the time scale of a second following a large disturbance [32]. Due to the voltage dip, induction motors decelerate dramatically or may stall if the electrical torque cannot overcome the mechanical load. The behavior of the motors depends on the mechanical torque characteristics and the motor inertia. Stalling of a motor near the end of a feeder may cause the stalling of other motors [185]. As a consequence they draw a very high reactive current at low power factor depressing the voltage magnitudes. The stalling of induction motors has been identified as main reason for Fault Induced Delayed Voltage Recovery (FIDVR) which is the phenomenon whereby system voltage remains at significantly reduced levels for several seconds after a transmission fault has been cleared [33]. In case load dynamics attempt to restore power consumption beyond the capability of the transmission system, voltage collapse may occur due to excessive voltage deviation from normal permissible limits [1]. Hence, the major challenges are that the systems transition from post-contingency to new operation point should not violate any dynamic limits and the new operation point needs to be stable [186].

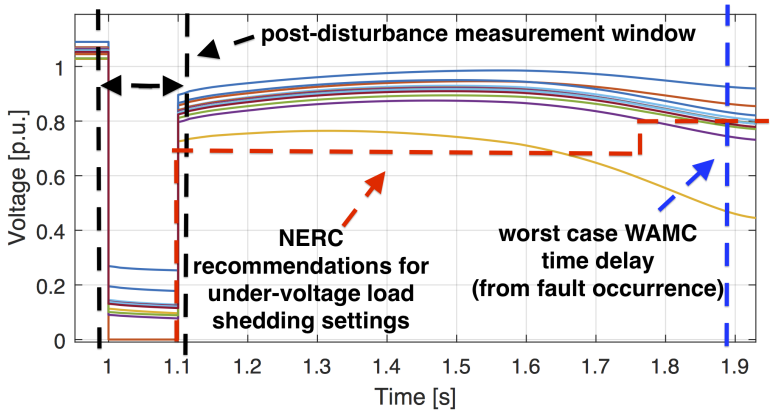

Figure 7.1: Example of a voltage collapse scenario with the visualization of the post-disturbance measurement window and the NERC recommendation for under-voltage load shedding.

Dynamic voltage limits after a contingency required by different utilities are provided for example in [187].

Since the short-term voltage instability is usually following a disturbance perturbing the system state away from equilibrium, the dynamics are complex making the voltage stability analysis a challenging problem [188]. The complexity of monitoring the voltage stability of the power system is further related to the system size, as well as the presence of various sources of parametric and modelling uncertainties in power system dynamics, which could cause unreliable stability predictions [189].

The increasing penetration of induction motor loads (e.g., air-conditioners), as well as the more intensive usage of the transmission system makes today's power systems more vulnerable to the short-term voltage instability [190]. At the same time, the increasing deployment of Phasor Measurement Units (PMUs) has made it possible to obtain high-resolution, real-time dynamic state information of the power grid. These measurements result in a large amount of data collection of the system behavior enabling us to develop methods to monitor, predict, and enhance system stability in real-time. In particular, as an accurate model is difficult to establish as the operating conditions constantly change. Although, PMUs allow the development of Wide-Area Monitoring and Control (WAMC) systems using numerous PMUs system-wide and communication to gather all the data, the communication delay may prohibit WAMC systems to be effective against short-termin voltage instability. In fact, in [191], the authors address the communication delays, which include propagation delays, router queuing delays, data transmission delays and phasor data concentrators data aggregation delays, between the PMUs and the control actuator. The authors determine delays between $50\,\mathrm{ms}$ and $78\,\mathrm{ms}$ depending on the Information and Communication Technology (ICT) infrastructure configuration. However, they argue that the PMU data frame losses additionally need to be considered to obtain a robust WAMC system. In WAMC applications the computation is performed with the most recent PMU data frames available, however, theses data frames would be outdated in case of data frame losses, since the most recent measurements sent by the PMU are lost during data transfer to the central control unit. Thus, data frame losses induce an additional time delay resulting in even higher average time delays between $172\,\mathrm{ms}$ and $872\,\mathrm{ms}$ depending on the ICT configuration [191].

Thus, relying on communication comes with the risk of communication faults or loss, and introduces

a significant time delay between measurement and actuator which for certain faults could be too large to be acceptable. For instance, in case of potential load driven short-term voltage instability (or fast evolving transient instability) the time delay induced by communication between PMUs and a central control unit may limit the possibility of saving the system. In Fig. 7.1, the worst-case WAMC time delay (not including communication loss) is visualized as blue, dashed line. It is worth noting that at the time instance of $872\,\mathrm{ms}$ after the fault, the WAMC does not even have any post-disturbance measurements yet but has just received the measurements at the moment when the disturbance occurred. However, the voltages already violate the recommendation of the North American Electric Reliability Corporation (NERC) for under-voltage load shedding [192], visualized in Fig. 7.1 as red, dashed line. For this reason, most control and protection schemes are decentralized and based on local measurements. Among several examples, the control at the HVDC terminals, for instance, is usually based on PI-controllers reacting to the measured voltage magnitude / active power.

7.2 Literature Review

While most research in short-term voltage stability uses classical fully populated dynamic models in time-domain simulations, mostly sped up by distributed architecture and earlier termination [193], there is less work done using a data driven approach. Nevertheless, it is possible to distinguish between two main different directions of research in the data driven short-term voltage stability analysis:

- Approaches using mathematical functions as stability metrics
- Data-driven approaches using Artificial Intelligence (AI), Machine Learning (ML), and / or Data Mining (DM)

The group of mathematical functions as stability metrics basically sums up approaches, which directly apply certain methods involving specific mathematical functions on real-time measurement. In [194], the authors use a direct stability analysis based on transient energy functions. In [188, 195–197], the authors use the Lyapunov exponent as stability metric. By determining the sign of the Lyapunov exponent, the authors are able to determine whether the voltage trajectories diverge/converge.

In [198], the authors describe a novel analytical method to analyze short-term voltage stability using a transient PV-plane. This method was also already proposed to be used in a control structure to increase the dynamic voltage support capability of a photovoltaic systems [199].

In [200], the authors propose an index to detect voltage stability based on monitoring changes in active power transferred to a weak area and the apparent conductance seen by the bus, which is related to the Thévenin impedance matching approach that is frequently used for long-term voltage stability assessment. They claim that an extension of this approach proposed to monitor long-term voltage stability would make it possible to monitor short-term voltage stability.

Further, the use of singular value decomposition showed promising results for predicting long-term voltage instability and also detecting topology changes [201].

On the other hand, there are many approaches using data-driven approaches. A review of the methods used at the different stages (i.e. Database Generation, Input and Output Definition,

Knowledge Extraction, Validation) is provided by Zhang et al. in [202]. Previous works mainly used the knowledge of the measurements at all nodes in the system to enable a quite precise stability monitoring and prediction [168, 169, 203–207]. While several authors propose the use of Artificial Neuro Networks (ANNs) [208–211], other propose to use Support Vector Machine (SVM) methods [212–214] or Extreme Learning Machine (ELM) methods [215]. Other interesting approaches are based on Decision Tree (DT), which might be more comprehensible for system operators [143, 169, 216–221].

In [222], the authors provide an extensive case study comparing the accuracy of detecting pre-emergency states of the power system for different learning techniques including various DT, SVM and ANN methods. The results indicate the best results for DT and SVM methods. Further, the authors emphasize the ability of DTs to uncover the intrinsic mechanism governing physical processes, and to provide a clear description in terms of tractable system parameters as attractive aspects compared to other machine learning approaches.However, such an approach requires numerous PMUs and relies on communication. Nevertheless, there has been very little work on data-driven methods using only *local* PMU measurements for stability assessment: Existing approaches include the application of DTs for transformer protection [223], and for high impedance fault detection [224]. In [225], the authors propose a response-based DT approach for an out-of-step relaying application. In [226], the authors use Long Short-Term Memory (LSTM) networks and SVM to predict the occurrence of faults based on measurement data.

7.3 Contributions

In contrast to these previous works, we raise the question whether we could enhance the system performance by supporting the local control of e.g. HVDC terminals with data-driven tools using local post-disturbance data only. Given that it is possible to predict that the system will become unstable, or violate under-voltage load-shedding relay settings, before it becomes visible in the voltage magnitude, the local control could act earlier avoiding load-shedding or even voltage collapse. That means, while the voltages in Fig. 7.1 directly after the fault seem to recover, i.e. the voltage difference between set-point and measurement actually decreases, the system is still moving towards collapse shortly afterwards. If it would be possible to predict the system instability right after the post-disturbance measurement window (shown in black, dashed lines in Fig. 7.1), relying only on local measurements, the system could potentially be saved by fast local corrective control actions.

The contribution of this work is the first stage towards such a corrective control: the efficient data-driven early stability assessment of faults in the extended neighbourhood of a strategic node which will later trigger appropriate early actions. Future work will focus on the complete design of the corrective control response to such events. Especially for faults that severely affect the voltage, the focus on faults in the extended neighborhood of a strategic node is reasonable, due to the limited, relatively local, impact of reactive power support.

This work includes the following contributions: (a) we propose two data-driven approaches of assessing the system stability after faults in the extended neighbourhood of a strategic node using local post-disturbance measurements only. First, a single-level approach is presented, then a two-level approach is presented where the first-level classifier determines the fault location and the second-level classifier determines the criticality of that fault. Further, (b) we evaluate and compare the accuracy of different supervised machine learning methods and (c) evaluate the robustness of

these approaches against changes in the grid and the load configuration in a case study. Thus, compared with existing literature, this work focuses on *local*, data-driven approaches for stability predictions which could be used to trigger early corrective control actions.

The remainder of this work is structured as follows: First, the underlying concepts of extended neighborhood and post-disturbance measurements are introduced in detail, followed by a brief introduction of the supervised machine learning methods. Then, the proposed approaches are introduced. Finally, a case study is presented.

7.4 Definitions

The question is whether it is possible to assess and predict the system stability after faults in the extended neighbourhood of a strategic node using a limited time-window of only local post-disturbance measurements. Thus, let us first define the extended neighbourhood of the strategic node, followed by a description of the limited time window of local post-disturbance measurements.

7.4.1 Definition of the extended Neighbourhood of a Strategic Node

For a graph $G(V, E)$, where V is the set of vertices, and E is the set of edges, we define vertex 1 as strategic node. Then, two vertices 1, 2 are *adjacent* or *neighbours*, if {1, 2} is an edge of G. The set of neighbours of a vertex V in G is denoted by $N_V(G)$ [155].

If vertices 2, 3 are also neighbours, i.e. {2, 3} is an edge of G, then vertex 3 is an extended neighbour of vertex 1. The set of extended neighbours of a vertex v in G is denoted by $N_v^e(G)$.

Thus, for the small example of graph G in Fig. 7.2, the set of neighbours of the strategic node 1 is $N_1(G) = \{2, 4\}$ with the connecting edges marked as red, dashed lines, while the set of extended neighbours is $N_1^e(G) = \{3, 5, 6, 7\}$ with the connecting edges marked as blue, dotted lines.

7.4.2 Post-disturbance Measurement Window

Triggered by a fault and the characteristic subsequent drop of the voltage magnitude, the local measurements within a certain time-window are used as predictor variables and inputs for the supervised machine learning methods described in the following subsections. Since we focus on faults in the extended neighbourhood of the strategic node, the time window starts with one sample before the characteristic voltage magnitude drop and ends one sample after the characteristic rise of the voltage magnitude when the fault is cleared with a trip of the corresponding lines.

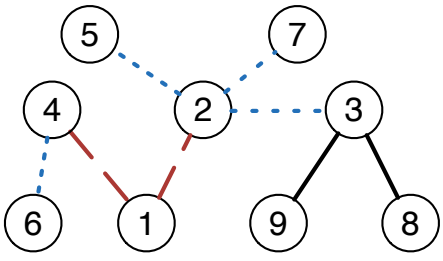

Figure 7.2: Graph G.

Thus, as shown in Fig. 7.1, at $t = 1\,\mathrm{s}$ a line fault occurred in the extended neighbourhood of the strategic node. The fault is cleared after $100\,\mathrm{ms}$ with a trip of the corresponding line. With a sampling rate of the PMUs of 60 Hz, the time window between the first measurement and last measurement used for the prediction lies between $t = 0.9833\,\mathrm{s}$ and $t = 1.125\,\mathrm{s}$, shown in Fig. 7.1 as black, dashed lines. If it is possible to assess a stability purely based on this limited local information, control actions can be initiated significantly faster than by a WAMC which has a time delay of anywhere between $172\,\mathrm{ms}$ and $872\,\mathrm{ms}$.

7.5 Modeling

As such fault measurements in form of real PMU data are rare if available at all, this work uses PSS/e as simulation tool to create the required data. As the complex dynamics of short-term voltage instability affect the analysis of the phenomena, time-domain simulations with a detailed modeling of the load are required in order to analyze short-term voltage stability [185]. Following similar studies, this work uses complex load models 'CLODBL', shown in Fig. 7.3. A more detailed description is given in [227]. Note that the proposed methods are not limited to specific models or model parameters.

> The CLOD model replaces the constant MVA, current, and impedance load with a composition of loads as shown in [Fig. 7.3]. These loads consist of large and small induction motors, discharge lighting, constant MVA load, and a static load response. Also included are transformer saturation effects and an equivalent distribution feeder and transformer impedance. Some general comments and modeling considerations for the CLOD model:
>
> - The model assumes that the load bus voltage is 0.98 pu, and adjusts the transformer tap ratio at initialization until that load bus voltage is attained.
> - The motor curves for the large and small induction motor models are provided in the instruction manual. These motors models represent large and small motors with inertia constant H = 1.0 sec and H = 0.6 sec, respectively.
> - The model does not consider single-phase induction motors such as residential air conditions.
> - The distribution system equivalent modeled as (R+jX)/P0 represents the transformer and/or feeder impedance; however, this does not represent shunt compensation at the substation or down the feeder.
> - Under-load tap changing is not considered in the transformer model.
> - Discharge lighting is modeled as constant current real part and imaginary part proportional to the voltage raised to 4.5 power. Voltage between 0.65-0.75 pu exhibits a linear reduction. For any voltage less than 0.65 pu, the load is assumed extinguished (no load).
>
> [227]

The configuration is chosen as suggested in [185] as $15\,\%$ large motors, $45\,\%$ small motors, $1\,\%$ transformer exciting current, $20\,\%$ discharge lighting, $5\,\%$ constant power and $14\,\%$ remaining loads.

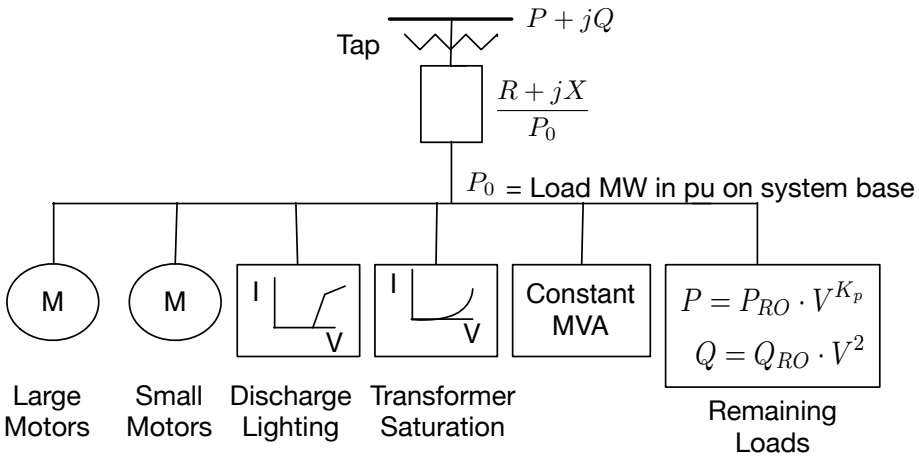

Figure 7.3: Complex Load Model: 'CLODBL'. Adapted from: [13].

7.6 Methodology

The different supervised machine learning methods used in this work have been introduced in section 2.5. Here, we introduce the different data sets and point out two different approaches about how to apply these supervised machine learning methods.

For each fault we create a data set containing numerous scenarios using various load levels and generation patterns. A single scenario is defined as a set of *local* measurements at the strategic node of a specific fault using a specific generation pattern and load level. The scenarios of each of all the different faults are split into randomly chosen $80\,\%$ for the training set and $20\,\%$ for the test set. Then, all training sets and all test sets of the different faults are accumulated to a global training and a global test set. Thus, both global sets consist of an equal share of scenarios of all the different considered faults.

The decision tree classifiers developed in this chapter are trained using the gini-index as splitting criteria as introduced in section 2.5. Moreover, in order to avoid false positive classifications, i.e. unstable scenarios classified as stable, we raised the cost of these misclassifications. Cost-complexity pruning is used as pruning method minimizing $C_\alpha(T) = c(T) + \alpha \times |T|$ for a set of subtrees T_x developed using cross-validation within the test set.

The SVM classifiers have been been trained with standardized data and auto kernel scaling, i.e. the software uses a heuristic procedure to select the scale value. The heuristic procedure uses subsampling [42].

7.6.1 Single Level Approach

In a single level approach, the described supervised machine learning methods are used to train classifiers on the global training set trying to distinguish acceptable scenarios from unacceptable scenarios according to specified criteria.

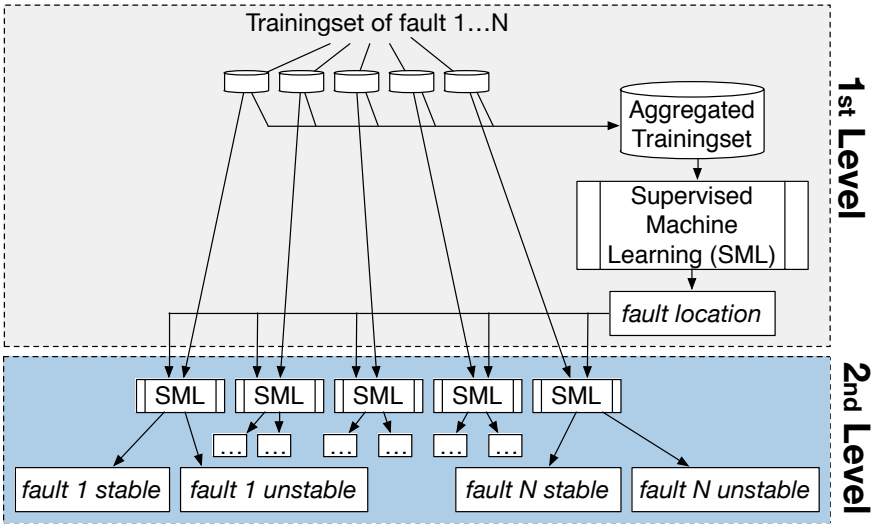

Figure 7.4: Two-Level Approach.

7.6.2 Two-Level Approach

The two-level approach is shown in Fig. 7.4. For the different machine learning methods, as a first step, we use the global training set to train classifiers that are able to determine the fault location. Then, at a second step, we use the individual training sets of each fault in order to train a second set of classifiers to distinguish between acceptable and unacceptable scenarios for each fault individually.

Thus, while the single level approach leads to a single classifier (e.g. classification tree), the two-level approach results in $N + 1$ classifiers, with N being the number of considered faults. The advantage of this approach is that it leads to smaller trees with potentially higher accuracy since different predictors are important to determine the stability boundary or the location of the fault.

The disadvantage is that misclassifications of the fault location occurring at the first level, lead to the use of classifiers specialized at different fault locations in the second level. However, the case study indicates that very high accuracies can be achieved for the first level classifiers and that even first-level misclassified scenarios are classified correctly on the second level with quite high accuracy. This is discussed in more detail in the case study.

7.6.3 Predictors

These methods consider local post-disturbance measurements only, i.e. we use the measurements of voltage and current magnitudes, voltage and current phase angles and active power and reactive power flows on the connected lines within the post-disturbance measurement window. Additionally, based on the simplified power flow equations, we calculate an approximate voltage phase angle difference of the strategic node and the neighbouring nodes:

$$\Delta\theta_{yz} = \arcsin\left(\frac{P_{yz} \cdot x_{yz}}{V_y^2}\right) \tag{7.1}$$

where P_{yz} is the active power flow between the strategic node y and the neighbouring node z, x_{yz} is the reactance of the corresponding line and V_y is the voltage magnitude at the strategic node.

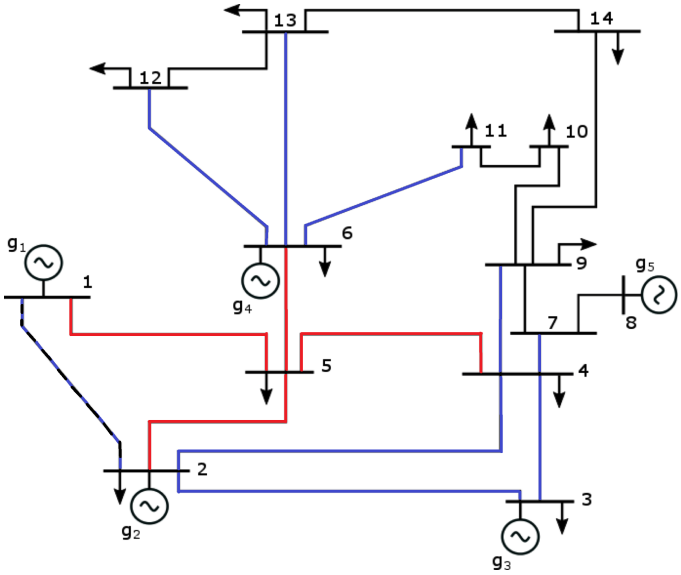

Figure 7.5: IEEE 14 Bus System. Source: **[Pub. E]**.

In addition to the local post-disturbance measurements, the global pre-disturbance steady state data of the system is used, i.e. voltage magnitudes and voltage phase angles of all buses and the phase angle differences between the buses before the disturbance. Since the pre-disturbance information of the system is not time critical, it is expected to be available e.g. through the SCADA system.

7.7 Case Study

The IEEE 14 Bus system, shown in Fig. 7.5, is used as test system. As we did not have PMU data available, we created a large enough data set by running time-domain simulations of a large number of scenarios using PSS/e.

At buses 2 to 6, we use complex load models 'CLODBL', shown in Fig. 7.3. The configuration is chosen as suggested in [185] as $15\,\%$ large motors, $45\,\%$ small motors, $1\,\%$ transformer exciting current, $20\,\%$ discharge lighting, $5\,\%$ constant power and $14\,\%$ remaining loads. The remaining loads are modeled as constant power loads.

In this study, we chose bus 5 as strategic node and applied the data-driven dynamic stability assessment based only on local measurements. In general any bus could be selected. With bus 5 being a very central node, with $N_5(G) = \{1,\, 2,\, 4,\, 6\}$ and $N_5^e(G) = \{3,\, 7,\, 9,\, 11,\, 12,\, 13\}$, this choice allows us to challenge the assessment with many different faults. Thus, we considered all line faults of one of the lines directly connected to bus 5 (red lines) as well as those in the extended neighborhood (blue lines). The line between bus 1 and bus 2 would in general be in the extended neighborhood, however, this line appears to be very critical for the system, leading to mostly unacceptable scenarios. Thus, this fault is very easy to predict leading to a very high accuracy. Hence, it was not considered in order not to overestimate the observed overall prediction accuracy.

We created simulation data for 12 contingencies, each for 441 different generation patterns (i.e. with $P_{gen,1}$ being the slack bus we vary the generator outputs between zero and P_{max} in $10\,\mathrm{MW}$ ($P_{gen,2/3}$) and $12.5\,\mathrm{MW}$ ($P_{gen,4/5}$) steps, respectively. Moreover, this is done at 13 different load

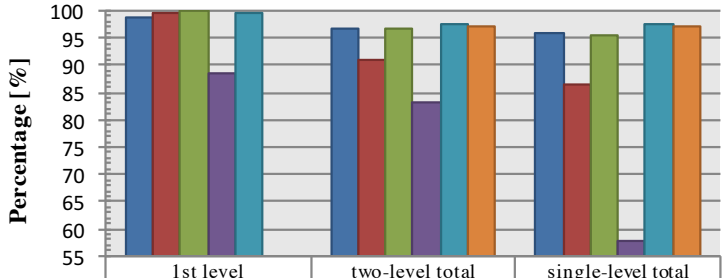

	1st level	two-level total	single-level total
DT	98.82	96.75	95.79
SVM (lin)	99.42	91.13	86.53
SVM (cubic)	100.00	96.55	95.48
AdaBoost	88.47	83.19	57.59
RUSBoost	99.65	97.55	97.40
LogitBoost	0.00	97.18	97.00

Figure 7.6: Accuracies of the single level and two-level approach.

levels (between 70 % and 112.5 %). This results in total of over 63'000 scenarios and more than 70 GB of raw data. For the robustness analysis in the second part of the case study over 20'000 additional scenarios are created with the details given in that subsection.

The PMUs are assumed to provide 60 samples per second. We assumed that all line faults are cleared after 100 ms by tripping the corresponding line without re-closing it. Scenarios are declared as unacceptable if the voltage trajectories fulfill the NERC recommendations for under voltage load-shedding settings. That means: After fault clearing, a minimum of 70% of nominal voltage should be maintained at any bus and not fall below 80% for more than 40 cycles at load buses [192].

7.7.1 Single Level

The results for the different supervised machine learning approaches are shown in Fig. 7.6 in which the prediction accuracies of the test set for the single level approach are given in the last column. The results indicate that quite high accuracies can be achieved using only local post-disturbance measurements. Although the linear SVM and the AdaBoost ensemble achieve unacceptable accuracies of 57.6 % and 86.5 %, a single DT achieves 95.5 %, while the ensemble methods LogitBoost and RUSBoost achieve even higher accuracies of 97 % and 97.4 %, respectively.

Thus, compared to literature where accuracies between 96 % and 99 % have been reported for approaches using global measurements [171, 210, 219], we observe that we can achieve similar accuracies with our single-level approach, based only on local measurements, as outlined in this work.

7.7.2 Two-Level Approach

The results of the two-level approach are shown in Fig. 7.6 as well and numerical values are given in the second column for just the 1st level and in the third column for both levels combined. The accuracies of the different supervised learning algorithms are given for the test set. Since LogitBoost is not capable of classifying more than two classes, the best first level classifier (SVM cubic 100 % accuracy) was used within the first level, while the LogitBoost algorithm was used in the second level to assess the stability of the different faults.

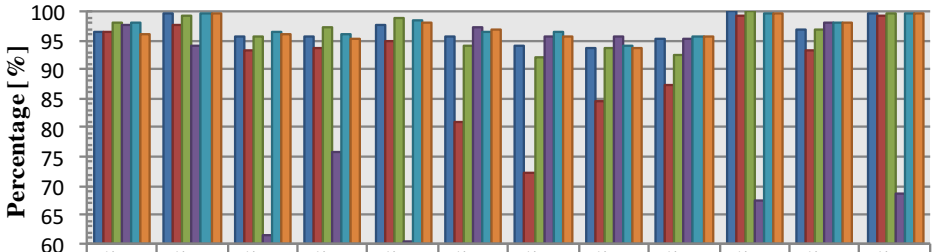

	line 1-5	line 2-3	line 2-4	line 2-5	line 3-4	line 4-5	line 4-7	line 4-9	line 5-6	line 6-11	line 6-12	line 6-13
DT	96.52	99.65	95.56	95.62	97.73	95.72	93.95	93.69	95.34	99.91	96.77	99.56
SVM (lin)	96.30	97.73	93.10	93.58	94.99	80.89	72.02	84.62	87.16	99.21	93.11	99.30
SVM (cubic)	97.87	99.21	95.65	97.45	98.68	94.15	92.25	93.57	92.52	99.91	96.77	99.83
AdaBoost	97.53	94.15	61.63	75.87	60.30	97.21	95.84	95.84	95.25	67.54	98.17	68.76
RUSBoost	97.98	99.48	96.60	96.23	98.58	96.60	96.31	94.20	95.69	99.83	98.25	99.83
LogitBoost	96.19	99.56	96.22	95.32	97.92	96.77	95.56	93.57	95.78	99.83	98.08	99.65

Figure 7.7: Accuracies of different supervised machine learning methods for the second level (i.e. different line faults) within the two-level approach.

It is shown that very high accuracies can be achieved for the first level assessment, i.e. the fault location determination, with SVM cubic reaching $100\,\%$ accuracy. Only the AdaBoost method achieves an unacceptable low accuracy of $88.5\,\%$. It is worth mentioning that the misclassifications of all methods are limited to the lines of the extended neighborhood. That means that the methods sometimes fail to distinguish between faults on those lines connecting extended neighbour nodes to the same neighbour node, since they share similar characteristics in the local measurements at the strategic node. For example, faults on the lines between bus 6 and 11 and bus 6 and 12 are misclassified as each other.

In order to raise the accuracy at the first level, we examined a modification to our approach. By clustering these lines prone to misclassifications, i.e. those connecting extended neighbor buses to the same neighbor bus, accuracies of $100\,\%$ can be achieved with all methods. However, this came at the cost of reducing the accuracies of the second level assessment, resulting at the end in a reduction of the overall assessment accuracy.

It is worth mentioning that, because the misclassification at the first level occurs only within small groups of specific faults, and these faults show similar characteristics in the local measurements at the strategic node, the classifiers of each of these faults share also similarities. This allows to achieve a high accuracy of $95.3\,\%$ in the acceptable / unacceptable classification, even if due to the misclassification at the first level a classifier corresponding to a different fault is used.

The results of the second level assessment are shown for all supervised machine learning methods in Fig. 7.7. It is shown that most methods (DT, SVM cubic, LogitBoost and RUSBoost) achieve accuracies between $93\,\%$ and $99.9\,\%$. It, is also shown that the accuracies vary quite noticeably for the different faults and the different supervised machine learning methods. Unlike one might expect, the accuracies of faults on lines not directly connected to the strategic node (bus 5) are not lower compared to those on lines directly connected to it. Further, the performance of the supervised machine learning methods varies for the different faults, i.e. that e.g. AdaBoost underperforms for specific faults with very low accuracies of e.g. $60.3\,\%$ (fault on the line between bus 3 and 4), but at the same time AdaBoost outperforms the remaining methods for other faults:

e.g. $97.2\,\%$ (fault on the line 4-5). Thus, it is shown that it could be beneficial to choose different supervised machine learning methods within the second level assessment in order to increase the overall accuracy.

As indicated by the overall accuracies given in Fig. 7.6, it is shown that the overall accuracies can slightly be increased with the two-level assessment compared to the single level assessment while at the same time reducing the size of the trees. Similar to the single level assessment the highest accuracy can be achieved using the RUSBoost ensemble method with $97.6\,\%$ accuracy. However, in case we combine the best performing machine learning method of each fault we can further increase the accuracy to $97.8\,\%$ using all different machine learning methods except SVM (lin) at least once.

7.7.3 Robustness Analysis

One issue data-driven approaches are often criticized for is their robustness against changes in the system. Therefore, the following subsections analyze in detail how the approach reacts to changes in the grid, i.e. an outage of a line outside of the extended neighbourhood of the strategic node, and to changes of the load configuration.

Robustness against Changes in the Grid Topology

For the analysis of the robustness against changes in the grid topology, we change the system by taking offline the line between bus 13 and 14. This is a line that is not included in the stability assessment but that is directly connected to a bus $\in N_5^e(G)$. Thus, a rather high impact is expected compared to changes in the grid further away from the assessed region.

We created 110 scenarios for each of the same 13 load levels for each of the faults on the lines between the buses '2-4', '4-5', '4-9', '5-6', '6-11', '6-12', '6-13'. These scenarios are tested with the classifiers obtained with the initial grid status. The results are shown in Fig. 7.8. As expected the accuracies of all second level classifiers decrease significantly, even the accuracies of the first level classifiers, i.e. the fault location detection is significantly lower. The single level classifiers show similar results.

Although this supports the criticism on data-driven tools, we believe this issue can be solved, at least for changes in the grid. Since the SCADA system and state estimator will track potential changes in the grid, different classifiers could be trained for every outage which are then activated in case changes in the grid are detected. This, however, remains to be tested.

Robustness against Changes in the Load Configuration

For the analysis of the robustness against changes in the load configuration, we created two new load configurations of all dynamic loads:

- configuration 1: $20\,\%$ large motors, $35\,\%$ small motors, $1\,\%$ transformer exciting current, $15\,\%$ discharge lighting, $10\,\%$ constant power and $19\,\%$ remaining loads.
- configuration 2: $17.5\,\%$ large motors, $42.5\,\%$ small motors, $1\,\%$ transformer exciting current, $17.5\,\%$ discharge lighting, $7.5\,\%$ constant power and $14\,\%$ remaining loads.

We created 110 scenarios for the same 13 load levels for each of the faults on the lines between the buses '2-4', '4-5', '4-7', '5-6' for each of both configurations. These scenarios are tested with the classifiers obtained with the initial load configuration.

The analysis shows that the more the configuration differs from the initial configuration the classifier was trained with, the more the accuracy of the classifier decreases. That means that the results for configuration 1 are worse than for configuration 2. The accuracy decrease is similar for all supervised machine learning methods ($\approx 5 - 15$ percentage points for configuration 2 depending on the fault) except for SVM (cubic) which loses between 5 and 30 percentage points for configuration 2 depending on the fault. While the first level classifiers are not impacted by other load configurations, the accuracy of the single level classifiers decreases similarly to the second level classifiers.

Based on these results, new classifiers are trained using the initial training set enriched by the additional scenarios of configuration 1. This provides an indication whether classifiers trained for a range of configurations (initial configuration + configuration 1) are capable of identifying a configuration somewhere within this range.

The results indicate that the accuracies are even lower compared to the previous analysis which demonstrates that additional predictors helping to distinguish between load configurations are necessary. However, since this approach is supposed to learn from real PMU data and load configuration changes follow mostly patterns through the day, the week and seasons of the year [227], additional predictors as the time of the day, the weekday and the date will help to distinguish between them and therefore increase the accuracy compared to this simplified test. Thus, in a real system if the classifier is trained with seasonal measurement data, we believe the accuracy would not necessarily decrease that much. This, however, remains to be tested.

7.8 Conclusion and Outlook

Two data-driven stability assessment methods based on *local* measurements have been proposed in this work. Compared to a wide-area monitoring and control system, these methods enable

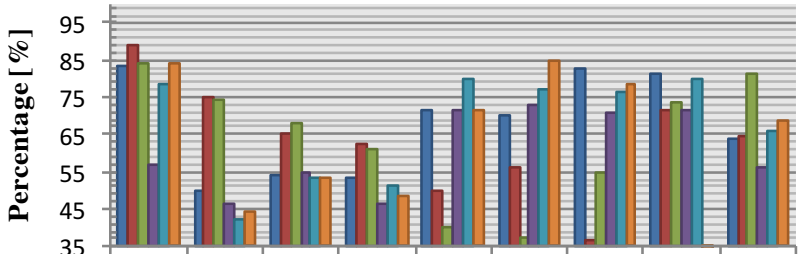

	line 2-4	line 4-5	line 4-9	line 5-6	line 6-11	line 6-12	line 6-13	first level	single level
DT	83.78	49.72	54.05	53.41	71.45	70.34	83.02	81.00	63.70
SVM (lin)	88.95	75.31	65.14	62.33	49.97	55.86	36.87	71.33	64.77
SVM (cubic)	84.06	74.69	67.91	61.07	40.40	37.01	55.02	73.69	81.16
AdaBoost	56.99	46.71	54.61	46.66	71.45	72.77	70.82	71.79	56.29
RUSBoost	78.81	42.52	53.64	51.04	79.83	77.20	76.78	80.16	66.29
LogitBoost	83.92	44.34	53.71	48.61	71.38	85.03	78.59	0.00	68.73

Figure 7.8: Accuracies of the supervised machine learning methods for specific faults after taking line '13-14' offline.

control actions to be initiated significantly faster at similar prediction accuracies, with the two-level approach performing better than the single level approach.

Most of the tested methods demonstrated a very good performance, with four out of six methods achieving accuracies over $96\,\%$. The highest performance was achieved with SVM and ensemble methods reaching accuracies up to $97.6\,\%$.

Further, the robustness of the approaches against changes in the system topology and the load configuration has been investigated. We observed that the performance, especially for some methods, reduced below acceptable levels. However, we expect that communication with SCADA, or integration of the methods proposed in this work to a local state estimator, could help to maintain a robust good performance against topology changes. Concerning varying load configurations, additional predictors need to be considered. According to [227], loads follow typical (time related) patterns. If such information is included, higher accuracies for varying loads could potentially be achieved. Both assumptions still need to be verified in future work though.

Given that none of the data-driven methods achieves $100\,\%$ prediction accuracy in any scenario, these approaches could not completely replace local control and protection schemes. However, the proposed methods enable fast instability predictions with high accuracy based on local post-disturbance measurements even before a potential subsequent voltage collapse becomes visible in the voltage magnitude. Thus, they indicate high potential to support and enhance local control and protection systems enabling potentially fast local corrective control actions.

While also literature shows that more complex machine learning methods are capable of achieving higher accuracies, there is a trade-off between performance and the ability for the user to intuitively interpret the results. So, the first step towards an application of a data-driven methodology that supports and enhances local control is probably more likely to be based on an easily comprehensible machine learning method as for instance a decision tree which admittedly performs slightly worse but enables a good understanding of the decision making process. Nevertheless, future work should also investigate the performance of more complex machine learning methods as e.g. LSTM networks which have demonstrated good performance in predicting fault occurrences [226] or other fields as fault detection in railway applications [228] or sensor node fault detection in wireless sensor networks [229].

As this study was just the first step towards a data-driven local support method enhancing power system stability, there are plenty of steps to take in future work. The methods have to be tested in larger systems, it has to be investigated how a potential instability prediction could exactly be used within the control system of e.g. a HVDC terminal. Initial thoughts as changing the prioritization between active and reactive power enabling reactive power at the costs of a reduction of the active power transfer or determining an artificial optimal error trajectory as input to the voltage controller enhancing its response need to be investigated in detail and developed further based on the results. Thus, this work should be seen as an initial study towards an interesting study topic which potentially could enhance power system stability.

CHAPTER 8

Conclusion and Outlook

This thesis focused on important aspects of the integration of Multi-Terminal High-Voltage Direct Current (MT-HVDC) grids and the application of data-driven methods in power systems to increase power system security. As a first step, we investigated the potential of AC and HVDC lines in Europe; we found that several new HVDC lines are indispensable in the future European transmission network to meet the renewable energy source (RES) integration targets of the European Union. Ideally, these lines must become parts of a MT-HVDC grid in order to minimize costs and increase reliability. Based on this study, we developed a policy recommendation highlighting that a coordinated upgrade of both AC and DC network is essential to achieve the full potential of either technology.

As such a MT-HVDC grid would most likely not be built at once by a single vendor but rather be developed by a step-wise integration of already existing on- and offshore inter-connectors, we investigated potential multi-vendor interoperability issues and the impact of different control structures on power system stability. Following the in-depth analysis, two specific dc voltage droop control structures are recommended based on their superior performance in the studies. Moreover, a methodology has been developed allowing to determine the operation space of an arbitrary MT-HVDC with freely selectable requirements. This methodology could be used by a third party using the specific models of different vendors in order to identify potential interoperability issues for specific project topologies. In [130], Oliver Despouys from RTE suggests such an approach as a way to circumvent any potential intellectual property theft threads which otherwise appear by demanding the vendors to exchange their control algorithms to ensure interoperability.

Considering that VSC-HVDC systems do not only introduce new challenges but also new opportunities, such preventive and corrective control. Taking also into account the increasing availability of measurement data, and the recent advances in data-driven approaches, we develop methods allowing us to enrich and use the available measurement data to increase power system security. As historical data often contain limited number of abnormal situations, simulation data are necessary to accurately determine the security boundary. Therefore, we developed a modular and efficient database generation method for data-driven security assessment of power systems which is scalable to large systems and detailed models. Leveraging advancements in convex relaxation techniques and complex network theory approaches, we develop a highly parallelizable algorithm which efficiently explores the search space and can determine the security boundary with extremely high accuracy. Our approach is highly scalable, modular, and achieves drastic speed-ups compared with existing methods.

Moreover, using the data, we take a more holistic view, and we combine the data-driven security assessment with optimization for operations and markets. Thereby, we leverage advantages of controlability of VSC-HVDC, efficient data generation and data-driven methods to minimize power system operation costs. By deriving tractable decision rules from the databases, we implement security considerations in the form of line flow limits in market-clearing and power system

operation algorithms. Our approach allows to enlarge the feasible space to the real non-convex feasible space leading to more cost-efficient still secure dispatch results mitigating redispatching actions. Thus, we incorporate detailed small-signal stability and preventive-(corrective) security considerations into market-clearing and power system operation methods. Case studies highlight the superior performance of our methods compared to current approaches. Moreover, given the capabilities of Mixed-Integer Linear Programming (MILP) solvers, these methods are scalable to medium and large systems.

Finally, inspired by the development of the data-driven security assessment, we developed a first proof-of-concept of how such methods can not only assess security, but also predict the criticality of faults based on local measurements only without requiring communication. Ideally, such a method could be developed into a local control support method for HVDC terminals enabling the HVDC terminal potentially not only to react to measurements but act on stability predictions and thereby potentially prevent fast evolving short-term voltage stability problems.

8.1 Future work

With increasing discussions of potential MT-HVDC grid developments in Europe, more research is required on several different aspects for an optimal integration in daily operation of power systems:

(i) Potential multi-vendor interoperability issues need to be investigated in detail, ideally using control replicas of the different vendors. Our proposed methodology could then be used by a third party in order to identify potential interoperability issues for specific project topologies.

(ii) The flexibility and corrective control capability of a MT-HVDC grid should be explored. The proposed security constrained OPF methods should be developed further by incorporation uncertainty by using chance constrains. So far the uncertainty of RES is separated from the problem in that sense that we rely on a precise forecast. However, the next step is to include the uncertainty within the OPF allowing us to include more detailed probabilistic forecasts. Then, using chance constraints we could ensure that the dispatch is always secure for the given confidence intervals. Moreover, the databases should be enriched by time-domain simulations ensuring the feasibility of the trajectory from pre-disturbance to post-disturbance state.

(iii) The proposed database generation method should be extended in order to incorporate HVDC lines and allow to create databases considering corrective control actions. This would allow to create a case study of the data-driven preventive-corrective SC-OPF on a larger network.

(iv) The concept of enhancing control structures by data-driven control support methods should be investigated in detail. Given the classification and prediction performance of machine learning approaches, we foresee high potential in increasing the capabilities of control structures. As a first step, we could imagine using the data-driven support methods for determining the optimal control gains for the specific operating conditions. Finally, given increasing accuracies and generalization capabilities of machine learning methods, we could imagine that data-driven control support methods could enable control structures not only to react to measurements but act on (stability) predictions.

Bibliography

[1] P. Kundur, J. Paserba, V. Ajjarapu, G. Andersson, A. Bose, C. Canizares, N. Hatziargyriou, D. Hill, A. Stankovic, C. Taylor, T. Van Cutsem, and V. Vittal, "Definition and Classification of Power System Stability," *IEEE Transactions on Power Systems*, vol. 21, no. 3, pp. 1387–1401, 2004.

[2] European Network of Transmission System Operators (ENTSO-E), "Net Transfer Capacities (NTC) Available Transfer Capacities (ATC)," European Network of Transmission System Operators (ENTSO-E), Tech. Rep., 2000.

[3] K. Van den Bergh, J. Boury, and E. Delarue, "The Flow-Based Market Coupling in Central Western Europe: Concepts and definitions," *Electricity Journal*, vol. 29, no. 1, pp. 24–29, 2016. [Online]. Available: http://dx.doi.org/10.1016/j.tej.2015.12.004

[4] C. Zhang and Y. Ma, Eds., *Ensemble Machine Learning*. Springer Science+Business Media, Inc., 2012.

[5] J. Beerten, S. D'Arco, and J. A. Suul, "Frequency-dependent cable modelling for small-signal stability analysis of VSC-HVDC systems," *IET Generation, Transmission & Distribution*, vol. 10, no. 6, 2016.

[6] S. D'Arco, J. A. Suul, and M. Molinas, "Implementation and Analysis of a Control Scheme for Damping of Oscillations in VSC-based HVDC Grids," in *16th International Power Electronics and Motion Control Conference and Exposition*, Antalya, Turkey 21-24, 2014, pp. 586–593.

[7] F. Mei, "Small - Signal Modelling and Analysis of Doubly - Fed Induction Generators in Wind Power," Ph.D. dissertation, Impeial College London, 2008. [Online]. Available: https://spiral.imperial.ac.uk/handle/10044/1/4249

[8] L. M. Fernández, F. Jurado, and J. R. Saenz, "Aggregated dynamic model for wind farms with doubly fed induction generator wind turbines," *Renewable Energy*, vol. 33, no. 1, pp. 129–140, 2008. [Online]. Available: http://linkinghub.elsevier.com/retrieve/pii/S0960148107000250

[9] E. Prieto-Araujo, A. Egea-Alvarez, S. F. Fekriasl, and O. Gomis-Bellmunt, "DC voltage droop control design for multi-terminal HVDC systems considering AC and DC grid dynamics," *IEEE Transactions on Power Delivery*, vol. 31, no. 2, pp. 575 – 585, 2015.

[10] R. Preece and J. V. Milanovic, "Efficient Estimation of the Probability of Small-Disturbance Instability of Large Uncertain Power Systems," *IEEE Trans. on Power Systems*, vol. 31, no. 2, pp. 1063–1072, 2016.

[11] S. Kodsi and C. Canizares, "Modeling and simulation of IEEE 14-bus system with FACTS controllers," University of Waterloo, Waterloo, Canada, Tech. Rep., 2003.

[12] KUL Energy Institute, "Fact Sheet: Cross-border electricity trading - towards flow-based market coupling," *KUL Energy Institute*, no. February, pp. 1–5, 2015.

[13] Power Technologies Inc., "Chapter 19: Load Modeling," *Program Application Guide: Volume II*.

[14] S. Akkari, E. Prieto-Araujo, J. Dai, O. Gomis-Bellmunt, and X. Guillaud, "Impact of the DC cable models on the SVD analysis of a Multi-Terminal HVDC system," in *19th Power Systems Computation Conference (PSCC)*, Genoa, 2016, pp. 1–6.

[15] F. Milano, *Power System Modelling and Scripting*. Springer-Verlag Berlin Heidelberg, 2010.

[16] P. M. Anderson and A. A. Fouad, "Power Systems Control and Stability," Ames, Iowa, USA, p. 464, 1977.

[17] D. V. Hertem, O. Gomis-Bellmunt, and J. Liang, Eds., *HVDC grids: for offshore and supergrid of the future*. Wiley-IEEE Press, 2016.

[18] S. Saeed, "A Snapshot of Flexible AC Transmission Systems (FACTS) Market in Europe," Power Technology Research, Tech. Rep., 2018. [Online]. Available: https://powertechresearch.com/a-snapshot-of-flexible-ac-transmission-systems-facts-market-in-europe/

[19] Bundesnetzagentur, "Quartalsbericht zu Netz- und Systemsicherheitsmaßnahmen Gesamtjahr und Viertes Quartal 2017," Bundesnetzagentur für Elektrizität, Gas, Telekommunikation, Post und Eisenbahnen, Bonn, Tech. Rep., 2018. [Online]. Available: https://www.bundesnetzagentur.de/SharedDocs/Downloads/DE/Allgemeines/Bundesnetzagentur/Publikationen/Berichte/2018/Quartalsbericht{_}Q4{_}Gesamt{_}2017.pdf?{_}{_}blob=publicationFile{&}v=3

[20] M. Laux, "Redispatch in Deutschland," BDEW Bundesverband der Energie- und Wasserwirtschaft e.V., Berlin, Tech. Rep., 2018. [Online]. Available: https://www.bdew.de/media/documents/Awh{_}20180212{_}Bericht{_}Redispatch{_}Stand{_}Februar-2018.pdf

[21] United Nations Framework Convention on Climate Change, "The Paris Agreement," United Nations, Paris, Tech. Rep., 2015. [Online]. Available: https://treaties.un.org/doc/Treaties/2016/02/2016021506-03PM/Ch{_}XXVII-7-d.pdf

[22] European Network of Transmission System Operators (ENTSO-E), "TYNDP 2018 - Scenario Report," European Network of Transmission System Operators (ENTSO-E), Tech. Rep., 2018. [Online]. Available: https://www.entsoe.eu/Documents/TYNDPdocuments/TYNDP2018/Scenario{_}Report{_}2018{_}Final.pdf?Web=1

[23] 50Hertz Transmission GmbH, Amprion GmbH, TenneT TSO GmbH, and TransnetBW GmbH, "Hochspannungs-Gleich- strom-Übertragung | Netzentwicklungsplan," 2018. [Online]. Available: https://www.netzentwicklungsplan.de/de/wissen/hochspannungs-gleich-strom-uebertragung [Accessed: 2018-05-28]

[24] A. Orths, A. Hiorns, R. van Houtert, L. Fisher, and C. Fourment, "The European North Seas Countries' Offshore Grid initiative - The way forward," *2012 IEEE Power & Energy Society General Meeting. New Energy Horizons - Opportunities and Challenges*, pp. 1–8, 2012.

[25] TenneT Holding B.V and TenneT TSO B.V., "Three TSOs sign agreement on North Sea Wind Power Hub," 2017. [Online]. Available: https://northseawindpowerhub.eu/23-march-2017-three-tsos-sign-agreement-on-north-sea-wind-power-hub/ [Accessed: 2018-05-28]

[26] G. Bathurst and P. Bordignan, "Delivery of the Nan'ao Multi-terminal VSC-HVDC System," in *Cigré International Symposium - Across Borders - HVDC Systems and Market Integration*, no. December 2013, Lund, 2015, pp. 1–12.

[27] R. Eriksson, "Coordinated Control of HVDC Links in Transmission Systems," Ph.D. dissertation, KTH, 2011.

[28] F. Capitanescu, J. L. Martinez Ramos, P. Panciatici, D. Kirschen, A. Marano Marcolini, L. Platbrood, and L. Wehenkel, "State-of-the-art, challenges, and future trends in security constrained optimal power flow," *Electric Power Systems Research*, vol. 81, no. 8, pp. 1731–1741, 2011.

[29] F. Capitanescu, "Critical review of recent advances and further developments needed in AC optimal power flow," *Electric Power Systems Research*, vol. 136, pp. 57–68, 2016.

[30] T. V. Cutsem, "Instability of Voltage Source Converters in weak AC grid conditions : a case study," in *IEEE PES General Meeting*, Chicago, USA, 2017, pp. 1–24.

[31] EirGrid, "Operating Security Standards," EirGrid, Tech. Rep. April, 2010. [Online]. Available: http://www.eirgridgroup.com/site-files/library/EirGrid/Operating-Security-Standards-December-2011.pdf

[32] C. D. Vournas, S. Member, and E. G. Potamianakis, "Investigation of Short-term Voltage Stability Problems and Countermeasures," in *IEEE PES Power Systems Conference and Exposition*, New York, 2004, pp. 385 – 391.

[33] C. A. Baone, Y. Xu, and J. D. Kueck, "Local voltage support from distributed energy resources to prevent air conditioner motor stalling," *Innovative Smart Grid Technologies Conference, ISGT 2010*, pp. 1–6, 2010.

[34] Synchronized Measurement Subcommittee of North American Electric Reliability Corporation (NERC), "Fault Induced Delayed Voltage Recovery (FIDVR) Advisory," North American Electric Reliability Corporation (NERC), Tech. Rep. July, 2014. [Online]. Available: https://www.nerc.com/comm/PC/SynchronizedMeasurementSubcommittee/FIDVRAlert07-2015.pdf

[35] North American Electric Reliability Corporation - Transmission Issues Subcommittee and System Protection and Control Subcommittee, "A Technical Reference Paper Fault-Induced Delayed Voltage Recovery," North American Electric Reliability Corporation, Tech. Rep., 2009.

[36] The European Commission, "COMMISSION REGULATION (EU) 2017/ 1485 - of 2 August 2017 - establishing a guideline on electricity transmission system operation," The European Commission, Tech. Rep. 2, 2017. [Online]. Available: http://eur-lex.europa.eu/legal-content/EN/TXT/PDF/?uri=CELEX:32017R1485{&}from=EN

[37] Bundesnetzagentur, "Market Coupling - Kopplung der europäischen Stromgroßhandelsmärkte," 2016. [Online]. Available: https://www.bundesnetzagentur.de/DE/Sachgebiete/ElektrizitaetundGas/Unternehmen{_}Institutionen/HandelundVertrieb/EuropMarktkopplung/MarketCoupling.html [Accessed: 2018-08-12]

[38] NERC, "Available Transfer Capability Definitions and Determination," *North American Electric Realiability Council*, no. June, pp. 1–42, 1996.

[39] L. A. Wehenkel, *Automatic Learning Techniques in Power Systems*. Boston/London/Dordrecht: Kluwer Academic Publishers, 1998.

[40] T. Hastie, R. Tibshirani, and J. Friedman, *The Elements of Statistical Learning*, 2nd ed. Springer Science+Business Media, Inc., 2009.

[41] The MathWorks Inc., "Matlab 2017b," Natick, Massachusetts, United States.

[42] MathWorks, "Statistics and Machine Learning Toolbox," 2018. [Online]. Available: https://se.mathworks.com/help/stats/index.html [Accessed: 2018-09-15]

[43] J. Brownlee, *Machine Learning Mastery With Python*, 1st ed., Melbourne, 2016. [Online]. Available: https://machinelearningmastery.com/machine-learning-with-python/

[44] R. Eriksson, "On the centralized nonlinear control of HVDC systems using Lyapunov theory," *IEEE Transactions on Power Delivery*, vol. 28, no. 2, pp. 1156–1163, 2013.

[45] ABB, "Economic and environmental advantages," 2018. [Online]. Available: https://new.abb.com/systems/hvdc/why-hvdc/economic-and-environmental-advantages [Accessed: 2018-09-15]

[46] O. E. Oni, K. I. Mbangula, and I. E. Davidson, "A Review of LCC-HVDC and VSC-HVDC Technologies and Applications," in *16th International Conference on Environment and Electrical Engineering (EEEIC) IEEE*, vol. 1, no. 3, Florence, 2016.

[47] P. Sauer and M. Pai, *Power System Dynamics and Stability*, M. Horton, Ed. New Jersey: Prentice-Hall, Inc., 1998.

[48] I. Wolfram Research, "Mathematica," Champaign, Illinois, 2018.

[49] R. D. Zimmerman, C. E. Murillo-Sánchez, and R. J. Thomas, "MATPOWER: Steady-state operations, planning, and analysis tools for power systems research and education," *IEEE Transactions on Power Systems*, vol. 26, no. 1, pp. 12–19, 2011.

[50] D. Mondal, A. Chakrabarti, and A. Sengupta, *Power System Small Signal Stability Analysis and Control*, 1st ed. Academic Press 2014, 2014. [Online]. Available: http://linkinghub.elsevier.com/retrieve/pii/B9780128005729000056

[51] V. Akhmatov, M. Callavik, C. M. Franck, S. E. Rye, T. Ahndorf, M. K. Bucher, H. Muller, F. Schettler, and R. Wiget, "Technical guidelines and prestandardization work for first HVDC Grids," *IEEE Transactions on Power Delivery*, vol. 29, no. 1, 2014.

[52] P. Kundur, *Power system stability and control*. McGraw-Hill Professional, 1994.

[53] V. Blasko and V. Kaura, "A new mathematical model and control of a three-phase AC-DC voltage source converter," *IEEE Transactions on Power Electronics*, vol. 12, no. 1, pp. 116–123, 1997.

[54] V. Kaura and V. Blasko, "Operation of a phase locked loop system under distorted utility conditions," *IEEE Transactions on Industry Applications*, vol. 33, no. 1, pp. 58–63, 1997.

[55] W. Wang, M. Barnes, and O. Marjanovic, "Droop control modelling and analysis of multi-terminal VSC-HVDC for offshore wind farms," in *10th IET Int. Conf. on AC and DC Power Transmission*, Birmingham, 2012.

[56] C. Gavriluta, I. Candela, A. Luna, A. Gomez-Exposito, and P. Rodriguez, "Hierarchical Control of HV-MTDC Systems With Droop-Based Primary and OPF-Based Secondary," *IEEE Transactions on Smart Grid*, vol. 6, no. 3, pp. 1502–1510, 2015.

[57] O. Ramos-Leanos, J. L. Naredo, J. Mahseredjian, C. Dufour, J. A. Gutierrez-Robles, and I. Kocar, "A wideband line/cable model for real-time simulations of power system transients," *IEEE Transactions on Power Delivery*, vol. 27, no. 4, pp. 2211–2218, 2012.

[58] H. Kolstad, *Control of an Adjustable speed Hydro utilizing field programmable devices*. Trondheim: Ph.D Dissertation, 2002.

[59] J. A. Suul, S. D'Arco, P. Rodríguez, and M. Molinas, "Impedance-compensated grid synchronisation for extending the stability range of weak grids with voltage source converters," *IET Generation, Transmission & Distribution*, vol. 10, no. 6, pp. 1315–1326, 2016.

[60] L. Zhang, "Modeling and Control of VSC-HVDC Links Connected to Weak AC Systems," Ph.D. dissertation, KTH Royal Institute of Technology, 2010.

[61] M. Malinowski, M. P. Kazmierkowski, and S. Bernet, "New simple active damping of resonance in three-phase PWM converter with LCL filter," in *IEEE International Conference on Industrial Technology 2005*. IEEE, 2005, pp. 861–865.

[62] O. Mo, M. Hernes, and K. Ljøkelsøy, "Active damping of oscillations in LC-filter for line connected , current controlled , PWM voltage source converters Keywords Basic control system," in *Proc. of the 10th European Conference on Power Electronics and Applications, EPE 2003*, Toulouse, France, 2003, pp. 1–10.

[63] C. Bajracharya, M. Molinas, J. A. Suul, and T. Undeland, "Understanding of tuning techniques of converter controllers for VSC-HVDC," in *Proceedings of the Nordic Workshop on Power and Industrial Electronics*, Espoo, Finland, 2008, p. 8.

[64] C. D. Barker and R. Whitehouse, "Autonomous converter control in a multi-terminal HVDC system," in *9th IET International Conference on AC and DC Power Transmission*, London, 2010, pp. 1–5.

[65] O. Gomis-Bellmunt, J. Liang, J. Ekanayake, and N. Jenkins, "Voltage-current characteristics of multiterminal HVDC-VSC for offshore wind farms," *Elec.Power Syst. Research*, vol. 81, no. 2, pp. 440–450, 2011.

[66] L. Xu, L. Yao, and M. Bazargan, "DC grid management of a multi-terminal HVDC transmission system for large offshore wind farms," in *Int. Conf. on Sust. Power Gen. and Supply*, 2009, pp. 1–7.

[67] F. D. Bianchi and O. Gomis-Bellmunt, "Droop control design for multi-terminal VSC-HVDC grids based on LMI optimization," in *50th IEEE Conf. on Decision and Control and Europ. Control Conf.*, Orlando, 2011.

[68] L. Xu and L. Yao, "DC voltage control and power dispatch of a multi-terminal HVDC system for integrating large offshore wind farms," *Renewable Power Generation, IET*, vol. 5, no. 3, pp. 223–233, 2011.

[69] E. Prieto-Araujo, F. D. Bianchi, A. Junyent-Ferre, and O. Gomis-Bellmunt, "Methodology for Droop Control Dynamic Analysis of Multiterminal VSC-HVDC Grids for Offshore Wind Farms," *IEEE Transactions on Power Delivery*, vol. 26, no. 4, pp. 2476–2485, 2011.

[70] R. T. Pinto, S. Rodrigues, P. Bauer, and J. Pierik, "Operation and control of a multi-terminal DC network," in *IEEE ECCE Asia Downunder*, Melbourne, 2013, pp. 474–480.

[71] Y. Chen, G. Damm, and A. Benchaib, "Multi-Time-Scale Stability Analysis and Design Conditions of a VSC Terminal with DC Voltage Droop Control for HVDC Networks," in *53rd IEEE Conference on Decision and Control*, Los Angeles, CA, 2014.

[72] J. Liang, T. Jing, O. Gomis-Bellmunt, J. Ekanayake, and N. Jenkins, "Operation and Control of Multiterminal HVDC Transmission for Offshore Wind Farms," *IEEE Transactions on Power Delivery*, vol. 26, no. 4, pp. 2596–2604, 2011.

[73] B. K. Johnson, R. H. Lasseter, F. L. Alvarado, and R. Adapa, "Expandable multiterminal dc systems based on voltage droop," *IEEE Transactions on Power Delivery*, vol. 8, no. 4, 1993.

[74] S. Zhou, J. Liang, J. B. Ekanayake, and N. Jenkins, "Control of multi-terminal VSC-HVDC transmission system for offshore wind power generation," in *44th Int. Universities Power Eng. Conf.*, Glasgow, 2009.

[75] F. Thams, J. A. Suul, S. D'Arco, M. Molinas, and F. W. Fuchs, "Stability of DC Voltage Droop Controllers in VSC HVDC Systems," in *PowerTech, Eindhoven 2015*, Eindhoven, 2015.

[76] P. Rault, F. Colas, X. Guillaud, and S. Nguefeu, "Method for small signal stability analysis of VSC-MTDC grids," in *IEEE Power and Energy Society General Meeting*, San Diego, 2012.

[77] J. Dragon, L. Werner, and J. Hanson, "Effects of DC Voltage Droop Characteristics on Contingency Behaviour of AC / DC Systems," in *49th Int. Universities' Power Eng. Conf. (UPEC)*, Cluj-Napoca, 2014.

[78] T. M. Haileselassie and K. Uhlen, "Impact of DC Line Voltage Drops on Power Flow of MTDC Using Droop Control," *IEEE Transactions on Power Systems*, vol. 27, no. 3, pp. 1441–1449, 2012.

[79] ——, "Precise control of power flow in multiterminal VSC-HVDCs using DC voltage droop control," in *IEEE Power and Energy Society General Meeting*, San Diego, 2012.

[80] ——, "Primary frequency control of remote grids connected by multi-terminal HVDC," in *IEEE Power and Energy Society General Meeting*, Minneapolis, 2010, pp. 1–6.

[81] G. Stamatiou and M. Bongiorno, "Decentralized converter controller for multiterminal HVDC grids," in *15th European Conference on Power Electronics and Applications (EPE)*, 2013, pp. 1–10.

[82] F. Mei and B. C. Pal, "Modelling and small-signal analysis of a grid connected doubly-fed induction generator," *2005 IEEE Power Engineering Society General Meeting*, vol. 3, pp. 2101–2108, 2005.

[83] B. Pal and F. Mei, "Modelling adequacy of the doubly fed induction generator for small-signal stability studies in power systems," *Renewable Power Generation, IET*, vol. 2, no. 3, pp. 181–190, 2008.

[84] F. Wu, X.-P. Zhang, K. Godfrey, and P. Ju, "Small signal stability analysis and optimal control of a wind turbine with doubly fed induction generator," *Generation, Transmission & Distribution, IET*, vol. 1, no. 5, pp. 751 – 760, 2007.

[85] J. Padron and A. Lorenzo, "Calculating Steady-State Operating Conditions for Doubly-Fed Induction Generator Wind Turbines," *IEEE Transactions on Power Systems*, vol. 25, no. 2, pp. 922–928, 2010.

[86] H. Wang, Y. Zhang, and Q. Zhou, "Wind Farm Model with DFIG for Small Signal Stability Study," in *4th International Conference on Electric Utility Deregulation and Restructuring and Power Technologies*, 2011, pp. 303–307.

[87] J. Serrano-González and R. Lacal-Arántegui, "Technological evolution of onshore wind turbines—a market-based analysis," *Wind Energy*, vol. 19, pp. 2171–2187, 2016.

[88] Z. Zhang, A. Chen, A. Matveev, R. Nilssen, and A. Nysveen, "High-power generators for offshore wind turbines," *Energy Procedia*, vol. 35, no. 1876, pp. 52–61, 2013.

[89] L. Fernández, C. García, J. Saenz, and F. Jurado, "Equivalent models of wind farms by using aggregated wind turbines and equivalent winds," *Energy Conversion and Management*, vol. 50, no. 3, pp. 691–704, 2009.

[90] A. Ellis and E. Muljadi, "Wind power plant representation in large-scale power flow simulations in WECC," in *2008 IEEE Power and Energy Society General Meeting - Conversion and Delivery of Electrical Energy in the 21st Century*, vol. 87158, 2008, pp. 1–6.

[91] P. W. Sauer, M. A. Pai, and J. Chow, *Power Systems Dynamics and Stability*, 2nd ed. John Wiley & Sons, Ltd Registered, 2018.

[92] J. Beerten, S. D Arco, and J. Suul, "Identification and Small-Signal Analysis of Interaction Modes in VSC MTDC Systems," *IEEE Transactions on Power Delivery*, vol. 31, no. 2, pp. 888 – 897, 2016.

[93] European Commission, "Energy Roadmap 2050," European Commission, Tech. Rep. April, 2012. [Online]. Available: http://www.roadmap2050.eu/

[94] Aloys Nghiem and I. Pineda, "Wind Energy in Europe: Scenarios For 2030," Wind Europe, Tech. Rep. September, 2017. [Online]. Available: https://windeurope.org/wp-content/uploads/files/about-wind/reports/Wind-energy-in-Europe-Scenarios-for-2030.pdf

[95] International Energy Agency, "IEA wind TCP 2016 Annual Report," International Energy Agency, Tech. Rep., 2016. [Online]. Available: https://community.ieawind.org/publications/ar

[96] B. Chabot, "Onshore and Offshore Wind Power Capacity Factors: How Much they Differ Now and in the Future? - A case study from Denmark," *Erneuerbare Energien*, pp. 1–9, sep 2013. [Online]. Available: https://www.erneuerbareenergien.de/files/smfiledata/3/1/7/2/7/1/V2BC37NhCFWindDK.pdf

[97] G. Ellis and G. Ferraro, "The social acceptance of wind energy Title: Social acceptance of wind energy," Joint Research Centre (JRC), Tech. Rep., 2016. [Online]. Available: http://publications.jrc.ec.europa.eu/repository/bitstream/JRC103743/jrc103743{_}2016.7095{_}src{_}en{_}socialacceptanceofwind{_}am-gffinal.pdf

[98] European Wind Energy Association, "The European offshore wind industry key 2015 trends and statistics," European Wind Energy Association, Tech. Rep. January, 2015. [Online]. Available: http://scholar.google.com/scholar?hl=en{&}btnG=Search{&}q=intitle:The+European+offshore+wind+industry+-+key+trends+and+statistics+2012{#}1

[99] Niharika, S. Verma, and V. Mukherjee, "Transmission expansion planning: A review," *2016 International Conference on Energy Efficient Technologies for Sustainability (ICEETS)*, pp. 350–355, 2016.

[100] R. Hemmati, R. A. Hooshmand, and A. Khodabakhshian, "State-of-the-art of transmission expansion planning: Comprehensive review," *Renewable and Sustainable Energy Reviews*, vol. 23, pp. 312–319, 2013.

[101] S. Lumbreras and A. Ramos, "The new challenges to transmission expansion planning. Survey of recent practice and literature review," *Electric Power Systems Research*, vol. 134, pp. 19–29, 2016.

[102] S. Lumbreras, A. Ramos, F. Banez-Chicharro, L. Olmos, P. Panciatici, C. Pache, and J. Maeght, "Large-scale transmission expansion planning: from zonal results to a nodal expansion plan," *IET Generation, Transmission & Distribution*, vol. 11, no. 11, pp. 2778–2786, 2017.

[103] German Energy Agency, "e-Highway2050," 2013. [Online]. Available: http://www.e-highway2050.eu/e-highway2050/ [Accessed: 2018-04-09]

[104] M. Majidi-Qadikolai and R. Baldick, "A Generalized Decomposition Framework for Large-Scale Transmission Expansion Planning," *IEEE Transactions on Power Systems*, vol. 33, no. 2, pp. 1635–1649, 2018.

[105] E3M Lab/NTUA and IIASA, "Technical report on Member State results of the EUCO policy scenarios," E3MLab & IIASA, Tech. Rep. December, 2016. [Online]. Available: https://ec.europa.eu/energy/sites/ener/files/documents/20161219{_}-{_}technical{_}report{_}on{_}euco{_}scenarios{_}primes.pdf

[106] European Network of Transmission System Operators (ENTSO-E), "Ten Year Network Development Plan (TYNDP) 2016," 2016. [Online]. Available: https://tyndp.entsoe.eu/2016/[accessedon10April2018] [Accessed: 2018-04-09]

[107] ——, "ENTSO-E Statistical Factsheet 2016," 2018. [Online]. Available: https://docstore.entsoe.eu/Documents/Publications/Statistics/Factsheet/entsoe{_}sfs{_}2016{_}web.pdf [Accessed: 2018-04-17]

[108] ——, "Power Statistics - Montly Domestic Values," 2016. [Online]. Available: https://www.entsoe.eu/data/power-stats/monthly-domestic/ [Accessed: 2018-04-09]

[109] The Federal Government, "Perspectives for Germany: Our Strategy for Sustainable Development (in English)," The Federal Government, Tech. Rep., 2002. [Online]. Available: https://m.bundesregierung.de/Content/EN/StatischeSeiten/Schwerpunkte/Nachhaltigkeit/Anlagen/perspektives-for-germany-langfassung.pdf?{_}{_}blob=publicationFile{&}v=1

[110] Bundesverband WindEnergie, "Bundesverband WindEnergie - Netze," 2018. [Online]. Available: https://www.wind-energie.de/themen/netze[accessedon10April2018] [Accessed: 2018-04-09]

[111] Bundesverband Solarwirtschaft E.V., "Ausbau und Ertüchtigung des Niederspannungsnetzes zur Aufnahme großer Mengen an Photovoltaik," Bundesverband Solarwirtschaft E.V., Tech. Rep., 2012. [Online]. Available: https://www.solarwirtschaft.de/fileadmin/media/pdf/bsw{_}hintergr{_}netzausbau.pdf

[112] I. Staffell and S. Pfenninger, "Using bias-corrected reanalysis to simulate current and future wind power output," *Energy*, vol. 114, pp. 1224–1239, 2016.

[113] S. Pfenninger and I. Staffell, "Long-term patterns of European PV output using 30 years of validated hourly reanalysis and satellite data," *Energy*, vol. 114, pp. 1251–1265, 2016.

[114] ——, "Renewables.ninja," 2015. [Online]. Available: https://www.renewables.ninja/ [Accessed: 2018-04-17]

[115] T. Overbye, Xu Cheng, and Yan Sun, "A comparison of the AC and DC power flow models for LMP calculations," in *37th Annual Hawaii International Conference on System Sciences, 2004. Proceedings of the*, 2004, p. 9 pp.

[116] S. Chatzivasileiadis, "Power System Planning and Operation Methods Integrating the Controllability of HVDC," Ph.D. dissertation, ETH Zurich, 2013. [Online]. Available: http://e-collection.library.ethz.ch/eserv/eth:7678/eth-7678-02.pdf

[117] ABB, "Introducing HVDC," ABB, Tech. Rep., 2014. [Online]. Available: www.abb.com

[118] T. M. Haileselassie and K. Uhlen, "Power System Security in a Meshed North Sea HVDC Grid," *Proceedings of the IEEE*, vol. 101, no. 4, pp. 978–990, 2013.

[119] T. K. Vrana, J. Beerten, R. Belmans, and O. B. Fosso, "A classification of DC node voltage control methods for HVDC grids," *Electric Power Systems Research*, vol. 103, pp. 137–144, 2013.

[120] R. T. Pinto, S. F. Rodrigues, and P. Bauer, "Comparison of direct voltage control methods of multi-terminal DC (MTDC) networks through modular dynamic models," in *Proceedings of the 2011-14th European Conference on Power Electronics and Applications (EPE 2011)*, Birmingham, 2011.

[121] W. Wang, M. Barnes, and O. Marjanovic, "Stability Limitation and Analytical Evaluation of Voltage Droop Controllers for VSC MTDC," *CSEE Journal of Power and Energy Systems*, vol. 4, no. 2, pp. 238–249, 2018.

[122] C. Buchhagen, C. Rauscher, A. Menze, and J. Jung, "BorWin1 - First Experiences with harmonic interactions in converter dominated grids," *International ETG Congress 2015; Die Energiewende - Blueprints for the new energy age*, pp. 27–33, 2015.

[123] H. Saad, "Performance Analysis of INELFE link with control replicas," in *Workshop of 'Real-Time simulations to support installation and operation of HVDC/FACTS on transmission grids' durin Cigré Sessions 2016*, 2016.

[124] T. M. Haileselassie, M. Molinas, and T. Undeland, "Multi-terminal VSC-HVDC system for integration of offshore wind farms and green electrification of platforms in the North Sea," in *Nordic Workshop on Power and Industrial Electronics (NORPIE/2008)*, Espoo, Finland, 2008, p. 8.

[125] T. K. Vrana, "System Design and Balancing Control of the North Sea Super Grid," Ph.D. dissertation, NTNU, Trondheim, 2013.

[126] A. Endegnanew, J. Beerten, and K. Uhlen, "Dynamic interactions between asynchronous grids interconnected through an MTDC system A." in *Cigré International Symposium - Across Borders - HVDC Systems and Market Integration*, 2015.

[127] Y. Liu, A. Raza, K. Rouzbehi, B. Li, D. Xu, and B. Walliams, "Dynamic Resonance Analysis and Oscillation Damping of Multi-Terminal DC Grids," *IEEE Access*, vol. 3536, no. c, 2017.

[128] A. Bayo-Salas, J. Beerten, E. Prieto-Araujo, O. Gomis-Bellmunt, and D. Van Hertem, "Mitigation of harmonic interactions by the VSC-HVDC converter in variable networks," *IET Conference Publications*, vol. 2017, no. CP709, pp. 1–8, 2017.

[129] N. A. Cutululis, "Multi-terminal DC grid for offshore wind (MEDOW)," DTU Wind Energy, Tech. Rep., 2018. [Online]. Available: http://orbit.dtu.dk/files/146792252/MEDOW{_}Final{_}Report{_}April2018.pdf

[130] R. Parsons, "Direct current grids: interoperability is a key factor for their development," youris.com GEIE, pp. 1–2, 2018. [Online]. Available: https://euagenda.eu/publications/direct-current-grids-interoperability-is-a-key-factor-for-their-development [Accessed: 2018-06-14]

[131] H. Saad, X. Guillaud, J. Mahseredjian, S. Dennetiere, and S. Nguefeu, "MMC Capacitor Voltage Decoupling and Balancing Controls," *IEEE Transactions on Power Delivery*, vol. 30, no. 2, pp. 704–712, 2014.

[132] J. Beerten, R. Eriksson, D. V. Hertem, and S. Member, "A New Approach to HVDC Grid Voltage Control Based on Generalized State Feedback," in *Proceedings of 2014 IEEE PES General Meeting*, 2014, pp. 1–5.

[133] P. Apkarian, V. Bompart, and D. Noll, "Non-smooth structured control design with application to PID loop-shaping of a process," *Int. J. Robust Nonlinear Control*, no. 17, 2007.

[134] T. K. Vrana, Y. Yang, D. Jovcic, S. Dennetière, J. Jardini, and H. Saad, "The CIGRE B4 DC Grid Test System," Cigre, Tech. Rep., 2013.

[135] G. Pinares, L. B. Tjernberg, L. A. Tuan, C. Breitholtz, and A.-A. Edris, "On the analysis of the dc dynamics of multi-terminal VSC-HVDC systems using small signal modeling," *2013 IEEE Grenoble Conference*, pp. 1–6, 2013.

[136] Maxima CAS Development Team, "Maxima, a Computer Algebra System," p. GNU General Public License (GPL), 2015.

[137] I. Konstantelos, G. Jamgotchian, S. Tindemans, P. Duchesne, S. Cole, C. Merckx, G. Strbac, and P. Panciatici, "Implementation of a Massively Parallel Dynamic Security Assessment Platform for Large-Scale Grids," *IEEE Transactions on Smart Grid*, vol. 8, no. 3, pp. 1417–1426, 2017.

[138] V. Krishnan, J. D. McCalley, S. Henry, and S. Issad, "Efficient database generation for decision tree based power system security assessment," *IEEE Trans. on Power Systems*, vol. 26, no. 4, pp. 2319–2327, 2011.

[139] C. Coffrin, D. Gordon, and P. Scott, "NESTA, The NICTA Energy System Test Case Archive," 2014. [Online]. Available: http://arxiv.org/abs/1411.0359

[140] L. Wehenkel, M. Pavella, E. Euxibie, and B. Heilbronn, "Decision tree based transient stability method a case study," *IEEE Transactions on Power Systems*, vol. 9, no. 1, pp. 459–469, 1994.

[141] N. Hatziargyriou, G. Contaxis, and N. Sideris, "A decision tree method for on-line steady state security assessment," *IEEE Transactions on Power Systems*, vol. 9, no. 2, pp. 1052–1061, 1994.

[142] I. Genc, R. Diao, V. Vittal, S. Kolluri, and S. Mandal, "Decision tree-based preventive and corrective control applications for dynamic security enhancement in power systems," *IEEE Transactions on Power Systems*, vol. 25, no. 3, pp. 1611–1619, 2010.

[143] C. Liu, Z. H. Rather, Z. Chen, C. L. Bak, and P. Thogersen, "Importance sampling based decision trees for security assessment and the corresponding preventive control schemes: The Danish case study," in *IEEE PowerTech*, Grenoble, 2013, pp. 1–6.

[144] C. Liu, K. Sun, Z. Chen, Z. H. Rather, C. L. Bak, P. Thogersen, and P. Lund, "A Systematic Approach for Dynamic Security Assessment and the Corresponding Preventive Control Scheme Based on Decision Trees," *IEEE Transactions on Power Systems*, vol. 29, no. 2, pp. 717–730, 2014.

[145] C. Hamon, M. Perninge, and L. Söder, "An importance sampling technique for probabilistic security assessment in power systems with large amounts of wind power," *Electric Power Systems Research*, vol. 131, pp. 11–18, 2016.

[146] M. Sun, I. Konstantelos, S. Tindemans, and G. Strbac, "Evaluating composite approaches to modelling high-dimensional stochastic variables in power systems," *19th Power Systems Computation Conference*, 2016.

[147] I. Konstantelos, M. Sun, S. Tindemans, S. Issad, P. Panciatici, and G. Strbac, "Using Vine Copulas to Generate Representative System States for Machine Learning," *IEEE Transactions on Power Systems*, vol. PP, no. c, p. 1, 2018.

[148] E. Nuño Martinez, N. Cutululis, and P. Sørensen, "High dimensional dependence in power systems: A review," *Renewable and Sustainable Energy Reviews*, vol. 94, no. March 2017, pp. 197–213, 2018. [Online]. Available: https://doi.org/10.1016/j.rser.2018.05.056

[149] D. K. Molzahn, "Computing the Feasible Spaces of Optimal Power Flow Problems," *IEEE Transactions on Power Systems*, vol. 32, no. 6, pp. 4752–4763, 2017.

[150] J. Lavaei and S. H. Low, "Zero duality gap in optimal power flow problem," *IEEE Transactions on Power Systems*, vol. 27, no. 1, pp. 92–107, 2012.

[151] D. K. Molzahn, J. T. Holzer, B. C. Lesieutre, and C. L. Demarco, "Implementation of a Large-Scale Optimal Power Flow Solver Based on Semidefinite Programming," *IEEE Transactions on Power Systems*, vol. 28, no. 4, pp. 3987–3998, 2013.

[152] A. Venzke and S. Chatzivasileiadis, "Convex Relaxations of Security Constrained AC Optimal Power Flow under Uncertainty," in *Power Systems Computation Conference (PSCC)*, Dublin, Ireland, 2018.

[153] R. Albert, I. Albert, and G. L. Nakarado, "Structural Vulnerability of the North American Power Grid," *Physical Review E - Statistical, Nonlinear, and Soft Matter Physics*, vol. 69, no. 2, 2004.

[154] J. Fang, C. Su, Z. Chen, H. Sun, and P. Lund, "Power System Structural Vulnerability Assessment based on an Improved Maximum Flow Approach," *IEEE Transactions on Smart Grid*, 2016.

[155] R. Diestel, *Graph Theory*, 5th ed. Springer-Verlag, 2016, vol. 173.

[156] A. Dwivedi, X. Yu, and P. Sokolowski, "Analyzing power network vulnerability with maximum flow based centrality approach," *IEEE Int. Conf. on Industrial Informatics*, pp. 336–341, 2010.

[157] A. Dwivedi and X. Yu, "A maximum-flow-based complex network approach for power system vulnerability analysis," *IEEE Transactions on Industrial Informatics*, vol. 9, no. 1, pp. 81–88, 2013.

[158] S. Greene, I. Dobson, and F. L. Alvarado, "Sensitivity of the loading margin to voltage collapse with respect to arbitrary parameters," *IEEE Transactions on Power Systems*, vol. 12, no. 1, pp. 262–272, 1997.

[159] R. Zárate-Miñano, F. Milano, and A. J. Conejo, "An OPF methodology to ensure small-signal stability," *IEEE Transactions on Power Systems*, vol. 26, no. 3, pp. 1050–1061, 2011.

[160] M. Cain, R. O'Neill, and A. Castillo, "History of Optimal Power Flow and Formulations," Federal Energy Regulatory Comission, Tech. Rep. December, 2012. [Online]. Available: http://www.ferc.gov/industries/electric/indus-act/market-planning/opf-papers/acopf-1-history-formulation-testing.pdf

[161] Federal Energy Regulatory Commission, "Recent ISO Software Enhancements and Future Software and Modeling Plans," Federal Energy Regulatory Commission, Tech. Rep., 2011. [Online]. Available: https://www.ferc.gov/industries/electric/indus-act/rto/rto-iso-soft-2011.pdf

[162] P. Li, J. Qi, J. Wang, H. Wei, X. Bai, and F. Qiu, "An SQP method combined with gradient sampling for small-signal stability constrained OPF," *IEEE Transactions on Power Systems*, vol. 32, no. 3, pp. 2372–2381, 2017.

[163] C. Y. Chung, L. Wang, F. Howell, and P. Kundur, "Generation Rescheduling Methods to Improve Power Transfer Capability Constrained by Small-Signal Stability," *IEEE Transactions on Power Systems*, vol. 19, no. 1, pp. 524–530, 2004.

[164] S. K. Kodsi and C. A. Cañizares, "Application of a stability-constrained optimal power flow to tuning of oscillation controls in competitive electricity markets," *IEEE Transactions on Power Systems*, vol. 22, no. 4, pp. 1944–1954, 2007.

[165] J. E. Condren and T. W. Gedra, "Expected-security-cost optimal power flow with small-signal stability constraints," *IEEE Transactions on Power Systems*, vol. 21, no. 4, pp. 1736–1743, 2006.

[166] P. Li, B. Li, H. Wei, and Y. Yang, "Eigenvalue-optimisation-based optimal power flow with small-signal stability constraints," *IET Generation, Transmission & Distribution*, vol. 7, no. 5, pp. 440–450, 2013.

[167] M. Chavez-Lugo, C. R. Fuerte-Esquivel, C. A. Canizares, and V. J. Gutierrez-Martinez, "Practical Security Boundary-Constrained DC Optimal Power Flow for Electricity Markets," *IEEE Transactions on Power Systems*, vol. 31, no. 5, pp. 3358–3368, 2016.

[168] L. Wehenkel, "Decision tree approach to power systems security assessment," *Int. Journal of Elec. Power & Energy Systems*, vol. 15, no. 1, pp. 13–36, 1993.

[169] K. Sun, "An Online Dynamic Security Assessment Scheme Using Phasor Measurements and Decision Trees," *IEEE Transactions on Power Systems*, vol. 22, no. 4, pp. 1935–1943, 2007.

[170] E. Voumvoulakis, A. E. Gavoyiannis, and N. D. Hatziargyriou, "Decision trees for dynamic security assessment and load shedding scheme," in *PES General Meeting, 2006. IEEE*, no. 2, Montreal, Quebec, Canada, 2006, pp. 1–7.

[171] W. D. Oliveira, J. P. Vieira, U. H. Bezerra, D. A. Martins, and B. d. G. Rodrigues, "Power system security assessment for multiple contingencies using multiway decision tree," *Electric Power Systems Research*, vol. 148, pp. 264–272, 2017.

[172] C. Liu, Z. H. Rather, Z. Chen, and C. L. Bak, "An overview of decision tree applied to power systems," *International Journal of Smart Grid and Clean Energy*, pp. 413–419, 2013.

[173] Y. Xu, Z. Y. Dong, R. Zhang, and K. Po Wong, "A decision tree-based on-line preventive control strategy for power system transient instability prevention," *International Journal of Systems Science*, vol. 45, no. 2, pp. 176–186, 2014.

[174] Gurobi Optimization, "Gurobi Optimizer Reference Manual," 2015. [Online]. Available: http://www.gurobi.com

[175] R. A. Jabr, "A conic quadratic format for the load flow equations of meshed networks," *IEEE Transactions on Power Systems*, vol. 22, no. 4, pp. 2285–2286, 2007.

[176] A. G. Expösito and E. R. Ramos, "Reliable load flow technique for radial distribution networks," *IEEE Transactions on Power Systems*, vol. 14, no. 3, pp. 1063–1069, 1999.

[177] B. Kocuk, S. S. Dey, and X. A. Sun, "New Formulation and Strong MISOCP Relaxations for AC Optimal Transmission Switching Problem," *IEEE Transactions on Power Systems*, vol. 32, no. 6, pp. 4161–4170, 2017.

[178] R. D. Zimmerman and C. E. Murillo-Sánchez, "MATPOWER 6.0 User's Manual," Power Systems Engineering Research Center (PSerc), Tech. Rep., 2016. [Online]. Available: http://www.pserc.cornell.edu/matpower/manual.pdf

[179] H. Hijazi, C. Coffrin, and P. V. Hentenryck, "Convex quadratic relaxations for mixed-integer nonlinear programs in power systems," *Mathematical Programming Computation*, vol. 9, no. 3, pp. 321–367, 2017.

[180] J. Beerten and R. Belmans, "Development of an open source power flow software for high voltage direct current grids and hybrid AC/DC systems: MATACDC," *IET Generation, Transmission & Distribution*, vol. 9, no. 10, pp. 966–974, 2015.

[181] U.S.-Canada Power System Outage Task Force, "Final Report on the August 14, 2003 Blackout in the United States and Canada: Causes and Recommendations," U.S.-Canada Power System Outage Task Force, Tech. Rep. April, 2004. [Online]. Available: https://www3.epa.gov/region1/npdes/merrimackstation/pdfs/ar/AR-1165.pdf

[182] S. Larsson and E. Ek, "The black-out in southern Sweden and eastern Denmark, 23 September, 2003," in *IEEE Power Engineering Society General Meeting*, 2004, pp. 1–5.

[183] A. Berizzi, "The Italian 2003 blackout," *IEEE Power Engineering Society General Meeting, 2004.*, vol. 2, no. September, pp. 1673–1679, 2004.

[184] Power System Dynamic Performance Committee Power System Stability Subcommittee, "Voltage Stability Assessment : Concepts , Practices and Tools," IEEE Power & Energy Society, Tech. Rep., 2002.

[185] J. A. D. De Leon and B. Kehrli, "The modeling requirements for short-term voltage stability studies," *IEEE PES Power Systems Conference and Exposition (PSCE)*, pp. 582–588, 2006.

[186] A. Tiwari and V. Ajjarapu, "Addressing short term voltage stability problem - Part I: Challenges and plausible solution directions," in *Proceedings of the IEEE Power Engineering Society Transmission and Distribution Conference*, Dallas, TX, USA, 2016, pp. 1–5.

[187] D. Shoup, J. Paserba, and C. Taylor, "A survey of current practices for transient voltage dip/sag criteria related to power system stability," *IEEE PES Power Systems Conference and Exposition, 2004.*, pp. 1499–1506, 2005.

[188] S. Dasgupta, M. Paramasivam, U. Vaidya, and V. Ajjarapu, "PMU-based model-free approach for short term voltage stability monitoring," in *IEEE Power and Energy Society General Meeting*, San Diego, California, USA, 2012, pp. 1–8.

[189] ——, "PMU-Based Model-Free Approach for Real-Time Rotor Angle Monitoring," *IEEE Transactions on Power Systems*, vol. 30, no. 5, pp. 2818–2819, 2015.

[190] I. D. D. Leon, J.a. and C. Taylor, "Understanding and solving short-term voltage stability problems," in *IEEE Power Engineering Society Summer Meeting,*, vol. 2, San Diego, California, USA, 2002, pp. 745–752.

[191] K. Zhu and L. Nordström, "Design of wide-area damping systems based on the capabilities of the supporting information communication technology infrastructure," *IET Generation, Transmission Distribution*, vol. 8, no. 4, pp. 640–650, 2014.

[192] Transmission Issues Subcommittee of the North American Electric Reliability Council, "Guidelines for Developing an Under Voltage Load Shedding (UVLS) Evaluation Program," North American Electric Reliability Council, Tech. Rep., 2006.

[193] R. Schainker, P. Miller, W. Dubbelday, P. Hirsch, and G. Zhang, "Real-Time Dynamic Security Assessment," *IEEE Power and Energy Magazine*, vol. 4, no. 2, pp. 51–58, 2006.

[194] H.-D. Chang, C.-C. Chu, and G. Cauley, "Direct stability analysis of electric power systems using energy functions: theory, applications, and perspective," *Proceedings of the IEEE*, vol. 83, no. 11, pp. 1497–1529, 1995.

[195] S. Dasgupta, M. Paramasivam, U. Vaidya, and V. Ajjarapu, "Real-time monitoring of short-term voltage stability using PMU data," *IEEE Transactions on Power Systems*, vol. 28, no. 4, pp. 3702–3711, 2013.

[196] A. Reddy, K. Ekmen, V. Ajjarapu, and U. Vaidya, "PMU based real-time short term voltage stability monitoring - Analysis and implementation on a real-time test bed," *2014 North American Power Symposium (NAPS)*, pp. 1–6, 2014.

[197] S. Vakili, Q. Zhao, and L. Tong, "Bayesian Quickest Short-term Voltage Instability Detection in Power Systems," in *54th IEEE Conference on Decision and Control (CDC)*, Osaka, Japan, 2015, pp. 7214–7219.

[198] K. Kawabe and K. Tanaka, "Analytical method for short-term voltage stability using the stability boundary in the P-V plane," *IEEE Transactions on Power Systems*, vol. 29, no. 6, pp. 3041–3047, 2014.

[199] K. Kawabe, Y. Ota, A. Yokoyama, and K. Tanaka, "Novel Dynamic Voltage Support Capability of Photovoltaic Systems for Improvement of Short-Term Voltage Stability in Power Systems," *IEEE Transactions on Power Systems*, vol. PP, no. 99, 2016.

[200] C. D. Vournas, C. Lambrou, and P. Mandoulidis, "Voltage Stability Monitoring from a Transmission Bus PMU," *IEEE Transactions on Power Systems*, vol. PP, no. 99, pp. 1–9, 2016.

[201] J. M. Lim and C. L. DeMarco, "SVD-Based Voltage Stability Assessment From Phasor Measurement Unit Data," *IEEE Transactions on Power Systems*, vol. 31, no. 4, pp. 2557–2565, 2016.

[202] R. Zhang, H. K. Polytechnic, H. Kong, Y. Xu, Z. Y. Dong, K. Meng, and Z. Xu, "Intelligent Systems for Power System Dynamic Security Assessment : Review and Classification," in *4th International Conference on Electric Utility Deregulation and Restructuring and Power Technologies (DRPT)*, Weihai, China, 2011, pp. 134–139.

[203] T. van Cutsem, L. Wehenkel, M. Pavella, B. Heilbronn, and M. Goubin, "Decision tree approaches to voltage security assessment," *IEE Proc.- Generation, Transmission and Distribution*, vol. 140, no. 3, p. 189, 1993.

[204] N. V. Tomin, V. G. Kurbatsky, D. N. Sidorov, and A. V. Zhukov, "Machine Learning Techniques for Power System Security Assessment," *IFAC-PapersOnLine*, vol. 49, no. 27, pp. 445–450, 2016.

[205] K. Morison, X. Wang, A. Moshref, and A. Edris, "Identification of voltage control areas and reactive power reserve; An advancement in on-line voltage security assessment," in *IEEE PES GM: Conversion and Delivery of Elec. Energy in the 21st Century*, 2008.

[206] J. Huang, A. Valette, M. Beaudoin, K. Morrison, A. Moshref, M. Provencher, and J. Sun, "An Intelligent System for Advanced Dynamic Security Assessment," in *Powercon 2002: International Conference on Power System Technology*, vol. 1, 2002, pp. 220–224.

[207] Cigre Working Group C4.601, "Review of on-line dynamic security assessment tools and techniques," Cigre, Tech. Rep., 2007.

[208] D. Devaraj and J. Preetha Roselyn, "On-line voltage stability assessment using radial basis function network model with reduced input features," *International Journal of Electrical Power and Energy Systems*, vol. 33, no. 9, pp. 1550–1555, 2011.

[209] D. Q. Zhou, U. D. Annakkage, and A. D. Rajapakse, "Online Monitoring of Voltage Stability Margin Using an Artificial Neural Network," *IEEE Transactions on Power Systems*, vol. 25, no. 3, pp. 1566–1574, 2010.

[210] Y. Xu, R. Zhang, J. Zhao, Z. Y. Dong, D. Wang, H. Yang, and K. P. Wong, "Assessing Short-Term Voltage Stability of Electric Power Systems by a Hierarchical Intelligent System," *IEEE Trans. on Neural Networks and Learning Sys.*, vol. 27, no. 8, pp. 1686–1696, 2016.

[211] H. Shah, K. Verma, and M. Ieee, "PMU-ANN based Approach for Real Time Voltage Stability Monitoring," in *2016 IEEE 6th International Conference on Power Systems (ICPS)*, New Delhi, India, 2016, pp. 1–5.

[212] M. Mohammadi and G. B. Gharehpetian, "Application of multi-class support vector machines for power system on-line static security assessment using DT - Based feature and data selection algorithms," *Journal of Intelligent and Fuzzy Systems*, vol. 20, no. 3, pp. 133–146, 2009.

[213] P. Duraipandy and D. Devaraj, "On-Line Voltage Stability Assessment using Least Squares Support Vector Machine with Reduced Input Features," in *International Conference on Control, Instrumentation, Communication and Computational Technologies (ICCICCT)*, no. January, Kumaracoil, Thuckalay Tamilnadu Kanyakumari District, India, 2014, pp. 1070–1074.

[214] J. Cepeda, J. L. Rueda, D. G. Colome, and I. Erlich, "Data-mining-based approach for predicting the power system post-contingency dynamic vulnerability status," *International Transactions on Electrical Energy Systems*, vol. 36, no. E1, pp. 51–66, 2014.

[215] P. Duraipandy and D. Devaraj, "Extreme Learning Machine Approach for Real Time Voltage Stability Monitoring in a Smart Grid System using Synchronized Phasor Measurements," *Journal of Electrical Engineering Technol.*, vol. 11, no. 6, pp. 1527–1534, 2016.

[216] H. Mohammadi, G. Khademi, D. Simon, and M. Dehghani, "Multi-Objective Optimization of Decision Trees for Power System Voltage Security Assessment," in *Annual IEEE Systems Conference (SysCon)*, no. March, Orlando, Florida, 2016, pp. 1–6.

[217] A. Khatib, R. Nuqui, M. Ingram, and A. Phadke, "Real-time estimation of security from voltage collapse using synchronized phasor measurements," *IEEE Power Engineering Society General Meeting, 2004.*, vol. 2, pp. 582–588, 2004.

[218] R. Diao, K. Sun, V. Vittal, R. J. O'Keefe, M. R. Richardson, N. Bhatt, D. Stradford, and S. K. Sarawgi, "Decision tree-based online voltage security assessment using PMU measurements," *IEEE Transactions on Power Systems*, vol. 24, no. 2, pp. 832–839, 2009.

[219] M. Beiraghi and A. M. Ranjbar, "Online Voltage Security Assessment Based on Wide-Area Measurements," *IEEE Transactions on Power Delivery*, vol. 28, no. 2, pp. 989–997, 2013.

[220] S. M. Shahrtash and H. Khoshkhoo, "Fast online dynamic voltage instability prediction and voltage stability classification," *IET Generation, Transmission & Distribution*, vol. 8, no. 5, pp. 957–965, 2014.

[221] I. Kamwa, S. Samantaray, and G. Joos, "Development of Rule-Based Classifiers for Rapid Stability Assessment of Wide-Area Post-Disturbance Records," *IEEE Transactions on Power Systems*, vol. 24, no. 1, pp. 258–270, 2009.

[222] V. Kurbatsky and N. Tomin, "Identification of Pre-Emergency States in the Electric Power System on the Basis of Machine Learning Technologies," in *12th World Congress on Intelligent Control and Automation (WCICA) June*, no. 14, Guilin, China, 2016, pp. 378–383.

[223] Yong Sheng and S. Rovnyak, "Decision trees and wavelet analysis for power transformer protection," *IEEE Transactions on Power Delivery*, vol. 17, no. 2, pp. 429–433, 2002.

[224] Y. Sheng and S. M. Rovnyak, "Decision tree-based methodology for high impedance fault detection," *IEEE Transactions on Power Delivery*, vol. 19, no. 2, pp. 533–536, 2004.

[225] S. Rovnyak, G. Li, and K. Mei, "One-shot controls for preventing loss of synchronism," in *IEEE PES GM*, vol. 4, 2003.

[226] S. Zhang, Y. Wang, M. Liu, and Z. Bao, "Data-Based Line Trip Fault Prediction in Power Systems Using LSTM Networks and SVM," *IEEE Access*, vol. 6, pp. 7675–7686, 2017.

[227] NERC, "Dynamic Load Modeling," North American Electric Reliability Corporation (NERC), Tech. Rep. December, 2016.

[228] T. de Bruin, K. Verbert, and R. Babuska, "Railway Track Circuit Fault Diagnosis Using Recurrent Neural Networks," *IEEE Transactions on Neural Networks and Learning Systems*, vol. 28, no. 3, pp. 523–533, 2017.

[229] A. Moustapha and R. Selmic, "Wireless Sensor Network Modeling Using Modified Recurrent Neural Networks: Application to Fault Detection," *IEEE Transactions on Instrumentation and Measurement*, vol. 57, no. 5, pp. 981–988, 2008.

A. Appendix

A.1 Data of the Pan-European Transmission System in 2016 and 2030

Table A.1: Net demand, RES energy and consumption per country 2016

Country	AT	BE	DK	FR	DE	HR	GR	HU	IT	NL	PL	ES	CH	UK	PT	SK	BG	FI	SE	RO	NO	IE	CZ	LU	RS	SI	AL	ME	MK	BA	Total
Consumption according to ENTSO-E (TWh)	69.98	84.77	33.87	478.33	504.38	17.55	51.08	41.77	313.41	114.20	152.47	249.67	62.59	374.81	49.08	28.71	37.59	84.79	138.88	53.43	131.86	26.84	65.10	6.48	38.89	13.76	7.09	3.23	7.08	12.35	3262.42
Wind energy in distribution level (TWh)	3.84	0.24	0.00	0.47	50.68	0.85	2.64	0.44	14.94	0.00	6.27	35.12	0.07	0.00	11.81	0.00	1.04	0.00	0.00	5.40	0.00	0.00	0.32	0.08	0.00	0.00	0.00	0.00	0.11	0.00	134.31
Solar energy in distribution level (TWh)	0.93	2.70	0.63	7.73	33.53	0.06	3.65	0.03	21.55	1.54	0.12	12.95	0.45	0.00	0.78	0.55	1.03	0.00	0.00	1.59	0.00	0.00	2.08	0.10	0.00	0.24	0.07	0.00	0.03	0.00	92.34
Bio fuel energy in distribution level (TWh)	0.00	3.42	2.98	4.13	40.70	0.33	0.25	1.65	16.85	3.47	7.22	3.40	0.32	13.84	2.69	1.63	0.27	10.74	8.98	0.45	0.00	0.00	4.20	0.05	0.00	0.17	0.00	0.00	0.04	0.00	127.78
Geothermal in distribution level (TWh)	0.00	0.00	0.00	0.00	0.17	0.00	0.00	0.00	0.00	5.87	0.00	0.00	0.00	0.00	0.00	0.00	0.00	0.00	0.00	0.00	0.00	0.00	0.00	0.00	0.00	0.00	0.00	0.00	0.00	0.00	6.04
Renewable waste in distribution level (TWh)	0.00	1.21	1.40	2.34	4.97	0.00	0.00	0.40	2.41	0.00	0.00	0.79	0.64	0.08	0.00	0.00	0.00	0.00	1.23	0.00	0.00	0.06	0.00	0.00	0.00	0.00	0.00	0.00	0.00	0.00	15.53
Hydro in distribution level (TWh)	15.85	0.30	0.02	12.09	20.90	4.30	3.47	0.30	38.80	0.10	1.40	28.32	13.20	4.50	12.59	1.55	3.50	0.00	0.00	15.44	0.00	0.00	2.00	0.12	0.00	4.40	0.00	0.00	1.60	3.40	188.15
Other RES in distribution level (TWh)	3.06	0.04	0.00	0.00	1.46	0.07	1.30	0.00	0.00	0.00	0.00	0.04	1.37	0.00	0.00	0.03	0.00	0.00	0.00	0.00	0.00	0.15	0.00	0.00	0.00	0.13	0.00	0.00	0.00	0.00	7.65
Net demand (TWh)	46.31	76.86	28.84	451.59	351.98	11.93	39.77	38.95	218.86	103.23	137.45	169.06	46.54	356.40	21.21	24.95	31.75	74.05	128.68	30.54	131.86	26.63	56.50	6.12	38.89	8.83	7.02	3.23	5.31	8.94	2682.24

Table A.2: Net demand, RES energy and consumption per country 2030

Country	AT	BE	DK	FR	DE	HR	GR	HU	IT	NL	PL	ES	CH	UK	PT	SK	BG	FI	SE	RO	NO	IE	CZ	LU	RS	SI	AL	ME	MK	BA	Total
Consumption according to ENTSO-E (TWh)	76.92	95.56	39.00	500.80	575.31	18.09	54.76	42.31	316.55	118.08	184.86	273.40	72.19	371.20	49.39	32.73	33.63	89.68	158.20	60.47	150.45	29.89	71.32	8.14	43.25	15.57	9.29	5.20	11.09	12.55	3519.84
Wind energy in distribution level (TWh)	3.84	0.24	0.00	0.47	50.68	0.85	2.64	0.44	14.94	0.00	6.27	35.12	0.07	0.00	11.81	0.00	1.04	0.00	0.00	5.40	0.00	0.00	0.32	0.08	0.00	0.00	0.31	0.51	0.31	1.96	137.28
Solar energy in distribution level (TWh)	5.89	6.03	0.63	7.73	33.53	1.88	11.04	1.15	21.55	4.48	0.76	12.95	0.00	0.00	3.78	0.70	1.10	0.02	0.00	1.59	0.72	0.02	2.69	0.34	0.00	1.51	0.01	0.00	0.05	0.00	120.14
Bio fuel energy in distribution level (TWh)	0.00	3.36	7.27	15.20	50.47	0.00	1.27	2.14	26.28	19.18	18.26	9.49	0.00	178.52	2.88	2.25	0.38	0.00	9.65	0.83	0.00	2.01	0.00	0.18	0.00	0.48	0.00	0.00	0.00	0.00	350.12
Hydro in distribution level (TWh)	15.85	3.50	0.02	12.09	75.46	4.35	3.98	0.32	68.06	0.10	5.81	34.92	13.20	0.00	16.19	1.55	5.53	0.00	0.00	15.44	4.60	1.82	3.43	5.89	8.84	8.77	6.79	3.01	1.89	3.30	324.74
Other RES in distribution level (TWh)	6.78	0.00	0.00	0.04	0.00	0.09	0.00	0.00	0.00	0.00	0.00	0.00	0.04	0.00	0.00	0.00	0.00	0.04	0.00	0.00	0.00	0.00	0.04	0.00	0.04	0.00	0.00	0.04	0.04	0.00	7.17
Net demand (TWh)	44.57	82.42	31.08	465.28	365.17	10.91	35.83	38.26	185.72	94.32	153.76	180.91	58.88	192.69	14.74	28.22	25.57	89.62	148.54	37.20	145.12	26.04	64.84	1.64	34.36	4.80	2.18	1.64	8.80	7.29	2580.40

A.2 Parameters of the MT-HVDC Models

Table B.3: Base values of per unit system and parameters used in section 4.7.

Parameter	Value
Rated voltage, $V_{S,LL,RMS}$	220 kV
Rated power, $S_{b,gsvsc}$	1200 MVA
Rated power, $S_{b,wfvsc}$	$2 \cdot 1200$ MVA
Rated dc voltage, V_{dc}	400 kV
Rated angular frequency, ω_b	$2\pi 50\,\mathrm{s}^{-1}$
Base value for voltage defined as peak value of phase voltage, V_b	$\sqrt{\frac{2}{3}} V_{S,LL,RMS}$
Base value for currents defined as peak value or rated RMS, I_b	$\frac{S_b}{\sqrt{3} V_{S,LL,RMS}}$
Base value for impedance, Z_b	$\frac{V_b}{I_b}$
Base value for filter inductance, L_b	$\frac{Z_b}{\omega_b}$
Base value for filter capacitance, C_b	$\frac{1}{\omega_b Z_b}$
Line resistance, R	$0.011\,\Omega/\mathrm{km}$
Line inductance, L	$2.615\,\mathrm{mH/km}$
Line capacitance, C	$0.1908\,\mu\mathrm{F/km}$
Cable distances	67 km
Equivalent dc capacitor, c_{dc}	4.2 p.u.
Grid voltage, $\hat{v}_g$	1 p.u.
Filter inductance, l_f	0.08 p.u.
Filter resistance, r_f	0.003 p.u..
Filter capacitance, c_f	0.074 p.u.
Grid inductance, l_g	0.2 p.u.
Grid resistance, r_g	0.01 p.u.
Reactive power reference, q^*	0 p.u.
Ac voltage reference, $v^*_{o,d,wf}$	1 p.u.
Low-Pass filter frequency, ω_{AD}	20 p.u.
Active damping parameter (GSVSCs), $k_{ad,gsvsc}$	0.2 p.u.
Active damping parameter (WFVSC), $k_{ad,wfvsc}$	1 p.u.

Table B.4: Parameters of the freq. dependent cable model used in section 4.5, 4.6 and 6.6 [14].

$r_{dc,z1} = 1.1724 \cdot 10^{-1}\,\Omega/\mathrm{km}$	$l_{dc,z1} = 2.2851 \cdot 10^{-4}\,\mathrm{H/km}$
$r_{dc,z2} = 8.2072 \cdot 10^{-2}\,\Omega/\mathrm{km}$	$l_{dc,z2} = 1.5522 \cdot 10^{-3}\,\mathrm{H/km}$
$r_{dc,z3} = 1.1946 \cdot 10^{-2}\,\Omega/\mathrm{km}$	$l_{dc,z3} = 3.2942 \cdot 10^{-3}\,\mathrm{H/km}$
$g_{cs} = 7.6333 \cdot 10^{-11}\,\mathrm{S/km}$	$c_{cs} = 1.9083 \cdot 10^{-7}\,\mathrm{F/km}$

Table B.5: Base values of per unit system and parameters used in section 6.6.

Parameter	Value
Rated voltage, $V_{S,LL,RMS}$	345 kV
Rated power, $S_{b,gsvsc}$	100 MVA
Rated power, $S_{b,wfvsc}$	100 MVA
Rated dc voltage, V_{dc}	400 kV
Rated angular frequency, ω_b	$2\pi 50\,\mathrm{s}^{-1}$
Base value for voltage defined as peak value of phase voltage, V_b	$\sqrt{\frac{2}{3}}V_{S,LL,RMS}$
Base value for currents defined as peak value or rated RMS, I_b	$\frac{S_b}{\sqrt{3}V_{S,LL,RMS}}$
Base value for impedance, Z_b	$\frac{V_b}{I_b}$
Base value for filter inductance, L_b	$\frac{Z_b}{\omega_b}$
Base value for filter capacitance, C_b	$\frac{1}{\omega_b Z_b}$
Cable distances	100 km
Equivalent dc capacitor, c_{dc}	4.2 p.u.
Grid voltage, $\hat{v}_g$	1 p.u.
Filter inductance, l_f	0.1643 p.u.
Filter resistance, r_f	0.001 p.u..
Filter capacitance, c_f	0.0887 p.u.
Grid inductance, l_g	0.1121 p.u.
Grid resistance, r_g	0.0015 p.u.
Low-Pass filter frequency, ω_{AD}	20 p.u.
Active damping parameter (GSVSCs), $k_{ad,gsvsc}$	1 p.u.
Active damping parameter (WFVSC), $k_{ad,wfvsc}$	1 p.u.

Table B.6: Parameters of the three terminal grid used in section 4.5 and 4.6.

Parameters	Value	Units
GSC/WFC DC link capacitor c_{dc}	150	μF
WFC rated power P_3	700	MW
Reference voltage E^*	400	kV
Nominal power P_1, P_2	350	MW
Nominal voltage V_{ac}	195	kV
Nominal frequency f	50	Hz
Short circuit ratio (SCR)	5	-
Grid Thévenin X_n/R_n ratio	10	-
Coupling inductance L_c	0.2	pu
Coupling resistance R_c	0.01	pu
Capacitor filter impedance X_f	5.88	pu

A.3 Parameters of the Multi-Machine Models

Table C.7: Generator data for the IEEE 14 bus system adapted from [15] and used in chapter 5 & 6.

Machine and AVR parameters					
Parameters	g_1	g_2	g_3	g_4	g_5
MVA	615	60	60	25	25
r_a (pu)	0.0031	0.0031	0.0031	0.0041	0.0041
H (s)	5.148	6.54	6.54	5.06	5.06
D (pu)	2	2	2	2	2
x_d (pu)	0.8979	1.05	1.05	1.25	1.25
x'_d (pu)	0.2995	0.1850	0.1850	0.232	0.232
x_q (pu)	0.646	0.98	0.98	1.22	1.22
x'_q (pu)	0.646	0.36	0.36	0.715	0.715
x''_q (pu)	0.4	0.13	0.13	0.12	0.12
x_l (pu)	0.2396	0	0	0.134	0.134
T'_{do} (s)	7.4	6.1	6.1	4.75	4.75
T''_{do} (s)	0.03	0.04	0.04	0.06	0.06
T'_{qo} (s)	0.31	0.3	0.3	1.5	1.5
T''_{qo} (s)	0.033	0.099	0.099	0.21	0.21
K_a	120	20	20	20	20
$V_{R_{max}}$ (pu)	9.9	2.05	1.7	2.2	2.2
T_a (s)	0.02	0.02	0.02	0.02	0.02
K_e (pu)	1.0	1.0	1.0	1.0	1.0
T_e (s)	0.19	1.98	1.98	0.70	0.70
K_f (s)	0.0012	0.001	0.001	0.001	0.001
T_f (s)	1.0	1.0	1.0	1.0	1.0
A_e	0.0006	0.0006	0.0006	0.0006	0.0006
B_e (1/pu)	0.9	0.9	0.9	0.9	0.9
Economic data					
c_{lin} (€/MWh)	10	12.5	15	17.5	20

Table C.8: Generator data for the NESTA 162 bus system adapted from [16] and used in chapter 5

	Machine, AVR and PSS parameters																						
Gen.	MVA	t'_{do} (s)	t''_{do} (s)	t'_{qo} (s)	t''_{qo} (s)	h (s)	x_d (pu)	x'_d (pu)	x''_d (pu)	x_q (pu)	x'_q (pu)	x''_q (pu)	x_l (pu)	$\gamma_{d,1}$ (pu)	$\gamma_{d,2}$ (pu)	$\gamma_{q,1}$ (pu)	$\gamma_{q,2}$ (pu)	r_a (pu)	k_A	t_E (s)	k_F (s)	t_F (s)	d (pu)	$v_{R_{max}}$ (pu)	$v_{R_{min}}$ (pu)
g_1	1217	0.6341	0.0041	0.1446	0.1190	46.9800	0.1631	0.0333	0.0271	0.1577	0.0955	0.0271	0.0220	0.4513	48.5551	0.0694	12.6614	0.0002	38.5469	0.0014	0.000	0.0048	2.0	60.8409	-60.8409
g_2	566	0.8614	0.0066	0.1159	0.0127	13.6800	0.4327	0.0574	0.0441	0.4143	0.1005	0.0441	0.0318	0.4805	20.2942	0.1790	11.9499	0.0009	41.0169	0.0010	0.0001	0.2051	2.0	60.3030	-60.3030
g_3	1282	0.5813	0.0038	0.1326	0.0109	46.9800	0.0150	0.0305	0.0248	0.1446	0.0875	0.0248	0.0202	0.4513	52.9692	0.0694	13.8124	0.0002	35.3347	0.0013	0.0000	0.0044	2.0	55.7708	-55.7708
g_4	186	3.7290	0.0172	0.2786	0.0406	6.3400	0.8599	0.1208	0.2000	0.8281	0.1979	0.2000	0.1500	-1.7123	-92.8880	1.0438	-0.9153	0.0014	13.0208	0.0014	0.0005	0.0048	2.0	10.0	-10.0
g_5	180	2.3900	0.0134	0.2167	0.0316	6.3400	0.6688	0.0940	0.1556	0.6441	0.1539	0.1556	0.1167	-1.7123	-119.4274	1.0438	-1.1768	0.0011	10.1273	0.0014	0.0004	0.0048	2.0	7.7778	-7.7778
g_6	1151	0.6341	0.0041	0.1446	0.1190	46.9800	0.1631	0.0436	0.0271	0.1577	0.0955	0.0271	0.0220	0.2361	35.3652	0.0694	12.6614	0.0002	38.5469	0.0014	0.0000	0.0048	2.0	60.8409	-60.8409
g_7	148	3.5831	0.0403	1.2499	0.1817	4.3100	1.2808	0.2492	0.1800	1.2666	0.8133	0.1800	0.2775	3.4452	86.4039	-0.1820	2.2060	0.0028	145.8252	0.7933	0.0003	0.8333	2.0	30.4543	-30.4543
g_8	189	2.3900	0.0134	0.2167	0.0316	6.3400	0.6688	0.0940	0.1556	0.6441	0.1539	0.1556	0.1167	-1.7123	-119.4274	1.0438	-1.1768	0.0011	10.1273	0.0014	0.0004	0.0048	2.0	7.7778	-7.7778
g_9	1005	0.5230	0.0025	0.0322	0.0430	33.1200	0.0152	0.0367	0.0245	0.1369	0.0898	0.0216	0.0169	0.3838	31.1193	0.0645	12.8330	0.0283	31.4123	0.0785	0.0047	0.0785	2.0	90.7625	-90.7625
g_{10}	2590	0.0404	0.0003	0.0092	0.1190	46.9800	0.0104	0.0021	0.0017	0.0101	0.0061	0.0017	0.0014	0.4513	761.4322	0.0694	198.5536	0.0	2.4581	0.0001	0.0	0.0003	2.0	3.8797	-3.8797
g_{11}	591	0.7831	0.0060	0.1054	0.1190	13.6800	0.3934	0.0522	0.0401	0.3766	0.0914	0.0401	0.0289	0.4805	22.3236	0.1790	13.1449	0.0009	37.2881	0.0009	0.0001	0.1865	2.0	54.8209	-54.8209
g_{12}	580	0.9571	0.0073	0.1288	0.1190	13.6800	0.4808	0.0638	0.0490	0.4603	0.1117	0.0490	0.0353	0.4805	18.2648	0.1790	10.7549	0.0010	45.5743	0.0011	0.0001	0.2279	2.0	67.0033	-67.0033

Table C.9: Generator data for the NESTA 162 bus system adapted from [16] and used in chapter 5

	Machine, AVR and PSS parameters							
Gen.	A_e	B_e (1/pu)	t_R (s)	t_A (s)	k_E (pu)	k_ω (pu)	k_P (pu)	k_V (pu)	t_ω (pu)
g_1	0.0125	0.0368	0.0010	0.0019	0.0964	2.7500	0.0300	0.0300	0.0030
g_2	0.0125	0.9000	0.001	0.0733	0.2051	2.7500	0.0300	0.0300	0.0030
g_3	0.0115	0.0337	0.0010	0.0017	0.0884	2.7500	0.0300	0.0300	0.0030
g_4	0.0007	0.7153	0.0010	0.1042	0.2051	2.7500	0.0300	0.0300	0.0030
g_5	0.0005	0.5563	0.0010	0.0810	0.2051	2.7500	0.0300	0.0300	0.0030
g_6	0.0125	0.0368	0.0010	0.0019	0.0964	2.7500	0.0300	0.0300	0.0030
g_7	0.0022	1.2189	0.0010	0.0417	0.2051	2.7500	0.0300	0.0300	0.0030
g_8	0.0005	0.5563	0.0010	0.0810	0.2051	2.7500	0.0300	0.0300	0.0030
g_9	0.0001	0.1220	0.0010	0.0149	0.0785	10.7500	0.0300	0.0300	0.0030
g_{10}	0.0008	0.0023	0.0010	0.0001	0.0061	2.7500	0.0300	0.0300	0.0030
g_{11}	0.0125	0.9000	0.0010	0.0666	0.1865	2.7500	0.0300	0.0300	0.0030
g_{12}	0.0125	0.9000	0.0010	0.0814	0.2279	2.7500	0.0300	0.0300	0.0030

A.4 DFIG Parameters

Table D.10: DFIG parameters

DFIG parameters	
Parameters	Value
h_{tot} (s)	4.1
t'_o (pu)	10
l_m (pu)	4
l'_s (pu)	$1.01 l_m$
l_{rr} (pu)	$1.005\, l'_s$
k_{mrr} (pu)	$\frac{l_m}{l_{rr}}$
l_s (pu)	$l'_s - l_m \cdot k_{mrr}$
k_0 (pu)	0.1018
k_{p1} (pu)	0.6
k_{p2} (pu)	0.27
k_{p3} (pu)	1.48
k_{i1} (pu)	80.4
k_{i2} (pu)	5.1
k_{i3} (pu)	219

Collection of relevant publications

Journals

[**Pub. A**] F. Thams, R. Eriksson, and M. Molinas, "Interaction of Droop Control Structures and its Inherent Effect on the Power Transfer Limits in Multi- terminal VSC-HVDC," IEEE Transactions on Power Delivery, vol. 32, no. 1, pp. 182-192, 2017.

[**Pub. B**] F. Thams, A. Venzke, R. Eriksson, and S. Chatzivasileiadis, "Efficient Database Generation for Data-driven Security Analysis of Power Systems," IEEE Transactions of Power Systems, 2018, under review.

Conferences

[**Pub. C**] F. Thams, S. Chatzivasileiadis, E. Prieto-Araujo, and R. Eriksson, "Disturbance Attenuation of DC Voltage Droop Control Structures in a Multi-Terminal HVDC Grid," in Power Tech, Manchester, 2017.

[**Pub. D**] F. Thams, S. Chatzivasileiadis, and R. Eriksson, "DC Voltage Droop Control Structures and its Impact on the Interaction Modes in Interconnected AC-HVDC Systems," in International Conference on Innovative Smart Grid Technologies (ISGT) Asia, Auckland, 2017.

[**Pub. E**] F. Thams, L. Halilbašić, P. Pinson, S. Chatzivasileiadis, and R. Eriksson, "Data-Driven Security-Constrained OPF," in 10th Bulk Power Systems Dynamics and Control Symposium - IREP, Espinho, 2017.

[**Pub. F**] L. Halilbašić, F. Thams, A. Venzke, S. Chatzivasileiadis, and P. Pinson, "Data-Driven Security-Constrained AC-OPF for Operations and Markets," 20th Power Systems Computation Conference, Dublin, 2018.

Further Publications

[**Pub. G**] L. Halilbašić, F. Thams and S. Chatzivasileiadis, "BEST PATHS Deliverable 13.1: Technical and economical scaling rules for the implementation of demo results," Technical Report, Technical University of Denmark, 2018, under review.

[Pub. A] Interaction of Droop Control Structures and its Inherent Effect on the Power Transfer Limits in Multi- terminal VSC-HVDC.

Interaction of Droop Control Structures and its Inherent Effect on the Power Transfer Limits in Multi-terminal VSC-HVDC

F. Thams, *Graduate Student Member, IEEE,* R. Eriksson, *Senior Member, IEEE,* M. Molinas, *Member, IEEE*

***Abstract*—Future multi-terminal HVDC systems are expected to utilize dc voltage droop controllers and several control structures have been proposed in literature. This paper proposes a methodology to analyse the impact of various types of droop control structures using small-signal stability analysis considering all possible combinations of droop gains. The different control structures are evaluated by the active power transfer capability as a function of the droop gains, considering various possible stability margins. This reveals the flexibility and robustness against active power flow variations, due to disturbances for all the implementations. A case study analyzing a three terminal HVDC VSC-based grid with eight different kinds of droop control schemes points out that three control structures outperform the remaining ones. Additionally, a multi-vendor case is considered where the most beneficial combinations of control structures has been combined in order to find the best performing combination.**

***Index Terms*—Power system stability, Power transmission, stability, HVDC transmission, AC-DC power converters, Stability analysis, Control system analysis, State-space methods**

I. Introduction

THE rising number of offshore wind farm projects far away from the coast, as well as the need to connect those often remote RES to the major load centers, led to an increase of interest in HVDC technology in the last decade. The first commercial application of HVDC transmission was built in 1954 between Gotland and the Swedish mainland based on mercury valves [1]. Since then, most HVDC links based on line commutated converters (LCC) were built in point-to-point connections besides few exceptions (e.g. in Sardinia-Corsica-Italy and Quebec New England [2]).

The appearance and development of HVDC transmission based on voltage source converter (VSC) and its advantages compared to HVDC based on LCC raised the interest in connecting more than two terminals to a multi-terminal grid. These advantages include the capability of controlling active and reactive power independently, the capability to supply weak grids and especially the ease of achieving power flow reversal.

In Europe, ten countries of the North sea region formed the North Seas Countries Offshore Grid Initiative (NSCOGI) in order to explore the best way to establish an offshore HVDC grid [3]. In China, however, two multi-terminal HVDC (MT-HVDC) grids have already been built [4], [5].

Due to the little experience with multi-terminal grids, the control of such a HVDC grid is an emerging research topic. The operational reliability is a crucial aspect due to the significant economic impact of any malfunction. In case of a MT-HVDC system it is preferable to have a distributed control architecture, where multiple units are actively participating in the control of the grid based on local measurements. This leads to an inherently higher robustness against outages. Further, a distributed control architecture is more effective in case of power fluctuations that exceed the available control range of a single terminal [6], [7]. This is reflected by the fact that the vendors participating in the European HVDC Study Group prefer droop control or droop control together with deadband as control structure for distributed voltage control [8]. Additionally, the applicability of droop control is proven by its use in the Nanao MT-HVDC grid [4].

In technical literature several alternative droop control schemes have been proposed [6], [9]–[18], which have been categorized in a simple framework in [19].

The general operation principle for all the dc voltage droop implementations is identical, i.e. each implementation contains two control loops, in order to assume a linear relationship between current respectively active power and dc voltage. However, it was shown that the choice of control objective for the first respectively the second loop, as well as the tuning, has a significant impact on the dynamic performances and the stability properties. This is especially important to consider in case of a MT-HVDC grid built by different vendors.

Although small-signal stability analysis has been carried out in MT-HVDC grids, a comparison of different dc voltage droop control structures is still missing. To the best knowledge of the authors, there does not exist any analysis to determine the most beneficial and flexible control structure in the context of a MT-HVDC grid yet. Further, there do not exist any studies on using different kinds of droop control structures within one grid and their impact on each other.

The contribution of this work encloses a methodology for a stability analysis of different droop control implementations, regarding the active power transfer capability as a function

This project is co-funded by the European Unions Seventh Framework Programme for Research, Technological Development and Demonstration under the grant agreement no. 612748.

F. Thams is with the Center of Electric Power and Energy (CEE), Technical University of Denmark (DTU), DK-2800 Kgs. Lyngby, Denmark (e-mail: fltha@elektro.dtu.dk).

Robert Eriksson was with the Center for Electric Power and Energy (CEE), Technical University of Denmark (DTU), DK-2800 Kgs. Lyngby, Denmark. He is now with the Swedish National Grid (e-mail: errobban@gmail.com).

M. Molinas is with the Department of Engineering Cybernetics, Norwegian University of Science and Technology (NTNU), 7491 Trondheim, Norway (e-mail: marta.molinas@ntnu.no).

of the droop gains. This methodology is applied to analyse a MT-HVDC grid, which extends the work in [19], to emphasize the impact of different control structures. In the study case the flexibility against active power flow variations and robustness against disturbances will be compared and analyzed for all the various implementations.
Additionally, the stability limits of the most promising configurations will be analyzed and the limitations discussed in more detail. This will also provide further insight on how different droop controlled converters influence each other. Moreover, in contrast to previous publications, this work will investigate the consequences resulting from using different implementations simultaneously at different converter stations.
This paper is structured in four main parts. After the introduction a general model will be introduced and then the used methodology for analyzing the power transfer capability will be explained. Finally, a case study of a three terminal grid will be introduced and the findings will be discussed.

II. MATHEMATHICAL MODEL

A general mathematical model of a VSC-HVDC terminal with simplified ac grid will be presented in the following sections. This model is based on the single VSC configuration introduced in [20]. In order to develop a multi-terminal grid, an arbitrary number of those terminals and lines can be connected.

A. Model Conventions

Upper case letters represent physical values of the electrical circuit, whereas lower case letters define per unit quantities. The apparent power rating of the converter and the peak value of the rated phase voltage serve as base values for the used per unit system. The modelling of the electrical system and the control of the ac-side will be presented in a synchronous reference frame (SRF), using the amplitude-invariant Park Transformation. The d-axis voltage vector is aligned with the voltage vector, v_o, at the corresponding filter capacitor, c_f, and the q-axis is leading the d-axis by $90°$ [1]. SRF equations will be noted in complex space vector notation according to

$$\mathbf{x} = x_d + j \cdot x_q. \tag{1}$$

B. Electrical System

As shown in Fig. 1, a simplified but appropriate model for this analysis is used. The focus on the outer control loop, as well as the emphasis on small signal analysis, justifies this simplification for a multi-terminal grid in order to minimize the large computational burden.

1) Electrical System on the AC Side: As shown in Fig. 1, a simplified model of the ac grid is assumed, using an LC filter as the grid interface of the VSC and a Thévenin equivalent representation of the grid. The state-space equations can be

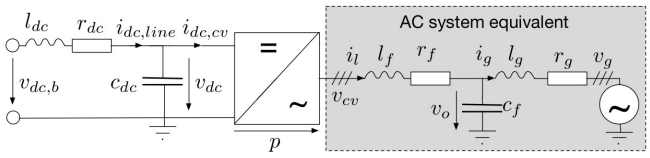

Fig. 1. Model of a VSC-HVDC terminal connected to a single dc line

obtained as given below, where the per unit grid frequency is denoted as ω_g and the base angular frequency as ω_b [21], [22].

$$\frac{d\mathbf{i}_l}{dt} = \frac{\omega_b}{l_f}\mathbf{v}_{cv} - \frac{\omega_b}{l_f}\mathbf{v}_o - \left(\frac{r_f\omega_b}{l_f} + j \cdot \omega_g\omega_b\right)\mathbf{i}_l \tag{2}$$

$$\frac{d\mathbf{v}_o}{dt} = \frac{\omega_b}{c_f}\mathbf{i}_l - \frac{\omega_b}{c_f}\mathbf{i}_g - j \cdot \omega_g\omega_b\mathbf{v}_o \tag{3}$$

$$\frac{d\mathbf{i}_g}{dt} = \frac{\omega_b}{l_g}\mathbf{v}_o - \frac{\omega_b}{l_g}\mathbf{v}_g - \left(\frac{r_g\omega_b}{l_g} + j \cdot \omega_g\omega_b\right)\mathbf{i}_g \tag{4}$$

The power balance between ac and dc side is given below. It is based on the assumption of an ideal lossless average model for the converter.

$$v_{cv,d} \cdot i_{l,d} + v_{cv,q} \cdot i_{l,q} = v_{dc} \cdot i_{dc,cv} \tag{5}$$

2) Electrical System on the DC Side: On the dc side, the lines are represented as single pi-equivalents, where the capacitances are incorporated in the dc capacitance of the corresponding converter, as given in (6).

$$c_{dc} = \frac{c_{dc,line}}{2} + c_{dc,vsc} \tag{6}$$

It is worth to note that this is a simplified model, which can approximate only the lowest frequency resonant peak of the cable [12]. But, on the other hand, D'Arco argues in [20], this approach also resembles the worst case scenario with respect to LC oscillations. This is due to the fact that the oscillatory effects are condensed in a single frequency, instead of being spread on several frequencies as in a real cable. This modeling approach can also be justified by the results of [23], indicating that for an appropriate sizing of the capacitor the impedance

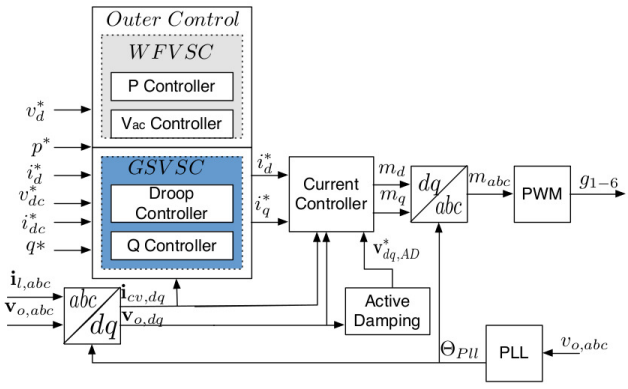

Fig. 2. Control system GSVSC and WFVSC differ by outer controllers, GSVSCs differ by chosen droop control structure (CS)

seen by the VSC is almost identical. The equations for the dynamics at the dc capacitors are given by:

$$\frac{dv_{dc}}{dt} = \frac{\omega_b}{c_{dc}} i_{dc,line} - \frac{\omega_b}{c_{dc}} i_{dc,cv} \tag{7}$$

Whereas the dc line dynamics according to the defined current flow are given by:

$$\frac{di_{dc,line}}{dt} = \frac{\omega_b}{l_{dc}} v_{dc,b} - \frac{\omega_b}{l_{dc}} v_{dc} - \frac{\omega_b r_{dc}}{l_{dc}} i_{dc,line} \tag{8}$$

C. Control System

The control system consists of an active damping of LC filter oscillations for the ac side, a current controller, a PLL and an outer controller. The outer control depends on the connected ac grid, which is explained in more detail in the outer loop controller subsection. An overview of the control system is given in Fig 2. The corresponding equations are given in the following subsections.

1) PLL: The VSC is assumed to be synchronized with the corresponding ac grid through a PLL, modelled as shown in Fig. 3 [22], [24]. An inverse tangent function is used on the low-pass filtered estimated phase voltages $\mathbf{v}_{PLL}$ to approximate the actual phase angle error $\Delta\Theta_{v,PLL}$. Followed by a PI controller in order to derive the frequency of the tracked voltages. The corresponding equations are given as:

$$\frac{d\mathbf{v}_{PLL}}{dt} = -\omega_{LP,PLL}\mathbf{v}_{PLL} + \omega_{LP,PLL}\mathbf{v}_o \tag{9}$$

$$\frac{d\epsilon_{PLL}}{dt} = \tan^{-1}\left(\frac{v_{PLL,q}}{v_{PLL,d}}\right) \tag{10}$$

$$\frac{d\Delta\Theta_{v,PLL}}{dt} = \omega_b \Delta\omega_{PLL} \tag{11}$$

with ϵ_{PLL} representing the integrator state of the PI controller and $\Delta\Theta_{PLL}$ the phase angle deviation between the grid voltage, $\mathbf{v}_g$, and the orientation of the PLL. $\Delta\omega_{PLL}$ describes the grid frequency deviation. The deviation variables are necessary for the modeling of the PLL in the SRF. While the actual voltage vector phase angle, Θ_{PLL}, obtained, as shown in Fig. 3, is needed for the transformation between stationary and rotating reference frame.

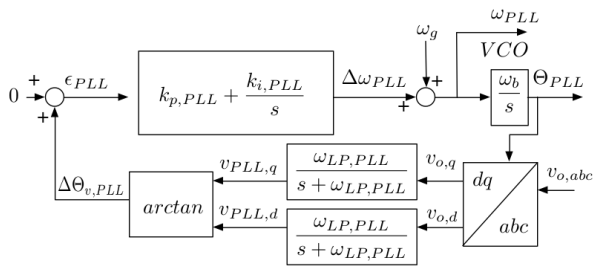

Fig. 3. Phase Locked Loop

2) Active Damping of LC Filter Oscillations: An active damping of LC filter oscillations is implemented, based on injecting a component, $\mathbf{v}^*_{AD}$, to the converter output voltage, which is in counter-phase with the detected oscillations [25], [26].

$$\mathbf{v}^*_{AD} = k_{AD}\left(\mathbf{v}_o - \phi\right) \tag{12}$$

$$\frac{d\phi}{dt} = \omega_{AD}\mathbf{v}_o - \omega_{AD}\phi \tag{13}$$

While ω_{AD} represents the cut-off frequency and ϕ the integrator states of the low-pass filter, k_{AD} is used as tuning parameter depending on the dynamic response of the system.

3) Inner Current Control Loop: The inner current control is based on vector control in the synchronous reference frame, tuned by modulus optimum criterion [27]. Considering two conventional PI controllers with decoupling terms and voltage feed-forward, the converter output voltage reference, $\mathbf{v}^*_{cv}$, can be defined as:

$$\mathbf{v}^*_{cv} = k_{pc}(\mathbf{i}^*_l - \mathbf{i}_l) + k_{ic}\gamma + jl_f\omega_{PLL}\mathbf{i}_l + \mathbf{v}_o - \mathbf{v}^*_{AD} \tag{14}$$

with γ, k_{pc} and k_{ic} representing the integrator state, the proportional and integral gain of the PI controller.

4) Outer Loop Controller: The outer loop control structure is the main difference between the terminals. Here, a distinction is made between VSC terminals, which are supposed to take part in the dc voltage control, and those which are not. The former are most likely connected to rather strong grids, hence those terminals are called grid side VSC (GSVSC) in the following. The latter is most likely connected to rather weak grids, where the focus lies on maximizing the power output as it is for wind farms, hence those are called wind farm VSC (WFVSC) in the following. This paper focuses on the outer loop control structure of the GSVSCs, in particular how different droop control structures influence the power transfer limits of the whole system.

a) Wind Farm Converter (WFVSC): For a VSC terminal representing a wind farm, a conventional active power controller is providing the d-axis current reference. The q-axis reference is provided by an ac voltage controller. The equations are given as:

$$i^*_{l,d,wf} = k_{pcd,wf}\left(p^*_{wf} - p_{wf,ac}\right) + k_{icd,wf}\chi_{d,wf} \tag{15}$$

$$i^*_{l,q,wf} = k_{pcq,wf}\left(v^*_{o,d,wf} - v_{o,d,wf}\right) + k_{icq,wf}\chi_{q,wf} \tag{16}$$

with $\chi_{d/q}$, $k_{pcd/q}$ and $k_{icd/q}$ representing the integrator state, the proportional and integral gain of the PI controller.

b) Grid Side Converter (GSVSC): The q-axis current reference for a VSC terminal connected to a strong grid is provided by a reactive power controller.

$$i^*_{l,q,g} = k_{pcq,g}\left(q^*_g - q_g\right) + k_{icq,g}\chi_{q,g} \tag{17}$$

The d-axis current reference is provided by one of the various dc voltage droop controllers, identified and categorized in [19] and shown in Fig. 4. The block diagrams of the corresponding droop controller indicate that these droop controllers differ regarding:

- power or current based droop implementations
- the choice of the second variable (besides dc voltage): current / power measured on ac or dc side
- the choice on which variable the droop gain k_{droop} is applied, i.e. which variable is controlled in the first and which in the second loop

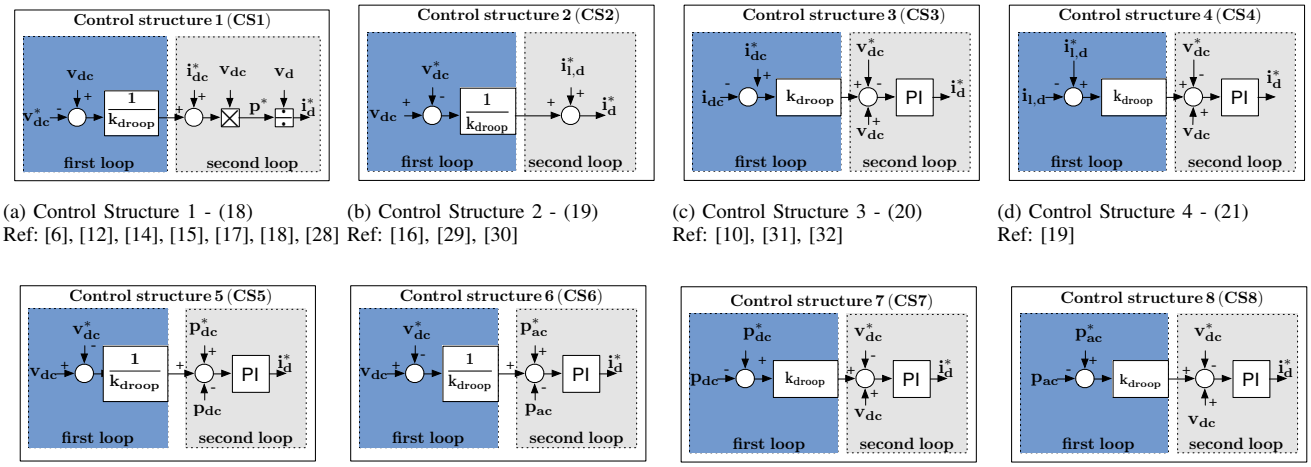

(a) Control Structure 1 - (18) Ref: [6], [12], [14], [15], [17], [18], [28]

(b) Control Structure 2 - (19) Ref: [16], [29], [30]

(c) Control Structure 3 - (20) Ref: [10], [31], [32]

(d) Control Structure 4 - (21) Ref: [19]

(e) Control Structure 5 - (22) Ref: [11], [33]–[35]

(f) Control Structure 6 - (23) Ref: [35]

(g) Control Structure 7 - (24) Ref: [36], [37]

(h) Control Structure 8 - (25) Ref: [37]

Fig. 4. Analysed DC Voltage Droop Control Structures

The corresponding equations of those controllers are given in (18)-(25) in the order of control structure (CS) 1 to 8.

$$\text{CS1:}\quad i^*_{l,d,g} = \frac{\left(\frac{v_{dc}-v^*_{dc}}{k_{droop}} + i^*_{dc}\right)\cdot v_{dc}}{v_{o,d}} \tag{18}$$

$$\text{CS2:}\quad i^*_{l,d,g} = \frac{v_{dc}-v^*_{dc}}{k_{droop}} + i^*_{ac} \tag{19}$$

$$\text{CS3:}\quad i^*_{l,d,g} = k_{pcd,g}\left((i^*_{dc}-i_{dc})\cdot k_{droop} + v_{dc} - v^*_{dc}\right) + k_{icd,g}\chi_{d,g} \tag{20}$$

$$\text{CS4:}\quad i^*_{l,d,g} = k_{pcd,g}\left((i^*_{ac}-i_{ac})\cdot k_{droop} + v_{dc} - v^*_{dc}\right) + k_{icd,g}\chi_{d,g} \tag{21}$$

$$\text{CS5:}\quad i^*_{l,d,g} = k_{pcd,g}\left(\frac{v_{dc}-v^*_{dc}}{k_{droop}} + p^*_{dc} - p_{dc}\right) + k_{icd,g}\chi_{d,g} \tag{22}$$

$$\text{CS6:}\quad i^*_{l,d,g} = k_{pcd,g}\left(\frac{v_{dc}-v^*_{dc}}{k_{droop}} + p^*_{ac} - p_{ac}\right) + k_{icd,g}\chi_{d,g} \tag{23}$$

$$\text{CS7:}\quad i^*_{l,d,g} = k_{pcd,g}\left((p^*_{dc}-p_{dc})\cdot k_{droop} + v_{dc} - v^*_{dc}\right) + k_{icd,g}\chi_{d,g} \tag{24}$$

$$\text{CS8:}\quad i^*_{l,d,g} = k_{pcd,g}\left((p^*_{ac}-p_{ac})\cdot k_{droop} + v_{dc} - v^*_{dc}\right) + k_{icd,g}\chi_{d,g} \tag{25}$$

III. METHODOLOGY

The differences between the various dc voltage droop controllers are analyzed in terms of active power transfer capability as a function of the droop gains of the connected GSVSCs using droop control. That means by using eigenvalue analysis, the eigenvalue movement is analyzed for a variation of the disturbances (= power injection at uncontrolled dc nodes / WFVSCs) and a variation of the droop gains. The sensitivity of certain eigenvalues for a variation of these parameters is shown in Fig. 5. For each combination of these parameters, the nonlinear system is linearized and the steady state is evaluated with respect to the chosen requirements for an acceptable operation point. These requirements can be chosen by the user applying the method and could include e.g. specific stability margins and / or current / voltage limitations. This analysis will basically result in a set of acceptable operation points, which are plotted with respect to the power transferred at a specific terminal. The surfaces of this area of acceptable operation points in this plot illustrate the upper and lower boundary (both directions of power flow) of acceptable operation for a specific combination of droop gains at each terminal. This set of acceptable operation points varies with respect to the chosen requirements. In contrast to other publications using small signal analysis, this methodology helps to determine the range of acceptable operation for a specific terminal within a multi-terminal grid for various control structures with all possible droop gain combinations and any arbitrary requirement. This operating range is expressed as a range of possible power flows at that terminal for a specific droop gain combination. Therefore, it is referred to as active power transfer capability (APTC) in the following.

Finally, the steady states at the boundary of the APTC are analyzed by a participation factor analysis, in order to identify the states associated with the modes causing the violation of a specific stability margin. This provides insight in determining the origin of the boundary and identifies which part of the system is provoking the limit.

Here, this analysis is used to illustrate the focus of this paper: revealing the impact of the choice of the droop control structure on the APTC for different exemplary requirements for an acceptable operation point. Since the models differ only in terms of the droop control structures, this analysis allows to determine which effect each control structure has on the APTC of each terminal and the whole system. Further, it reveals which control structures are more beneficial than others in terms of the APTC. Additionally, in the planning phase of a multi-vendor multi-terminal HVDC grid, probably

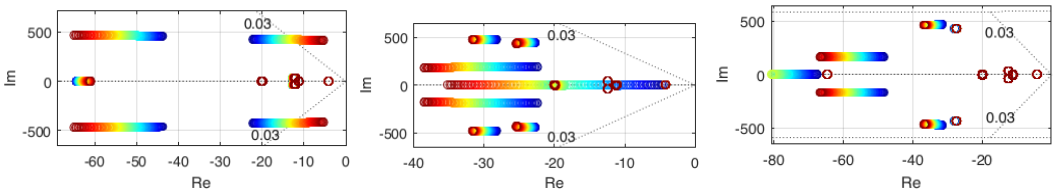

Fig. 5. Visualization of the sensitivity of certain eigenvalues and the stability margin of a minimum damping ratio of 3%. The pole movement is shown for a variation of a) p_{wf} from 0 p.u. (blue) to 1 p.u. (red), b) k_{droop} from 0 (blue) to 0.1 (red) and c) k_{droop_gs2} from 0 p.u. (blue) to 0.1 p.u. (red) for otherwise fixed values of $p_{wf} = 0$ pu, $k_{droop} = 0.1$ p.u. and $k_{droop,gs2} = 0.1$ p.u.

using different kind of droop control structures, the analysis facilitates to determine more or less beneficial combinations of control structures. Moreover, by analyzing these boundaries along the variation of the droop gains, it provides insight on how the choice of the droop gain values affects the APTC during operation. Additionally, it indicates whether a certain ratio of the droop gain values may be beneficial for maximizing the APTC.

A. Flowchart of the Methodology

The methodology is shown in detail in Fig. 6, as an example for a three terminal model, as it is used in the case study. The methodology can, however, also be applied to other topologies, the visualization of the APTC just becomes more challenging in case of a higher number of terminals.

First, a range of values for the droop gains, as well for the disturbance resembled by the power injection of the uncontrolled dc node, needs to be defined. Here, the values of the disturbances will define the power flow, while the droop gains will define the power sharing between the terminals. In the case study, a value range of $0.0001\,\text{p.u.} \leq k_{droop} \leq 0.1\,\text{p.u.}$ and $-2\,\text{p.u.} \leq p^*_{wf} \leq 2\,\text{p.u.}$ was chosen, however, the ranges can be chosen by the user applying the method according to the analyzed system. Additionally, any arbitrary requirement for an acceptable operation point can be chosen, which can include (several) stability margins and/or current/voltage requirements. Then, the first combination of values is chosen and the nonlinear system obtained from the aforementioned equations is linearized for the given inputs. It is analyzed whether the steady state meets current and voltage limits and whether the eigenvalues satisfy the requirements of various possible stability margins. Depending on the results, the operation points are saved correspondingly and the next combination of values is analyzed.

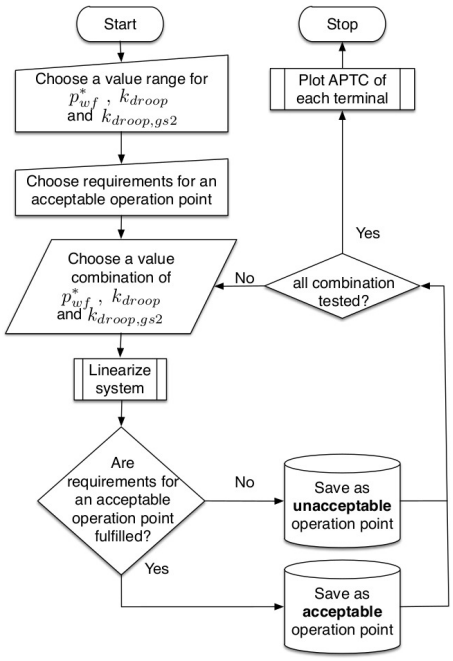

Fig. 6. Flowchart of Methodology

B. Requirements for an acceptable Operation Point

As aforementioned any arbitrary requirement for an acceptable operation point can be chosen by the user applying the method. Since there are no grid codes or standardized requirements for acceptable operation points in MT-HVDC grids defined yet, in the case study the APTC is analyzed for three possible requirements in order to investigate whether a certain requirement (current/voltage limit or stability margin) limits specific control structures more than others.

1) Voltage and Current Limits: First, the APTC are analyzed only with respect to fulfill the current and voltage limits. Here, these limits are chosen according to the Cigré B4 DC Grid test system, i.e. the dc voltage operational frame is assumed to be between 0.95 p.u. and 1.05 p.u., while the maximum current in the dc cable is set to 2265 A [38].

2) Damping Ratio $\geq$ 3%: A minimum damping ratio of 3% is demanded for all eigenvalues [39].

3) Maximum DC Voltage deviation of 5%: The performance of the control structures can be analysed by means of the singular value representation of the system transfer function matrices, $E_w(j\omega)$, according to [40]. The singular value representation can be obtained as:

$$\sigma_i(E_w(j\omega)) = \sqrt{\lambda_i(E_w^T(j\omega)E_w(j\omega))} \tag{26}$$

where λ_i is the i-eigenvalue of the matrix. The maximum singular value, $\overline{\sigma}(G(j\omega))$, indicates the maximum amplification of the corresponding inputs by the system seen from a specific output. The analysed inputs and outputs are the disturbance

(wind power input) and the dc voltage errors at the GSVSCs. In [40] the authors derive the maximum gain the singular value representation should not exceed, in case a maximum voltage error of 10% of the nominal value at each terminal is assumed. Here, it is adapted to the per unit system and a maximum deviation of 5% is chosen as stability margin:

$$\overline{\sigma}(E_w(0)) \leq \frac{\|e(0)\|_2}{\|w(0)\|_2} = 20\log_{10}\left(\frac{\sqrt{e_{gsvsc1}+e_{gsvsc2}}}{p_{wfvsc}}\right) = 20\log_{10}\left(\frac{\sqrt{(1\cdot 0.05)^2\cdot 2}}{1}\right) = -23.01\,\text{dB} \tag{27}$$

IV. CASE STUDY

A symmetric three terminal grid is derived from the aforementioned model, as shown in Fig. 8 (the ac sides are equal for all terminals as indicated by the ac system equivalent of the general model).

The GSVSCs use each one of the eight different droop control structures. First, both GSVSCs use the same CSs in order to detect the ones with highest APTC and highest damping ratios. Then, the most promising ones are combined with each other in order to determine the most beneficial combination of droop control structures. Each of these models consists of 52-54 states depending on the dc voltage droop implementations used. All models have been derived using Maxima [41].

The analysis depends obviously on the given parameters and should therefore be selected as they appear in the system. In this case study, the dc voltage reference values for both GSVSCs are set to 1 p.u., while the current and active power reference values of the GSVSCs are set to 0.1 p.u.. The numerical values for the gains of the droop controller have been selected with respect to the aforementioned reference values to ensure comparable performances. In particular, if a PI controller is present, its tuning has been set to achieve a 5% overshoot for a 5% step in the dc voltage reference with a fast rise time of approx. 8 ms and a settling time of a few tens of milliseconds. Thus, it is chosen to be very fast compared to suggestions in the literature of up to few 100 ms [8] in order to approach the limits of the VSC. Additionally, a second tuning with a rise time in the range of tens of milliseconds and a settling time of 100 ms is used as reference case.

In order to ensure comparability but also not to be limited by the VSC representing the wind farm, the active damping of both GSVSCs are tuned equally, whereas a higher damping factor is chosen for the WFVSC.

All parameter and base values are given in appendix. The dc parameters are scaled into per unit by using the same base frequency as for the ac side, as shown in appendix. This results in apparently high values for per unit inductance and capacitance, however, these parameters are corresponding to a dc cable of about 67 km [20].

All used models are verified by time domain simulations with equivalent non-linear models built in Matlab SimPowerSystems, two validation plots are shown in Fig. 7.

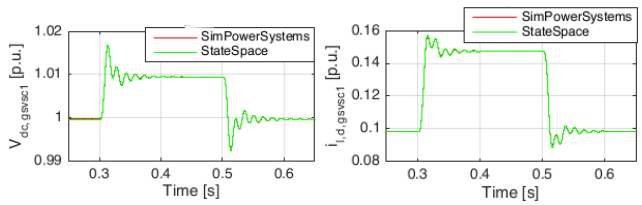

(a) (b)

Fig. 7. Validation of the small signal model by a time domain simulation and comparison with a non-linear model built in Matlab SimPowerSystems. (Response of a) $v_{dc,gs1}$ and b) $i_{l,d}$ to a 10% step in p^*_{wf}).

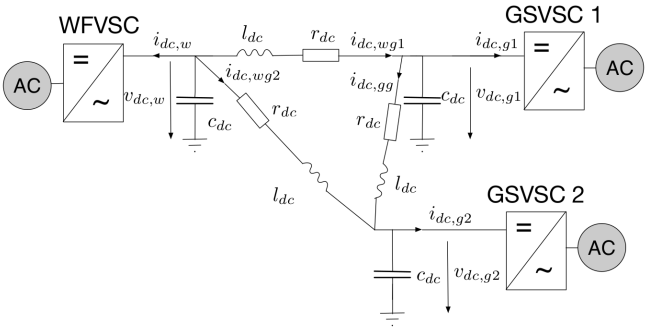

Fig. 8. Model of the dc grid

A. Analysis of the Case where both GSVSCs use the same CS

In this scenario the same control structure is used at GSVSC1 and GSVSC2. This is done in order to determine the operation ranges for each CS for the various requirements.

In the following the APTCs are given for the case where the only requirements considered are the system stability ($Re\{\lambda\} \leq 0$) and the voltage and current limits given in the subsection III-B1. The impact of the remaining requirements are discussed in the corresponding subsections and highlighted in the respective tables. The APTC of the case in which both GSVSCs use CS 8 is shown in Fig. 9. Fig. 9a shows the maximum power transfer in both directions of one terminal for all combinations of k_{droop} and $k_{droop,gs2}$. That means with the given current definition shown in Fig. 1, the upper surface resembles the inverter limit of that GSVSC while the lower surface resembles the rectifier limit of that GSVSC. The area between both surfaces is the area of stable and acceptable operation points. Thus, the APTC of a single

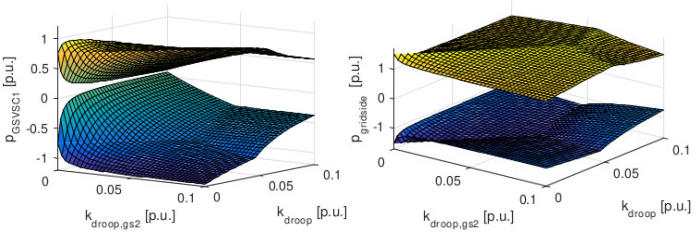

(a) (b)

Fig. 9. APTC of a) GSVSC1 and b) the sum of both GSVSCs ($p_{gridside}$)

TABLE I
COMPARISON OF MAXIMUM APTC OF A SINGLE GSVSC FOR VARIOUS CONTROL STRUCTURES
REQUIREMENTS: FULFILLED, FULFILLED BUT CLOSE TO BOUNDARY, NOT FULFILLED

	Fast Response Time					Slow Response Time				
Control Structure	Max Range p_{gsvsc1}	Damping Ratio of lowest damped EV l. limit	Damping Ratio of lowest damped EV u. limit	$\overline{\sigma}(E_w(0))$ lower limit	$\overline{\sigma}(E_w(0))$ upper limit	Max Range p_{gsvsc1}	Damping Ratio of lowest damped EV l. limit	Damping Ratio of lowest damped EV u. limit	$\overline{\sigma}(E_w(0))$ lower limit	$\overline{\sigma}(E_w(0))$ upper limit
CS 1	1.14 p.u.	0.14%	13.88%	-46.1 dB	-46.3 dB					
CS 2	1.17 p.u.	5.27%	0.02%	-54.4 dB	-54.5 dB					
CS 3	2.23 p.u.	6.86%	7.62%	-51 dB	-51.6 dB	2.23 p.u.	0.35%	6.19%	-50.8 dB	-51.4 dB
CS 4	2.23 p.u.	7.26%	7.72%	-51.4 dB	-52 dB	2.16 p.u.	0.41%	6.14%	-51.1 dB	-51.8 dB
CS 5	1.34 p.u.	0.05%	13.1%	-27.2 dB	-27.4 dB	1.87 p.u.	0.03%	9.49%	-30.5 dB	-30.8 dB
CS 6	1.38 p.u.	0.15%	15.41%	-26 dB	-26.3 dB	1.87 p.u.	0.08%	10.31%	-30.5 dB	-30.8 dB
CS 7	2.24 p.u.	8.6%	7.6%	-51 dB	-51.5 dB	2.24 p.u.	4.9%	6.7%	-50.8 dB	-51.4 dB
CS 8	2.24 p.u.	6.8%	7.6%	-51 dB	-51.6 dB	2.24 p.u.	0.32%	6.15%	-50.8 dB	-51.4 dB

terminal indicates for which power flow variations a stable and acceptable operation can be achieved for that terminal for all droop gain value combinations. In the optimal case, each terminal should achieve an APTC $\geq 2\,\mathrm{p.u.}$ for a wide range of droop gain combinations in order to be able to withstand disturbances and power flow variations up to its rated power in both power flow directions.

The APTC for the sum of both GSVSCs ($p_{gridside}$), shown in Fig. 9b, indicates how much power can be transferred from the WFVSC to the GSVSCs (upper limit) and how much could be transferred from both GSVSCs to an uncontrolled dc node (lower limit). In this scenario the WFVSC should be imagined not as wind farm, but as a weak grid not participating in the dc voltage control.

When analyzing the APTC of the various CSs, it is of main interest to find the maximum APTC value of a single terminal, i.e. exemplary for CS 8 to determine the droop gain combination where the range between the upper and lower limit is the highest in Fig. 9a. Further, it is of main interest to find the maximum APTC value for the whole $p_{gridside}$ (Tab. I & Tab. III), since in the case of just maximizing the APTC of a single terminal the APTC of the second terminal will be minimized at the same time, as shown in Fig. 9a (maximum at $k_{droop} = 0.0001$ and $k_{droop,gs2} = 0.1$, but minimum at $k_{droop} = 0.1$ and $k_{droop,gs2} = 0.0001$). Thus, the maximum APTC for the whole $p_{gridside}$ is resembled by the maximum range between the upper and lower boundary in Fig. 9b.

Additionally, the eigenvalues with the lowest damping ratio at both limits have been analyzed in order to determine possible limitations and differences between the CSs (Tab. II, Tab. IV). Both analyses have been carried out once for each investigated tuning in order to be able to point out the consequences of a different tuning.

1) Analysis of the maximum APTC of a single terminal: The results of the analysis of the maximum APTC of a single terminal in the case both terminals use the same CS is given in Tab. I. The participation factor analysis of the lowest damped eigenvalues at both limits is given in Tab. II.

The results indicate that the four CSs, where the dc voltage is controlled in the second loop, outperform the remaining CSs. That means, CS 3, 4, 7 and 8 achieve a significant larger APTC. Additionally, they achieve significant lower maximum singular values in steady state, $\overline{\sigma}(E_w(0))$. However, all CSs fulfill the requirements of the stability margin minimizing the voltage deviation ($\overline{\sigma}(E_w(0)) \geq -23.01\,\mathrm{dB}$). The results indicate further that the results are almost the same for the slow tuning.

For all CSs the APTC of a single terminal is maximized in case the difference of the droop gains is high, which minimizes the APTC of the second terminal at the same time, as shown above

TABLE II
PARTICIPATION FACTOR ANALYSIS FOR MAXIMUM APTC OF A SINGLE GSVSC
GSVSC1 + AC GRID 1, GSVSC2 + AC GRID 2, WFVSC +AC GRID, DC GRID

	Fast Response Time							
Control Structure	Highest participation factors of lowest damped EV lower limit				upper limit			
CS 1	32% $i_{g,d,g1}$	30% $v_{o,d,g1}$	18% $v_{o,q,g1}$	17% $i_{g,q,g1}$	45% $v_{o,q,g1}$	43% $i_{g,q,g1}$	5% $i_{l,q,g1}$	3% $\chi_{q,g1}$
CS 2	50% $i_{l,d,g1}$	50% $v_{dc,g1}$	\	\	37% $i_{g,d,wf}$	26% $v_{o,d,wf}$	11% $\chi_{d,wf}$	8% $v_{o,q,wf}$
CS 3	25% $i_{dc,wg2}$	22% $v_{dc,w}$	21% $v_{dc,g2}$	13% $i_{dc,wg1}$	31%$v_{o,d,g1}$	26% $i_{g,d,g1}$	17% $v_{o,q,g1}$	16% $i_{g,q,g1}$
CS 4	24% $i_{dc,wg2}$	23% $v_{dc,w}$	21% $v_{dc,g2}$	13% $i_{dc,wg1}$	31%$v_{o,d,g1}$	26% $i_{g,d,g1}$	17% $v_{o,q,g1}$	16% $i_{g,q,g1}$
CS 5	39% $i_{g,d,g1}$	29% $v_{o,d,g1}$	10% $v_{dc,g1}$	8% $v_{o,q,g1}$	32% $v_{o,d,g2}$	26% $i_{g,d,g2}$	16% $v_{o,q,g2}$	15% $i_{g,q,g2}$
CS 6	39% $i_{g,d,g1}$	29% $v_{o,d,g1}$	8% $v_{dc,g1}$	8% $v_{o,q,g1}$	32% $v_{o,d,g2}$	25% $i_{g,d,g2}$	18% $v_{o,q,g2}$	16% $i_{g,q,g2}$
CS 7	30% $v_{o,q,g2}$	27% $i_{g,q,g2}$	19% $v_{o,d,g2}$	19% $i_{g,d,g2}$	31% $v_{o,d,g1}$	26% $i_{g,d,g1}$	18% $v_{o,q,g1}$	16% $i_{g,q,g1}$
CS 8	25% $i_{dc,wg2}$	23% $v_{dc,w}$	21% $v_{dc,g2}$	13% $i_{dc,wg2}$	31% $v_{o,d,g1}$	26% $i_{d,g,g1}$	18% $v_{o,q,g1}$	16% $i_{g,q,g1}$
	Slow Response Time							
CS 3	23% $v_{dc,w}$	23% $i_{dc,wg2}$	17% $i_{dc,wg1}$	16% $v_{dc,g2}$	24% $v_{dc,g1}$	24% $i_{dc,gg}$	23% $v_{dc,g2}$	7% $\chi_{d,g1}$
CS 4	23% $v_{dc,w}$	22% $i_{dc,wg2}$	17% $i_{dc,wg1}$	16% $v_{dc,g2}$	23% $i_{dc,gg}$	23% $v_{dc,g1}$	23% $v_{dc,g2}$	7% $\chi_{d,g1}$
CS 5	39% $v_{dc,w}$	20% $i_{dc,wg1}$	12% $i_{dc,wg2}$	9% $v_{dc,g2}$	38% $v_{o,d,g1}$	27% $i_{g,d,g1}$	10% $v_{o,q,g1}$	9% $i_{g,q,g1}$
CS 6	39% $v_{dc,w}$	20% $i_{dc,wg1}$	12% $i_{dc,wg2}$	9% $v_{dc,g2}$	28% $v_{o,d,g2}$	24% $i_{g,d,g2}$	22% $v_{o,q,g2}$	20% $i_{g,q,g2}$
CS 7	34% $v_{dc,g1}$	21% $i_{dc,wg1}$	11% $v_{dc,w}$	11% $\chi_{d,g1}$	34% $v_{dc,g1}$	24% $i_{dc,wg1}$	12% $v_{dc,w}$	11% $\chi_{d,g1}$
CS 8	23% $i_{dc,wg2}$	23% $v_{dc,w}$	17% $i_{dc,wg1}$	16% $v_{dc,g2}$	25% $v_{dc,g1}$	24% $i_{dc,gg}$	23% $v_{dc,g2}$	8% $\chi_{d,g1}$

TABLE III
COMPARISON OF MAXIMUM APTC OF SUM OF GSVSCs FOR VARIOUS CONTROL STRUCTURES
REQUIREMENTS: FULFILLED, FULFILLED BUT CLOSE TO BOUNDARY, NOT FULFILLED

	Fast Response Time					**Slow Response Time**				
Control Structure	Max Range $p_{gridside}$	Damping Ratio of lowest damped EV l. limit	Damping Ratio of lowest damped EV u. limit	$\overline{\sigma}(E_w(0))$ lower limit	$\overline{\sigma}(E_w(0))$ upper limit	Max Range $p_{gridside}$	Damping Ratio of lowest damped EV l. limit	Damping Ratio of lowest damped EV u. limit	$\overline{\sigma}(E_w(0))$ lower limit	$\overline{\sigma}(E_w(0))$ upper limit
CS 1	1.97 p.u.	0.23%	13.92%	-26 dB	-27.3 dB					
CS 2	1.95 p.u.	0.16%	0.19%	-23.7 dB	-24 dB					
CS 3	3.02 p.u.	6.19%	8.22%	-61.3 dB	-62 dB	2.9 p.u.	0.002%	5.8%	-27.3 dB	-29 dB
CS 4	2.97 p.u.	8.98%	7.99%	-36.6 dB	-37.3 dB	2.97 p.u.	2.21%	5.87%	-28.9 dB	-29.6 dB
CS 5	2.48 p.u	0.06%	15.49%	-26.4 dB	-26.7 dB	2.76 p.u.	0.5%	11.12%	-26.4 dB	-26.7 dB
CS 6	2.55 p.u	0.05%	17.04%	-26.4 dB	-26.7 dB	2.77 p.u.	0.03%	12.14%	-26.5 dB	-26.9 dB
CS 7	2.47 p.u	0.1%	9.2%	-32 dB	-32.3 dB	2.59 p.u.	0.07%	7.26%	-28.8 dB	-29.1 dB
CS 8	3.02 p.u	6.7%	8.37%	-53.5 dB	-53.9 dB	2.97 p.u.	0.08%	5.6%	-27.8 dB	-28.2 dB

in Fig. 9a. The reason for this is the current limit of 2265 A (= 0.755 p.u.), which limits the current for each line and therefore makes it necessary to minimize the power transfer of the second terminal, in order to transfer as much power as possible from the WSVSC through all three cables to one specific terminal. This might make the results rather specific for this topology, however, the analysis still points out which CSs are capable of withstanding large droop gain deviations within a MT-HVDC grid without leading to instability (in rectifier mode). This is indicated by the very low damping ratios of the lowest damped eigenvalues at the lower limit for CS 1, 2, 5 and 6, as shown in Tab. II. This means further that the APTC of those CSs decreases further for a stability margin demanding a minimum damping ratio of 3%, which leads to an even bigger deviation between the highest and lowest APTC of the various CSs.

The participation factor analysis in Tab. II shows further, which states have a participation in the modes of those eigenvalues with the lowest damping ratio. In fact, in case of the fast tuning, the eigenvalues corresponding to the very low damping ratios at the lower limit (CS 1, 5&6) are related to the GSVSC1, i.e. the GSVSC transferring as much power as possible from the ac to the dc side. Hence, the instability is caused by the terminal and the connected ac grid.

While in case of the slower tuning, the damping ratios at the lower limit do not differ so much anymore, i.e. the ones of the better performing CSs decrease while the damping ratios of the remaining ones remain low. Only CS 7 still fulfills the stability margin in this case. Further, with the slower tuning, the lower limit is related to oscillation within the dc grid for all CSs, as the participation factor analysis indicates (Tab. II). Thus, a faster tuning leads to better damped dc oscillations.

2) Analysis of the maximum APTC of the sum of both GSVSCs: The results of the maximum APTC of all GSVSCs are given in Tab. III. It is shown that the CSs 3 and 8 still outperform the others in case of the fast tuning. While CS 4 still achieves a comparable APTC, CS 3 and 8 achieve significant lower maximum singular values in steady state, $\overline{\sigma}(E_w(0))$, i.e. smaller voltage deviation induced by a variation of the active power of the WFVSC.

The results indicate further that in order to maximize the APTC of all GSVSCs equal droop gains (or small deviations) are preferable, the only exception here is CS 7.

The analysis additionally shows that with slower tuning the maximum singular values of CS 3, 4, 7 and 8 decrease, while the ones of CS 5 and 6 remain approximately constant. Further, with that tuning, the APTC of the CSs 5, 6 and 7 increase while the ones of 3 and 8 decrease, which brings the APTC of all CSs closer to each other. Hence, the various CSs tend to favor different tunings / the impact of the tuning on the CSs

TABLE IV
PARTICIPATION FACTOR ANALYSIS FOR MAXIMUM APTC OF THE SUM OF BOTH GSVSCs
GSVSC1 + AC GRID 1, GSVSC2 + AC GRID 2, WFVSC +AC GRID, DC GRID

	Fast Response Time							
Control Structure	Highest participation factors of lowest damped EV lower limit				upper limit			
CS 1	37% $i_{g,d,g1}$	30% $v_{o,d,g1}$	11% $v_{o,q,g1}$	10% $i_{g,q,g1}$	45% $v_{o,q,g2}$	42% $i_{g,q,g1}$	5% $i_{l,q,g2}$	2% $\chi_{q,g2}$
CS 2	46% $v_{dc,w}$	24% $i_{dc,wg1}$	24% $i_{dc,wg2}$	2% $v_{dc,g2}$	37% $i_{g,d,wf}$	26% $v_{o,d,wf}$	11% $\chi_{d,wf}$	8% $v_{o,q,wf}$
CS 3	26% $v_{dc,w}$	15% $\chi_{d,g1}$	15% $\chi_{d,g2}$	11% $v_{dc,g1}$	15%$v_{o,d,g1}$	15% $v_{o,d,g2}$	13% $i_{g,d,g1}$	13% $i_{g,q,g2}$
CS 4	19% $v_{dc,w}$	18% $i_{dc,wg1}$	17% $v_{dc,g1}$	16% $i_{dc,wg2}$	29%$v_{o,d,g2}$	25% $i_{g,d,g2}$	19% $v_{o,q,g2}$	17% $i_{g,q,g2}$
CS 5	19%$i_{g,d,g1}$	19% $i_{g,d,g2}$	15% $v_{o,d,g1}$	15% $v_{o,d,g2}$	18% $v_{o,q,g1}$	18% $v_{o,q,g2}$	17% $i_{g,q,g1}$	17% $i_{g,q,g2}$
CS 6	19% $i_{g,d,g1}$	19% $i_{g,d,g2}$	15% $v_{o,d,g2}$	15% $v_{o,d,g1}$	17% $v_{o,q,g1}$	17% $v_{o,q,g2}$	16% $i_{g,q,g1}$	16% $i_{g,q,g2}$
CS 7	34% $i_{g,d,g2}$	31% $v_{o,d,g2}$	16% $v_{o,q,g2}$	14% $i_{g,q,g2}$	32% $v_{o,d,g1}$	26% $i_{g,d,g1}$	17% $v_{o,q,g1}$	15% $i_{g,q,g1}$
CS 8	25% $v_{dc,w}$	15% $\chi_{d,g1}$	15% $\chi_{d,g2}$	11% $v_{dc,g1}$	15% $v_{o,d,g1}$	15% $v_{o,d,g2}$	13% $i_{g,d,g1}$	13% $i_{g,d,g2}$
	Slow Response Time							
CS 3	23% $v_{dc,w}$	19% $i_{dc,wg1}$	19% $i_{dc,wg2}$	13% $v_{dc,g1}$	24% $i_{dc,gg}$	23% $v_{dc,g1}$	23% $v_{dc,g2}$	6% $\chi_{d,g1}$
CS 4	24% $v_{dc,w}$	17% $\chi_{d,g1}$	20% $\chi_{d,g2}$	13% $v_{dc,g1}$	24% $i_{dc,gg}$	24% $v_{dc,g1}$	24% $v_{dc,g2}$	7% $\chi_{d,g2}$
CS 5	38% $v_{dc,w}$	16% $i_{dc,wg1}$	16% $i_{dc,wg2}$	8% $\chi_{d,g2}$	17% $v_{o,d,g1}$	17% $v_{o,d,g2}$	13% $i_{g,d,g1}$	13% $i_{g,d,g2}$
CS 6	38% $v_{dc,w}$	16% $i_{dc,wg1}$	16% $i_{dc,wg2}$	7% $\chi_{d,g1}$	34% $v_{o,d,g1}$	26% $i_{g,d,g1}$	16% $v_{o,q,g1}$	14% $i_{g,q,g1}$
CS 7	37% $i_{g,d,g2}$	32% $v_{o,d,g2}$	12% $v_{o,q,g2}$	11% $i_{g,q,g2}$	34% $v_{dc,g1}$	25% $i_{dc,wg1}$	13% $v_{dc,w}$	10% $\chi_{d,g1}$
CS 8	21% $v_{dc,w}$	19% $i_{dc,wg1}$	19% $i_{dc,wg2}$	14% $v_{dc,g1}$	25% $i_{dc,gg}$	24% $v_{dc,g1}$	24% $v_{dc,g2}$	6% $\chi_{d,g1}$

varies for the different CSs.
The damping ratios of the lowest damped eigenvalues, given in Tab. IV, indicate significant difference between the CSs. In fact, a stability margin demanding a minimum damping ratio of 3% with a fast tuning will further decrease the APTC of all CSs except 3, 4 and 8. This will lead to even higher APTC deviation between the various CSs. The lowest damped eigenvalues of the lower limit of all these three cases are related to the dc grid and the droop controller. Whereas in all other cases (except CS 2) the lowest damped eigenvalues of the lower limit are related to ac values of either GSVSC1 or GSVSC2. Given the low damping ratios of those eigenvalues, for CSs 1, 5 ,6 and 7 the lower limit is caused by the ac side oscillations of one of the GSVSCs.
The lowest damped eigenvalues of the upper limit on the other hand have for all CSs a comparable high damping ratio, except for CS 2, where the upper limit is apparently related to oscillations within the ac grid of the WFVSC.

3) Conclusion for both GSVSCs using the same CS: Two important aspects of the APTC have been analyzed, first the maximization of power transfer of a single terminal and then the maximization of APTC of the whole system. The CSs 3, 4 and 8 outperform the remaining CSs in both aspects. In both cases, they obtain wider APTC, higher damping ratios of the lowest damped eigenvalue, as well significant lower maximum singular values. Furthermore, the maximum APTC is only limited by the current limitations.
Additionally, the impact of two different tunings have been compared. The tuning hardly impacts the analysis of maximizing the APTC of a single terminal, while the influence on the second analysis is not negligible. It is obvious that a faster damping leads to better damped dc oscillations. This is indicated by the comparison of the eigenvalue movement for a variation of k_{droop} in Fig. 10. It is obvious that both pairs of complex eigenvalues with $Im\{\lambda\} \approx \pm 400$ are moved to regions with higher damping ratio in the left half-plane. A participation factor analysis indicates that these eigenvalues are related to dc states.
Further, it has been shown that all CSs are not limited by a set of maximum singular values. The damping ratio stability margin on the other hand is limiting specific CSs while others are fulfilling this stability margin without further limitation of the APTC. Hence, in case of demanding a minimum damping ratio of 3%, the differences between the APTC of the various CSs will be even more significant.

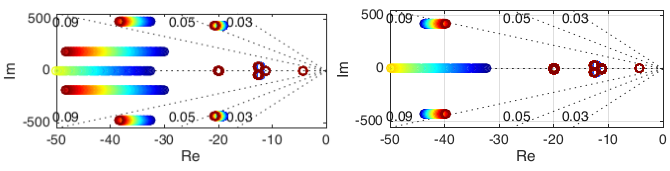

(a) Slow Tuning (b) Fast Tuning

Fig. 10. Movement of the EV and the damping ratios for a variation of $k_{droop} = 0$ p.u. (blue) to 0.1 p.u. (red) in case both GSVSCs use CS 3

TABLE V
MAXIMUM APTC - REQUIREMENTS: ■ FULFILLED

Control Structures	Max Range $p_{gridside}$	$\overline{\sigma}(E_w(0))$ l. limit	$\overline{\sigma}(E_w(0))$ u. limit	Low. Damp. Ratio l. limit	Low. Damp. Ratio u. limit
4 & 3	3.02 p.u.	-61.33 dB	-61.99 dB	6.2 %	8.2 %
8 & 3	3.02 p.u.	-53.5 dB	-53.95 dB	6.7 %	8.4 %
8 & 4	3.02 p.u.	-61.33 dB	-61.99 dB	6.2 %	8.2 %

B. Analysis of the Case where both GSVSCs use different CSs

In order to determine the consequences of combining different CSs within one grid and finding the most beneficial combination, the most promising CSs from the previous analysis have been combined. Thus, GSVSC1 and GSVSC2 will use different droop control structures with the fast tuning in the following. In particular, the combinations of CS 3, 4 and 8 have been analyzed in detail, due to the most promising results in the previous section.
The analysis indicates that the results for a maximization of the APTC of the single terminal do not differ from the previous analysis for the specific CSs. Thus, the focus is put on the maximization of the APTC of the whole system, the results are given in Tab. V. All the three combinations fulfill all requirements and achieve the same APTC. However, both combinations including CS 4 achieve lower maximum singular values than the combination of CS 8 & CS 3, which leads to lower voltage deviation at the GSVSCs induced by a power variation of the WFVSC. The maximum APTC of all these three combinations is limited by the current limit. Thus, with cables enabling a higher current limit the APTC will be further increased. However, this does not imply that for other current limitations different combinations of CSs might be more beneficial, since in the previous analysis it was already shown that these three CSs outperform the remaining once already with this current limit.

V. Conclusion

This paper presented a methodology to determine the active power transfer capability of single terminals within a MTDC grid. A case study was used to analyze deviations in the APTC, considering different stability margins due to the use of various dc voltage droop control structures and two different tunings. It was shown that fast tuning leads to better damping of dc oscillations. Further, it was shown that three different CSs outperform the remaining five. These three have been combined with each other in order to determine the most beneficial combination. In fact, a combination of a control structure using the dc voltage and the ac current (CS 4) with either a control structure using dc voltage and active power measured on the ac side (CS 8) or using dc voltage and dc current (CS 3) leads to even lower voltage deviation induced by power variations of the wind farm. However, additional studies are needed to verify the results for other topologies.

References

[1] P. Kundur, N. J. Balu, and M. G. Lauby, *Power system stability and control*. McGraw-Hill Professional, 1994.

[2] A. Y. Nilanjan Ray Chaudhuri, Balarko Chaudhuri, Rajat Majumder, *Multi-Terminal Direct-Current Grids: Modeling, Analysis, and Control*. Hoboken, New Jersey (USA): John Wiley & Sons, Inc., 2014.

[3] A. Orths, A. Hiorns, R. van Houtert, L. Fisher, and C. Fourment, "The European North Seas Countries' Offshore Grid initiative - The way forward," *2012 IEEE Power & Energy Society General Meeting. New Energy Horizons - Opportunities and Challenges*, pp. 1–8, 2012.

[4] G. Bathurst and P. Bordignan, "Delivery of the Nan'ao Multi-terminal VSC-HVDC System," in *Cigré International Symposium - Across Borders - HVDC Systems and Market Integration*, no. December 2013, Lund, 2015, pp. 1–12.

[5] L. I. Xuan, M. A. Yulong, Y. U. E. Bo, M. A. Weimin, and C. Dong, "Study on Discharge Characteristics of DC System in Zhoushan Multi-Terminal VSC-HVDC Transmission Project," in *Cigré International Symposium - Across Borders - HVDC Systems and Market Integration*, Lund, 2015.

[6] C. D. Barker and R. Whitehouse, "Autonomous converter control in a multi-terminal HVDC system," in *9th IET International Conference on AC and DC Power Transmission, 2010*. London: IET, 2010, pp. 1–5.

[7] T. M. Haileselassie and K. Uhlen, "Power System Security in a Meshed North Sea HVDC Grid," *Proceedings of the IEEE*, vol. 101, no. 4, pp. 978–990, 2013.

[8] V. Akhmatov, M. Callavik, C. M. Franck, S. E. Rye, T. Ahndorf, M. K. Bucher, H. Muller, F. Schettler, and R. Wiget, "Technical guidelines and prestandardization work for first HVDC Grids," *IEEE Transactions on Power Delivery*, vol. 29, no. 1, 2014.

[9] R. T. Pinto, S. F. Rodrigues, and P. Bauer, "Comparison of direct voltage control methods of multi-terminal DC (MTDC) networks through modular dynamic models," in *Proceedings of the 2011-14th European Conference on Power Electronics and Applications (EPE 2011)*, Birmingham, 2011.

[10] J. Liang, T. Jing, O. Gomis-Bellmunt, J. Ekanayake, and N. Jenkins, "Operation and Control of Multiterminal HVDC Transmission for Offshore Wind Farms," *IEEE Transactions on Power Delivery*, vol. 26, no. 4, pp. 2596–2604, 2011.

[11] P. Rault, F. Colas, X. Guillaud, and S. Nguefeu, "Method for small signal stability analysis of VSC-MTDC grids," *2012 IEEE Power and Energy Society General Meeting*, 2012.

[12] W. Wang, M. Barnes, and O. Marjanovic, "Droop control modelling and analysis of multi-terminal VSC-HVDC for offshore wind farms," in *10th IET International Conference on AC and DC Power Transmission*, 2012, pp. 1–6.

[13] T. M. Haileselassie and M. Molinas, "Multi-terminal VSC-HVDC system for integration of offshore wind farms and green electrification of platforms in the North Sea," in *Nordic Workshop on Power and Industrial Electronics (NORPIE/2008)*, 2008.

[14] O. Gomis-Bellmunt, J. Liang, J. Ekanayake, and N. Jenkins, "Voltage-current characteristics of multiterminal HVDC-VSC for offshore wind farms," *Electric Power Systems Research*, vol. 81, no. 2, pp. 440–450, 2011.

[15] L. Xu, L. Yao, and M. Bazargan, "DC grid management of a multi-terminal HVDC transmission system for large offshore wind farms," in *International Conference on Sustainable Power Generation and Supply, 2009*. IEEE, 2009, pp. 1–7.

[16] R. T. Pinto, S. Rodrigues, P. Bauer, and J. Pierik, "Operation and control of a multi-terminal DC network," *IEEE ECCE Asia Downunder 2013*, pp. 474–480, 2013.

[17] F. D. Bianchi and O. Gomis-Bellmunt, "Droop control design for multi-terminal VSC-HVDC grids based on LMI optimization," in *50th IEEE Conference on Decision and Control and European Control Conference*, 2011, pp. 4823–4828.

[18] L. Xu and L. Yao, "DC voltage control and power dispatch of a multi-terminal HVDC system for integrating large offshore wind farms," *Renewable Power Generation, IET*, vol. 5, no. 3, pp. 223–233, 2011.

[19] F. Thams, J. A. Suul, S. D'Arco, M. Molinas, and F. W. Fuchs, "Stability of DC Voltage Droop Controllers in VSC HVDC Systems," in *PowerTech, Eindhoven 2015*, Eindhoven, 2015.

[20] S. D'Arco, J. A. Suul, and M. Molinas, "Implementation and Analysis of a Control Scheme for Damping of Oscillations in VSC-based HVDC Grids," in *16th International Power Electronics and Motion Control Conference and Exposition*, Antalya, Turkey 21-24, 2014, pp. 586–593.

[21] V. Blasko and V. Kaura, "A new mathematical model and control of a three-phase AC-DC voltage source converter," *IEEE Transactions on Power Electronics*, vol. 12, no. 1, pp. 116–123, 1997.

[22] V. Kaura and V. Blasko, "Operation of a phase locked loop system under distorted utility conditions," *IEEE Transactions on Industry Applications*, vol. 33, no. 1, pp. 58–63, 1997.

[23] C. Gavriluta, I. Candela, A. Luna, A. Gomez-Exposito, and P. Rodriguez, "Hierarchical Control of HV-MTDC Systems With Droop-Based Primary and OPF-Based Secondary," *IEEE Transactions on Smart Grid*, vol. 6, no. 3, pp. 1502–1510, 2015.

[24] H. Kolstad, *Control of an Adjustable speed Hydro utilizing field programmable devices*. Trondheim: Ph.D Dissertation, 2002.

[25] M. Malinowski, M. P. Kazmierkowski, and S. Bernet, "New simple active damping of resonance in three-phase PWM converter with LCL filter," in *IEEE International Conference on Industrial Technology 2005*. IEEE, 2005, pp. 861–865.

[26] O. Mo, M. Hernes, and K. Ljøkelsøy, "Active damping of oscillations in LC-filter for line connected, current controlled, PWM voltage source converters," in *10th European Conference on Power Electronics and Applications 2003*, 2003.

[27] C. Bajracharya, M. Molinas, and J. A. Suul, "Understanding of tuning techniques of converter controllers for VSC-HVDC," in *Proceedings of the Nordic Workshop on Power and Industrial Electronics*, 2008.

[28] E. Prieto-Araujo, F. D. Bianchi, A. Junyent-Ferre, and O. Gomis-Bellmunt, "Methodology for Droop Control Dynamic Analysis of Multiterminal VSC-HVDC Grids for Offshore Wind Farms," *IEEE Transactions on Power Delivery*, vol. 26, no. 4, pp. 2476–2485, 2011.

[29] R. L. Hendriks, G. C. Paap, and W. L. Kling, "Control of a multiterminal VSC transmission scheme for connecting offshore wind farms," *European Wind Energy Conference*, 2007.

[30] Y. Chen, G. Damm, and A. Benchaib, "Multi-Time-Scale Stability Analysis and Design Conditions of a VSC Terminal with DC Voltage Droop Control for HVDC Networks," in *53rd IEEE Conference on Decision and Control*, Los Angeles, CA, 2014.

[31] B. K. Johnson, R. H. Lasseter, F. L. Alvarado, and R. Adapa, "Expandable multiterminal dc systems based on voltage droop," *IEEE Transactions on Power Delivery*, vol. 8, no. 4, 1993.

[32] S. Zhou, J. Liang, J. B. Ekanayake, and N. Jenkins, "Control of multi-terminal VSC-HVDC transmission system for offshore wind power generation," in *Proceedings of the 44th International Universities Power Engineering Conference , 2009*, 2009.

[33] J. Dragon, L. Werner, and J. Hanson, "Effects of DC Voltage Droop Characteristics on Contingency Behaviour of AC / DC Systems," in *49th International Universities' Power Engineering Conference (UPEC)*, Cluj-Napoca, 2014.

[34] T. M. Haileselassie and K. Uhlen, "Impact of DC Line Voltage Drops on Power Flow of MTDC Using Droop Control," *IEEE Transactions on Power Systems*, vol. 27, no. 3, pp. 1441–1449, 2012.

[35] ——, "Precise control of power flow in multiterminal VSC-HVDCs using DC voltage droop control," *2012 IEEE Power and Energy Society General Meeting*, pp. 1–9, 2012.

[36] ——, "Primary frequency control of remote grids connected by multi-terminal HVDC," *Power and Energy Society General Meeting, 2010 IEEE*, pp. 1–6, 2010.

[37] G. Stamatiou and M. Bongiorno, "Decentralized converter controller for multiterminal HVDC grids," in *15th European Conference on Power Electronics and Applications (EPE), 2013*. IEEE, 2013, pp. 1–10.

[38] T. K. Vrana, Y. Yang, D. Jovcic, S. Dennetière, J. Jardini, and H. Saad, "The CIGRE B4 DC Grid Test System," Cigre, Tech. Rep., 2013.

[39] G. Pinares, L. B. Tjernberg, L. A. Tuan, C. Breitholtz, and A.-A. Edris, "On the analysis of the dc dynamics of multi-terminal VSC-HVDC systems using small signal modeling," *2013 IEEE Grenoble Conference*, pp. 1–6, 2013.

[40] E. Prieto-Araujo, A. Egea-Alvarez, S. F. Fekriasl, and O. Gomis-Bellmunt, "DC voltage droop control design for multi-terminal HVDC systems considering AC and DC grid dynamics," *IEEE Transactions on Power Delivery*, vol. 31, no. 2, pp. 575 – 585, 2015.

[41] Maxima CAS Development Team, "Maxima, a Computer Algebra System," p. GNU General Public License (GPL), 2015.

APPENDIX

TABLE VI
BASE VALUES OF PER UNIT SYSTEM AND PARAMETERS

Parameter	Value
Rated voltage, $V_{S,LL,RMS}$	$220\,\mathrm{kV}$
Rated power, $S_{b,gsvsc}$	$1200\,\mathrm{MVA}$
Rated power, $S_{b,wfvsc}$	$2 \cdot 1200\,\mathrm{MVA}$
Rated dc voltage, V_{dc}	$400\,\mathrm{kV}$
Rated angular frequency, ω_b	$2\pi 50\,\mathrm{s}^{-1}$
Base value for voltage defined as peak value of phase voltage, V_b	$\sqrt{\frac{2}{3}} V_{S,LL,RMS}$
Base value for currents defined as peak value or rated RMS, I_b	$\frac{S_b}{\sqrt{3} V_{S,LL,RMS}}$
Base value for impedance, Z_b	$\frac{V_b}{I_b}$
Base value for filter inductance, L_b	$\frac{Z_b}{\omega_b}$
Base value for filter capacitance, C_b	$\frac{1}{\omega_b Z_b}$
Line resistance, R	$0.011\,\Omega/\mathrm{km}$
Line inductance, L	$2.615\,\mathrm{mH/km}$
Line capacitance, C	$0.1908\,\mu\mathrm{F/km}$
Cable distances	$67\,\mathrm{km}$
Equivalent dc capacitor, c_{dc}	$4.2\,\mathrm{p.u.}$
Grid voltage, $\hat{v}_g$	$1\,\mathrm{p.u.}$
Filter inductance, l_f	$0.08\,\mathrm{p.u.}$
Filter resistance, r_f	$0.003\,\mathrm{p.u.}$.
Filter capacitance, c_f	$0.074\,\mathrm{p.u.}$
Grid inductance, l_g	$0.2\,\mathrm{p.u.}$
Grid resistance, r_g	$0.01\,\mathrm{p.u.}$
Reactive power reference, q^*	$0\,\mathrm{p.u.}$
Ac voltage reference, $v^*_{o,d,wf}$	$1\,\mathrm{p.u.}$
Low-Pass filter frequency, ω_{AD}	$20\,\mathrm{p.u.}$
Active damping parameter (GSVSCs), $k_{ad,gsvsc}$	$0.2\,\mathrm{p.u.}$
Active damping parameter (WFVSC), $k_{ad,wfvsc}$	$1\,\mathrm{p.u.}$

Florian Thams received the B.Sc. and M.Sc. in Business Administration and Engineering from the Christan Albrechts University of Kiel, Germany, in 2012 and 2015, respectively. From February 15 to June 15 he joined the Center of Electric Power and Energy at the Technical University of Denmark (DTU) as Research Assistant. Currently he is pursuing his PhD at the same institute working within the EU BestPath project.

Robert Eriksson Robert Eriksson (M06) received his M.Sc. and Ph.D. degrees in electrical engineering from the KTH Royal Institute of Technology, Stockholm, Sweden, in 2005 and 2011, respectively. He held a position as Associate Professor with the Center for Electric Power and Energy (CEE), DTU Technical University of Denmark between 2013 and 2015. He is currently employed by the Swedish National Grid, focusing on research and development, at the Department of Market and System development. His research interests include power system dynamics and stability, HVDC systems, dc grids, and automatic control.

Marta Molinas Marta Molinas (M'94) received the Diploma degree in electromechanical engineering from the National University of Asuncion, Asuncion, Paraguay, in 1992; the Master of Engineering degree from Ryukyu University, Japan, in 1997; and the Doctor of Engineering degree from the Tokyo Institute of Technology, Tokyo, Japan, in 2000. She was a Guest Researcher with the University of Padova, Padova, Italy, during 1998. From 2004 to 2007, she was a Postdoctoral Researcher with the Norwegian University of Science and Technology (NTNU) and from 2008-2014 she has been professor at the Department of Electric Power Engineering at the same university. She is currently Professor at the Department of Engineering Cybernetics, NTNU. Her research interests include stability of power electronics systems, harmonics, instantaneous frequency, and non-stationary signals from the human and the machine. She is Associate Editor for the IEEE Journal JESTPE, IEEE PELS Transactions and Editor of the IEEE Transactions on Energy Conversion. Dr. Molinas has been an AdCom Member of the IEEE Power Electronics Society from 2009 to 2011.

[Pub. B] Efficient Database Generation for Data-driven Security Assessment of Power Systems.

Efficient Database Generation for Data-driven Security Assessment of Power Systems

Florian Thams, *Student Member, IEEE,* Andreas Venzke, *Student Member, IEEE,*
Robert Eriksson, *Senior Member, IEEE,* Spyros Chatzivasileiadis, *Senior Member, IEEE*

***Abstract*—Power system security assessment methods require large datasets of operating points to train or test their performance. As historical data often contain limited number of abnormal situations, simulation data are necessary to accurately determine the security boundary. Generating such a database is an extremely demanding task, which becomes intractable even for small system sizes. This paper proposes a modular and highly scalable algorithm for computationally efficient database generation. Using convex relaxation techniques and complex network theory, we discard large infeasible regions and drastically reduce the search space. We explore the remaining space by a highly parallelizable algorithm and substantially decrease computation time. Our method accommodates numerous definitions of power system security. Here we focus on the combination of N-1 security and small-signal stability. Demonstrating our algorithm on IEEE 14-bus and NESTA 162-bus systems, we show how it outperforms existing approaches requiring less than 10% of the time other methods require.**

***Index Terms*—Convex relaxation, data-driven, power system analysis, small-signal stability**

I. Introduction

SECURITY assessment is a fundamental function for both short-term and long-term power system operation. Operators need to eliminate any probability of system failure on a sub-hourly basis, and need to guarantee the security of supply in the long-term, having the required infrastructure and operating practices in place. All these functions require the assessment of thousands of possibilities with respect to load patterns, system topology, power generation, and the associated uncertainty which is taking up a more profound role with the increased integration of renewable energy sources (RES). Millions of possible operating points violate operating constraints and lead to an insecure system, while millions satisfy all limitations and ensure safe operation. For systems exceeding the size of a few buses it is impossible to assess the total number of operating points, as the problem complexity explodes. Therefore, computationally efficient methods are necessary to perform a fast and accurate dynamic security assessment.

Numerous approaches exist in the literature proposing methods to assess or predict different types of instability, e.g. transient, small-signal, or voltage instability. Recently, with the abundance of data from sensors, such as smart meters and phasor measurement units, machine learning approaches have emerged showing promising results in tackling this problem [1]–[4]. Due to the high reliability of the power system operation, however, historical data are not sufficient to train such techniques, as information related to the security boundary or insecure regions is often missing. For that, simulation data are necessary.

This paper deals with the fundamental problem that most of the dynamic security assessment (DSA) methods are confronted with before the implementation of any algorithm: the generation of the necessary dataset which is required for the development of dynamic security classification approaches. With this work we aim to propose a modular and scalable algorithm that can map the secure and insecure regions, and identify the security boundaries of large systems in a computationally efficient manner.

There are two main challenges with the generation of such a database. First, the problem size. It is computationally impossible to assess all possible operating points for systems exceeding a few tens of buses. Second, the information quality. Dynamic security assessment is a non-convex and highly nonlinear problem. Generating an information-rich and not too large dataset can lead to algorithms that can be trained faster and achieve higher prediction accuracy.

The efforts to develop a systematic and computationally efficient methodology to generate the required database have been limited up to date. In [5], [6] re-sampling techniques based on post-rule validation were used to enrich the database with samples close to the boundary. Genc et al. [7] propose to enrich the database iteratively with additional points close to the security boundary by adding operating points at half the distance of the already existing operating points at the stability boundary. In [2], [8]–[11], the authors propose to use importance sampling methods based on Monte-Carlo variance reduction (MCVR) technique, introducing a bias in the sampling process such that the representation of rare events increases in the assessment phase. In [12], the authors propose a composite modelling approach using high dimensional historical data.

This work leverages advancements in several different fields to propose a highly scalable, modular, and computationally efficient method. Using properties derived from convex relaxation techniques applied on power systems, we drastically reduce the search space. Applying complex network theory approaches, we identify the most critical contingencies boosting the efficiency of our search algorithms. Based on steepest descent methods, we design the exploration algorithm in a highly parallelizable fashion, and exploit parallel computing to reduce computation time. Compared with existing approaches, our method achieves a speed-up of 10 to 20 times, requiring less than 10% of the time other approaches need to achieve the same results.

F. Thams, A. Venzke, and S. Chatzivasileiadis are with the Center for Electric Power and Energy (CEE), Technical University of Denmark (DTU), Kgs. Lyngby, Denmark. E-mail: {fltha, andven, spchatz} @elektro.dtu.dk.

R. Eriksson is with the Department of Market and System Development, Svenska kraftnät, Sundbyberg, Sweden. E-mail: robert.eriksson@svk.se

The contributions of this work are the following:

- We propose a computationally efficient and highly scalable method to generate the required datasets for the training or testing of dynamic security assessment methods. Our approach requires less than 10% of the time existing methods need for results of similar quality.
- Our method is modular and can accommodate several types of security boundaries, including transient stability and voltage stability. In this paper, we demonstrate our approach considering the combination of N-1 security and small signal stability.
- Besides the database generation, the methodology we propose can be easily employed in real-time operation, where computationally efficient techniques are sought to explore the security region in case of contingencies around the current operating point.

The remainder of this paper is organized as follows: First, a set of terms are defined in Section II. In Section III, we describe the challenges of the database generation for data-driven security analysis. Section IV provides an overview of the methodology, which we detail in the two subsequent sections. Section V describes how we reduce the search space, while Section VI describes the highly parallelizable exploration of the remaining space. We demonstrate our methods in Section VII. Section VIII concludes the paper.

II. Definitions

1) Security boundary: the boundary γ dividing the secure from the insecure region; (a) can correspond to a specific stability boundary, e.g. small-signal stability or voltage stability, (b) can represent a specific stability margin, i.e. all operating points not satisfying the stability margin belong to the insecure region, (c) can be a combination of security indices, e.g. the intersection of operating points that are both N-1 secure and small-signal stable. Note that our proposed method can apply to any security boundary the user needs to consider.

2) HIC – High Information Content: the set Ω of operating points in the vicinity of the security boundary γ, see (2) [10]. This is the search space of high interest for our methods as it separates the secure from insecure regions.

3) DW – Directed Walk: we use this term to denote the steepest descent path our algorithm follows, starting from a given initialization point, in order to arrive close to the security boundary.

III. Challenges of the Database Generation

Determining the secure region of a power system is an NP-hard problem. In an ideal situation, in order to accurately determine the non-convex secure region we need to discretize the whole space of operating points with an as small interval as possible, and perform a security assessment for each of those points. For a given system topology, this set consists primarily of all possible combinations of generator and load setpoints (NB: if the system includes tap-changing transformers, and other controllable devices, the number of credible points increases geometrically). Thus, in a classical brute force approach, the number of points to be considered is given by:

$$|\Psi| = \Lambda \cdot \prod_{i=1}^{N_G-1} \left(\frac{P_i^{max} - P_i^{min}}{\alpha} + 1 \right), \tag{1}$$

where N_G is the number of generators i, P_i^{max} and P_i^{min} is their maximum and minimum capacity, α is the chosen discretization interval between the generation setpoints, and Λ represents the number of different load profiles. For example, for the IEEE 14 bus system [13] with 5 generators and a discretization interval of $\alpha = 1\,\text{MW}$, a classical brute force approach requires $|\Psi| \approx 2.5 \cdot 10^6$ operating points to be assessed for a single load profile. It can be easily seen that security assessment of large systems can very fast result in an intractable problem. For example, in the NESTA 162 bus system [14], a brute force approach would require the analysis of $7 \cdot 10^{29}$ points. It becomes clear that the efficient database generation is one of the major challenges for the implementation of data-driven tools in power system security analysis. In this effort, we need to balance the trade-off between two partially contradicting goals: keep the database as small as possible to minimize computational effort, but contain enough data to determine the security boundary as accurately as possible. To better illustrate our approach, in Fig. 1 we show all possible operating points of two generators for a certain load profile in a system. Focusing on small-signal stability here, we define the security boundary γ as a certain level of minimum damping ratio, which corresponds to our stability margin. All safe operating points, with a damping ratio below γ, are plotted in blue, while operating points that do not fulfill the stability margin are plotted in yellow. From Fig.1, it is obvious that if we are able to assess all points close to γ, it is easy to classify the rest of the points. By that, the size of the required database can be significantly reduced. In the remainder of this paper, we will call the set of operating points in the vicinity of γ as the set of *high information content (HIC)*, defined as follows:

$$\Omega = \{OP_k \in \Psi \mid \gamma - \mu < \gamma_k < \gamma + \mu\}, \tag{2}$$

with γ_k denoting the value of the chosen stability margin for operating point OP_k and μ representing an appropriate small value to let $|\Omega|$ be large enough to describe the desired security boundary with sufficient accuracy. The value of μ depends on the chosen discretization interval in the vicinity of the boundary. In Fig. 1, the HIC set, i.e. all points $OP_k \in \Omega$, is visualized as the grey area surrounding γ. In this small example, we were able to assess all possible operating points and accurately determine the HIC area. For large systems this is obviously not possible. As a result, in the general case, the main challenge is to find the points OP_k which belong to the HIC area $|\Omega|$.

To put the difference between $|\Psi|$ and $|\Omega|$ in perspective: for the small signal stability analysis of the IEEE 14 bus

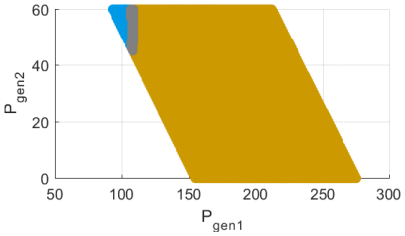

Fig. 1. Scatter plot of all possible operating points of two generators for a certain load profile. Operating points fulfilling the stability margin and outside the high information content (HIC) region ($\gamma_k > 3.25\%$) are marked in blue, those not fulfilling the stability margin and outside HIC ($\gamma_k < 2.75\%$) are marked in yellow. Operating points located in the HIC region ($2.75\% < \gamma_x < 3.25\%$) are marked in grey.

system, the classical brute force approach requires the analysis of $|\Psi| \approx 2.5 \cdot 10^6$ operating points (OPs) for a single load profile. By assuming a required damping ratio of $\gamma = 3\,\%$, and $\mu = 0.25\,\%$, the HIC set, defined as $\Omega = \{OP_k \in \Psi \mid 2.75\,\% < \gamma_k < 3.25\,\%\}$, reduces the analysis to only 1457 points (here, γ refers to the damping ratio of the lowest damped eigenvalue). In other words, by assessing only $0.06\,\%$ of all data points, we can accurately determine the whole secure region of this example.

This small amount of required operating points to assess has actually worked as an obstacle for one of the most popular approaches in previous works: importance sampling. Importance sampling re-orients the sampling process towards a desired region of interest in the sampling space, while also preserving the probability distribution. Thus, it requires that the initial sampling points include sufficient knowledge about the desired region of interest. However, the smaller the proportion of the region of interest is in respect to the entire multi-dimensional space, the larger the initial sample size needs to be to include a sufficient number of points within the desired region of interest. Therefore, the use of expert knowledge [5], [6], [10], regression models [2] or linear sensitivities [10] are proposed to determine the desired region and reduce the search space. However, since this search space reduction is based on a limited initial sample size, it entails the risk of either missing regions of interest not represented in the initial sample or requires a large initial sample which increases computational burden. Furthermore, previous works [7], [10] often use expert knowledge to reduce the burden of the N-1 security assessment to a few critical contingencies. Our proposed method does not require expert knowledge and avoids potential biases by not separating the knowledge extraction from the sampling procedure.

IV. Methodology

We divide the proposed methodology in two main parts. First, the search space reduction by the elimination of a large number of infeasible (and insecure) operating points. Second, the directed walks: a steepest-descent based algorithm to explore the search space and accurately determine the security boundary. During the search space reduction, we exploit properties of convex relaxation techniques to discard large infeasible regions. In order to reduce the problem complexity, we employ complex network theory approaches which allow us to identify the most critical contingencies. Finally, designing the directed walks as a highly parallelizable algorithm, we use parallel computing capabilities to drastically reduce the computation time.

The different parts are described in detail in the following sections. Our algorithm starts by uniformly sampling the search space using the Latin Hypercube Sampling (LHS) method, to generate initialization points for the subsequent steps (Section V-A). Following that, we propose a convex grid pruning algorithm, which also considers contingency constraints, to discard infeasible regions and reduce the search space (Section V-B). In Section V-C, we leverage complex network theory approaches to identify the most critical contingencies. The identified contingency set is crucial both for the grid pruning algorithm, and for subsequent steps within the Directed Walks. After resampling the now significantly reduced search space, we use these samples as initialization points for the Directed Walk (DW) algorithm, described in Section VI. In order to achieve an efficient database generation, the goal of the algorithm is to traverse as fast as possible large parts of the feasible (or infeasible) region, while carrying out a high number of evaluations inside the HIC region. This allows the algorithm to focus on the most relevant areas of the search space in order to accurately determine the security boundary. The DWs are highly parallelizable, use a variable step size depending on their distance from the security boundary, and follow the direction of the steepest descent. Defining the secure region as the N-1 secure *and* small signal stable region in our case studies, we demonstrate how our method outperforms existing importance sampling approaches, achieving a 10 to 20 times speed-up.

V. Reducing the Search Space

A. Choice of Initialization Points

An initial set of operating points is necessary to start our computation procedure. Using the Latin Hypercube Sampling (LHS), we sample the space of operating points to select the initialization points η. Besides the initialization points at the first stage, η_1, our method requires the finer selection of initialization samples, η_2 and η_3 during the reduction of the search space in two subsequent stages, as will be explained later. We use the same sampling procedure at all stages. The Latin hypercube sampling (LHS) aims to achieve a uniform distribution of samples across the whole space. Dividing each dimension in subsections, LHS selects only one sample from each subsection of each parameter, while, at the same time, it maximizes the minimum distance between the samples [2]. An even distribution of the initialization points over the multi-dimensional space is of high importance in order to increase the probability that our method does not miss any infeasible region or any HIC region. The number of initialization points $|\eta|$ is a tuning factor which depends on the specific system under investigation. In general, quite sparse discretization intervals are used for the search space reduction procedures in the first two stages of our approach, η_{1-2}, while a more dense discretization interval is used for the directed walks at a later stage, η_3. Suitable values are discussed in the case study. While LHS allows an even sampling, it is very computationally expensive for high-dimensional spaces and large numbers of initialization points. Thus, for larger systems there is a trade-off between initial sampling and computation time, that needs to be considered.

B. Grid Pruning Algorithm For Search Space Reduction

Given the η_1 initialization points from the first stage, the aim of this stage is to reduce the search space by eliminating infeasible operating regions. For that, we use a grid pruning algorithm which relies on the concept of convex relaxations. The algorithm is inspired by [15], where it was developed to compute the feasible space of small AC optimal power flow (OPF) problems. In this work, we introduce a grid pruning algorithm which determines infeasible operating regions considering not only the intact system but also all N-1 contingencies.

Convex relaxations have been recently proposed to relax the non-convex AC-OPF to a semidefinite program [16]. A corollary of that method is that the resulting semidefinite relaxation provides an infeasibility certificate: If an initialization point is infeasible for the semidefinite relaxation, it is guaranteed to be infeasible for the non-convex AC-OPF problem. This property is used in our grid pruning algorithm.

The semidefinite relaxation introduces the matrix variable W to represent the product of real and imaginary parts of the complex bus voltages, (for more details the interested reader is referred to [16], [17]). Defining our notation, the investigated power grid consists of $\mathcal{N}$ buses, where $\mathcal{G}$ is the set of generator buses. We consider a set of line outages C, where the first entry of set C corresponds to the intact system state. The following auxiliary variables are introduced for each bus $i \in \mathcal{N}$ and outage $c \in C$:

$$Y_i^c := e_i e_i^T Y^c \tag{3}$$

$$\mathbf{Y}_i^c := \frac{1}{2}\begin{bmatrix} \Re\{Y_i^c + (Y_i^c)^T\} & \Im\{(Y_i^c)^T - Y_i^c\} \\ \Im\{Y_i^c - (Y_i^c)^T\} & \Re\{Y_i^c + (Y_i^c)^T\} \end{bmatrix} \tag{4}$$

$$\bar{\mathbf{Y}}_i^c := \frac{-1}{2}\begin{bmatrix} \Im\{Y_i^c + (Y_i^c)^T\} & \Re\{Y_i^c - (Y_i^c)^T\} \\ \Re\{(Y_i^c)^T - Y_i^c\} & \Im\{Y_i^c + (Y_i^c)^T\} \end{bmatrix} \tag{5}$$

$$M_i := \begin{bmatrix} e_i e_i^T & 0 \\ 0 & e_i e_i^T \end{bmatrix} \tag{6}$$

Matrix Y^c denotes the bus admittance matrix of the power grid for outage c, and e_i is the i-th basis vector. The initialization points η_1 from stage A (see Section V-A) correspond to both feasible and infeasible operating points for the AC power flow. Given a set-point P^* for the generation dispatch (corresponding to initialization point η_1^*), (7) – (13) compute the minimum distance from P^* to the closest feasible generation dispatch. Obviously, if P^* is a feasible generation dispatch, the minimum distance is zero.

$$\min_{W^c} \sqrt{\sum_{i\in\mathcal{G}} (\mathrm{Tr}\{\mathbf{Y}_i^0 W^0\} + P_{D_i} - P_i^*)^2} \tag{7}$$

$$\text{s.t. } \underline{P}_{G_i} \le \mathrm{Tr}\{\mathbf{Y}_i^c W^c\} + P_{D_i} \le \overline{P}_{G_i} \quad \forall i \in \mathcal{N}\, \forall c \in C \tag{8}$$

$$\underline{Q}_{G_i} \le \mathrm{Tr}\{\bar{\mathbf{Y}}_i^c W^c\} + Q_{D_i} \le \overline{Q}_{G_i} \quad \forall k \in \mathcal{N}\, \forall c \in C \tag{9}$$

$$\underline{V}_i^2 \le \mathrm{Tr}\{M_i W^c\} \le \overline{V}_i^2 \quad \forall i \in \mathcal{N}\, \forall c \in C \tag{10}$$

$$W^c \succeq 0 \quad \forall c \in C \tag{11}$$

$$\mathrm{Tr}\{\mathbf{Y}_i^c W^c\} = \mathrm{Tr}\{\mathbf{Y}_i^0 W^0\} \quad \forall i \in \mathcal{G}\backslash\{\text{slack}\}\, \forall c \in C \tag{12}$$

$$\mathrm{Tr}\{M_i W^c\} = \mathrm{Tr}\{M_i W^0\} \quad \forall k \in \mathcal{G}\, \forall c \in C \tag{13}$$

The matrix variable W^0 refers to the intact system state. The terms $\underline{P}_{G_i}$, $\overline{P}_{G_i}$, $\underline{Q}_{G_i}$, $\overline{Q}_{G_i}$ are the maximum and minimum active and reactive power limits of the generator at bus i, respectively. The active and reactive power demand at bus i is denoted with the terms P_{D_i} and Q_{D_i}. The bus voltages at each bus i are constrained by upper and lower bounds $\overline{V}_i$ and $\underline{V}_i$. In case of an outage, the generator active power and voltage set-points remain fixed (12) – (13), as traditional N-1 calculations do not consider corrective control. To reduce the computational complexity of the semidefinite constraint (11), we apply a chordal decomposition according to [17] and enforce positive semidefiniteness only for the maximum cliques of matrix W^c.

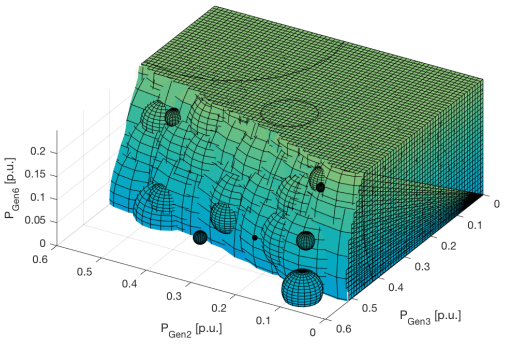

Fig. 2. Search space reduction obtained by the proposed grid pruning algorithm for the IEEE 14 bus system. Operating points within the structure formed by superimposed spheres are infeasible considering N-1 security.

To obtain an objective function linear in W^0, we introduce the auxiliary variable R and replace (7) with:

$$\min_{W^c, R} \quad R \tag{14}$$

$$\text{s.t.} \sqrt{\sum_{i\in\mathcal{G}} (\mathrm{Tr}\{\mathbf{Y}_i^0 W^0\} + P_{D_i} - P_i^*)^2} \le R \tag{15}$$

The convex optimization problem (8) – (15) guarantees that the hypersphere with radius R around the operating point P^* does not contain any points belonging to the non-convex feasible region, considering both the intact system state and the contingencies in set C. Note that the obtained closest generation dispatch $P_i^0 = \mathrm{Tr}\{\mathbf{Y}_i^0 W^0\} + P_{D_i}$ is feasible in the relaxation but not necessarily in the non-convex problem. Hence, with R we obtain a lower bound of the distance to the closest feasible generation dispatch in the non-convex problem.

In a procedure similar to [18], we apply an iterative algorithm for the grid pruning: First, given η_1 initialization points, we solve (8) – (15) without considering contingencies, i.e. $C = \{0\}$. Using the determined hyperspheres, we eliminate the infeasible operating regions and, using LHS, we resample the reduced search space to select a reduced set of initialization points η_2. In the next stage, given η_2, we determine the five most critical contingencies (see section V-C for more details) and resolve (8) – (15). We remove all resulting infeasible regions from the set η_2, and using LHS we resample the remaining feasible region to determine the initialization set η_3. The number of considered contingencies is a trade-off between the amount of obtained infeasible points and the required computational time to solve the semidefinite relaxation.

As an example, we consider the IEEE 14 bus system in a scenario where all but three generators (P_{gen2-4}) are fixed to specific values. Considering the five most critical contingencies, and using our proposed convex grid pruning algorithm, the search space is reduced by 65.34 %. This is visualized in Fig. 2; the colored area shows the discarded regions of infeasible points as determined by the superposition of the spheres.

C. Determining the Most Critical Contingencies

From the definition of N-1 security criterion it follows that a single contingency suffices to classify an operating point as infeasible. Most of the unsafe operating points, however, belong to the infeasible regions of several contingencies.

As a result, focusing only on a limited number of *critical* contingencies, we can accurately determine a large part of the N-1 insecure region, thus reducing the search space without the need to carry out a redundant number of computations for the whole contingency set. This drastically decreases the computation time.

The goal of this section is to propose a methodology that determines the most critical contingencies, which can then be used both in the convex grid pruning algorithm (8) – (15), and in the step direction of the DWs in Section VI-2. While classical N-1 analyses are computationally demanding, recent approaches based on complex network theory showed promising results while requiring a fraction of that time. Refs. [19], [20] propose fast identification of vulnerable lines and nodes, using concepts such as the (extended) betweenness or the centrality index.

The centrality index used in [20], and first proposed for power systems in [21], [22], is based on a classical optimization problem in complex network theory, known as maximum flow problem. The index refers to the portion of the flow passing through a specific edge in the network. Components with higher centrality have a higher impact on the vulnerability of the system, and thus have higher probability to be critical contingencies.

Similar to [20], we adopt an improved max-flow formulation for the power system problem, which includes vertex weights, and extends the graph with a single global source and a single global sink node. The improved formulation accounts for the net load and generation injections at every vertex, avoids line capacity violations resulting from the superposition of different source-sink combinations, and decreases computation time. Contrary to [20], however, we use a modified definition of the centrality index. While Fang et al. [20] analyze the most critical contingencies for all generation and demand patterns, we are interested in the most critical contingency for every *specific* load and generation profile, i.e. for every operating point OP_k. Thus, for each operating point OP_k we define the centrality index as:

$$C_{ij}^{(k)} = f_{ij,actual}^{(k)} / f_{max}^{(k)}. \tag{16}$$

where $f_{ij,actual}^{(k)}$, are the actual flows for that operating point OP_k, and $f_{max}^{(k)}$ represents the maximum possible flow between global source and global sink node for the same case. Thus, at every operating point OP_k, the lines are ranked according to their contribution to the maximum flow in the system. The higher their centrality index is, the more vulnerable becomes the system in case they fail, and as a result they are placed higher in the list of most critical contingencies.

The case study includes a brief discussion about the performance of this vulnerability assessment for the investigated systems. Despite the drastic decrease in computation time and its general good performance, the proposed approach still includes approximations. As we will see in Sections VI-7–VI-8, we take all necessary steps to ensure that we have avoided any possible misclassification.

VI. Directed Walks

1) Variable Step Size: As mentioned in Section III, to achieve an efficient database generation our focus is to assess a sufficiently high number of points inside the HIC area, while traverse the rest of the space faster and with fewer evaluations. To do that, we propose to use a variable step size α depending on the distance d of the operating point from the security boundary γ. The distance $d(OP_k)$ of the operating point under investigation is defined as:

$$d(OP_k) = |\gamma_k - \gamma|, \tag{17}$$

with γ_k being the stability index value for operating point OP_k. Then, for OP_k we define the variable step size α_k as follows:

$$\alpha_k = \begin{cases} \epsilon_1 \cdot P^{max}, & \text{if } d(OP_k) > d_1 \\ \epsilon_2 \cdot P^{max}, & \text{if } d_1 \geq d(OP_k) > d_2 \\ \epsilon_3 \cdot P^{max}, & \text{if } d_2 \geq d(OP_k) > d_3 \\ \epsilon_4 \cdot P^{max}, & \text{otherwise} \end{cases}, \tag{18}$$

where P^{max} is the vector of generator maximum capacities, ϵ_{1-4} are scalars, and for distances d_{1-3} holds $d_1 > d_2 > d_3$. Since the system is highly nonlinear (in our case study for example we are searching for the minimum damping ratio considering N-1 security, i.e. $\Gamma + 1$ different nonlinear systems superimposed), the exact step size required to reach the HIC region cannot be constant and determined a-priori. Thus, the step size is gradually reduced as we approach the security boundary in order not to miss any points within the HIC region. This is illustrated in Fig. 3.

It follows that distances d_{1-3} and the corresponding ϵ_{1-4} are tuning factors, to be chosen depending on the desired speed, granularity, precision and given system size. Factors found useful for given systems are discussed in the case study.

2) Determining the Step Direction: After identifying the step size, we need to determine the direction of the next step. Our goal is to traverse the feasible (or infeasible) region as fast as possible, and enter the HIC region. To do that, at every step we follow the steepest descent of the distance metric $d(OP_k)$, as shown in (19).

$$OP_{k+1} = OP_k - \alpha_k \cdot \nabla d(OP_k) \tag{19}$$

where α_k is the step size for OP_k, defined in (18), and $\nabla d(OP_k)$ is the gradient of $d(OP_k)$. As the distance is a function of the chosen stability index, it is user specific and $\nabla d(OP_k)$ in the discrete space shall be determined by a suitable sensitivity measure, which differs for different stability indices. If the focus is on voltage stability for example, the associated margin sensitivities could be used [23]. It is stressed that our method is suitable for any sensitivity capable of measuring the distance to the chosen stability index. In the case studies of this paper, we focus on small-signal stability and, as described in the next paragraph, we pick the damping ratio sensitivity as a suitable measure.

Normally, at every step k we should measure distance d for all $N-1$ contingencies, select the minimum of those distances and based on that, determine the next step size and direction. Having thousands of initialization points η_3 implies checking along all possible dimensions and $N-1$ contingencies at every step of thousands of directed walks. Beyond a certain system size, this becomes computationally intractable. Instead, we take advantage of the critical contingency identification procedure described in Section V-C, and at every step we measure distance d assuming the most critical contingency for

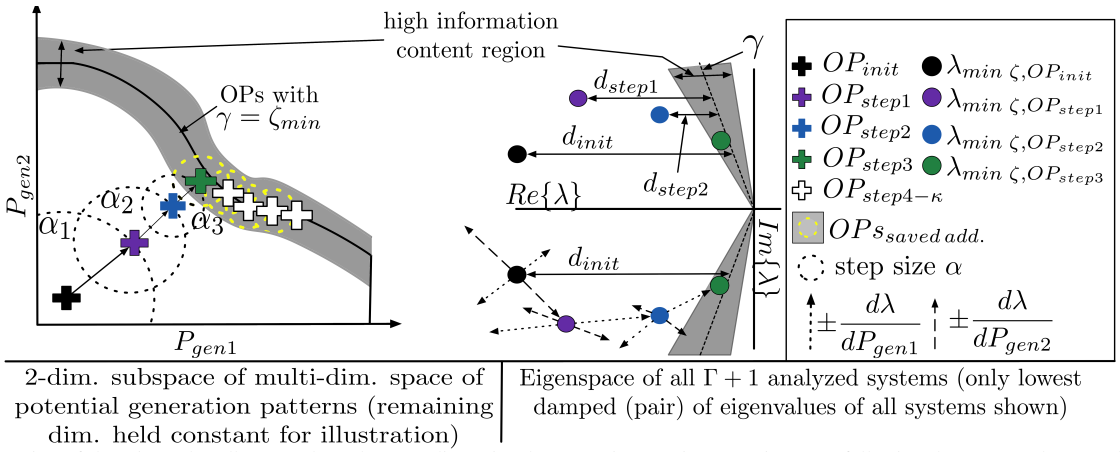

Fig. 3. Illustration of the Directed Walk (DW) through a two dimensional space using varying step sizes, α_i, following the steepest descent of distance, d.

OP_k. This reduces the required analysis from $\Gamma+1$ systems to one system, which drastically decreases the computation time. Following steps in this procedure, as described later, ensure that this approximation is sufficient and there is an accurate detection of the security boundary as soon as we enter the HIC region.

3) Sensitivity Measure for Small-Signal Stability: We determine the step direction by the sensitivity of the damping ratio, ζ, of the system representing the most critical contingency, Γ_i. This requires to compute the eigenvalue sensitivity which, in turn, depends on the state matrix $\mathbf{A_{\Gamma_i}}$ (for more details about forming state matrix A the reader is referred to [24]). Thus, the sensitivity of eigenvalue λ_n to a system parameter ρ_i is defined as

$$\frac{\partial \lambda_n}{\partial \rho_i} = \frac{\psi_n^T \frac{\partial \mathbf{A_{\Gamma_i}}}{\partial \rho_i} \phi_\mathbf{n}}{\psi_n^T \phi_n}. \tag{20}$$

ψ_n^T and ϕ_n are the left and right eigenvectors, respectively, associated with eigenvalue λ_n [24]. Defining $\lambda_n = \sigma_n + j\omega_n$, and with $\zeta = \frac{-\sigma_n}{\sqrt{\sigma_n^2+\omega_n^2}}$, we can determine the damping ratio sensitivity, $\frac{\partial \zeta_n}{\partial \rho_i}$ as

$$\frac{\partial \zeta_n}{\partial \rho_i} = \frac{\partial}{\partial \rho_i}\left(\frac{-\sigma_n}{\sqrt{\sigma_n^2+\omega_n^2}}\right) = \omega_n \frac{(\sigma_n \frac{\partial \omega_n}{\partial \rho_i} - \omega_n \frac{\partial \sigma_n}{\partial \rho_i})}{(\sigma_n^2+\omega_n^2)^{\frac{3}{2}}}. \tag{21}$$

Due to the fact that the computation of $\frac{\partial \mathbf{A_{\Gamma_i}}}{\partial \rho_i}$ is extremely demanding, it is usually more efficient to determine the damping ratio sensitivity of ζ to ρ_i by a small perturbation of ρ_i. The whole process is illustrated in Fig. 3. The parameters ρ_i correspond to the power dispatch of two generators. The DW is illustrated following the steepest descent of damping ratio considering the lowest damped eigenvalue of the system representing the most critical contingency Γ_i.

4) Parallelization of the Directed Walks: Directed Walks are easily parallelizable. In our case studies, we have used 80 cores of the DTU HPC cluster for this part of our simulations. To ensure an efficient parallelization and not allow individual processes take up unlimited time, we set a maximum number of steps of DWs, κ_{max}. The tuning of κ_{max} is discussed in the case studies in Section VII.

5) Entering the HIC region: As soon as a DW enters the HIC region, two additional processes take place. First, all points surrounding the current operating point are assessed as well, as they may be part of Ω. This is indicated in Fig. 3 by the yellow circles. Second, we allow the DW to move along only a single dimension (the dimension is still selected based on the steepest descent) and with the minimum step size. This ensures that we collect as many points within the HIC region as possible.

6) Termination of the Directed Walks: Each DW terminates if the next step arrives at an operating point already existing in the database. The termination criterion excludes operating points that were collected as "surrounding points" of a current step (see Section VI-5).

7) Full N-1 contingency check: After all DWs have been performed for every initialization point in parallel, we evaluate all safe (and almost safe) operating points in the database against all possible contingencies to ensure that no violations occur. More formally, we assess all operating points in the final database with $\gamma_k \geq \gamma - \mu$ for all remaining Γ systems to ensure that a possible false identification of the most critical contingency does not affect the stability boundary detection. This allows us to guarantee a high level of accuracy in determining the security boundary. Despite, this being the most computationally expensive step of our method, accounting for over 50% of the required time, in absence of expert knowledge this procedure is required for any method reported in the literature [8], [9]. The difference is, however, that our approach manages to discard a large volume of not relevant data before this step, and, as a result, outperforms existing methods by being at least 10 to 20 times faster.

8) Final Set of Directed Walks: The maximum number of steps κ_{max}, although helpful for the efficient parallelization of the DWs, may result in DWs that have not sufficiently explored the search space. In this final step, for any DWs that have reached κ_{max} while inside the HIC region, we perform an additional round of DW to explore as thoroughly as possible the HIC region. The final points from the previous round serve as initialization points.

VII. Case Studies

In the first case study, the efficient database generation method is applied on the IEEE 14 bus system. We measure the efficiency improvement compared with the brute force approach (BF), and we demonstrate how our method outperforms importance sampling techniques. It is impossible to carry out the comparison with the BF approach in larger systems, as BF becomes intractable. In the second case study, we demonstrate the scalability of our method to larger systems, such as the

TABLE I
RESULTS: IEEE 14 BUS SYSTEM

Required time	Time in % w.r.t. BF	OPs in Ω found	Method	η_1 / η_2 / η_3 / κ_{max}
2.56 min	0.46 %	95.13 %	DWs	0 / 200 / 2k / 10
2.99 min	0.54 %	98.9 %	DWs	0 / 200 / 2k / 15
2.94 min	0.53 %	97.80 %	DWs	0 / 200 / 2k / 20
3.77 min	0.68 %	100 %	DWs	0 / 200 / 2k / 25
2.94 min	0.53 %	97.80 %	DWs	0 / 200 / 1k / 20
3.48 min	0.74 %	99.93 %	DWs	0 / 200 / 3k / 20
4.80 min	0.86 %	100 %	DWs	0 / 200 / 5k / 20
37.0 min	6.66 %	100 %	Importance Sampling (IS)	
556 min	100 %	100 %	Brute Force (BF)	

NESTA 162 bus system [14]. The case studies in this paper use the combination of N-1 security and small-signal stability for the definition of the security boundary. It should be stressed though that the proposed methodology proposes a general framework and is applicable to a number of other stability metrics or power system models.

A. Small-Signal Model

A sixth order synchronous machine model [25] with an Automatic Voltage Regulator (AVR) Type I (3 states) is used in this study. With an additional state for the bus voltage measurement delay this leads to a state-space model of $10 \cdot N_G$ states, with N_G representing the number of generators in the grid. In case of the NESTA 162 bus system, all generators are addtionally equipped with Power System Stabilizers (PSS) type 1 adding an additional state per generator. The small signal models were derived using Mathematica, the initialization and small signal analysis were carried out using Matpower 6.0 [13] and Matlab. Reactive power limits of the generators are enforced. For a detailed description of the derivation of a multi-machine model, the interested reader is referred to [26]. Machine parameters are taken from [27].

B. IEEE 14 bus system

Carrying out the first case study on a small system, where the BF approach is still tractable, allows us to verify that our method is capable of finding 100 % of the points belonging to the HIC region. To ensure comparability, all simulations used 20 cores of the DTU HPC cluster.

Network data is given in [13], machine parameters are given in [3]. The considered contingencies include all line faults (except lines 7-8 and 6-13[1]). Due to the BF approach, we know that 1457 operating points belong to the HIC set, i.e. with $2.75\,\% < \zeta < 3.25\,\%$. The grid pruning without considering any contingency does not reduce the search space in this case study; this is because all possible combinations of generation setpoints do not violate any limits for the given load profile. Thus, η_1 is chosen as 0 and we directly start with the contingency-constrained grid pruning considering the five most critical contingencies. Table I compares the performance of our method with the BF approach and an Importance Sampling (IS) approach [8]. Our method is capable of creating a database including *all* points of interest in 3.77 min; that is 0.68 % of the time required by the BF approach (9.26 hours; 147 times faster). The proposed method is also significantly faster (approx. 10 times) than an Importance Sampling approach (31.60 min).

One of the major advantages of our method is the drastic search space reduction through the grid pruning and the most critical contingency identification. In this case study, grid pruning eliminated up to 70.13 % of all $\approx 2.5 \cdot 10^6$ potential operating points (the number varies based on the number of initialization points). At the same time, performing every DW step for the single most critical contingency, we reduce the required assessment from $\Gamma + 1$ systems to 1 system. In larger systems the speed benefits will be even more pronounced, e.g. 14-bus: $\Gamma + 1 = 19$ contingencies are reduced to 1 (most critical); 162-bus: $\Gamma + 1 = 160$ contingencies reduced to 1.

Table I also compares the method's performance for different numbers of initialization points η_{1-3} and maximum number of DW steps κ_{max}. In this system, choosing a higher number of maximum steps instead of a higher number of initialization points leads to time savings. The same holds in larger systems, as shown in Table II.

In the highlighted case of Table I, the required computation time for the different parts of our method is split as follows: 26.67 % (60.31 s) for the grid pruning considering the 5 most critical contingencies (200 operating points); 53.1 % (120.12 s) for the Directed Walks; and 20.24 % (45.78 s) for the final N-1 check of all operating points. Grid pruning eliminates 1149 from the $\eta_3 = 2000$ initialization points, resulting in 851 feasible starting points for the DWs. The most critical contingency is detected correctly in 94.55 % of cases.

C. NESTA 162 bus system

A BF approach with a 1 MW step size for this system requires the assessment of $7.6 \cdot 10^{29}$ operating points for a single load profile; this is computationally intractable. The set of considered contingencies includes 159 line faults[1]. To ensure comparability, all simulations for the 162-bus system have been performed using 80 cores of the DTU HPC cluster.

Compared to the IEEE 14 bus system, the problem size (potential # of OPs) is 23 orders of magnitude larger while the problem complexity (# of faults) increased 6.2 times. Table II presents the results of our method compared with an Importance Sampling approach [8]. As the BF approach for this system is intractable, the exact number of points within the HIC region (set Ω) is unknown. Therefore, the focus here is on demonstrating that within similar time frames, our proposed method is capable of finding substantially more unique operating points inside Ω. Indeed, our approach identifies approx. three orders of magnitude more HIC points that an Importance Sampling approach (183'295 vs 901 points).

In the highlighted case of Table II, the computation time is split as follows: 3.44 h (9.28 %) for LHS (3 stages), 1.85 h (4.98 %) for both stages of grid pruning, 7.04 h (18.98 %) for the DWs, and 24.75 h (66.76 %) for the final N-1 check of all operating points of interest. This highlights that the most computationally expensive part is the complete N-1 analysis and shows why our proposed method is significantly faster than others: (i) we reduce the search space by eliminating infeasible N-1 points through the grid pruning algorithm, (ii) we evaluate most points only for one contingency and discard

[1]The IEEE 14-bus and the NESTA 162-bus systems, based on the available data, are not $N-1$ secure for all possible contingencies. The outage of those specific lines lead to violations (e.g. voltage limits, component overloadings, or small-signal instability) that no redispatching measure can mitigate. This would not have happened in a real system. In order not to end up with an empty set of operating points, and still use data publicly available, we choose to neglect these outages.

TABLE II
RESULTS: NESTA 162 BUS SYSTEM

Req. time	Unique OPs in Ω	Method	η_1 / η_2 / η_3 / κ_{max}
9.35 h	3118	Directed Walks	30k / 120k / 800k / 5
13.17 h	4166	Directed Walks	30k / 120k / 800k / 10
14.57 h	25046	Directed Walks	30k / 120k / 800k / 20
29.78 h	150790	Directed Walks	30k / 120k / 800k / 30
37.07 h	183295	Directed Walks	30k / 120k / 800k / 40
13.36 h	16587	Directed Walks	100k / 200k / 800k / 5
18.20 h	45040	Directed Walks	100k / 200k / 800k / 10
35.70 h	901	Importance Sampling (IS)	

all with $\zeta < 2.75\,\%$, and (iii) the method can largely be scheduled in parallel.

VIII. Conclusions

This work proposes an efficient database generation method that can accurately determine power system security boundaries, while drastically reducing computation time. Such databases are fundamental to any DSA method, as the information in historical data is not sufficient, containing very few abnormal situations. This topic has not received the appropriate attention in the literature, with the few existing approaches proposing methods based on importance sampling.

Our approach is highly scalable, modular, and achieves drastic speed-ups compared with existing methods. It is composed of two parts. First, the search space reduction, which quickly discards large infeasible regions leveraging advancements in convex relaxation techniques and complex network theory approaches. Second, the "Directed Walks", a highly parallelizable algorithm, which efficiently explores the search space and can determine the security boundary with extremely high accuracy. Using a number of initialization points, a variable step size, and based on a steepest descent method, the "Directed Walk" algorithm traverses fast through large parts of feasible (or infeasible) regions, while it focuses on the high information content area in the vicinity of the security boundary. Our case studies on the IEEE 14-bus and the NESTA 162-bus system demonstrate the high scalability and excellent performance of our algorithm, being able to identify up to 100% of the operating points around the security boundary, while achieving computational speed-ups of over 10 to 20 times, compared with an importance sampling approach. Our approach is modular, not dependent on the initial sampling set (as importance sampling is), and agnostic to the security criteria used to define the security boundary. Criteria to be used include N-1 security, small-signal stability, voltage stability, or a combination of several of them. The method can find application in off-line security assessment, in real-time operation, and in machine learning and other data-driven applications, providing a computationally efficient way to generate the required data for training and testing of new methods.

IX. Acknowledgements

This work has been supported by the EU-FP7 Project "Best Paths", grant agreement no. 612748, and by the Danish ForskEL project "Best Paths for DK", grant agreement 12264.

References

[1] I. Konstantelos, G. Jamgotchian, S. Tindemans, P. Duchesne, S. Cole, C. Merckx, G. Strbac, and P. Panciatici, "Implementation of a Massively Parallel Dynamic Security Assessment Platform for Large-Scale Grids," *IEEE Transactions on Smart Grid*, vol. 8, no. 3, pp. 1417–1426, 2017.

[2] R. Preece and J. V. Milanovic, "Efficient Estimation of the Probability of Small-Disturbance Instability of Large Uncertain Power Systems," *IEEE Trans. on Power Systems*, vol. 31, no. 2, pp. 1063–1072, 2016.

[3] F. Thams, L. Halilbašic, P. Pinson, S. Chatzivasileiadis, and R. Eriksson, "Data-Driven Security-Constrained OPF," in *10th Bulk Power Systems Dynamics and Control Symposium - IREP*, Espinho, 2017, pp. 1–10.

[4] L. Halilbašic, F. Thams, A. Venzke, S. Chatzivasileiadis, and P. Pinson, "Data-driven Security-Constrained AC-OPF for Operations and Markets," in *XX Power Systems Computation Conference*, Dublin, 2018.

[5] L. Wehenkel, M. Pavella, E. Euxibie, and B. Heilbronn, "Decision tree based transient stability method a case study," *IEEE Transactions on Power Systems*, vol. 9, no. 1, pp. 459–469, 1994.

[6] N. Hatziargyriou, G. Contaxis, and N. Sideris, "A decision tree method for on-line steady state security assessment," *IEEE Transactions on Power Systems*, vol. 9, no. 2, pp. 1052–1061, 1994.

[7] I. Genc, R. Diao, V. Vittal, S. Kolluri, and S. Mandal, "Decision tree-based preventive and corrective control applications for dynamic security enhancement in power systems," *IEEE Transactions on Power Systems*, vol. 25, no. 3, pp. 1611–1619, 2010.

[8] C. Liu, Z. H. Rather, Z. Chen, C. L. Bak, and P. Thogersen, "Importance sampling based decision trees for security assessment and the corresponding preventive control schemes: The Danish case study," in *IEEE PowerTech*, Grenoble, 2013, pp. 1–6.

[9] C. Liu, K. Sun, Z. Rather, Z. Chen, C. Bak, P. Thogersen, and P. Lund, "A systematic approach for dynamic security assessment and the corresponding preventive control scheme based on decision trees," *IEEE Transactions on Power Systems*, vol. 29, no. 2, 2014.

[10] V. Krishnan, J. D. McCalley, S. Henry, and S. Issad, "Efficient database generation for decision tree based power system security assessment," *IEEE Trans. on Power Systems*, vol. 26, no. 4, pp. 2319–2327, 2011.

[11] C. Hamon, M. Perninge, and L. Söder, "An importance sampling technique for probabilistic security assessment in power systems with large amounts of wind power," *Electric Power Systems Research*, vol. 131, pp. 11–18, 2016.

[12] M. Sun, I. Konstantelos, S. Tindemans, and G. Strbac, "Evaluating composite approaches to modelling high-dimensional stochastic variables in power systems," *19th Power Systems Computation Conference*, 2016.

[13] R. D. Zimmerman, C. E. Murillo-Sánchez, and R. J. Thomas, "MATPOWER: Steady-state operations, planning, and analysis tools for power systems research and education," *IEEE Transactions on Power Systems*, vol. 26, no. 1, pp. 12–19, 2011.

[14] C. Coffrin, D. Gordon, and P. Scott, "NESTA, The NICTA Energy System Test Case Archive," pp. 1–26, 2014. [Online]. Available: http://arxiv.org/abs/1411.0359

[15] D. K. Molzahn, "Computing the Feasible Spaces of Optimal Power Flow Problems," *IEEE Transactions on Power Systems*, vol. 32, no. 6, pp. 4752–4763, 2017.

[16] J. Lavaei and S. H. Low, "Zero duality gap in optimal power flow problem," *IEEE Transactions on Power Systems*, vol. 27, no. 1, pp. 92–107, 2012.

[17] D. K. Molzahn, J. T. Holzer, B. C. Lesieutre, and C. L. Demarco, "Implementation of a Large-Scale Optimal Power Flow Solver Based on Semidefinite Programming," *IEEE Transactions on Power Systems*, vol. 28, no. 4, pp. 3987–3998, 2013.

[18] A. Venzke and S. Chatzivasileiadis, "Convex Relaxations of Security Constrained AC Optimal Power Flow under Uncertainty," in *Power Systems Computation Conference (PSCC) 2018*, June 2018.

[19] R. Albert, I. Albert, and G. L. Nakarado, "Structural Vulnerability of the North American Power Grid," *Physical Review E - Statistical, Nonlinear, and Soft Matter Physics*, vol. 69, no. 2, 2004.

[20] J. Fang, C. Su, Z. Chen, H. Sun, and P. Lund, "Power System Structural Vulnerability Assessment based on an Improved Maximum Flow Approach," *IEEE Transactions on Smart Grid*, 2016.

[21] A. Dwivedi, X. Yu, and P. Sokolowski, "Analyzing power network vulnerability with maximum flow based centrality approach," *IEEE Int. Conf. on Industrial Informatics*, pp. 336–341, 2010.

[22] A. Dwivedi and X. Yu, "A maximum-flow-based complex network approach for power system vulnerability analysis," *IEEE Transactions on Industrial Informatics*, vol. 9, no. 1, pp. 81–88, 2013.

[23] S. Greene, I. Dobson, and F. L. Alvarado, "Sensitivity of the loading margin to voltage collapse with respect to arbitrary parameters," *IEEE Transactions on Power Systems*, vol. 12, no. 1, pp. 262–272, 1997.

[24] P. Kundur, *Power system stability and control*. McGraw-Hill Professional, 1994.

[25] P. Sauer and M. Pai, *Power System Dynamics and Stability*, M. Horton, Ed. New Jersey: Prentice-Hall, Inc., 1998.

[26] F. Milano, *Power System Modelling and Scripting*. Springer-Verlag Berlin Heidelberg, 2010.

[27] P. M. Anderson and A. A. Fouad, "Power Systems Control and Stability," Ames, Iowa, USA, p. 464, 1977.

[Pub. C] Disturbance Attenuation of DC Voltage Droop Control Structures in a Multi-Terminal HVDC Grid.

Disturbance Attenuation of DC Voltage Droop Control Structures in a Multi-Terminal HVDC Grid

Florian Thams and Spyros Chatzivasileiadis
Center for Electric Power and Energy (CEE)
Technical University of Denmark
{fltha} / {spchatz} @elektro.dtu.dk

Eduardo Prieto-Araujo
CITCEA-UPC
Universitat Politècnica de Catalunya
eduardo.prieto-araujo@citcea.upc.edu

Robert Eriksson
Market and System Development
Svenska Kraftnät
robert.eriksson@svk.se

***Abstract*—DC voltage droop control is seen as the preferred control structure for primary voltage control of future multi-terminal HVDC systems. Different droop control structures have been proposed in literature which can be classified in eight categories. This paper contributes to an analysis of the disturbance rejection of these droop control structures. The approach is based on multi-variable frequency response analysis where both ac and dc grid dynamics are incorporated. In particular, the amplification of dc voltage oscillations due to wind power variations is analyzed using singular value analysis. Further, the impact of dc cable modeling on the results is discussed. In addition, it is shown that the maximum singular value limits, frequently used in literature for MIMO-analysis, are not sufficient to prove that the impact of certain disturbances on analyzed outputs is within a certain boundary. It is necessary to verify the results by a multiple input single output analysis of the transfer functions connecting the inputs with the highest amplified output.**

***Index Terms*—HVDC transmission, Wind energy integration, Control system analysis, State-space methods**

I. Introduction

The present trend of developing offshore wind farms with increasing distance from shore raised the interest in HVDC based on voltage source converters (VSC). VSC-HVDC entails several advantages compared to HVDC based on line-commutated converters such as smaller converter size or the capability to supply weak grids. Further, the ease of changing rapidly the power direction and enabling parallel connections makes VSC-HVDC the most appropriate technology for a multi-terminal HVDC (MT-HVDC) grid. However, only a few multi-terminal VSC-HVDC systems have been built world-wide while many ideas and projects have been proposed [1].

Due to the very little experience with MT-HVDC grids, there is no standardization of the control structure for such grids yet. It is acknowledged in academia and industry that it is preferable to have a distributed control architecture [2], as it makes the grid more resilient against the significant impact of any single malfunction. Thus, it is preferable to have multiple units actively participating in the control of the dc grid voltage instead of having it controlled by a single converter. One of the preferred control structures, enabling power sharing between several converters, is dc voltage droop control. In technical literature, however, several alternative droop control schemes have been discussed [3]–[22]. Here, we collect them all and evaluate their performance by their disturbance attenuation.

This work is co-funded by the European Unions Seventh Framework Programme for Research, Technological Development and Demonstration under the grant agreement no. 612748.

In general, a droop control scheme introduces a linear relationship between two electrical variables. In the specific case of dc voltage droop control for MT-HVDC, the dc voltage is used in each implementation, so that the droop gain, k_{droop}, defines the deviation of V_{dc} for a variation of the other electric variable:

$$V_{dc} = V_{dc}^* + k_{droop}(y^* - y) \tag{1}$$

y^* and V_{dc}^* are the set points and V_{dc}, y are the measured electric variables respectively. The second electric variable, y, can either represent the dc current, I_{dc}, one component of the ac current, I_{ac}, the active power measured on the dc side, P_{dc}, or the active power measured on the ac side, P_{ac}. They can be categorized by two different types of generalized structures, depending on whether the dc voltage is used within the first loop (Type2 (V_{dc}-y)) or the second loop (Type1 (y-V_{dc})) as shown in Fig. 1. This leads to a total of 8 different dc voltage droop control structures, shown in Fig. 2.

In [9] a methodology was proposed to analyse the multi-variable frequency response for one specific dc voltage droop control structure (CS). This work was extended in [23] using the methodology to design a droop controller using certain requirements based on maximum singular value (SV) limits. However, to the knowledge of the authors no previous work is done on analysing and comparing the performance of all the different CSs in terms of multi-variable frequency response.

The contributions of this paper include the following: First, we perform an analysis and comparison of the multi-variable frequency response of the eight different CSs. Second, we compare the results for a frequency dependent and a conventional π-equivalent dc cable model indicating how the usage of the latter might lead to overrated resonance peaks. We also perform a participation factor analysis of the eigenvalues

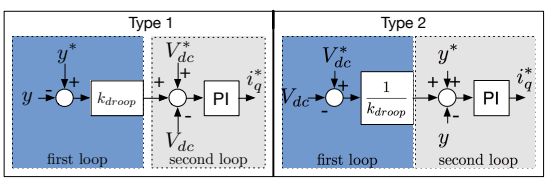

Fig. 1. Generalized droop control structures.

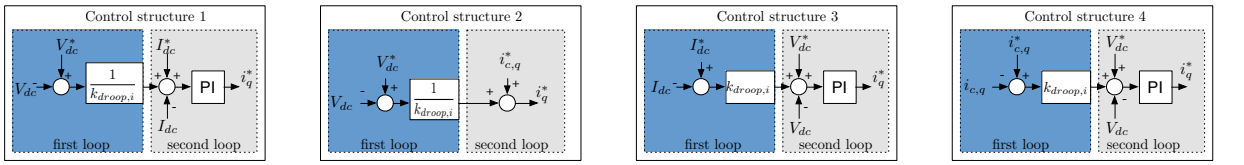

(a) CS1 (V_{dc}-I_{dc}) - [3]–[9]. (b) CS2 (V_{dc}-I_{ac}) - [10], [11]. (c) CS3 (I_{dc}-V_{dc}) - [12]–[14]. (d) CS4 (I_{ac}-V_{dc}) - [15].

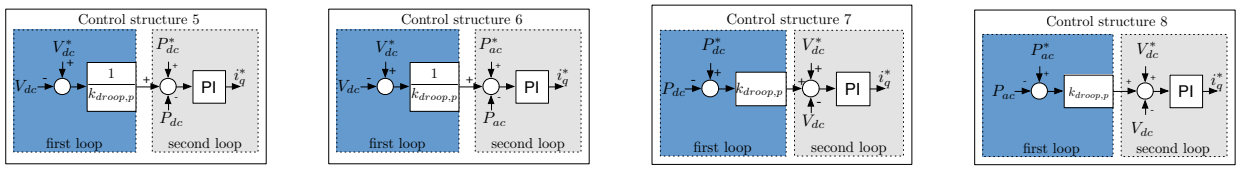

(e) CS5 (V_{dc}-P_{dc}) - [17]–[20]. (f) CS6 (V_{dc}-P_{ac}) - [20]. (g) CS7 (P_{dc}-V_{dc}) - [21], [22]. (h) CS8 (P_{ac}-V_{dc}) - [22].

Fig. 2. Analysed dc voltage droop control structures.

corresponding to the resonance peaks in order to determine the origin of resonance peaks observed in the singular value representation. Third, we point out that the maximum SV limits frequently used for multiple input multiple output (MIMO) analysis in literature (e.g. [23], [24]) are not sufficient to prove that the impact of specific disturbances on analyzed outputs is within a certain boundary. Due to the fact that these maximum SV limits implicitly assume the same amplification at every output, it is necessary to verify them by a multiple input single output (MISO) analysis of the transfer functions connecting the inputs with the highest amplified output.

This paper is structured as follows: First, the methodology will be introduced, then the analyzed model will be presented followed by a discussion of the results.

II. Methodology

The methodology enables the analysis of the different dc voltage droop control structures considering all the dynamics of a generic multi-terminal HVDC system. The control structure of a generic multi-terminal HVDC system is illustrated in Fig. 3. The wind farms are assumed to control the ac grid voltage and angle and to export all available active power. Thus their active power in-feed into the dc grid is considered as uncontrolled disturbance for the distributed droop voltage control scheme. Based on this scheme the closed loop transfer function matrices combining the converters and both ac and dc grid dynamics can be calculated:

$$\mathbf{E}_w(s) = \frac{\mathbf{z}(s)}{\mathbf{w}(s)} = \frac{(\Delta V_{dc,1}(s) \ \cdots \ \Delta V_{dc,M}(s))^T}{(P_{wf,N+1}(s) \ \cdots \ P_{wf,M}(s))} \tag{2}$$

$$\mathbf{U}_w^{uiq}(s) = \frac{\mathbf{u}_{iq}(s)}{\mathbf{w}(s)} = \frac{(i_{c,1}^{q*}(s) \ \cdots \ i_{c,N}^{q*}(s))^T}{(P_{wf,N+1}(s) \ \cdots \ P_{wf,M}(s))} \tag{3}$$

where $\mathbf{E}_w(s)$ is the transfer function matrix relating the power induced into the HVDC grid by the wind farms, $\mathbf{w}_i$, with the dc voltage deviations at all terminals, $\mathbf{z}_i$, with $k = 1 \ldots N$ representing the grid side converters (GSCs) while $k = N+1 \ldots M$ resemble the connected wind farms. The transfer function matrix $\mathbf{U}_w^{uiq}(s)$ relates accordingly the wind farm power, $\mathbf{w}$, with $\mathbf{u}_{iq}$, the active current loop references of the current loops of the different GSCs.

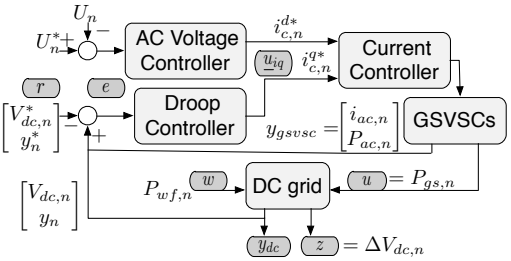

Fig. 3. Control structure of multi-terminal HVDC grid.

The performance of the control structures is analysed by means of the singular value representation of the system transfer function matrix, $\mathbf{E}_w(s)$, which can be obtained as:

$$\sigma_i(\mathbf{E}_w(j\omega)) = \sqrt{\lambda_i(\mathbf{E}_w^T(j\omega)\mathbf{E}_w(j\omega))} \tag{4}$$

where λ_i is the i-eigenvalue of the matrix. The maximum SV $\overline{\sigma}(\mathbf{E}_w(j\omega))$ indicates the maximum amplification of the corresponding inputs by the system seen from a specific output. Here, we analyse which effect the wind power input ($\mathbf{w}$ in Fig. 3) has on the dc voltage deviations ($\mathbf{z}$) at all HVDC terminals. Thus, according to [23], in case a maximum voltage error of 10% (ϵ_v) of the nominal value at each terminal should not be exceeded, the maximum singular value $\overline{\sigma}(\mathbf{E}_w(j\omega))$ can be derived as:

$$\overline{\sigma}(\mathbf{E}_w(j\omega)) \leq \frac{\|\mathbf{z}(j\omega)\|_2}{\|\mathbf{w}(j\omega)\|_2} = 20\log_{10}\left(\frac{\sqrt{\sum_{k=1}^{M}(V_{dc,k}\cdot\epsilon_v)^2}}{\sqrt{\sum_{k=N+1}^{M}P_{wf,k}^2}}\right) \tag{5}$$

In addition, in [23] the authors derive the maximum gain the SV representation of the transfer function $\mathbf{U}_r^{uiq}(j\omega)$ should not exceed. As given in (3), these transfer functions indicate the impact of the wind power in-feed on the active current loop references of the different GSCs. This maximum gain corresponds to a maximum allowed current flowing through

the GSCs of $110\,\%$ (ϵ_i) of the nominal current value, i_n.

$$\overline{\sigma}(\mathbf{U}_w^{uiq}(j\omega)) \leq \frac{\|\mathbf{u}_{iq}(j\omega)\|_2}{\|\mathbf{w}(j\omega)\|_2} = 20\log_{10}\left(\frac{\sqrt{\sum_{k=1}^{N}(i_{n,k}\cdot\epsilon_i)^2}}{\sqrt{\sum_{k=N+1}^{M}P_{wf,k}^2}}\right) \tag{6}$$

However, by using the L_2-norm these limits calculate the maximum energy of the error caused by the disturbances that would lead to a $10\,\%$ voltage deviation / $110\,\%$ nominal current at each terminal. Hence, these limits assume implicitly that the deviation of the outputs is the same for all outputs, i.e. e.g. the dc voltage deviation is the same at each terminal in the whole grid. However, this is not true and since the exact deviation at the less deviating terminals is not known in advance it can therefore not be considered in the calculation. Therefore, we will show that it is necessary to validate the results by analysing the transfer functions from the chosen disturbances to that output which experiences the highest deviation. That means, to calculate the maximum error, ϵ, of the most deviating output by using $\overline{\sigma}$ of the MISO analysis to solve (5) and (6) for ϵ while neglecting the sum in the numerator considering only the single most deviating output.

Extending the SV analysis, we analyzed the eigenvalues, λ_i, in terms of their damping ratio, ζ, and damped circular frequency, ω_d, in order to determine those eigenvalues corresponding to the resonance peaks in the SV representation. Then, we derived the participation matrix, $\mathbf{\Gamma}$, enabling us to detect the participation factor, Γ_{ki}, of the k-state in the i-th mode [25]:

$$\mathbf{\Gamma} = \{\Gamma_{ki}\} = \{v_{ki}l_{ik}\} \tag{7}$$

where v_{ki} and l_{ki} are the k-th entry of the i-th right ($\mathbf{v_i}$) respective left ($\mathbf{l_i}$) eigenvectors of $\mathbf{A}$. Hence, the participation factor analysis allows to determine the origin of the resonance peaks.

III. Modeling

The modeling is done according to the generic multi-terminal grid derived in [23]. A three terminal grid is used as case study with two GSCs connected by LC filters to two different equivalent ac grids, modeled as Thévenin equivalent. An overview is shown in Fig. 4. The GSCs are assumed to be synchronized to the ac grids through a Phase Locked Loop (PLL) and operated with conventional current controllers in the Synchronous Reference Frame (SRF). The current controllers of the GSCs are tuned by the Internal Model Control (IMC) technique designed to track references with a settling time of $10\,\mathrm{ms}$ [26]. Saturation limits are included in the control scheme, in order not to exceed the maximum current ratings of the converters. Both GSCs are assumed to use one of the eight dc voltage droop control structures, shown in Fig. 2. In order to achieve a comparable performance of power and current based droop control structures, the following is done:

- The droop gains were chosen as $k_{droop,p} = \frac{1}{25}\frac{\mathrm{V}}{\mathrm{kW}}$ as suggested in [23].
- The droop gains used within the power and current based droop controller should be comparable. Thus, the relation derived in [27] and given in (8) is used to determine the current based droop gains, $k_{droop,i_{dc}}$, that are equivalent to the power based droop gains, $k_{droop,p}$. The current based droop gain used for the CSs combining V_{dc} and I_{ac} needs to be scaled additionally (9), due to the higher range of I_{ac}. However, due to the non-linearity of power based droop control, the approximation holds only for a small deviation of the voltage.

$$k_{droop,i_{dc}} = \frac{V_{dc}^*}{\frac{1}{k_{droop,p}} - I_{dc}^*} \tag{8}$$

$$k_{droop,i_{ac}} = \frac{I_{dc}^*}{i_{c,q}^*}\cdot k_{droop,i_{dc}} \tag{9}$$

- The tuning of the outer controllers is based on optimization based robust control techniques [28] determining the tuning of the controllers $K(s)$ minimizing the H_∞ norm $\left\|T_{w,r\to y}(K)\right\|_\infty$, where $T_{w,r\to y}(K)$ denotes the closed loop transfer functions from the disturbance, $\mathbf{w}$, respectively the references, $\mathbf{r}$, to the measurements, $\mathbf{y}$. A comparable tuning for a chosen settling time of $100\,\mathrm{ms}$ [26] was achieved using pre- and post-compensators.

Only the response of CS2(V_{dc}-I_{ac}) differs, due to the absence of a PI controller, since the droop gain already serves as proportional controller connecting V_{dc} and i_q creating the necessary reference variable for the current controller. Hence, the dynamics of CS2(V_{dc}-I_{ac}) are determined by the current controller, which was tuned independently of the outer CS.

The impact of two different dc line models are compared. First, the results are discussed for a conventional π-equivalent model from the Cigré B4 DC grid test system, in which the capacitors at both ends are the results of incorporating all capacitors connected in parallel. This is a simplified model, but it is considered appropriate, as D'Arco also argues in [29], since the chosen model represents the worst case scenario with respect to LC oscillations. This is due to the fact that the oscillatory effects are condensed in a single frequency, instead of being spread on several frequencies as

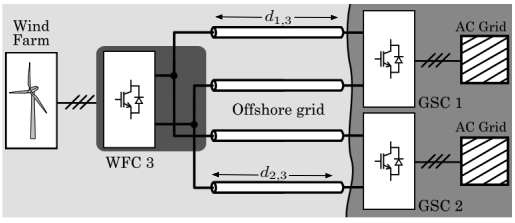

Fig. 4. Three terminal VSC-HVDC grid [23].

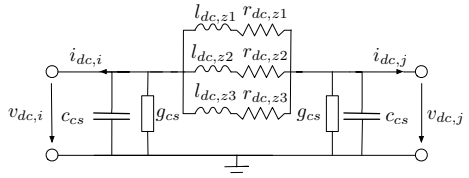

Fig. 5. Approximation of frequency dependent π dc cable model [30].

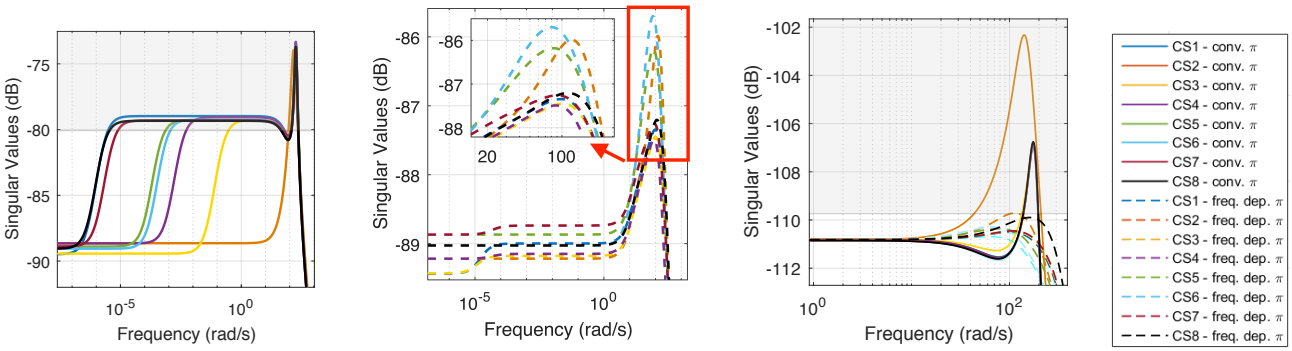

Fig. 6. Singular value representation of a) $E_w(j\omega)$ (wind power input - dc voltage deviation) for a π-equivalent dc cable model and b) $E_w(j\omega)$ for a 'frequency dependent π' cable model, c) $\mathbf{U}_r^{uiq}(j\omega)$) (wind power input - current controller reference) for both models and d) the legend for all graphs.

in a real cable. The model parameters are chosen according to [23]. In [24], however, the authors argue that for SVD studies the conventional π model may not be accurate enough. Therefore, in a second step, the results are compared to the case where a 'frequency dependent π' cable model, introduced in [30], is implemented. The model, shown in Fig. 5, is called 'frequency dependent π' since the additional parallel branches are calculated to fit the frequency response of a wide-band cable model [24], [31].

IV. Case Study

The analysis is performed for a scenario where both GSCs use the same dc voltage droop control structure and the same droop gain values. The results are compared for the different dc cable models and examined with a participation factor analysis in order to detect the origin of the resonance peaks.

The wind farm is assumed to inject maximum power into the HVDC grid, since this leads to the highest gains of the SV representation. Thus, it represents the worst case scenario. The linearized model is verified by an equivalent non-linear model built in Matlab Simulink, which also provides the steady state initial values.

The results of the SV analysis of $\mathbf{E}_w(j\omega)$ and $\mathbf{U}_r^{uiq}(j\omega)$ for both dc cable models are shown in Fig. 6. The maximum SV leading to a max. of $10\,\%$ voltage deviation at each terminal and to max. $110\,\%$ of the nominal current flowing through the GSCs have been calculated as $\overline{\sigma}(\mathbf{E}_w(j\omega)) \leq -80.09\,\mathrm{dB}$ and $\overline{\sigma}(\mathbf{U}_w^{uiq}(j\omega)) \leq -109.74\,\mathrm{dB}$. The area exceeding those limits has been faded gray in Fig. 6.

A. Cable model: conventional π

The SV representations of $\mathbf{E}_w(j\omega)$ (Fig. 6a) are very similar for all CSs besides CS2($V_{dc} - I_{ac}$), which, however, is the only droop control structure without a PI-controller. All CSs besides CS2($V_{dc} - I_{ac}$) exceed the limit of $-80.09\,\mathrm{dB}$ already for $\omega \ll 1$ with values around $-79.3\,\mathrm{dB}$. CS2($V_{dc} - I_{ac}$) stays at approx. $-89\,\mathrm{dB}$ for $\omega \leq 1$. For higher frequencies the SV representations of all CSs indicate a peak at a resonance frequency: CS2($V_{dc} - I_{ac}$) at $145.5\,\mathrm{rad/s}$ (=23.2 Hz), all remaining CSs: at approx. $180\,\mathrm{rad/s}$ (=28.6 Hz). Here, all CSs exceed the limit with a maximum $\overline{\sigma}(\mathbf{E}_w(j\omega))$ of approx. $-73.6\,\mathrm{dB}$. Hence, all CSs would exceed the limit of a maximum dc voltage deviation of 10% in case those frequencies are excited.

The SV representations of $\mathbf{U}_r^{uiq}(j\omega)$ (Fig. 6c) show that all CSs achieve in steady state a $\overline{\sigma}(\mathbf{U}_r^{uiq}(j\omega))$ of $-110.8\,\mathrm{dB}$. Thus, all CSs comply with the limit. However, similar to the previous analysis, the SV representations of $\mathbf{U}_r^{uiq}(j\omega)$ indicate a resonance peak for all CSs at the same resonance frequencies leading to maximum SVs of $-102.2\,\mathrm{dB}$ (CS2($V_{dc} - I_{ac}$)) to $-106.8\,\mathrm{dB}$ (all remaining CSs). Thus, none of the CSs complies with the limit for the whole frequency range.

The deviation from the results obtained in [23], where only CS6(V_{dc}-P_{ac}) was analyzed, are due to the varied cable length (here $d_{1,3} = 200\,\mathrm{km}$, $d_{2,3} = 300\,\mathrm{km}$ instead of $d_{1,3} = 100\,\mathrm{km}$, $d_{2,3} = 150\,\mathrm{km}$) as well as the fact that the dc voltage deviation at the wind farm is also considered. Here, a smaller droop gain would be necessary to comply with the derived limits. Hence, the analysis shows that with this cable model the choice of the droop gains is closely related to the length of the cables as well as the capacitance size of the wind farm converter.

In the SISO case, the SV analysis is equivalent to the bode diagram of the corresponding transfer function. In the MIMO case, however, the maximum SV is the maximum gain for any input direction, hence the SV representation is not just the sum of the bode diagrams of the corresponding transfer functions. Nevertheless, it is possible to determine the eigenvalues causing the resonance peaks by examining the damped circular frequencies and ratios of the corresponding transfer functions. The corresponding eigenvalues have been examined by a participation factor analysis in order to identify the source of the resonance peak. The analysis is done for the case where both GSCs use CS1(V_{dc}-I_{dc}). However, further analyses showed that the results can be generalized for the remaining CSs.

The analyses showed that the resonance peak of CS1(V_{dc}-I_{dc}) in Fig. 6a is related to a pair of complex eigenvalues, with a damping ratio of $14.5\,\%$. The participation factor analysis of this pair of complex eigenvalues causing the resonance peak is shown in Fig. 7. It indicates, that the peak is mainly related to the dc voltage at the wind farm, $V_{dc,3}$, the currents in the

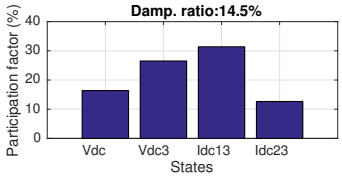

Fig. 7. Participation factor analysis of the complex pair of eigenvalues causing the resonance peak in case of CS1(V_{dc}-I_{dc}).

dc lines, $I_{dc,13}$ and $I_{dc,23}$ as well as the dc voltage at GSC1, V_{dc}. Similar results with varying damping ratios are obtained for the analysis of the resonance peaks of the remaining CSs. Hence, the resonance peaks, i.e. the maximum possible amplifications of dc voltage oscillations, are always related to dc values at the wind farm. The results are also similar for the analysis of eigenvalues corresponding to the peaks of the SV representation of the transfer function matrix $\mathbf{U}_w^{uiq}(s)$, which resembles the control action. Hence, in contrast to the usual practice that the wind farm converter does not participate in the dc voltage control, the results indicate that a participation or an additional damping of dc voltage oscillations at this point could be feasible.

B. Cable model: frequency dependent π

The frequency dependent π model enables the droop control structures to react faster without causing instability, which results in a better disturbance attenuation. Hence, the results for $E_w(j\omega)$ (Fig. 6b) indicate lower SVs for the whole frequency range for all CSs, however, with slightly bigger differences between them. While in steady state, the maximum SVs of all CSs are comparable, with CS1(V_{dc}-I_{dc}) achieving the lowest with $-89.5\,\mathrm{dB}$. The differences are caused by the different tunings and the fact that (8) is only an approximation of the non-linear control behavior of active power and dc voltage [27].

For frequencies $\geq 10\,\frac{\mathrm{rad}}{\mathrm{s}}$, CS4($I_{ac}$-$V_{dc}$) achieves the lowest $\overline{\sigma}(\mathbf{E}_w(j\omega))$ with $-87.49\,\mathrm{dB}$ at a frequency of $88\,\mathrm{rad/s}$ (=$14\,\mathrm{Hz}$). The highest maximum singular value is obtained by CS6($V_{dc}-P_{ac}$) with $-85.7\,\mathrm{dB}$, closely followed by CS2(V_{dc}-I_{ac}) ($-85.99\,\mathrm{dB}$) and CS5(V_{dc}-P_{dc}) ($-86.18\,\mathrm{dB}$).

Although it seems, as if all CSs stay far below the $10\,\%$ voltage deviation limit ($-80.09\,\mathrm{dB}$), it is not possible to calculate the maximum dc voltage deviation from these dB values using (5), since the dc voltage deviation at each converter differs. Assuming the same deviation for all outputs, as (5) and (6) do, a maximum deviation of $4.27\,\%$ (CS4(I_{ac}-V_{dc})) and $5.26\,\%$ (CS6($V_{dc}-P_{ac}$)) would be achieved. However, the deviations are not the same, in fact, the highest deviation can be observed at the wind farm, due to the fact that there is no dc voltage control at this point and the input is not damped by a cable. Hence, if we only consider the transfer function from wind power input to dc voltage deviation at the wind farm converter we can calculate a maximum voltage deviation of $5.74\,\%$ (CS4(I_{ac}-V_{dc})) and $6.73\,\%$ (CS6($V_{dc}-P_{ac}$)) using (5). Thus, in contrast to what is implicitly assumed in (5) and (6), when deriving a maximum SV limit in the MIMO analysis, it always needs to be considered that the output deviation might not be the same at every output. Since the deviation at the less deviating terminals is not known in advance and can therefore not be considered in the calculation, the transfer functions from the disturbances to the highest deviating output (MISO analysis) should be analysed additionally in order to verify the results.

The analysis of the control action, i.e. the SV representation of $\mathbf{U}_w^{uiq}(j\omega)$ (Fig. 6c), for the various CSs indicates small differences between the different CSs. Here, only CS2($V_{dc}-I_{ac}$) exceeds the limit of $-109.74\,\mathrm{dB}$ slightly. Although the remaining CSs do not exceed the limit, it is necessary to analyse the transfer function from the wind power input to the highest deviating output, the current reference at the converter station closest to the wind farm, GSC1. It indicates that only CS4(I_{ac}-V_{dc}) would comply with the boundary of max. $110\,\%$ of the nominal current flowing through GSC1. While - in case the frequencies corresponding to the resonance peaks are excited by the input signal - the current exceeds from $111\,\%$ (CS5(V_{dc}-P_{dc})) up to $120\,\%$ (CS8(P_{ac}-V_{dc})) of the nominal current for the remaining CSs.

Analysing the eigenvalues of CS1(V_{dc}-I_{dc}), a complex pair of eigenvalues with similar participation factors as the one leading to the resonance peak in the conventional π model can be identified at the damping frequency of $327.44\,\mathrm{rad/s}$ (=$52.1\,\mathrm{Hz}$) with a damping ratio of $52.2\,\%$. Hence, the different dc cable parameters lead to a change in the resonance frequency and a significantly higher damping.

C. Discussion

The results show that it is important to use a more accurate frequency dependent cable model as it allows to perform a more accurate design of the distributed droop voltage control.

Further, it was shown that the maximum dc voltage deviation depends on the chosen dc voltage droop CS. In fact, for the topology chosen in the case study it can be minimized to $5.74\,\%$ by using CS4($I_{ac}-V_{dc}$) instead of $6.73\,\%$ with CS6($V_{dc}-P_{ac}$), which would allow the operator to operate the system closer to the nominal values, thus more efficiently.

Only CS4($I_{ac}-V_{dc}$) managed to comply also with the requirement of limiting the current flowing through the GSCs to 110% of the nominal current. The choice of a higher droop gain would allow all CSs to comply with that requirement, however, at the same time it would increase the dc voltage deviation. The effect is the same for all CSs, hence, the differences between them are comparable for different droop gains. Finally, the need for MISO analyses due to varying impact of the disturbance on the different HVDC terminals has been highlighted.

V. Conclusion

The impact of the various dc voltage droop control structures has been compared for two different dc cable models. It was shown that the possible amplification of dc oscillations depends up to a certain extent on the chosen dc voltage droop control structure. Finally, we showed that the maximum singular value limits, frequently used in literature for MIMO

analysis, is not sufficient to prove that the impact of specific disturbances on analyzed outputs is within a certain boundary. In fact, it is necessary to verify them by an analysis of the transfer functions connecting the disturbances with the highest deviating output (MISO analysis) due to an uneven impact of the disturbances on the different outputs.

REFERENCES

[1] D. V. Hertem, O. Gomis-Bellmunt, and J. Liang, Eds., *HVDC grids: for offshore and supergrid of the future*. Wiley-IEEE Press, 2016.

[2] V. Akhmatov, M. Callavik, C. M. Franck, S. E. Rye, T. Ahndorf, M. K. Bucher, H. Muller, F. Schettler, and R. Wiget, "Technical guidelines and prestandardization work for first HVDC Grids," *IEEE Transactions on Power Delivery*, vol. 29, no. 1, 2014.

[3] C. D. Barker and R. Whitehouse, "Autonomous converter control in a multi-terminal HVDC system," in *9th IET International Conference on AC and DC Power Transmission*, London, 2010, pp. 1–5.

[4] W. Wang, M. Barnes, and O. Marjanovic, "Droop control modelling and analysis of multi-terminal VSC-HVDC for offshore wind farms," in *10th IET Int. Conf. on AC and DC Power Transmission*, Birmingham, 2012.

[5] O. Gomis-Bellmunt, J. Liang, J. Ekanayake, and N. Jenkins, "Voltage-current characteristics of multiterminal HVDC-VSC for offshore wind farms," *Elec.Power Syst. Research*, vol. 81, no. 2, pp. 440–450, 2011.

[6] L. Xu, L. Yao, and M. Bazargan, "DC grid management of a multi-terminal HVDC transmission system for large offshore wind farms," in *Int. Conf. on Sust. Power Gen. and Supply*, 2009, pp. 1–7.

[7] F. D. Bianchi and O. Gomis-Bellmunt, "Droop control design for multi-terminal VSC-HVDC grids based on LMI optimization," in *50th IEEE Conf. on Decision and Control and Europ. Control Conf.*, Orlando, 2011.

[8] L. Xu and L. Yao, "DC voltage control and power dispatch of a multi-terminal HVDC system for integrating large offshore wind farms," *Renewable Power Generation, IET*, vol. 5, no. 3, pp. 223–233, 2011.

[9] E. Prieto-Araujo, F. D. Bianchi, A. Junyent-Ferre, and O. Gomis-Bellmunt, "Methodology for Droop Control Dynamic Analysis of Multiterminal VSC-HVDC Grids for Offshore Wind Farms," *IEEE Transactions on Power Delivery*, vol. 26, no. 4, pp. 2476–2485, 2011.

[10] R. T. Pinto, S. Rodrigues, P. Bauer, and J. Pierik, "Operation and control of a multi-terminal DC network," in *IEEE ECCE Asia Downunder*, Melbourne, 2013, pp. 474–480.

[11] Y. Chen, G. Damm, and A. Benchaib, "Multi-Time-Scale Stability Analysis and Design Conditions of a VSC Terminal with DC Voltage Droop Control for HVDC Networks," in *53rd IEEE Conference on Decision and Control*, Los Angeles, CA, 2014.

[12] J. Liang, T. Jing, O. Gomis-Bellmunt, J. Ekanayake, and N. Jenkins, "Operation and Control of Multiterminal HVDC Transmission for Offshore Wind Farms," *IEEE Transactions on Power Delivery*, vol. 26, no. 4, pp. 2596–2604, 2011.

[13] B. K. Johnson, R. H. Lasseter, F. L. Alvarado, and R. Adapa, "Expandable multiterminal dc systems based on voltage droop," *IEEE Transactions on Power Delivery*, vol. 8, no. 4, 1993.

[14] S. Zhou, J. Liang, J. B. Ekanayake, and N. Jenkins, "Control of multi-terminal VSC-HVDC transmission system for offshore wind power generation," in *44th Int. Universities Power Eng. Conf.*, Glasgow, 2009.

[15] F. Thams, J. A. Suul, S. D'Arco, M. Molinas, and F. W. Fuchs, "Stability of DC Voltage Droop Controllers in VSC HVDC Systems," in *PowerTech, Eindhoven 2015*, Eindhoven, 2015.

[16] F. Thams, R. Eriksson, and M. Molinas, "Interaction of Droop Control Structures and its Inherent Effect on the Power Transfer Limits in Multi-terminal VSC-HVDC," *IEEE Transactions on Power Delivery*, vol. 32, no. 1, pp. 182–192, 2017.

[17] P. Rault, F. Colas, X. Guillaud, and S. Nguefeu, "Method for small signal stability analysis of VSC-MTDC grids," in *IEEE Power and Energy Society General Meeting*, San Diego, 2012.

[18] J. Dragon, L. Werner, and J. Hanson, "Effects of DC Voltage Droop Characteristics on Contingency Behaviour of AC / DC Systems," in *49th Int. Universities' Power Eng. Conf. (UPEC)*, Cluj-Napoca, 2014.

[19] T. M. Haileselassie and K. Uhlen, "Impact of DC Line Voltage Drops on Power Flow of MTDC Using Droop Control," *IEEE Transactions on Power Systems*, vol. 27, no. 3, pp. 1441–1449, 2012.

[20] T. M. Haileselassie and K. Uhlen, "Precise control of power flow in multiterminal VSC-HVDCs using DC voltage droop control," in *IEEE Power and Energy Society General Meeting*, San Diego, 2012.

[21] T. M. Haileselassie and K. Uhlen, "Primary frequency control of remote grids connected by multi-terminal HVDC," in *IEEE Power and Energy Society General Meeting*, Minneapolis, 2010, pp. 1–6.

[22] G. Stamatiou and M. Bongiorno, "Decentralized converter controller for multiterminal HVDC grids," in *15th European Conference on Power Electronics and Applications (EPE)*, 2013, pp. 1–10.

[23] E. Prieto-Araujo, A. Egea-Alvarez, S. F. Fekriasl, and O. Gomis-Bellmunt, "DC voltage droop control design for multi-terminal HVDC systems considering AC and DC grid dynamics," *IEEE Transactions on Power Delivery*, vol. 31, no. 2, pp. 575 – 585, 2015.

[24] S. Akkari, E. Prieto-Araujo, J. Dai, O. Gomis-Bellmunt, and X. Guillaud, "Impact of the DC cable models on the SVD analysis of a Multi-Terminal HVDC system," in *19th Power Systems Computation Conference (PSCC)*, Genoa, 2016, pp. 1–6.

[25] I. J. Perez-Arriaga, G. C. Verghese, and F. C. Schweppe, "Selective Modal Analysis with Applications to Electric Power Systems, Part I: Heuristic Introduction," *IEEE Power Engineering Review*, vol. PER-2, no. 9, pp. 29–30, 1982.

[26] H. Saad, X. Guillaud, J. Mahseredjian, S. Dennetiere, and S. Nguefeu, "MMC Capacitor Voltage Decoupling and Balancing Controls," *IEEE Transactions on Power Delivery*, vol. 30, no. 2, pp. 704–712, 2014.

[27] T. K. Vrana, "System Design and Balancing Control of the North Sea Super Grid," Ph.D. dissertation, NTNU, Trondheim, 2013.

[28] P. Apkarian, V. Bompart, and D. Noll, "Non-smooth structured control design with application to PID loop-shaping of a process," *Int. J. Robust Nonlinear Control*, no. 17, 2007.

[29] S. D'Arco, J. A. Suul, and M. Molinas, "Implementation and Analysis of a Control Scheme for Damping of Oscillations in VSC-based HVDC Grids," in *16th International Power Electronics and Motion Control Conference and Exposition*, Antalya, Turkey 21-24, 2014, pp. 586–593.

[30] J. Beerten, S. D'Arco, and J. A. Suul, "Frequency-dependent cable modelling for small-signal stability analysis of VSC-HVDC systems," *IET Generation, Transmission & Distribution*, vol. 10, no. 6, 2016.

[31] O. Ramos-Leanos, J. L. Naredo, J. Mahseredjian, C. Dufour, J. A. Gutierrez-Robles, and I. Kocar, "A wideband line/cable model for real-time simulations of power system transients," *IEEE Transactions on Power Delivery*, vol. 27, no. 4, pp. 2211–2218, 2012.

[32] T. K. Vrana, Y. Yang, D. Jovcic, S. Dennetière, J. Jardini, and H. Saad, "The CIGRE B4 DC Grid Test System," Cigre, Tech. Rep., 2013.

[33] L. Zhang, "Modeling and control of VSC-HVDC links connected to weak AC systems," Ph.D. dissertation, 2010.

APPENDIX

TABLE I
PARAMETERS OF THE THREE-TERMINAL DC GRID. CIGRÉ B4 DC GRID TEST SYSTEM [32] AND AC GRIDS [33]

Parameters	Value	Units
Line resistance r_{dc}	0.0095	Ω/km
Line inductance l_{dc}	2.112	mH/km
Line capacitance c_{cs}	0.1906	μF/km
Cable distance $d13$	200	km
Cable distance $d23$	300	km
GSC/WFC DC link capacitor c_{dc}	150	μF
WFC rated power P_3	700	MW
Reference voltage E^*	400	kV
Nominal power P_1, P_2	350	MW
Nominal voltage V_{ac}	195	kV
Nominal frequency f	50	Hz
Short circuit ratio (SCR)	5	-
Grid Thévenin X_n/R_n ratio	10	-
Coupling inductance L_c	0.2	pu
Coupling resistance R_c	0.01	pu
Capacitor filter impedance X_f	5.88	pu

TABLE II
PARAMETERS OF THE FREQ. DEPENDENT CABLE MODEL [24]

$r_{dc,z1} = 1.1724 \cdot 10^{-1}\,\Omega/\mathrm{km}$	$l_{dc,z1} = 2.2851 \cdot 10^{-4}\,\mathrm{H/km}$
$r_{dc,z2} = 8.2072 \cdot 10^{-2}\,\Omega/\mathrm{km}$	$l_{dc,z2} = 1.5522 \cdot 10^{-3}\,\mathrm{H/km}$
$r_{dc,z3} = 1.1946 \cdot 10^{-2}\,\Omega/\mathrm{km}$	$l_{dc,z3} = 3.2942 \cdot 10^{-3}\,\mathrm{H/km}$
$g_{cs} = 7.6333 \cdot 10^{-11}\,\mathrm{S/km}$	$c_{cs} = 1.9083 \cdot 10^{-7}\,\mathrm{F/km}$

[Pub. D] DC Voltage Droop Control Structures and its Impact on the Interaction Modes in Interconnected AC-HVDC Systems.

DC Voltage Droop Control Structures and its Impact on the Interaction Modes in Interconnected AC-HVDC Systems

Florian Thams and Spyros Chatzivasileiadis
Center for Electric Power and Energy (CEE)
Technical University of Denmark
{fltha} / {spchatz} @elektro.dtu.dk

Robert Eriksson
Market and System Development
Svenska kraftnät
robert.eriksson@svk.se

***Abstract*—Different dc voltage droop control structures for future multi-terminal HVDC systems have been proposed in literature. This paper contributes to the evaluation of those structures by an analysis of their impact on the coupling of the interconnected subsystems. In particular, the modes of the systems are classified in different subsets according to the participation of the various subsystems. Those subsets are then evaluated qualitatively and quantitatively indicating which impact the choice of the droop control structure has on the degree of coupling between the connected ac and dc systems respectively the different HVDC converters. The lowest damped interaction modes of the different subsets are analyzed in more detail.**

***Index Terms*—HVDC transmission, Wind energy integration, Control system analysis, State-space methods**

I. Introduction

The increasing interest in renewable energy sources, often built far away from load centers, also raised interest in HVDC technology as enabler for long distance bulk power transmission. In particular, HVDC based on voltage source converter (VSC) is acknowledged as the appropriate technology for grid connection of offshore wind parks far away from the coast. Several advantages, such as the capability to support weak grids and the smaller converter size compared to HVDC based on line-commutated converter (LCC), makes it the preferred technology for this use case. Further, with VSC-HVDC technology enabling multi-terminal HVDC (MT-HVDC) systems, researchers started to think about larger overlay-grids, allowing the interconnection of different asynchronous areas, even a global grid [1]. However, so far only a few multi-terminal VSC-HVDC systems have been built worldwide [2]. Since even on a smaller scale such an MT-HVDC grid would most likely not be built at once but be developed by step-wise integration of already existing on- and offshore interconnectors, this would raise the question of the interoperability of HVDC systems from different vendors using potentially different control structures. Furthermore, such a system could potentially connect widely dispersed parts of the power system and even asynchronous systems demanding a carefully evaluation of potential interactions between converters in order to avoid potential propagation of disturbances between different subsystems.

The little experience with MT-HVDC systems is also the reason for the lacking standardization of the control structure for such grids. In academia and industry it is acknowledged that it is preferable to have a distributed control architecture to make the grid more resilient against the significant impact of any single malfunction. However, while different control schemes have been proposed, it remains unknown which control structure exactly each vendor is using. While one of the preferred options by academia and industry for the control of the grid side converters (GSCs) is dc voltage droop control [3], several alternative droop control schemes have been discussed in technical literature [4]–[19]. The different dc voltage droop control structures (CS) have been categorized and analyzed in terms of their inherent effect on the power transfer capability [15] and in terms of their disturbance attenuation [20]. Further, in [21] the authors analyze interaction modes and their sensitivity to droop gains and dc breaker inductances in a MT-HVDC system. However, to the best knowledge of the authors, there does not exist an analysis of the impact of the various CSs on the interaction modes between different subsystems. Thus, it remains unknown whether the choice of a certain CS results in an unfeasible stronger coupling of subsystems, as for instance the dc and the ac subsystems. In general, it is preferred to have those systems as decoupled as possible to minimize a potential spread of disturbances from one system into the other.

The contributions of this paper include the following: First, an analysis of the quantitative and qualitative coupling between the different subsystems will be provided for two different tunings of the converters, i.e. whether a certain CS imposes a higher degree of coupling reflected by a higher percentage of interaction modes and whether this also influences the damping ratio of the interaction modes. In particular, we will focus on the coupling between the dc and the ac systems and the coupling between the different HVDC converters. We will show how an increased transient response impacts the coupling of the different subsystems. Further, we will discuss

This work is co-funded by the European Unions Seventh Framework Programme for Research, Technological Development and Demonstration under the grant agreement no. 612748 and by the ForskEL-projekt 12264 Best Paths for DK.

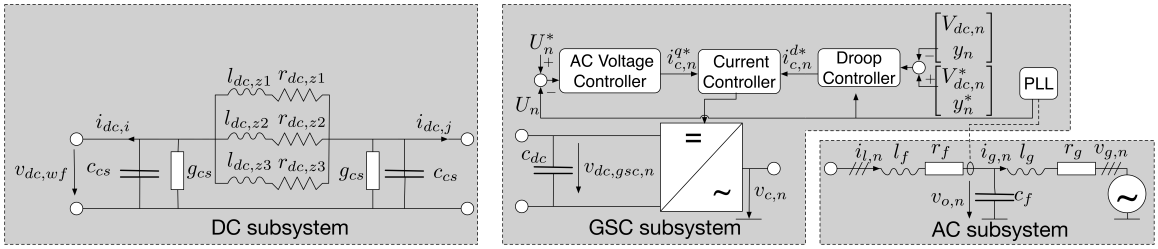

Fig. 1. Splitting of the different subsystems.

how a generalized feedback influences the coupling of those subsystems.

II. Methodology

In [21], the authors propose a methodology to identify and analyze interaction modes between converters in a HVDC system. Here, we adapt the strategy to evaluate how the choice of the CS influences the coupling of the different subsystems:

Given a general linearized model of a HVDC system, which is composed of various subsystems for every connected converter terminal and HVDC cable:

$$\dot{\mathbf{x}} = \mathbf{A}\mathbf{x} + \mathbf{B}\mathbf{u}, \qquad \mathbf{x}(0) = \mathbf{x}_0 \tag{1}$$

with $\mathbf{x} \in R^n$ being the state vector and $\mathbf{u} \in R^m$ the input vector. $\mathbf{A} \in R^n \times R^n$ and $\mathbf{B} \in R^n \times R^m$ are the known coefficient matrices of the steady state linearization around $\mathbf{x_0} \in R^n$.

First, a criterion is defined to distinguish between local modes and interaction modes. Here, interaction modes are defined as modes where at least two subsystems participate. Thus, the participation factors Γ_{ki} measuring the relative participation of the k-th state variable in the i-th mode are determined by:

$$\mathbf{\Gamma} = \{\Gamma_{ki}\} = \{v_{ki} l_{ik}\} \tag{2}$$

where $\mathbf{v}_{ki}$ and $\mathbf{l}_{ki}$ are the k-th entry of the i-th right ($\mathbf{v}_i \in R^{n_t}$) respective left ($\mathbf{l}_i \in R^{n_t}$) eigenvectors of $\mathbf{A}$. Then, $\Gamma^n_{ki} = \frac{\Gamma_{ki}}{\|\mathbf{\Gamma}_i\|}$ are the normalized participation factors. While $\mathbf{\Gamma}_i \in R^{n_t}$ contains the participation factors associated with mode i for all system states, $\|\cdot\|$ denotes the L_1-norm [21]. Further, the vector $\mathbf{\Gamma}^n_{\alpha,i} \in R^{n_\alpha}$ contains all normalized participation factors associated with mode i for all states of the subsystem α.

The overall participation for each subsystem α in mode i is defined as [21]:

$$\eta_{\alpha,i} = \frac{\|\mathbf{\Gamma}^n_{\alpha,i}\|}{\|\mathbf{\Gamma}^n_i\|} \tag{3}$$

with $\|\cdot\|$ denoting the L_1-norm. Focusing on interaction between specific subsystems I^α a set of interaction modes S^α can be defined as:

$$S^\alpha = \{i \mid \eta_{\alpha,i} \geq \chi, \forall\, \alpha \in I^\alpha\} \tag{4}$$

with $S^\alpha \subseteq S$, the set of all modes, and χ resembling a threshold chosen as 5% following the example in [21].

Here, two subsets of interaction modes are of particular interest:

- the interaction modes of the subset $S^{ac,dc} = \{i \mid (\eta_{dc,i} \geq \chi) \wedge ((\eta_{ac_1,i} \geq \chi) \vee \cdots \vee (\eta_{ac_N,i} \geq \chi)),\ \forall\ dc, ac_j \in I^{ac,dc}\}$. That means interaction modes with participation of at least one of the connected ac systems and the dc system, since it is preferred to have those systems as decoupled as possible to minimize a potential spread of disturbances from one system into the other.
- the interaction modes of the subset $S^{gsc} = \{i \mid (\eta_{gsc_1,i} \geq \chi) \wedge (\eta_{gsc_2,i} \geq \chi) \wedge \cdots \wedge (\eta_{gsc_N,i} \geq \chi),\ \forall\ gsc_j \in I^{gsc}\}$, i.e. interaction modes between all GSCs, indicating the degree of coupling within the dc grid.

These two subsets will be evaluated quantitatively, i.e. how many of all modes show this type of coupling, and qualitatively, i.e. where are the corresponding eigenvalues located, how critical are they and which states participate in particular?

III. Modeling

The modeling is done according to the generic MT-HVDC model derived in [22]. Each model consists of a number of three different kind of subsystems, shown in Fig. 1.

The ac subsystems are modeled as Thévenin equivalent with an LC-filter interface to the GSCs. Thus, the states corresponding to the ac subsystems, I^{ac_j}, with $j = 1, \ldots, N$, are the following:

$$\mathbf{x}_{ac,j} = \big[i_{g,d,j} \quad i_{g,q,j} \quad v_{o,d,j} \quad v_{o,q,j} \quad i_{l,d,j} \quad i_{l,q,j} \quad v_{o,d,meas,j} \quad v_{o,q,meas,j} \quad i_{l,q,meas,j} \quad P_{ac,meas,j}\big]. \tag{5}$$

Variables $i_{g,d/q,j}$, $i_{l,d/q,j}$ represent the grid current and the line current flowing through the converter. While $v_{o,d/q,j}$ represents the voltage at the point of common coupling (PCC), $v_{o,d/q,meas,j}$ resembles the delayed voltage measurement at the PCC. Further, $P_{ac,meas,j}$ and $i_{l,q,meas,j}$ represent the delayed active power measurement at the PCC and the delayed measurement of q- component of the current flowing though the converter used in the control loops.

The dc grid subsystem includes all dc cables, modelled as 'frequency dependent' π model where the additional parallel RL branches are calculated to fit the frequency response of a wide-band cable model [24], [25]. The model is illustrated in Fig. 1. In general, in a dc grid wind farm side converters (WFC) work as grid forming converter for the connected ac grid without controlling V_{dc}. Hence, due to the focus on the GSC control WFCs can be simplified to dc current sources

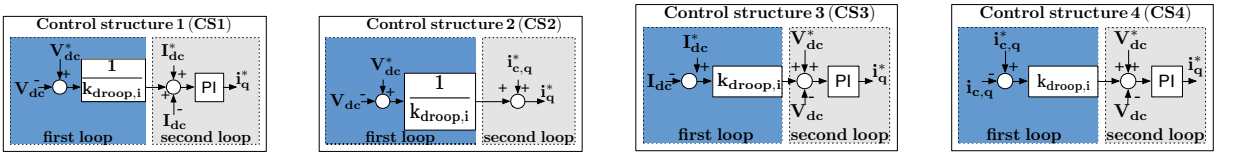

(a) CS1 (V_{dc}-I_{dc}) - [4]–[8]. (b) CS2 (V_{dc}-I_{ac}) - [9], [10]. (c) CS3 (I_{dc}-V_{dc}) - [11]–[13]. (d) CS4 (I_{ac}-V_{dc}) - [14].

(e) CS5 (V_{dc}-P_{dc}) - [16], [17]. (f) CS6 (V_{dc}-P_{ac}) - [23]. (g) CS7 (P_{dc}-V_{dc}) - [18], [19]. (h) CS8 (P_{ac}-V_{dc}) - [19].

Fig. 2. Analyzed dc voltage droop control structures [20].

representing an uncontrolled disturbance for the dc grid [22]. Thus, the states corresponding to the dc subsystem, I^{dc}, are:

$$\begin{aligned}\mathbf{x}_{dc} = \big[& I_{dc,z(l)} \quad I_{dc,z(l+1)} \quad I_{dc,z(l+2)} \quad \cdots \quad I_{dc,z(3M-2)} \\ & I_{dc,z(3M-1)} \quad I_{dc,z(3M)} \quad I_{dc,meas,l} \quad \cdots \quad I_{dc,meas,M} \\ & V_{dc,wf,k} \quad \cdots \quad V_{dc,wf,K}\big] \end{aligned} \tag{6}$$

with $I_{dc,z(l)}$ - $I_{dc,z(l+2)}$ representing the currents in the different branches of the $l = 1, \cdots, M$ different dc cables. Further, $I_{dc,meas,l}$ represents the delayed dc current measurements at the GSCs, shown in Fig. 1 as $I_{dc,i}$. The variable $V_{dc,wf,k}$ denotes the dc voltage at the $k = 1, \ldots, K$ WFCs.

The GSCs are assumed to be synchronized to the ac grids through a Phase Locked Loop (PLL) and operated with conventional current controllers in the Synchronous Reference Frame (SRF). The current controllers of the GSCs are tuned by the Internal Model Control (IMC) technique designed to track references with a settling time of 10 ms [26]. Saturation limits are included in the control scheme, in order not to exceed the maximum current ratings of the converters.

Both GSCs are assumed to use dc voltage droop control. In general, dc voltage droop control introduces a linear relationship between the dc voltage and a second electric variable, so that the droop gain, k_{droop}, defines the deviation of $V_{dc,j}$ for a variation of the other electric variable:

$$V_{dc,j} = V^*_{dc,j} + k_{droop}(y^*_j - y_j) \tag{7}$$

y^*_j and $V^*_{dc,j}$ are the set points and $V_{dc,j}$, y_j are the measured electric variables respectively. The second electric variable, y_j, can either represent the dc current, $I_{dc,j}$, one component of the ac current, $I_{ac,j}$, the active power measured on the dc side, $P_{dc,j}$, or the active power measured on the ac side, $P_{ac,j}$ [20]. Depending on whether the dc voltage is controlled in the first or the second loop this leads to a total of 8 different dc voltage droop control structures, shown in Fig. 2.

Further, to better control the power sharing between the converters after a converter outage the use of a generalized feedback signal using communication between the GSCs has been proposed [27] as an alternative to the eight CSs using local measurements only. The idea here is, to use a multiple-input feedback controller using all measured voltages deviations as inputs at every terminal, as given in:

$$\begin{bmatrix} \mathbf{\Delta I_{dc,1}} \\ \mathbf{\Delta I_{dc,2}} \\ \vdots \\ \mathbf{\Delta I_{dc,N}} \end{bmatrix} = \begin{bmatrix} g_{11} & g_{12} & \cdots & g_{1N} \\ g_{21} & g_{22} & \cdots & g_{2N} \\ \vdots & \vdots & \ddots & \vdots \\ g_{N1} & g_{N2} & \cdots & g_{NN} \end{bmatrix} \begin{bmatrix} \mathbf{\Delta V_{dc,1}} \\ \mathbf{\Delta V_{dc,2}} \\ \vdots \\ \mathbf{\Delta V_{dc,N}} \end{bmatrix} \tag{8}$$

with g_{xy} corresponding to the inverse of the droop gains, $\frac{1}{k_{droop}}$. Here, however, they are determined by an optimization problem considering the line resistances. Hence, the proposed generalized feedback controller is similar to CS1 (V_{dc}-I_{dc}) but differs by the fact that the generalized feedback controller uses measurements of all GSCs and additional corresponding droop gains.

A comparable performance of power and current based droop control structures and the generalized feedback controller is ensured by the following:

- The droop gains were chosen as $k_{droop,p} = \frac{1}{25}\frac{\text{V}}{\text{kW}}$ as suggested in [22].
- The droop gains used within the power and current based droop controller should be comparable. Thus, the relation derived in [28] is used to determine the current based droop gains, $k_{droop,i_{dc}}$, that are equivalent to the power based droop gains, $k_{droop,p}$:

$$k_{droop,i_{dc}} = \frac{V^*_{dc,j}}{\frac{1}{k_{droop,p}} - I^*_{dc,j}}. \tag{9}$$

  The current based droop gain used for the CSs combining $V_{dc,j}$ and $I_{ac,j}$ needs to be scaled additionally, due to the higher range of $I_{ac,j}$. However, due to the non-linearity of power based droop control, the approximation holds only for a small deviation of the voltage:

$$k_{droop,i_{ac}} = \frac{I^*_{dc,j}}{i^*_{c,q,j}} \cdot k_{droop,i_{dc}}. \tag{10}$$

- For a comparable performance of the generalized feedback control g_{11} and g_{22} are chosen as $\frac{1}{k_{droop,i} - \frac{k_{droop,i}}{2}}$, while g_{12} and g_{21} are chosen as $\frac{1}{k_{droop,i}/2}$.
- Two different for all droop control structures comparable tunings are chosen to show the impact of the tuning on the coupling of the different subsystems. The fast tuning leads

to a fast rise time of approx. 17 ms and a settling time of approx. 60 ms with an overshoot of approx. 5%. The slow tuning is reflected by an over-damped response without overshoot, a rise time of approx. 23 ms and a settling time of approx. 40 ms.

Only the response of CS2(V_{dc}-I_{ac}) differs, due to the absence of a PI controller, since the droop gain already serves as proportional controller connecting $V_{dc,j}$ and $i_{q,j}$ creating the necessary reference variable for the current controller. Hence, the dynamics of CS2(V_{dc}-I_{ac}) are determined by the current controller, which was tuned independently of the outer CS.

Thus, the GSC subsystems, I^{gsc_j}, with $j = 1, \ldots, N$, consist of the following states:

$$\mathbf{x}_{gsc,j} = \begin{bmatrix} pll_{d,j} & pll_{q,j} & \gamma_{d,j} & \gamma_{q,j} & \kappa_{d,j} & \kappa_{q,j} \\ & & V_{dc,j} & V_{dc,meas,j} & P_{dc,meas,j} \end{bmatrix} \quad (11)$$

with $pll_{d/q,j}$ corresponding to the integrator state of the phase-locked loop (PLL). While $\gamma_{d/q,j}$ and $\kappa_{d/q,j}$ represent the integrator states of the current, respective outer controllers, $V_{dc,j}$ and $V_{dc,meas,j}$ represent the dc voltage at the converter and its delayed measurement. Further, $P_{dc,meas,j}$ represents the delayed active power measurement at the GSC.

IV. Case Study

A three terminal grid, shown in Fig. 3, is chosen to evaluate which impact has the choice of the CS on the coupling of the different subsystems. The length of both lines is assumed to be 100 km, parameters are taken from [25]. Choosing the same droop control structure for both GSCs we obtain nine different scenarios (eight different droop CSs, one with generalized feedback). The parameters are given in the appendix. The WFC is assumed to inject maximum power into the HVDC grid with an equal power sharing between the converters. The linearized models are verified by equivalent non-linear models built in Matlab Simulink, which also provide the steady state initial values. As described in the methodology, we focus on two subsets of interaction modes, in particular $S^{ac,dc}$ and S^{gsc}.

A. Subset: AC/DC Interactions

Fig. 4 shows the size of the subset $S^{ac,dc}$ with respect to the set of all modes S in percent in black (fast tuning) and red (slow tuning) respectively. Further, it indicates the minimum damping ratio of the interaction modes in that subset in percent in blue (fast tuning) and green (slow tuning). The first observation is that the coupling of the dc and ac subsystems is affected by the choice of the CS. In fact, depending on the CS and the tuning this subset includes between 11.8 % (CS7 (P_{dc}-V_{dc}) and CS8 (P_{ac}-V_{dc})) and 21.6 % (CS6 (V_{dc}-P_{ac}))

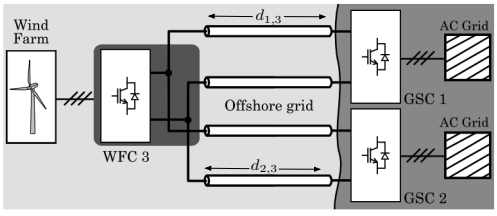

Fig. 3. Three terminal VSC-HVDC grid [22].

of all modes in case of the fast tuning. For the slow tuning it is spread between 0 % (CS3 (I_{dc}-V_{dc}) and CS7 (P_{dc}-V_{dc})) and 13.7 % (CS8 (P_{ac}-V_{dc})), considering that there exists no different tuning for (CS2 (V_{dc}-I_{ac}) due to the fact that the CS does not include a PI-controller within the droop controller. Further, unlike it might be intuitively expected the use of an ac measurement within the droop control structure does not necessarily lead to a higher degree of coupling. Further, Fig. 4 also indicates that the damping ratio of the most critical eigenvalue of this subset differs significantly for every CSs as well as for the different tunings (between 16.4 % (CS6 (V_{dc}-P_{ac})) and 29.3 % (CS3 (I_{dc}-V_{dc})) for the fast tuning and between 15 % (CS8 (P_{ac}-V_{dc})) and 100 % (CS1 (V_{dc}-I_{dc})) for the slow tuning, CS2 (V_{dc}-I_{ac}): 14.8 %). This indicates that not only the degree of coupling of the ac and dc grid depends on the choice and tuning of the CS, but also how well damped disturbances potentially spread between the subsystems.

It is remarkable that for all CSs but CS8 (P_{ac}-V_{dc}) an increased transient response (faster tuning) leads to a higher coupling and lower damping ratio, while it is the other way around for CS8 (P_{ac}-V_{dc}).

The analysis of the participation factors of the lowest damped modes indicates that CSs using the q-component of the ac current within the droop control structure (CS2 (V_{dc}-I_{ac}) and CS4 (I_{ac}-V_{dc})) create a stronger coupling between the outer control loops and therefore for specific modes a stronger coupling between the dc and ac systems. The analysis shows that in this case the subset I^{dc} participates with $\eta_{dc} = 9.4\,\%$ (CS4 (I_{ac}-V_{dc}) (fast tuning)) respectively $\eta_{dc} = 6.9\,\%$ (CS2 (V_{dc}-I_{ac}) in those modes which have a high participation of both ac voltage controllers and corresponding ac states, while in case other CSs are used the dc participation in these modes is $\leq 2.2\,\%$ (fast tuning).

Further, it is worth to mention that both CSs using the dc current (CS1 (V_{dc}-I_{dc}) and CS3 (I_{dc}-V_{dc})) lead to almost complete decoupling of the ac and dc systems in case of the slow tuning, i.e. there exists no (CS3 (I_{dc}-V_{dc})), respectively only very few very well damped eigenvalues. Further, in the fast tuning case, they lead to a medium coupling but all interaction modes are very well damped. In fact, unlike to the other CSs all eigenvalues but two corresponding to the interaction modes have a damping ratio of 100 % and the

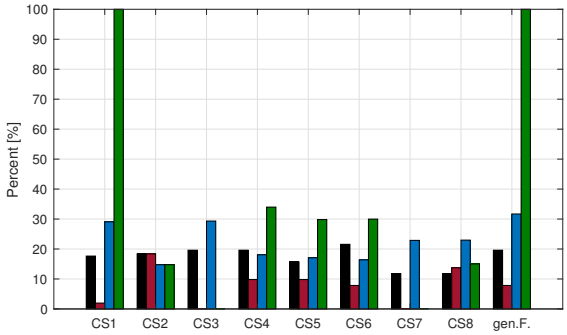

Fig. 4. Size of subset $S^{ac,dc}$ with respect to S in percent for the fast (black) and slow tuning (red). The minimum damping ratio of the corresponding eigenvalues of subset $S^{ac,dc}$ is shown in percent in blue for the fast and in green for the slow tuning.

two remaining ones have significant higher damping ratios ($\geq 29\,\%$) than the lowest damped eigenvalues corresponding to the interaction modes of all remaining CSs.

The impact of the generalized feedback controller can be evaluated by comparing the results of CS1 (V_{dc}-I_{dc}) with the scenario where both GSCs use the generalized feedback controller since they differ only by the use of the measurement signals and additional corresponding droop gains as indicated in III. Figure 4 shows that this leads to a slightly higher number of interaction modes ($21.6\,\%$ to $17.7\,\%$ (fast tuning), $7.8\,\%$ to $2\,\%$ (slow tuning)), hence a higher coupling between the subsystems as intuitively expected due to the communication between the converters. Further, in the fast tuning case, it leads to a slightly higher damping of that aforementioned pair of eigenvalues $31.6\,\%$ to $29.1\,\%$.

Thus, considering that it is preferable to have the ac and dc grid as decoupled as possible with as well damped interaction modes as possible CS7 (P_{dc}-V_{dc}) shows the best properties. For the slow tuning it leads to a complete decoupled system while for the fast tuning it leads to the most decoupled system and a medium damping (together with CS8 (P_{ac}-V_{dc})). Further, CS3 (I_{dc}-V_{dc}) leads to a complete decoupled system with the slow tuning as well. However, in case of the fast tuning a higher coupling of the system (with even though very well damped interaction modes) can be observed. Hence, the best results in particular for the slow tuning are observed for both CSs, combining V_{dc} with dc variables and controlling V_{dc} in the second loop.

On the other hand, CS2 (V_{dc}-I_{ac}) leads to a medium coupling of the systems (size of $S^{ac,dc}$= $18.3\,\%$ of S) and the lowest damping of the most critical interaction mode ($14.8\,\%$). However, considering that TSOs allow damping ratios as low as 3% in their systems, the values of all CSs are not critical in terms of system security. Nevertheless, significant differences between the CSs have been shown.

B. Subset: Converter Interactions

Fig. 5 shows the size of the subset S^{gsc} with respect to the set of all modes S in percent in black (fast tuning) and red (slow tuning) respectively. Further, it indicates the minimum damping ratio of the interaction modes in that subset in percent in blue (fast tuning) and green (slow tuning). The figure shows a high degree of coupling of the two converters and that also the degree of coupling between the different converters depends on the choice of the CS and the tuning, since the size of the subset S^{gsc} varies between $43.1\,\%$ (CS4 (I_{ac}-V_{dc}) and CS6 (V_{dc}-P_{ac})) and $54.9\,\%$ (CS5 (V_{dc}-P_{dc}) and CS7 (P_{dc}-V_{dc})) of S (fast tuning) and between $41.2\,\%$ (CS1 (V_{dc}-I_{dc}) and CS3 (I_{dc}-V_{dc})) and $54.9\,\%$ (CS5 (V_{dc}-P_{dc})) of S. The choice of CS2 (V_{dc}-I_{ac}) leads to $38.8\,\%$ of all modes having a participation of at least $5\,\%$ of both converters.

Further, it is shown that not only the degree of coupling depends on the chosen CS and its damping but also how well those interaction modes are damped. The blue (fast) and green (slow) bars in Fig. 5 indicate minimum damping ratios between $3.3\,\%$ (CS4 (I_{ac}-V_{dc})) and $10\,\%$ (CS6 (V_{dc}-P_{ac})) (fast) and between $10.1\,\%$ (CS7 (P_{dc}-V_{dc})) and $14.3\,\%$ (CS8 (P_{ac}-V_{dc})) (slow), hence significant differences and close to critical damping ratios for CS4 (I_{ac}-V_{dc}). The choice of CS2 (V_{dc}-I_{ac}) leads to a minimum damping ratio of $5.4\,\%$.

Thus, the best performing CS from the previous subset, CS7 (P_{dc}-V_{dc}), leads to a comparably medium (slow) / high (fast) degree of coupling between the GSCs and a comparably low (slow) / medium (fast) level of damping ratio with respect to the other CSs. The second place, CS3 (I_{dc}-V_{dc}), leads to a low (slow) / medium (fast) degree of coupling and comparably low (slow) / medium (fast) damping ratios.

The analysis of the participation factors of the lowest damped modes indicates that all lowest damped modes are related to the outer control loops (mostly ac voltage controllers) and the corresponding ac variables. Thus, the previous observed stronger coupling between the outer control loops in case the q-component of the ac current is used within the droop control structure (CS2 (V_{dc}-I_{ac} and CS4 (I_{ac}-V_{dc}) (fast tuning)) also leads to a lower damping of the most critical interaction modes of the system. However, apart from this and the fact that CSs combining I_{dc} with V_{dc} with a slow tuning lead to a comparably low degree of coupling of the GSCs, there is no clear tendency that a specific combination of variables or order of control loops is better or worse in general within this subsets.

The generalized feedback leads to a higher degree of coupling ($49\,\%$ to $45.1\,\%$) as intuitively expected due to communication between the converters, however, it does not improve the damping of the most critical interaction mode.

C. Discussion

It has been shown that the choice of the CSs as well as the tuning influences the degree of coupling between the different subsystems. Further, a CS leading to a low degree of coupling of dc and ac systems does not consequently also lead to a lower degree of coupling within the dc grid. Additionally, a trade-off between the degree of coupling of the subsystems, the damping of the interaction modes and the response time of the converters was observed.

A CS controlling V_{dc} in the second loop and combining it

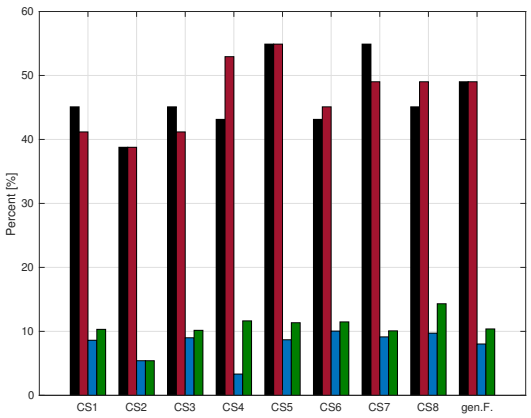

Fig. 5. Size of subset S^{gsc} with respect to S in percent for the fast (black) and slow tuning (red). The minimum damping ratio of the corresponding eigenvalues of subset S^{gsc} is shown in percent in blue for the fast and in green for the slow tuning.

with a second dc variable (I_{dc}/P_{dc}) is in particular with a slow tuning preferable for a decoupling of the dc and ac subsystems. On the other hand, a CS combining V_{dc} with I_{dc} and a slow tuning leads to a comparably low degree of coupling within the dc grid. Thus, CS3 (I_{dc}-V_{dc}) achieves overall the best results with a comparably slow transient response. For a fast response the results are not as clear as for the slow response with different CSs having advantages in different subsets. Considering the higher importance of the subset $S^{ac,dc}$, CS8 (P_{ac}-V_{dc}) is a good candidate for a fast transient response, since it leads to the most decoupled dc and ac subsystems with a comparably medium damping ratio.

Finally, a generalized feedback increases the coupling of the subsystems and the damping of specific but not all interaction modes.

V. Conclusion

This paper presented an analysis of the impact the choice of the droop control structure and its tuning have on the degree of coupling of different subsystems in an interconnected AC/MT-HVDC system. It was shown that the choice of the droop control structure and its tuning influence the degree of coupling of the dc grid with the connected ac grids as well as the degree of coupling between the GSCs. Further, it also influences how well the corresponding interaction modes are damped.

References

[1] S. Chatzivasileiadis, D. Ernst, and G. Andersson, "The Global Grid," *Renewable Energy*, vol. 57, pp. 372–383, 2013.

[2] D. V. Hertem, O. Gomis-Bellmunt, and J. Liang, Eds., *HVDC grids: for offshore and supergrid of the future*. Wiley-IEEE Press, 2016.

[3] V. Akhmatov, M. Callavik, C. M. Franck, S. E. Rye, T. Ahndorf, M. K. Bucher, H. Muller, F. Schettler, and R. Wiget, "Technical guidelines and prestandardization work for first HVDC Grids," *IEEE Transactions on Power Delivery*, vol. 29, no. 1, 2014.

[4] C. D. Barker and R. Whitehouse, "Autonomous converter control in a multi-terminal HVDC system," in *9th IET International Conference on AC and DC Power Transmission*, London, 2010, pp. 1–5.

[5] W. Wang, M. Barnes, and O. Marjanovic, "Droop control modelling and analysis of multi-terminal VSC-HVDC for offshore wind farms," in *10th IET Int. Conf. on AC and DC Power Transmission*, Birmingham, 2012.

[6] O. Gomis-Bellmunt, J. Liang, J. Ekanayake, and N. Jenkins, "Voltage-current characteristics of multiterminal HVDC-VSC for offshore wind farms," *Elec.Power Syst. Research*, vol. 81, no. 2, pp. 440–450, 2011.

[7] L. Xu, L. Yao, and M. Bazargan, "DC grid management of a multi-terminal HVDC transmission system for large offshore wind farms," in *Int. Conf. on Sust. Power Gen. and Supply*, 2009, pp. 1–7.

[8] F. D. Bianchi and O. Gomis-Bellmunt, "Droop control design for multi-terminal VSC-HVDC grids based on LMI optimization," in *50th IEEE Conf. on Decision and Control and Europ. Control Conf.*, Orlando, 2011.

[9] R. T. Pinto, S. Rodrigues, P. Bauer, and J. Pierik, "Operation and control of a multi-terminal DC network," in *IEEE ECCE Asia Downunder*, Melbourne, 2013, pp. 474–480.

[10] Y. Chen, G. Damm, and A. Benchaib, "Multi-Time-Scale Stability Analysis and Design Conditions of a VSC Terminal with DC Voltage Droop Control for HVDC Networks," in *53rd IEEE Conference on Decision and Control*, Los Angeles, CA, 2014.

[11] J. Liang, T. Jing, O. Gomis-Bellmunt, J. Ekanayake, and N. Jenkins, "Operation and Control of Multiterminal HVDC Transmission for Offshore Wind Farms," *IEEE Transactions on Power Delivery*, vol. 26, no. 4, pp. 2596–2604, 2011.

[12] B. K. Johnson, R. H. Lasseter, F. L. Alvarado, and R. Adapa, "Expandable multiterminal dc systems based on voltage droop," *IEEE Transactions on Power Delivery*, vol. 8, no. 4, 1993.

[13] S. Zhou, J. Liang, J. B. Ekanayake, and N. Jenkins, "Control of multi-terminal VSC-HVDC transmission system for offshore wind power generation," in *44th Int. Universities Power Eng. Conf.*, Glasgow, 2009.

[14] F. Thams, J. A. Suul, S. D'Arco, M. Molinas, and F. W. Fuchs, "Stability of DC Voltage Droop Controllers in VSC HVDC Systems," in *PowerTech, Eindhoven 2015*, Eindhoven, 2015.

[15] F. Thams, R. Eriksson, and M. Molinas, "Interaction of Droop Control Structures and its Inherent Effect on the Power Transfer Limits in Multi-terminal VSC-HVDC," *IEEE Transactions on Power Delivery*, vol. 32, no. 1, pp. 182–192, 2017.

[16] P. Rault, F. Colas, X. Guillaud, and S. Nguefeu, "Method for small signal stability analysis of VSC-MTDC grids," in *IEEE Power and Energy Society General Meeting*, San Diego, 2012.

[17] T. M. Haileselassie and K. Uhlen, "Impact of DC Line Voltage Drops on Power Flow of MTDC Using Droop Control," *IEEE Transactions on Power Systems*, vol. 27, no. 3, pp. 1441–1449, 2012.

[18] T. M. Haileselassie and K. Uhlen, "Primary frequency control of remote grids connected by multi-terminal HVDC," in *IEEE Power and Energy Society General Meeting*, Minneapolis, 2010, pp. 1–6.

[19] G. Stamatiou and M. Bongiorno, "Decentralized converter controller for multiterminal HVDC grids," in *15th European Conference on Power Electronics and Applications (EPE)*, 2013, pp. 1–10.

[20] F. Thams, S. Chatzivasileiadis, E. Prieto-Araujo, and R. Eriksson, "Disturbance Attenuation of DC Voltage Droop Control Structures in a Multi-Terminal HVDC Grid," in *PowerTech*, Manchester, 2017.

[21] J. Beerten, S. D Arco, and J. Suul, "Identification and Small-Signal Analysis of Interaction Modes in VSC MTDC Systems," *IEEE Transactions on Power Delivery*, vol. 8977, no. c, pp. 1–1, 2015.

[22] E. Prieto-Araujo, A. Egea-Alvarez, S. F. Fekriasl, and O. Gomis-Bellmunt, "DC voltage droop control design for multi-terminal HVDC systems considering AC and DC grid dynamics," *IEEE Transactions on Power Delivery*, vol. 31, no. 2, pp. 575 – 585, 2015.

[23] T. M. Haileselassie and K. Uhlen, "Precise control of power flow in multiterminal VSC-HVDCs using DC voltage droop control," in *IEEE Power and Energy Society General Meeting*, San Diego, 2012.

[24] J. Beerten, S. D'Arco, and J. A. Suul, "Frequency-dependent cable modelling for small-signal stability analysis of VSC-HVDC systems," *IET Generation, Transmission & Distribution*, vol. 10, no. 6, 2016.

[25] S. Akkari, E. Prieto-Araujo, J. Dai, O. Gomis-Bellmunt, and X. Guillaud, "Impact of the DC cable models on the SVD analysis of a Multi-Terminal HVDC system," in *19th Power Systems Computation Conference (PSCC)*, Genoa, 2016, pp. 1–6.

[26] H. Saad, X. Guillaud, J. Mahseredjian, S. Dennetiere, and S. Nguefeu, "MMC Capacitor Voltage Decoupling and Balancing Controls," *IEEE Transactions on Power Delivery*, vol. 30, no. 2, pp. 704–712, 2014.

[27] J. Beerten, R. Eriksson, D. V. Hertem, and S. Member, "A New Approach to HVDC Grid Voltage Control Based on Generalized State Feedback," pp. 1–5, 2014.

[28] T. K. Vrana, "System Design and Balancing Control of the North Sea Super Grid," Ph.D. dissertation, NTNU, Trondheim, 2013.

[29] T. K. Vrana, Y. Yang, D. Jovcic, S. Dennetière, J. Jardini, and H. Saad, "The CIGRE B4 DC Grid Test System," Cigre, Tech. Rep., 2013.

[30] L. Zhang, "Modeling and control of VSC-HVDC links connected to weak AC systems," Ph.D. dissertation, 2010.

Appendix

TABLE I
PARAMETERS OF THE THREE-TERMINAL DC GRID. CIGRÉ B4 DC GRID TEST SYSTEM [29] AND AC GRIDS [30]

Parameters	Value	Units
GSC/WFC DC link capacitor c_{dc}	150	μF
WFC rated power P_3	700	MW
Reference voltage E^*	400	kV
Nominal power P_1, P_2	350	MW
Nominal voltage V_{ac}	195	kV
Nominal frequency f	50	Hz
Short circuit ratio (SCR)	5	-
Grid Thévenin X_n/R_n ratio	10	-
Coupling inductance L_c	0.2	pu
Coupling resistance R_c	0.01	pu
Capacitor filter impedance X_f	5.88	pu

[Pub. E] Data-Driven Security-Constrained OPF.

Data-Driven Security-Constrained OPF

Florian Thams, Lejla Halilbašić, Pierre Pinson, and Spyros Chatzivasileiadis
Center for Electric Power and Energy (CEE)
Technical University of Denmark (DTU)
Kgs. Lyngby, Denmark
Email: {fltha, lhal, ppin, spchatz} @elektro.dtu.dk

Robert Eriksson
Market and System Development
Svenska kraftnät
Sundbyberg, Sweden
robert.eriksson@svk.se

***Abstract*—In this paper we unify electricity market operations with power system security considerations. Using data-driven techniques, we address both small signal stability and steady-state security, derive tractable decision rules in the form of line flow limits, and incorporate the resulting constraints in market clearing algorithms. Our goal is to minimize redispatching actions, and instead allow the market to determine the most cost-efficient dispatch while considering all security constraints. To maintain tractability of our approach we perform our security assessment offline, examining large datasets, both from measurements and simulations, in order to determine stable and unstable operating regions. With the help of decision trees, we transform this information to linear decision rules for line flow constraints. We propose conditional line transfer limits, which can accurately capture security considerations, while being less conservative than current approaches. Our approach can be scalable for large systems, accounts explicitly for power system security, and enables the electricity market to identify a cost-efficient dispatch avoiding redispatching actions. We demonstrate the performance of our method in a case study.**

I. Introduction

Market-clearing processes and security assessment are separated in most electricity markets [1]. Market operators determine the economic dispatch in an auction based on Optimal Power Flow algorithms (OPFs) considering only a few physical limitations, such as generation and line flow limits. Transmission System Operators (TSOs), in charge of the secure and reliable system operation, determine actual physical bounds and carry out necessary redispatching measures. In order to optimally establish secure system operation and avoid expensive redispatching actions, market-clearing processes need to account for security considerations. To this end, algorithms are required, which capture the security requirements imposed by TSOs while at the same time being scalable and rapidly deployable in market-clearing auctions. We propose conditional line transfer limits as preventive security measures, which are optimally chosen in market-clearing auctions.

Security requirements include the N-1 criterion and stability margins. The N-1 criterion guarantees safe system operation even after the outage of any single component, while the stability margin ensures that oscillations caused by small disturbances are sufficiently damped. Security-Constrained OPF algorithms (SC-OPFs), i.e. OPFs which explicitly account for security criteria, have primarily focused on the N-1 criterion. Constraints, which for example ensure small-signal stability, are based on differential algebraic equations and cannot be included in the OPF as linear or non-linear constraints in a straightforward way. The authors in [1] and [2] use eigenvalue-sensitivities with respect to OPF decision variables to maintain tractability of small-signal stability constraints. However, both papers conclude that the required computational effort is a major challenge and the methods perform poorly when applied to larger systems. Additionally, compared to this paper, the method developed in [1] determines only the optimal redispatching action of the TSO and does not incorporate small-signal stability constraints in market-clearing auctions. An online preventive control strategy accounting for contingencies and transient stability was developed in [3]. The security considerations are translated to generator capacity limits of the most critical generators, which are included as hard constraints in the OPF. This approach, however, does not allow the market participants to bid all their available capacity and imposes very conservative bounds, which can prevent the deployment of cheaper generation capacity. In [4] a security boundary-constrained DC-OPF ensuring voltage and small-signal stability is proposed, where hyperplanes are used to linearly approximate the security boundary. Thus, operating points outside the convex space constructed by the hyperplanes are not considered in the OPF.

The contribution of this paper is a data-driven SC-OPF, which (a) incorporates the N-1 criterion, (b) ensures small-signal stability and compliance with stability margins, (c) avoids the complex reformulation of small-signal stability constraints inside the OPF by incorporating decision rules, (d) is applicable to large systems, (e) allows for a fast online solution as all computation related to the small-signal model is done offline and (f) encapsulates all security considerations for the OPF in conditional transfer limits of the lines. Traditionally, transfer limits, which are calculated by TSOs and provided to market operators, tend to be very robust and can lead to an inefficient use of the network. In this paper, we derive conditional transfer limits in the form of decision rules, which can be easily incorporated in OPF algorithms using Mixed Integer Linear Programming (MILP) and allow the market to optimally decide on power flows which will always guarantee power system security. Furthermore, this SC-OPF is not limited to market operation but it can also be used to minimize losses in the system or for other objectives.

For this purpose, a large database of operating points is created using a small-signal model of the system. The operating

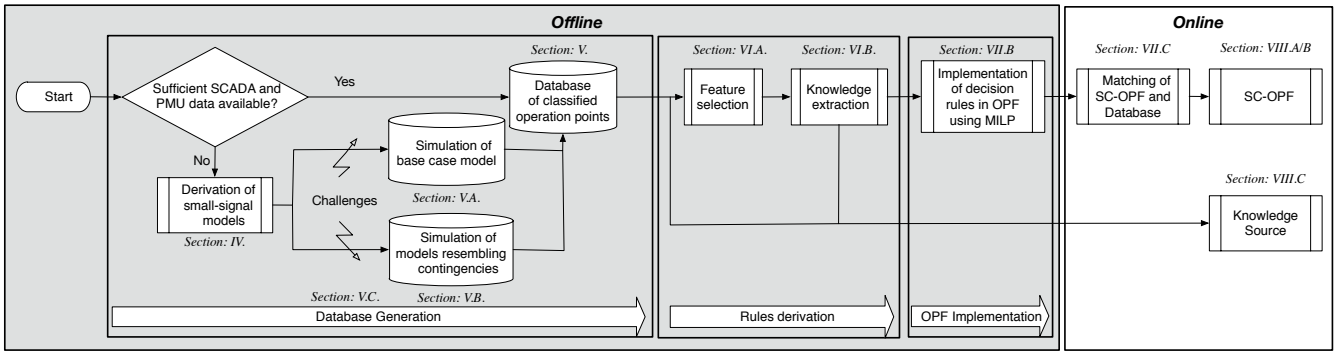

Fig. 1. Proposed Methodology.

points are evaluated for small-signal stability and classified according to their compliance with required stability margins and the N-1 security criterion. Decision tree learning tools are then applied to derive decision rules suitable for implementation in OPF problems, thereby reducing the complexity of the SC-OPF. This allows for a more detailed modeling of the system given that all computations with respect to the small-signal model are done offline and not within the OPF. Less constraints are used compared to conventional SC-OPFs, which makes the method suitable for large systems.

The remainder of this paper is organized as follows: Section II introduces small-signal stability. An overview of the methodology to derive the SC-OPF is given in section III. The small-signal model and database creation are described in section IV and V, followed by a summary of the methodology for feature selection and knowledge extraction in section VI. Section VII describes the implementation of small-signal stability constraints in an OPF problem, while the application of the proposed method is demonstrated in section VIII. Finally, section IX concludes the paper.

II. Small-Signal Stability

Small-signal stability assessment belongs to standard practice for almost all power system operators. In [5], a joint Cigre and IEEE Task Force defines small-signal rotor angle stability as the ability of a power system to maintain synchronism under small disturbances. They conclude that small-signal (or small disturbance) stability depends on the initial operating point and that nowadays instability is usually a result of insufficient damping of oscillations.

Small-signal instability is associated with one or more complex eigenvalues, whose real parts become positive [1]. Usually, TSOs determine a certain stability margin in terms of minimum damping ratio which should not be violated at any time to ensure a secure operation of the system.

Although power system stabilizers (PSS) and other damping controllers have been proposed and shown to be effective in improving small-signal stability, the authors of [6] argue that it is usually not possible to design a damping controller for all possible operating conditions, which makes additional remedial measures necessary. Thus, an OPF considering small-signal stability constraints may be an efficient way to avoid such operating conditions and therefore small-signal stability problems.

III. Method

The methodology to derive the data-driven SC-OPF proposed in this paper is shown as a flowchart in Fig. 1.

The first part consists of the data generation block. If available, data from phasor measurement units (PMUs) could be used. Further, if SCADA data is available a state estimator could be used to map the data into a power system model to perform the required simulations. However, due to the unavailability of such data we used data obtained by simulation of small-signal models in this paper. The derivation of such models is described in section IV, while the consideration of N-1 security and the challenges of the data generation are discussed in the following subsections. The result of this first part of the methodology is a large database of operating points which are classified for the base case as well as for credible contingencies. This is described in section V. The second part of the methodology uses this database to derive rules, which can later be incorporated in the OPF formulation. The second part includes feature selection and knowledge extraction and is described in section VI. The third part consists of implementing such rules in the OPF algorithm using MILP (section VII). Finally, the SC-OPF is tested in a case study in section VIII.

IV. Modeling

In order to create a database of possible operating points for which we can perform a small-signal stability assessment, we first need to derive a small-signal model.

A sixth order synchronous machine model [7] with an Automatic Voltage Regulator (AVR) Type I (3 states) is used in this study. With an additional state for the bus voltage delay this leads to a state-space model of $10m$ states, with N_G representing the number of generators in the grid. The model is based on the following assumptions without loss of generality:

- Stator and network transients are neglected.

- Constant mechanical torque is assumed as a result of neglecting turbine governor dynamics.
- The damping torque is assumed to be linear.

For a detailed description of the derivation of a multi-machine model, the interested reader is referred to [7], [8]. The relevant equations are briefly summarized in Appendix A. The small-signal models are derived symbolically until equation (A2), due to the fact that the symbolic inversion of the Jacobian given in (35) is computationally extremely demanding, if not impossible (for larger systems). The symbolic derivation enables us to initialize the model for every possible combination of load and generation using Matpower 6.0 [9].

The small-signal model is adjusted to account for the N-1 criterion by explicitly incorporating the outage of a single component. Thus, the multi-machine model of the base case, i.e. without any contingency, is adapted for every credible contingency resulting in $\Gamma + 1$ different small signal models. Variable Γ represents the number of considered contingencies.

V. Database Generation

The required database contains the necessary information on possible operating points of the system including their stability and stability margins. This set of credible operating points contains all possible combinations of generator dispatches corresponding to typical load patterns. Thus, in general, depending on the number of generators in the grid, N_G, their maximum capacity, P_i^{max}, the number of load patterns, Λ and the minimum generation bid size, α, the number of operating points in this set is given by:

$$\Psi = \Lambda \cdot \prod_{i=1}^{N_G-1} \left(\frac{P_i^{max}}{\alpha} + 1 \right). \tag{1}$$

Obviously, this number corresponds to only one approach. The study of how to define and determine the whole space of operating points is equally important and needs to be addressed. We will discuss this in more detail in subsection V-C. Thus, (1) provides only a first impression of the size of the required database and which variables influence the database size specifically.

In case that PMU and SCADA data is available for all credible operating points, the necessary database for the base case already exists. Noise reduction and data correction methods might be necessary and the data needs to be analyzed with respect to the stability margin of the operating points. However, it is very likely that there does not exist data for all credible contingencies, thus additional simulations will be necessary. Hence, a state estimator could be used to map the SCADA data into a power system model to perform additional simulations.

A. Base Case

If PMU / SCADA data is not (sufficiently) available for the base case, i.e. considering the whole grid without contingencies, (additional) simulations are necessary. The base case model is initialized for every (missing) operating point using ac power flow in Matpower 6.0 [9]. Each operating point is examined for small signal stability considering the chosen stability margin and classified as "fulfilling the stability margin" or "not fulfilling the stability margin". The results are saved in a database together with the necessary information of the operating point. The necessary information depends on the chosen mapping of the operating points between the ac and dc power flow and is described in more detail in section VI-A.

B. N-1 Security

In order to evaluate the N-1 security of the system, Γ different small signal models adjusted for all considered contingencies are also initialized for all Ψ operating points. Here, however, the choice of the slack bus in the ac power flow used for initializing the various contingency models may differ between the contingencies considered. Ideally the distributed slack buses should be chosen according to the location of the primary reserves, which balance the power mismatch in case of the specific contingency based on the experience of the TSO. The operating points are classified according to the outcome of the small signal analysis of the different contingency models.

The database contains all necessary information of the operating points and the results of the small signal analyses for the base case and all considered contingencies.

C. Challenges

The data generation is one major challenge of this approach. In particular, two partially contradicting goals exist:

- keeping the database as small as possible to minimize computational demand
- determining the stability boundary as precise as possible

Large grids with many generators lead to a very large database if all possible operating points were evaluated as seen in (1). However, since the goal is to determine line flow limits it is not really necessary to analyze all possible combinations of generation patterns as indicated in Fig. 2. The figure shows the

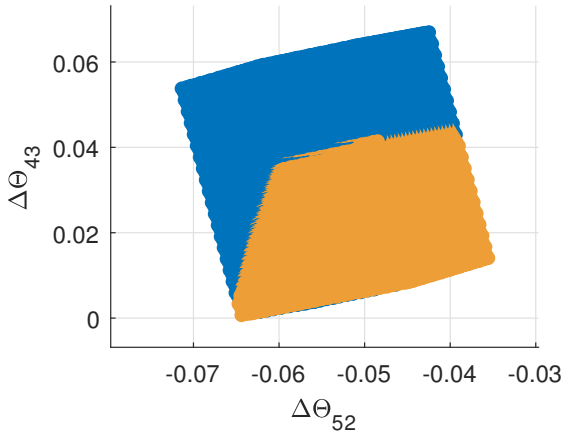

Fig. 2. Scatter plot of two angle differences, which correspond to line flow limits, for all operating points. Operating points fulfilling the stability margin (3%) are marked in orange, those not fulfilling the stability margin in blue.

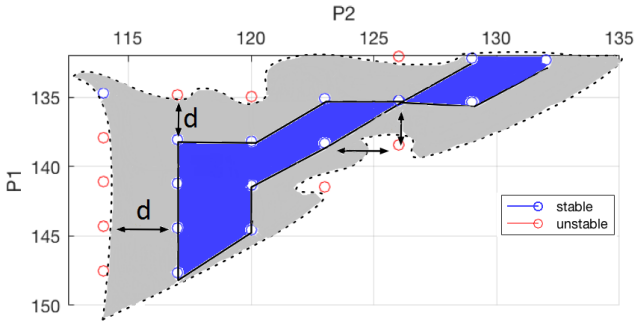

Fig. 3. Step size (d) of simulation needs to be chosen in a way that the area of stable operating points (purple) is maximized while the area of uncertain/potentially stable operating points (grey) which lies between stable (blue) and unstable (red) operating points is minimized.

area of operating points fulfilling the stability margin (orange) and the area of operating points not fulfilling the stability margin (blue). Thus, by focusing on the stability boundary and neglecting operating points far away from the boundary the database can be reduced. This can be achieved by e.g. using the existing knowledge of experienced engineers at TSOs.

Furthermore, we want to determine the stability boundary as accurately as possible, in order to provide the most cost-efficient line flow limits without increasing risk. Thus, in the area around the stability boundaries the step size between the operating points should be smaller than the minimum bid size leading to an even larger database. Hence, the appropriate distance between the different simulated operating points is an important issue. It was shown in [10] that eigenvalues associated with Hopf bifurcations vary smoothly with respect to power changes. Nonetheless, Fig. 3 indicates that it is important, in particular at the boundary, to find the step size d of active power variation ΔP, which minimizes the area of not simulated operating points (i.e., grey area), whose stability is uncertain. Smaller distances lead to a larger data sample and are computationally more demanding, whereas larger distances lead to inaccuracies and potentially higher costs due to more conservative boundaries. The computational efficiency depends on the method used for the database generation, including the appropriate choice of operating points to be analyzed. Although carried out offline, the database generation may represent a major obstacle. In future work we plan on investigating methods to minimize the computational demand without losing accuracy.

VI. Feature Selection and Knowledge Extraction

The creation of the database is followed by the feature selection, which determines the level of conservatism of the line flow limits. The knowledge extraction constitutes the final step in the offline derivation of the decision rules.

A. Feature Selection

In order to be able to substitute simulation data with PMU data in the future, only easily accessible variables should be considered as inputs. The goal is to incorporate all security considerations into conditional transfer limits, which provide the boundaries for the market and keep the complexity of the SC-OPF comparably low.

The transfer limits for the market-clearing are derived from the data obtained by using ac power flow as initialization for the small signal models. Since market operations are usually based on linearized dc power flow equations, the main issue here is to achieve a good mapping between the ac power flow operating points and the dc power flow points. This mapping is needed due to the fact that for the same generation pattern the line flows in an ac power flow can differ (significantly) from the ones in a dc power flow depending on the voltages and angles in the system. Thus, a better mapping of operating points leads to more accurate and less conservative line flow limits.

We focused on three different approaches to determine the active power transfer limits. Eq. (2) shows the active power transfer over a line $n-m$ based on the full AC power flow equations.

$$F_{nm} = |V_n||V_m| \left(G_{nm}\cos(\theta_n - \theta_m) + B_{nm} sin(\theta_n - \theta_m)\right), \quad (2)$$

where F_{nm} and V_n denote the active power flow between nodes n and m and the voltages at node i, respectively. G_{nm} and B_{nm} correspond to the conductance and susceptance of the line.

1) Standard DC Approximation: The standard dc approximation is based on the following assumptions:

- the resistance of the lines is very small compared to the reactance resulting in: $G = 0$ and $B_{nm} = \frac{-1}{x_{nm}}$
- the angle difference between adjacent nodes is small allowing for the sine to be replaced by its argument
- voltage magnitudes $|V_n|$ are equal to 1 p.u..

The line flows are then given by:

$$F_{nm} = \frac{\theta_n - \theta_m}{x_{nm}}. \quad (3)$$

2) Less conservative approximation: More accurate line flows can be computed if nodal voltage magnitudes and the sine of the angle difference are accounted for:

$$F_{nm} = \frac{|V_n||V_m| \sin(\theta_n - \theta_m)}{x_{nm}}. \quad (4)$$

3) Exact Mapping of DC and AC operating points: The most precise mapping of the dc and ac operating points has been achieved by incorporating the mapping into the data generation. We derived the line losses of the ac power flow of each generation pattern and included them as additional loads in a subsequent dc power flow. The losses are added to the nodes in the following way:

$$P_{Loss,n} = \frac{1}{2} \cdot \sum_{m \in I_n} \left(F_{nm} + F_{mn}\right), \quad (5)$$

where F_{nm} and F_{mn} represent the line flows obtained from the ac power flow analysis and I_n denotes the set of nodes connected to node n. The dc power flow is thus augmented by the loss approximation of the corresponding ac power flow

and the obtained line flows of the dc power flow represent an exact mapping of operating points.

B. Knowledge Extraction

This paper proposes classification trees as knowledge extraction/classification methods. A classification tree is a subset of decision trees (DT) where the decision outcome, called "target variable", can take a finite set of values. A complete introduction to DT theory for power systems can be found in [11]. Within the generated databases containing all operating points, we distinguish between those "fulfilling the stability margin" and those "not fulfilling the stability margin". TSOs require stability margins to ensure sufficient damping of oscillations. The classification tree is used to reveal patterns of the interconnection between observation attributes and target variables with the goal of using these patterns as decision rules to predict the decision outcome of new observations. These attributes of observations used as decision variables are called "predictors". A simple example of a DT is shown in Fig. 4. It contains nodes, branches and terminal decisions. At each node a test of a predictor splits the data set into subsets according to the test result. The branches connecting this node with the nodes one level below represent the possible test outcomes. The leaf nodes with terminal decisions constitute the final classification of the input observation. The use of a DT instead of other data mining or machine learning techniques provides a better understanding of the entire system's small-signal stability and what influence different parts of the system have. Moreover, we can define conditional transfer limits by using an appropriate feature selection and associating all full DT paths from the root to the leaves with binary decision variables. The optimal dispatch is then chosen by allowing only one path to be activated.

Note that before training the DT, the database should be analyzed with respect to the potential problem of skewed classes, i.e. it needs to be examined whether one class ("fulfilling the stability margin" / "not fulfilling the stability margin") is significantly over-represented compared to the other. If this is the case, three options exist: (a) limiting the number of the over-represented class by neglecting the appropriate amount of samples, (b) over-sampling the minority class or (c) raising the cost of misclassifying the minority class. While option (a) might leave out exactly the most important information close to the stability boundary, (b) degrades the learning speed due to duplicate instances. Option (c) allows to introduce risk-aversion, which might lead to more conservative and less cost-efficient transfer limits. This however, can be improved through smaller step sizes during the analysis described in V-C.

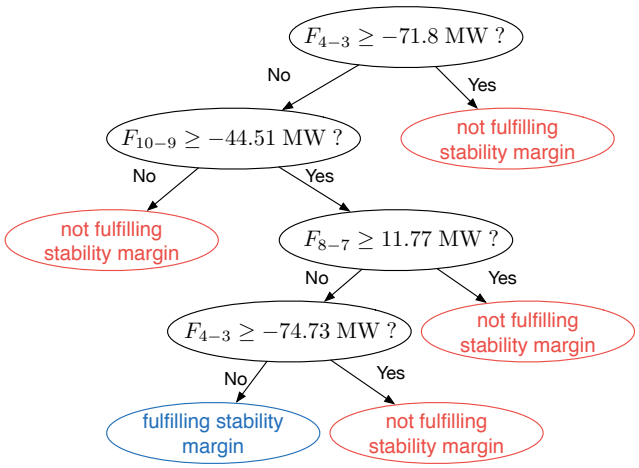

Fig. 4. A simple example of a decision tree

The DT is trained using a subset of the whole database, called training set A. The derived rules are tested using another subset B of the database with $A \cup B = \emptyset$.

It is worth mentioning that although DTs achieve pretty high accuracies, there will always be misclassifications, which in theory could cause unstable solutions of the proposed data-driven SC-OPF. However, actions have been taken to minimize, if not completely avoid this threat. First, by increasing the cost for misclassifications of unstable cases we reduce the misclassifications in this direction. This, however, might also cause less cost-efficient line flow limits. Further, by choosing a certain stability margin and differentiating between "fulfilling the stability margin" and "not fulfilling the stability margin", instead of "stable" and "unstable", we can reduce the risk even further, since misclassifications do not necessarily lead to instability, but just to lower stability margins than required - at least in all scenarios tested in this paper. This is discussed in more detail in section VIII-B.

Finally, in order to avoid over-fitting, the obtained trees need to be pruned appropriately. Different pruning techniques will be investigated in future work.

VII. OPF Implementation

As usual in market applications, the network is modeled using a linear DC approximation.

A. Standard DC Optimal Power Flow (DC-OPF)

The objective function to be minimized represents the total generation cost (6). The optimization problem is formulated as follows:

$$\min_{\mathbf{P_G}} \sum_{i=1}^{N_G} c_{G,i} P_{G,i}, \tag{6}$$

$$\text{s.t.} \sum_{i=1}^{N_G} P_{G,i} - \sum_{n=1}^{N_B} P_{D,n} = 0, \tag{7}$$

$$-\mathbf{F_L^{max}} \leq \mathbf{PTDF} \cdot \left(\mathbf{P_G} - \mathbf{P_D}\right) \leq \mathbf{F_L^{max}} \tag{8}$$

$$\mathbf{0} \leq \mathbf{P_G} \leq \mathbf{P_G^{max}}, \tag{9}$$

where symbols in bold denote matrices or vectors. N_G and N_B refers to the number of generators and buses, respectively. Equality constraint (7) ensures balance between total generation and total demand. Demand $\mathbf{P_D}$ is assumed to be inelastic and thus, not a decision variable. Power Transfer Distribution

Factors (PTDF) are used to translate net injections into line flows, which are constrained to their line flow limits $F_{L,i}^{max}$ in Eq. (8). Eq. (9) constrains the generator outputs below capacity limits.

B. Security Constrained OPF (SC-OPF)

The SC-OPF ensuring N-1 security and small signal stability extends the standard DC-OPF by including additional constraints representing *conditional line transfer limits*, derived from the decision tree in Section VI-B. The DT is incorporated into the optimization using Mixed Integer Linear Programming (MILP). Each full path p from the root to a leaf node is represented by a set of minimum and maximum line transfer limits $\mathbf{F_{L,p}^{min}}$ and $\mathbf{F_{L,p}^{max}}$, respectively. Eq. (8) is replaced by:

$$\mathbf{PTDF} \cdot \left(\mathbf{P_G} - \mathbf{P_D}\right) \leq \mathbf{F_{L,p}^{max}} y_p + \mathbf{F_L^{max}}(1 - y_p) \quad \forall p \in P \quad (10)$$

$$\mathbf{PTDF} \cdot \left(\mathbf{P_G} - \mathbf{P_D}\right) \geq \mathbf{F_{L,p}^{min}} y_p - \mathbf{F_L^{max}}(1 - y_p) \quad \forall p \in P, \quad (11)$$

where P is the set of full paths representing the decision tree. Note that the conditional line transfer limits do not limit the flows symmetrically as in Eq. (8), i.e. the lower bound does not necessarily correspond to the negative upper bound. Each path is associated with a binary variable y_p, which, if chosen, ensures the activation of the corresponding conditional line flow limits or otherwise, leaves the usual line flow limits unchanged. The number of binary variables corresponds to the number of leaf nodes in the DT. The choice of line limits to one path only is constrained through $\sum_p y_p = 1$.

C. Matching of SC-OPF and Database

In contrast to the operating points saved in the database, losses are not inherently considered in the standard DC-OPF or SC-OPF described above. Thus, the operating points resulting from the OPFs need to be matched with the ones saved in the database by incorporating losses. Due to the fact that the optimal power flow is not known prior to delivering the line flow limits and the line flows and losses vary depending on the generation pattern, an initial best guess of the optimal operating point is crucial to achieve a good matching. By searching the database for the cheapest operating point (assuming that costs are known a priori), which fulfills the stability margin and meets the load level, we found a "best guess" operating point, whose losses were incorporated in the standard DC-OPF and the SC-OPF according to (5). The losses of the "best guess" OP are determined through an ac power flow analysis. The DC-OPF and SC-OPF are thus augmented by a loss approximation and yield more realistic results.

VIII. Case Study

The proposed method ensuring small signal stability and N-1 security is applied to the IEEE 14 bus test system shown in Fig. 5. All parameters are given in the appendix.

The small signal models were derived using Mathematica, the initialization and small signal analysis were carried out using Matlab and Matpower 6.0 [13]. All DC-OPF simulations were carried out in Python using the Gurobi Optimizer [14].

A minimum damping ratio of 3% is chosen as stability margin. We chose to require the same minimum damping ratio also for the steady states obtained after an outage of a single element during the N-1 security analysis. However, this could also be chosen differently by e.g. allowing lower damping ratios after certain faults.

The system has been simulated for several load levels (±20%) and various step sizes between the generation patterns. Generator g_1 has been chosen as the slack bus, also in all N-1 scenarios, due to the small size of the other generators. Since the IEEE 14 Bus system is not N-1 stable, a few contingencies and reactive power limits could not be considered for the N-1 security assessment. All line faults have been considered except for a fault on the line connecting bus 1 and bus 2. All bus faults have been analyzed, except for a fault at bus 1 and bus 2. These contingencies could not be considered because either they lead to instability / violation of the AVR limits for any operating point of the considered load patterns (bus 1) or the stable operating points are not stable for the remaining contingencies. Hence, this would leave us with an empty set of feasible operating points and therefore we had to neglect these contingencies.

First, we will compare the results of the novel data driven SC-OPF, when using different features for mapping the operating points of ac and dc power flows. Then, we will investigate the impact of various step sizes between the generation patterns on the results of the data-driven SC-OPF, i.e. different accuracies and database sizes. Finally, we will discuss additional benefits of data-driven approaches.

A. Comparison between Standard DC-OPF and Data-driven SC-OPF using different Mapping Approaches

The comparison between the data-driven SC-OPFs using different mapping approaches is done using a 2.5 MW step size during the data generation. Table I lists the results of both

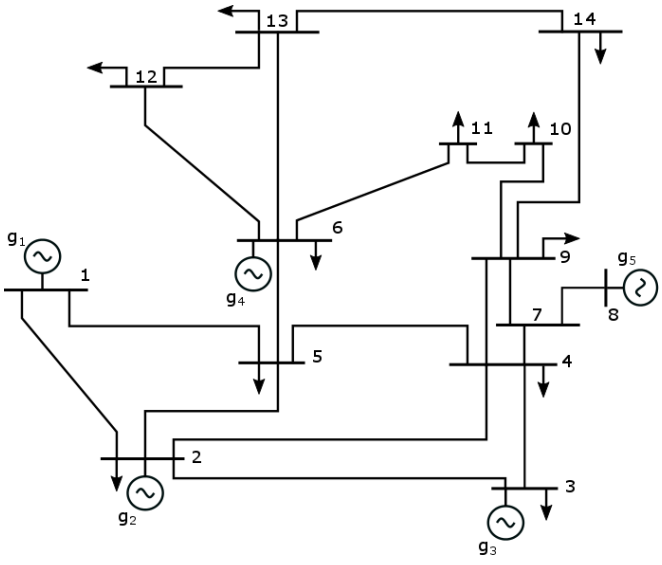

Fig. 5. IEEE 14 Bus System [12].

TABLE I
RESULTS OF STANDARD DC-OPF AND DATA-DRIVEN SC-OPF USING DIFFERENT MAPPING APPROACHES

	DC-OPF (w. losses)	Best Guess (Data Based)	SC-OPF (clas. DC)		SC-OPF (less con. DC)		SC-OPF (exact)	
Dispatch (MW)			1. Run	2. Run	1. Run	2. Run	1. Run	2. Run
g_1	275.5509	183.73	165.962	165.262	176.535	176.297	184.106	184.127
g_2	0	55	60	60	60	60	60	60
g_3	0	27.5	26.603	26.671	22.51	22.616	24.628	24.906
g_4	0	2.5	16.17	15.687	9.689	9.582	0	0
g_5	0	0	0	0	0	0	0	0
Total Cost (€)	2755.5	2981.1	3091.63	3077.21	3022.56	3019.9	2960.48	2964.87
Min. damping ratio (%)	-20.33%	4.07%	9.73%	9.59%	6.59%	6.57%	2.98%	3.05%
Cost of Security (€)	-	225.59	336.12	321.7	267.05	264.39	204.97	209.36

the standard DC-OPF and the SC-OPF using different features of the database, in particular the three different mapping approaches described in VI-A. Additionally, the database best guess operating point is listed, which is used for determining the losses to be incorporated in the OPFs.

Table I shows that the standard DC-OPF fails to ensure N-1 security, since for this generation pattern the most critical pair of eigenvalues of the most critical fault in the N-1 security assessment (Fault at Bus 5) indicates a negative damping ratio, i.e. instability. The most critical eigenvalues of those faults in the N-1 security assessment violating the minimum required stability margin of 3% are shown in Fig. 6. It shows that all SC-OPFs ensure N-1 security of the system by a change of the generation pattern resulting in the most critical eigenvalues of the same faults being moved into the left half-plane, i.e. in the safe area with a minimum damping ratio larger than the required stability margin.

The figure visualizes also that the operating points obtained by the SC-OPFs using different mapping approaches vary by their minimum damping ratio, which reflects the more conservative line flow limits in case of both dc approximations compared with the exact mapping approach. These more conservative line flow limits lead consequently also to higher cost of security, as indicated in Tab. I.

Finally, Tab. I indicates also the importance of the matching of operating points, i.e. the importance of the best guess of power flow. While in the 1st run column of the SC-OPFs the losses are implemented according to the data based best guess, the 2nd run uses the result of the 1st run as initial best guess. In this case, the loss distribution and therefore the line flows are more accurate, i.e. more comparable to dc power flows obtained in the data generation. Thus, the matching of operating points is improved which leads to better results in all cases.

B. Comparison of different Step Sizes between the analyzed Generation Patterns

Table II shows various aspects and results for the database generation of a SC-OPF comparing different step sizes used during data generation.

Obviously, following the simple approach with constant step size between each analyzed generation pattern the database size grows as indicated in (1). However, as discussed in V-C there exist improvement potential on which we will focus in future work. Further, the required simulation time is related to the database size. It naturally increases with the number of operating points. The database was generated using 20 cores in parallel on the high performance computing farm at DTU.

The tree accuracy is also related to the available database size. In general, it should be easier to differentiate between the case fulfilling the stability margin and not fulfilling the stability margin if there is a higher step size in between the analyzed generation patterns. This is reflected in Tab. II by the decreasing number of false prediction with risk with increasing step size. False predictions with risk are those predictions which falsely predict operating points not fulfilling the stability margin as "fulfilling the stability margin". The results show that the chosen risk averse approach, discussed in section VI-B, which increases the costs of this kind of false predictions, works fine since the vast majority of false predictions is made in the other direction. This is indicated by the small percentage of these kind of false predictions within the total number of false predictions.

However, on the other hand there exists also less data for training which may decrease the tree accuracy as indicated in Tab. II. This also leads to potentially shorter trees resembled by a smaller number of binary variables and a faster execution time, shown in Tab. III.

Table II supports also the discussion in section V-C about the importance of the step size, in particular close to the boundary. This is reflected by the significantly increasing number of risky false predictions with increasing step size when the DTs are tested with the database of the other step sizes. Here, the DTs of 2.5 MW and 5 MW are tested on the 1 MW database while the 1 MW DT is tested on the 2.5 MW database. It is shown that a wider step size in between the generation patterns leads to potentially more and unsafer risky false predictions, as indicated by the increasing number of false predictions with risk and the decreasing minimum damping ratio of those false predictions.

However, the tree accuracy should not be confused with the cost efficiency of the line flow limits resembled by the generation costs. All SC-OPFs with the different step sizes lead to points fulfilling the required stability margin. Here, we used two runs using the 1st run as initialization for the 2nd run as described in the previous subsection.

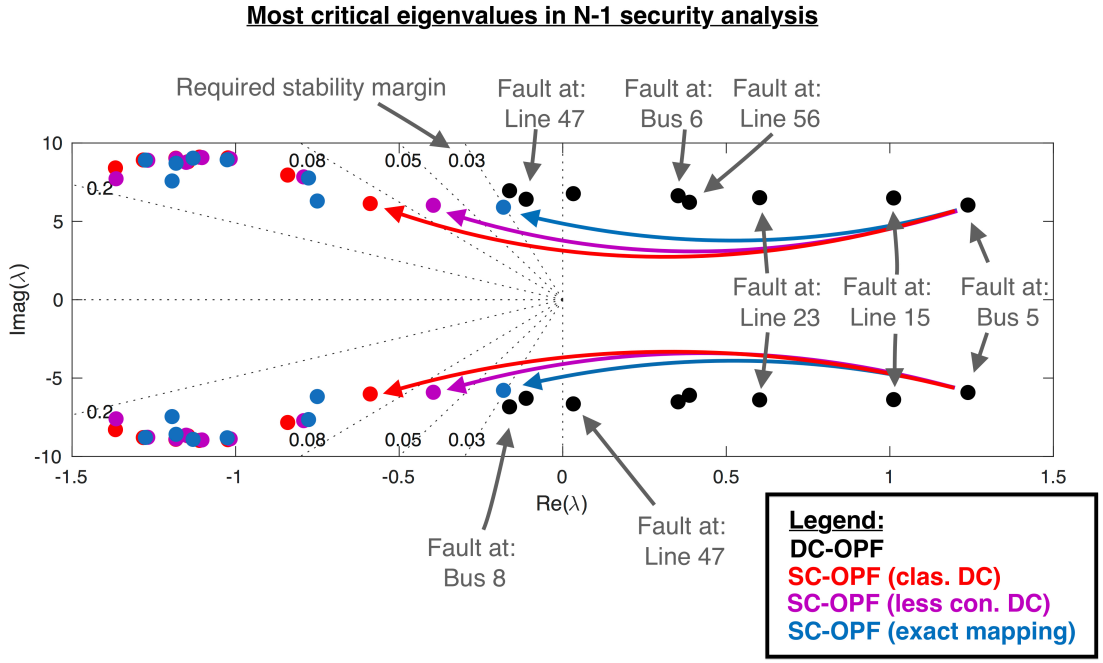

Fig. 6. Visualization of the location of the most critical eigenvalues in the N-1 security analysis for the DC-OPF (black), SC-OPF using the classical dc approximation approach (red), SC-OPF using the less conservative dc approximation approach (purple) and SC-OPF using the exact mapping approach. The faults corresponding to the critical eigenvalues are denoted in grey. The small signal models resembling the faults differ by the base case in that way that they consider the disconnection of the corresponding elements. Any contingency not violating the stability margin requirement of 3% is neglected.

TABLE II
DATABASE ANALYSIS FOR DIFFERENT STEP SIZES

step size	1 MW	2.5 MW	5 MW
# operating points, Ψ	2515396	75625	6084
Simulation time	8.17 h	15.11 min	1.29 min
Training set			
Tree accuracy	99.86%	99.77%	98.9%
False prediction w. risk	55	1	0
% of false pred.	1.54%	0.57%	0
Min. damp. ratio of risky false pred.	2.89%	2.76%	-
Using database of other step sizes as test set			
Tree accuracy	99.79%	99.03%	97.64%
False prediction w. risk	36	9111	13298
% of false pred.	23.08%	37.34%	22.44%
Min. damp. ratio of risky false pred.	2.73%	1.37%	0.82%

TABLE III
DATA-DRIVEN SC-OPF RESULTS FOR DIFFERENT STEP SIZES

Data-driven SC-OPF			
step size	1 MW	2.5 MW	5 MW
Bin. var.	616	35	28
Exec. time	26.64s	1.08s	0.98s
Generation cost	2965.4€/h	2964.9€/h	2959.2€/h
Minimum margin	3.03%	3.05%	3.42%
Generation (MW)			
g_1	187	193.50	183.3213
g_2	60	42.72	58.0360
g_3	18.7	24.73	27.46
g_4	3.7	0	0
g_5	0	0	0

Table III shows that in fact the SC-OPF using the widest step size leads to the cheapest operating point. This is due to the wider uncertain area in between the analyzed operating points (see Fig. 3) resulting in more relaxed line flow limits. However, the difference is very small (max. 6.2€). It is important to emphasize that, although the widest step size achieves the best performance in this particular scenario, smaller step sizes are safer as discussed before and indicated in Tab. II.

C. Additional Benefit of the Data-driven Approach

Besides the possibility to deliver cost-efficient line flow limits the data-driven approach provides the additional benefit of serving as an easy accessible source of knowledge for the TSO which could be useful during normal operation but in particular during training of new employees.

First, similar as visualized in Fig. 6, the database enables the user to get an overview which faults are the most critical for any operation point. Unlike for the specific generation pattern provided by the DC-OPF this may only be a single fault.

Second, the use of a DT instead of other knowledge extraction methods provides the user with additional comprehensible knowledge about safe and unsafe line flows in the system. By just visualizing the tree as e.g. in Fig. 4 the user is able to

access this valuable comprehensive information, which would not be possible by most other knowledge extraction methods, which work mostly like a black-box from the outside.

IX. Conclusion

A novel data-driven SC-OPF method ensuring small-signal stability has been proposed. It uses a small-signal model for data generation, and classification trees for the knowledge extraction. Conditional transfer limits in the form of decision rules are derived from the decision tree and implemented in the OPF problem by means of Mixed Integer Linear Programming. We investigated the impact of different features for the mapping of operating points from the ac to the dc space and emphasized specific aspects of this method, e.g. the importance of matching the operating points. Additionally, we discussed the challenges of this method, such as the problems arising when using a wide step size (in particular at the stability boundary). Finally, we emphasized the additional benefits of the data-driven approach as it serves as a source of knowledge of the system. The case study indicates a good performance.

Acknowledgment

This work is supported by the EU project Best Paths under the 7th Framework Programme, Grant Agreement No. 612748 and by the ForskEL-projekt 12264 Best Paths for DK.

Appendix

A. Small-Signal Model

1) Notation:

α_{ik}	Angle of the ik-th entry of the network bus admittance matrix.
δ_i	Rotor angle of generator i.
ω_i	Rotor speed of generator i.
ω_s	Synchronous rotor speed.
Ω	Base synchronous frequency.
ψ_{d,q_i}	Magnetic flux of generator i.
D_i	Additional damping Torque of generator i.
e'_{d,q_i}	Transient voltage of generator i in d-/q-axis.
e_{fd_i}	Field voltage of generator i.
H_i	Inertia constant of generator i.
$i_{d,q}$	Current of generator i in d-/q-axis.
K_{A_i}	Amplifier gain of generator i.
K_{E_i}	Self-excited constant used for of generator i.
K_{F_i}	Stabilizer gain used for of generator i.
m	Number of machines.
n	Number of buses.
r_{F_i}	Output of the stabilizer of generator i.
r_{a_i}	Armature resistance of generator i.
$S_{E_i}(E_{fd_i})$	Saturation function of generator i.
T_{A_i}	Time constant of the voltage regulator of gen. i.
$T'_{d0,q0_i}$	Transient time const. of d-/q-axis of generator i.
$T''_{d0,q0_i}$	Sub-transient time const. of d-/q-axis of gen. i.
T_{E_i}	Exciter time constant of generator i.
T_{F_i}	Time constant of the stabilizer of generator i.
T_{M_i}	Mechanical torque of generator i.
v_{ref_i}	Reference voltage of generator i.
v_{R_i}	Output of the voltage regulator of generator i.
$v_{R,max}$	Limit of the voltage regulator of generator i.
x'_{d,q_i}	Transient reactance of generator i in d-/q-axis.
x_{l_i}	Leakage reactance of generator i in d-/q-axis.
x_{d,q_i}	Synchronous reactance of gen. i in d-/q-axis.
x''_{d,q_i}	Sub-transient reactance of gen. i in d-/q-axis.
Y_{ik}	Magnitude of the ik-th entry of the network bus admittance matrix.

2) Model: The multi-machine model can be described with $10m$ differential algebraic equations (12)-(23) and $6m$ algebraic equations: $2m$ equations defining stator fluxes (24)-(25), $2m$ stator equations (26)-(27), and $2n$ network equations (28)-(29). For a more detailed desciption the interested reader is referred to [8].

$$\frac{d\delta_i}{dt} = \Omega(\omega_i - \omega_s) \tag{12}$$

$$\frac{d\omega_i}{dt} = \frac{1}{2H_i}\left(T_{M_i} - \psi_{d,i} i_{q,i} + \psi_{q,i} i_{d,i} - D_i(\omega_i - \omega_s)\right) \tag{13}$$

$$\frac{de'_{q_i}}{dt} = (-e'_{q_i} - (x_{d_i} - x'_{d_i})(i_{d_i} - \gamma_{d2,i}\psi''_{d,i} \tag{14}$$

$$- (1 - \gamma_{d1,i}) i_{d,i} + \gamma_{d2,i} e'_{q,i}) + e_{fd_i})/T'_{d0_i} \tag{15}$$

$$\frac{de'_{d_i}}{dt} = (-e'_{d_i} - (x_{q_i} - x'_{q_i})(i_{q_i} - \gamma_{q2,i}\psi''_{q,i} \tag{16}$$

$$- (1 - \gamma_{q1,i}) i_{q,i} + \gamma_{q2,i} e'_{d,i}))/T'_{q0_i} \tag{17}$$

$$\frac{d\psi''_{d_i}}{dt} = (-\psi''_{d,i} + e'_{q,i} - (x'_{d,i} - x_{l,i}) i_{d,i})/T''_{d0,i} \tag{18}$$

$$\frac{d\psi''_{q_i}}{dt} = (-\psi''_{q,i} + e'_{d,i} - (x'_{q,i} - x_{l,i}) i_{q,i})/T''_{q0,i} \tag{19}$$

$$\frac{dv_{h_i}}{dt} = \frac{v_{b,i} - v_{h,i}}{T_{r,i}} \tag{20}$$

$$\frac{dv_{R_i}}{dt} = \frac{K_{A_i}(v_{ref,i} - v_{h,i} - r_{f,i} - \frac{K_{f,i}}{T_{f,i}} e_{fd_i}) - v_{R_i}}{T_{A_i}} \tag{21}$$

$$\frac{dr_{F_i}}{dt} = -\frac{r_{F_i}}{T_{F_i}} - \frac{K_{F_i}}{(T_{F_i})^2} e_{fd_i} \tag{22}$$

$$\frac{de_{fd_i}}{dt} = -\frac{K_{E_i} + S_{E_i}(e_{fd_i})}{T_{E_i}} e_{fd_i} + \frac{v_{R_i}}{T_{E_i}} \tag{23}$$

$$0 = \psi_{d,i} + x''_{d,i} i_{d,i} - \gamma_{d1,i} e'_{q,i} - (1 - \gamma_{d1,i})\psi''_{d,i} \tag{24}$$

$$0 = \psi_{q,i} + x''_{q,i} i_{q,i} + \gamma_{q1,i} e'_{d,i} - (1 - \gamma_{q1,i})\psi''_{q,i} \tag{25}$$

$$0 = r_{a,i} + i_{d,i} + \psi_{q,i} + v_{d,i} \tag{26}$$

$$0 = r_{a,i} + i_{q,i} - \psi_{d,i} + v_{q,i} \tag{27}$$

for $i = 1, 2, 3, \ldots, m$.
and

$$0 = P_{G_i} + P_{L_i}(V_i) - \textstyle\sum_{k=1}^{n} V_i V_k Y_{ik} \cos(\theta_i - \theta_k - \alpha_{ik}) \tag{28}$$

$$0 = Q_{G_i} + Q_{L_i}(V_i) - \textstyle\sum_{k=1}^{n} V_i V_k Y_{ik} \sin(\theta_i - \theta_k - \alpha_{ik}) \tag{29}$$

for $i = 1, 2, 3, \ldots, m, m+1, \ldots, n$.
with

$$P_{G_i} = I_{d_i} V_i \sin(\delta_i - \theta_i) + I_{q_i} V_i \cos(\delta_i - \theta_i) \tag{30}$$

$$Q_{G_i} = I_{d_i} V_i \cos(\delta_i - \theta_i) - I_{q_i} V_i \sin(\delta_i - \theta_i) \tag{31}$$

for $i = 1, 2, 3, \ldots, m$.
The equations can be combined, linearized and rewritten in matrix notation as:

$$\begin{bmatrix} \mathbf{\Delta\dot{X}} \\ \mathbf{0} \\ \mathbf{0} \end{bmatrix} = \begin{bmatrix} \mathbf{A} & \mathbf{B_1} & \mathbf{B_2} \\ \mathbf{C_1} & \mathbf{D_{11}} & \mathbf{D_{12}} \\ \mathbf{C_2} & \mathbf{D_{21}} & \mathbf{D_{22}} \end{bmatrix} \begin{bmatrix} \mathbf{\Delta X} \\ \mathbf{\Delta Z_1} \\ \mathbf{\Delta Z_2} \end{bmatrix} + \begin{bmatrix} \mathbf{E_1} \\ 0 \\ 0 \end{bmatrix} \mathbf{\Delta U} \tag{32}$$

with $\mathbf{X} = [\mathbf{X}_1^T, \ldots, \mathbf{X}_m^T]^T$ and
$\mathbf{X}_i = [\delta_i \ \omega_i \ e'_{q_i} \ e'_{d_i} \ \psi'_{d,i} \ \psi'_{q,i} \ v_{h,i} \ v_{R_i} \ r_{F_i} \ e_{fd_i}]^T$ including the machine state variables and $\mathbf{\Delta Z_1} = [\theta_1 \ v_{b,1} \ldots v_{b,m}]^T$ including the voltage angle of the slack bus as well as the voltage magnitudes of the generator buses. $\mathbf{\Delta Z_2} = [\theta_2 \ldots \theta_n \ v_{b,m+1} \ldots v_{b,n}]^T$ includes the voltage angles of the remaining buses and the voltage magnitudes of the load buses. The system matrix A_{sys} with dimension $10m \, x \, 10m$ fulfilling the equation

$$\mathbf{\Delta\dot{X}} = \mathbf{A}_{sys}\mathbf{\Delta X} + \mathbf{E\Delta U} \tag{33}$$

can be obtained as:

$$\mathbf{A}_{sys} = \mathbf{A} - [\mathbf{B}_1 \ \mathbf{B}_2][\mathbf{J}_{AE}]^{-1} \begin{bmatrix} \mathbf{C}_1 \\ \mathbf{C}_2 \end{bmatrix} \tag{34}$$

with

$$[\mathbf{J}_{AE}] \quad = \quad \begin{bmatrix} \mathbf{D_{11}} & \mathbf{D_{12}} \\ \mathbf{D_{21}} & \mathbf{D_{22}} \end{bmatrix} \tag{35}$$

representing the network algebraic Jacobian.

B. Parameters

TABLE IV
GENERATOR DATA ADAPTED FROM [8]

Machine and AVR parameters					
Parameters	g_1	g_2	g_3	g_4	g_5
MVA	615	60	60	25	25
r_a (pu)	0.0031	0.0031	0.0031	0.0041	0.0041
H (s)	5.148	6.54	6.54	5.06	5.06
D (pu)	2	2	2	2	2
x_d (pu)	0.8979	1.05	1.05	1.25	1.25
x'_d (pu)	0.2995	0.1850	0.1850	0.232	0.232
x_q (pu)	0.646	0.98	0.98	1.22	1.22
x'_q (pu)	0.646	0.36	0.36	0.715	0.715
x''_q (pu)	0.4	0.13	0.13	0.12	0.12
x_l (pu)	0.2396	0	0	0.134	0.134
T'_{do} (s)	7.4	6.1	6.1	4.75	4.75
T''_{do} (s)	0.03	0.04	0.04	0.06	0.06
T'_{qo} (s)	0.31	0.3	0.3	1.5	1.5
T''_{qo} (s)	0.033	0.099	0.099	0.21	0.21
K_a	120	20	20	20	20
$V_{R_{max}}$ (pu)	9.9	2.05	1.7	2.2	2.2
T_a (s)	0.02	0.02	0.02	0.02	0.02
K_e (pu)	1.0	1.0	1.0	1.0	1.0
T_e (s)	0.19	1.98	1.98	0.70	0.70
K_f (s)	0.0012	0.001	0.001	0.001	0.001
T_f (s)	1.0	1.0	1.0	1.0	1.0
A_e	0.0006	0.0006	0.0006	0.0006	0.0006
B_e (1/pu)	0.9	0.9	0.9	0.9	0.9
Economic data					
c_{lin} (€/MWh)	10	12.5	15	17.5	20

REFERENCES

[1] R. Zárate-Miñano, F. Milano, and A. J. Conejo, "An OPF Methodology to Ensure Small-Signal Stability," *IEEE Transactions on Power Systems*, vol. 26, no. 3, pp. 1050–1061, 2011.

[2] J. E. Condren and T. W. Gedra, "Expected-Security-Cost Optimal Power Flow With Small-Signal Stability Constraints," *IEEE Transactions on Power Systems*, vol. 21, no. 4, pp. 1736–1743, 2006.

[3] Y. Xu, Z. Y. Dong, R. Zhang, and K. P. Wong, "A Decision Tree-Based Online Preventive Control Strategy for Power System Transient Instability Prevention," *International Journal of Systems Science*, vol. 45, no. 2, pp. 176–186, 2014. [Online]. Available: http://dx.doi.org/10.1080/00207721.2011.626906

[4] M. Chávez-Lugo, C. R. Fuerte-Esquivel, C. A. Canizares, and V. J. Gutierrez-Martinez, "Practical Security Boundary-Constrained DC Optimal Power Flow for Electricity Markets," *IEEE Transactions on Power Systems*, vol. 31, no. 5, pp. 3358–3368, Sept 2016.

[5] P. Kundur, J. Paserba, V. Ajjarapu, G. Andersson, A. Bose, C. Canizares, N. Hatziargyriou, D. Hill, A. Stankovic, C. Taylor, T. Van Cutsem, and V. Vittal, "Definition and Classification of Power System Stability," *IEEE Transactions on Power Systems*, vol. 21, no. 3, pp. 1387–1401, 2004.

[6] C. Y. Chung, L. Wang, F. Howell, and P. Kundur, "Generation Rescheduling Methods to Improve Power Transfer Capability Constrained by Small-Signal Stability," *IEEE Transactions on Power Systems*, vol. 19, no. 1, pp. 524–530, 2004.

[7] P. Sauer and M. Pai, *Power System Dynamics and Stability*, M. Horton, Ed. New Jersey: Prentice-Hall, Inc., 1998.

[8] F. Milano, *Power System Modelling and Scripting*. Springer-Verlag Berlin Heidelberg, 2010, no. 1.

[9] R. D. Zimmerman, C. E. Murillo-sánchez, R. J. Thomas, L. Fellow, and A. M. Atpower, "MATPOWER : Steady-State Operations , Systems Research and Education," *Power*, vol. 26, no. 1, pp. 12–19, 2011.

[10] C. A. Cañizares, N. Mithulananthan, and F. Milano, "Linear Performance Indices to Predict Oscillatory Stability Problems in Power Systems," *IEEE Transactions on Power Systems*, vol. 19, no. 2, pp. 1104–1114, 2004.

[11] L. A. Wehenkel, *Automatic Learning Techniques in Power Systems*. Boston/London/Dordrecht: Kluwer Academic Publishers, 1998.

[12] S. Kodsi and C. Canizares, "Modeling and Simulation of IEEE 14-Bus System with FACTS Controllers," University of Waterloo, Waterloo, Canada, Tech. Rep., 2003.

[13] R. D. Zimmerman, C. E. Murillo-Sanchez, and R. J. Thomas, "Matpower: Steady-state operations, planning, and analysis tools for power systems research and education," *IEEE Transactions on Power Systems*, vol. 26, no. 1, pp. 12–19, Feb 2011.

[14] Gurobi Optimization, "Gurobi Optimizer Reference Manual," 2015. [Online]. Available: http://www.gurobi.com

[Pub. F] Data-driven Security-Constrained AC-OPF for Operations and Markets.

Data-driven Security-Constrained AC-OPF for Operations and Markets

Lejla Halilbašić, Florian Thams, Andreas Venzke, Spyros Chatzivasileiadis, Pierre Pinson
Center for Electric Power and Energy
Technical University of Denmark
Kongens Lyngby, Denmark
{lhal, fltha, andven, spchatz, ppin}@elektro.dtu.dk

***Abstract*—In this paper, we propose a data-driven preventive security-constrained AC optimal power flow (SC-OPF), which ensures small-signal stability and N-1 security. Our approach can be used by both system and market operators for optimizing redispatch or AC based market-clearing auctions. We derive decision trees from large datasets of operating points, which capture all security requirements and allow to define tractable decision rules that are implemented in the SC-OPF using mixed-integer nonlinear programming (MINLP). We propose a second-order cone relaxation for the non-convex MINLP, which allows us to translate the non-convex and possibly disjoint feasible space of secure system operation to a convex mixed-integer OPF formulation. Our case study shows that the proposed approach increases the feasible space represented in the SC-OPF compared to conventional methods, can identify the global optimum as opposed to tested MINLP solvers and significantly reduces computation time due to a decreased problem size.**

***Index Terms*—Security-constrained OPF, small-signal stability, convex relaxation, mixed-integer non-linear programming.**

I. Introduction

The Security-Constrained Optimal Power Flow (SC-OPF) is an important tool for power system operation and planning in order to maintain power system security. The SC-OPF identifies optimal preventive control actions compliant with the N-1 criterion, which ensure that the system can withstand the loss of any major component without violating system constraints. To this end, the constraint set of the conventional OPF is extended to include all considered contingency scenarios. The SC-OPF can be applied at different planning stages to either determine an optimal and N-1 secure dispatch or to identify optimal redispatching actions closer to real-time. SC-OPFs are non-linear and non-convex problems with both continuous and discrete variables. A major drawback of conventional SC-OPF algorithms is the problem size and the negligence of stability requirements [1], which cannot be expressed as linear or non-linear constraints and are therefore difficult to incorporate in a straightforward way. We address both challenges by using a data-driven approach to preventive SC-OPF, which is computationally tractable and based on decision trees that capture all N-1 and small-signal stability considerations. We extend our previous work in [2] to an AC-OPF context with the intention to bridge the gap between power system operation and markets. We incorporate the knowledge extracted from the data in the OPF using convex Mixed-Integer Programming (MIP) and relax the non-convex AC power flow equations through a Second Order Cone (SOC) relaxation. We further use the data to strengthen the relaxation. To the authors' knowledge, this is the first SC-OPF formulated as a Mixed-Integer Second Order Cone Program (MISOCP). Our approach combines the advantages of convex MIP and data analytics and allows for a fast online solution. It extends the feasible space in order to reflect the true non-convex area of operation and includes the true optimal solution.

Research in SC-OPF algorithms has primarly investigated the N-1 security criterion and the reduction of the associated computational burden, while less focus has been put on stability requirements. However, only enforcing the N-1 criterion does not necessarily guarantee stability and hence, feasiblity of the solution. In order to translate small-signal stability constraints to an OPF context, eigenvalue-sensitivities with respect to OPF decision variables are used in [3] and [4]. However, the required computational effort and the scalability of the proposed methods are still major challenges. In [5] hyperplanes are used to approximate the security boundary and are incorporated in a DC-OPF. Operating points outside the convex space constructed by the hyperplanes are neglected though, increasing the likelihood of missing the optimal solution.

The authors in [6] have identified the Security-Constrained AC-OPF as the "ultimate goal" for market software to be used by Independent System Operators (ISO) across the US. They outline the oversimplification of current software, often requiring operator intervention and resulting in suboptimal solutions due to inaccurate ISO models, which only use estimates for reactive power and voltage constraints. Improved modeling of voltage and stability constraints can lead to more realistic dispatch decisions and better market signals, resulting in up to 10% cost savings worldwide [7]. The relative amount of potential savings will increase over the course of the coming decades due to the ongoing electrification of the entire energy industry. Electricity market participants in the US are already saving over half a billion dollars annually as a result of the implementation of MIP in day-ahead and real-time markets

This work is supported by the European project BEST PATHS, Grant No. 612748, and the ForskEL-project 12264 BestPaths for DK.

[8]. Due to significant improvements since the 1990s, MIP has been widely applied accross various industries, increasing expertise, which only reinforces further development of MIP approaches.

SOCP has gained increased attention for power system applications as it is computationally less demanding than other relaxations, such as Semi-Definite Programming (SDP). Furthermore, it can be extended to mixed-integer problems, where the SDP relaxation fails even on small scales. MISOCP has been introduced for OPF problems incorporating optimal transmission switching and capacitor placement in [9] and [10]. The challenge in SOCP for OPF problems lies in convexifying the coupling contraint between voltage angles and SOC variables, which are introduced to remove the non-convexities arising from the AC power flow equations. Several strengthening techniques have been proposed in [9] and [10], which significantly contribute to the advancement of MISOCP for real-life applications. However, these techniques still do not achieve to avoid optimality gaps and can be computationally demanding, negating the benefit of convex MIP solvers.

The main contribution of this work is a data-driven SC-OPF algorithm formulated as a MISOCP, which (a) can be used by system operators as a security analysis tool (e.g., for redispatch), (b) can be used by market operators, approaching the "ultimate goal" for market software [6], (c) incorporates the N-1 security criterion, (d) ensures small-signal stability for the base case and all considered contingencies, (e) is scalable, (f) exploits the maturity of convex MIP solvers in order to identify the optimal operating point within a non-convex and possibly disjoint stability area, (g) can be solved fast, as all computation related to the small-signal stability assessment and N-1 criterion is done offline and the OPF problem size is significantly decreased, (h) uses data to stregthen the relaxation, (i) can be solved to global optimality where tested non-convex solvers fail and (j) alleviates the need for iterative contingency analyses, which are currently used by system operators to define the boundaries of the secure system space.

The remainder of this paper is organized as follows: Section II describes the proposed methodology including the derivation of decision rules from data and focuses mainly on the incorporation of those rules in nonlinear and non-convex SC-OPF algorithms. Section III presents results from a case study. Section IV concludes and gives an outlook on future work.

II. Method

Our approach consists of an offline security assessment, which includes the database generation and derivation of decision rules, and an online SC-OPF, which incorporates the decision rules ensuring power system security. The database generation, stability analysis and knowledge extraction have been discussed in more detail in our previous work [2] and we will only highlight the main features here. This work focuses mainly on the implementation of the decision rules in AC-OPF algorithms and applications of the proposed method.

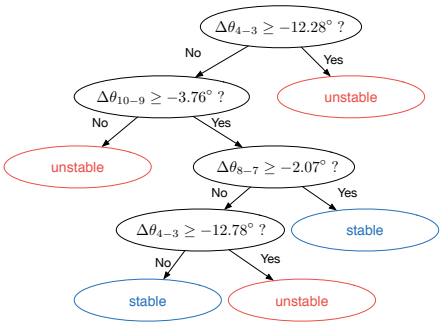

Figure 1. A simple illustrative decision tree.

A. Offline Security Assessment

A large database of operating points is created for various load levels based on AC power flow calculations. All possible generation patterns corresponding to the specified load levels are evaluated using specified step sizes to discretize the space of possible dispatch combinations. In order to perform the small-signal stability assessment of the simulated operating points, small-signal models are derived for the base case and all considered contingencies. A database is generated, which contains the operating points together with the information on whether they are stable or unstable. Challenges related to the computational demand of the database generation, the appropriate choice of discretization intervals and the determination of the stability boundary have been addressed in [2]. Ongoing work focuses on further improvements.

Once the database is generated, decision rules based on appropriate features, that need to be selected, can be derived for the OPF, which will lead the solution to a stable operating region. These features have to be easily accessible in an AC-OPF formulation to allow for a fast online computation. Voltage angle differences along transmission lines are explicitly modeled in both the security analysis and the AC-OPF, representing coupling variables. Among the tested features, they have proven to most efficiently capture all security requirements and are thus chosen as features for the knowledge extraction (i.e., the derivation of the decision rules). Additionally, if approximations of the OPF are used, which do not explicitly model voltage angles, angle differences can be translated to line capacity limits using appropriate mapping strategies as explained in [2]. We employ decision trees (DTs) as the knowledge extraction method, as they are comprehensible and easy to interpret for the operator. They are trained based on the selected features. Moreover, the conditional rules defined by the DT can be directly incorporated through binary variables in an optimization problem. A simple illustrative example is shown in Fig. 1.

We refer to our previous work for details on the small-signal models, the DT generation including the reduction of mislassifications and the dependence of the DT accuracy on the database size/discretization [2].

B. Preventive SC-OPF - Current Practice

The traditional preventive SC-OPF (PSC-OPF) aims at finding the optimal least-cost dispatch ensuring N-1 security. It extends the conventional nonlinear and non-convex AC-OPF by including additional constraints to ensure feasibility of the identified solution after the occurrence of any specified contingency. The AC-OPF is given as follows:

$$\min_{\mathbf{x}} \sum_{i=1}^{N_G} C_i\Big(P_i^G\Big), \tag{1}$$

$$\text{s.t. } P_i^G - P_i^D = G_{ii}V_i^2 + \sum_{j=1,j\neq i}^{N_B} V_iV_j\Big(G_{ij}\cos(\theta_{ij}) + B_{ij}\sin(\theta_{ij})\Big), \quad \forall i \in \mathcal{N} \tag{2}$$

$$Q_i^G - Q_i^D = -B_{ii}V_i^2 + \sum_{j=1,j\neq i}^{N_B} V_iV_j\Big(G_{ij}\sin(\theta_{ij}) - B_{ij}\cos(\theta_{ij})\Big), \quad \forall i \in \mathcal{N}, \tag{3}$$

$$\underline{\mathbf{x}} \leq \mathbf{x} \leq \overline{\mathbf{x}}, \tag{4}$$

$$\theta_{\text{ref}} = 0, \tag{5}$$

where $\mathbf{x}$ represents the set of optimization variables including active power generation $\mathbf{P^G}$, reactive power generation $\mathbf{Q^G}$, voltage magnitudes $\mathbf{V}$ and voltage angles θ. $\mathcal{N}$ denotes the set of buses. The objective function (1) minimizes active power generation costs. Constraints (2) and (3) ensure active and reactive power balance at all nodes, where G_{ij} and B_{ij} represent the real and imaginary parts of the bus admittance matrix, respectively. Constraint (4) limits all decision variables within their upper and lower bounds. Equation (5) sets the voltage angle of the reference bus to zero. Line flow limits are not explicitly included here, as we derive limits from the security analysis, which will be introduced later.

Control variables (e.g., active and reactive power generation, transformer tap position etc.) in the PSC-OPF are not allowed to change from pre- to post-contingency states. The problem size of the OPF increases to $N_c + 1$ compared to the conventional AC-OPF, where N_c denotes the number of contingencies, rendering SC-OPFs computationally very demanding. The computational burden of SC-OPFs, especially for large systems with many considered contingencies, is a major challenge. Another challenging factor is the inclusion of system dynamics, i.e. stability considerations, in SC-OPF algorithms. Given that they cannot be incorporated as linear or nonlinear constraints in a straightforward way, common practice is to impose tighter constraints. Such conservative bounds on the feasible space should allow the system to return to a steady-state equilibrium after a fault event, but also lead to costly and suboptimal solutions.

Net Transfer Capacities (NTC) constitute one example of such conservatism. NTCs are maximum cross-zonal capacities available for trade on the day-ahead market, which are derived based on the N-1 security criterion, accounting for thermal and stability limitations [11]. NTCs are fixed line flow limits, which are determined by transmission system operators (TSOs) in each direction of cross-border lines prior to the day-ahead market-clearing. Improvements towards a more accurate representation of the physical reality of power systems have been achieved by introducing Flow-Based Market Coupling (FBMC), where a simplified European network representation is accounted for in the market-clearing. Critical branches (CBs) inside of and between zones are identified, which could potentially be congested and limit the cross-border trade. All CBs are represented through Power Transfer Distribution Factors (PTDFs) and instead of assuming only one fixed NTC value for each cross-border line, all constraints imposed by the CBs are considered. Thus, a larger secure domain is offered to the market compared to static NTC approaches as depicted in Fig. 2. The market is then able to determine the optimal combination of commercial capacities between zones. Nonetheless, even flow based NTCs only capture one convex region of the entire feasible space and do not represent the non-convex reality of power system operations.

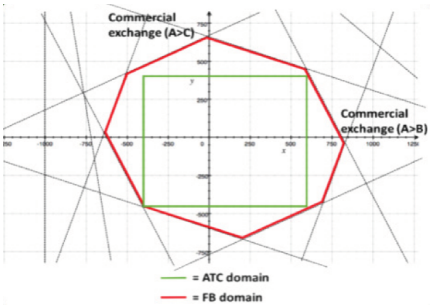

Figure 2. Security domain of Flow-Based Market Coupling (FBMC) and Available Transfer Capacity (ATC) [12]. ATCs are NTCs reduced by long-term capacity nominations.

C. Improving the Preventive SC-OPF Using Data

To address the challenges described above, we propose a data-driven approach to SC-OPFs, which we introduced in previous work [2]. Non-convex and discontinous feasibility spaces are captured using decision trees, which define conditional constraints on appropriate decision variables, such as voltage angle differences $\theta_{ij} = \theta_i - \theta_j$ along transmission lines. Each branch p of the DT contains a set of minimum and maximum voltage angle differences and leads to a different region of the feasibility space, one of which contains the least-cost, optimal solution. A visual illustration of our approach is depicted in Fig. 3. Instead of defining bounds that contain only one of the three stable regions depicted in the shades of blue, conditional rules allow to capture the entire feasible region within the red frame. The DT is incorporated in the SC-OPF using Mixed-Integer Programming (MIP). Each full branch is associated with a binary variable y_p, which if chosen, activates the corresponding upper and lower bounds on angle differences, or otherwise, leaves the original bounds unchanged:

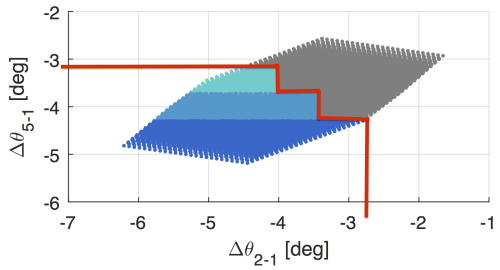

Figure 3. Illustrative example of non-convex space.

$$y_p \cdot \underline{\theta_{ij,p}} - (1-y_p)\cdot\overline{\theta_{ij}} \le \theta_{ij} \le y_p \cdot \overline{\theta_{ij,p}} + (1-y_p)\cdot\overline{\theta_{ij}}, \quad \forall (i,j)\in\mathcal{L}, \forall p \in \mathcal{P}. \quad (6)$$

$\mathcal{L}$ and $\mathcal{P}$ denote the set of lines and DT branches/paths, respectively. Only one DT branch, i.e. one set of minimum and maximum bounds on angle differences, can be chosen, which is imposed by adding constraint $\sum_{p\in\mathcal{P}} y_p = 1$.

The data-driven SC-OPF is thus formulated as a Mixed-Integer Non-linear Program (MINLP), which is a NP-hard problem. One of the main contributions of this paper is that we relax the non-convex AC power flow equations using a Second Order Cone relaxation and obtain a SC-OPF formulated as a Mixed-Integer Second Order Cone Program (MISOCP), which is a convex mixed-integer program that can be solved efficiently by already existing solvers.

D. Relaxing the Data-driven SC-OPF

The SOC formulation of the OPF problem is based on [13], [14] and [9]. New variables are introduced to capture the nonlinearities and non-convexities of the AC power flow equations: (a) $u_i := V_i^2$, (b) $c_{ij} := V_i V_j \cos(\theta_{ij})$ and (c) $s_{ij} := -V_i V_j \sin(\theta_{ij})$. The AC-OPF is transformed from the space of $\mathbf{x} := \{\mathbf{P^G}, \mathbf{Q^G}, \mathbf{V}, \theta\}$ variables to the space of $\mathbf{x_{SOC}} := \{\mathbf{P^G}, \mathbf{Q^G}, \mathbf{u}, \mathbf{c}, \mathbf{s}\}$ variables and is given by:

$$\min_{\mathbf{x_{SOC}}} \sum_{i=1}^{N_G} C_i\left(P_i^G\right) \quad (7)$$

$$\text{s.t. } P_i^G - P_i^D = G_{ii}u_i + \sum_{j=1, j\neq i}^{N_B}\left(G_{ij}c_{ij} - B_{ij}s_{ij}\right), \quad \forall i \in \mathcal{N} \quad (8)$$

$$Q_i^G - Q_i^D = -B_{ii}u_i - \sum_{j=1, j\neq i}^{N_B}\left(G_{ij}s_{ij} + B_{ij}c_{ij}\right), \quad \forall i \in \mathcal{N} \quad (9)$$

$$c_{ij} = c_{ji}, \quad s_{ij} = -s_{ji}, \quad \forall (i,j)\in\mathcal{L} \quad (10)$$

$$c_{ij}^2 + s_{ij}^2 = u_i u_j, \quad \forall (i,j)\in\mathcal{L} \quad (11)$$

$$\underline{V_i}^2 \le u_i \le \overline{V_i}^2, \quad \forall i \in \mathcal{N}. \quad (12)$$

Active and reactive power generation are constrained by their usual limits and are not explicitly mentioned. The non-convex quadratic equality constraint (11) is relaxed through a second-order cone constraint: $c_{ij}^2 + s_{ij}^2 \le u_i u_j$. The SOC formulation of the OPF problem (7)-(12) is exact for radial networks and the optimal voltage angles can be recovered by solving:

$$\theta_i - \theta_j = \text{atan2}(s_{ji}^*, c_{ij}^*), \quad \forall (i,j)\in\mathcal{L}, \quad (13)$$

where * indicates the optimal solution obtained from the SOC-OPF. For meshed networks the above formulation is a strict relaxation, potentially resulting in solutions, which are infeasible for the original AC-OPF [9]. Reintroducing voltage angle variables and constraint (13) in problem (7)-(12) would render the SOC formulation exact for meshed networks, but also non-convex. Various convex approximations of constraint (13) have been proposed [9], [13]. In this paper we use a sequential conic procedure as proposed in [13], where the arctan function is linearized using a Taylor series expansion.

Conditional bounds on voltage angles are introduced using binary variables as described in Section II-C. Known limits on angle differences can also be used to define bounds on the SOC variables $\mathbf{c}$ and $\mathbf{s}$:

$$y_p \cdot \tan(\underline{\theta_{ij,p}}) \cdot c_{ij} - (1-y_p)\cdot\tan(\overline{\theta_{ij}})\cdot c_{ij} \le s_{ji}, \quad \forall (i,j)\in\mathcal{L}, \forall p \in \mathcal{P}, \quad (14)$$

$$y_p \cdot \tan(\overline{\theta_{ij,p}}) \cdot c_{ij} + (1-y_p)\cdot\tan(\overline{\theta_{ij}})\cdot c_{ij} \ge s_{ji}, \quad \forall (i,j)\in\mathcal{L}, \forall p \in \mathcal{P}. \quad (15)$$

Otherwise, the SOC variables c_{ij} and s_{ij} are only constrained by their implied upper and lower bounds $\pm\overline{V_i V_j}$, which in practice can be very loose. In order to tighten the relaxation, we determine the values for c_{ij} and s_{ij} along all lines (i,j) for each operating point in the generated database and extract their minimum and maximum values to obtain tighter variable bounds.

III. Case Study

We evaluate the performance of the proposed data-driven SC-OPF ensuring small-signal stability and N-1 security on a modified version of the IEEE 14 bus test system [15]. Our case study consists of three parts. First, we compare the convex MISOCP formulation of the algorithm to a data-driven MINLP implementation and a standard (i.e., not data-driven) preventive SC-OPF. Its low computational effort makes the proposed MISOCP suitable for AC based market-clearing auctions as envisaged in the US. In Europe, however, electricity markets will probably continue to rely on DC approximations. To this end, we show how the proposed method can also be used by TSOs for optimizing redispatching actions in order to ensure N-1 security and small-signal stability after the market-clearing. Finally, we analyze how the data-driven approach coupled with MIP notably extends the feasible space of the OPF.

The network data is given in [16] with some modifications introduced in [2]. Note that additionally the voltage setpoints of generators 4 and 5 are changed to 1.02 p.u. and 1.01 p.u., respectively, and the reactive power of generator 1 is limited within ± 990 Mvar. The considered contingencies include all line and bus faults, except for faults at buses 1,

2 and 6. These would lead to either instability/AVR limit violations or operating points, which are unstable for the remaining contingencies. Note that the standard PSC-OPF does not incorporate stability considerations, but only extends the constraint set to account for the defined N-1 contingencies. Bus 1 with generator g_1 has been chosen as the slack bus for the base case and all N-1 cases. A step size of 0.5 MW was chosen for discretizing the possible operating range and generating the database of operating points used for deriving the decision tree. See [2] for a comparison of test cases with different discretization intervals. The minimum damping ratio of an operating point over the base case and all N-1 cases is used as a metric for small-signal stability. As usual in power system operation, we define a security margin by requiring a minimum damping ratio of 3%. The derived DT contains 136 leaf nodes, out of which 74 point to operating regions, which are small-signal stable for the base case and all considered contingencies. Thus, 74 binary variables are used to define conditional constraints on voltage angle differences along lines and incorporate the stable regions in the data-driven SC-OPF. Note that 1.34 million operating points have been evaluated for this case study, from which more than 88 000 fulfill the required minimum damping ratio. We derive the DT based on three different load levels (base case, $\pm 20\%$). The data-driven SC-OPF was performed for all three levels seperately. Given that they showed very similar results, we present our results for the base case only. The voltage magnitude at generator buses is set to the corresponding generator voltage setpoint in order to ensure an appropriate voltage profile, which is fundamental to a secure system operation.

The small-signal analysis was performed using Matlab and Matpower 6.0 [16]. The MISOCP was implemented in Python using the Gurobi Optimizer. The standard PSC-OPF (i.e., NLP) and the MINLP implementation of the data-driven SC-OPF were carried out in GAMS. BONMIN and COUENNE were used for solving the MINLPs, while CONOPT was used for the NLP.

A. Comparison of Preventive and Data-driven SC-OPFs

Table I lists the results of all three SC-OPF implementations. It can be observed that all implementations based on decision trees result in operating points, which exhibit minimum damping ratios that are non-negative and are thus stable for the base case and all considered N-1 contingencies. The solution of the standard PSC-OPF however is unstable for a fault at bus 5 and line 1-2, respectively. Thus, the identified preventive control actions do not fullfill the system's security requirements and would call for redispatching measures. As the PSC-OPF results in an operating point, which does not reflect the small-signal stability requirements, its total cost is lower than the other solutions. All three data-driven implementations result in different leaf nodes of the DT and thus in different regions of the feasible space with various degrees of conservatism. Higher damping ratios are also reflected by higher costs. All solutions include a stability margin, but only the most conservative result achieves a minimum damping ratio of more than 3%. This can

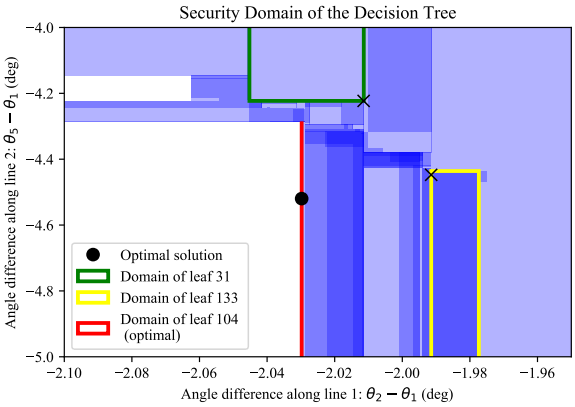

Figure 4. Non-convex security domain of the DT as a function of the angle differences along lines 1 and 2. The blue shaded areas represent the stable regions defined by all DT branches. The darker the color, the more domains of different DT branches overlap. Note that the actual security domains covered by the different leaf nodes do not overlap and might even be disjoint, which however cannot be depicted by only two dimensions.

be explained by the fact that (a) the OPF is not limited to the specified discretization intervals of 0.5 MW, as used for the database generation and (b) DTs are not 100% accurate leading to missclassifications. For cases, where the minimum damping ratio is a hard constraint, higher values can be required when deriving the DT in order to avoid violations. Fig. 4 illustrates the stable domain covered by all DT leaf nodes as a function of the angle differences along lines 1 and 2. The rectangles indicate the domains covered by the three different leaf nodes obtained from the data-driven SC-OPF implementations with the location of the corresponding solution pointed out. It can be seen that the stable domain is non-convex and that safer operating points exhibiting higher damping ratios are located further away from the stability boundary.

The known scalability issues of COUENNE [10], which is a global optimization solver, lead to significantly higher execution times compared to BONMIN, which employs heurisitic methods for non-convex MINLPs. Also, the default settings for both solvers include a relative tolerance gap of 10% terminating the computation as soon as a solution is found, which lies within 10% of the true objective value. This explains the choice of different leaf nodes. However, even reducing the tolerance value does not change the outcome indicating that neither of the solvers is able to provide the best integer solution. The MISOCP is able to find the optimal integer solution, which has been verified by manually imposing the bounds defined by each DT branch. Specifically, we solved 74 AC-OPFs consecutively, one for each DT branch and imposed the corresponding bounds in order to determine the DT branch, which contains the least-cost, optimal NLP solution. Leaf node 104 actually contains the bounds, which result in the least-cost NLP solution. Notably, in this test case, the MISOCP relaxation is exact, i.e. its solution is feasible to the nonlinear, non-convex AC-OPF formulation and corresponds to the global optimum of the non-convex problem.

TABLE I
RESULTS OF STANDARD PSC-OPF AND DATA-DRIVEN SC-OPF IMPLEMENTED AS MINLP AND MISOCP.

		Standard PSC-OPF	**Data-driven SC-OPF**		
		NLP	**MINLP**		**MISOCP**
			COUENNE	BONMIN	
Cost	(€/h)	3022.83	3445.09	3381.21	3365.95
Runtime	(s)	10.06	1000.16	96.16	5.58
Iterations*	(-)	-	-	-	4
Min. damping ratio	(%)	unstable	3.27	2.97	2.53
Leaf node	(-)	-	31	133	104

* The number of iterations refers to the sequential conic algorithm used to approximate constraint (13) with a chosen convergence tolerance of 10^{-6}.

Nonetheless, given that the MISOCP formulation is still a relaxation, identified solutions can be infeasible for the original problem. Therefore, we propose to use the MISOCP primarily to identify the optimal DT branch and hence the linear bounds on the feasible space, such that the optimal solution is included. Once these are known and the feasible space has been reduced, the integer variables can be omitted and a common AC-OPF (i.e., NLP) with the previously identified bounds on angle differences imposed as linear constraints can be performed to identify feasible and secure preventive control actions. The MISOCP solution serves as a lower bound and can validate the optimality of the AC-OPF solution.

Table I also outlines the savings in online computation time of the proposed SC-OPF method. The data-driven approach outperforms the usual PSC-OPF by more than 40%, while at the same time incorporating more security requirements. Naturally, the computation time depends on the size of the DT and the number of binary variables used to represent it. Even though introducing binaries increases the OPF complexity, this side effect is offset by a significantly reduced overall size of the SC-OPF. While the PSC-OPF increases 32-fold when considering 31 contingencies, the proposed data-driven approach increases less than 4-fold for the same amount of contingencies. As indicated by constraint (6), $(2 \times N_L \times N_P + 1)$ additional linear inequality constraints are added, where N_L and N_P denote the number of network lines and DT paths, respectively. Hence, the complexity of the resulting MISOCP is primarily determined by the N_L SOC constraints $c_{ij}^2 + s_{ij}^2 \leq u_i u_j$ and the N_P binary variables.

Furthermore, given that the problem is a convex MIP, which can be solved efficiently by already existing solvers that are able to handle up to a few thousand binaries, the amount of discrete variables is not expected to be an obstacle. While solvers for MISOCPs have not yet reached the maturity of MILP solvers, recent work has demonstrated how general convex MIPs can be solved to global optimality by a sequence of MILPs using polyhedral outer approximations and continuous convex programs [17]. Large-scale instances of a similar type of problem class with up to 3000 binary variables and quadratic constraints have successfully been solved in [18] using state-of-the-art solvers and employing heuristic methods. The size of the DT is directly determined by the size of the dataset, which it is derived from. Hence, a more efficient method to generate the database of operating points, appropriate pruning of the DT and techniques to decompose the data-driven optimization are aspects that require a deeper analysis and are promising approaches to enhance the scalability performance of the method. One approach already used in the industry would be to focus only on the most critical N-1 contingencies and angle differences.

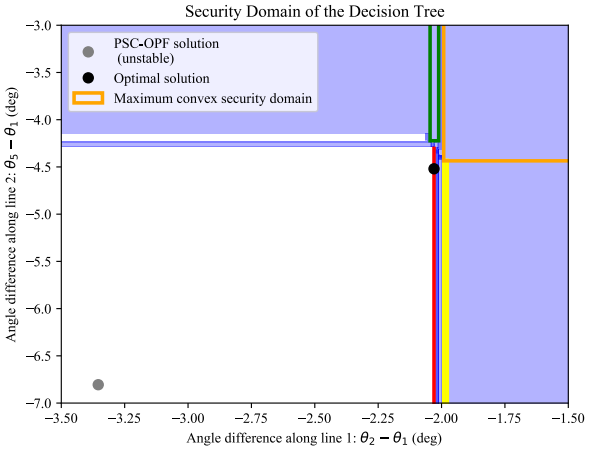

Figure 5. Visualization of redispatch and maximum convex security domain, which can be covered by one leaf node only.

B. Optimizing Redispatch

The method can be used by TSOs to identify optimal redispatching actions, where for example the market-based day-ahead dispatch, if identified as unstable, is redirected through the DT to a secure domain. We have reformulated the MISOCP in order to optimize redispatching actions, assuming that the costs of generator up- and down-regulation correspond to its marginal cost. Generators are assumed to be paid for up-regulation and charged for savings resulting from down-regulation. We have used the unstable solution of the standard PSC-OPF listed in Table I as an input to the redispatch and successfully shifted the operating point to leaf node 104. The cost of redispatch amounts to 343.12€, which corresponds to the original difference in objective values between the PSC-OPF and MISOCP. The MISOCP, if implemented at the market stage, could result in more than 10% cost savings for the system operator and better reflects the locational impact of stability requirements.

C. Enlarging the Feasible Space

The generated database contains 1.34 million operating points, out of which 6.57% fulfill the 3% minimum damping

ratio and define the feasible space of operation. We have evaluated how much of the entire stable region is covered by each individual leaf node, i.e. how many operating points fulfill the constraints imposed by the corresponding DT branch. All leaf nodes cover in total 99.91% of the considered stability region, where leaf node 7 accounts for most of it, capturing 77.78% of the entire feasible space. The implied bounds of leaf node 7 are depicted in Fig. 5. If we had considered the stability requirements in the OPF only by imposing bounds, which define a convex space, as it is currently done in practice, we would have been able to capture at most 77.78% of the feasible space, thereby also missing the optimal solution as can be seen in Fig. 5. Thus, our approach to incorporate the information provided by the database in the optimization problem through binary variables allows us to enlarge the feasible space by more than 28%, enclosing the remaining 22.13%, which are covered by the DT.

IV. Conclusion and Future Work

In this paper we propose a data-driven approach to preventive SC-OPF, which ensures N-1 security and small-signal stability and uses decision trees to capture the non-convex and possibly disjoint space of stable operating points. We propose a new approach to translate data, which operators usually already have available from dynamic simulations, and include them in a simple way in an optimization framework. Binary variables are used to represent the knowledge extracted from the data giving rise to two levels of non-convexities: one that refers to the integrality of the binary variables and another one that concerns the AC power flow equations. We eliminate the latter using a SOC relaxation and obtain a convex MISOCP. MISOCPs generalize convex mixed-integer quadratic programs, for which solvers have already reached a high level of maturity. The proposed method reduces the overall problem size by avoiding to explicitly include all considered contingencies and incorporates stability requirements, both of which have been major challenges in SC-OPFs. Finally, we have shown that by using data coupled with MIP in (SC-)OPFs we can enlarge the feasible space represented in the OPF by more than 28%.

The relaxed data-driven SC-OPF can be used to determine the optimal bounds (i.e., the optimal DT branch) on the feasible space, such that secure preventive control actions are ensured. Considering that the DT represents a non-convex operating space, identified preventive actions can be less conservative than those determined by current approaches. The need for iterative contingency analyses to identify suitable control actions is alleviated. The MISOCP formulation of the SC-OPF can be used by market operators as a market-clearing tool due to its low online computational effort but also by TSOs to determine optimal redispatching actions and the bounds on angle differences, which allow accommodating the redispatch.

In future work, we are planning to: (a) include uncertainties and corrective control policies for relaxed OPFs, which we developed in [19], (b) exploit the decomposable structure of the MISOCP to separate discrete and continuous variables and apply decomposition techniques with convergence guarantees resulting from the convex problem properties, (c) improve the database generation and determination of the stability boundary, which directly determines the DT size and (d) apply the method to larger systems.

References

[1] F. Capitanescu, J. M. Ramos, P. Panciatici, D. Kirschen, A. M. Marcolini, L. Platbrood, and L. Wehenkel, "State-of-the-art, challenges, and future trends in security constrained optimal power flow," *Electric Power Systems Research*, vol. 81, no. 8, pp. 1731 – 1741, 2011.

[2] F. Thams, L. Halilbašić, P. Pinson, S. Chatzivasileiadis, and R. Eriksson, "Data-Driven Security-Constrained OPF," *10th IREP Symposium - Bulk Power Systems Dynamics and Control*, 2017.

[3] R. Zárate-Miñano, F. Milano, and A. J. Conejo, "An OPF Methodology to Ensure Small-Signal Stability," *IEEE Transactions on Power Systems*, vol. 26, no. 3, pp. 1050–1061, 2011.

[4] J. E. Condren and T. W. Gedra, "Expected-Security-Cost Optimal Power Flow With Small-Signal Stability Constraints," *IEEE Transactions on Power Systems*, vol. 21, no. 4, pp. 1736–1743, 2006.

[5] M. Chávez-Lugo, C. R. Fuerte-Esquivel, C. A. Canizares, and V. J. Gutierrez-Martinez, "Practical Security Boundary-Constrained DC Optimal Power Flow for Electricity Markets," *IEEE Transactions on Power Systems*, vol. 31, no. 5, pp. 3358–3368, Sept 2016.

[6] M. B. Cain, R. P. O'Neill, and A. Castillo, "History of Optimal Power Flow and Formulations - Optimal Power Flow Paper 1," 2012. [Online]. Available: https://www.ferc.gov/industries/electric/indus-act/market-planning/opf-papers/acopf-1-history-formulation-testing.pdf

[7] FERC Joint Boards on Security Constrained Economic Dispatch, "Study and Recommendations Regarding Security Constrained Economic Dispatch (SCED) in the Northeast by the Joint Board on Economic Dispatch for the Northeast Region," 2006. [Online]. Available: https://www.ferc.gov/industries/electric/indus-act/joint-boards/south-recom.pdf

[8] FERC Staff, "Recent ISO Software Enhancements and Future Modeling Plans," 2011. [Online]. Available: https://www.ferc.gov/industries/electric/indus-act/rto/rto-iso-soft-2011.pdf

[9] B. Kocuk, S. S. Dey, and X. Sun, "New Formulation and Strong MISOCP Relaxations for AC Optimal Transmission Switching Problem," *IEEE Transactions on Power Systems*, 2017, (in press).

[10] H. Hijazi, C. Coffrin, and P. V. Hentenryck, "Convex Quadratic Relaxations for Mixed-Integer Nonlinear Programs in Power Systems," NICTA, Tech. Rep., 2013.

[11] ENTSO-E, "Principles for Determining the Transfer Capacities in the Nordic Power Market," 2017.

[12] KU Leuven Energy Institute, "EI Fact Sheet: Cross-border Electrcity Trading: Towards Flow-based Market Coupling," 2015. [Online]. Available: http://set.kuleuven.be/ei/factsheets

[13] R. A. Jabr, "A Conic Quadratic Format for the Load Flow Equations of Meshed Networks," *IEEE Transactions on Power Systems*, vol. 22, no. 4, pp. 2285–2286, Nov 2007.

[14] A. G. Esposito and E. R. Ramos, "Reliable Load Flow Technique for Radial Distribution Networks," *IEEE Transactions on Power Systems*, vol. 14, no. 3, pp. 1063–1069, Aug 1999.

[15] S. Kodsi and C. Canizares, "Modeling and Simulation of IEEE 14-Bus System with FACTS Controllers," University of Waterloo, Waterloo, Canada, Tech. Rep., 2003.

[16] R. D. Zimmerman, C. E. Murillo-Sanchez, and R. J. Thomas, "MATPOWER: Steady-State Operations, Planning, and Analysis Tools for Power Systems Research and Education," *IEEE Transactions on Power Systems*, vol. 26, no. 1, pp. 12–19, Feb 2011.

[17] M. Lubin, E. Yamangil, R. Bent, and J. P. Vielma, "Polyhedral approximation in mixed-integer convex optimization," *ArXiv e-prints*, Jul. 2016.

[18] A. Bley, A. M. Gleixner, T. Koch, and S. Vigerske, "Comparing MIQCP Solvers to a Specialised Algorithm for Mine Production Scheduling," in *Modeling, Simulation and Optimization of Complex Processes*. Berlin, Heidelberg: Springer Berlin Heidelberg, 2012, pp. 25–39.

[19] A. Venzke, L. Halilbasic, U. Markovic, G. Hug, and S. Chatzivasileiadis, "Convex Relaxations of Chance Constrained AC Optimal Power Flow," *IEEE Transactions on Power Systems*, 2017, (in press).

Department of Electrical Engineering
Center for Electric Power and Energy (CEE)
Technical University of Denmark
Elektrovej, Building 325
DK-2800 Kgs. Lyngby
Denmark

www.elektro.dtu.dk/cee
Tel: (+45) 45 25 35 00
Fax: (+45) 45 88 61 11
E-mail: cee@elektro.dtu.dk